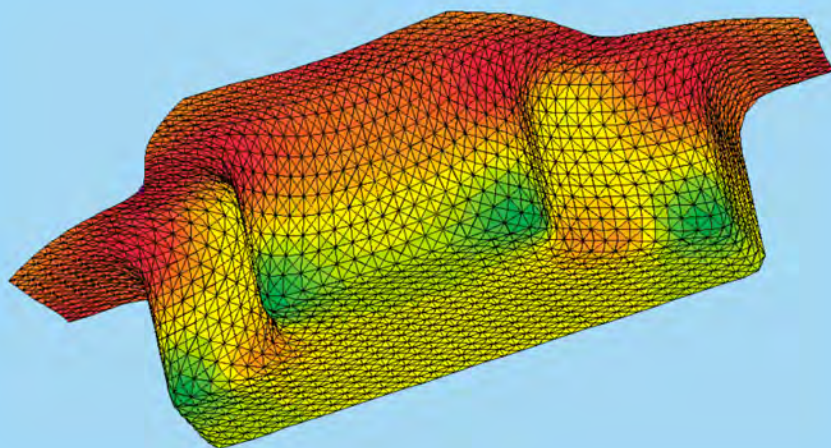


INSTITUTE OF FUNDAMENTAL TECHNOLOGICAL RESEARCH
POLISH ACADEMY OF SCIENCES

39th SOLID MECHANICS CONFERENCE
BOOK OF ABSTRACTS

Z.L. Kowalewski (Editor)



Zakopane, Poland
September 1–5, 2014

39th Solid Mechanics Conference
Book of Abstracts

ACKNOWLEDGMENTS FOR SUPPORT TO

PLATINUM SPONSORS

Spectro-Lab
Laboratoria Przyszłości



INSTRON

elhys **MTS**

SILVER SPONSOR

NANOVEA

A Better Measure.

OTHER SPONSORS



Politechnika Krakowska
im. Tadeusza Kościuszki

NATIONAL
INSTRUMENTS

BIURO
INŻYNIERSKIE
MACIEJ
ZAJACZKOWSKI

WYŁĄCZNY
PRZEDSTAWICIEL
FIRMY HBM NA
TERYTORIUM POLSKI
HBM
AUTORYZOWANY KONTAKT: 011 41 41 41

INSTITUTE OF FUNDAMENTAL TECHNOLOGICAL RESEARCH
P O L I S H A C A D E M Y O F S C I E N C E S

39th Solid Mechanics Conference

Book of Abstracts

Editor:

Zbigniew L. Kowalewski

Coeditors:

Zbigniew Ranachowski

Jacek Widłaszewski

WARSZAWA – ZAKOPANE

2014

© Copyright by Institute of Fundamental Technological Research PAN
Warszawa 2014

ISBN 978-83-89687-89-0

The selection and presentation of material and the opinion expressed in this publication are the sole responsibility of the authors concerned.

No responsibility is assumed by the Publishers for any injury and/or damage to persons or property as a matter of products liability, negligence or otherwise, or from any use or operation of any method, products, instructions or ideas contained in the material herein.

Technical editor: Joanna Żychowicz-Pokulniewicz

Produced by:



Institute of Fundamental Technological Research PAN
02-106 Warszawa, ul. Pawińskiego 5B
www.ippt.pan.pl



Drukarnia Braci Grodzickich Sp.J.
05-500 Piaseczno, ul. Geodetów 47A
www.dbg.com.pl



39th Solid Mechanics Conference
Zakopane, Poland, September 1–5, 2014



Preface

There is a long tradition to organize Solid Mechanics Conferences in different locations of Poland to cover all areas of active research in mechanics of materials and structures including interactive fields.

Initially the series of Polish Solid Mechanics Conferences have been organized by the Institute of Fundamental Technological Research of the Polish Academy of Sciences since 1953, when the first conference was held in Karpacz, located on the south of Poland. At the beginning, these conferences had mainly national character and concentrated mostly on problems of elasticity, plasticity and structural mechanics. Later on, they became international conferences with considerable participation of scientists from Poland as well as from foreign countries and with much wider scope covering most important and actual aspects of solid mechanics.

The aim of this conference has been thought to serve as a place for scientific discussion of the research community working in different areas of contemporary mechanics of solids and structures.

This volume contains extended abstracts of papers accepted for presentation at the 39th Solid Mechanics Conference, Zakopane, 1–5 September, 2014. The program of the Conference includes 8 plenary lectures, 11 keynote sectional lectures, 2 special lectures, 4 sponsors lectures and contributed presentations which can be roughly classified into the following specific topics.

- Computational Aspects of Mechanics of Solids – 12 papers
- Continuum Mechanics, Elasticity and Plasticity – 17 papers
- Dynamics of Solids and Structures – 6 papers
- Experimental Mechanics – 16 papers
- Fracture, Damage and Fatigue of Materials – 10 papers
- Geomechanics – 7 papers
- Mechanics of Composites, Porous Media – 8 papers
- Micromechanics, Interfaces and Multi-Scale Modelling – 4 papers
- Plates and Shells – 18 papers
- Smart Materials and Structures – 10 papers
- Structural Mechanics, Optimization and Reliability Analysis – 6 papers
- Poster Session – 18 papers

The Solid Mechanics Conferences have maintained for 61 years high scientific standard and served as a forum for exchange of new ideas and research information. A great number of participants either from Poland or foreign countries delivered here lectures many times and certainly remember the period when they first time came as young beginning researchers, now presenting general or key-note lectures as eminent scientists. It is our pleasure to see again old friends to whom we shared our ideas and enthusiasm for mechanics. It is also a great pleasure to meet here young generation of researchers working in new fields and contributing new important results.

We wish all participants a fruitful and enjoyable conference time in beautiful Zakopane and look forward with confidence to SOLMECH 2014 in the hope that it will break new ground in our chosen area of interest and to be of great benefit to all those who participate.

On behalf of the organizers, we would like to express our gratitude to the students and scientists who attended this conference.

Finally, it is my great pleasure to express my cordial thanks to all members of the Scientific Committee, to all members of the Local Organizing Committee, to all supporting institutions (all names enclosed separately), and to the Global Wings – official Conference Partner – for their help which cannot be overestimated.

Warsaw, July 31, 2014

Chairman
of the 39th Solid Mechanics Conference

Zbigniew L. Kowalewski

Organizers

The 39th Solid Mechanics Conferences is organized by the Institute of Fundamental Technological Research under the auspices of Committee on Mechanics, both of the Polish Academy of Sciences.

Scientific Committee

Badur J.	Kowalczyk P.	Pietraszkiewicz W.
Basista M.	Kowalewski Z.	Pietrzyk M.
Borkowski A.	Kubik J.	Rojek J.
Burczyński T.	Łodygowski T.	Skoczeń B.
Dłużewski P.	Mróz Z.	Stupkiewicz S.
Gutkowski W.	Nowicki A.	Szefer G.
Holnicki-Szulc J.	Perzyna P.	Tejchman J.
Kleiber M.	Petryk H.	Tylikowski A.
Kosiński W.	Pęcherski R.	Wiśniewski K.
Kotulski Z.	Pieczyska E.	

Organizing Committee

Zbigniew Kowalewski – Chairman of the Conference
Zbigniew Ranachowski – Scientific Secretary
Paweł Grzywna Agnieszka Rutecka
Dominik Kukla Jacek Widłaszewski
Tomasz Libura Joanna Żychowicz-Pokulniewicz
Urszula Czubacka – Secretary

Thematic Sessions and Their Organizers

Computational Aspects of Solid Mechanics:

J. Eberhardsteiner (Austria) & T. Burczyński (Poland)

Continuum Mechanics, Elasticity and Plasticity

(Special Session in Memory of Prof. Piotr Perzyna):

H. Altenbach (Germany), B. Skoczeń (Poland) & R. Pęcherski (Poland)

Dynamics of Solids and Structures:

R. Iwankiewicz (Germany) & Z. Kotulski (Poland)

Experimental Mechanics

(Special Session in Memory of Prof. Wojciech Szczepiński):

N.K. Gupta (India) & A. Rusinek (France)

Fracture, Damage and Fatigue of Materials:

D.R. Hayhurst (UK) & Z. Nowak (Poland)

Geomechanics:

Z. Mróz (Poland), S. Pietruszczak (Canada) & J. Tejchman (Poland)

Mechanics of Composites, Porous Media:

P. Kowalczyk (Poland) & J. Rojek (Poland)

Micromechanics, Interfaces and Multi-Scale Modelling:

S.A. Meguid (Canada) & H. Petryk (Poland)

Plates and Shells:

W. Pietraszkiewicz (Poland) & K. Wiśniewski (Poland)

Smart Materials and Structures:

H. Tobushi (Japan) & E. Pieczyska (Poland)

Structural Mechanics, Optimization and Reliability Analysis:

J. Holnicki-Szulc (Poland) & T. Szolc (Poland)

Contents

Preface	5
-------------------	---

Plenary Lectures

H. Altenbach, V. A. Eremeyev – <i>Mechanics of Nanostructures</i>	17
J. Füssl, M. Lukacevic, G. Kandler, J. Eberhardsteiner – <i>Mechanical Behavior of Wood – a Bridge from Microstructure to Structural Applications by Means of Computational Methods</i>	19
N. K. Gupta – <i>Plasto-Mechanics of Large Deformation Under Impact Loading</i>	21
S. A. Meguid – <i>Multiscale Modeling of Multifunctional Aerospace Nanocomposites: Challenges and Oportunities</i>	23
K. Nalepka, R. B. Pęcherski – <i>Plastic Flow and Failure of Solids. Modelling across Scales</i>	25
K. Wiśniewski, E. Turska – <i>Recent Improvements in Mixed/Enhanced Shell Elements with Drilling Rotation</i>	27
R. Zaera, J.A. Rodríguez-Martínez, G. Vadillo, J. Fernández-Sáez, D. Rittel, A. Rusinek, R. Pesci, S. Osovski, T. Cohen – <i>Deformation of Dynamically Phase Transforming Metals in Adiabatic Conditions: Thermal Effects and Instabilities</i>	29

Computational Aspects of Solid Mechanics

D. Dębski, P. Źach – <i>Review of Hyperelastic Material Use in Damper at Sub-Zero Temperatures</i>	33
P. Dłużewski, M. Maździarz, P. Tazowski – <i>Third-Order Elastic Coefficients and Logarithmic Strain in Finite Element Modelling of Anisotropic Elasticity</i>	35
A. Gialos, V. Zeimpekis, N.D. Alexopoulos, S. Riekehr, N. Kashaev – <i>Integrated Laser Beam Welded Structures for Aircraft Applications: Manufacturing, Weight Saving and Testing Aspects</i>	37
G. Hénap, L. Szabó – <i>Analytical Solution of an Elastic-Plastic Wedge Subjected to Uniform Shear on its Face</i>	39
P. Landkammer, P. Steinmann – <i>On Recursive Strategies for Inverse Form Finding in Metal Forming Applications</i>	41
J. Lengiewicz, P. Sadowski, S. Stupkiewicz – <i>Finite Element Modelling of Elastohydrodynamic Lubrication in the Finite Deformation Regime</i>	43
D. Lumelskyy, J. Rojek, R. Pęcherski, F. Grosman, M. Tkocz – <i>Numerical Investigation of Influence of Friction on Strain Distribution and Forming Limit Curve in Nakazima Formability Test</i>	45
Z. Nowak, F. Grosman, D. Lumelskyy, M. Nowak, R.B. Pęcherski, J. Rojek, M. Tkocz – <i>Metal Cup Deep Drawing Processes – Numerical Simulation and Experimental Verification</i>	47

M. Romanowicz – <i>Region of Higher Misalignment in Carbon Fiber Reinforced Polymers as an Initiator for Kink Band Formation</i>	49
H. Šimonová, D. Lehký, Z. Keršner, V. Veselý, J. Macur – <i>Relationships between Mechanical Fracture and Durability Parameters of Selected Concretes</i>	51
J. Tabin, B. Skoczeń – <i>Slip Bands Evolution During Discontinuous Plastic Flow in 304 Austenitic Stainless Steels at Liquid Helium Temperature (4.2 K)</i>	53
Z. Więckowski, E. Misztalska – <i>Stress-Based Finite Element Method for Nearly Incompressible and Incompressible Materials</i>	55

Continuum Mechanics, Elasticity and Plasticity

Professor Piotr Perzyna – In Memoriam	59
A. Bajkowski, R. Kulchytsky-Zyhailo – <i>Effect of Interlayer on Stresses in Coating under Normal and Tangential Loading</i>	63
M. Chudzicka-Adamczak, T. J. Hoffmann – <i>Dilatational and Non-Dilatational Strain in Coaxial Cable</i>	65
H. Egner, W. Egner, P. Sulich – <i>Effect of Temperature Rate in Modeling Nonisothermal Low Cycle Fatigue of Steel</i>	67
H. Egner, M. Ryś – <i>Effect of Phase Transformation Rate on the Response of Elastic-Plastic Two-Phase Material Subjected to Cyclic Loading at Cryogenic Temperatures</i>	69
H. Egner, M. Ryś – <i>On the Thermodynamic Modeling of Coupling between Plasticity, Damage and Phase Transformation</i>	71
A. Ganczarski, M. Adamski – <i>Tertragonal or Hexagonal Symmetry of Failure Tsai-Wu Criterion for Transversely Isotropic Materials</i>	73
M. Karyakin, I. Pozdnyakov, N. Shubchinskaya – <i>The Equilibrium and Stability of the Nonlinearly Elastic Cylinder with Internal Stresses under Tension and Inflation</i>	75
W. Kosiński, W. Oliferuk, K. Kochanowski, A. Adamowicz – <i>Inverse Problem for Heat Conduction Equation in IR Thermography</i>	77
D.R. McArthur, L.J. Sudak – <i>Arbitrary Piezoelectric Inclusion with Weakly and Highly Conducting Imperfect Interface</i>	79
A. Młeczek, P. Kłosowski – <i>Identification of Parameters of Bodner-Partom Viscoplastic Model for Aluminum Alloy at Elevated Temperature</i>	81
V. Nežerka, J. Antoš, P. Tesárek, J. Zeman – <i>Two-Scale Modeling Approach for Prediction of Masonry Column Failure</i>	83
R. Ortwein, B. Skoczeń – <i>Skakedown Mechanism in Round Rods Subjected to Cyclic Torsion at Cryogenic Temperatures</i>	85
B. Skoczeń – <i>Plastic Strain and Radiation Induced Phenomena Between Absolute Zero and Room Temperature</i>	87
M. Somr, P. Kabele – <i>Magma Flow Caused by Inverted Density Stratification</i>	89
W. Sumelka, J. Fernández-Sáez, R. Zaera – <i>Small-Scale Effect in the Framework of Fractional and Eringen Non-Local Models</i>	91
A. Uscilowska, M. Kulczynska – <i>An Elastic-Plastic Torsion of a Profile – Comparison of Meshless Methods Implementations</i>	93

B. Wcisło, J. Pamin – <i>Thermomechanical Modeling of Elastic-Plastic Materials Undergoing Large Deformations</i>	97
--	----

Dynamics of Solids and Structures

L. Domagalski, J. Jędrysiak – <i>Large Amplitude Forced Vibrations of Micro-Periodic Slender Beams</i>	101
A. Goodarzi, H. M. Shodja, B. Hashemian – <i>Dynamic Stress Concentration Factor Around an Embedded Nano-Cavity in the Context of Couple Stress Theory</i>	103
S. Kokot, Z. Zembaty, P. Bobra – <i>Application of Rotation Rate Sensors to Improve Structural Health Monitoring of Beams in Flexure</i>	105
D. Pisarski – <i>On Real-Time Distributed Adaptation of Structures Subjected to Travelling Loads</i>	107
A. Vaz-Romero, J. A. Rodríguez-Martínez, A. Arias – <i>Interplay Between Stress Waves Propagation and Flow Localization in the Dynamic Tensile Test: Application to Steel Sheets</i>	109
R. Wiszowaty, G. Mikułowski, K. Sekuła, J. Biczuk – <i>Application of Piezoelectric Actuators for the Gas Valve Opening Control</i>	111

Experimental Mechanics

Professor Wojciech Szczepiński – <i>In Memoriam</i>	115
N.D. Alexopoulos, S.K. Kourkoulis, P. Poulin – <i>Sensing of Cement Mortar with Embedded Polyvinyl Alcohol–Carbon Nanotube Fiber</i>	117
B. Augustyniak, M. Chmielewski, L. Piotrowski, P. Maciakowski – <i>Stress Evaluation in Steel Elements with Novel Barkhausen Effect Meter</i>	119
G. Hloupis, I. Stavrakas, I. Dakanali, A. Kyriazopoulos, D. Triantis – <i>Natural Time Analysis of Acoustic Emissions when Cement Mortar Specimens are Subjected to Three Point Bending Loading</i>	121
J. Janiszewski – <i>Methodological Remarks on Conducting High-Strain Rate Testing with the Use of SHPB Technique</i>	123
S.K. Kourkoulis, E.D. Pasiou, I. Stavrakas, G. Hloupis, D. Triantis, K. Moutzouris – <i>An Experimental Study of the Mechanical Response of a Typical Epistyles' Connection Under Pure Shear</i>	125
L. Kruszka, W. Moćko, E. Cadoni, L. Fenu – <i>Effect of Fibre Content on Static and Dynamic Properties of Fibre Reinforced Concrete</i>	127
P. Lymperta, S.K. Kourkoulis, P. Poulin, N.D. Alexopoulos – <i>Piezoelectric Behavior of Aeronautical GFRP with Embedded Strain Sensor under Bending Loads</i> .	129
K. Makowska, Z.L. Kowalewski – <i>Microstructural Assessment and Magnetic Structuroscopy of Middle-Carbon Steel after Simulated Creep</i>	131
I. Markiewicz – <i>Design with SADSf Method and Analyses of Elastic Properties of Torsion-Loaded Structures Based on Double-Tee Sections</i>	133
A. Ohtsuki – <i>A New Method for Measuring Young's Modulus of Thin Multi-Layered Materials Using Postbuckling Behavior</i>	135
W. Oliferuk, M. Maj – <i>Energy Storage Rate Components</i>	137

P. Sadowski, S. Stupkiewicz – <i>Estimation of the Effective Properties of Composites with Inclusions of Diverse Shapes and Properties</i>	139
G. Stefanou, S.K. Kourkoulis, Z. Velonaki, E. Lymperaki, N.D. Alexopoulos – <i>Fracture Toughness of Aeronautical Aluminum Alloys 6156 and 2024 for Different Artificial Aging Conditions</i>	141
T. Szymczak, Z.L. Kowalewski – <i>Analysis of Tensile Force Variation Due to Application of Cyclic Torsion for a Range of Frequency Levels</i>	143
Z. Velonaki, S.K. Kourkoulis, W. Dietzel, N.D. Alexopoulos – <i>Mechanical Behaviour of Aluminum Alloy 2198 Under Different Corrosion Exposure Times</i> . . .	145
J. Widłaszewski – <i>Application of the Inherent Strain Method in Modeling of Laser Thermal Forming</i>	147

Fracture, Damage and Fatigue of Materials

Y. Akinci, O. C. Celik – <i>Parametric Study on Collapse Investigation in Steel Vierendeel Beams</i>	151
P. Fiborek – <i>Defects and Non-Destructive Detection Methods for Adhesive Bonds in Composite Structures – Preliminary Study</i>	153
A. Kaczyński – <i>An Anticrack in a Transversely Isotropic Space Under a Remote Uniform Heat Flow</i>	155
A. Knitter-Piątkowska, M. Guminiak – <i>Damage Detection in Plate Structures Using Wavelet Transformation</i>	157
C. V. Kukudzhanov, A. V. Kolomiets – <i>Deformation and Fracture of the Preliminary Damaged Material under the Impact of Electric Current</i>	159
G. Mejak – <i>Effective Linear Elastic Properties of a Solid with Periodic Distribution of Penny Shaped Cracks</i>	161
W. Moćko – <i>Influence of the Fatigue Loadings on the Residual Stress-Strain Characteristic of the Engineering Materials</i>	163
T. Paris, A. Migliarini – <i>Abnormal Fracture in Titanium Alloy TA6V</i>	165
A. Rutecka, P. Grzywna – <i>Metal Matrix Composites under Fatigue Conditions</i> . . .	167
G. Socha, L. Dietrich – <i>Evolution of Damage for P91 Steel under Cyclic Load</i>	169

Geomechanics

S. K. Kourkoulis – <i>The Brazilian-Disc- and the Ring-Tests as Means to Determine the Tensile Strength of Brittle Materials: Some New Insights</i>	173
I. Marczewska, J. Rojek, R. Kačianauskas – <i>Micro-Macro Dependency for Elastic Constants in a Numerical Model of Granular Material</i>	175
S. Pietruszczak, M. Oboudi – <i>On the Description of Inherent/Induced Anisotropy in Porous Media</i>	177
A. Pożarycki, T. Garbowski – <i>Soft Computing in Mechanical Characterization of Pavement Structures</i>	179
R. Staroszczyk – <i>Modelling of Sea Ice Flow by the Smoothed Particle Hydrodynamics Method</i>	181
Z. Więckowski – <i>Analysis of Soil-Fluid-Structure Interaction Problems by Material Point Method</i>	183

- A. V. Zaitsev, A.V. Kutergin, Yu.V. Sokolkin, A.A. Fukalov** – *Exact Analytical Solutions to Problems on Equilibrium State of Elastic Anisotropic Heavy Spheres and Cylinders and Their Applications to Geomechanical Problems* 185

Mechanics of Composites, Porous Media

- T. Burczyński, A. Mrozek** – *Atomistic Models of Polycrystalline and Porous Structures* 189
- S. Hernik** – *New Hybrid Weight Homogenization Rule for Fiber-Reinforced Orthotropic Composite* 191
- K. Kowal-Michalska, Z. Kołakowski** – *Inelastic Buckling of Thin-Walled FML Columns by Elastic Asymptotic Solutions* 193
- Z. S. Metaxa, E. P. Favvas, C. Mercader, F. Poulin, N. D. Alexopoulos** – *A Preliminary Study on the Development of Graphene/Cement Based Nanocomposites* 195
- P. Papanikos** – *Finite Element Modelling of the Mechanical Behavior of Polymers Reinforced by Randomly Distributed Carbon Nanotubes* 197
- Z. Ranachowski, D. Józwiak-Niedźwiedzka, P. Ranachowski, A. Pawełek, S. Kudela Jr., T. Dvorak** – *The Analysis of Pore Distribution and Pore Connectivity in Concrete Samples Using X-Ray Microtomography* 199
- M. Svanadze** – *Boundary Value Problems in the Theory of Thermoelasticity of Double-Porosity Materials* 201
- I. Yu. Zubko, V. I. Kochurov, R. S. Gorodilov** – *Finding Second-Order Nonsymmetric Thermoelastic Properties of Graphene Monolayer using Lattice Statics Approach* 203

Micromechanics, Interfaces and Multi-Scale Modelling

- K. Frydrych, K. Kowalczyk-Gajewska, S. Stupkiewicz** – *Modelling of Microstructure Evolution in hcp Polycrystals on Non-Proportional Strain Paths* 207
- P. Hołobut, M. Kurza, A. Macios, J. Lengiewicz** – *Evolving Microstructures for Scalable Actuation in Programmable Matter* 209
- S. Schmauder** – *Recent Developments in Atomistic and Atomistic-Continuum Modelling for Materials Development* 211
- A. Zmitrowicz** – *Variational Settings in Mechanics of Wear* 213

Plates and Shells

- S. Burzyński, J. Chróścielewski, W. Witkowski** – *Some Aspects of Buckling in Geometrically and Materially Nonlinear Cylindrical Shells* 217
- N. Chinchaladze** – *On a Variational Problem for a Cusped Elastic Prismatic Shells in Case of the Third Model of Vekua'S Hierarchical Model* 219
- S. Fialko** – *Quadrilateral Flat Shell Finite Element for Simulation of Reinforced Concrete Structural Elements* 221
- M. Gohnert** – *Natural Shapes Applied to Shell Structures* 223
- B. Gulua** – *Vekua's Hierarchical Models of the Second Type for Elastic Shallow Shells* 225
- P. Jarzębski, K. Wiśniewski** – *On Parallelization of the Loop Over Elements for Composite Shell Computations* 227

G. Knor, J. Holnicki-Szulc – <i>Modelling Propagation of Lamb Waves in CFRP Plates for Damage Detection</i>	229
A.M. Kolesnikov – <i>Wrinkling of Inflated Elastic Curved Tube Under Pure Bending</i> . .	231
V. Konopińska, W. Pietraszkiewicz – <i>Irregular Base Surface in the Resultant Thermo-mechanics of Shells</i>	233
Ch. F. Markides, S. K. Kourkoulis – <i>Elliptically Perforated Circular Discs Under Parabolic Pressure</i>	235
P. Kowalczyk, J. Rojek, R. Stocki, T. Bednarek, P. Tazowski, R. Lasota, D. Lumelsky, K. Wawrzyk <i>NUMPRESS – Integrated Computer System for Analysis and Optimization of Industrial Sheet Metal Forming Processes: Numerical Investigation of Square Cup Drawing</i>	237
E. Pruchnicki – <i>Two-Dimensional Model of Fifth Order for the Combined Bending, Stretching and Shearing of Shells Derived from Three-Dimensional Elasticity: General Approach and Application to Cylindrical Shells</i>	239
D. Ribarić, G. Jelenić – <i>Distortion-Immune 9-Node Quadrilateral Thick Plate Finite Elements That Satisfy Constant-Bending Patch Test</i>	241
B. Tomczyk – <i>Tolerance Models of Stability Problems for Micro-Periodic Cylindrical Shells</i>	243
B. Tóth – <i>A Comparative Study of New Dual-Mixed h- and p-Version Cylindrical Shell Finite Elements for Elastostatic Problems</i>	245
W. Wagner, J. Läufer – <i>On the Influence of Shell-Kinematics on the Failure Behaviour of Composite Shell Structures</i>	247
A. Wirowski, M. Rabenda, B. Michalak – <i>Modelling of Thin Skeletal Annular Plates with Dense System of Ribs</i>	249
Ł. Żmuda-Trzebiatowski – <i>Comparison of Buckling Resistance of Columns Modelled by Beam and Shell Elements Using Non-Linear Analysis</i>	251

Smart Materials and Structures

V. Dunić, E. Pieczyska, N. Busarac, R. Slavković, V. Slavković – <i>Partitioned Thermo-Mechanical Coupling of SMA Constitutive Model</i>	255
T. Ikeda – <i>Analysis of Effect of Loading Frequency on Stress-Strain-Temperature Relationship of Shape Memory Alloys</i>	257
K. Kowalczyk-Gajewska, E. Pieczyska, M. Maj, M. Staszczak, M. Majewski, M. Cristea, H. Tobushi – <i>Two-Phase Model of Shape Memory Polymers at Finite Strains: Formulation and Experimental Verification</i>	259
R. Matsui, R. Takenouchi – <i>Transformation and Deformation Properties of Functionally Graded Shape Memory Alloy Fabricated by SPS and Rolling Processes</i> . .	261
E. A. Pieczyska – <i>Ferromagnetic Single Crystal Shape Memory Alloy Subjected to Subsequent Compression Cycles</i>	263
P. Sowa, A. Biborski, R. Kozubski, E. V. Levchenko, A. V. Evteev, I. V. Belova, G. E. Murch – <i>Ordering and Segregation Processes in Binary Intermetallic Nanofilms with Triple Defects: Atomistic Simulations</i>	265
M. Staszczak, E. A. Pieczyska, M. Maj, K. Kowalczyk-Gajewska, M. Cristea, H. Tobushi, S. Hayashi – <i>Estimation of Shape Fixity and Shape Recovery – Crucial Parameters for Shape Memory Polymer Applications</i>	267

K. Takeda, R. Matsui, H. Tobushi, N. Levintant-Zayonts, S. Kucharski – <i>Deformation and Fatigue Properties of Nitrogen Ion Implanted TiNi Shape Memory Alloy</i>	269
K. Takeda, R. Matsui, H. Tobushi, E.A. Pieczyska – <i>Stress Relaxation and Stress Recovery of TiNi Shape Memory Alloy in Stress-Controlled Subloop Loading</i> . . .	271
M. Xia, Q. Sun – <i>Jump Phenomenon of Thermomechanical Responses in Nonlinear Torsional Vibration of NiTi Tube</i>	275

Structural Mechanics, Optimization and Reliability Analysis

M. Kotełko, P. Lis – <i>Probabilistic Approach to the Load-Carrying Capacity Estimation of Thin-Walled Structural Members</i>	279
A. Marek, T. Garbowski – <i>Sensitivity Analysis in Homogenization Process of Corrugated Paperboards</i>	281
I. Pączelt, Z. Mróz – <i>Analysis of Steady Wear States for Monotonic and Periodic Sliding</i>	283
T. Tokunaga, D. Szeliga, K. Matsuura, M. Ohno, M. Pietrzyk – <i>Sensitivity Analysis for the Indirect Extrusion of Mg Alloy with Al Coating</i>	285
T. Ueda, S. Shimizu, G. Fujita, N. Tanaka – <i>Flange Vertical Buckling of Hybrid Steel Girders under Bending</i>	287
A.V. Zaitsev, I.Yu. Zubko, O.Yu. Isaev, D.M. Karavaev, V.S. Koksharov, D.V. Smirnov, A.M. Khanov – <i>Mathematical Model for Inelastic Deformation of Flexible Graphite O-Ring Seals and Seal Packs under Their Exploitation in Stop Valves</i>	289

Poster Session

V. Baklanov – <i>Dynamic Model Aircraft Engine from the Solid to Multicoupling System (on Experimental Studies of Dynamic Compliance Engine Housing)</i>	293
P. Drzymała, J. Bonarski, Z. Ranachowski – <i>The Role of Microstructure in Deformation Mechanisms in Extruded AZ31 Magnesium Alloy</i>	295
A. Klasik, K. Pietrzak, N. Sobczak, K. Makowska, D. Rudnik – <i>Wetting-Bonding Relationship in Lead-Free Solder Joints for High Temperature Applications</i>	297
S.K. Kourkoulis, G.E. Exadaktylos – <i>Prismatic Beams Made of Shellstone under Three-Point Bending: Implications Due to the Transverse Isotropy</i>	299
S.K. Kourkoulis, E.D. Pasiou – <i>A Validated Numerical Model for the Response of Typical Parthenon Epistyles' Connections under Pure Shear</i>	303
M.S. Kozieñ, D. Smolarski – <i>Formulation of the Spectral Direct Method for Cycle Counting of Bimodal Multiaxial Stress</i>	305
D. Kukla, P. Grzywna, Z.L. Kowalewski – <i>Assessment of Damage Development Due to Fatigue of 2017 Aluminum Alloy on the Basis of Conductivity Measurements</i>	307
P. Kulak, J. Piwnik, T. Węgrzyn, D. Sieteski, Ł. Wszółek – <i>Innovative Micro Welding Technologies</i>	309
T. Libura, W. Moćko, Z.L. Kowalewski – <i>A New Version of Hopkinson Bar Testing Stand for Determination of Dynamic Tensile Characteristics</i>	311

M. Maj, A. Klasik, K. Pietrzak, D. Rudnik – <i>Mechanical Low Cycle Fatigue (LCF) Test and Its Modified (MLCF) Version</i>	313
J. Melcer – <i>Numerical and Experimental Analysis of a Bridge</i>	315
D. Mężyk – <i>Failure Frequency of Steam Pipelines – Operational Conclusions</i>	317
G. Mura – <i>Geometry Optimization Method of the Cores of the Energy-Absorbing Protective Panels</i>	319
K. Pietrzak, A. Klasik, K. Makowska, J.J. Sobczak, D. Rudnik – <i>Mechanical Properties of Aluminum Composites Reinforced with Al_2O_3 Particles After Multiple Remelting</i>	321
P. Sadowski, S. Kucharski, J. Lengiewicz, S. Stupkiewicz – <i>Soft Elastohydrodynamic Lubrication Problems in the Finite Deformation Regime: Experimental Testing and Modelling</i>	323
T. Szymczak, A. Brodecki, Z.L. Kowalewski – <i>An Effect of Technological Notches on Stress and Strain Distribution During Monotonic Tension</i>	325
T. Szymczak, A. Brodecki, A. Eminger, Z.L. Kowalewski – <i>Experimental Assessment of Ball Joints Operation Using Servo-Hydraulic Testing Systems</i>	327
A. Ustrzycka, B. Skoczeń – <i>Degradation of Material Properties Due to Evolution of Radiation Induced Damage</i>	329
Authors Index	331

Plenary Lectures

MECHANICS OF NANOSTRUCTURES

H. Altenbach¹, V. A. Eremeyev^{1,2}

¹Otto-von-Guericke-Universität, Magdeburg, Germany

²South Federal University & South Scientific Center of RASci, Rostov on Don, Russia

1. Introduction

During the last 50 years the nanotechnology is established as one of the advanced technologies manipulating matter on an atomic and molecular scale. By these approach new materials, devices or other structures possessing at least one dimension sized from 1 to 100 nm are developed. The question arises how structures composed of nanomaterials should be modeled. Two approaches are suggested - theories which take into account quantum mechanical effects since they are important at the quantum-realm scale and theories which are based on the classical continuum mechanics adapted to nanoscale problems. Here the second approach will be discussed in detail. It will be shown that the classical continuum mechanics with some improvements is enough for a sufficient description of the mechanical behavior of nanomaterials and -structures in many situations.

2. Governing equations of the classical continuum mechanics

The classical boundary-value problem of continuum mechanics takes the following form:

$$(1) \quad \nabla \cdot \boldsymbol{\sigma} + \mathbf{f} = 0, \quad \text{in } V, \quad \mathbf{n} \cdot \boldsymbol{\sigma}|_{\Omega_f} = \mathbf{t}, \quad \mathbf{n}|_{\Omega_u} = 0.$$

Here for simplicity we restricted ourselves by infinitesimal deformations, ∇ is the three-dimensional gradient (nabla) operator, $\boldsymbol{\sigma}$ is the stress tensor, \mathbf{u} is the displacements, V and $\Omega = \Omega_f \cup \Omega_u$ are the volume of the solid and its surface, respectively. \mathbf{f} and \mathbf{t} are the volume and surface external forces. The constitutive equations are given as follows: $\boldsymbol{\sigma} = \mathbf{C} : \boldsymbol{\varepsilon}$.

3. Improvements in the case of nanoscale problems

There are various models extended the classical continuum mechanics to the nanoscale. Recently, the Gurtin-Murdoch model [1] and its generalizations are widely applied for nanomechanics, see [2–4]. From the mechanical point of view the model [1] can be described as an elastic body with glued on its surface an elastic membrane. The stress resultants acting in the membrane are the surface stress tensor $\boldsymbol{\tau}$. As a result the additional constitutive equations for the surfaces stresses are required. The boundary-value problem of surface elasticity transforms to

$$(2) \quad \nabla \cdot \boldsymbol{\sigma} + \mathbf{f} = 0 \quad \text{in } V, \quad \mathbf{n} \cdot \boldsymbol{\sigma}|_{\Omega_f} = \mathbf{t}, \quad \mathbf{n}|_{\Omega_u} = 0, \quad (\mathbf{n} \cdot \boldsymbol{\sigma} - \nabla_S \cdot \boldsymbol{\tau})|_{\Omega_s} = \mathbf{t},$$

where ∇_s is the surface nabla operator and $\Omega = \Omega_f \cup \Omega_u \cup \Omega_s \equiv \partial V$. Equation (2)₄ is the generalisation of the classical Laplace-Young equations used in the theory of capillarity where instead of tensor-valued field $\boldsymbol{\tau}$ the scalar surface tension are introduced.

It is worth to mention other approaches for definition of surface phenomena related with strain-gradient theories [5] or [6]. These approaches are based on unified constitutive equations for the bulk and surface behaviour.

For determination of material parameters for surface constitutive equations the atomistic simulations are widely used, see [7, 8].

4. Application to plates and shells

Presence of surface stresses changes dramatically the effective (apparent) properties of materials, see [2-4]. Here we discuss effective stiffness parameters for plates and shells of nano-sized thickness. The basic equations are, see [9, 10],

$$\begin{aligned} \nabla_S \cdot \mathbf{T}^* + \mathbf{q} &= 0, \quad \nabla_S \cdot \mathbf{M}^* + \mathbf{T}_\times^* + \mathbf{m} = 0, \quad \mathbf{T}^* = \mathbf{T} + \mathbf{T}_S, \quad \mathbf{M}^* = \mathbf{M} + \mathbf{M}_S, \\ (3) \quad \mathbf{T} &= \langle (\mathbf{A} - z\mathbf{B})^{-1} \cdot \boldsymbol{\sigma} \rangle, \quad \mathbf{M} = -\langle (\mathbf{A} - z\mathbf{B})^{-1} \cdot z\boldsymbol{\sigma} \times \mathbf{n} \rangle, \quad \langle (\dots) \rangle = \int_{-h/2}^{h/2} (\dots) G dz, \\ \mathbf{T}_S &= \boldsymbol{\tau}_+ + \boldsymbol{\tau}_-, \quad \mathbf{M}_S = -\frac{h}{2}(\boldsymbol{\tau}_+ - \boldsymbol{\tau}_-) \times \mathbf{n}, \quad \mathbf{B} = -\nabla_S \mathbf{n}, \quad G = \det(\mathbf{A} - z\mathbf{B}). \end{aligned}$$

In (3) \mathbf{T}^* and \mathbf{M}^* are effective stress resultants and couple stress tensors, \mathbf{T}_S and \mathbf{M}_S are stress resultants tensors related with surface stresses $\boldsymbol{\tau}_+$ and $\boldsymbol{\tau}_-$, \mathbf{q} and \mathbf{m} are the surface loads. Tensors \mathbf{T}_S and \mathbf{M}_S are given by $\mathbf{T}_S = 2\tau_0\mathbf{A} + C_1^S\boldsymbol{\varepsilon} + C_2^S\mathbf{A}\text{tr}\boldsymbol{\varepsilon}$, $\mathbf{M}_S = -[D_1^S\boldsymbol{\kappa} + D_2^S\mathbf{A}\text{tr}\boldsymbol{\kappa}] \times \mathbf{n}$, where $C_1^S = 4\mu^S$, $C_2^S = 2\lambda^S$, $D_1^S = h^2\mu^S$, $D_2^S = D\nu + h^2\lambda^S/2$, $\boldsymbol{\varepsilon}$ and $\boldsymbol{\kappa}$ are 2D strain measures: $\boldsymbol{\varepsilon} = \frac{1}{2}(\nabla_S \mathbf{w} \cdot \mathbf{A} + \mathbf{A} \cdot (\nabla_S \mathbf{w})^T)$, $\boldsymbol{\kappa} = \frac{1}{2}(\nabla_S \boldsymbol{\theta} \cdot \mathbf{A} + \mathbf{A} \cdot (\nabla_S \boldsymbol{\theta})^T)$, \mathbf{w} and $\boldsymbol{\theta}$ are the vectors of translations and rotations. Stiffness parameters significantly depend on surface elastic moduli μ^S and λ^S . In particular, the effective tangential and bending stiffness are given by

$$C^* \equiv C_1 + C_2 = C + 4\mu^S + 2\lambda^S, \quad D^* \equiv D_1 + D_2 = D + h^2\mu^S + h^2\lambda^S/2.$$

Other examples of an effective properties of materials with surface stresses including surface viscoelasticity, residual surface stresses, etc, will be also discussed.

References

1. M.E. Gurtin, A.I. Murdoch (1975). A continuum theory of elastic material surfaces, *Arch. Rat. Mech. Analysis*, **57**, 291–323.
2. H.L. Duan, J. Wang, B.L. Karihaloo (2008). Theory of elasticity at the nanoscale, *Advances in Applied Mechanics*, **42**, 1–68.
3. J. Wang, Z. Huang, H. Duan, S. Yu, X. Feng, G. Wang, W. Zhang, T. Wang (2011). Surface stress effect in mechanics of nanostructured materials, *Acta Mechanica Solida Sinica*, **24**, 52–82.
4. A.A. Javili, A.A. Mc Bride, P. Steinmann (2013). Thermomechanics of solids with lower-dimensional energetics: On the importance of surface, interface, and curve structures at the nanoscale. A unifying review, *Appl. Mech. Rev.*, **65**, 010802-31.
5. R.D. Mindlin (1965). Second gradient of strain and surface-tension in linear elasticity, *Int. J. Solids Struct.*, **1**, 417–438.
6. H. Ibach (1997). The role of surface stress in reconstruction, epitaxial growth and stabilization of mesoscopic structures, *Surface Science Reports*, **29**, 195–263.
7. V.B. Shenoy, R.E. Miller (2000). Size-dependent elastic properties of nanosized structural elements, *Nanotechnology*, **11**, 139–147.
8. V.B. Shenoy (2005). Atomistic calculations of elastic properties of metallic FCC crystal surfaces, *Physical Review B*, **71**, 094104-11.
9. H. Altenbach, V.A. Eremeyev (2011). On the shell theory on the nanoscale with surface stresses, *Int. J. Engng Sci.*, **49**, 1294–1301.
10. H. Altenbach, V.A. Eremeyev, N.F. Morozov (2010). On equations of the linear theory of shells with surface stresses taken into account, *Mech. Solids*, **45**, 331–342.

MECHANICAL BEHAVIOR OF WOOD – A BRIDGE FROM MICROSTRUCTURE TO STRUCTURAL APPLICATIONS BY MEANS OF COMPUTATIONAL METHODS

J. Füssl, M. Lukacevic, G. Kandler, J. Eberhardsteiner

Institute for Mechanics of Materials and Structures, Vienna University of Technology, Austria

1. Introduction and motivation

Wood is a naturally grown material with excellent mechanical properties. Comparing mass density to representative strength value ratios of different common building materials, wood is a factor of three better than steel, considering tensile strength, and about ten times better than concrete, even with respect to compressive strength. Nevertheless, wood as structural bearing material is often countered with skepticism and therefore it is not used as extensively as its very good material behavior would suggest. Besides building physics and construction reasons, the main cause of this skepticism is the quite complex material behavior of wood, the huge variety due to hundreds of species and its strong inhomogeneity, resulting from branches and growth irregularities. Thus, to strengthen confidence in wood as load bearing material and to increase the competitiveness in comparison to other building materials, the following challenges can be formulated:

- Determination of the mechanical clear wood properties as a function of wood species and the location in the stem.
- Quantification of the influence of inhomogeneities (knots and knot groups) and growth irregularities (global and local fiber deviations) on the effective mechanical properties of timber boards.
- Consideration of the material variability within timber boards in general, and linking this variability to stochastic information of the effective properties of wood-based products.

2. Modeling approach

A comprehensive modeling approach, covering all these points, was developed at the Institute for Mechanics of Materials and Structures of Vienna University of Technology (TU Wien). Basically, the whole concept can be divided into three parts: (i) the identification of the timber board morphology, (ii) the identification of material properties at different scales of observation, and (iii) the determination of the effective behavior including variability of wood products.

The starting point of this approach is an individual wooden board, produced in sawmills by cutting of logs, and the goal of the first part is a reconstruction of the board morphology as accurately as possible. This can be done in two different ways. On the one hand, 2D fiber angle information on all four surfaces of wooden boards was extracted from laser scanning data. From that surface information, a 3D fiber distribution can be approximated with appropriate interpolation methods (natural or nearest neighbor [1]). On the other hand, about 90 knot groups were reconstructed manually by scanning the board surfaces digitally and approximating knots with rotationally symmetric cones. A detailed description of this procedure can be found in [2]. In the following, a 3D fiber course around the identified knots can be generated and finally a 3D model of the wooden board morphology is obtained.

The second part of this concept aims at identifying mechanical properties of wooden boards based on the morphological information gained within the first part. From this point on, two different modeling strategies with different priorities must be distinguished.

On one side, focus is laid on the stochastic nature of wooden boards, requiring simplifications regarding morphology and material behavior, and on the other side, the complexity of the material and the 3D geometry is taken into account very accurately, at the cost of material variability. Without considering random variables, a numerical finite element (FE) model [2] was developed based on the 3D model of morphology described before. Within this model, the orthotropic elastic clear wood material properties are determined by means of a micromechanical model developed by Hofstetter *et al.* [3], the failure criterion of Tsai and Wu is used to define local failure and stress redistribution effects are used to identify structural failure. A comprehensive validation of this numerical simulation tool by means of full-field deformation measurements is presented in [4].

For the second modeling strategy, with the material variability as the main focus, the elastic stiffness tensor from the micromechanical model is directly linked to an approximation of the 3D fiber course, obtained through interpolation of the 2D fiber angle information, leading to 3D elastic property distributions within wooden boards. These distributions serve as input to a stochastic analysis tool, which will be described in the following.

Part three of the concept deals with the determination of effective material properties and related stochastic information of wood-based products. The stochastic approach consists of two parts: (i) The development of an appropriate random process model based on previously acquired data (realizations), in our case stiffness distributions, and (ii) the implementation into a stochastic FE model where the mechanical and stochastic problem is coupled. Parallel to this, the deterministic FE model for wooden boards was extended to GLT and CLT elements.

3. Conclusions

Referring to the challenges mentioned within the motivation the following conclusions can be drawn:

- The application of a micromechanical model at cell wall level as well as an unit cell FE model at cell level allows for the determination of material properties depending on (micro)structural characteristics and therefore as a function of wood species. Additionally, the influence of clear wood density variations within a stem on the material properties can be taken into account.
- The performance of a 3D numerical model for wooden boards was validated by means of full-field deformation measurements on four-point bending tests to failure, showing that both, elastic strain fields as well as structural failure, can be predicted very accurately. The determination of effective material properties, taking the inhomogeneity of wooden boards into account, is thus possible.
- An automated identification of wooden board morphologies, using laser scanning data or possibly in the future data from computer tomography, delivers appropriate input for stochastic FE models. The error influenced by required simplifications regarding material behavior or morphology, respectively, should be assessed with deterministic models. A strong interaction between these two approaches ensures that reliable effective properties, including stochastic information, of wood products are obtained.

References

1. A. Olsson, J. Oscarsson, E. Serrano, B. Källsner, M. Johanson, B. Enquist (2013). Prediction of timber bending strength and in-member cross-sectional stiffness variation on basis of local wood fibre orientation, *European Journal of Wood and Wood Products*, **71**, 3, 319–333.
2. M. Lukacevic, J. Füssl (2014). Numerical simulation tool for wooden boards with a physically based approach to identify structural failure, *European Journal of Wood and Wood Products* (to be published).
3. K. Hofstetter, C. Hellmich, J. Eberhardsteiner (2005). Development and experimental validation of a continuum micromechanics model for the elasticity of wood, *European Journal of Mechanics A/Solids*, **24**, 1030–1053.
4. M. Lukacevic, J. Füssl, M. Griessner, J. Eberhardsteiner (2014). Performance assessment of a numerical simulation tool for wooden boards with knots by means of full-field deformation measurements, *Strain* (to be published).

PLASTO-MECHANICS OF LARGE DEFORMATION UNDER IMPACT LOADING

N. K. Gupta

Supercomputer Education and Research Centre, Indian Institute of Science Bangalore, India

I consider it an honour to have been invited to deliver this lecture in the 39th Solid Mechanics Conference and thank Prof. Zbigniew Kowalewski for giving me this opportunity.

Several studies have appeared in recent years, which present formulations that describe plasto-mechanics of large deformation and attempt to bring together various facets affecting the deformation. However, many problems relating to the deformation modes and mechanics involved in such phenomenon and their dependence on various parameters like strain rate, inertia, history of loading, annealing and thermal processes, and geometry are still not fully understood. Structured experiments become necessary to study the phenomenon in its varied aspects, and provide plausible description, assumptions and parameters needed for realistic analysis of such problems based on the mechanics observed.

In this paper, an overview of observations on plasto-mechanics in some of our large deformation studies and resulting collapse modes in relation to absorption of kinetic energy, which are of interest, involving thin walled structures of varying geometry and size and subjected to impact of a drop hammer, projectiles of different features and blast loading, is presented in a hope that plausible explanation for these having been found, would help in further understanding of the phenomenon and its dependence on different parameters.

Plasto-mechanics of structural elements like tubes of circular and non-circular cross-sections, spherical shells, and conical frusta are extensively studied for their application in the design of devices for absorbing kinetic energy in situations of a crash or an accident. Axially crushed thin walled tubes are perhaps the most investigated structural elements. Their progressive collapse is either axi-symmetric due to local axial and radial buckling or diamond due to local circumferential buckling. It is however seen that the size of the specimen, annealing process, and the presence of any discontinuity or eccentricity (Fig. 1) influence the mode of deformation very much. Typical load-deformation curves of such structures, their collapse modes and deformed shapes and their dependence on various parameters are discussed.

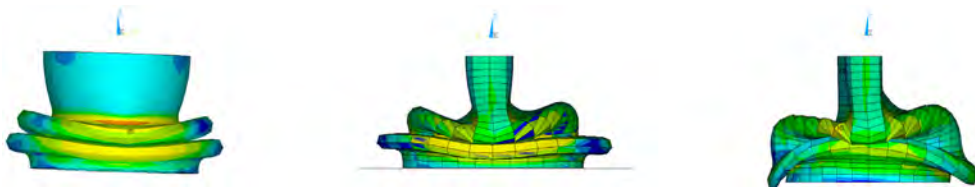


Fig. 1. Collapse modes of tubes with 0.03 mm, 0.3 mm, 0.5 mm thickness eccentricity.

Composite thin shells, such as tubes, frusta, and domes are potential candidates for their use as energy absorbing elements. Their deformation and failure mechanism is highly complicated (Fig. 2) and rather difficult to analyse. This includes fracture in fibers, matrix, and fibre-matrix interface in tension, compression, and shear. This class of materials still

MULTISCALE MODELING OF MULTIFUNCTIONAL AEROSPACE NANOCOMPOSITES: CHALLENGES AND OPORTUNITIES

S. A. Meguid

Mechanics and Aerospace Design Laboratory, University of Toronto, Canada

1. Tailoring of nanocomposites

It has been recognised for some time that the mechanical, electrical and thermal properties of polymeric materials can be engineered by fabricating composites that are comprised of different volume fractions of one or more reinforcing phases. Traditionally, polymeric materials have been reinforced with carbon or glass micro fibres to improve their mechanical properties and a variety of metallic and/or organic fillers for electrical and thermal property enhancements.

These composite materials have been used in a wide variety of applications in automotive, aerospace, mass transit, and nuclear industries. Rarely, however, have traditional fillers been able to substantially improve a combination of these properties. As time has progressed, practical realization of such composites has begun to shift from micro-scale composites to nanocomposites, taking advantage of the unique combination of mechanical, electrical and thermal properties of *nanofillers*; *viz.*, fillers with a characteristic dimension below 100 nm.

There are a number of advantages associated with dispersing nanofillers in polymeric materials. Whilst some credit can be attributed to the intrinsic properties of the fillers, most of these advantages stem from the extreme reduction in filler size combined with the large enhancement in the specific surface area and interfacial area they present to the matrix phase. In addition, whereas traditional composites use over 40% by weight of the reinforcing phase, the dispersion of just a few weight percentages of nanofillers into polymeric matrices could lead to dramatic changes in their mechanical [1, 2] and electrical [3, 4] properties with added functionalities.

2. Multifunctionality using carbon nanotubes

Perhaps the most widely used and studied nano-filler is carbon nanotube (CNT). CNTs are highly unusual electrical conductors, the strongest known fibers, and excellent thermal conductors. In fact, some CNTs are stronger than steel, lighter than aluminum, and more conductive than copper. Theoretical and experimental studies have shown that CNTs exhibit extremely high tensile modulus (~ 1 TPa) and strength (~ 150 GPa). Depending on their atomic structure, CNTs can be either metallic or semiconducting with experimental measurements showing intrinsic electrical conductivities of approximately 10^5 to 10^6 S/m for metallic nanotubes and 10 S/m for semiconducting nanotubes. Furthermore, CNTs exhibit large phonon mean free paths that result in high thermal conductivities which have been theoretically estimated to be in the range of 6000–3000 W/mK. In addition, CNTs exhibit high flexibility, low density (1.3 to 1.4 g/cm³), and large aspect ratios (1000 s). Due to this unique combination of physical and multifunctional properties, CNTs have emerged as excellent candidates for use as tailoring agents in polymeric materials to yield next generation multifunctional composite materials.

The ability to tailor the mechanical, electrical and thermal properties of polymeric materials through the dispersion of CNTs depends on several important factors relating to the physical and mechanical properties on CNTs, dispersion techniques, CNTs loading, type of polymer used and the molecular chains. For example, at a concentration of only

0.1 wt% of CNTs, the volume resistivity of certain polymers can be decreased by over eight orders of magnitude. The limit that governs the sudden transition between insulating and conducting behavior is known as *the percolation threshold*. Earlier work also shows that the addition of as little as 0.1 wt% of CNTs in an epoxy matrix can increase the fracture toughness by upwards of 20% with further improvements observed for amino-functionalized nanotubes. In comparison, the thermal conductivity of cured nanotube-epoxy composites show a minimal and near insignificant increase with nanotube content; less than 0.5% for a concentration of 0.5 wt% of CNTs. Furthermore, the mechanical properties of nanocomposites have been shown to increase significantly when the CNTs are chemically modified to form reactive bridges with the surrounding polymer chains; a process known as functionalization. In this context, the same CNTs can be shown to provide a wide range of improvements in the mechanical properties from this surface modification process.

3. Objectives and scope

We are currently developing multifunctional nanoreinforced composites for the aerospace industry. In this presentation, I shall address (i) the interfacial properties of nanoreinforced polymer composites and (ii) the electrical properties of CNT-Tailored thermoset polymer. In (i), we will determine the interfacial shear strength (ISS) by simulating a nanotube pull-out experiment using both molecular dynamics and atomistic based continuum. An atomistic description of the problem, which is based on the use of a representative volume element (RVE), is achieved by implementing constitutive relations that are derived solely from interatomic potentials (Fig. 1). Specifically, both non-bonded interface, where only the van der Waals (vdW) interactions are assumed to exist, and cohesively bonded C-C interfaces are studied. The effects of CNT embedded length, the number of vdW interactions, the thickness of the interface on ISS are investigated and discussed. In (ii), Monte-Carlo simulations are conducted to determine the electrical conductivity of CNT percolated network which is based on electron transport theory and periodic boundary conditions in a representative cell.

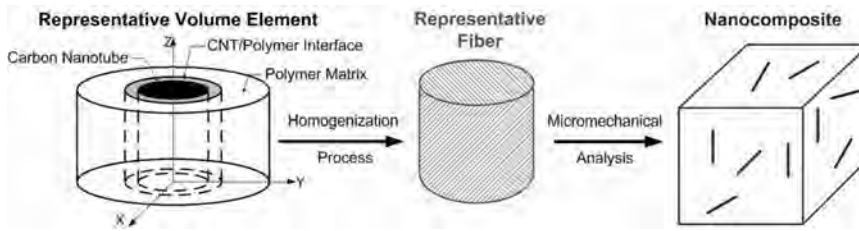


Fig. 1. Multiscale modeling of nanocomposite using RVE.

Acknowledgments

The author wishes to acknowledge the financial support of Natural Sciences and Engineering Research Council of Canada. He also wishes to thank Drs. J. Wernik and W.S. Bao for helpful discussions and input.

References

1. J.M. Wernik, S.A. Meguid (2011). Recent developments in multifunctional nanocomposites using CNTs, *Applied Mechanics Reviews*, **63**, 5, 050801.
2. J.M. Wernik, B.J. Cornwell-Mott, S.A. Meguid (2012). Determination of the interfacial properties of CNTs reinforced polymer composites using atomistic based continuum model, *Int. J. Solid Struct.*, **49**, 13, 1852–1863.
3. W.S. Bao, S.A. Meguid (2012). A novel approach to predict the electrical conductivity of multifunctional nanocomposites, *Mechanics of Materials*, **46**, 129–138.
4. W.S. Bao, S.A. Meguid *et al.* (2011). Modelling electrical conductivities of nanocomposites with aligned CNTs, *Nanotechnology*, **22**, 48, 485704.

PLASTIC FLOW AND FAILURE OF SOLIDS. MODELLING ACROSS SCALES

K. Nalepka¹, R. B. Pęcherski²

¹Department of Strength and Fatigue of Materials and Structures, Faculty of Mechanical Engineering and Robotics, AGH University of Science and Technology

Al. Mickiewicza 30, 30-059 Krakow, Poland, e-mail: knalepka@agh.edu.pl

²Department of Mechanics of Materials, Institute of Fundamental Technological Research, Polish Academy of Sciences

A. Pawińskiego 5B, 02-106 Warsaw, Poland, e-mail: rpecher@ippt.pan.pl

1. Introduction

The aim of the presentation is to discuss the classical problems of elastic limit criteria from the perspective of basic quantum mechanical approach [1]. In the case of metallic solids the multiscale mechanisms of plastic deformation and failure are analysed [2]. In particular, the role of shear banding responsible for plastic flow is elucidated [3].

New and original aspects of the presentation are related with our recent studies on metal-ceramic composites. Final functional and mechanical properties of such materials depend largely on interface microstructures [4]. Particularly, it concerns to nanocomposites. Therefore, in cooperation with specialists of leading research centers in Poland, we undertook experimental and theoretical studies on microstructures of metal/ceramic interfaces. As an example, copper/ sapphire nanocomposites were considered. As a result of the carried out research, the interface microstructure of Cu/ α -Al₂O₃ nanocomposites obtained by the pulsed laser deposition (PLD) method is reconstructed [5]. The synthesized heterostructures were examined using the aberration corrected high-resolution transmission electron microscopy (Cs-HRTEM) and the electron backscatter diffraction (EBSD). The results reveal that copper deposited by a laser pulse on the (0 0 0 1) α -Al₂O₃ surface

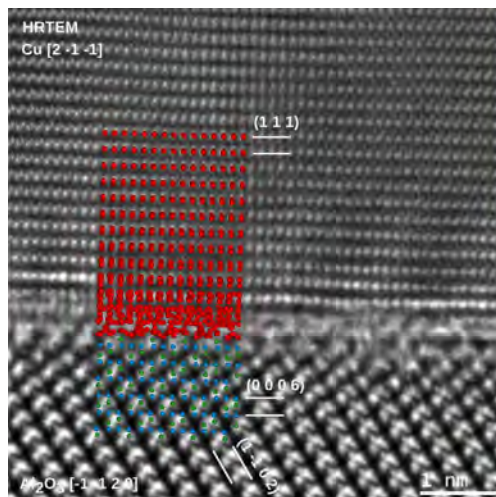


Fig. 1. Atomistic reconstruction (Cu, Al, and O atoms are denoted by red, green and blue spheres, respectively) compared with Cs-HRTEM image.

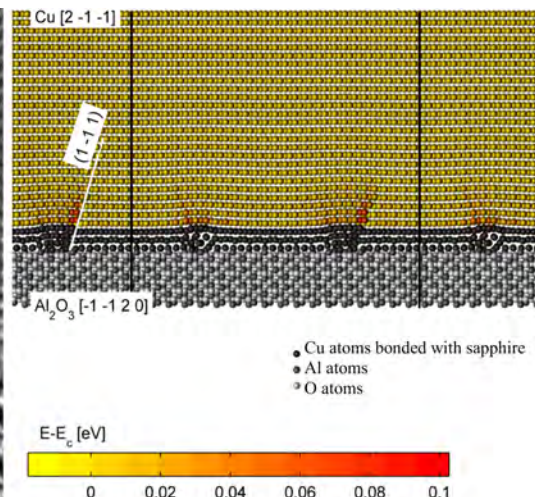


Fig. 2. Distribution of energy changes relative to the equilibrium state per atom in the copper section with the thickness 8 Å.

forms islands (the Volmer-Weber growth type) with one main orientation. In the preferred arrangement, the close packed planes and directions of copper are parallel to their equivalents in sapphire: $(1\ 1\ 1)[-1\ 0\ 1]\text{Cu} \parallel (0\ 0\ 0\ 1)[0\ 1\ -1\ 0]\alpha\text{-Al}_2\text{O}_3$. This gives an opportunity to form a strong bonding at the phase boundary. EBSD studies showed that the identified disorientation is also characteristic for copper matrix composites reinforced by sapphire particles. The strong bonding between Cu and $\alpha\text{-Al}_2\text{O}_3$ induces structural changes in the $(1\ 1\ 1)$ Cu layer nearest the substrate and leads to plastic deformations in subsequent layers (Fig. 1, 2). In consequence, the Cu/ $\alpha\text{-Al}_2\text{O}_3$ interface becomes the semi-coherent system. The lattice matching regions of the individual Cu layers are significantly lowered, which results in formation of the system of partially dissociated dislocations in the close packed planes $\{1\ -1\ 1\}$. The reconstructed interface is used for Cs-HRTEM image simulation. A good accordance with the experimental results indicates that the proposed model correctly maps the microstructure at the phase boundary of the synthesized nanocomposite.

The reconstruction is obtained by Molecular Dynamic and Static (MD and MS) simulations under the assumption that the sapphire substrate is rigid, while the copper undergoes deformations according to the model of interatomic interactions by A.F. Voter [6]. The interatomic potential is specified by a new method which is based on symmetry of considered material (S-B method) [7, 8]. According to the proposed approach, in the equilibrium state, the cohesive energy and eigenvalues of the elasticity tensor \mathbf{C} predicted by the model are consistent with the experimental data. Additionally, the pressure in the crystal should amount to zero. The derived conditions take a simpler form than those proposed in the literature thanks to double application of material symmetry: at the continuum and atomistic level. At the first of them, symmetry determines the spectral decomposition of the elasticity tensor, which enables to formulate the initial form of parameterization relationships. The obtained conditions undergo further simplifications at the atomistic level due to application of orthogonality relations in the point group of the considered crystal. The proposed specification method enables us to assess accuracy with which a model reproduces arbitrary processes of small strains. It is shown that errors in eigenvalues of the tensor \mathbf{C} constitute extreme values of errors with which a model predicts energy densities stored during elastic deformations. Formulated S-B conditions are used to specify the Voter model. The obtained potential more accurately reproduces processes of small strains (Fig. 3) and the key paths of large deformations [7]. At the end perspectives of further research on the strength of the Cu/ $\alpha\text{-Al}_2\text{O}_3$ interface are discussed.

References

1. K. Nalepka, R.B. Peçherski, T. Fraś, M. Nowak (2014). Inelastic flow and failure of metallic solids. Material effort: study across scales, in: T. Łodygowski, A. Rusinek (eds.), *Constitutive Relations under Impact Loadings. Experiments, Theoretical and Numerical Aspects*, CISM International Centre for Mechanical Sciences, vol. 552, Udine, 245–285.
2. R.B. Peçherski (1983). Relation of microscopic observations to constitutive modelling of advanced deformations and fracture initiation of viscoplastic materials, *Archives of Mechanics*, **35**, 257–277.
3. R.B. Peçherski (1998). Macroscopic effects of micro-shear banding in plasticity of metals, *Acta Mechanica*, **131**, 203–224.
4. K. Nalepka, R.B. Peçherski (2009). Modelling of the interatomic interactions in the Copper crystal applied in the structure $(111)\text{Cu} \parallel (0001)\text{Al}_2\text{O}_3$, *Archives of Metallurgy and Materials*, **54**, 511–522.
5. K. Nalepka, J. Hoffman, S. Kret, P. Nalepka, Z. Szymanski (2014). *Applied Physics A*, DOI: 10.1007/s00339-014-8317-3, in press.
6. Y. Mishin, M.J. Mehl, D.A. Papaconstantopoulos, A.F. Voter, J.D. Kress (2001). *Physical Review B*, **63**, 224106.
7. K. Nalepka (2012). *Computational Materials Science*, **56**, 100–107.
8. K. Nalepka (2013). *Bulletin of the Polish Academy of Sciences: Technical Sciences*, **61**, 441–450.

RECENT IMPROVEMENTS IN MIXED/ENHANCED SHELL ELEMENTS WITH DRILLING ROTATION

K. Wiśniewski¹, E. Turska²

¹Institute of Fundamental Technological Research, Warsaw, Poland

²Polish Japanese Institute of Information Technology, Warsaw, Poland

1. Introduction

The purpose of the presentation is to summarize features of our recent formulation of mixed/enhanced four-node shell elements based on the Hu-Washizu (HW) functional *with* rotational degrees of freedom and illustrate their numerical performance [1–5].

The drilling rotation, defined as the rotation about the shell director, is not naturally present in the shell equations derived from the non-polar Cauchy continuum for the Reissner hypothesis and Green strain. To alleviate this restriction, we consider the *extended configuration* space, consisting of the deformation $\chi \in R^3$ and rotations $\mathbf{Q} \in SO(3)$ subjected to the Rotation Constraint (RC) equation $skew(\mathbf{Q}^T \mathbf{F}) = \mathbf{0}$, where $\mathbf{F} = \nabla \chi$. For shells, \mathbf{Q} is reduced to the rotation at the reference surface \mathbf{Q}_0 and only the drilling component (12) of the RC equation, $[skew(\mathbf{Q}_0^T \mathbf{F})]_{12} = 0$, is used. This approach enables us to use standard constitutive equations for shells; in contrast to the Cosserat-type shells, which also use the drilling rotation but need specialized constitutive equations.

2. Shell pure HW functional with rotations

Mixed finite elements were pioneered by Pian in 1964 and a lot of work has been done since then to improve their theoretical foundations and performance. In the class of four-node elements, the best seem to be the ones based on the three-field Hu-Washizu (HW) functional; they exhibit a higher accuracy of displacements and stresses and significantly better convergence properties in non-linear problems than other elements, such as the enhanced strain (EAS or EADG) elements.

Our formulation is based on the 2nd Piola-Kirchhoff stress \mathbf{S} and the Green strain $\mathbf{E}(\mathbf{u}) = \frac{1}{2}(\mathbf{F}^T \mathbf{F} - \mathbf{I})$. For 3D formulation, the Lagrange multiplier method is used to append the RC equation to the HW functional,

$$(1) F_{\text{HW}}(\mathbf{u}, \mathbf{Q}, \mathbf{S}^*, \mathbf{E}^*, \mathbf{T}^*) = \int_{\mathbf{v}} \{W(\mathbf{E}^*) + \mathbf{S}^* \cdot [\mathbf{E}(\mathbf{u}) - \mathbf{E}^*] + \mathbf{T}^* \cdot skew(\mathbf{Q}^T \mathbf{F})\} dV - F_{\text{ext}},$$

where $W(\mathbf{E}^*)$ is the strain energy expressed by the independent strain \mathbf{E}^* , and \mathbf{S}^* is the independent stress which serves as the Lagrange multiplier for the difference of strains \mathbf{E}^* and $\mathbf{E}(\mathbf{u})$. Besides, \mathbf{T}^* is the skew-symmetric Lagrange multiplier for the RC equation $skew(\mathbf{Q}^T \mathbf{F}) = \mathbf{0}$.

To derive the HW functional for shells, we use the Reissner shell kinematics,

$$(2) \quad \mathbf{x}(\zeta) = \mathbf{x}_0 + \zeta \mathbf{Q}_0 \mathbf{t}_3, \quad \zeta \in [-1, +1],$$

where \mathbf{x}_0 is a position of the reference surface and \mathbf{t}_3 is the shell director. The rotation of the reference surface \mathbf{Q}_0 is parameterized by the canonical rotation vector. For this kinematics, the Green strain linearized in ζ becomes $\mathbf{E}(\zeta) \approx \boldsymbol{\varepsilon} + \zeta \boldsymbol{\kappa}$. Let us also assume

the independent strain in the analogous form, $\mathbf{E}^*(\zeta) \approx \boldsymbol{\varepsilon}^* + \zeta \boldsymbol{\kappa}^*$. Then, by integration of the HW functional of Eq. (1) over the shell thickness, we obtain its shell counterpart,

$$(3) \quad F_{\text{HW}}^{\text{sh}} = \int_{\mathbf{A}} \{W^{\text{sh}}(\boldsymbol{\varepsilon}^*, \boldsymbol{\kappa}^*) + \mathbf{N}^* \cdot [\boldsymbol{\varepsilon}(\mathbf{u}, \mathbf{Q}_0) - \boldsymbol{\varepsilon}^*] + \mathbf{M}^* \cdot [\boldsymbol{\kappa}(\mathbf{u}, \mathbf{Q}_0) - \boldsymbol{\kappa}^*] + F_{\text{RC}}^{\text{drill}}\} dA - F_{\text{ext}}^{\text{sh}},$$

where \mathbf{N}^* and \mathbf{M}^* are defined as the integrals of \mathbf{S}^* and $\zeta \mathbf{S}^*$ over the shell thickness, and \mathbf{A} is the area of the shell reference surface. The drilling RC part is used in the Perturbed Lagrange (PL) form,

$$(4) \quad F_{\text{RC}}^{\text{drill}} = T^* [\text{skew}(\mathbf{Q}_0^{\text{T}} \mathbf{F})]_{12} - (1/2\gamma)(T^*)^2$$

where T^* is the (scalar) Lagrange multiplier and $\gamma \in (0, \infty)$ is the regularization parameter. Note that seven fields ($\mathbf{u}, \mathbf{Q}_0, \mathbf{N}^*, \mathbf{M}^*, \boldsymbol{\varepsilon}^*, \boldsymbol{\kappa}^*, T^*$) are used in $F_{\text{HW}}^{\text{sh}}$. This methodology yields pure shell HW functional, the shell element for which performs very well but requires a large number of parameters and so is not efficient.

3. Shell partial HW functionals with rotations

In an alternative approach, we derive the shell HW functional differently. First, the 3D potential energy functional is integrated, to obtain its shell counterpart

$$(5) \quad F_{\text{PE}}^{\text{sh}} = \int_{\mathbf{A}} W^{\text{sh}}(\boldsymbol{\varepsilon}, \boldsymbol{\kappa}) dA - F_{\text{ext}}^{\text{sh}}.$$

Then, we construct the *partial* shell HW functional for selected strain components only while still using the potential energy functional for the other components. The so-derived functionals can be used to select the “optimal” formulation, which ensures the required numerical performance using a minimum number of parameters. For instance, in the HW29 shell element, we use the HW functional only for the 0-th order strain components $\varepsilon_{\alpha\beta}$ and $\varepsilon_{\alpha 3}$ ($\alpha, \beta = 1, 2$),

$$(6) \quad F_{\text{HW}}^{\text{sh}} = \int_{\mathbf{A}} \{W^{\text{sh}}(\varepsilon_{\alpha\beta}^*, \varepsilon_{\alpha 3}^*, \kappa_{\alpha\beta}) + N_{\alpha\beta}^* [\varepsilon_{\alpha\beta} - \varepsilon_{\alpha\beta}^*] + N_{\alpha 3}^* [\varepsilon_{\alpha 3} - \varepsilon_{\alpha 3}^*] + F_{\text{RC}}^{\text{drill}}\} dA - F_{\text{ext}}^{\text{sh}}.$$

Using such a methodology, we have developed several mixed/enhanced shell elements based on the Hu-Washizu functional *with* rotational degrees of freedom, [1–4]. Numerical examples will illustrate various aspects of their performance, such as: accuracy, radius of convergence, required number of iterations of the Newton method or the arc-length method and time of computations. Additionally, examples enabling comparisons with our new HW elements using only translational degrees of freedom will be provided.

References

1. K. Wiśniewski, E. Turska (2012). Four-node mixed Hu-Washizu shell element with drilling rotation, *Int. J. Num. Meth. Engng*, **90**, 506–536.
2. K. Wiśniewski (2010). *Finite Rotation Shells. Basic Equations and Finite Elements for Reissner Kinematics*, CIMNE-Springer.
3. K. Wiśniewski, W. Wagner, E. Turska, F. Gruttmann (2010). Four-node Hu-Washizu elements based on skew coordinates and contravariant assumed strain, *Computers & Structures*, **88**, 1278–1284.
4. K. Wiśniewski, E. Turska (2009). Improved four-node Hu-Washizu elements based on skew coordinates, *Computers & Structures*, **87**, 407–424.
5. K. Wiśniewski, E. Turska (2006). Enhanced Allman quadrilateral for finite drilling rotations, *Comp. Meth. Appl. Mech. Engng.*, **195**, 44–47, 6086–6109.

DEFORMATION OF DYNAMICALLY PHASE TRANSFORMING METALS IN ADIABATIC CONDITIONS: THERMAL EFFECTS AND INSTABILITIES

R. Zaera¹, J. A. Rodríguez-Martínez¹, G. Vadillo¹, J. Fernández-Sáez¹, D. Rittel²,
A. Rusinek³, R. Pesci⁴, S. Osovski⁵, T. Cohen⁶

¹Dept. of Continuum Mechanics and Structural Analysis, University Carlos III of Madrid, Spain

²Faculty of Mechanical Engineering, Technion, Israel

³LaBPS, National Engineering School of Metz (ENIM), France

⁴LEM3, ENSAM-Arts et Métiers ParisTech, France

⁵Materials Science and Engineering, University of North Texas, USA

⁶ Department of Mechanical Engineering, MIT, USA

1. Effects of adiabatic heating and microstructural evolution in plastic localization and energy absorption

Energy absorption is a relevant discipline in many industries like automotive, aircraft, rail transportation or marine engineering. In these industrial sectors structural elements, specifically designed to undergo plastic deformation, are used for energy absorption applications. To gain knowledge in the energy absorption behavior of ductile materials is crucial in design of structures potentially subjected to accidental impact and collision.

Most energy absorbers are usually made up of metallic materials that: (1) keep a high value of the stress upon deformation and (2) show a large value of strain at failure. This second requirement is strongly dependent on the onset of plastic localization which triggers material failure. Although localization and fracture are essentially different events, the first one is an early indication of ultimate structural failure and therefore it is commonly used as a reference for evaluating the energy absorption capacity.

In order to delay localization, materials with a high strain hardening are preferred for energy-absorption applications. Among the metallic materials having these specific features, steel grades showing Strain Induced Martensitic Transformation (SIMT) are widely used for energy absorption under dynamic solicitations. Their ability to transform from the initial face-centered cubic austenite phase γ to body-centered cubic martensite α' during plastic deformation is comparable to a dynamic composite effect and causes a remarkable hardening. Multiphase Transformation Induced Plasticity (TRIP) steels and metastable austenitic grades are representative examples of steels exhibiting SIMT. Martensitic transformation kinetics is strongly influenced by temperature; as the temperature rises due to the dissipation of plastic work and the release of latent heat upon martensitic nucleation, austenite stability increases thereby limiting the transformation. Therefore a strong coupling is expected to exist between SIMT hardening and temperature softening in these alloys. Both SIMT hardening and thermal softening are key features in the initiation of plastic instabilities.

Together with phase transformation, Dynamic Recrystallization (DRX), a process in which nucleation and growth of new strain-free grains replace the deformed microstructure, is a relevant microstructural evolution phenomenon which takes place in a wide variety of metals and alloys (such as OFHC copper or Ti6Al4V) upon plastic deformation. DRX softens the material thus having a strong influence in the onset of plastic instabilities, as pointed out by Osovski *et al.* [1]. Similarly to SIMT alloys, recrystallization releases latent heat that has to be considered as a source of temperature increase.

Within this context, we show here our recent contributions to the analysis of the role of microstructural and thermal effects on the localization of plastic deformation in dynamically deforming solids. Two different modeling methodologies are used: linear stability technique and finite element simulations, both of them accounting for the essential features of adiabatic heating, and hardening or softening induced by microstructural transformation processes. The different heat sources involved in the temperature increase of the material have been considered. These are the latent heat released due to the exothermic character of the microstructural transformation and the dissipation of plastic work. The analysis sheds light on experimental results available in the literature reporting unusual (greater than one) values for the Taylor–Quinney coefficient [2].

The study covers a wide range of key loading states representative of dynamic applications: necking [3–6], perforation [7], cavitation phenomena [8] and shear. This permits to identify the conditions (both loading type and rate), for which the microstructural or thermal effects may either contribute or decrease the capacity of the material to dissipate energy.

Acknowledgments

The authors from the University Carlos III of Madrid are indebted to the Ministerio de Ciencia e Innovación de España (Projects DPI/2011-24068 and DPI/2011-23191) for the financial support.

References

1. S. Osovski, D. Rittel, A. Venkert (2013). The respective influence of microstructural and thermal softening on adiabatic shear localization, *Mech. Mater.*, **56**, 11–22.
2. R. Zaera, J.A. Rodríguez-Martínez, D. Rittel (2013). On the Taylor-Quinney coefficient in dynamically phase transforming materials. Application to 304 stainless steel, *Int. J. Plasticity*, **40**, 185–201.
3. R. Zaera, J.A. Rodríguez-Martínez, A. Casado, J. Fernández-Sáez, A. Rusinek, R. Pesci (2012). A constitutive model for analyzing martensite formation in austenitic steels deforming at high strain rates, *Int. J. Plasticity*, **29**, 77–101.
4. R. Zaera, J.A. Rodríguez-Martínez, G. Vadillo, J. Fernández-Sáez (2014). Dynamic necking in materials with strain induced martensitic transformation, *J. Mech. Phys. Solids*, **64**, 316–337.
5. J.A. Rodríguez-Martínez, D. Rittel, R. Zaera, S. Osovski (2013). Finite element analysis of AISI 304 steel sheets subjected to dynamic tension: the effects of martensitic transformation and plastic strain development on flow localization, *Int. J. Impact Engng.*, **53**, 206–216.
6. J.A. Rodríguez-Martínez, G. Vadillo, R. Zaera, J. Fernández-Sáez, D. Rittel (2014). An analysis of microstructural and thermal softening effects in dynamic necking, *Mech. Mater.*, in press.
7. J.A. Rodríguez-Martínez, A. Rusinek, R. Pesci, R. Zaera (2013). Experimental and numerical analysis of the martensitic transformation in AISI 304 steel sheets subjected to perforation by conical and hemispherical projectiles, *Int. J. Solids Struct.*, **50**, 339–351.
8. J.A. Rodríguez-Martínez, T. Cohen, R. Zaera (2014). Approaching steady cavitation: the time scale in hypervelocity cavity expansion in work hardening and transformation hardening solids, (submitted to *Int. J. Impact. Engng.*).

Session

**Computational Aspects
of
Solid Mechanics**

REVIEW OF HYPERELASTIC MATERIAL USE IN DAMPER AT SUB-ZERO TEMPERATURES

D. Dębski, P. Żach

Warsaw University of Technology, Institute of Machine Design Fundamentals, Poland

The undesirable result in the suspension systems of machines is the phenomenon of curvilinear wheel movement, which is the consequence of the so called ‘shimmy effect’, which is consequential to the occurrence of the self-induced vibrations in vehicle movement groups, perpendicular to the direction of its movement. The movement line of a wheel has a sinusoidal shape in relation to the movement line of the whole vehicle. This phenomenon occurs in airplanes (vibrations of self-setting undercarriage front and rear wheels during take-off, landing and taxiing), motorbikes and bicycles (oscillation of the front suspension by the axle head frame) and in cars (vibrations of the front suspension). The self-induced, shimmy type vibrations occur in the stabilization and free(slow)-variable conditions. Polymers can be in one of the following three physical states depending on their temperature: glassy, elastic or plastic. The physical and mechanical properties of these materials are related to each of these phases. Property changes such as stiffness, viscosity, hardness, etc occur during the transition of the polymer from one state to another.

The dependence of polymer relaxation time t to the temperature dependence is expressed by (1):

$$(1) \quad t = t_0 \left(\frac{\Delta H}{RT} \right),$$

where: t_0 – characteristic time constant for a given material, ΔH – initial process of enthalpy, R – universal gas constant.

The relaxation times are small in the range of the glass transition temperature and melting temperature values, and that’s why the decaying warp time is short. Above the material’s flow temperature T_f , when $RT = \Delta H$ (in accordance to formula (1)), the relaxation times tend to zero.

Based on the research results by Williams, Landel and Ferry [1], the relativity between the output polymer viscosity, η and temperature, T is (2):

$$(2) \quad \ln \left(\frac{\eta}{\eta_{T_g}} \right) = \frac{-C_1(T - T_g)}{C_2 + (T - T_g)}$$

where: η_{T_g} – viscosity of the glass transition temperature T_g , T – process temperature [K], C_1 , C_2 – specific constants to a particular polymer.

The temperature also affects body deformation. It usually causes a change of volume and the appropriate corresponding coordinates of tensor deformation in a thermally isotropic material is given by the formula (3):

$$(3) \quad \varepsilon_{ij}^T = \alpha_T T \delta_{ij}$$

where: α_T is the coefficient of thermal expansion, T – temperature increase, δ_{ij} – a change in length relative to initial length.

The following experimental studies of viscoelastic structures have been made in order to assess the effect of plastic temperature on machinery teams: segmented polyurethane Epunit elastomer, made by a team of Dr Eng. Anna Boczkowska, in the Institutional Research Program of Warsaw University of Technology in 2006, which was attended by two teams from the Institute of Mechanical Engineering and Department of Materials

Science and Engineering (Dr. Eng. Anna Boczkowska) under the direct supervision of Prof. Eng. Jerzy Osiński [2] and terpolimer EPDM (ethylene-propylene-diene).

Phenomenas occurring in materials during labor will be the response to coercion with external force, which was described by the nonlinear equation in general form (4):

$$(4) \quad Q(t) = m\ddot{x} + K_n(x, \dot{x}, T).$$

Considering that K_n is a function describing coupled nonlinear elasticity and damping, equation (4) can be written in the form (5):

$$(5) \quad Q(t) = m\ddot{x} + C(x, \dot{x}, T) + K(x, \dot{x}, T).$$

An additional program was developed for compression test simulation, in which approximations of nonlinear functions are received in equation (6), using polynomials – coefficients damping $C_{01} \div C_{06}$ and $C_1 \div C_6$ and elasticity coefficients $k_1 \div k_6$ are entered as data. Hysteresis loop is determined. The coefficients C_{0n} , C_n and k_n are variables until the cancellation of the surface area of the loop obtained from experimental studies. The analysis is performed in real time thereby allowing the observation of the impact of the individual components of formula (6) curve. The value of the area, limited with field curves which has become a criterion for model fitting, is also calculated.

$$(6) \quad my''[t] + \frac{1}{2}(C_{01}y'[t]) \left(1 + \text{Sign} \left[t - \frac{t_k}{2}\right]\right) + (C_{02}y'[t]^2) \left(1 + \frac{1}{2}\text{Sign} \left[t - \frac{t_k}{2}\right]\right) \\ + \frac{1}{2}(C_{03}y'[t]^3) \left(1 + \text{Sign} \left[t - \frac{t_k}{2}\right]\right) + \frac{1}{2}(C_{04}y'[t]^4) \left(1 + \text{Sign} \left[t - \frac{t_k}{2}\right]\right) \\ + \frac{1}{2}(C_{05}y'[t]^5) \left(1 + \text{Sign} \left[t - \frac{t_k}{2}\right]\right) + \frac{1}{2}(C_{06}y'[t]^6) \left(1 + \text{Sign} \left[t - \frac{t_k}{2}\right]\right) \\ + C_1y'[t] + C_2y'[t]^2 + C_3y'[t]^3 + C_4y'[t]^4 + C_5y'[t]^5 + C_6y'[t]^6 \\ + k_1y[t] + k_2y[t]^2 + k_3y[t]^3 + k_4y[t]^4 + k_5y[t]^5 + k_6y[t]^6 = F \sin \left[\frac{\pi t}{t_k}\right]$$

where: m – mass of analyzed sample, C_n , C_{0n} , k_n – material constants, t_k – final time, Sign – zero function.

Numerical calculations were made using a package of programs designed for mathematical calculations like MATHEMATICA v. 7.0. Making use of ready-made application to determine the estimated size of the Epunit 2 and Epunit 3 materials deformation energy for different strains (30%, 40% and 50%) and EPDM thermopolymers – the field is contained between the curves describing the hysteresis loop.

The aim of this article is to develop a selective method of a hyper-deformable material for use in a self-induced, shimmy type damper vibration in the chassis (undercarriage) of a small airplane. The specification of this system makes sure that the damper works in all possible weather conditions during operation. This means there is need for it to be able to operate efficiently in Poland where temperature reaches -30°C . It is our goal to use an appropriate material whose properties are able to change at the lowest degree of temperature changes. The selection was accomplished after research of several materials properties. The non-linear description way of hyper-deformable damping materials was also proposed.

References

1. J. D. Ferry (1980). *Viscoelastic Properties of Polymers*, John Wiley, New York.
2. A. Boczkowska, K. Babski, J. Osiński, P. Żach (2008). Modeling of characteristics at compression and functional properties of hyperelastic polyurethane materials applied in mechanical engineering, *Polimery*, **53**, 554–550.

THIRD-ORDER ELASTIC COEFFICIENTS AND LOGARITHMIC STRAIN IN FINITE ELEMENT MODELLING OF ANISOTROPIC ELASTICITY

P. Dłużewski, M. Maździarz, P. Tazowski

Institute of Fundamental Technological Research, Pawińskiego 5B, 02-106 Warszawa, Poland

1. Introduction

Contrary to higher order elastic constants for momentum stresses the second (classical) and third-order elastic coefficients (TOEC) for symmetric elasticity are measured and tabulated successfully with good accuracy for tens of years. In the classical experimental measurements of TOEC, the correct recalculation of instantaneous stiffness changes onto TOEC has an important role. A similar problem arises in the constitutive and finite element (FE) modelling. Namely, because of a very strong dependency of TOEC on the strain measure choice, the constitutive and FE modelling of elastic materials is considered here in terms of different finite strain measures. To this aim, the known analytical formulae for calculation of two first derivatives of the isotropic tensor function of tensor variable are verified by means of the finite difference method. In result, the revised formulae are used for calculation of the tangent stiffness matrix. This paper closes with some remarks on the use of TOEC in finite element modelling.

2. Third-order elastic coefficients

TOEC are often determined from ab-initio calculation as well as by measurement the effect of stress on the ultrasonic wave speeds in crystals. Usually, the coefficients are determined in relation to the Green strain [1, 4, 3]. Assume the following strain energy function for elastic material

$$(1) \quad \psi(\hat{\varepsilon}) = \frac{1}{\hat{\rho}} \left[\frac{1}{2!} \hat{c}_{\dot{y}kl} \hat{\varepsilon}^{\dot{y}} \hat{\varepsilon}^{kl} + \frac{1}{3!} \hat{C}_{\dot{y}klmn} \hat{\varepsilon}^{\dot{y}} \hat{\varepsilon}^{kl} \hat{\varepsilon}^{mn} \right],$$

where \hat{c} and \hat{C} are tensors of the second- and third-order elastic coefficients determined in relation to a given strain measure; $\hat{\rho}$ is the mass density in the reference configuration. Each of strain measures from the Seth-Hill family can be recalculated to another one from the same family, according to the transformation rule

$$(2) \quad \hat{\varepsilon}'(\hat{\varepsilon}) = \begin{cases} \frac{1}{m'} [(m\hat{\varepsilon} + \mathbf{1})^{m'/m} - \mathbf{1}] & \text{for } m \neq 0 \wedge m' \neq 0, \\ \frac{1}{m'} [\exp(m'\varepsilon) - \mathbf{1}] & \text{for } m = 0 \wedge m' \neq 0, \\ \frac{1}{m} \ln(m\hat{\varepsilon} + \mathbf{1}) & \text{for } m \neq 0 \wedge m' = 0, \end{cases}$$

where m is the real number taking a role of an additional elastic constant. For fixed second-order elastic coefficients the instantaneous stiffness of anisotropic Hookeans in the relaxed configuration is invariant with respect to the choice of the finite strain measure. Contrary to that, TOEC corresponding to the given instantaneous stiffness curve depend very strongly on the strain measure choice. In other words, two experimenters measuring the same instantaneous stiffness change under loading can determine two dramatically different sets of TOEC dependently on the strain measure used. Simultaneously, both of

them can speak on quite the same change of instantaneous stiffness under loading. In order to hold the same instantaneous stiffness evolution in vicinity of the relaxed state, TOEC must be recalculated to the equivalent values corresponding to the strain measure used, for the Seth-Hill strain measures the formula for recalculation takes form

$$(3) \quad \widehat{C}'_{ijklmn} = \widehat{C}_{ijklmn} + (m - m') [\mathcal{J}_{ijkl}{}^{\infty} \hat{c}_{\infty mn} + \mathcal{J}_{klmn}{}^{\infty} \hat{c}_{\infty ij} + \mathcal{J}_{mnij}{}^{\infty} \hat{c}_{\infty kl}],$$

where \mathcal{J} is the sixth-order proper-symmetric unit tensor. As an example, consider the instantaneous stiffness changes for silicon crystal originally recalculated onto TOEC for Green strain by Johal and Dunstan [3], see Table 1 for $m = 2$. The second-order elastic coefficients were $c_{11} = 166$, $c_{12} = 64$, $c_{44} = 80$ GPa. The mentioned TOEC have been recalculated here onto equivalent ones that refer to the Biot and logarithmic strain measures, see rows 3 and 4. Additionally, in the last row the strain measure has been chosen in such a way to get a Hookean material for which the second-order bulk modulus vanishes.

Table 1. Third-order elastic coefficients [GPa] for silicon related to different strain measures.

m	\widehat{C}_{111}	\widehat{C}_{112}	\widehat{C}_{123}	\widehat{C}_{144}	\widehat{C}_{155}	\widehat{C}_{456}	$\partial\widehat{B}/\partial\hat{\varepsilon}$
2	-815	-450	-75	16	-307	-82	-1124
1	-317	-386	-75	48	-170	-22	-928
0	181	-322	-75	80	-32	38	-544
-2.155	1254	-184	-75	149	266	167	0

Acknowledgments

This research is supported by the project N N519 647640 founded by the Polish Ministry of Science and Higher Education.

References

1. K. Brugger (1964). Thermodynamic definition of higher order elastic coefficients, *Physical Review*, **133**, 6A, 1611–1612.
2. P. Dłużewski (2000). Anisotropic hyperelasticity based upon general strain measures, *Journal of Elasticity*, **60**, 2, 119–129.
3. A.S. Johal, D.J. Dunstan (2006). Reappraisal of experimental values of third-order elastic constants of some cubic semiconductors and metals, *Physical Review B*, **73**, 024106.
4. R.N. Thurston, K. Brugger (1964). Third-order elastic constants and the velocity of small amplitude elastic waves in homogeneously stressed media, *Physical Review*, **133**, 6A, 1604–1610.

INTEGRATED LASER BEAM WELDED STRUCTURES FOR AIRCRAFT APPLICATIONS: MANUFACTURING, WEIGHT SAVING AND TESTING ASPECTS

A. Gialos¹, V. Zeimpekis¹, N. D. Alexopoulos¹, S. Riekehr², N. Kashaev²

¹University of the Aegean, Department of Financial and Management Engineering
Chios Island, Greece

²Helmholtz-Zentrum Geesthacht, Institute of Materials Research, Materials Mechanics
Geesthacht, Germany

1. Introduction

Due to their high stiffness-to-weight and strength-to-weight ratios, aluminum alloys have been the dominant aircraft materials for many decades. In order to compete the decreasing tendency of Al usage in aero structures (in contrary to composites), aluminum alloy producers are making a huge effort in developing lighter and more weldable alloys. Aluminum sheet manufacturers develop materials that could compete with composites and try to maintain their dominant position among the aircraft materials. They have now focused all their attention in lithium containing aluminum alloys, not only because weight can be saved, but also because weldability of Al-Cu and Al-Zn alloys can be improved. These alloys can be welded, thus eliminating thousands of rivets resulting in a lighter and stronger integral structure. They offer lower density than conventional aluminium alloys and direct weight reduction of about 5%. The improved property balance i.e. corrosion resistance, fatigue [1], fatigue crack growth rate, strength and toughness, allows further weight reduction up to 20% through adapted design, and reduction of aircraft maintenance costs as well [2, 3].

In the present work, the target was to compare in principle T joint as well as a typical four-stringer aircraft structure manufactured with LBW process and innovative aluminum alloys against a structure manufactured with the riveting process and conventional aluminum alloys. Various parameters of the above fostered technologies were compared and explicitly discussed. The environmental (carbon) footprint of the two structures was calculated in order to assess the “greenness” of the two technologies that assure a sustainable life cycle of the final product. A series of parameters was investigated: (a) the carbon footprint and the energy consumption of manufacturing process, (b) the operating materials, and (c) all sorts of produced waste. The GHG emissions were calculated for each activity, and the relevant global warming potential (GWP) factors were used to convert them to CO₂ emissions.

2. Manufacturing

Laser beam welding process is adopted for the aluminum alloys to manufacture (a) T-joint configuration AA2198 as skin and AA2196 as stringer as well as (b) butt joint configuration AA2198 with AA2198 for the realization of future fuselage structures. T-joints and butt joints with optimal process configuration are produced and the effect of different process parameters is examined on the microstructure, tensile, fatigue and fracture toughness properties of the welded specimens, Fig. 1.

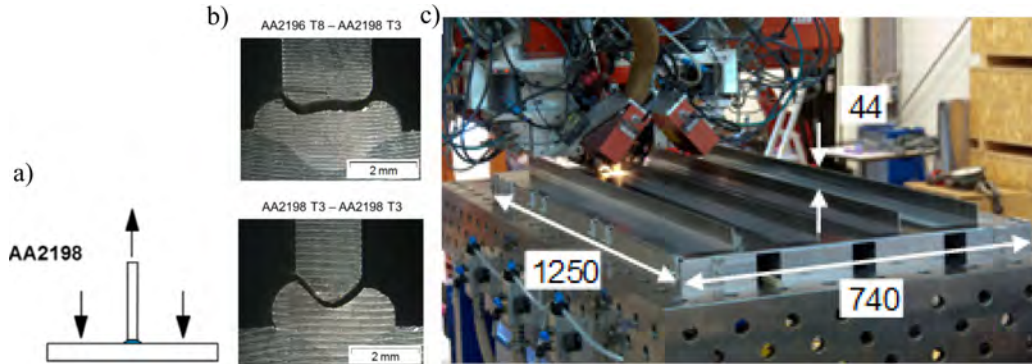


Fig. 1. a) Typical sketch of the pull-out test, b) microstructure results of the pull-out tests [4] and c) welded demonstrator panel manufactured at HZG from aluminum alloy AA2198.

3. Comparison between the two processes

The main goal of this work is to directly compare the two manufacturing processes in terms of mechanical properties, weight, manufacturing cost, lead processing time and CO₂ equivalent emissions. Preliminary results showed that calculated weight saving is essential; when using innovative Al-Li alloys and LBW process, the weight saving exceeds 22% when compared to the conventional riveted manufacturing process with conventional aluminum alloys, e.g. 2024. For the consideration of a serial production of one such a four-stringer demonstrator, total process time is essentially shortened by approximately 15%. However, calculated manufacturing costs showed that such an LBW demonstrator seems to cost more than double when compared to the riveted one. Finally, the carbon footprint of the LBW demonstrator was calculated to be 49% lower than the respective riveted demonstrator.

Acknowledgments

The authors gratefully acknowledge the financial support of the European Union (Clean Sky EU-JTI Platform) under the thematic call: JTI-CS-2013-1-ECO-065 “Extrapolation and technical and economic study of a Laser Beam Welding technology” (Grant Agreement No: 620091).

References

1. N.D. Alexopoulos, E. Migklis, A. Stylianos, D.P. Myriounis (2013). Fatigue behavior of the aeronautical Al-Li (2198) aluminum alloy under constant amplitude loading, *Int. J. Fatigue*, **56**, 95–105.
2. J. Montgomery (July 2007). Aircraft primary structure and materials, *National Institute of Aerospace Workshop, Revolutionary Aircraft for Quiet Communities*, Hampton, VA.
3. J.C. Williams, E.A. Starke (2003), Progress in structural materials for aerospace systems, *Acta Materialia*, **51**, 5775–5799.
4. J. Enz, S. Riekehr, V. Ventzke, N. Kashaev, N. Huber (2012). Prozessoptimierung fuer das Laserstrahlsschweißen von hochfesten Aluminium-Lithium-Legierungen, *Schweißen und Schneiden*, **64**, 482–485.

ANALYTICAL SOLUTION OF AN ELASTIC-PLASTIC WEDGE SUBJECTED TO UNIFORM SHEAR ON ITS FACE

G. Hénap, L. Szabó

Department of Applied Mechanics, Budapest University of Technology and Economics
H-1111 Budapest, Műegyetem rkp. 5., Hungary

1. Introduction

Analytical solutions for elastic-plastic infinite wedges were first proposed by Naghdi et. al. The complete plane-strain solution is given in [1] for Tresca's and Mises' yield criteria assuming incompressible material and uniform pressure on one edge. This was later extended for compressible material using Tresca's yield criterion [2]. The solution for uniform surface traction has been discussed by Murch and Naghdi [3]. The plane stress case for uniform pressure was proposed by Kachanov [4] then the complete solution for Mises' yield criterion was published by Kalnins [5].

The aim of this work is to present a new closed form analytical elastic-plastic solution for an infinite wedge subjected to uniform shear on its face. Plane stress condition and Mises' yield criterion are considered. This solution can be useful to validate numerical methods (e.g. finite element method). Besides the formulation of the equations, the clarity of the results are also important for practical applications. The comparison of the analytical results with the numerical solution is also presented.

2. Solution of the problem

The outline of the problem is seen in Fig. 1. The angle of the wedge is 90 degree. Depending on the magnitude of the traction one or two plastic zones emerge. It is more convenient to use polar system since the stress and strain components only depend on the tangential coordinate.

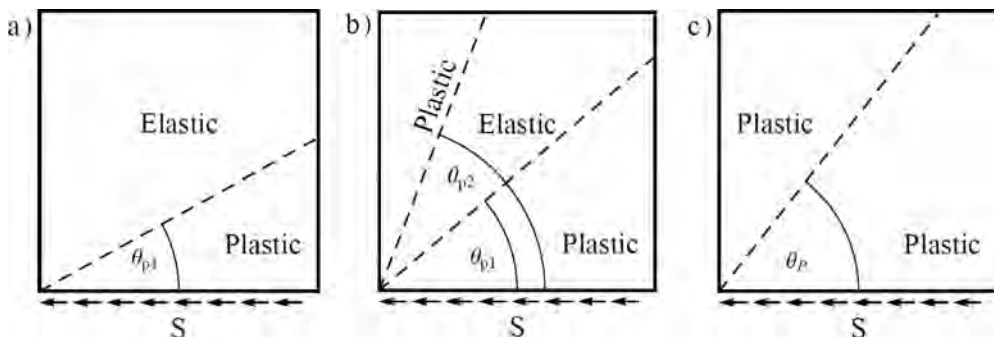


Fig. 1. Model of the infinite wedge, the loading parameter $\xi = S/\sigma_Y$: a) $0.4276 < \xi < 0.5184$, b) $0.5184 < \xi < 0.5503$, c) $\xi = 0.5503$.

Using the yield condition and the equilibrium equation the differential equation of the tangential stress in the plastic domain is:

$$(1) \quad \sigma_\theta''^2 + 2\sigma_\theta\sigma_\theta'' + 3\sigma_\theta'^2 + 4\sigma_\theta^2 - 4\sigma_Y^2 = 0,$$

which has the solution in form

$$(2) \quad \sigma_\theta(\theta) = \frac{3\sigma_Y}{2\sqrt{2}}C_1 - \frac{\sigma_Y\sqrt{8-9C_1^2}}{2\sqrt{6}}\sin(2\theta + 2C_2),$$

where σ_Y is the yield stress. The radial and shear stress components are obtainable from the equilibrium equations and the integration constants are determined from the boundary conditions. Using the Prandtl-Reuss equations the strain rates can be expressed by

$$(3) \quad \dot{\epsilon}_r = \frac{1}{E}(\dot{\sigma}_r - \nu\dot{\sigma}_\theta) + \dot{\lambda}s_r, \quad \dot{\epsilon}_\theta = \frac{1}{E}(\dot{\sigma}_\theta - \nu\dot{\sigma}_r) + \dot{\lambda}s_\theta,$$

where according to the compatibility equation

$$(4) \quad \dot{\lambda} = \dot{L}_1(\xi) + \dot{L}_2(\xi)G(\xi, \theta),$$

where

$$(5) \quad G(\xi, \theta) = \frac{\ln \left[\frac{-3\xi + \sqrt{2+3\xi^2} + \sqrt{1-3\xi^2} \tan(\theta)}{3\xi + \sqrt{2+3\xi^2} - \sqrt{1-3\xi^2} \tan(\theta)} \right]}{4\sqrt{2+3\xi^2}}.$$

In order to identify the unknown functions \dot{L}_1 and \dot{L}_2 it is necessary to express the displacement rates [6] that have the form

$$(6) \quad \begin{aligned} \dot{u}_r &= r\dot{\epsilon}_r + K_2 \cos \theta - K_1 \sin \theta, \\ \dot{u}_\theta &= \int r(\dot{\epsilon}_\theta - \dot{\epsilon}_r)d\theta - K_1 \cos \theta - K_2 \sin \theta + K_3r - \psi(\dot{L}_2). \end{aligned}$$

Along the elastic-plastic boundary, the values of the stress and strain fields computed from the elastic and plastic domain are equal. Using this condition $\dot{\lambda}$ is given, therefore the strain components in (3) can be integrated.

References

1. P.M. Naghdi (1957). Stresses and Displacements in an Elastic-Plastic Wedge, *J. Appl. Mech.*, **79**, 98–104.
2. D.R. Bland, P.M. Naghdi (1958). A Compressible Elastic, Perfectly Plastic Wedge, *J. Appl. Mech.*, **25**, 239–242.
3. S.A. Murch, P.M. Naghdi (1958). On the Infinite Elastic, Perfectly Plastic Wedge Under Uniform Surface Traction, *Proc. 3rd U.S. Nat. Congr. Appl. Mech.*, 611–624.
4. L.M. Kachanov (1957). Elastic-Plastic Equilibrium of a Wedge in Plane Stress State, *Prikl. Math. Mekh.*, **21**, 413–418.
5. A. Kalnins (1959). On Plane Stress Solution of a Compressible Wedge With the Use of Mises' Yield Condition, *J. Appl. Mech.*, **26**, 676–678.
6. J. Chakrabarty (2006). *Theory of Plasticity*, 3rd ed. Elsevier, United Kingdom.

ON RECURSIVE STRATEGIES FOR INVERSE FORM FINDING IN METAL FORMING APPLICATIONS

P. Landkammer, P. Steinmann

Chair of Applied Mechanics, University of Erlangen-Nuremberg, Germany

1. Introduction

The presentation is concerned with the problem of inverse form finding which aims to determine the optimal initial configuration of a workpiece, see Fig. 1a. In this case the desired end configuration that is obtained after a forming process, the boundary conditions and the applied loads are known, see Fig. 1b. Inputting the optimal initial configuration a subsequent FEM computation then has to result in exactly the desired deformed configuration. The equivalent stresses and strains occurring in the computed end configuration are additionally depicted in Fig. 1c and 1d.

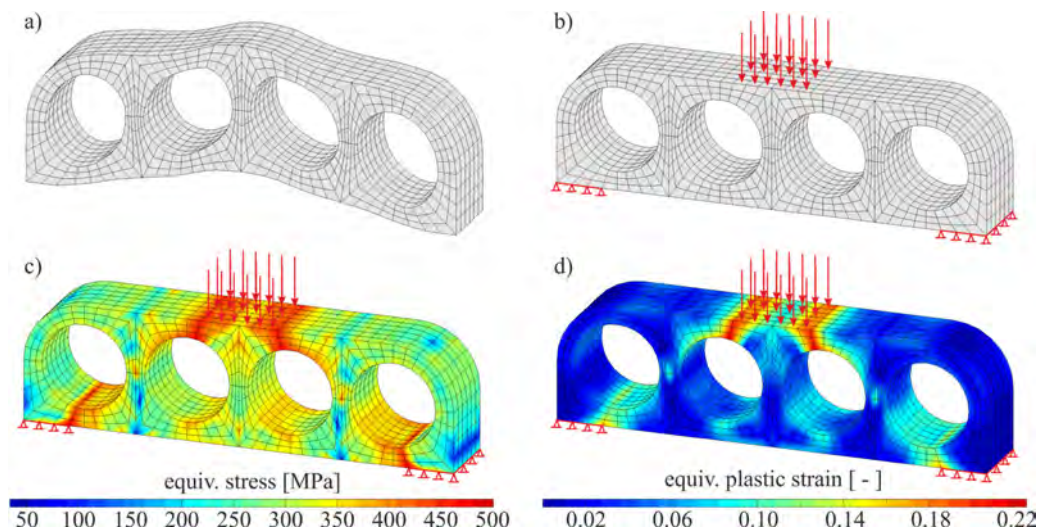


Fig. 1. An example of an optimal initial configuration of a workpiece which results in exactly the desired end configuration after the forming simulation.

Knowing the optimal blank design of a workpiece for a given forming process saves time and costs for experiments. Inverse form finding is therefore of special interest for metal forming applications.

2. Recursive strategies for inverse form finding

On the one hand there exist recursive strategies for solving the form finding problem by pure geometrical considerations. In the context of sheet metal forming Kim *et al.* [1] for example takes the difference between the computed and the desired end configuration into account. In a similar way this is also applicable to three dimensional models in bulk metal forming processes. The benefit of these geometrical approaches is the simple adaptability to commercial software by subroutine procedures.

On the other hand Germain *et al.* [2] presented a new form finding strategy for isotropic elasto-plasticity. The corresponding algorithm uses the inverse mechanical formulation which is also denoted as inverse finite element method. This method formulates the mechanical weak form with respect to the nodal positions of the end configuration as proposed by Govindjee and Mihalic [3]. Switching between the inverse and the common direct mechanical formulation, while fixing the internal plastic variables in the inverse step, uniquely detects the optimal undeformed configuration iteratively. Landkammer *et al.* [4] and [5] recently presented an extension of this approach to combinations of orthotropic elasto-plasticity. The benefit of using this new algorithm is the stability and the efficiency in contrast to pure geometrical approaches. Even for examples with large plastic strains only a few iterations are required to detect an appropriate initial configuration.

3. Conclusion

In this presentation different strategies for solving the inverse form finding problem in elasto-plasticity are introduced. Within examples of metal forming applications the efficiency and convenience of these two recursive approaches are compared to each other.

Acknowledgment

The authors are grateful to the German Research Foundation (DFG) for supporting the investigations in the project “*Manufacturing of complex functional components by using a new metal forming process – Sheet-Bulk metal forming*” (SFB/TR73: <http://www.tr-73.de>).

References

1. J.-Y. Kim, N. Kim, M.-S. Huh (2000). Optimal blank design of an automobile sub-frame, *Journal of Materials Processing Technology*, **101**, 31–41.
2. S. Germain, P. Landkammer, P. Steinmann (2013). On a recursive formulation for solving inverse form finding problems in isotropic elastoplasticity, *Advanced Modelling in Simulation and Science (AMSES)*, submitted.
3. S. Govindjee, P.-A. Mihalic (1996). Computational methods for inverse finite elastostatics, *Comp. Meth. Appl. Mech. Engrg.*, **136**, 47–57.
4. P. Landkammer, S. Germain, P. Steinmann (2013). On inverse form finding for orthotropic plasticity, *Computer Assisted Methods in Engineering and Science (CAMES)*, accepted.
5. P. Landkammer, S. Germain, P. Steinmann (2014). Optimum blank design by using the FEM based on inverse motion in orthotropic elasto-plasticity, *Proceedings in Applied Mathematics and Mechanics (PAMM)*, submitted.

FINITE ELEMENT MODELLING OF ELASTOHYDRODYNAMIC LUBRICATION IN THE FINITE DEFORMATION REGIME

J. Lengiewicz, P. Sadowski, S. Stupkiewicz

Institute of Fundamental Technological Research, Warsaw, Poland

1. Introduction

In a variety of tribological systems, hydrodynamic lubrication is coupled with the large deformation of one or both contacting bodies. Contact problems of this kind are called soft elastohydrodynamic lubrication (soft-EHL) problems, and can be applied to analysis of elastomeric seals, various biotribological systems, and others.

In the modelling of hydrodynamic lubrication, the necessity to properly incorporate the cavitation phenomenon poses difficulties because the cavitation boundary is a part of the solution (free-boundary problem). The problem appears even more demanding if severe nonlinearities due to elastohydrodynamic coupling are additionally included. Fully coupled formulation for this class of problems, suitable for monolithic solution scheme in a FE framework, has been recently developed in [1, 2]. However, the analysis was only limited to two dimensional case, and the simple penalty method was used to enforce the mass-conservation condition only in approximate manner, see [3] for more detailed discussion.

2. Finite element treatment of the model

In this work, a mixed, two-field formulation of the mass-conserving cavitation model is developed, which is equivalent to the classical JFO theory. The two-field formulation is preserved in the consistently derived weak form, and is expressed in terms of the hydrodynamic pressure and a complementary variable λ related to the lubricant density. The corresponding complementarity condition is enforced using a non-smooth constraint function. This approach is similar to the augmented Lagrangian method [4] and primal-dual active set strategy [5]. The final discretized problem is solved for both variables in a monolithic scheme, using a semi-smooth Newton method.

3. Numerical examples

Several examples have been analyzed within this work. The convergence behavior and other properties of the proposed method have been checked, with the use of simple two-dimensional benchmark tests, cf. e.g., Fig. 1.

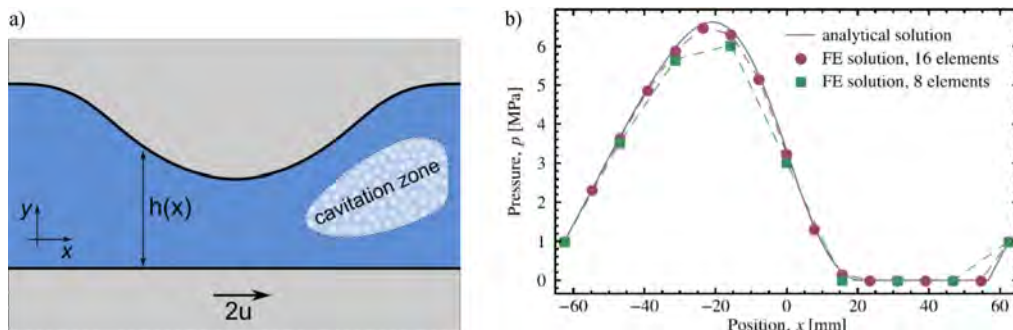


Fig. 1. EHL problem: a) 2D schematic and b) pressure field for simple 2D benchmark test.

One computationally demanding three-dimensional soft-EHL problem has also been analyzed, in which a hyperelastic ball is slid over a rigid flat. The proposed model proved to be suitable for a particular mesh refinement technique (hanging-node technique) used in the zones of high pressure gradients. The distribution of the lubricant film thickness, contact pressure, and void fraction in the cavitation zone is shown in Fig. 2. A characteristic ridge, seen in the film-thickness plots, i.e., Figs. 2a and 3a, is in a qualitative agreement with experimental observations, e.g., [6]. The analysis of the overall friction coefficient, for different velocities and different loads, cf. Fig. 3b, shows the effect of drop of the friction coefficient with increasing load.

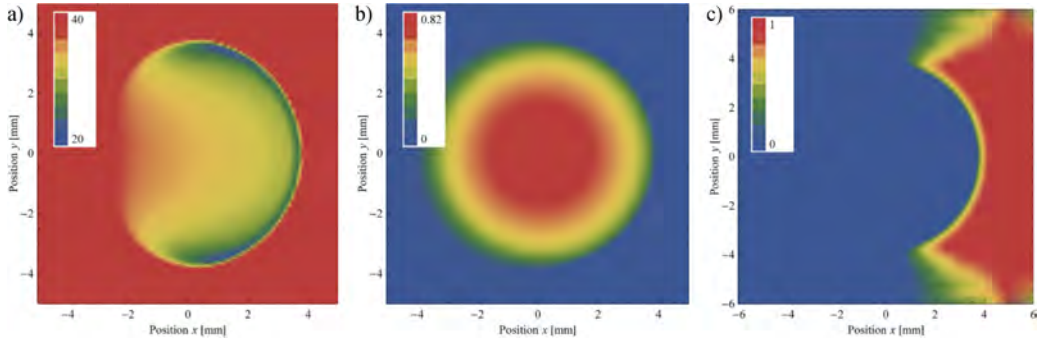


Fig. 2. Maps of: a) film thickness h [μm], b) pressure p [MPa], and c) complementary variable λ , obtained for $u = 400$ mm/s. In Fig. c, the region of $\lambda > 0$ constitutes the cavitation zone.

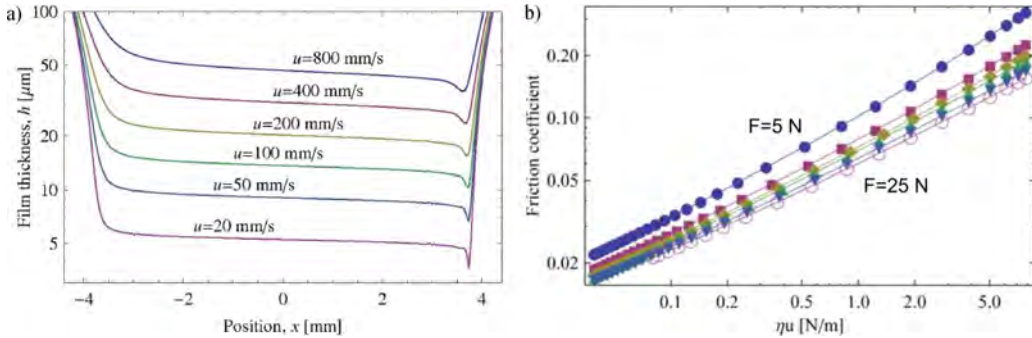


Fig. 3. 3D soft-EHL problem: a) film thickness at $y = 0$ cross-section for load $F = 13$ N for different velocities u , and b) friction coefficient for different velocities and different normal loads.

References

1. S. Stupkiewicz, A. Marcinişzyn (2009). Elastohydrodynamic lubrication and finite configuration changes in reciprocating elastomeric seals, *Tribol. Int.*, **42**, 615–627.
2. S. Stupkiewicz (2009). Finite element treatment of soft elastohydrodynamic lubrication problems in the finite deformation regime, *Comp. Mech.*, **44**, 605–619.
3. J. Lengiewicz, M. Wichrowski, S. Stupkiewicz (2014). Mixed formulation and finite element treatment of the mass-conserving cavitation model, *Tribol. Int.*, **72**, 143–155.
4. P. Alart, A. Curnier (1991). A mixed formulation for frictional contact problems prone to Newton like solution methods, *Comp. Meth. Appl. Mech. Engrg.*, **92**, 353–375.
5. M. Hintermueller, K. Ito, K. Kunisch (2003). The primal-dual active set strategy as a semismooth Newton method, *SIAM J. Optim.*, **13**, 865–888.
6. L. Mourier, D. Mazuyer, A.A. Lubrecht, C. Donnet (2006). Transient increase of film thickness in micro-textured EHL contacts, *Tribol. Int.*, **39**, 1745–1756.

NUMERICAL INVESTIGATION OF INFLUENCE OF FRICTION ON STRAIN
DISTRIBUTION AND FORMING LIMIT CURVE
IN NAKAZIMA FORMABILITY TEST

D. Lumelsky¹, J. Rojek¹, R. Pęcherski¹, F. Grosman², M. Tkocz²

¹Institute of Fundamental Technological Research, Warsaw, Poland

²Silesian University of Technology, Krasinskiego 8, 40-019 Katowice, Poland

1. Introduction

This paper presents numerical investigations of the influence of friction in the contact between sheet and a punch on sheet deformation in Nakazima type formability tests. The Nakazima test [1] is one of the most commonly used tests to study experimentally formability of metal sheets. It consists in stretching of a sheet specimen by means of a hemispherical punch until occurrence of fracture.

Friction, affecting strain paths in a tested specimen, is usually undesired phenomenon in formability tests, therefore different measures are taken to reduce friction. In the Nakazima tests, either oil, grease or polymer foils should be used as lubricant systems [1]. Tribological conditions should be adjusted so that fracture occurs within a distance less than 15% of the punch diameter away from the apex of the dome. The failure location is very sensitive to friction. Even small increase of friction displaces the location of fracture [2].

The aim of this study has been to numerically identify frictional conditions in a selected case of the Nakazima test and study numerically effect of change of friction on forming limit curve (FLC). Numerical simulations have been performed assuming the data corresponding to own laboratory tests carried out for the steel grade HC380LA 1.5 mm thick.

2. Numerical investigation of influence of friction on strain distribution and FLC

Numerical analyses have been performed using the authors' own computer explicit dynamic finite element program. Sheet was discretized with a linear shell triangular elements BST [3]. The material has been considered assuming the Hill'48 model. The tools have been modelled as rigid bodies whose surfaces has been discretized with triangular facets. Frictional contact between the tool and sheet has been treated using the Coulomb model of friction. Deformation process has been analyzed under prescribed motion of the punch. Strain distribution obtained in numerical simulations for circular specimens and various friction conditions are compared with experimental results on the forming limit diagram in Fig. 1. A good agreement between numerical predictions and experimental data can be easily seen.

Influence of friction on forming limits has been studied numerically using specimens with different width which allows us to receive the full range of conditions needed to build a FLC. The results in the form of numerically determined FLC along with strain paths are shown in Fig. 2. The fracture localization was obtained by post-processing time histories of major and minor strains and their first and second derivatives. A peak of the major strain acceleration in the failure zone determined the onset of localized fracture. With the increase of friction strain path deflects toward the plain strain from equibiaxial and uniaxial tension strain state. The increase in friction causes the narrowing of the area of possible deformations of the material.

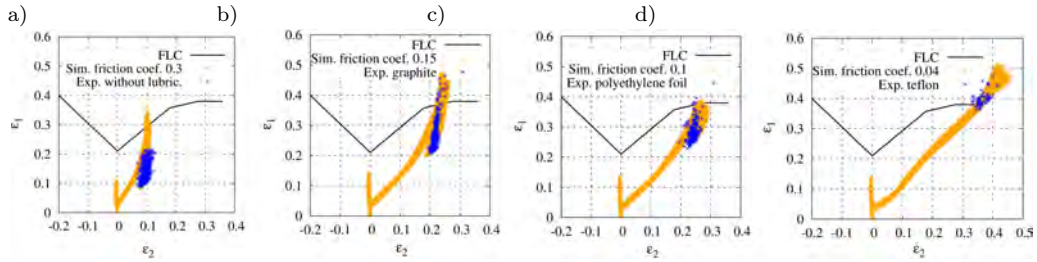


Fig. 1. Strain path in circular specimen obtained numerically in bulging test under different friction conditions: a) without a lubricant, b) graphite, c) a polymer film, d) Teflon.

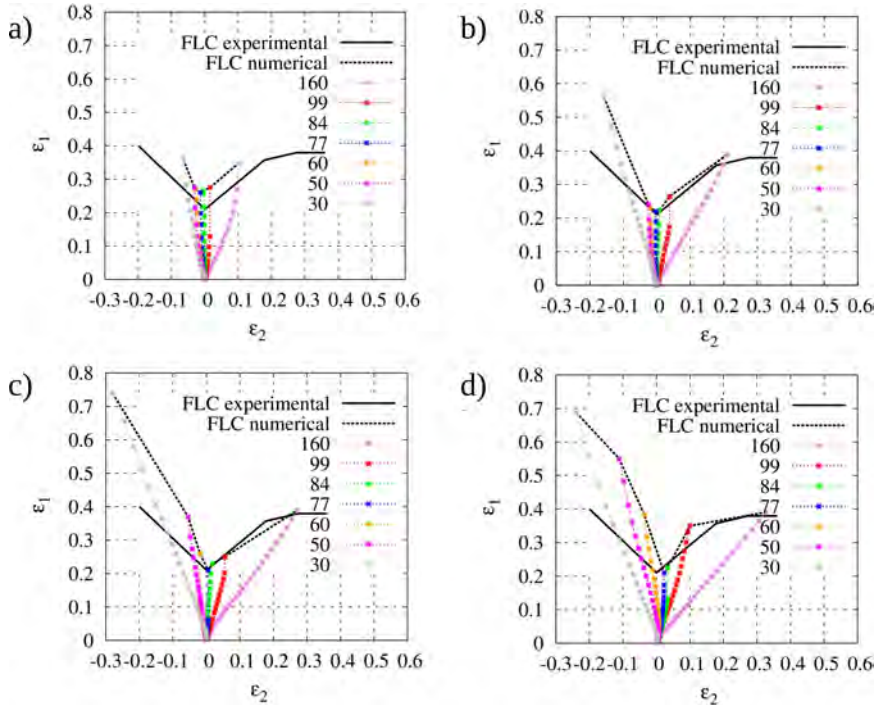


Fig. 2. Comparison of strain distribution in circular specimen obtained numerically and experimentally in bulging test under different tribological conditions: a) without a lubricant, b) graphite, c) a polymer film, d) Teflon.

Acknowledgments

The authors acknowledge funding from: (1) European Regional Development Fund within the framework of the Innovative Economy Program, project number POIG.01.0 3.01-14-209/09, acronym NUMPRESS, (2) National Science Centre through research project No. 2311/B/ T02/2011/406.

References

- ISO 1200 4-2 (2008). Metallic materials – Sheet and strip – Determination of forming-limit curves. Part 2: Determination of forming-limit curves in the laboratory.
- Larsson M., Mattiasson K., Sigvant M. (2007). Some observations on failure prediction in sheet metal forming, *Proc. 6th European LS-DYNA Users' Conf.*, 5.93-5.102.
- Rojek J., Oñate E. (1999). Sheet springback analysis using a simple shell triangle with translational degrees of freedom only, *Int. Journal of Forming Processes*, **1**, 75–296.

METAL CUP DEEP DRAWING PROCESSES – NUMERICAL SIMULATION AND EXPERIMENTAL VERIFICATION

Z. Nowak¹, F. Grosman², D. Lumelskyy¹, M. Nowak¹, R.B. Pęcherski¹,
J. Rojek¹, M. Tkocz²

¹Institute of Fundamental Technological Research, Polish Academy of Sciences, Warsaw, Poland

²Silesian University of Technology, Katowice, Poland

1. Introduction

Finite element method is an efficient numerical tool to analyse problems of the sheet metal forming processes in particular cup drawing and stamping. Proper description of material properties is crucial for accurate analysis. In particular, the anisotropy and asymmetry of elastic range, which is related with strength differential effect (SDE), of considered materials play an important role in finite element simulation. For metal forming analysis with use of traditional models many experimental tests are usually needed to obtain the adequate description of anisotropic behaviour of metal sheets. Therefore, the search for new models, which are based on simplified description of the effects of anisotropy and SDE requiring less experimental tests seems to be justified.

The paper presents the application of a new yield criterion for the transversal isotropy of metal sheets under plane stress conditions. The proposed criterion is based on the study of yield criteria accounting for the SDE and anisotropy made by W. Burzyński [1]. The system of equations describing the sheet metal forming process is solved by the algorithm using the return mapping procedure. Plane stress constraint is incorporated into the Newton-Raphson iteration loop. The proposed algorithm is verified by performing the numerical calculations using shell elements of the commercial FEM software ABAQUS/EXPLICIT with own VUMAT subroutine. The Fig. 1 shows deformation of the square DP600 steel blank at the punch stroke 40 mm for the cup deep drawing with application of the proposed yield condition Eq. (1) with the isotropic power hardening law.

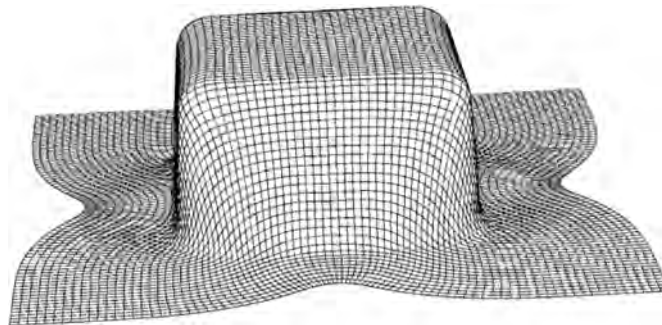


Fig. 1. Deformation of the square blank at the punch stroke 40 mm for the cup deep drawing.

2. Yield condition

To perform finite element simulations of cup deep drawing processes, three independent values of yield strength ($\sigma_Y^T, \sigma_Y^C, \tau_Y$) are required, which can be obtained from: the

uniaxial tensile test, uniaxial compression test and shear test. The proposed yield condition is based on the analysis of limit condition for transversally isotropic solids. In the case of plane stress state the yield condition takes the following form:

$$(1) \quad f = \frac{1}{2k_1} \left\{ 3(k_1 - 1)p + \sqrt{9(k_1 - 1)^2 p^2 + 4k_1 q^2} \right\} - \sigma_Y^T(\bar{\varepsilon}_p) = 0$$

where

$$p = \frac{\sigma_x + \sigma_y}{3}, \quad q = \sqrt{\sigma_x^2 + \sigma_y^2 + R_B \sigma_x \sigma_y + (2 - R_B) \sigma_{xy}^2}, \quad R_B = 2 - \frac{1}{k_1 k_2^2} - \frac{2}{k_2} + \frac{2}{k_1 k_2},$$

and $k_1 = \sigma_Y^C / \sigma_Y^T$, $k_2 = f(\sigma_Y^T, \sigma_Y^C, \tau_Y)$.

3. Cup deep drawing process

The aim of the paper is to simulate the metal cup deep drawing process and verify the computational results with own experimental data obtained in the laboratory of the co-authors from the Silesian University. Additionally, the independent calculations were performed with use of the known plasticity model, which is based on the anisotropy yield condition proposed by Hill in 1948. The model was implemented in finite element program NUMPRESS – EXPLICIT to perform the simulation of the discussed cup deep drawing process. The comparison and detail discussion of two sets of data obtained in both numerical simulations with the results of experimental observations of the same process and the results of measurement of the change of thickness of drawn cup along chosen paths leads to interesting conclusions regarding the possible applications of the proposed simplified model.

Acknowledgments

The research reported in the paper was partly obtained in the framework of the research project NUMPRESS carried out in IPPT PAN (Poland), co-funded by European Regional Development Fund grant nr: POIG.01.03.01-14-209/09.

References

1. W. Burzyński (2009). Selected passages from Włodzimierz Burzyński doctoral dissertation "Study on material effort hypotheses", *Engng. Trans.*, **57**, 3–4, 185–215, published originally in Polish: W. Burzyński (1928). Studium nad hipotezami wyciężenia, *Nakładem Akademii Nauk Technicznych*, 1–192, Lwów.

REGION OF HIGHER MISALIGNMENT IN CARBON FIBER REINFORCED POLYMERS AS AN INITIATOR FOR KINK BAND FORMATION

M. Romanowicz

Department of Mechanical Engineering, Bialystok University of Technology, Poland

1. Introduction

In order to study the post-critical response of fiber reinforced composites subjected to longitudinal compression, computational micromechanics usually uses models with an idealized uniform distribution of fiber waviness. Generally, there are two types of such models. In the first one, the longitudinal sides of model are free from constraints (see for example Ref. [1–2]). In the second one, periodic boundary conditions are prescribed on the longitudinal sides of model (see for example Ref. [3–4]). It is believed that the predictions of the first model should tend to the results obtained from the second model for a sufficiently large number of fibers. Unfortunately, a distinct difference in the deformation of the two models is observed. The free boundary conditions allow the deformation to localize along an antisymmetric band crossing the entire width of the model, provided that the geometry of fiber waviness is antisymmetric with respect to the longitudinal direction. On the contrary, the periodic boundary conditions force the deformation to be symmetric regardless of the geometry of fiber waviness. As a consequence of this, the model with free boundary conditions and uniform waviness can ensure a realistic inclination of kink bands, contrary to the periodic model with uniform waviness in which the kink-band angle is indirectly set to zero degree.

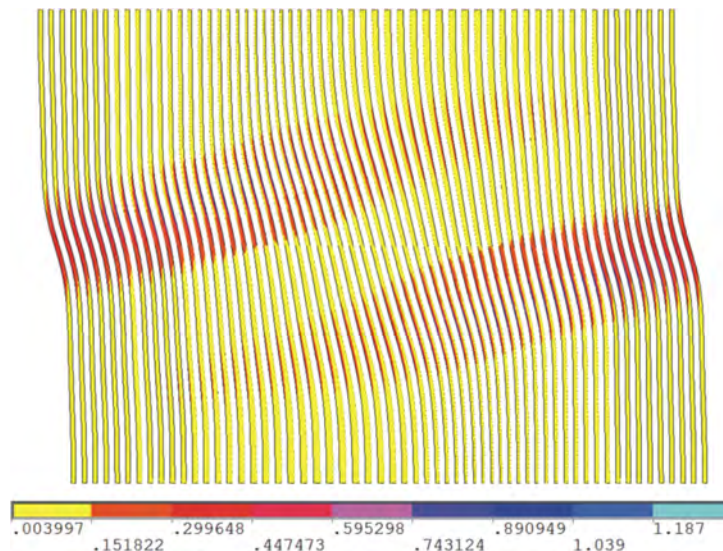


Fig. 1. Contour plot of the effective plastic strain in the matrix predicted from the model with centrally located imperfection at the post buckling stage of deformation.

2. Micromechanical model

The present work shows an alternative approach for predicting the compressive response of long fiber composites based on a periodic model with non-uniform waviness. The main novelty of this work lies in the fact that the mechanism of kink band formation at a finite region of fiber misalignment has been successfully modeled using the periodic model (Fig. 1). In particular, the proposed model correctly simulates the formation of inclined bands of bent fibers as a result of the interaction of local fiber instabilities and material nonlinearities. The most important feature of this model is that a stress concentration can develop only in the interior due to increasing amplitude of the fiber imperfection in contrast to existing models in which stress concentrations at free edges dominate. Comparison of such a model with those reported in the literature on compressive failure showed that it calculates the limit load equally well as the periodic model with uniform waviness and predicts the post-critical events equally well as the model with free edge boundary conditions. For more details on the proposed computational model, see Ref. [5].

Acknowledgments

The financial support of the National Science Centre of Poland under contract DEC-2011/03/D/ST8/04817 is acknowledged with thanks.

References

1. S. Kyriakides, R. Arseculeratne, E.J. Perry, K.M. Liechti (1995). On the compressive failure of fiber reinforced composites, *Int. J. Solids Struct.*, **32**, 689–738.
2. P. Prabhakar, A.M. Waas (2013). Interaction between kinking and splitting in the compressive failure of unidirectional fiber reinforced laminated composites, *Compos. Struct.*, **98**, 85–92.
3. E.G. Guynn, O.O. Ochoa, W.L. Bradley (1992). A parametric study of variables that affect fiber microbuckling initiation in composite laminates: Part I analyses, *J. Comp. Mater.*, **26**, 1594–1611.
4. R. Gutkin, S.T. Pinho, P. Robinson, P.T. Curtis (2010). Micro-mechanical modeling of shear-driven fibre compressive failure and of fibre kinking for failure envelope generation in CFRP laminates, *Compos. Sci. Technol.*, **70**, 1214–1222.
5. M. Romanowicz (2013). Initiation of kink bands from regions of higher misalignment in carbon fiber reinforced polymers, *J. Compos. Mater.*, doi:10.1177/0021998313498106.

RELATIONSHIPS BETWEEN MECHANICAL FRACTURE AND DURABILITY PARAMETERS OF SELECTED CONCRETES

H. Šimonová, D. Lehký, Z. Keršner, V. Veselý, J. Macur

Brno University of Technology, Faculty of Civil Engineering, Brno, Czech Republic

1. Introduction

Present research is aimed at the relationships between parameters of selected cement-based composites which describe their durability and which quantify the content of microcracks, the resistance to stable and unstable fracture propagation, respectively. Most attention is paid here to the concrete surface layer.

Permeability of the material which determines for example its transport properties is significantly related to the quality of the surface layer. The permeability of concrete with dense aggregate depends mainly on the porosity of cement paste structure and is affected, among others, by cracks wider than 10^{-4} m resulting from the process of concrete hardening. These cracks (microcracks) are being connected together under external loading of the investigated concrete structure and create major cracks causing a significant reduction of durability or even serious damage of the structure. The relation of the structural durability and the content of microcracks in the material (or the material's resistance against crack initiation and propagation) is therefore obvious.

2. Materials, specimens and fracture tests

Tests were conducted on four sets of specimens differing in the material. Concrete of each set of specimens was different in dosage of Portland cement CEM I 42.5 R. Reference mixture (marked as REF) contains 250 kg/m^3 of cement. The other mixtures, marked 0/1, 0/2 and 0/3, contain 305, 355 and 455 kg/m^3 of cement, respectively. Additional details regarding the concrete mixture compositions can be found in [1].

Beam specimens (of nominal dimensions $100 \times 100 \times 400 \text{ mm}$) with central notch on bottom edge were subjected to three-point bending (3PB) fracture tests. The notches were made with a diamond blade saw. The notches depths were approximately equal to 30% of the depth of the specimen. The span length was equal to 300 mm. Three specimens from each set were tested at the age of 28 days. The fracture tests were carried out using a Heckert FPZ 100/1 testing machine with the load range of 0–10 kN.

3. Results

Load versus displacement diagrams ($P-d$ diagrams) were recorded during the 3PB fracture experiments. Values of modulus of elasticity and parameters of the cohesive crack model (particularly the fracture energy and tensile strength) were identified from corrected $P-d$ diagrams [2] by inverse analysis using FraMePID-3PB software [3]. The cornerstone of the method is an artificial neural network which transfers the input data obtained from the fracture test to the desired material parameters.

Selected results obtained in the analysis are introduced in Table 1: Elasticity modulus E , fracture energy G_F , tensile strength f_t , compressive strength f_c ; these values are completed by the so called “durability parameters” – bond strength (by pull-off) f_h , resistance of cement concrete surface to water and defrosting chemicals (after 25 cycles)

ρ_a and depth of penetration of water under pressure d_w . Correlation matrix of all these parameters is presented in Table 2.

Table 1. Mean values (coefficients of variation in %) of selected parameters of concretes studied.

Parameter/Concrete	REF	0/1	0/2	0/3
E [GPa]	25.3 (9.6)	25.9 (6.8)	33.93 (-)	35.0 (11.4)
G_F [J/m ²]	155.1 (13.4)	174.2 (14.9)	153.7 (28.0)	133.9 (28.4)
f_t [MPa]	1.6 (3.4)	2.1 (4.5)	3.6 (9.0)	3.2 (8.5)
f_c [MPa]	21.4 (0.5)	33.3 (0.8)	44.9 (1.0)	55.6 (3.6)
f_h [MPa]	3.0 (5.6)	3.5 (8.9)	3.9 (12.6)	4.1 (9.2)
ρ_a [g/m ²]	125.3 (31.0)	53.3 (7.5)	54.3 (4.4)	66.5 (7.7)
d_w [mm]	98 (7.8)	34 (11.8)	35 (14.2)	24 (24.1)

Table 2. Correlation coefficients of selected parameters of concretes studied.

	E	G_F	f_t	f_c	f_h	ρ_a	d_w
E	1.00						
G_F	-0.75	1.00					
f_t	0.95	-0.51	1.00				
f_c	0.93	-0.64	0.88	1.00			
f_h	0.92	-0.54	0.92	0.99	1.00		
ρ_a	-0.51	-0.12	-0.68	-0.68	-0.77	1.00	
d_w	-0.67	0.15	-0.74	-0.85	-0.90	0.95	1.00

4. Conclusions

Mechanical fracture parameters obtained by identification from records of 3PB fracture test on concrete specimens with central edge notch were introduced in this paper. These parameters were accompanied with “durability parameters” and correlation coefficients of all these parameters values were presented.

Acknowledgment

This outcome has been achieved with the financial support of the Czech Science Foundation, project GA CR 13-18870S.

References

1. M. Matysík, L. Topolář, P. Daněk, T. Vymazal, I. Plšková (2014). The effect of concrete quality on the acoustic emission parameters during three-point bending fracture test, *Advanced Materials Research*, **897**, 149–152.
2. P. Frantík, J. Průša, Z. Keršner, J. Macur (2007). About stability loss during displacement-controlled loading, in: *Proceeding of International Conference on Fibre Concrete 2007*, Prague, ISBN 978-80-01-03740-9.
3. D. Lehký, Z. Keršner, D. Novák (2013). FraMePID-3PB software for material parameter identification using fracture tests and inverse analysis, *Advances in Engineering Software*, **63**, 1–8.

SLIP BANDS EVOLUTION DURING DISCONTINUOUS PLASTIC FLOW IN 304 AUSTENITIC STAINLESS STEELS AT LIQUID HELIUM TEMPERATURE (4.2 K)

J. Tabin, B. Skoczeń

Institute of Applied Mechanics, Faculty of Mechanical Engineering, Cracow University of Technology

1. Introduction

FCC metals and alloys belong to the group of engineering materials massively applied at cryogenic temperatures. These materials, loaded in such extreme conditions, often manifest discontinuous plastic flow (DPF). Complex nature of the flow instability that occurs at extremely low temperatures has been investigated by several authors, among them: Basinski (1957) [1], Obst and Nyilas (1991) [2], Zaiser and Hähner (1997) [3], Skoczeń (2013) [4]. Zaiser and Hähner attribute discontinuous nature of plastic flow at low temperatures to strain rate softening instabilities and point out similarities between the low temperature phenomena and the Portevin – Le Chatelier (PLC) effect that occurs at room temperature. A new physically based constitutive model of discontinuous plastic flow including the relevant thermodynamic background has been developed by Skoczeń et al. [4]. The DPF is described by the mechanism of local catastrophic failure of lattice barriers (for instance Lomer–Cottrell locks) under the stress fields related to the accumulating edge dislocations. The failure of LC locks leads to massive motion of released dislocations accompanied by stepwise increase of the strain rate. Therefore, the DPF appears in the stress-strain curve in the form of oscillations of stress against strain (the so-called serrations). Each serration is accompanied by considerable increase of temperature, related to dissipation of plastic power and the thermodynamic instability. Single serration shows usually similar pattern: after the initial elastic process, smooth plastic flow occurs until the abrupt drop of stress. For the austenitic steel, in the next stage the relaxation takes place, after which the beginning of elastic stage is immediately observed.

2. Experimental data

The measurements carried out at cryogenic temperatures require rather sophisticated equipment (Fig. 1) in order to obtain the correct experimental conditions and test results.

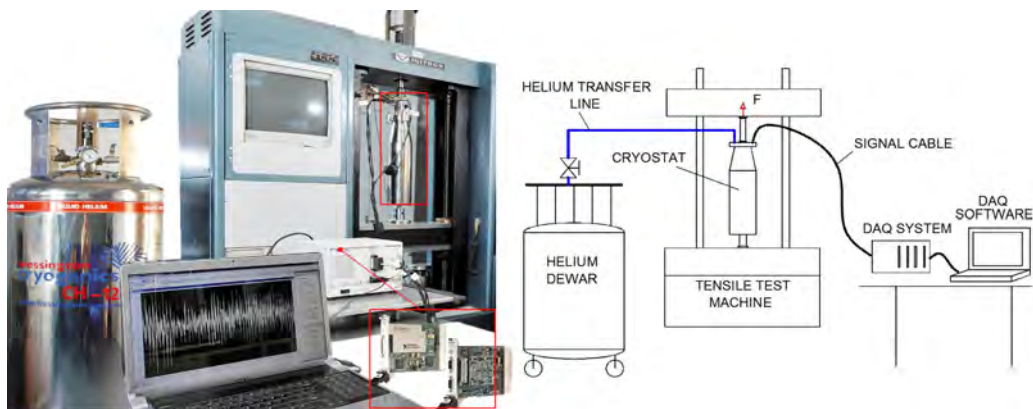


Fig. 1. Experimental set-up for testing the samples at extremely low temperatures.

The present paper is focused on the extension of physically based constitutive model of DPF (Skoczeń *et al.*, 2013) to include experimentally observed evolution of slip bands in the austenitic stainless steels (Fig. 2). Based on the own experimental data, collected during several campaigns of tensile tests carried out on stainless steel samples (304) immersed in liquid helium (4.2 K), it turns out that the generated slip bands move along the gauge part of the specimen (from grip to grip).

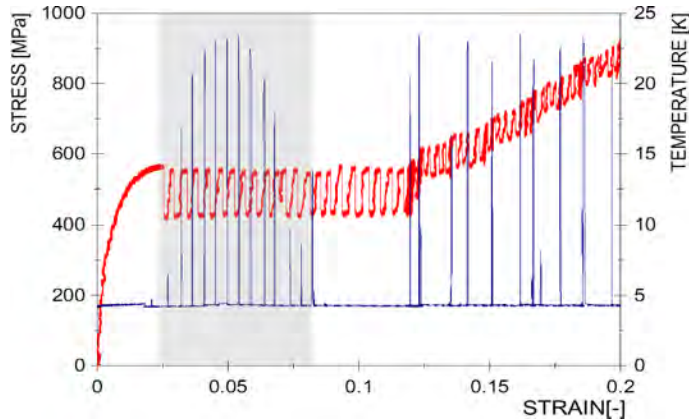


Fig. 2. Tensile test for 304. Stress-strain curve (red) accompanied by the temperature profile (blue). Experimental identification of slip bands evolution.

Previous models did not include the above mentioned phenomenon. Therefore, the basic idea of the updated model is associated with the assumption that RVE travels together with the slip band during the tensile test.

3. RVE based multi-axial constitutive model of DPF

New multi-axial constitutive model shows important feature of discontinuous plastic flow: the serrations may take place in two or three directions simultaneously. Moreover, the oscillations of temperature associated with serrations can be predicted by knowing the plastic power dissipated during the DPF and the thermodynamic properties of materials in the range of temperatures between absolute zero and T_0 or T_1 (material dependent). Thus, based on heat conduction equation, it is possible to obtain a correlation between the temperature oscillations, given fixed spatial position of the temperature sensor and travelling RVE associated with the slip band. These conclusions have rather fundamental meaning for thin-walled structures operating at extremely low temperatures like heat exchangers, corrugated expansion bellows or vacuum chambers.

Acknowledgments

Grant of Polish National Science Centre 2284/B/T02/2011/40 is gratefully acknowledged.

References

1. Basinski Z.S. (1957). The instability of plastic flow of metals at very low temperatures. *Proceeding of the Royal Society of London, Series A*, **240**, 229–242.
2. Obst B., Nyilas A. (1991). Experimental evidence on the dislocation mechanism of serrated yielding in f.c.c. metals and alloys at low temperatures, *Materials Science and Engineering*, **A137**, 141–150.
3. Hahn P., Zaiser M. (1997). From mesoscopic heterogeneity of slip to macroscopic fluctuations of stress and strain, *Acta Materialia*, **45**, 3, 1067–1075.
4. B. Skoczeń, J. Bielski, J. Tabin (2014). Multiaxial constitutive model of discontinuous plastic flow at cryogenic temperatures, *International Journal of Plasticity*, **55**, 198–218.

STRESS-BASED FINITE ELEMENT METHOD FOR NEARLY INCOMPRESSIBLE AND INCOMPRESSIBLE MATERIALS

Z. Więckowski, E. Misztalska

Łódź University of Technology, Łódź, Poland

1. Problem description

The finite element method (FEM) is a major tool in computational mechanics among many other numerical methods. Due to different choices of main unknowns, there are three basic approaches to FEM: displacement-based, stress-based and mixed methods. The displacement FE model is the most widely used and extensively developed, because of its versatility as well as its easiness in computational implementation. The mixed interpolation approach has also been employed successfully while the stress-based formulation is presented rather rarely. This paper puts forward the application of the stress-based FEM in the analysis of nearly incompressible and incompressible materials. It is well known that the displacement formulation based on the minimum principle of potential energy functional performs poorly in the case of material incompressibility. In this model, for three dimensional and plane strain problems when Poisson's ratio approaches number 0.5, the common multiplier in the elasticity matrix goes to infinity which makes the displacement formulation of FEM not applicable. The case of Poisson's ratio close to 0.5 leads to an ill-conditioned system of equations. Obtaining the accurate solution is possible but requires much finer element mesh than in a comparable analysis of a compressible material. These types of numerical difficulties can be avoided by the use of the mixed method (e.g. [1]) and are not encountered in the stress-based formulation of FEM, but the last approach has been very seldom presented in literature. In the present paper, the stress-based FE model is employed. The statically admissible stress field is constructed by means of a stress function which is approximated with the help of finite elements of class C^1 . The stress boundary conditions are satisfied using the Lagrange multiplier method.

2. Example

An elastic body subjected to the plane strain state is considered. The body has a rectangular cross-section with dimensions $2 \text{ m} \times 1 \text{ m}$. The body is subjected to normal inward load distributed uniformly on the upper surface with magnitude of 1 MPa, and for $x \in [0, 0.5] \text{ m}$ and $x \in [1.5, 2.0] \text{ m}$ on the lower surface with magnitude of 2 MPa, where x denotes the horizontal coordinate axis. The following data has been applied in the computations: Young's modulus, $E = 1 \text{ GPa}$, Poisson's ratio, $\nu = 0.4999$.

Two types of stress-based elements have been used in computations: the triangular (HCT) element introduced by Hsieh, Clough and Tocher and the rectangular (BFS) one by Bogner, Fox and Schmit [3]. The obtained results have been compared with those obtained by the use of the mixed ($u-p$) method where the displacement field is approximated inside an element region with polynomials of the second order while the average normal stress (the pressure) with the linear function. Four sets of computational meshes with various sizes of elements ($h = 0.5, 0.25, 0.125$ and 0.0625 m) have been utilized to check the rate of convergence of the methods. In Figure 1, a map of the normal horizontal stress component is shown for the left half of the computational region. The results related to the mesh with $h = 0.25 \text{ m}$ are depicted in the figure. It is seen that the field of stress component σ_{xx} obtained by the use of HCT element is much smoother (smaller discontinuities are observed on elements' edges) than that gained by the mixed $u-p$ method.

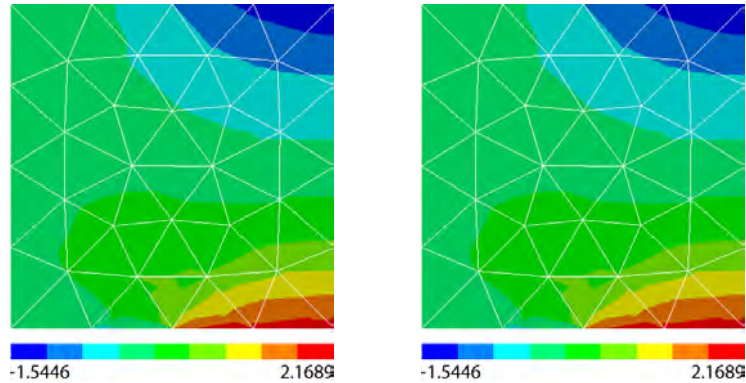


Fig. 1. Horizontal normal stress component obtained by the stress-based (left) and mixed $u-p$ (right) methods.

The convergence rate of the stress-based approach has been checked by plotting the relation between $\log((U - U_0)/U_0)$ and $\log(h)$, where U is the value of strain energy calculated for meshes coarser than the finest one, U_0 is the strain energy value obtained in the case of the finest mesh which is used here as a reference value. The relation is shown in Figure 2 for two types of stress-based elements and the 8-node element of the mixed method. The plot shows that the convergence of the equilibrium finite element approach is remarkably faster than the convergence of the mixed method.

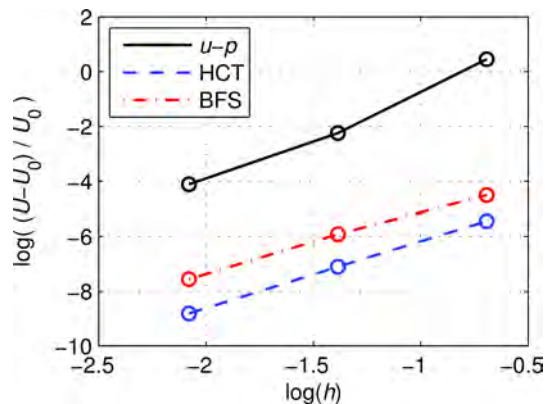


Fig. 2. Strain energy–element size relation for three types of elements.

It is noticeable that the stress-based method does not need any additional effort in the case of full incompressibility ($\nu = 0.5$). On the contrary, in this case, the mixed method in which zeros appear on the main diagonal of the final system of algebraic equations requires such an additional remedy. Some computational tools have restrictions with respect to the value of Poisson's ratio, e.g. program ANSYS [2] requires that $\nu \leq 0.49999$. In the present paper, the results based on the mixed formulation have been found using this program.

References

1. K.J. Bathe (1996). *Finite Element Procedures*, Prentice-Hall, New Jersey, 276–297.
2. Documentation for ANSYS, Release 11.0.
3. Z. Więckowski, S.K. Youn, B.S. Moon (1999). Stress-based finite element analysis of plane plasticity problems, *Int. J. Numer. Meth. Eng.*, **44**, 1505–1525.

Session

**Continuum Mechanics,
Elasticity and Plasticity**

organized in memory of

Professor Piotr Perzyna

Professor Piotr Perzyna (1931–2013)



Piotr Perzyna was born August 1, 1931 in Niedźwiada near Łowicz. In the years 1946–1951 he attended the Secondary School named after J. Poniatowski in Łowicz, in 1951 he began his studies at the Warsaw University of Technology. The beginnings of his research and teaching activities date back to his student days. In 1953, while still a student at the Faculty of Mechanical Engineering, Technology and Construction of the Warsaw University of Technology, he was hired as an assistant in the Department of Mechanics directed by prof. Waław Olszak. On 28 June 1956 he graduated and received his Master Degree in Engineering. Further scientific work of Professor was carried out in the newly established Institute of Fundamental Technological Research, Polish Academy of Sciences (IPPT PAN) in Warsaw. Professor Perzyna had been involved in this research centre for more than 45 years, being successively employed in the Department of Mechanics of Continuous Media at the positions of: senior assistant since 1956, assistant professor since 1959, associate professor since 1964, professor extraordinarius since 1971, and full professor since 1978. Since January 1964 Professor Perzyna was Head of the Laboratory of Theory of Viscoplasticity, and since February 1979 he was Head of the Laboratory of Theory of Inelastic Materials in IPPT PAN until retirement. Since 1974 he was a member of the Scientific Council of IPPT PAN, presiding in many of its committees. For three terms he served as Head of the Section of Solid Mechanics in Committee of Mechanics of PAN.

In 1959, in IPPT PAN, he received a PhD degree in Technical Sciences (supervised by Prof. Waław Olszak), and on 25 April 1963 he received a degree of Doctor of Sciences. In the years 1961–1962 he held a postdoctoral position in the team of Prof. William Prager, the Division of Applied Mathematics, Brown University, Providence, R.I., USA.

In the years 1963–1973 he taught a monographic series of lectures on the Theory of Plasticity and Thermodynamics of Inelastic Materials at the Faculty of Mathematics,

University of Warsaw. In the years 1969-1970 he was an NSF Senior Fellow at the Department of Engineering Mechanics, University of Kentucky, Lexington, USA. In 1982 and 1985 he worked as an CNRS Visiting Professor at Université Poitiers in France, and in 1982 he was a Visiting Professor at Brown University, Providence, R.I., USA. In 1985 he worked as a Visiting Professor at MIT, Cambridge, Mass., USA, and as a Visiting Professor at Tokyo University, Japan. In 1988-1991 he was an DFG Visiting Professor at the Universität Hannover in Germany.

Solid mechanics was Professor's main area of research. Professor Piotr Perzyna was a co-founder of a new discipline – the theory viscoplasticity. His work in this area became the basis for extensive research in a number of domestic and foreign scientific centres. Research and results achieved in the field of constitutive modelling of inelastic materials for describing localization and damage are of special interest. Professor Piotr Perzyna proposed an original way of description within the realm of the thermodynamic structure with internal parameters. The choice of a set of internal parameters is justified by both the physical basics and experimental observations. This concept has been widely used for investigation of the location and damage phenomena in monocrystals and polycrystalline materials by analytical methods. This period had also resulted in formulating the criteria of localization of plastic deformation. Due to this, a detailed research on the influence of different effects on the occurrence of the phenomenon of localization was done. Professor Piotr Perzyna also achieved original results in the field of instability research of plastic flow processes and in the theory of damage. The results of these studies are of particular importance for the development of numerical methods and computer simulation of plastic flow processes. The developed numerical procedures are stable and allow to study the phenomena of localization and damage. This makes them widely cited and further developed in a number of national and international research centres.

Professor Piotr Perzyna obtained very interesting results in the field of thermodynamics of inelastic materials, as well as for dynamical and wave problems. His work in the field of description of the mechanical properties of irradiated materials were of great practical and cognitive importance. It is worth noting that subjects of PhD dissertations in various foreign centres (e.g. Delft University of Technology, MIT, Tokyo University, George Washington University, Grenoble University, Barcelona University of Technology) are often inspired by the results of Professor Perzyna's research.

Many chapters in the currently published scientific monographs on the theory of plasticity describe in detail Professor Piotr Perzyna's results in the theory of viscoplasticity and constitutive modelling for describing localization and damage. After retirement he did not change his way of life and remained active in the work of the Scientific Council of the Institute of Fundamental Technological Research of the Polish Academy of Sciences, came to the Institute several times a week, was actively involved as an advisor, colleague and co-author of articles with his younger colleagues or students. He was still creative and looking for new topics. For example, in the recent years, he worked with passion on the issues of existence of Hamilton's variational principle for dissipative bodies and possible consequences of the invariance of the functional of action, and a joint publication with Witold Kosinski in the Archives of Mechanics is the result of this activity.

Professor Piotr Perzyna participated in a large number of international conferences and had been invited to their scientific committees and to deliver plenary lectures. Since 1964, he participated in all International Congresses of Theoretical and Applied Mechanics (IUTAM), presenting there papers based on his own research. At the Congress of IUTAM in Toronto in 1980, he was asked to deliver a plenary lecture. He participated in many IUTAM Symposia and EUROMECH Colloquia. He was the organizer of international conferences, responsible for the scientific level of these meetings. Because of his extensive, friendly contacts he had always been able to accumulate the most prominent scientists at these meetings, providing the highest level to the events. He organized three EUROMECH Colloquia himself in 1972, 1979, and 1986. He was also the main organizer of the XVI-th Polish Conference of Solid Bodies (Krynica 1974) and XXXIII-th Confer-

ence on Solid Mechanics (Zakopane, 2000). In 1978, 1980, 1988, and 1997, he organized international courses at the European Centre for Mechanics CISM in Udine, Italy. In 1981–1986 Professor Piotr Perzyna was a member of the European Committee for Mechanics (EUROMECH).

Since 1964, for 30 years he was a member of the Editorial Board of the Archive of Applied Mechanics and Engineering Transactions. From 1972 to 2002 he was a member of the Editorial Board of the Library of the Applied Mechanics, IPPT PAN. In the years 1991–1996 he was a member of the Advisory Board of the International Journal of Plasticity, Pergamon Press; from 1990 to 1996, a member of the Advisory Board of International Journal of Impact Engineering, Pergamon Press; and from 1992 to 1998, a member of the Advisory Board of the JSME International Journal of Mechanics and Material Engineering, the Japan Society of Mechanical Engineers; from 1992 to 1997 a member of the Advisory Board of the European Journal of Mechanics.

The creative achievements of Professor include six scientific monographs, two university textbooks, and about 270 original scientific works, the vast majority of which were published in reputable journals currently covered by Thomson Reuters databases. Professor's publications are widely cited, and a few of them belong to the most frequently cited Polish works in the field of technical and mathematical sciences (works from the years 1963, 1966, 1971, 1978). The theory of viscoplasticity created by Professor is widely discussed also in the most significant monographs published in prominent scientific publishing houses. Moreover, Professor is author or co-author of more than twenty books, including one of the first in the world books on plasticity in 1966. Citations of Professor's work are not limited to the publications listed in the Web of Science databases. Hundreds of doctoral and postdoctoral works referring to the issue of plasticity always discuss the fundamental results of Professor Perzyna.

Looking at the impressive number of his international research internships, professors' visits, and travels to the most prestigious conferences in the world, one can say without a doubt that he belonged to a small group of truly world scientists, for whom, even during the difficult years of our post-war history, borders did not constitute a major barrier.

Professor Piotr Perzyna had supervised 17 completed PhD theses. 9 of his co-workers gained degrees of Doctors of Sciences, and 7 became professors. Professor also inspired many other researchers, and the value of scientific discussions with him could not be underestimated. He was a researcher who excellently and effectively directed research topics of discussion participants or seminar panelists. There is a numerous group of co-workers who do not change the presented statistics, but who truly belong to the group of his students; thanks to Professor, Polish mechanics maintains and strengthens its position in the scientific world. The names of his doctoral students in the alphabetical order are: Angel Baltov, Józef Bejda, Paweł Dłużewski, Aldona Drabik, Kurt Frischmuth, Tadeusz Jeske, Witold Kosiński, Sumio Murakami, Zdzisław Nowak, Anna Pabjanek, Ryszard Pęcherski, Amalia Pielorz, Jacek Rońda, Katarzyna Szmit-Saxton, Tomasz Wierzbicki, and Włodzimierz Wojno.

Professor was a very demanding promoter, but also an excellent and highly respected professional, colleague, and friend. His enthusiasm, high standards of ethics, and scientific honesty in an effort to solve research problems, to find an explanation of the observed phenomena, and his approach to research in general, shaped the minds of generations of co-workers. Many of his students and graduate students have become well-known scholars in Poland and beyond its borders. For example, Tomasz Wierzbicki is a professor at MIT, Angel Baltov for many years worked as the scientific director of the Bulgarian Academy of Sciences, Sumio Murakami was a professor at Nagoya University, Witold Kosiński was a professor at the Polish-Japanese Institute of Information Technology, where he worked for six years as a vice-rector for research, and Aldona Drabik is the general vice-rector there, Kasia Szmit-Saxton has been for many years a professor at Loyola University in New Orleans, Paweł Dłużewski and Ryszard Pęcherski are professors at the IPPT PAN, and Kurt Frischmuth is a professor at the University of Rostock.

Professor Perzyna was the winner of prestigious awards. In 1960, the M.T. Huber Prize, Division IV of the Polish Academy of Sciences; in 1968, the State team award of II degree; in 1974 and 1978, awards of the Scientific Secretary of the Polish Academy of Sciences; in 1984, individual State award of II degree; and in 1993, together with prof. Erwin Stein from Hanover (Doctor Honoris Causa of Poznań University of Technology), Max Plank Research Award (Max Plank Society and the Humboldt Association). Professor Piotr Perzyna was awarded the Chevalier Cross of the Polonia Restituta Order.

We will remember Professor Piotr Perzyna as a scientific authority, inspirer, teacher and an outstanding scientist in the field of solid mechanics, the creator of the widely used theory of viscoplasticity, a specialist in problems of thermodynamics of materials, damage dynamics, and wave propagation.

**EFFECT OF INTERLAYER ON STRESSES IN COATING
 UNDER NORMAL AND TANGENTIAL LOADING**

A. Bajkowski, R. Kulchytsky-Zhyhailo

Białystok University of Technology, Faculty of Mechanical Engineering
 Department of Mechanics and Applied Computer Science, Białystok, Poland

1. Introduction

Coatings are used to improve the tribological properties of the surface, it enables to reduce coefficient of friction between cooperating elements and increase the resistance to adverse thermal and chemical influence of an environment. Often the maximum tensile stress was taken as the factor which caused fracture initiation. Research described in literature [1–3] shows that in the homogeneous coating at the interface with base the tensile stresses may occur. These stresses are lower when the gradient interlayer was introduced.

2. Problem formulation

In the present work the homogeneous half-space with inhomogeneous coating was considered. The coating was composed of homogeneous top layer and gradient interlayer (Fig. 1). Mechanical properties of the base, interlayer and top layer were described by the Young's moduli and the Poisson's ratios, respectively E_0, ν_0 , E_1, ν_1 and E_2, ν_2 . Surface of the considered inhomogeneous half-space was under normal p and tangential $t_x = fp$ loading (f – coefficient of friction) subjected in circular area Ω of radius a . Distribution of the loading is elliptical: $p(r) = p_{\max}\sqrt{1-r^2}$, where: r, z – dimensionless cylindrical coordinates which refer to radius of loading area. Between components of considered medium the ideal mechanical contact conditions were satisfied.

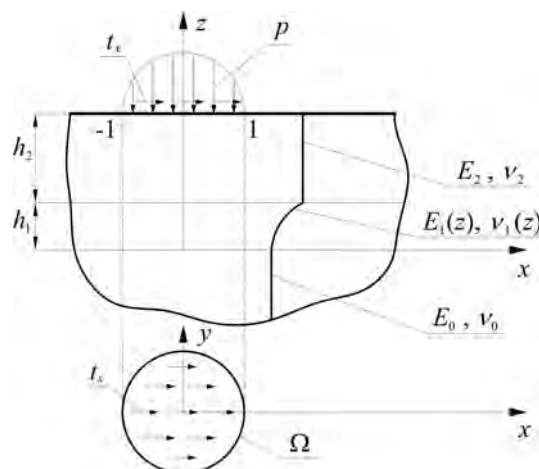


Fig. 1. Scheme of the problem.

3. Method of solution

Problem of the elasticity in the interlayer is described by partial differential equations with variable coefficients. Analytic solution of these equations is known only in rare special cases. One of these cases, when change of the function is described by power function will be considered in present paper.

The problem relay on solve the elasticity equations in every component of analysing inhomogeneous half-space with satisfying the boundary conditions:

- 1) loading of the surface of inhomogeneous half-space;
- 2) perfect contact condition between components of the half-space (continuous of the displacement and stress vector on the interlayers);
- 3) decline the value of components of stress tensor in infinity.

Solution of the problem was obtained using the two-dimensional integral Fourier transform, similar to the described in the works [4, 5]. General solution of the problem in the Fourier transform space contain unknown functions of integral transformation parameters. These functions can be obtain solving of the system of linear equations which were formed fulfilling the boundary conditions in the transform space. Using the inverse Fourier transform we get components of stress tensor in integral form. Integrals along the angular coordinate introduced in the plane of integral transform were calculated analytically. Integrals along the radial coordinate in internal points of the considered inhomogeneous half-space were calculated numerically using the Gaussian quadrature. Calculating the integrals describing the stresses on the surface ($z = h$), the asymptotic behaviour of the integrands along the polar coordinates approaching to infinity was taken into consideration.

4. Summary

In the present work we focus on the influence of the thickness of the components of coating, its mechanical properties and coefficient of friction to distribution on the first principal stress. Value of coefficient of friction have influence on the tensile stresses on surface of the considered half-space. It has been shown that introduction of the gradient interlayer caused significant decrease of the tensile stress on the interlayer between base and coating. The occurrence of interlayer only marginally increase the tensile stresses on the surface of the considered half-space.

Acknowledgment

This work was carried out within the project “Analysis of stress caused by contact pressure in a homogeneous body with a gradient coating”. The Project is financed by the resources of National Science Centre (Poland) given according to decision No. DEC-2011/03/N/ST8/04212.

References

1. N. Schwarzer (2000). Coating due to analytical modelling of mechanical contact problems on multilayer systems, *Surf. Coat. Technol.*, **133–134**, 397–402.
2. G.M. Bragallini, M.P. Cavatorta, P. Sainsot (2003). Coated contact: a strain approach, *Tribology Int.*, **36**, 935–941.
3. R. Kulchytsky-Zhyhailo, G. Rogowski (2010). Stresses in hard coating due to a rigid spherical indenter on a layered elastic half-space, *Tribology Int.*, **43**, 9, 1592–1601.
4. R. Kulchytsky-Zhyhailo, A. Bajkowski (2011). Elastic half space with inhomogeneous coating under the action of tangential forces, *Materials Science*, **46**, 6, 735–746.
5. R. Kulchytsky-Zhyhailo, A. Bajkowski (2012). Analytical and numerical methods of solution of three-dimensional problem of elasticity for functionally graded coated half-space, *Int. J. Mech. Sci.*, **54**, 105–112.

DILATATIONAL AND NON-DILATATIONAL STRAIN IN COAXIAL CABLE

M. Chudzicka-Adamczak¹, T. J. Hoffmann²

¹Polytechnic Institute, Stanisław Staszic State School of Higher Vocational Education, Pila, Poland

²Polytechnic Faculty, The President Stanisław Wojciechowski Higher Vocational State School
Kalisz, Poland

1. Introduction

This paper is an attempt to combine two approximations: magnetostatics and the mechanical statics of material. The model of infinitely long and resilient cable with circular symmetry is considered. In such an approximation, the magnetic field intensity and the Maxwell stress tensor components are determined from the equation of magnetostatics. The dilatational and non-dilatational strains caused by the Maxwell stress tensors are derived from the static motion Lamé's equations. The results are presented in the graphs in non-dimensional form.

2. Momentum balance and the static motion Lamé's equations in electromagnetic field

In the mechanics of deformable media the momentum balance of system has a form:

$$(1) \quad \rho \frac{Dv_k}{Dt} + \mathcal{D}_t(\mathbf{D} \times \mathbf{B})_k = \partial_l \mathfrak{S}_{kl} + f_k^{GL},$$

where: $\frac{D(\cdot)}{Dt}$ – material derivative, \mathfrak{S}_{kl} – complete stress tensor (the sum of Maxwell stress tensor (T_{kl}) and mechanical stress tensor (t_{kl})), $(\mathbf{D} \times \mathbf{B})_k$ – complete momentum density, f_k^{GL} – complete volume force.

The series of motion equations: [2–4] is derived from the above balance. In particular, static equations, where volume force are omitted:

$$(2) \quad \partial_l \mathfrak{S}_{kl} = 0.$$

In static approximation, the time derivatives are identically equal zero.

Using the static equation (2) for linear isotropic elasticity, the following equation can be written in index notation:

$$(3) \quad c_2^2 \partial_j \partial_j u_k + (c_1^2 - c_2^2) \partial_k \partial_j u_j = c_M^2 H_j (\partial_k H_j - \partial_j H_k),$$

where: $c_2^2 = \frac{G}{\rho}$ – square of the phase velocity of transverse elastic wave, $c_1^2 = \frac{\lambda + 2G}{\rho}$ – square of phase velocity of longitudinal elastic wave, $c_M^2 = \frac{\mu}{\rho}$ – permeability of conductor,

and $c_M^2 H_j (\partial_k H_j - \partial_j H_k) = -\frac{1}{\rho} (\text{div} \check{T})_k$.

A well-known equation of differential calculus of operators

$$\partial_j \partial_j u_k = \partial_k \partial_j u_j = \varepsilon_{klm} \varepsilon_{spr} \partial_l \partial_p u_r$$

is used and the equation (3) a new form is obtained:

$$(4) \quad \partial_i (c_1^2 \vartheta) + \varepsilon_{ijk} \partial_j (-c_2^2 2\omega_k) \partial_i (\partial_j u_j) = c_M^2 H_j (\partial_i H_j - \partial_j H_i),$$

where: $\vartheta = \partial_j u_j$ – relative dilatational change, $\omega_k = \frac{1}{2} \varepsilon_{klm} \partial_l u_m$ – rotation vector.

The divergence of equation (4) is calculated with the following result:

$$(5) \quad c_1^2 \partial_i \partial_i \vartheta = c_M^2 [(\partial_k H_i)^2 - (\partial_i H_k)].$$

The above equation describes balance dilatational strains caused by function on the right side of this equation. Calculating the rotation of equation (4) there is:

$$(6) \quad c_2^2 \partial_i \partial_i \omega_l = \frac{c_M^2}{2} \varepsilon_{ljk} [\partial_j H_i (\partial_k H_i - \partial_i H_k) + H_i (\partial_j \partial_k H_i - \partial_j \partial_i H_k)].$$

The above equation describes the balance of non-dilatational strains expressed by rotation vector. The right side of equation (6) caused these strains. All considerations are based on the classical method of elasticity theory of the decomposition of displacements field for non-dilatational and dilatational strains [5]. It is worth to underline that each of this form of strains has a source in magnetic interactions.

In the paper the dilatational and non-dilatational strains were determined in all the layers of the coaxial cable, in copper wire, insulation, copper mesh and outside insulation for all types of coaxial cables. The above results were presented on the graphs in the non-dimensional form.

References

1. J.D. Jackson (1997). *Classical Electrodynamics*, PWN Warszawa [in Polish].
2. L.D. Landau, E.M. Lifszyc (1960). *Electrodynamics of Continuous Media*, PWN Warszawa [in Polish].
3. A.C. Eringen, G.A. Maugin (1990). *Electrodynamics of Continua*. Vol. 1. Springer-Verlag, New York.
4. G. A. Maugin (1988). *Continuum Mechanics of Electromagnetic Solids*, North Holland, Amsterdam.
5. W. Nowacki (1970). *Theory of Elasticity*, PWN, Warszawa [in Polish].
6. T.J. Hoffmann, M. Chudzicka-Adamczak (2009). The Maxwell stress tensor for magnetoelastic materials, *International J. of Eng. Science*, **47**, 735–741.

EFFECT OF TEMPERATURE RATE IN MODELING NONISOTHERMAL LOW CYCLE FATIGUE OF STEEL

H. Egner¹, W. Egner¹, P. Sulich²

¹Institute of Applied Mechanics, Faculty of Mechanics, Cracow University of Technology, Cracow, Poland

²PhD student in the Institute of Applied Mechanics, Faculty of Mechanics, Cracow University of Technology, Cracow, Poland

1. Introduction

In the present analysis a constitutive and numerical modeling is performed to describe the fatigue behavior of steel in non-isothermal conditions. Two constitutive models are considered: 2M1C (2 mechanisms-1 yield criterion) model derived by Cailletaud and Sai [1] and identified by Velay et al. [2] is extended to account for the effect of temperature change. The second model is the classical Armstrong-Frederick formulation, also extended to include nonisothermal effects. Numerical simulations are performed, which indicate the significant influence of temperature rate on the response of both constitutive models when cyclic thermomechanical loading is considered.

2. Basic assumptions and equations

The RVE based 2M1C constitutive model is based on the following assumptions: (1) Thermo-elastic-viscoplastic material is considered. The complete set of state variables consists of two observable variables: elastic strain and absolute temperature, and four internal variables: two kinematic and two isotropic plastic hardening variables. (2) Small strains are assumed. Total strain is partitioned into an elastic, inelastic and thermal components, while inelastic strain can be partitioned itself into two different strain mechanisms inducing the cyclic softening: the decrease of the dislocation density inherited from the quench treatment, and the carbide coarsening. (3) The state equations result from the assumed form of the state potential, which is here the Helmholtz free energy, decomposed into thermo-elastic and thermo-viscoplastic terms. (4) Non-associated thermo-viscoplasticity is assumed. The detailed formulation of the dissipation potential, as well as the evolution equations of internal state variables, are given in [2]. (5) The plastic strain range memorization effect is included through additional internal state variables [3]. (6) To investigate qualitatively the influence of temperature rate on the response of a dissipative material in nonisothermal conditions, the extended evolution equations of thermodynamic conjugate forces are derived in this paper for both 2M1C and Armstrong-Frederick models, taking into account additional terms related to temperature rate, which were not included in the basic models.

3. Results

The extended constitutive models were implemented into numerical procedures by the use of Mathematica software. Three load cases were simulated: (i) thermomechanical cycles referring to a numerical test done by Chaboche [4] (see Fig. 1), (ii) in-phase thermomechanical loading, and (iii) out-of-phase thermomechanical loading.

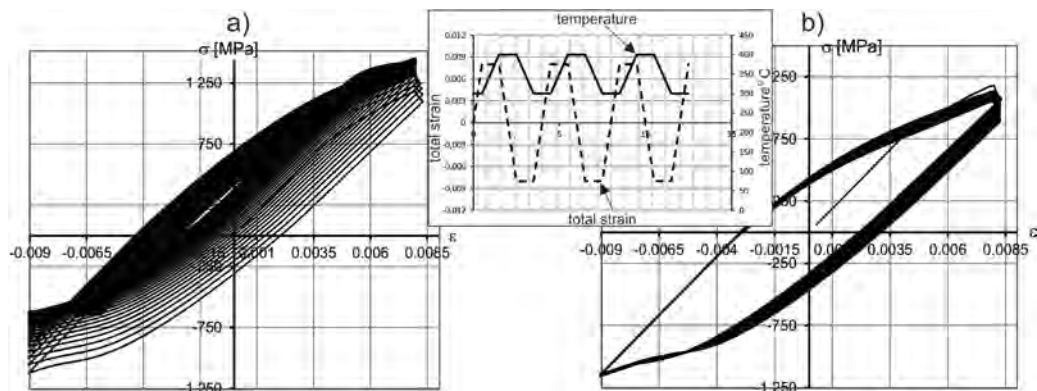


Fig. 1. Hysteresis loops for: a) temperature rate disregarded; b) temperature rate included.

The stress-strain loops for two cases: (a) temperature rate disregarded, and (b) temperature rate included are presented in Fig. 1ab. Qualitatively different results are obtained: without temperature rate terms the response exhibits cyclic hardening due to unreasonable shift of hysteresis loops along the stress axis, while including additional temperature rate terms allows for preserving stable behavior (cyclic softening is observed). Such effect was already indicated by Chaboche [4], and is more significant for materials exhibiting cyclic hardening (the shift of stress-strain loops is mitigated if cyclic softening takes place).

4. Conclusions

The results obtained in the presented research indicate that coupling between temperature and dissipative phenomena taking place in a material has a significant influence on the response of a constitutive model in non-isothermal conditions. Disregarding the rate of temperature in the evolution of thermodynamic forces related to hardening effects may lead to erroneous results, especially when solving high temperature problems, such as fire conditions or thermal shock.

Acknowledgments

The financial support under grant number 2011/03/B/ST8/05132 from the National Science Centre is gratefully acknowledged.

References

1. G. Cailletaud, K. Saï (1995). Study of plastic/viscoplastic models with various inelastic mechanisms, *Int. J. Plast.*, **11**, 991–1005.
2. V. Velay, G. Bernhart, L. Penazzi (2006). Cyclic behavior modeling of a tempered martensitic hot work tool steel, *Int. J. Plast.*, **22**, 459–496.
3. K. Saï (2011). Multi-mechanism models: Present state and future trends, *Int. J. Plast.*, **27**, 250–281.
4. J.L. Chaboche (2008). A review of some plasticity and viscoplasticity constitutive theories, *Int. J. Plast.*, **24**, 1642–1693.

**EFFECT OF PHASE TRANSFORMATION RATE ON THE RESPONSE
OF ELASTIC-PLASTIC TWO-PHASE MATERIAL SUBJECTED
TO CYCLIC LOADING AT CRYOGENIC TEMPERATURES**

H. Egner¹, M. Rys²

¹Institute of Applied Mechanics, Faculty of Mechanics, Cracow University of Technology,
Cracow, Poland

²PhD student in the Institute of Applied Mechanics, Faculty of Mechanics
Cracow University of Technology, Cracow, Poland

1. Introduction

There is a large variety of materials suitable for applications at extremely low temperatures. Among metallic materials we can often find austenitic stainless steels, applied for components of superconducting magnets and cryogenic transfer lines. Some of them (like bellows expansion joints) are subjected to particularly severe conditions: thermo-mechanical cycles between room temperature and 1.9K associated with axial displacements of the order of the bellows free length, and internal pressure up to 2 MPa.

The present paper is focused on constitutive and numerical modeling of austenitic stainless steels applied to cyclic loadings at very low temperatures. A special attention is paid to proper modelling of coupling between plasticity and phase transformation, under the assumption of small strains.

2. Basic assumption and equations of the model

The RVE based constitutive model presented in the paper is an extension of the existing models [1, 2]. It is based on the following assumptions: (1) the elastic-plastic two-phase material subjected to cyclic loading in isothermal conditions is considered; (2) the secondary phase inclusions are randomly distributed and oriented in the matrix, therefore, the current state of the phase transformation can be described by the simplest scalar variable ξ being the volume fraction of the secondary phase in the representative volume element; (3) to properly simulate the response of a material subjected to cyclic loading, the extended evolution equations for thermodynamic conjugate forces (back stress X_{ij}^p and drag stress R^p) are derived, accounting for additional terms related to phase transformation rate (full coupling, cf [3]), which were not included in the existing models [1, 2], see Table 1.

Table 1. Evolution laws for thermodynamic conjugate forces related to hardening.

	Partial coupling	Full coupling
$\dot{X}_{ij}^p =$	$\frac{2}{3}C^p(\xi)\dot{\alpha}_{ij}^p$	$+\frac{1}{C^p}\frac{\partial C^p}{\partial \xi}X_{ij}^p\dot{\xi}$
$\dot{R}^p =$	$b^p(R_\infty^p - R^p)\dot{r}^p$	$+\left[\frac{1}{R_\infty^p}\frac{\partial R_\infty^p}{\partial \xi}R^p + (R_\infty^p - R^p)r^p\frac{\partial b^p}{\partial \xi}\right]\dot{\xi}$

3. Numerical results

Two load cases were simulated: (i) uniaxial tension test, and (ii) strain controlled cyclic loading with constant strain amplitude. The results show that introducing full coupling in the state equations has significant meaning for proper numerical simulation of the real material behavior. Regarding the phase transformation rate in the kinetic equations allows for better fitting with the experimental results (Fig. 1). Disregarding the phase transformation rate leads also to unreasonable drift of back-stress loops (Fig. 2ab), which is inconsistent with the respective state equations.

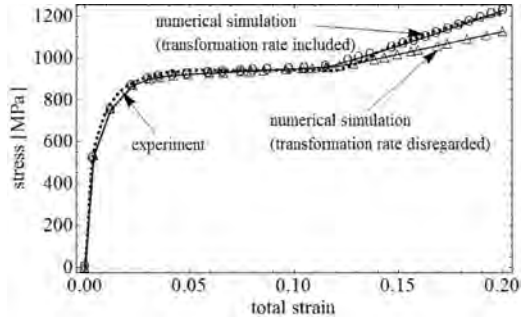


Fig. 1. Uniaxial tension test of 316L stainless steel at 4.2 K.

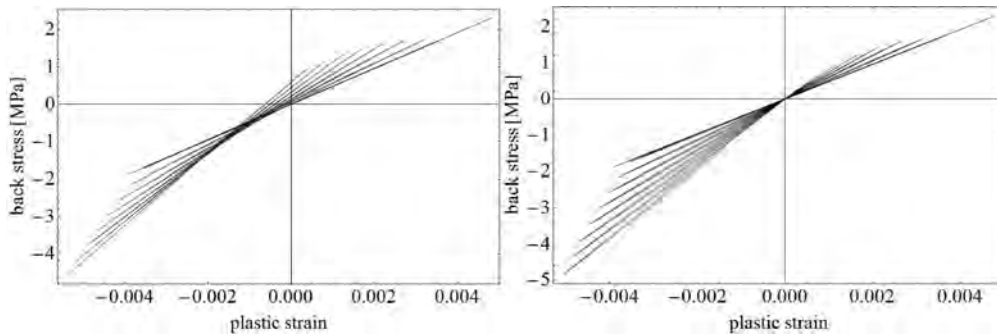


Fig. 2. Back stress versus plastic strain: a) transformation rate disregarded; b) transformation rate included.

4. Conclusions

In the presented work it is shown that full plastic-phase transformation coupling in kinetic equations of thermodynamic forces (when not only the influence of current state of phase transformation on the plastic material parameters is regarded, but also the rate of transformation is included) is necessary for proper numerical simulation of a material response under cyclic mechanical loading.

Acknowledgments

The financial support under grant number 2011/03/B/ST8/05132 from the National Science Centre is gratefully acknowledged.

References

1. M. Sitko and B. Skoczeń (2012). Effect of $\gamma - \alpha'$ phase transformation on plastic adaptation to cyclic loads at cryogenic temperatures, *Int. J. Solids Struct.*, **49**, 613–634.
2. C. Garion, B. Skoczeń, S. Sgobba (2006). Constitutive modelling and identification of parameters of the plastic strain induced martensitic transformation in 316 L stainless steel at cryogenic temperatures, *Int. J. Plast.*, **22**, 7, 1234–1264.
3. H. Egner (2012). On the full coupling between thermo-plasticity and thermo-damage in thermodynamic modeling of dissipative materials, *Int. J. Solids Struct.*, **49**, 279–288.

ON THE THERMODYNAMIC MODELING OF COUPLING BETWEEN PLASTICITY, DAMAGE AND PHASE TRANSFORMATION

H. Egner¹, M. Rys²

¹Institute of Applied Mechanics, Faculty of Mechanics
Cracow University of Technology, Cracow, Poland

²PhD student in the Institute of Applied Mechanics, Faculty of Mechanics
Cracow University of Technology, Cracow, Poland

1. Introduction

In this work, a thermodynamically consistent elastic-plastic-damage two-phase material model is introduced. A special attention is paid to proper modelling of coupling between all dissipative phenomena considered, under the assumption of small strains.

2. Basic assumptions and equations of the model

In our constitutive modelling we adopt the well-known formalism of thermodynamics of irreversible processes with internal state variables, and the local state method [1, 2]. In this approach a central hypothesis is that the state of a material is entirely determined by certain values of some independent variables, called variables of state. This type of approach is particularly well adapted to the formulation of constitutive equations for deformable solids with several dissipative phenomena.

In the definition of our constitutive model we follow a common three-stage procedure:

(1) *Stage 1: the choice of the state variables*

The two-phase continuum is composed of the primary phase matrix and secondary phase inclusions, randomly distributed and randomly oriented in the matrix. Therefore, the current state of the phase transformation can be described by the simplest scalar variable ξ being the volume fraction of the secondary phase in the representative volume element. In the presented analysis the matrix material is subjected to plastic deformation and ductile damage development, whereas the inclusions show purely brittle response. Such assumption corresponds for example to inelastic strain induced $\gamma - \alpha'$ phase transformation in austenitic stainless steels at cryogenic temperatures (the yield stress of martensite fraction is at cryogenic temperatures much higher than the yield stress of austenite). For the description of the current state of damage we therefore introduce two second order damage tensors, for ductile damage in primary phase (\mathbf{D}^p) and for brittle damage in secondary phase inclusions (\mathbf{D}^s). The total material degradation in the RVE is describe by the average damage tensor \mathbf{D}^{avg} , being a superposition of the ductile and brittle parts. For this reason a function of the volume fraction ξ of the secondary phase is introduced to define the general mixture rule. The mixed isotropic/kinematic plastic hardening is included, represented by the two classical plastic state variables α^p and r^p ; also damage hardening is possible, represented by damage state variables related to kinematic and isotropic hardening.

The effective state variables are defined using the total energy equivalence hypothesis. It is worth pointing out that this enables the systematic definition of pairs of effective variables that can be indifferently used either in stress or in strain spaces by the simple

application of the Legendre-Fenchel transformation. Moreover, it leads to symmetric physical properties affected by anisotropic damage, and allows naturally to achieve a strong coupling between damage and all other variables, without neglecting any interaction between the various phenomena regarded.

- (2) *Stage 2: the definition of the state potential from which the state relations (between strain-like variables and their dual forces) will be derived*

We construct a state potential as a closed, convex and scalar-valued function of the overall state variables, which is here the Helmholtz' free energy. The state relations are deduced from the fundamental Clausius-Planck inequality. The kinetic equations of force-like variables are then obtained by taking time derivatives. Various coupling terms appear in the kinetic equations, that are necessary for proper description of a material behavior, especially when cyclic loading is considered [3].

- (3) *Stage 3: the choice of the dissipation potential from which the rate equations of state variables will be derived*

Once the force-like variables are known from the state relations, it remains to define the flux variables so that the volumic dissipation is always non-negative. In order to define the evolution equations pertaining to dissipative phenomena, the existence of a potential of dissipation is assumed in the form of a positive, convex, closed and scalar-valued function of force-like variables, with the associated state variables able to serve as parameters. The flux variables are obtained based on the hypothesis of normal dissipation in the form of ordinary differential equations of the first order. In our model it is assumed that both ductile damage and phase transformation mechanisms are governed by plasticity, with single consistency multiplier $\dot{\lambda}^p$ (strong dissipation coupling), while for brittle damage the separate loading function is proposed.

3. Conclusions

The proposed model of elastic-plastic-damage two-phase material contains important new features in comparison with the existing formulations:

- Total energy hypothesis is applied instead of commonly used strain energy hypothesis. The advantages of this approach are pointed out.
- Damage evolution both in primary and secondary phases is regarded, under the conditions of variable volume fraction of both phases.
- In the kinetic equations of force-like variables different coupling terms are present, which are usually disregarded in the existing models.
- Thermodynamic consistency of the formulation of the elastic-plastic-damage two-phase material is proved.

Acknowledgment

This work has been supported by the National Science Centre through the Grant No. 2284/B/T02/2011/40.

References

1. K. Saanouni (2012). *Damage Mechanics in Metal Forming: Advanced Modeling and Numerical Simulation*, ISTE/Wiley, London O.C.
2. S. Murakami (2012). *Continuum damage mechanics: A continuum mechanics approach to the analysis of damage and fracture*, Springer-Verlag.
3. H. Egnér (2012). On the full coupling between thermo-plasticity and thermo-damage in thermodynamic modeling of dissipative materials, *Int. J. Solids Struct.*, **49**, 279–288.

TETRAAGONAL OR HEXAGONAL SYMMETRY OF FAILURE TSAI-WU CRITERION FOR TRANSVERSELY ISOTROPIC MATERIALS

A. Ganczarski, M. Adamski

Cracow University of Technology, Cracow, Poland

Present work deals with modeling of failure criteria for transversely isotropic materials. Analysis comprises two classes of symmetry: classical Tsai–Wu tetragonal and new Tsai–Wu based hexagonal. Detail analysis of both classes of symmetry with respect to their advantages as well as limitations is presented. Finally, simple comparison of differences between limit curves corresponding to cross sections by plane of transverse isotropy is done.

1. Introduction – Tsai–Wu failure criterion

Transversely isotropic Tsai–Wu criterion of initial failure [5]

$$(1) \quad \frac{\sigma_x^2 + \sigma_y^2}{k_{tx}k_{cx}} + \frac{\sigma_z^2}{k_{tz}k_{cz}} - \left(\frac{2}{k_{tx}k_{cx}} - \frac{1}{k_{tz}k_{cz}} \right) \sigma_x \sigma_y - \frac{\sigma_z(\sigma_x + \sigma_y)}{k_{tz}k_{cz}} + \left(\frac{4}{k_{tx}k_{cx}} - \frac{1}{k_{tz}k_{cz}} \right) \tau_{xy}^2 + \frac{\tau_{yz}^2 + \tau_{zx}^2}{k_{zx}^2} + \left(\frac{1}{k_{tx}} - \frac{1}{k_{cx}} \right) (\sigma_x + \sigma_y) + \left(\frac{1}{k_{tz}} - \frac{1}{k_{cz}} \right) \sigma_z = 1.$$

contains only 5 independent material coefficients that refer to appropriate tensile and compressive strengths k_{tx} , k_{cx} , k_{tz} , k_{cz} and shear strength k_{zx} . It is obvious that material coefficients in plane of transverse isotropy that precede terms $\sigma_x \sigma_y$ and τ_{xy} are not fully independent since they contain not only in plane tensile and compressive stresses k_{tx} , k_{cx} but also out of transverse isotropy plane tensile and compressive stresses k_{tz} , k_{cz} . Consequently, Eq. (1) can be classified as the tetragonal transversely isotropic Hill's criterion of initial failure.

2. Convexity loss in case of high orthotropy

Applicability range of Tsai–Wu orthotropic criterion (1) to properly describe initiation of failure in some engineering materials that exhibit high orthotropy degree, is bounded by a possible ellipticity loss of the limit surface. Other words, a physically inadmissible degeneration of the single convex and simply connected elliptic limit surface into two concave hyperbolas surfaces occur. The following inequality bounds the range of applicability for Tsai–Wu criterion [3, 1]

$$(2) \quad \frac{1}{k_{tz}k_{cz}} \left(\frac{4}{k_{tx}k_{cx}} - \frac{1}{k_{tz}k_{cz}} \right) > 0.$$

Substitution of the dimensionless parameter $R = 2(k_{tz}k_{cz}/k_{tx}k_{cx}) - 1$, (extension of that by Hosford and Backhofen [2]), leads to the simplified restriction $R > -0.5$. If the above inequality does not hold, elliptic cross sections of the limit surface degenerate to two hyperbolic branches and the lack of convexity occurs. To illustrate this limitation, the failure curve in the plane of transverse isotropy ($\sigma_x \sigma_y$) for various R -values, is sketched in Fig. 1a. It is observed that when R , starting from $R = 3$, approaches the limit $R = -0.5$, the curves change from closed ellipses to two parallel lines, whereas for $R < -0.5$, concave hyperbolas appear.

3. Modified Tsai–Wu based hexagonal failure criterion

Except the tetragonal transversely isotropic Tsai–Wu criterion Eq. (1) one can introduce hexagonally isotropic Tsai–Wu yield criterion

$$(3) \quad \frac{\sigma_x^2 - \sigma_x \sigma_y + \sigma_y^2}{k_{tx} k_{cx}} + \frac{\sigma_z^2}{k_{tz} k_{cz}} - \frac{\sigma_z(\sigma_x + \sigma_y)}{k_{tz} k_{cz}} + 3 \frac{\tau_{xy}^2}{k_{tx} k_{cx}} + \frac{\tau_{yz}^2 + \tau_{zx}^2}{k_{zx}^2} + \left(\frac{1}{k_{tx}} - \frac{1}{k_{cx}} \right) (\sigma_x + \sigma_y) + \left(\frac{1}{k_{tz}} - \frac{1}{k_{cz}} \right) \sigma_z = 1.$$

Both the Tsai–Wu transversely isotropic initial failure criteria: tetragonal Eq. (1) and new hexagonal type (3) are compared for columnar ice, the experimental date of which was established by Ralston [4]: $k_{tx} = 1.01$ MPa, $k_{cx} = 7.11$ MPa, $k_{tz} = 1.21$ MPa, $k_{cz} = 13.5$ MPa, in plane of transverse isotropy Fig. 1b.

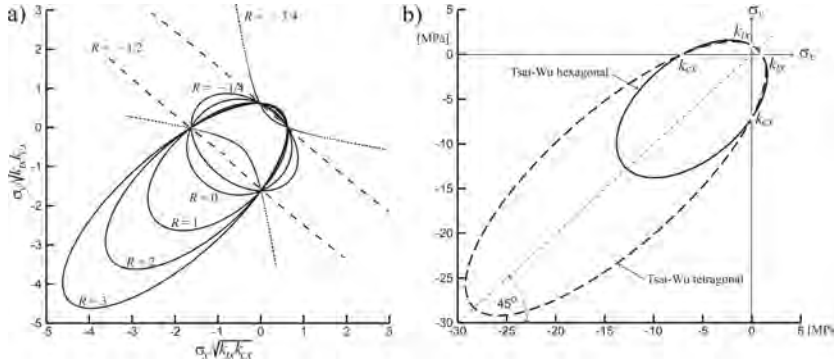


Fig. 1. Initial failure criteria for transversely isotropic materials: a) convexity loss of tetragonal Tsai–Wu criterion in case of high orthotropy degree, b) comparison of Tsai–Wu tetragonal and hexagonal criteria in case of columnar ice.

It is worth to emphasize that the tetragonal transversely isotropic Tsai–Wu failure criterion Eq. (1) contains 5 independent crushing stresses contrary to the hexagonal transversely isotropic Tsai–Wu failure criterion Eq. (3) containing only 4 independent crushing stresses. Both transversely isotropic failure criteria perform cylindrical surfaces in the space of principal stresses, but the tetragonal one is represented by elliptic cylinder the axis of which is parallel to the hydrostatic axis contrary to the hexagonal one, which represents elliptic cylinder the axis of which is not equally inclined to principal stress axes. Hence, transversely isotropic Tsai–Wu failure criterion of hexagonal class does not satisfies deviatoric property, that is a consequence of its coincidence with Huber–von Mises–Hencky criterion in the plane of transverse isotropy (in sense of saving the same ratio between semi axes of the ellipse) as well as a property of saving cylindrical nature despite of high ratio of orthotropy. Obviously, a choice of appropriate transversely failure criterion either tetragonal Eq. (2) or hexagonal Eq. (3) depends on coincidence with experimental tests done on real materials, that can subjected one or other class of symmetry.

References

1. A. Ganczarski and J. Skrzypek (2013). *Mechanika nowoczesnych materiałów*. Wyd. Pol. Krak.
2. W.F. Hosford, W.A. Backhofen (1964). *Strength and plasticity of textured metals*, in: W.A. Backhofen et al. (Eds), *Fundamentals of deformation processing*, Syracuse Univ. Press, 259–298.
3. N.S. Ottosen, M. Ristinmaa (2005). *The mechanics of constitutive modeling*. Elsevier, Amsterdam.
4. T.D. Ralston (1997). *Yield and plastic deformation of ice crushing failure*, *ICSI.AIDJEX Symposium on Sea Ice-Processes and Models*, Seattle, Washington.
5. S.T. Tsai, E.M. Wu (1971). *A general theory of strength for anisotropic materials*. *Int. J. Numer. Methods. Engng.*, 38, 2083–2088.

THE EQUILIBRIUM AND STABILITY OF THE NONLINEARLY ELASTIC CYLINDER WITH INTERNAL STRESSES UNDER TENSION AND INFLATION

M. Karyakin, I. Pozdnyakov, N. Shubchinskaya

Southern Federal University, Rostov-on-Don, Russia

Internal stresses caused by defects of crystal lattice draw an attention by the reason of a big impact to actual mechanical behavior such as plasticity, creep, destruction and so on [1]. In the context of elasticity theory of finite strains much motivation for the research comes from soft tissue biomechanics, and for a recent discussion of internal stresses in artery walls. In the present work some issues of effects of internal stresses on the equilibrium and stability of elastic cylinders were studied within the framework of nonlinear elasticity.

We present results on the two kinds of isolated defects: the wedge disclination and screw dislocation. To describe the mechanical properties of a cylinder two constitutive models for compressible elastic solid were used: John material (also called harmonic material) [2] and Blatz & Ko material [3]. The specific energy function W for these models has the following form, respectively

$$(1) \quad W = \frac{1}{2}\lambda \text{tr}(\mathbf{U} - \mathbf{I}) + \mu \text{tr}(\mathbf{U} - \mathbf{I})^2,$$

where λ, μ – material parameters, \mathbf{U} – the right stretch tensor, \mathbf{I} – the identity tensor, and

$$(2) \quad W = \frac{1}{2}\mu(1 - \beta) \left[I_2 I_3^{-1} + \frac{1}{\alpha}(I_3^\alpha - 1) - 3 \right] + \frac{1}{2}\mu\beta \left[I_1 + \frac{1}{\alpha}(I_3^{-\alpha} - 1) - 3 \right],$$

where α, β, μ – material parameters, I_k ($k = 1, 2, 3$) – principal invariants of the right Cauchy–Green deformation tensor. The first model is usually used to account for geometrical nonlinearities while the second one describes physical nonlinearities also.

To model tension/compression as well as inflation of the hollow cylinder with wedge disclination at its axis we use following representation of the deformation:

$$(3) \quad R = P(r), \quad \Phi = \kappa\varphi, \quad Z = \gamma z,$$

where r, φ, z and R, Φ, Z – cylindrical coordinates in the reference and actual configuration, respectively, κ – parameter of the defect (proportional to the magnitude of the Frank vector of the disclination), γ – positive coefficient of the cylinder stretching or shortening. The function $R(r)$ in (3) describes radial (non-uniform, in general) displacement of the cylinder points.

The analysis of length changing of an unloaded cylinder due to the defect formation was performed. This changing is completely described by the dependence of γ on the disclination parameter κ at the absence of axial force. It was shown numerically that it is nonlinear effect and the elongation ($\gamma > 1$) or shortening ($\gamma < 1$) depends on material parameters of the mechanical models (1), (2). To verify the numerical results the asymptotic formula was obtained within the limits of the second-order effects theory [4]. To construct the solution of equilibrium equations in this case we replace $P(r)$ in (3) by a series in terms of powers of the parameter $\delta = \kappa - 1$. Considering the sequence of tasks corresponding to different powers of δ we obtain the analytical relationship between

length changing of the cylinder and material parameters. In particular, for the simplified version of Blatz & Ko model ($\alpha = 0.5$) the elongation–disclination relation has the form

$$\gamma - 1 = -\delta^2(0.121\beta - 0.0605).$$

To study the screw dislocation we consider the following presentation of the cylinder deformation

$$(4) \quad R = P(r), \quad \Phi = \varphi + \psi z, \quad Z = a\varphi + \gamma z.$$

Here a is the dislocation parameter connected with the value of the Burgers vector b by relation $a = |b|/(2\pi)$. In this case not only elongation or shortening of the cylinder but the torsion with a relative angle of twist ψ is also allowed.

The study of length of an unloaded cylinder containing isolated dislocation also revealed that change of length, i.e. dependence $\gamma = \gamma(a)$, is a nonlinear effect that depends on material parameters of the mechanical models. The asymptotic analysis similar to the disclination case was performed. Within the second order effects theory the relations for the length changing of the cylinder and for the twist angle ψ were obtained. For the simplified version of Blatz & Ko model they can be written as follows

$$\gamma - 1 = -a^2 \frac{(\rho_0^2 + 1)(\beta - 1)3 + (\rho_0^2 - 1)(8 - 3\beta)}{5(\rho_0^4 - 1)}, \quad \psi = \frac{-2a}{\rho_0^2 + 1},$$

where ρ_0 is the ratio of inner radius of the cylinder to the outer one.

To analyze the stability of a cylinder with isolated defect under tension and inflation the bifurcation approach was used based on linearization of the equilibrium equations in the neighborhood of the solutions obtained by means of the semi-inverse representations (3), (4). Search of the bifurcation points is based on the analysis of the homogeneous linear boundary value problem of a six order, whose coefficients depend on radial displacement function $P(r)$ found in the first stage. The bifurcation point is treated as such value of the “loading” parameter – it can be the parameter of the defect, κ or a , or value of inflating pressure or axial force – for which the linearized problem has a nontrivial solution.

For some material parameters of Blatz & Ko model the tension diagram of the solid cylinder has a maximum point followed by the falling region [5]. Special attention was given to the analysis of the influence of the inflation as well as defects parameters to the loading diagram and the deformation stability. It was shown, in particular, that the value of Poisson’s ratio has a significant effect on the stability of the cylinder containing the isolated defect. The influence of disclination on the stability loss at the inflation was also considered.

References

1. L.M. Zubov (1997). *Nonlinear Theory of Dislocations and Disclinations in Elastic Bodies*, Springer–Verlag, Berlin – Heidelberg – New York.
2. A.I. Lurie (1990). *Nonlinear Theory of Elasticity*, North-Holland, Amsterdam.
3. P.J. Blatz, W.L. Ko (1962). Application of Finite Elastic Theory to the Deformation of Rubbery Materials, *Trans. Soc. Rheology*, **6**, 223–251.
4. V.V. Kalashnikov, M.I. Karyakin (2006). Second-order effects and Saint Venant’s principle in the torsion problem of a nonlinear elastic rod, *Journal of Applied Mechanics and Technical Physics*, **47**, 6, 879–885.
5. M.I. Karyakin (2007). On the Specific Features of the Tension of Nonlinearly Elastic Specimens (in Russian). *Ecological Bulletin of Research Centers of the Black Sea Economic Cooperation*, no. 4, 43–48.

INVERSE PROBLEM FOR HEAT CONDUCTION EQUATION IN IR THERMOGRAPHY

W. Kosiński¹, W. Oliferuk², K. Kochanowski², A. Adamowicz²

¹Polish-Japanese Institute of Information Technology, Computer Science Department, Warsaw, Poland

²Faculty of Mechanical Engineering, Department of Mechanics and Applied Computer Science, Białystok, Poland

The paper presents two methods of inverse problem solution for the equation of heat conduction, what allows to determine the thermal diffusivity of materials using pulsed infrared thermography. Both methods are related to finding the time dependence of the temperature of an infinite plate surface, when the opposite surface of the plate is heated by a short heat pulse. The solutions obtained by the methods are compared with the time evolution of the temperature of the plate surface opposite to stimulated one measured by the means of an infrared (IR) camera. Such comparison allows to extract, from experimental data, the information about thermal diffusivity of the tested material.

1. Introduction

Progress in determining thermal properties of materials, such as thermal diffusivity, is possible owing to the development of the active infrared thermography techniques. Thermal diffusivity α characterizes the material in a complex way, because it includes the heat conductivity λ , the specific heat c and the mass density ρ of the material: $\alpha = \lambda/\rho c$.

One of active thermography techniques is the pulsed infrared thermography (PIRT), based on stimulation of the plate surface by a short heat pulse (few milliseconds) and recording the material response, as a time evolution of the temperature distribution on the opposite surface, by the means of an infrared (IR) camera. To obtain information about thermal diffusivity one needs to use the inverse problem solution of the heat conduction equation.

2. Solution of heat conduction equation for infinite plate stimulated by short heat pulse

If the surface of the plate is sufficiently large in comparison with the region of interest, it may be considered as infinite and then the one-dimensional model of heat conduction can be presumed. Then the heat transfer by convection and radiation is omitted, since these mechanisms in comparison with conduction are negligible.

2.1. Method a) The differential equation of heat conduction with initial and boundary conditions is:

$$(1) \quad \frac{\partial T}{\partial t} = \alpha \frac{\partial^2 T}{\partial z^2} + \frac{1}{\rho c} q, \quad T(z, t = 0) = T_0, \quad T(z, t = 0) = T_0, \quad \frac{\partial T}{\partial z}(z = g, t) = 0,$$

where q is the function of heat sources associated with the surface density of energy delivered to the specimen during its heat pulse stimulation. Assuming character of the heat source $q = \delta(t) \delta(z)$, using Fourier transform the solution of Eq. (1) was obtained in the series form. Taking into account the accuracy of temperature measurement, the series was properly truncated. In this way the following expression for the surface temperature of the specimen has been received:

$$(2) \quad T(z = g, t) = T_\infty - 2(T_\infty - T_0) \exp\left(-\frac{\pi^2 \alpha}{g^2} t\right), \quad \text{where } T_\infty = T(t \rightarrow \infty).$$

The logarithm of this equation has a linear character:

$$(3) \quad \ln(T_\infty - T) = \left(-\frac{\pi^2}{g^2}\alpha\right)t + \ln 2(T_\infty - T_0),$$

where $A = \pi^2\alpha/g^2$ is the tangent of the slope straight line to the timeline. So in this way one can determine the thermal diffusivity α . The drawback of the method is that the heat source has the form of Dirac deltas in time and in space, whereas the duration of the heat impulse is finite.

2.2. Method b) In this method, the stimulation of the plate surface by heat pulse was taken into account in boundary condition as the temperature dependence of time for $z = 0$ as $T(z = 0, t) = \varphi(t)$. Mathematical form of the function $\varphi(t)$ was found on the basis of temperature time evolution of the stimulated surface of the plate, which was measured by means of IR Thermography. Thus the formulated condition is entirely consistent with the experiment. The initial condition and the boundary condition for $z = g$ are the same as in the method a) Eqs. (1), hence we solve:

$$(4) \quad \frac{\partial T}{\partial t} = \alpha \frac{\partial^2 T}{\partial z^2}.$$

The approach developed by Karman is used to solve our problem, in which the thermal balance equation and the heat penetration function appear [1]. The profile of the temperature along the thickness of the plate is approximated by a polynomial function. The solution is obtained in terms of the known temperature boundary condition.

3. Experiment and results

In the experiment (Fig. 1) the surface of the tested plate is stimulated by the heat pulse and time evolution of the temperature of the opposite surface is recorded and analysed.

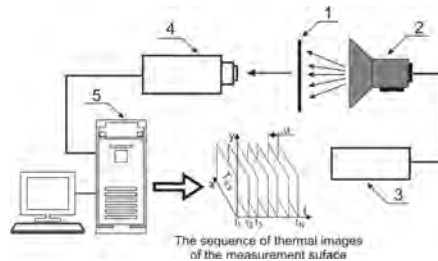


Fig. 1. Scheme of the measuring systems for determining the diffusivity of solids: 1 – plate, 2 – flash lamp, 3 – power supply, 4 – IR camera, 5 – computer with appropriate software.

Using the experimental results and the inverse problem solution (Eq. (4)) the thermal diffusivity α of the austenitic steel (316L) and aluminium alloy have been determined: $\alpha_s = 3.67 \cdot 10^{-6} \text{ m}^2/\text{s}$ and $\alpha_A = 9.43 \times 10^{-5} \text{ m}^2/\text{s}$, respectively.

References

1. T. Karman (1921). Über laminare und turbulente Reibung, *Zeitschrift für Angewandte Mathematik und Mechanik*, **1**, 233–252.
2. K. Kochanowski, W. Oliferuk, Z. Płochocki, A. Adamowicz (2014). Determination of thermal diffusivity of austenitic steel using infrared thermography, *Archives of Metallurgy and Materials*, **59**, 3.

ARBITRARY PIEZOELECTRIC INCLUSION WITH WEAKLY AND HIGHLY CONDUCTING IMPERFECT INTERFACE

D.R. McArthur, L.J. Sudak

University of Calgary, Alberta, Canada

1. Introduction

Piezoelectric composites can be found in a multitude of electrical and electromechanical systems and as such, the study of problems dealing with piezoelectric inclusions has received a considerable amount attention in recent years. Many of the recent works in this field analyze piezoelectric inclusions with at least one of the following simplifications; perfect bonding along the inclusion matrix interface or simple inclusion boundary geometry (such as a circle or an ellipse). In reality, these assumptions do not adequately describe the interaction between the inclusion and matrix across the boundary between them because they cannot account for phenomena such as interfacial damage and de-bonding.

2. Formulation

The present work circumvents the aforementioned issues by way of a particular form of the potential function postulated inside the inclusion as a Faber Series. This technique allows for the introduction of arbitrary inclusion geometry into the problem. Furthermore, the present work also incorporates the concept of a homogeneously imperfect interface across the inclusion boundary curve. In the present work two separate, but structurally similar, sets of boundary conditions are analyzed. First the inclusion matrix interface will be assumed to operate as a mechanically compliant, dielectrically weakly conducting interface, and then later as a mechanically compliant, dielectrically highly conducting interface. The generally accepted linear spring type model will be used for the homogeneously imperfect interface in both the elastic and electric boundary conditions. More specifically, the boundary conditions of the weakly conducting formulation are as follows

$$(1) \quad \sigma_{3r}^{(1)} = \sigma_{3r}^{(2)}, \quad D_1^{(1)} = D_r^{(2)},$$

$$(2) \quad u_3^{(2)} - u_3^{(1)} = \alpha \sigma_{3r}^{(1)}, \quad \varphi^{(2)} - \varphi^{(1)} = -\beta D_r^{(1)}, \quad z \in \partial L.$$

The corresponding boundary conditions for the highly conducting formulation are given by

$$(3) \quad \sigma_{3r}^{(1)} = \sigma_{3r}^{(2)}, \quad E_\theta^{(1)} = E_\theta^{(2)},$$

$$(4) \quad u_3^{(2)} - u_3^{(1)} = \eta \sigma_{3r}^{(1)}, \quad D_r^{(2)} - D_r^{(1)} = -\frac{\mu}{r} \frac{\partial E_\theta^{(1)}}{\partial \theta}, \quad z \in \partial L.$$

It should be noted that in Eq.'s (1)–(4) are the homogeneously imperfect interface parameters for the weakly and highly conducting boundaries, respectively. Superscripts and or subscripts labeled are to refer to the inclusion whereas refers to the matrix and is the boundary curve separating inclusion from matrix.

Postulating the existence of an analytic vector function $\mathbf{U}_i(z) = \frac{1}{2i}(\mathbf{f}_i(z) - \overline{\mathbf{f}_i(z)})$, $i = 1, 2$ the boundary value problems formed by Eq.'s (1)–(4) may be solved via the introduction of the Faber Series as the potential function inside the inclusion (when mapped into an image ξ plane)

$$(5) \quad \mathbf{f}_1(\xi) = \sum_{n=1}^{\infty} \mathbf{a}_n P_n(\xi) + \mathbf{a}_0, \quad \omega(\xi) \in D_1,$$

$$(6) \quad P_k(\xi) = \sum_{n=1}^{\infty} \beta_{k,n} \xi^{-n}, \quad |\xi| > 1, \quad k = 1, 2, 3, \dots$$

In Eq.'s (5), (6), $P_n(\xi)$ are the Faber polynomials expressed in the form of a Laurent series and $\beta_{k,n}$ are mapping coefficients. Through the process of analytic continuation the potential functions in both the inclusion and matrix can be determined explicitly. Following this procedure, the imperfect interface condition(s) shown in Eq.'s (2) and (4) may be evaluated and, after comparing coefficients from the LHS to the RHS of these equations, a linear system of algebraic equations may be developed to solve for the unknown Faber coefficients. For both the weakly and highly conducting formulations the linear system appears as follows

$$(7) \quad \begin{bmatrix} \Gamma_1 & \Gamma_2 & \Gamma_3 & \Gamma_4 \\ \Gamma_2 & \Gamma_1 & \Gamma_4 & \Gamma_3 \\ \Gamma_5 & \Gamma_6 & \Gamma_7 & \Gamma_8 \\ \Gamma_6 & \Gamma_5 & \Gamma_8 & \Gamma_7 \end{bmatrix} \begin{bmatrix} \mathbf{a}_s \\ \mathbf{a}_s \\ \mathbf{a}_e \\ \mathbf{a}_e \end{bmatrix} = \begin{bmatrix} \mathbf{F}_s^\infty \\ \mathbf{F}_s^\infty \\ \mathbf{F}_e^\infty \\ \mathbf{F}_e^\infty \end{bmatrix}.$$

The column vector consisting of the \mathbf{a}_s and \mathbf{a}_e are the unknown elastic and electric Faber coefficients, \mathbf{F}_s^∞ and \mathbf{F}_e^∞ are quantities derived from the far field loading conditions specific to the elastic and electric coefficients (respectively), and the Γ_i , $i = 1, 2, \dots, 8$ coefficients are composed of elements of the conformal mapping process (for the exterior domain) and the imperfect interface/material properties. With both the inclusion and matrix potential functions determined explicitly the stresses, electric displacements, and or electric fields present around the boundary of the inclusion may be determined explicitly.

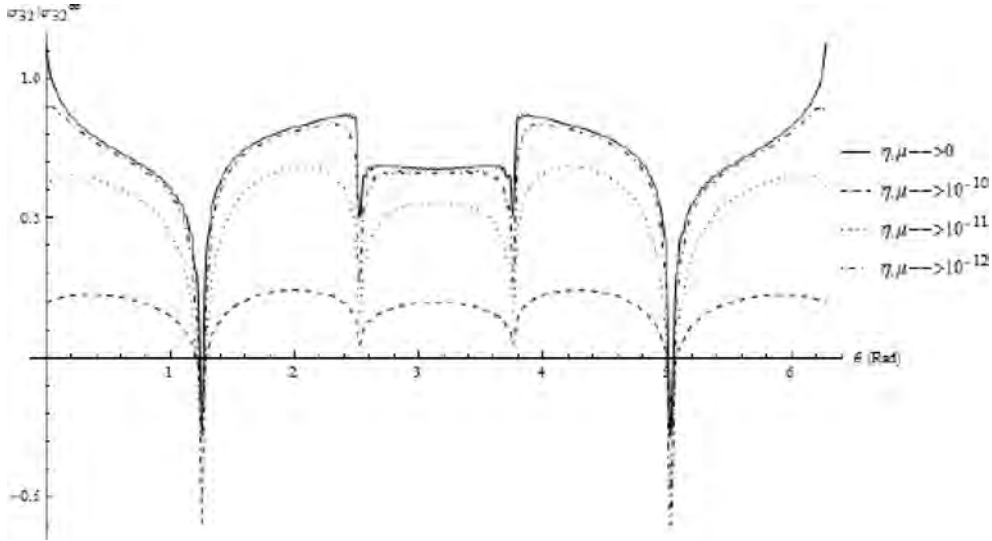


Fig. 1. Stress in a star shaped inclusion (BaTiO_3) embedded in (LiNbO_3) exposed to far field shear under the highly conducting formulation for various imperfect interface values.

From the numerical simulations, such as Fig. 1, it is clear that the stress peaks occur at the vertices of the star (which is to be expected) and the areas of highest stress fluctuation are seen in locations along the inclusion boundary curve where the normal is most weighted in the direction of the applied remote loading.

References

1. X. Wang, L.J. Sudak (2007). A piezoelectric screw dislocation interacting with an imperfect piezoelectric biomaterial interface, *Int. J. Sol. Struct.*, **44**, 3344–3358.
2. C.-F. Gao, N. Noda (2004). Faber series method for two-dimensional problems of an arbitrarily shaped inclusion in piezoelectric materials, *Acta Mech.*, **171**, 1–13.

IDENTIFICATION OF PARAMETERS OF BODNER-PARTOM VISCOPLASTIC MODEL FOR ALUMINUM ALLOY AT ELEVATED TEMPERATURE

A. Mleczek, P. Kłosowski

Faculty of Civil and Environmental Engineering, Gdansk, Poland

1. Introduction

At elevated temperature viscoplastic phenomenon should be taken into account in the description of dynamic material answer. Due to the fact that mechanical properties of body, which is subjected to dynamic forces beyond the plasticity limit, can be strain rate dependet. At the beginning of the twentieth century it has been noticed that during dynamic experiments the plasticity limit increases in comparison to static tests [1]. The classification of mechanical phenomenon in the displacement rate can be found in work [2]. Except of the change of the plasticity limit, strain rate changes mechanical behavior during loading process. It has been observed in experimental work about aluminum, steel, iron or magnesium [3]. Except of the strain rate dependency, material behavior is also temperature sensitive [4].

This study refers to determination the influence of temperature on the aluminum alloy. This effects was conduct on the basis of the parameters identification one of the Bodner-Partom viscoplastic model.

2. Materials and methods

The main purpose of this study is the identification of the Bodner-Partom viscoplastic model's parameters for the aluminum alloy. The additional purpose is the comparison of the parameters' values for tests at elevated temperature and tests at room conditions. The results have been verified by the numerical simulation of the laboratory tests. The material parameters have been calculated on the basis of the uniaxial tension test. Three tests at elevated temperature and one test at room temperature have been made for five different strain rates. The tests have been conducted on specimens cut out from 3 mm thick aluminum sheet. The tests have been performed on the strength machine Zwick/Roell Z400 with a mechanical extensometer and a thermal chamber.

The determination of the Bodner-Partom model's parameters has been made on the basis of the ideas presented in papers [5, 6] and [7]. The elastic and inelastic properties have been estimated using the approximation by the least-squares method in Marquard-Levensberg variant. The correctness assessment of the performed approximation has been verified on the basis of the correlation and determination coefficients.

3. Results

The identification results have been presented in Table 1. The last column contains the percentage differences between the values of the parameters, obtained in the process of identification at temperature of 120°C and those obtained at room conditions. The negative values indicate a decrease of the value of certain parameters at temperature of 120°C in relation to the temperature of 20°C.

Table 1. Results of parameters identification for the tests performed at elevated temperature (120°C).

Parameter	Unit	Average values of the parameters (120°C)	Average values of the parameters (120°C)	Percentage difference
D_0	s^{-1}	10.000	10.000	0.0
m_2	Pa^{-1}	$5.836 \cdot 10^{-5}$	$7.241 \cdot 10^{-5}$	-19.4
m_1	Pa^{-1}	$4.848 \cdot 10^{-6}$	$6.223 \cdot 10^{-6}$	-22.1
n	-	5.411	17.453	-69.0
R_0	Pa	$157.573 \cdot 10^6$	$145.226 \cdot 10^6$	8.5
D_1	Pa	$-14,116 \cdot 10^6$	$-17.892 \cdot 10^6$	21.1
R_1	Pa	$179.043 \cdot 10^6$	$166.348 \cdot 10^6$	7.6

4. Conclusions

The identification of the parameters of the Bodner-Partom viscoplastic model made at the temperature of 120°C and at the room temperature allows up to determine the temperature influence on the viscous properties of the material. Next, the average values of the viscoplastic parameters have been calculated and the results obtained at higher temperature have been compared with those obtained at room temperature. Substantial differences in the values of some parameters are observed, particularly a significant decrease of the parameter n by as much as 69%. This parameter takes into account changes of viscosity in the Bodner-Partom viscoplastic model. Similar differences of 20% have been recorded for three other parameters of the viscoplasticity law: m_2 , m_1 and D_1 . The performed identifications prove that temperature has a significant impact not only on the viscoplastic properties of the material, but also on the elastic properties. In both cases, the decrease in the value obtained at elevated temperatures in relation to room temperature is up to about 69%. Besides, it has been noted that at temperature of 120°C the values of the elasticity modulus slightly increase with increase of the strain rate. Such phenomenon has been not observed in the room temperature.

References

1. P. Ludwik (1909). *Elements of the technical mechanics*, Springer, Berlin (in German).
2. J.L. Duncan (1973). *Issues of creep and plasticity*, Materials Training Conference, Jablonna (in Polish).
3. F.H. Norton (1929). *The Creep of Steel at High Temperature*, McGraw Hill, New York.
4. P. Kłosowski, K. Woźnica (2007). *Nonlinear viscoplastic constitutive models in selected applications of structures analysis*, Ed. Gdańsk University of Technology, Gdańsk (in Polish).
5. K.S. Chan, U.S. Lindholm, S.R. Bodner, T.J. Hill, R.W. Weber, T.G. Meyer (1986). Constitutive modeling for isotropic materials (HOST), *Third Annual Status Report, NASA Report CR - 174980*.
6. S. Huang, A.S. Khan (1992). Modeling the mechanical behavior of 1100-0 aluminum at different strain rates by the Bodner-Partom model, *Int. J. Plasticity*, **8**, 501-517.
7. M.A. Rowley, E.A. Thornton (1996). Constitutive Modeling of the Visco-Plastic Response of Hastelloy - X and Aluminium Alloy 8009, *J. of Eng. Materials and Technology*, **118**, 19-27.

TWO-SCALE MODELING APPROACH FOR PREDICTION OF MASONRY COLUMN FAILURE

V. Nežerka, J. Antoš, P. Tesárek, J. Zeman

Department of Mechanics, Faculty of Civil Engineering, CTU in Prague, Czech Republic

1. Introduction

The use of masonry for the construction of load-bearing elements has been extensive throughout history. The craft was perfected mainly during the Roman period, when the basic understanding of structural behavior and development of suitable mortars allowed the construction of magnificent structures, attracting millions of tourists annually. The excessive loading and deterioration of the original materials evokes a concern about the durability of the ancient masonry structures, and their preservation became a frequently discussed issue. With respect to the enormous value of the structures, any intervention or repairs have to be done very carefully and after a rigorous assessment.

2. Basic assumptions and methods

Despite the enormous complexity of the mechanical behavior of masonry, the structural stability and safety of a structure can be assessed numerically thanks to available computational power of modern computers. Beside efficient computational methods, it is necessary to develop reliable constitutive models representing the materials, i.e. masonry blocks and mortar. In general, the mortar joints of historic masonry act as planes of weakness and decide about the performance of masonry elements. Therefore, we focused on an optimization of mortar with respect to the mechanical properties, while obeying the requirements defined by the authorities for cultural heritage, such as suitable chemical composition of its constituents [1].

To that purpose an analytical micromechanical model spanning several length-scales, based on the incremental form of the Mori-Tanaka method [2, 3], has been developed and successfully validated by experiments. Such strategy provides a computationally cheap estimate of mortar stiffness, tensile and compressive strength, and fracture energy. These effective mortar properties represent input data for a Finite Element (FE) model predicting the load-bearing capacity of masonry elements, with mortar modeled as a homogeneous inelastic material.

In particular, the present study is focused on the failure simulation of masonry columns eccentrically loaded in compression. The isotropic damage-plastic model proposed by Jirásek and Grassl [4] implemented in OOFEM software [5] has been adopted for the 3D FE analysis using linear tetrahedral elements.

3. Experimental analysis

The results of our calculations were compared to the experimentally obtained data on columns produced using lime-based mortar and common clay bricks. The full-scale testing was carried and the displacement field was monitored using a high-definition camera. Consequently, the corresponding strain field was evaluated using Digital Image Correlation (DIC) tool Ncorr [6]. In order to obtain stress-displacement diagrams and to check the results provided by DIC, the displacements were monitored in the column corners using extensometers attached to the face of columns.

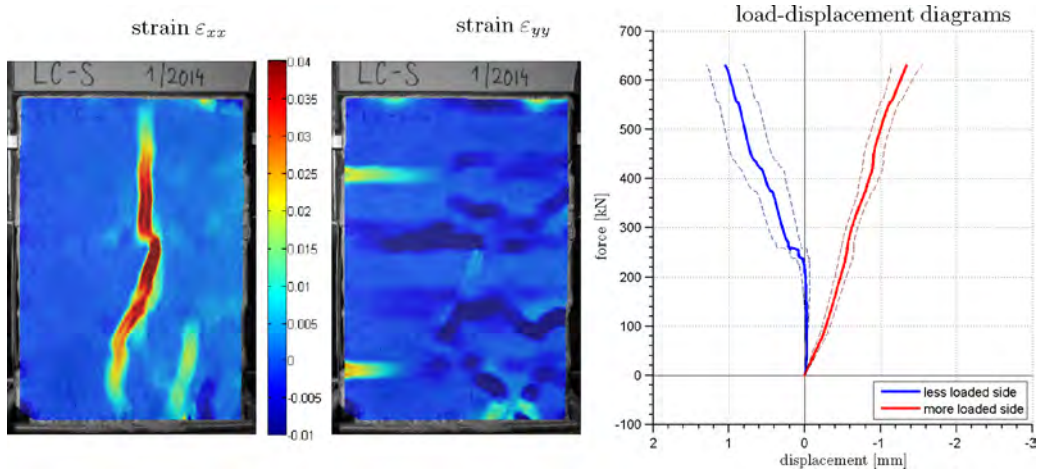


Fig. 1. Strain evolution during loading of columns (left and middle) and load-displacement diagrams (right).

4. Results and discussion

The results of our simulations indicate that the tensile strength of mortar and the bond strength at the interface between mortar and surrounding bricks have the major influence on the load-bearing capacity of masonry columns.

The experimental analysis confirmed that masonry columns lose their structural integrity after the mortar failure. Subsequently, a severe cracking affecting the entire column develops. Therefore, the attention should be paid on the development of strong mortars complying with the requirements established by the authorities for cultural heritage, and on the construction technology ensuring a proper bond between the mortar and surrounding masonry blocks.

Acknowledgments

This outcome has been supported by the Ministry of Culture of the Czech Republic, project No. DF11P01OVV008.

References

1. V. Nežerka, Z. Slížková, P. Tesárek, T. Plachý, D. Frankeová, V. Petráňová (submitted 2013). Comprehensive study on microstructure and mechanical properties of lime-pozzolan pastes, *Cem. Concr. Res.*
2. T. Mori, K. Tanaka (1973). Average stress in matrix and average elastic energy of materials with misfitting inclusions, *Acta Metall. Mater.*, **21**, 571–574.
3. Y. Benveniste (1987). A new approach to the application of Mori-Tanaka theory in composite materials, *Mech. Mater.*, **6**, 147–157.
4. P. Grassl, M. Jirásek (2006). Damage-plastic model for concrete failure, *Int. J. Solids Struct.*, **43**, 7166–7196.
5. B. Patzák, Z. Bittnar (2001). Design of object oriented finite element code, *Adv. Eng. Softw.*, **32**, 759–767.
6. J. Blaber (2014). *Ncorr digital image correlation software*, Georgia Institute of Technology.

SKAKEDOWN MECHANISM IN ROUND RODS SUBJECTED TO CYCLIC TORSION AT CRYOGENIC TEMPERATURES

R. Ortwein, B. Skoczeń

Institute of Applied Mechanics, Cracow University of Technology, Poland

1. Introduction

Austenitic stainless steels are very commonly used in structural applications both at room and cryogenic temperatures, almost down to absolute zero. Plastic strain induced phase transformation, often observed in these materials, causes changes of the microstructure from ductile and soft austenite to elastic and hard martensite. This phenomenon has been the subject of extensive studies during the past decades. In the present study, behavior of several austenitic stainless steels (304, 304L, 316L, 316LN) is investigated under cyclic torsion, at two temperatures: 77 K and 293 K. Torque versus angle of twist as well as the evolution of martensite content during monotonic and cyclic loading have been measured by means of Feritscope. This study has proved the possibility to create structural elements of variable microstructure (martensite and austenite content), that can be controlled via plastic strains distribution (function of the angle of twist).

2. Experimental methods and results

A cylindrical cryostat has been used for both test conditions (77 K, 293 K). Liquid nitrogen has been used as a coolant. Several samples of the same geometry have been machined from 4 types of austenitic stainless steels. The angle of twist has been measured on a printed scale with 0.5° accuracy. The torque was applied and measured by means of dedicated torque wrench. The content of martensite has been captured by using Feritscope MP3C. To measure martensite content, calibration of the device [2] as well as application of specific correction factors was necessary. After each half cycle (denoted as “hf” in Figs. 1, 2) the bar was removed from the cryostat, and the measurement was performed via Feritscope on the surface along the axis of the sample. In total, 10 full cycles were carried out and 17 samples have been tested; 8 were made of 304 stainless steel, and 3

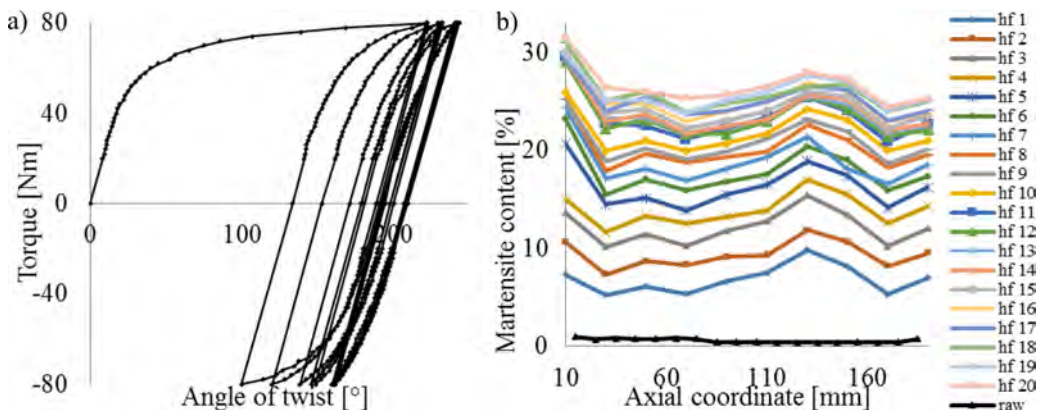


Fig. 1. a) Torque versus angle of twist for sample A2, ± 80 Nm, 10 cycles at 77 K; b) Martensite content evolution.

additional samples were made of each of three steels: 304L, 316L, 316LN. Two of these results are shown in Figs. 1 and 2.

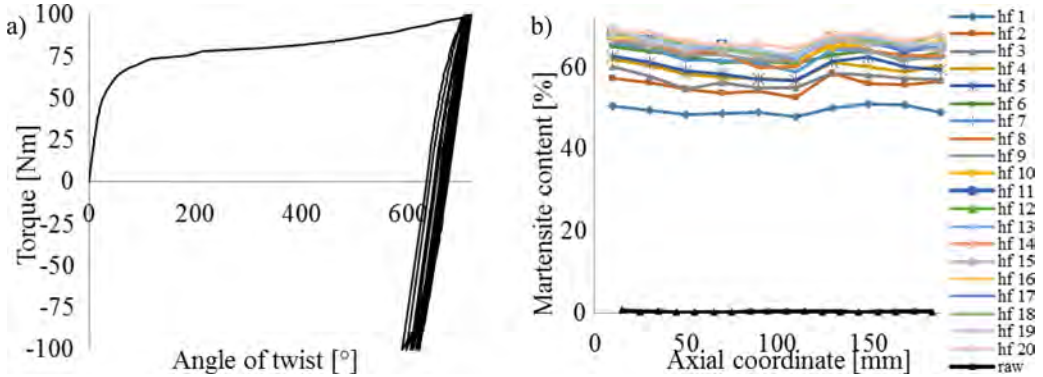


Fig. 2. a) Torque versus angle of twist for sample A4, ± 100 Nm, 10 cycles at 77 K; b) Martensite content evolution.

3. The constitutive model

Torque versus angle of twist and the martensite content can be obtained theoretically from the 3D constitutive model, developed previously by the authors. The nonlinear tangent stiffness and the kinetics of the phase transformation are described by Eqs. (1) [1]:

$$(1) \quad C_{MT}(\xi) = \frac{5 \cdot C_{a0}}{2(1 + \nu_a)} \frac{\xi \cdot (1 + h\xi)}{(1 - \xi)}, \quad \xi = A(T) \cdot (\gamma - \gamma_\xi) \cdot H[(\gamma - \gamma_\xi) \cdot (\xi_L - \xi)].$$

The torque versus the unit angle of twist equals:

$$(2) \quad M_{III}(\theta) = B_1 \cdot \theta^{-3} + B_2 \cdot \theta^{-2} + B_3 \cdot \theta^{-1} + B_4 + B_5 \cdot \theta^1 + B_6 \cdot \theta^2 + B_7 \cdot \theta^{-3} \cdot \ln[1 - A \cdot (\theta \cdot R - \gamma_\xi)] + B_8 \cdot \ln[1 - A \cdot (\theta \cdot R - \gamma_\xi)]$$

where ξ is the martensite content, $A(T)$, γ_ξ , ξ_L are material parameters and $A_1 \div A_3$ as well as $B_1 \div B_8$ are functions of the parameters of the constitutive model.

4. Conclusions

The main conclusion consists in the confirmation of the possibility to control the microstructure of the material by the plastic strains (by means of the angle of twist).

For cyclic loads, accelerated shakedown due to the evolution of microstructure has been observed in the course of numerical simulations. As it results from the structural evolution of two-phase continuum, where the elastic-plastic matrix is gradually replaced by the elastic inclusions, in the limit case where 100% of primary phase is replaced by the secondary phase the shakedown occurs by definition. This important and new conclusion has very practical meaning. As soon as the $\gamma \rightarrow \alpha'$ phase transformation begins, the evolution of material structure accelerates the process of adaptation of structural members to cyclic loads and, therefore, enhances their fatigue life when compared to the classical elastic-plastic structures.

References

1. B. Skoczeń (2007). Functionally graded structural members obtained via the low temperatures strain induced phase transformation, *Int. J. Solids Struct.*, **44**, 5182–5207.
2. J. Talonen, P. Aspegren, H. Hanninen (2004). Comparison of different methods for measuring strain induced α' -martensite content in austenitic steels, *Mater. Sci. Tech. Ser.*, **20**, 12, 1506–1512.

PLASTIC STRAIN AND RADIATION INDUCED PHENOMENA BETWEEN ABSOLUTE ZERO AND ROOM TEMPERATURE

B. Skoczeń

Institute of Applied Mechanics, Cracow University of Technology, Cracow, Poland

1. Plastic strain and radiation induced phenomena at cryogenic temperatures

Modern scientific instruments based on superconducting magnets generate ever increasing interest in the development and mathematical description of materials suitable for extremely low temperatures. Many of these materials undergo at low temperatures three distinct phenomena: discontinuous plastic flow (serrated yielding), plastic strain induced transformation from the parent phase to the secondary phase, and evolution of micro-damage. All three phenomena lead to irreversible degradation of lattice and accelerate the process of material failure. Discontinuous yielding is characteristic both of low and high stacking fault energy materials loaded beyond the yield point at very low temperatures. It represents oscillatory mode of deformation, reflects discontinuous nature of plastic flow and occurs below a specific temperature that represents transition from screw to edge dislocations mode. The plastic strain induced fcc-bcc phase transformation results from metastability of LSF metals and alloys at very low temperatures. The transformation process leads to creation of two-phase continuum where the parent phase coexists with the inclusions of secondary phase. The plastic strain and irradiation driven evolution of micro-damage at cryogenic temperatures represents a dissipative and irreversible process that leads to creation of micro-cracks and micro-void clusters and results in material “softening”.

2. Experiments

Given at least two contradictory theories (Basinski, 1957; Obst and Nyilas, 1991) developed in the past to explain serrated yielding there was a clear need to carry out additional experimental effort and to perform more precise tests in order to detect the real nature of this phenomenon. A crucial step has been achieved by mounting high sensitivity internal load cell in the proximity of the sample (inside the cryostat) and performing the measurements with the sampling frequency of 20 kHz. A comparison of the records obtained by means of the internal load cell with the values recorded by using the external load cell clearly shows that the drop of stress associated with each serration precedes the increase of temperature and the thermodynamic response is secondary with respect to the mechanical effect. Thus, the measurements reported explain the correct sequence of events when the plastic flow instability occurs.

3. Constitutive models

3.1. Discontinuous plastic flow. The main feature of serrated yielding consists in frequent abrupt drops of stress as a function of strain during monotonic loading. The mechanism of discontinuous yielding is related to formation of dislocation pile-ups at strong obstacles such as the Lomer-Cottrell (LC) locks during the strain hardening process. The back stresses of the piled-up groups block the motion of newly created dislocations. The local shear stress at the head of dislocation pile-up (τ_e) reaches the level of cohesive strength and the Lomer-Cottrell lock collapses by becoming a glissile dislocation. Such a local catastrophic event can trigger similar effects in the other groups of dislocations. Thus, the final result is massive and has collective character. Each “serration”

is accompanied by a considerable increase of temperature, related to the dissipation of plastic power. Surface density (B) of dislocation groups located at the Lomer-Cottrell locks reflects the readiness of lattice to plastic serration. It is assumed that the LC locks massively develop after a specific strain threshold has been reached and the increment of B is strictly related to the increment of accumulated plastic strain. The initial stages of the process reflect elastic-plastic loading under nearly isothermal conditions, corresponding to low excitation of the lattice. Under these circumstances (no thermal activation) the rate-independent plasticity can be applied. Thus, the yield surface has the standard form expressed by the deviatoric stress with kinematic and isotropic hardening included. Furthermore, it is assumed that the continuum containing LC locks obeys the associated flow rule. It is postulated in the present model that in every loading/unloading “cycle” the parameter B is accumulated from 0 as soon as the discontinuous plastic flow is triggered after a specific interaction curve in the $(B - \tau_e)$ space has been reached. Identification of parameters of the constitutive model is based on the experimental data collected during a campaign of tensile tests carried out on copper and stainless steel samples immersed in liquid helium (4.2 K).

3.2. Plastic strain induced phase transformation. The constitutive model used to describe mathematically the plastic strain induced fcc-bcc phase transformation at low temperatures involves strain hardening where two fundamental effects play an important role: interaction of dislocations with the martensite inclusions and increase in material tangent stiffness due to the mixture of harder martensite with softer austenite. The interaction of dislocations with the martensite inclusions is reflected by the hardening modulus that depends on the volume fraction of martensite. Here, a linear approximation, based on the micro-mechanical analysis, is used. On the other hand, evaluation of the material tangent stiffness of two-phase continuum is based on the classical homogenization scheme and takes into account the local tangent moduli of the components, as postulated by Hill, 1965. Mori-Tanaka homogenization algorithm is used to obtain the tangent stiffness operator of two-phase continuum (mixture of elastic martensite and elastic-plastic austenite).

3.3. Evolution of radiation induced micro-damage under plastic strains. Typical materials used for particle accelerators and target facilities (beam transport systems, magnetic horns, collimators etc.), subjected to flux of secondary particles of sufficiently high energy, suffer from formation of local defects in the form of interstitial atom/vacancy clusters (quantified by means of displacement per atom “dpa” unit). Most of defects remaining after irradiation and subsequent recombination are described in terms of porosity, coexisting with the classical micro-cracks and micro-voids of mechanical origin. Radiation induced micro-damage fields (voids and cavities) are computed based on NIEL (non-ionizing energy loss) and corresponding dpa distribution. The recombination effect is taken into account as a function of temperature during irradiation. Evolution of radiation induced micro-damage under the applied quasi-static or cyclic loads is described by means of Rice&Tracey and type Gurson kinetic laws. On the other hand, evolution of micro-damage fields of mechanical origin is described by means of the Garion-Skoczeń kinetic law (generalization of the classical Chaboche-Lemaitre model). The driving force of evolution of both types of micro-damage fields, coexisting in the same RVE, remains the accumulated plastic strain. Radiation induced micro-damage field is regarded mainly as isotropic, whereas the mechanically induced micro-damage field shows texture induced anisotropy. Combined damage representation is constructed in an additive way, as a sum of damage parameters/tensors individually related to both fields.

References

1. R. Ortwein, B. Skoczeń, J.Ph. Tock (2014). Micromechanics based constitutive modeling of martensitic transformation in metastable materials subjected to torsion at cryogenic temperatures, *International Journal of Plasticity*, **59**, 152–179.
2. B. Skoczeń, J. Bielski, J. Tabin (2014). Multiaxial constitutive model of discontinuous plastic flow at cryogenic temperatures, *International Journal of Plasticity*, **55**, 198–218.

MAGMA FLOW CAUSED BY INVERTED DENSITY STRATIFICATION

M. Somr, P. Kabele

Department of Mechanics, Faculty of Civil Engineering, CTU in Prague, Prague, Czech Republic

1. Introduction

Volcanic processes represent an enormous risk for the environment, climate and human society. Thus, a deeper understanding of geological conditions under which catastrophic events can occur is of a great importance and interest.

In this paper, we focus on the way how magma is transported from lower layers of the Earth through many kilometers of overlaying viscous and solid strata to shallow crustal layers. Geologists came up with several possibilities of the magma emplacement.

One of the theories, we particularly focus on, is a *diapirism*. The main reason why we are interested in this phenomenon is that there are still many researchers who question the diapirism as a possible mechanism responsible for the magma ascent, because it has never been conclusively proven that diapirs can reach the shallow crustal layers in a geologically reasonable time [1, 2].

2. Problem description

The diapirism is a subsurface flow of earth materials, which is caused by inverted density stratification. It means that one or more layers of a low density material are beneath materials of higher density. The diapir is generated from the magma plume in the mantle and it stalls its rise either when it reaches a region, where the density of a wall rock is similar to that of the diapir, or when the viscosity of the wall rock is too high. This usually happens somewhere in the crust, where the magma accumulates and forms a magma chamber.

After publishing papers of Grout [3] and Ramberg [4, 5], the diapirism became a popular theory explaining the ascent and emplacement of the magma. The ascent of magma can originate either from the Rayleigh-Taylor instability (gravitationally unstable configuration of viscous layers) or from a discrete region.

Researchers usually consider different rheologies of magma and host rock in order to reach as realistic model as possible, because behavior of most rock materials at very high temperature and pressure is unknown. Weinberg and Podladchikov [6] extended the Hadamard-Rybczynsky equation by three correction factors in order to describe the ascent of a viscous diapir composed of the Newtonian or power-law fluid through power-law wall rock. Another approach was chosen by Burov *et al.* [7], who employ a numerical model for assessment of deformation and heat transport. This strategy enables ductile, elastic, and brittle behavior simulations and a large-strain formulation is to solve stress, strain, and strain rate fields as a function of time.

3. Model

To numerically simulate the above-mentioned phenomena, we construct a finite element model in an object oriented finite element solver OOFEM [8].

Several experiments show that magmas, such as basalt heated above its liquidus temperature, behave as a Newtonian fluid [9]. Therefore, both magma and the host rock are considered to be viscous Newtonian fluids, which are immiscible. The diapir ascent is initiated from the Rayleigh-Taylor instability (as illustrated in Fig. 1).

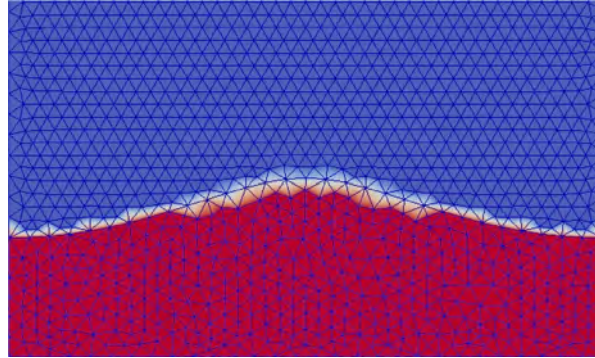


Fig. 1. Rayleigh-Taylor instability with the mesh and interface detail (magma represented by red and host rock by blue color).

The presented model is described as a transient incompressible flow using the Eulerian formulation with a fixed triangular finite element mesh, which is depicted in Fig. 1 as well. The flow is stabilized using the streamline-upwind / Petrov-Galerkin (SUPG) and the pressure-stabilizing / Petrov-Galerkin (PSPG) algorithms. It provides high accuracy solutions of advection-dominated problems and significantly improves a convergence rate in an iterative solution of large nonlinear systems of equations. It also allows utilizing equal-order interpolation functions for velocity and pressure. The volume of fluid (VOF) method is used to track the evolving shape and position of the fluid-fluid interface.

Since OOFEM was mostly used for simulation of large-scale free surfaces so far, it was unable to capture a surface tension, which was necessary to implement using the C++ language.

4. Results and discussion

Our model proves that the ascent velocity is greatly influenced by the viscosity of the host rock, while the effect of the magma viscosity is almost negligible. It also indicates the shape development of the diapir, which consequently affects the final shape of the magma chamber. The results are in the agreement with findings of geologists.

The shape and the depth of the chamber are especially important for predicting the risk of a caldera formation, which is a result of the magma chamber roof collapse. The process of the caldera formation is one of the most catastrophic geologic events that have occurred on the Earth's surface.

Acknowledgment

The financial support by the grant no. OHK1-089/14 is gratefully appreciated.

References

1. S.R. Paterson, R.H. Vernon, T.K. Fowler (1991). Aureole tectonics, *Rev. Mineral.*, **26**, 673–722.
2. J.D. Clemens, C.K. Mawer (1992). Granitic magma transport by fracture propagation, *Tectonophysics*, **204**, 339–360.
3. F.F. Grout (1945). Scale models of structures related to batholiths, *Am. J. Sci.*, **243**, 260–284.
4. H. Ramberg (1970). Model studies in relation to plutonic bodies, *Geol. J.*, **2**, 261–286.
5. H. Ramberg (1981). *Gravity, Deformation and the Earth's Crust*, Academic Press, London.
6. R.F. Weinberg, Yu. Podladchikov (1994). Diapiric ascent of magmas through power law crust and mantle, *J. Geophys. Res.*, **99**, 9543–9559.
7. E.B. Burov, C. Jaupart, L. Guillou-Frottier (2003). Ascent and emplacement of buoyant magma bodies in brittle-ductile upper crust, *J. Geophys. Res.*, **108**, 2177, doi: 10.1029/2002JB00190.
8. B. Patzák, Z. Bittnar (2001). Design of object oriented finite element code, *Adv. Eng. Softw.*, **32**, 759–767.
9. H.R. Shaw (1969). Rheology of basalt in the melting range, *J. Petrol.*, **10**, 510–535.

SMALL-SCALE EFFECT IN THE FRAMEWORK OF FRACTIONAL AND ERINGEN NON-LOCAL MODELS

W. Sumelka¹, J. Fernández-Sáez², R. Zaera²

¹Poznan University of Technology, Institute of Structural Engineering
Piotrowo 5 street, 60-969 Poznań, Poland, e-mail: wojciech.sumelka@put.poznan.pl

²Department of Continuum Mechanics and Structural Analysis, University Carlos III of Madrid
28911 Leganés, Madrid, Spain, e-mail: ppfer@ing.uc3m.es, ramon.zaera@uc3m.es

In this paper we present the comparison of two non-local formulations for small-scale effect modelling, namely fractional and Eringen models. The problem is illustrated by the analysis of 1D axial vibration of a nanorod. The discussion considers natural frequencies as a function of body dimensions and chosen length scale. For fractional model the influence of the order of fractional derivative is also discussed.

1. Introduction

Nowadays micro or nanostructures have increasing technological applications. Micro- or nano-electromechanical systems (MEMS or NEMS), incorporating beams or plates in the micro or nano length scale, have application in different fields of mechanics, as well as in biotechnology and biomedical fields. Due to the dimensions of these structures, which are small and comparable to molecular distances, size effects are significant in their mechanical behaviour.

Classical Continuum Mechanics (CCM), because of being length-scale independent, cannot handle size effect, thus non-local models are needed. In this paper two approaches will be contrasted, namely the Eringen non-local elastic model [1] and the Fractional Continuum Mechanics (FCM) with elastic behaviour [2].

2. Problem formulation

We consider a bar of constant cross section area, length L , density ρ and Young modulus E , in absence of external forces. The problem of 1D linear elasticity under FCM is governed by the following equation

$$E l_f^{\alpha-1} \frac{1}{2} \frac{\Gamma(2-\alpha)}{\Gamma(2)} \frac{\partial}{\partial x} \left({}^C_{x-l_f} D_x^\alpha u - {}^C_x D_{x+l_f}^\alpha u \right) = \rho \frac{\partial^2 u}{\partial t^2}$$

where x denotes space, t is time, u is displacement, l_f is a length scale in the fractional model, Γ is the Gamma function, ${}^C D^\alpha$ is the Riesz-Caputo differential operator and α is the order of the fractional differentiation. Alternatively this problem may be stated, under the hypotheses of the Eringen elastic non-local model, according to the following equation [3]:

$$E \frac{\partial^2 u}{\partial x^2} = \left(1 - (e_0 a)^2 \frac{\partial^2}{\partial x^2} \right) \rho \frac{\partial^2 u}{\partial t^2}$$

$l_g = e_0 a$ being the length scale for Eringen model. Assuming clamped-clamped boundary conditions, we may obtain the non-local eigenfrequencies of the rod ω_{NL} . In the case of FCM, the determination of natural frequencies requires solving an algebraic eigenproblem, due to the approximation of fractional spatial derivatives at discrete positions, whereas for the Eringen model the frequencies can be obtained in closed form (see Aydogdu [3]).

3. Numerical examples and discussion

In Fig. 1 the eigenfrequencies corresponding to the first vibration mode ($k = 1$), ω_{NL} of both FCM and Eringen models are compared with those obtained with CCM (local) model ω_L , for different orders of fractional derivative α , and four different values of the non-dimensional length-scale parameter $\bar{l} = \{0.1, 0.5, 1, 2\}$ ($\bar{l} = 2l_f/L$ for FCM, $\bar{l} = l_g/L$ for Eringen).

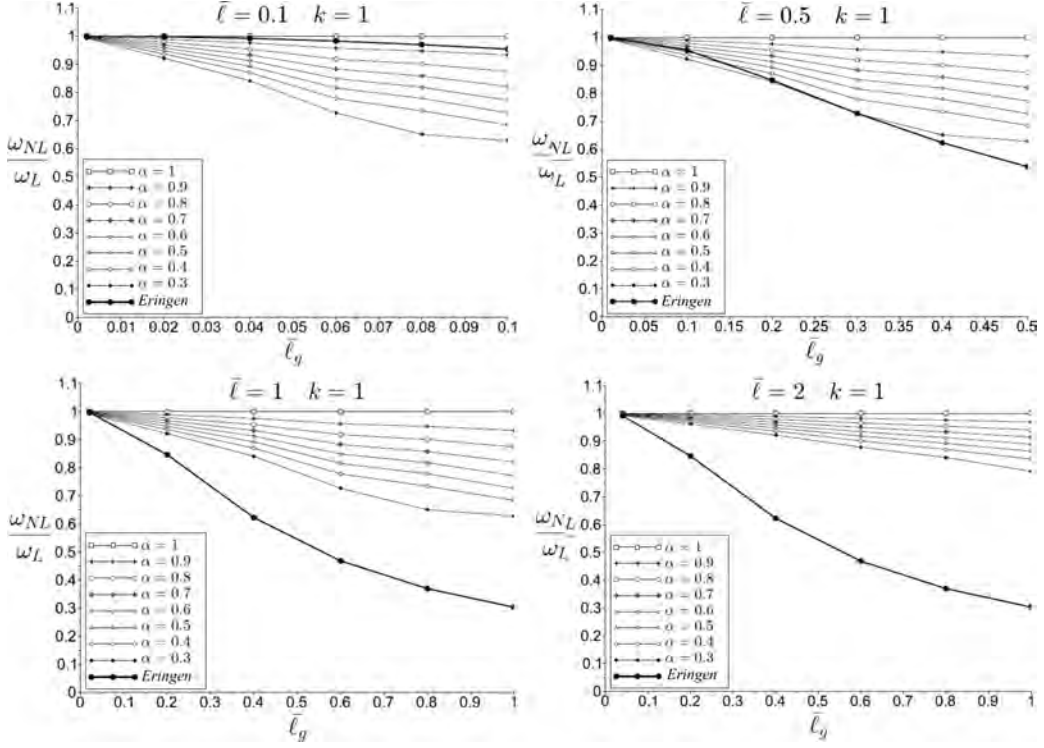


Fig. 1. Comparison of first eigenfrequency obtained with Eringen and FCM non-local models. Effect of length-scale parameter and fractional derivative order.

As shown ω_{NL} is dependent on length-scale parameter for both models, decreasing when \bar{l} increases, which strengthens the relevance of the length over which non-local effects are taken into account. Likewise, the solution of the FFC model depends on the value of the derivative order. Therefore α can be considered as an additional parameter in a non-local approach, offering more possibilities for reproducing the behavior of nanostructures. Moreover, using different types of fractional derivatives permit to obtain a closer approximation to the experimental observations. Certainly, this would also require additional results for a proper calibration.

References

1. A.C. Eringen (1972). Nonlocal polar elastic continua, *International Journal of Engineering Science*, **10**, 1–16.
2. W. Sumelka (2014). Application of fractional continuum mechanics to rate independent plasticity, *Acta Mechanica*, DOI: 10.1007/s00707-014-1106-4.
3. M. Aydogdu (2009). Axial vibration of the nanorods with the nonlocal continuum rod model, *Physica E*, **41**, 861–864.

AN ELASTIC-PLASTIC TORSION OF A PROFILE – COMPARISON OF MESHLESS METHODS IMPLEMENTATIONS

A. Uscilowska, M. Kulczyńska

Institute of Material Technology, Poznan University of Technology, Poznań, Poland

1. Introduction

This paper will be devoted to the problem of elastic-plastic torsion of a profile. For this problem there is no literature available, therefore considerations conducted in this paper will be based on literature about elastic-plastic torsion of a bar problem. This issue is well known and therefore widely described in literature so it's natural to use this knowledge to solve the problem of torsion of a profile.

In 1931 Nadai [8] presented a solution of an elastic-plastic solution. He invented the method of solving some cases of elastic-plastic torsion based on sand heap analogy. Next, Sadowsky [9] in 1941 extended the sand heap analogy to cross-section having one or more holes.

For some particular cases of the bar the exact solution is known, but in most cases coming from engineering it is not possible to find the exact solution by analytical way, It is necessary to use the numerical calculations to find the solution.

Recently, the meshless methods are developed and implemented to many engineering problems, including torsional problem. Mostly the elastic torsion is investigated. But there are few papers considering an elastic-plastic torsion of a bar, i. e. [7]. Authors implemented MFS for an elastic-plastic torsion of a prismatic rod. They presented results of numerical calculations for bar with square cross-section.

In present paper the comparison of three meshless methods is included. One of the method is MFS, proposed by [5]. Its numerical implementation was carried out by Mathon and Johnston [6]. This method has been applied to many engineering problems.

The second investigated method is KM, proposed by Kansa in 1999 in [3, 2].

The last method under consideration is the MAPS, presented by [1].

The novelty of this paper is the implementation of problem of the elastic-plastic torsion of a profile using Kansa Method and Method of Approximate Particular Solutions. The aim is to compare the results obtained by three methods and comparison of the effectiveness of these methods.

2. Problem description

There are some proposals of mathematical model of an elastic-plastic torsion of a bar in literature. In this paper the theory presented in [7] will be used and adapted to the problem of profile torsion. This approach involves the assumption that the displacements are the same as in elastic case of torsion.

The torsion of a profile is described by the following equation:

$$(1) \quad \frac{\partial^2 \phi}{\partial x^2} + \frac{\partial^2 \phi}{\partial y^2} = -2G\theta - g(x, y) \quad \text{in } \Omega$$

where ϕ is stress function, G is a shear modulus, θ is an angle of torsion, Ω is a region of a cross-section of a profile and $g(x, y)$ is a function given by formula:

$$(2) \quad g(x, y) = 2G \left(\frac{\partial \gamma_{xz}^p}{\partial y} - \frac{\partial \gamma_{yz}^p}{\partial x} \right) \quad \text{in } \Omega$$

where $\gamma_{xz}^p, \gamma_{yz}^p$ are the strains in plastic area of the profile cross-section. These strains depends on the stress function ϕ . For plastic range of torsion function $g(x, y)$ is greater than zero. It is obvious that for the elastic torsion equals zero. In this case the governing equation has form of Poisson equation.

For the torsion of a profile the boundary condition is given:

$$(3) \quad \phi = 0 \quad \text{on } \partial\Omega$$

where $\partial\Omega$ is the boundary of the region Ω .

3. Numerical solution

To solve the boundary value problem given by (1,3) the meshless methods (mentioned in Introduction) will be implemented. But, these implementation needs the application with other supporting methods and approaches.

The general algorithm is supported by Picard Iterations and is described by [4].

The very basic step in this procedure is to solve the boundary value problem consisting of Poisson equation and Cauchy-type boundary condition.

The three methods are proposed to solve the Cauchy boundary value problem with Poisson equation.

3.1. The Method of Fundamental Solutions. In this method it is assumed that the homogeneous solution may be approximated by a linear combination of special functions, known as fundamental solutions. Moreover, the inhomogeneous part of equation is approximated by a linear combination of Radial Basis Functions. So the approximation of the particular solution of the equation is a linear combination of the particular solutions for Radial Basis Functions.

3.2. The Kansa Method. The fundamental assumption of KM is that the solution of the Poisson-Cauchy boundary value problem is approximated by the linear combination of Radial Basis Functions. The real numbers, which are the coefficient of the linear combination of RBF are calculated by approximation of the inhomogeneous part of the equation by a linear combination of appropriate derivatives of RBF and approximation of the boundary conditions by of the linear combination of RBF.

3.3. The Method of Approximate Particular Solution. This method involves the approximation of the inhomogeneous part of Poisson equation by linear combination of Radial Basis Functions. Such approach gives the particular solution of the BVP in the form of a linear combination of the particular solutions for Radial Basis Functions. The homogeneous part of the solution is calculated by fulfilling the boundary condition by approximated homogeneous solution, which is in the form of a linear combination of the particular solutions for Radial Basis Functions.

4. Results of numerical experiment

The several types of the profiles have been investigated, i.e. the profiles with different cross-sections have been under consideration. The following shapes of the profile cross-section were investigated: C-, T- and Z-sections, and I-beam.

The results for the square cross-section will be presented on the conference.

Moreover the comparison of the accuracy of the results related to some parameters of the methods will be discussed.

5. Conclusions

The numerical algorithm considered in this paper is suitable for solving considered problem.

References

1. Chen C.S., Fan C.M., Wen P.H. (2012). The method of approximate particular solutions for solving certain partial differential equations, *Numerical Methods for Partial Differential Equations*, **28**, 2, 506–522.
2. Kansa E.J. (1999). Multiquadrics – a scattered data approximation scheme with applications to computational fluid-dynamics. I. Surface approximations and partial derivative estimates, *Computational Mathematical Applications*, **19**, 149–161.
3. Kansa E.J. (1999). Multiquadrics – a scattered data approximation scheme with applications to computational fluid-dynamics. II. Solutions to parabolic, hyperbolic and elliptic partial differential equations, *Computational Mathematical Applications*, **19**, 127–147.
4. Kolodziej J.A., Gorzelanczyk P. (2012). Application of method of fundamental solutions for elasto-plastic torsion of prismatic rods, *Engineering Analysis with Boundary Elements*, **36**, 81–86.
5. Kupradze V.D., Aleksidze M.A. (1964). The method of functional equations for the approximate solution of certain boundary value problems, *USSR Comput. Meth. Math. Phys.*, **4**, 82–126.
6. Mathon R., Johnston R.L. (1977). The approximate solution of elliptic boundary-value problems by fundamental solutions, *SIAM Journal on Numerical Analysis*, **14**, 638–650.
7. Mendelson A. (1968). *Plasticity: Theory and Application*, New York, Macmillan Company.
8. Nadai A. (1931). *Plasticity*, McGraw-Hill, New York.
9. Sadowsky M.A. (1941). An extension of the sand heap analogy in plastic torsion applicable to cross-section having one or more holes, *Journal of Applied Mechanics*, **8**, 166–168.

THERMOMECHANICAL MODELING OF ELASTIC-PLASTIC MATERIALS UNDERGOING LARGE DEFORMATIONS

B. Weisło, J. Pamin

Cracow University of Technology, Poland

1. Introduction

The paper deals with a coupled thermomechanical model which involves geometrical and material nonlinearities, i.e. large strains and plasticity, respectively. The influence of temperature on the behaviour of a material is significant. It can manifest itself in different ways: dependence of material parameters on temperature, thermal expansion or influence of the geometry change on the heat flux. What is more, during plastic deformation the heat production is observed. The presented material model includes full thermomechanical coupling and can reproduce complex response of a material.

In the paper the attention is focused on the aspects of the finite element implementation of the described model within symbolic-numerical computational tool. The application of this software requires the researcher to develop specific algorithms based on potentials derived from the weak forms of the governing equations.

2. Constitutive description

In this paper so-called energetic materials are considered, cf. [1]. The following constitutive model is derived using the classical multiplicative decomposition of the deformation gradient into its elastic and plastic component: $\mathbf{F} = \mathbf{F}^e \mathbf{F}^p$. The state of a material is expressed by the Helmholtz free energy potential which is assumed in a decoupled form [2]:

$$(1) \quad \psi(\mathbf{b}^e, T, \gamma) = \psi^e(\mathbf{b}^e) + \psi^{tm}(T, J) + \psi^T(T) + \psi^p(\gamma)$$

where the first part $\psi^e(\mathbf{b}^e)$ is related to the elastic response, the potential $\psi^{tm}(T, J)$ consists thermomechanical coupling responsible for thermal expansion, $\psi^T(T)$ is a purely thermal part and, finally, the term $\psi^p(\gamma)$ denotes the potential of isotropic strain hardening in plasticity. In Eq. (1) $\mathbf{b}^e = \mathbf{F} \mathbf{F}^{T}$ denotes the elastic left Cauchy-Green tensor, T is absolute temperature and $J = \det(\mathbf{F})$. On the basis of the free energy potential the state functions are obtained (Kirchhoff stress tensor, entropy and hardening function):

$$(2) \quad \boldsymbol{\tau} = 2 \frac{\partial \psi}{\partial \mathbf{b}^e} \mathbf{b}^e, \quad \eta = -\frac{\partial \psi}{\partial T}, \quad h = \frac{\partial \psi}{\partial \gamma}.$$

In the model the Huber-Mises-Hencky yield function F and linear isotropic hardening are adopted. The description is completed with the flow rule expressed through the Lie derivative of \mathbf{b}^e

$$(3) \quad -\frac{1}{2} \mathcal{L}_v \mathbf{b}^e = \dot{\gamma} \mathbf{N} \mathbf{b}^e$$

where \mathbf{N} denotes the normal to the yield function and $\dot{\gamma}$ is the plastic multiplier satisfying the KuhnTucker conditions:

$$(4) \quad \dot{\gamma} \geq 0, \quad F \leq 0, \quad \dot{\gamma} F = 0.$$

3. Balance laws

Due to the distinction between the reference and the current configuration in large strain analysis the governing equations can be formulated in material, see e.g. [3], or spatial description, e.g. [2]. The latter one is adopted in the presented model.

The analysed coupled problem is described with two governing equations. The first is the balance of linear momentum which can be formulated in local form as follows

$$(5) \quad \rho_0 \dot{\mathbf{v}} = J \operatorname{div} [\boldsymbol{\tau}/J] + \rho_0 \mathbf{B}.$$

The second governing equation is the energy balance which can be expressed in a temperature form [2]

$$(6) \quad c\dot{T} = J \operatorname{div} (-\mathbf{q}/J) + \mathcal{R}$$

where c is the heat capacity, \mathbf{q} denotes the Kirchhoff heat flux, \mathcal{R} is a heat source e.g. due to plastic dissipation, and $\operatorname{div}(\cdot)$ is the divergence computed with respect to Eulerian coordinates.

4. Implementation

The numerical simulations are performed using the symbolic-numerical packages *AceGen* (code generator) and *AceFEM* (finite element programme) in the Wolfram Mathematica environment [4]. To solve the set of nonlinear equations using the finite element method a standard Newton-Raphson iterative procedure is adopted. The code for computation finite element contribution to the global residual vector \mathbf{R}_{el} and to the tangent stiffness matrix \mathbf{K}_{el} is generated with *AceGen*. The important advantage of the application of the package is automatic differentiation which allows the researcher to compute the contribution to the consistent tangent matrix automatically on the basis of proper constitutive relations. A monolithic solution scheme is used. If the vector containing nodal unknowns (displacements and temperatures) is denoted with $\mathbf{p} = [\mathbf{u}_I, \mathbf{T}_I]$ then the contribution \mathbf{K}_{el} is calculated using relation:

$$(7) \quad \mathbf{K}_{el} = \frac{\partial \mathbf{R}_{el}}{\partial \mathbf{p}}.$$

For thermomechanical coupling the tangent matrix is non-symmetric.

In the paper the analysis is performed for three-dimensional problems and standard eight-noded finite elements with linear interpolation of both unknown fields are used. To avoid locking phenomenon which can be encountered for the volume-preserving plasticity the approach called *F-bar*, developed in Souza Neto *et al.* [5], is applied. The described model is tested using a rectangular bar and a perforated plate in tension with different boundary conditions.

References

1. G.A. Holzapfel (2000). *Nonlinear Solid Mechanics. A Continuum Approach for Engineering*, John Wiley & Sons, Ltd, Chichester.
2. J.C. Simo, C. Miehe (1992). Associative coupled thermoplasticity at finite strains: Formulation, numerical analysis and implementation, *Comput. Methods Appl. Mech. Engrg.*, **98**, 41–104.
3. J.C. Simo (1998). Numerical analysis and simulation of plasticity. In: P.G. Ciarlet and J.L. Lions (eds.), *Handbook of Numerical Analysis*, volume IV, 183–499, Elsevier Science B.V., Boca Raton.
4. J. Korelc (2009). Automation of primal and sensitivity analysis of transient coupled problems, *Computational Mechanics*, **44**, 631–649.
5. E.A. de Souza Neto, D. Peric, D.R.J. Owen (2008). *Computational methods for plasticity. Theory and applications*, John Wiley & Sons, Ltd, Chichester, UK.

Session

**Dynamics of Solids
and
Structures**

LARGE AMPLITUDE FORCED VIBRATIONS OF MICRO-PERIODIC SLENDER BEAMS

Ł. Domagalski, J. Jędrzyiak

Łódź University of Technology, Łódź, Poland

1. Introduction

The paper deals with forced vibrations of slender Euler-Bernoulli beams with bending and tensile stiffness and material density periodically varying along the beam axis. It is also assumed that the beam can interact with periodically inhomogeneous viscoelastic subsoil. A fragment of considered beam is depicted in Fig. 1.

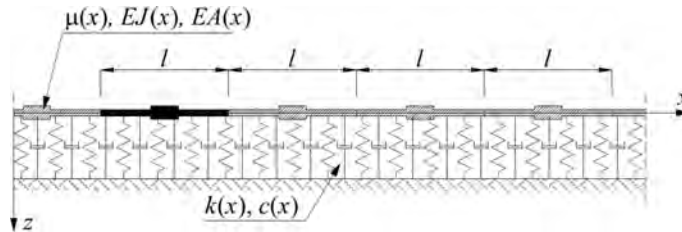


Fig. 1. A fragment of slender micro-periodic beam.

Problems of vibrations of such beams are described by the following system of coupled, nonlinear differential equations:

$$(1) \quad \begin{aligned} \partial \left[EA \left(\partial u_0 + \frac{1}{2} (\partial w)^2 \right) \right] &= 0, \\ \partial^2 (EJ \partial^2 w) - EA \left[\partial u_0 + \frac{1}{2} (\partial w)^2 \right] \partial^2 w + kw + c\dot{w} + \mu\ddot{w} &= q, \end{aligned}$$

cf. [2], where the transverse deflection, the longitudinal displacement, tensile and flexural stiffness, the elastic and damping coefficients of the subsoil, density of beam material per unit length and the transverse load are denoted by $w = w(x, t)$, $u_0 = u_0(x, t)$, $EA = EA(x)$, $EJ = EJ(x)$, $k = k(x)$, $c = c(x)$, $\mu = \mu(x)$, $q = q(x, t)$. In the case of considered beams, the coefficients of the aforementioned equations are highly-oscillating, non-continuous, periodic functions of the x -coordinate. This causes significant problems in obtaining analytical solutions.

Due to these difficulties, various methods averaging mechanical properties of the structure are used in the field of structural mechanics, cf. [1]. These methods lead to some approximate models of the considered problems. The actual structure is replaced with a corresponding one, with effective properties and the original mathematical model is replaced by differential equations with constant coefficients. These methods usually neglect the effect of the microstructure size.

2. The tolerance modeling approach

In this paper, in order to replace the original differential equations with highly oscillating coefficients with equations with constant coefficients, the concept and basic principles of tolerance modelling technique have been applied. This approach, cf. [6, 5, 4], was originally introduced for the purpose of analysis of thermomechanical problems of periodic

elastic composites. This technique was used in the vibration analysis of beams within the linear theory, cf. [3].

In the framework of the tolerance modelling approach it is assumed that the unknown transverse and longitudinal displacements undergo fluctuations due to the periodic inhomogeneity of the beam. Thus, they are decomposed into their averaged and fluctuating parts:

$$(2) \quad \begin{aligned} w(x, t) &= W(x, t) + h^A(x)V^A(x, t), & A = 1, \dots, N, \\ u_0(x, t) &= U(x, t) + g^K(x)T^K(x, t), & K = 1, \dots, M, \end{aligned}$$

where macro-displacements W , U , and the fluctuation amplitudes V^A , T^K are new basic unknowns, h^A and g^K stand for corresponding fluctuation shape functions.

Application of the tolerance averaging procedure, cf. [4], leads to the following system of equations:

$$(3) \quad \begin{aligned} &\partial \left[\langle EA \rangle \left(\partial U + \frac{1}{2}(\partial W)^2 \right) + \langle EA \partial g^K \rangle T^K + \frac{1}{2} \langle \underline{EA \partial h^A \partial h^B} \rangle V^A V^B \right] = 0, \\ &\quad \langle EJ \rangle \partial^2 W + \langle EJ \partial^2 h^A \rangle \partial^2 V^A + \langle \mu \rangle \ddot{W} + \langle k \rangle W + \langle \underline{kh^A} \rangle V^A + \langle c \rangle \dot{W} \\ &\quad \quad \quad + \langle \underline{ch^A} \rangle \dot{V}^A - \langle q \rangle + \partial(\langle \underline{EA \partial h^A \partial h^B} \rangle V^A V^B \partial W) \\ &+ \left[\langle EA \rangle \left(\partial U + \frac{1}{2}(\partial W)^2 \right) + \langle EA \partial g^K \rangle T^K + \frac{1}{2} \langle \underline{EA \partial h^A \partial h^B} \rangle V^A V^B \right] \partial^2 W = 0, \\ &\quad \langle EJ \partial^2 h^A \rangle \partial^2 W + \langle \partial^2 h^A EJ \partial^2 h^B \rangle V^B + \langle \underline{\mu h^A h^B} \rangle \ddot{V}^B + \langle \underline{ch^A} \rangle \dot{W} \\ &\quad \quad \quad + \langle \underline{ch^A h^B} \rangle \dot{V}^B + \langle \underline{kh^A} \rangle W + \langle \underline{kh^A h^B} \rangle V^B - \langle \underline{qh^A} \rangle \\ &\quad \quad \quad + \langle \underline{EA \partial h^A \partial h^B} \rangle \left(\partial U + \frac{1}{2}(\partial W)^2 \right) V^B + \langle \underline{EA \partial h^A \partial h^B} \rangle V^B (\partial W)^2 \\ &\quad \quad \quad + \frac{1}{2} \langle \underline{EA \partial h^A \partial h^B \partial h^C \partial h^D} \rangle V^B V^C V^D + \langle \underline{EA \partial g^L \partial h^A \partial h^B} \rangle V^B T^L = 0, \\ &\quad \langle EA \partial g^K \rangle (\partial U + \frac{1}{2}(\partial W)^2) + \langle EA \partial g^K \partial g^L \rangle T^L + \frac{1}{2} \langle \underline{EA \partial g^L \partial h^A \partial h^B} \rangle V^A V^B = 0. \end{aligned}$$

with constant coefficients. The underlined terms are dependent on the microstructure size parameter l .

3. Solutions and applications

The presented model can serve as a tool in parametric analysis of problems under consideration. Solutions to the tolerance model of slender periodic beams (3) can be obtained through an analytical-numerical method, using Galerkin orthogonalization and Runge-Kutta forward numerical integration. Results of the analysis of some specific problems of forced vibrations will be presented in the paper.

References

1. A. Bensoussan, J.L. Lions, G. Papanicolaou (1978). *Asymptotic analysis for periodic structures*, North-Holland, New York, 122–131.
2. A. Kacner (1969). *Beams and plates with variable thickness*, PWN, Warszawa (in Polish).
3. K. Mazur-Śniady (1993). Macro-dynamics of micro-periodic elastic beams, *J. Theor. Appl. Mech.*, **31**, 781–793.
4. Cz. Woźniak (ed.) (2010). *Mathematical modeling and analysis in continuum mechanics of microstructured media*, Wydawnictwo Politechniki Śląskiej, Gliwice.
5. Cz. Woźniak, B. Michalak, J. Jędrzyak (eds.) (2008). *Thermomechanics of microheterogeneous solids and structures*, Wydawnictwo Politechniki Łódzkiej, Łódź.
6. Cz. Woźniak, E. Wierzbicki (2000). *Averaging techniques in thermomechanics of composite solids*, Wydawnictwo Politechniki Częstochowskiej, Częstochowa.

DYNAMIC STRESS CONCENTRATION FACTOR AROUND AN EMBEDDED NANO-CAVITY IN THE CONTEXT OF COUPLE STRESS THEORY

A. Goodarzi¹, H. M. Shodja^{1, 2}, B. Hashemian¹

¹Department of Civil Engineering, Sharif University of Technology, Tehran, Iran

²Institute for Nanoscience and Nanotechnology, Sharif University of Technology, Tehran, Iran

It is well-known that classical theory of elasticity is not adequate in interpreting size effect observed in material behavior at nano scale. Also, this theory has deficiencies in describing phenomena of wave dispersion at high frequencies in which wavelengths are comparable with length scales associated with the microstructure of materials. Employment of higher order continuum theories such as micropolar and couple stress theory is a remedy to such dilemmas.

In the present study, elastodynamic stress fields of a scattered anti-plane shear wave due to an embedded circular cylindrical cavity is obtained in the context of couple stress theory. Applying couple stress theory gives rise to the appearance of a new characteristic length in the formulation. Dynamic stress concentration factors for different ratio of the characteristic length to radius of the cavity cross-section are presented. As a verification of the present formulations, the results for two limiting cases of static stress concentration factor within couple stress theory and dynamic stress concentration factor in the framework of classical theory of elasticity, are recovered.

1. Formulation in couple stress theory

In the framework of couple stress theory, micro-rotation and macro-rotation are equal to curl of displacement field, \mathbf{u} , [1]. Traction vector, \mathbf{T} and moment traction vector, \mathbf{M} on an arbitrary surface with unit outward normal \mathbf{n} are related to, respectively, stress tensor, $\boldsymbol{\sigma}$ and couple stress tensor, $\boldsymbol{\mu}$, such that $\mathbf{T} = \mathbf{n} \cdot \boldsymbol{\sigma}$, and $\mathbf{M} = \mathbf{n} \cdot \boldsymbol{\mu}$.

The asymmetric stress tensor can be decomposed into a symmetric ($\boldsymbol{\tau}$) and an anti-symmetric ($\boldsymbol{\alpha}$) parts, ($\boldsymbol{\sigma} = \boldsymbol{\tau} + \boldsymbol{\alpha}$). The symmetric part of stress and the couple stress, respectively, are related to the strain tensor $\boldsymbol{\varepsilon} = (1/2)(\nabla\mathbf{u} + \mathbf{u}\nabla)$ and curvature tensor ($\boldsymbol{\kappa} = (1/2)\nabla\nabla \times \mathbf{u}$ as $\boldsymbol{\tau} = \lambda\boldsymbol{\varepsilon} : \mathbf{I} + 2G\boldsymbol{\varepsilon}$ and $\boldsymbol{\mu} = 4\eta\boldsymbol{\kappa} + 4\tilde{\eta}\boldsymbol{\kappa}^T$, in which, λ , G , η and $\tilde{\eta}$ are Lamé type constants, [1]. Also, \mathbf{I} is the unit tensor and $\boldsymbol{\kappa}^T$ is transpose of curvature tensor. In the absence of body force and body couple, the equation of motion in terms of the displacement field is obtained as:

$$(1) \quad (1 - l^2\nabla^2)\nabla^2\mathbf{u} + \left(\frac{1}{1-2\nu} + l^2\nabla^2\right)\nabla\nabla \cdot \mathbf{u} = \frac{\rho}{G}\ddot{\mathbf{u}},$$

where ρ and ν are density and Poisson's ratio, respectively. Also $l = \sqrt{\eta/G}$, referred to as the couple stress characteristic length. $\ddot{\mathbf{u}}$ represents the acceleration vector.

2. Elastodynamic fields of a scattered anti-plane shear wave

Consider an incident anti-plane shear wave $u_z^i = u_0 \exp[i(k_1x - \omega t)]$ with amplitude, u_0 and frequency, ω propagating in an infinite elastic medium along the x -axis. Using Eq. (1), wavenumber $k_1 = \sqrt{-1 + \sqrt{1 + (2\omega l/c_0)^2}}/\sqrt{2}l$, where c_0 is the shear wave velocity in classical theory of elasticity. If the wave is scattered by an embedded circular cylindrical cavity whose axis in the z -direction and has radius a , the scattered wave u_z^s in polar coordinate is obtained as follows:

$$u_z^s = \sum_{n=0}^{\infty} \left(A_n H_n^{(1)}(k_1 r) + B_n K_n(k_2 r) \right) \cos(n\theta),$$

in which $k_2 = \sqrt{1 + \sqrt{1 + (2\omega l/c_0)^2}}/\sqrt{2}l$, and $H_n^{(1)}$ and K_n are the Hankel and modified Bessel functions of the first kind of order n . The coefficients A_n and B_n are calculated by applying appropriate interface conditions.

3. Dynamic stress concentration factor

Along the boundary of cavity ($r = a$) just inside the elastic medium, the dynamic stress concentration factor is defined as $\text{DSCF}(\theta, k_1 a) = |\sigma_{\theta z}^s + \sigma_{\theta z}^i|/\sigma_0$, in which σ_0 is the value of $|\sigma_{\theta z}^i|$ at $\theta = \pi/2$ measured from the positive direction of the x -axis. The superscript “ i ” and “ s ” imply stress fields corresponding to incident and scattered fields, respectively. The dynamic stress concentration factors (DSCF) for $l/a = 0, 0.5, 1$ and 1.5 , as a function of the normalized wavenumber, $k_1 l$ at $\theta = \pi/2$ are depicted in Fig. 1.

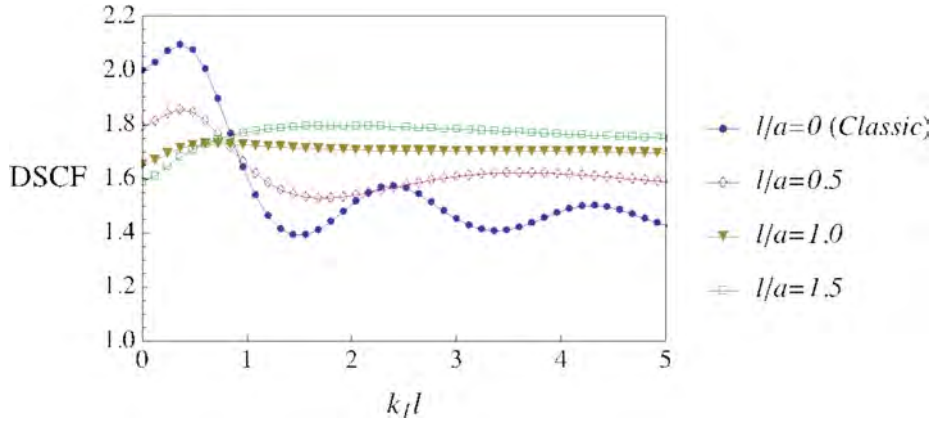


Fig. 1. Dynamic stress concentration factor around a cavity just inside the medium at $\theta = \pi/2$.

It is seen that as the size of the cavity becomes large as compared to the characteristic length, DSCF in couple stress theory for all wavenumbers tends to that of classical theory of elasticity. For normalized wavenumber above about 0.8, DSCF increases with decreasing the size of cavity. For the wavenumber below 0.8, this trend reverses. For the special case of dynamic problem in classical theory of elasticity ($l/a = 0$), DSCF is the exact results reported in [2]. Also, in the limiting case of the static problem ($k_1 l = 0$), the results reported by Lubarda [3] is recovered.

4. Conclusion

In the framework of couple stress theory, the value of dynamic stress concentration factors vary with the size of the cavity, provided that the size of the cavity cross-section and the wavelength of incident wave are comparable to the couple stress characteristic length.

References

1. R.D. Mindlin, H.F. Tiersten (1962). Effect of couple-stresses in linear elasticity, *Arch. Ration. Mech. Anal.*, **11**, 415–448.
2. A.C. Eringen, E.S. Suhubi (1975). *Elastodynamics: Linear theory*. Academic Press.
3. V.A. Lubarda (2003). Circular inclusions in anti-plane strain couple stress elasticity, *Int. J. Solids Struct.*, **40**, 3827–3851.

APPLICATION OF ROTATION RATE SENSORS TO IMPROVE STRUCTURAL HEALTH MONITORING OF BEAMS IN FLEXURE

S. Kokot, Z. Zembaty, P. Bobra

Opole University of Technology, Opole, Poland

1. Introduction

In structural health monitoring (*SHM*) of typical structures the damage is usually modeled as isolated “cuts” of structural elements, representing local losses of stiffness (e.g. [1]). However for some structures, (e.g. reinforced concrete (*r/c*) frames [2], buildings modeled as shear beams [3, 4] or masonry structures) the so called “damage” is diffused in wider areas and often accepted as inevitable. Monitoring of these type of structures require specific “reconstructions” of spatially distributed stiffness variations. Respective inverse problems demand application of advanced optimization algorithms and substantial computer power [5]. To improve damage detection or reconstruction, harmonic excitations of structures are often applied (e.g. [6–7]).

Recent numerical analyses suggest that measuring rotations of the beam axes may be particularly effective in monitoring structural behavior under vibrations [8, 9]. For this reason modern rotation rate sensors designed for geophysics [10], aircraft or rocket control are being recently applied as additional monitoring equipment in civil engineering [11, 12]. This can be beneficial in *SHM* because rotations of beams in bending are more sensitive to stiffness variations than their respective transversal motions. This problem is schematically depicted in Fig. 1 where in the lower picture fewer rotational & translational sensors give better information about the beam flexure than more number of only translational sensors (upper part of the figure).

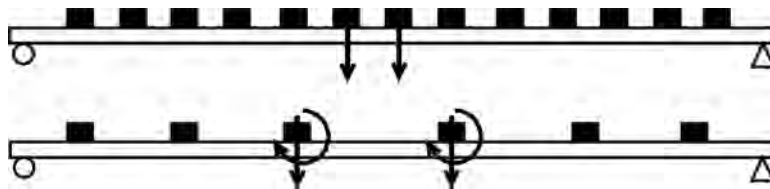


Fig. 1. Beam with traditional, translational accelerometers and rotation sensors.

The presentation planned for the *SolMech 2014* conference will be devoted to report the latest experiments in stiffness reconstructions of laboratory models of beams using the rotation rate sensors Horizon HZ- 100 – 100 compare with the conventional piezoelectric acceleration [11].

2. Problem statement

Consider matrix equation of motion of an undamped, discrete dynamic system under harmonic excitations, with angular frequency p and its familiar, algebraic solution:

$$(1) \quad \mathbf{M}\ddot{\mathbf{d}} + \mathbf{K}^d \mathbf{d} = \mathbf{P}_0 e^{ipt} \quad (\mathbf{K}^d p^2 \mathbf{M}) \mathbf{u} = \mathbf{P}_0$$

where \mathbf{K} , \mathbf{M} are stiffness and inertia matrices, \mathbf{d} (and its 2nd derivative) stand for vectors of displacements and accelerations, while vectors \mathbf{u} and \mathbf{P}_0 contain amplitudes of

displacements and forces. Using finite element method, the global stiffness matrix of damaged structure \mathbf{K}^d can be calculated with relative damage contribution α_i to i -th finite element. All the damage coefficients constitute vector of multipliers α which measuring losses stiffness of the structure ($0 < \alpha_i < 1$):

$$(2) \quad \mathbf{K}^d = \sum_{i=1}^n \mathbf{K}_i^{de} = \sum_{i=1}^n \alpha_i \mathbf{K}_i^{ue}.$$

Substituting (2) into (1)₂ leads to

$$(3) \quad \left(\sum_i^n \alpha_i \mathbf{K}_i^{ue} - p^2 \mathbf{M} \right) \mathbf{u} = \mathbf{P}_0$$

which can be used to compute displacement amplitudes for certain excitations and particular structural models. In order to quantify the difference between actual (measured) \mathbf{u}_m and reconstructed (computed) amplitudes \mathbf{u}_c following functional $\mathbf{J}(\alpha)$ is defined:

$$(4) \quad \mathbf{J}(\alpha) = \sum_{j=1}^{n_d} \left(\frac{u_j^c(\alpha) - u_j^m}{u_j^m} \right)^2.$$

3. Results and conclusion

In numerical simulations of ref. [9] it was demonstrated that by minimizing functional (4), up to 32 unknown coefficients α_i could be successfully computed. The experiment carried out on a cantilever plexi beam excited kinematically was limited only to three rotational sensors and three areas of stiffness loss (for details see ref. [11]). Nevertheless it showed that just these three rotational sensors enabled proper reconstruction of 15% stiffness losses.

References

1. Sohn H., Farrar C.R., Hemez F.M., Shunk D.D., Stinemates D.W., Nadler B.R. (2003), *A review of structural health monitoring literature: 1996–2001*, Los Alamos Ntl. Lab. Report.
2. Zembaty Z., Kowalski M., Pospisil S. (2006). Dynamic identification of a reinforced concrete frame in progressive states of damage, *Engineering Structures*, **28**, 668–681.
3. Gicev V., Trifunac M.D. (2009). Rotations in a shear-beam model of a seven-story building caused by nonlinear waves during earthquake excitation, *Structural Control & Health Monitoring*, **16**, 460–482.
4. Zembaty Z. (2007). Non-stationary random vibrations of a shear beam under high frequency seismic effects, *Soil Dynamics and Earthquake Engineering*, **27**, 1000–1011.
5. Liu G.R., Han X. (2003). *Computational inverse techniques in nondestructive evaluation*, CRC Press, Boca Raton.
6. Swiercz A., Kolakowski P., Holnicki-Szulc J. (2007). Structural damage identification using low frequency non-resonance harmonic excitation, *Key Engineering Materials*, **347**, 427–432.
7. Kokot S., Zembaty Z. (2009). Damage reconstruction of 3d frames using genetic algorithms with Levenberg-Marquardt local search, *Soil Dynamics & Earthquake Engineering*, **29**, 311–323.
8. Abdo M.A.-B., Hori M. (2002). A numerical study of structural damage detection using changes in the rotation of mode shapes, *Journal of Sound Vibration*, **251**, 227–239.
9. Kokot S., Zembaty Z. (2009). Vibration based stiffness reconstruction of beams and frames by observing their rotations under harmonic excitations – a numerical analysis, *Engineering Structures*, **31**, 1581–1588.
10. Igel H., Brokesova J., Evans J., Zembaty Z. (2012). Preface to the special issue on “Advances in rotational seismology”, *Journal of Seismology*, **16**, 571–572.
11. Zembaty Z., Kokot S., Bobra P. (2013). Application of rotation rate sensors in an experiment of stiffness ‘reconstruction’, *Smart Materials & Structures*, **22**, 7.
12. Schreiber K.U., Velikosev A., Carr A.J., Franco-Anaya R. (2009). The application of fiber optic gyroscopes for the measurement of rotations in structural engineering, *Bulletin of the Seismological Society of America*, **99**, 1207–1214.

ON REAL-TIME DISTRIBUTED ADAPTATION OF STRUCTURES SUBJECTED TO TRAVELLING LOADS

D. Pisarski

French National Institute for Research in Computer Science and Control, Grenoble, France

Institute of Fundamental Technological Research, Warsaw, Poland

1. The subject and the goals of the study

Problems of structures subjected to loads travelling with high velocity are of a special interest for practicing engineers. Numerous of analytical and numerical solutions are applied to solve the problems of transportation and robotic systems with a single or multi-point interactions such as train-track, vehicle-bridge or effector-guideway. These problems concern high vibration levels of both structures and travelling objects due to permanently increasing speed and load carrying capacity requirements.

The construction of new railway tracks or bridges with sufficiently higher load carrying capacity and ability to withstand dynamical stresses and strains is usually limited by costs. On the other hand, a static strengthening increases structure mass and often is restricted for technological reasons. To face undesired vibration effects a variety of control systems acting on both vehicle suspensions and structures have been proposed and put into practice. Active vehicle suspension systems are based on controlled rheological dampers that tend to improve the travelling comfort by keeping the passage trajectory as smooth and straight as possible [1]. For structural control, the objective is usually centered on a structure itself. Heavy and high power consumed force actuators are attached to a structure to stabilize it in the case of dangerous external excitations that occur, for instance, during earthquakes. A recent trend is to replace force actuators with semi-active rheological dampers. These solutions attract the engineers' interest due to significantly less power consumption. They are also safer in the case of a control system failure.

The use of semi-active supports for the structure subjected to a moving load was first proposed in [2]. By means of numerical simulations the authors demonstrated that for a wide range of travel velocity the switching damping strategies outperform standard passive solution. The idea was later extended in [3] and [4], where by introducing rigorous analysis and optimization techniques the authors concluded that even one switching action for each damper can provide very smooth load passages. The total deflection of the load trajectory from the straight line was reduced up to 50%.

The goal of this study is to design an efficient and easy for implementation feedback control system based on change of both damping and stiffness of structure supports. The system will be split into modules (often identified as “plug and play” tools). The functionality and incorporated computational procedures for every module will be the same. It will compute its optimal decision by using local state information and necessary information arriving from other controllers. The global time consuming optimization problem will be then divided into local problems of reduced size that can be solved on-line. A distributed control architecture is also convenient for system assembling and maintenance. In the case of failure, only the malfunctioning module needs to be replaced. In addition, a decentralization plays an important role for safety. Suppose a malfunction of the central computer computing the optimal decision for every controller. An incorrect signal is then sent to the whole control system that may drive the structure to dangerous states. In distributed control architecture this risk is reduced to local failures.

2. Research methodology

In the study, we consider the system as depicted in Fig. 1. The carrying structure or railway track is represented by one or two parallel spans. For the spans, the Euler-Bernoulli beam model is adapted.

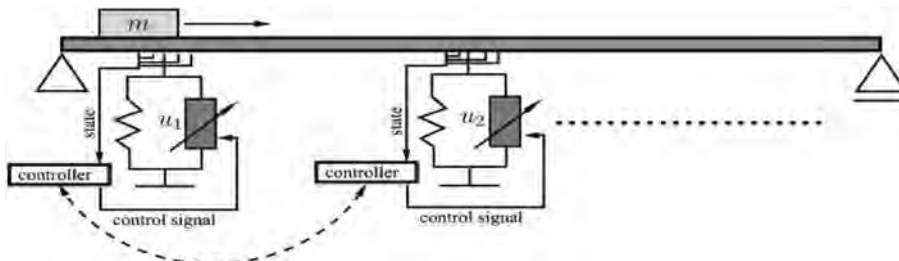


Fig. 1. A span supported by a distributed semi-active control architecture.

The beam is supported by a set of controlled supports (perceived as a set of modules). For control objective, we combine the smooth passage with reduced beam deflections. For control parameters we assume both damping and stiffness parameters. Eventually, the variable stiffness are meant to be approximately realized by relevant non-linear springs. Each of the supports is equipped with a controller that receives the information of its local state. It is also allowed to communicate with other controller or controllers under a relevant minimal communication topology (to be determined). Thus, the optimal controller decision is based on its local state and also on the information provided by the other controller (or controllers). The information arriving from one of the previous modules will be also triggering the controller to update his optimal decision. This must be done in advance, since the process of optimization takes some time and the optimal decision is supposed to be applied at the right time, i.e. when a load is passing the section corresponding to the controller. Therefore, at this stage two major problems are addressed. The first one is to find a proper controller communication topology taking into account performance, but also computational capabilities and simplicity in practical realization. The second one is to design a feedback structure for each of the controllers and a method that allows them to update the optimal decision in a reasonably short time. To solve these problems, analysis of controllability of distributed systems is performed and the methods of real-time optimization (based on the receding horizon control [5]) are applied. The analyzed model is represented by the following bilinear system of ODEs:

$$(1) \quad \dot{x} = A(t)x + \sum_{i=1}^m u_i B_i(t)x + F(t),$$

where x , u and F stands for the state, the set of control input and the travelling load excitation, respectively. The experimental validation of the proposed control method will be carried out by using the test stand operating in the Institute of Fundamental Technological Research.

References

1. Sh.J. Dyke, D. Giraldo (2002). Control of an elastic continuum when traversed by a moving oscillator, *Journal of Structural Control and Health Monitoring*, **14**, 197–217.
2. D. Pisarski, C. Bajer (2010). Semi-active control of 1D continuum vibrations under a travelling load, *Journal of Sound and Vibration*, **329**, 140–149.
3. D. Pisarski, C. Bajer (2010). Smart suspension system for linear guideways, *Journal of Intelligent and Robotic Systems*, **62**, 451–466.
4. C. Bajer, R. Bogacz (2000). Active control of beams under moving load, *Journal of Theoretical and Applied Mechanics*, **8**, 523–530.
5. Y. Wang, S. Boyd (2010). Fast Model Predictive Control Using Online Optimization, *IEEE Transactions on Control Systems Technology*, **18**, 267–278.

INTERPLAY BETWEEN STRESS WAVES PROPAGATION
AND FLOW LOCALIZATION IN THE DYNAMIC TENSILE TEST:
APPLICATION TO STEEL SHEETS

A. Vaz-Romero, J. A. Rodríguez-Martínez, A. Arias

Department of Continuum Mechanics and Structural Analysis, University Carlos III of Madrid, Spain

1. Introduction

Among the dynamic tests, the uniaxial tensile is one of the most commonly used. The first detailed investigations on high-velocity tension tests are dated to the mid-20th century. At that time a number of investigators focused their attention on developing reliable experimental methodologies to capture the mechanical properties under rapid loading of different metals and alloys [1–2]. The effect of testing velocity on the absorbed energy in the sample was demonstrated. In Mann’s words [1] the experimental data “*definitely showed that high velocity tests are essential to reveal the true dynamic properties of materials*”. This finding was a milestone in the investigation of dynamic behavior of materials. Moreover, the improvements in the tensile impact testing developed during this period pointed out a distinctive feature of the dynamic tensile test: there exists a correlation between fracture location and impact velocity. Under static (tensile) loading failure is invariably located in the middle of the gauge, while under impact loading, sample failure may occur at a different location. This correlation was described as being sample-size dependent. Years later, the one-dimensional theory of plastic waves propagation developed by Karman and others [3–4] was taken into account for the first time in interpreting the experimental results. Based on the processes of reflection and interaction of stress waves taking place in the sample during dynamic loading, the principles of stress wave propagation provided new insights into the interplay between fracture location and impact velocity [5]. In this regard, Rodríguez-Martínez *et al.* [6] recently claimed that fracture location away from the center of the sample reveals absence of mechanical equilibrium in the specimen, masking the actual constitutive performance of the material. Nevertheless, this key finding still requires further investigation. For this purpose, we present here an original experimental/numerical methodology to provide further insights into the interplay between stress waves propagation and flow localization in the dynamic tensile test.

2. Experiments

The material of this study is AISI 430 (ferritic) steel, supplied as 1mm thickness plates. Tensile samples were prepared along different in-plane directions: 0° (rolling direction), 45° and 90° (transverse direction). Static and dynamic experiments have been conducted. The static tests have been carried out using an INSTRON 8516 servo-hydraulic testing machine. The geometry and dimensions of the *static samples* are taken from Rodríguez-Martínez *et al.* [7], the gauge length being 20 mm. We observed that the material is largely isotropic. The dynamic tests have been carried out using an INSTRON VHS 8800 High Strain Rate servo-hydraulic machine within the range of applied velocities $0.5 \text{ m/s} < V_0 < 10 \text{ m/s}$. These experiments have been recorded using a high speed video camera Photon Ultima APX-RS. Dynamic specimens with different gauges lengths were prepared: 20 mm, 40 mm and 60 mm.

3. Finite elements

The computational analysis has been carried out using ABAQUS/Explicit. Finite element simulations have been conducted using different (distinctive) boundary and loading conditions:

1. Type I: modelling the tensile specimens subjected to the boundary and loading conditions applied in the experiments.
2. Type II: modelling the tensile specimens with prescribed initial velocity and stress fields which precludes stress waves propagation.

Following these 2 different configurations, numerical simulations are run within the range of loading velocities $0.5 \text{ m/s} < V_0 < 10 \text{ m/s}$ (the same range of velocities investigated experimentally).

4. Results and discussion

The experiments show the strong influence that loading velocity and specimen size have on the fracture location. Under static conditions, the fracture of the sample takes place in the center of the gauge. On contrary, flow localization occurs away from the center of the sample as we increase the applied velocity. The exact location depends on both, the applied velocity and the sample size. Strain localization occurs in a single point of the sample gauge, localization bands aligned with the direction of zero stretch-rate are observed. Finite element simulations of type I reproduce this experimental evidence and confirm that, as soon as the fracture moves from the center of the specimen, the sample is not in equilibrium. Moreover, numerical computations of the type II show that, in absence of stress waves, multiple localization points arise along the specimen gauge. The localization pattern is symmetric and the sample finds mechanical equilibrium no matter the value of the applied velocity. It is shown that, because of inertia effects, the spacing between localization points decreases as the loading rate increases.

Systematic confrontation of experiments and numerical computations of types I and II reveal the key role that stress waves play in the dynamic tensile tests. In particular, we provide here a detailed analysis of the mechanisms which dictate fracture location in the uniaxial impact testing of steel sheets.

Acknowledgments

The authors acknowledge the financial support from Ministerio de Ciencia e Innovación Project DPI/2011-24068.

References

1. H.C. Mann (1936). High-velocity tension-impact tests, *Proceedings ASTM*, **36**, 85.
2. D.S. Clark, G. Datwyler (1938). Stress-strain relations under tension impact loading, *Proceedings – American Society of Testing Materials*, **38**, 98.
3. T. Karman (1942). On the propagation of plastic deformation in solids, *NDRC Report No. A*, **29**, February 2.
4. H.A. Rakhmatulin (1945). Mechanics of unloading waves, *Prikladnaya Matematika i Mekhanika*, **9**, 91.
5. D.S. Clark, P.E. Duwez (1948). Discussion of the forces acting in tension impact test of materials, *Journal of Applied Mechanics*, **15**, A243.
6. J.A. Rodríguez-Martínez, D. Rittel, R. Zaera, S. Osovski (2013). Finite element analysis of AISI 304 steel sheets subjected to dynamic tension: the effects of martensitic transformation and plastic strain development on flow localization, *Int. J. Impact Eng.*, **53**, 206–216.
7. J.A. Rodríguez-Martínez, R. Pesci, A. Rusinek (2011). Experimental study on the martensitic transformation in AISI 304 steel sheets subjected to tension under wide ranges of strain rate at room temperature, *Mater. Sci. Eng. A.*, **528**, 5974–5982.

APPLICATION OF PIEZOELECTRIC ACTUATORS FOR THE GAS VALVE OPENING CONTROL

R. Wiszowaty¹, G. Mikułowski¹, K. Sekuła², J. Biczuk²

¹Institute of Fundamental Technological Research, Warsaw, Poland

²Adaptronica sp. z o.o., Łomianki, Poland

1. Introduction

In many cases during designing various technical installations arises a problem of choosing a proper gas valve that can meet the requirements following from distinct tasks. Imposed limitations concerning outline dimensions, flow capacity, opening/closing time, etc. could bring the designer to apply the valve actuated with piezoelectric actuators.

The presented paper concerns the topic of suitability piezoelectric actuators for the gas valve opening control. The valves' performance was considered in connection with the piezoactuators' motive properties that follow from the piezoelectric materials characteristics. The valves manufactured according to two structure concepts were investigated and compared. The former one was the poppet valve driven with Amplified Piezoelectric Actuator (APA®), Cedrat Technologies; Fig. 1. left) [1]. That solution was chosen due to relatively high stroke of the actuator. In the latter structure solution (Fig. 1 right) a cylindrical actuator was utilized for opening the valve by moving a plate having a matrix of overflow orifices apart from another plate with such a orifices located in different places than in the case of the first plate (the plates manufactured in this a way are called Hörbiger plates) [2].

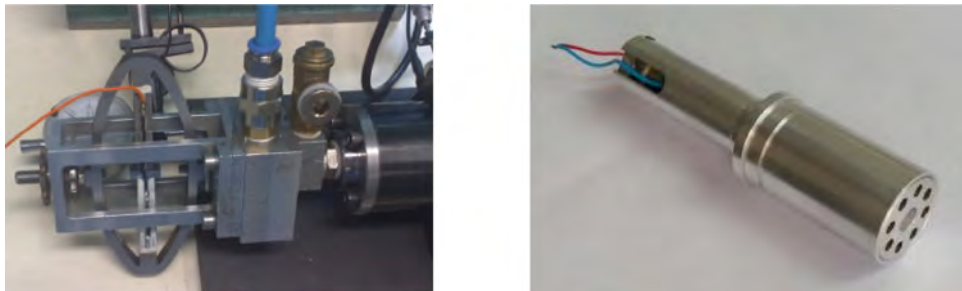


Fig. 1. Valve actuated by APA® (left) and by cylindrical actuator (right).

2. Piezoelectric actuator performance

Multilayer ceramic stacks, made of SONOX® P505 [3], were applied in both tested actuators and they operated by nominal driving signal voltages 150 and 200 V respectively. The elliptic stroke multiplier which belongs to the APA® structure enabled to achieve maximum stroke of 150 μm and ensured required piezostack preload¹). On the other hand, the cylindrical actuator performed maximum elongation of 80 μm . That parameter is significant from the point of view of maximum achievable gas mass flow rates on the valve. Blocking force of APA® equalled 1 kN, and 2.5 kN of cylindrical actuator initially preloaded with 750 N by the use of an external plate spring stack. This feature is crucial

¹Original device constructed by Cedrat was modified by replacing piezostacks with actuators made by CeramTec.

for the pressure ranges on the valve inlet and outlet by which the valve could be operable. Also there was a difference between overall dimensions of both actuators: APA® had $140 \times 70 \times 10$ mm, while cylindrical actuator – 66 mm longitude and 10 mm diameter.

3. Mass flow rates of the gas flowing through the valve

Measurements of mass flow rates of the gas passing the valve were performed by various inlet and outlet pressures. They were done with the stand consisting of two containers connected to the valve inlet and outlet respectively (Fig. 2).

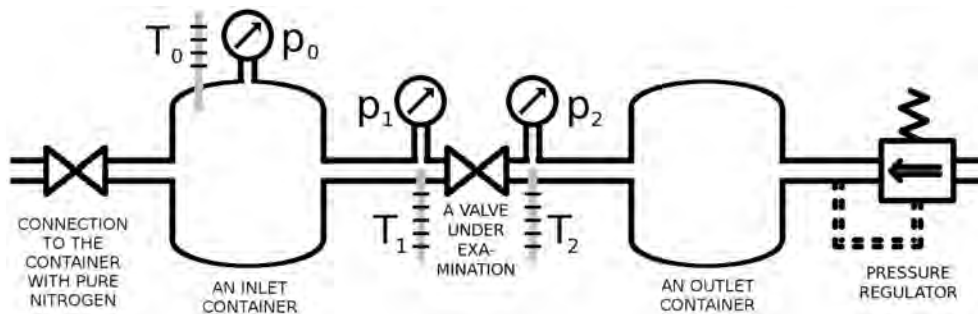


Fig. 2. Schematic of the setup used for obtaining valve characteristics.

During the conducted research there were performed series of experiments in which the gas flow between two containers through the investigated valve. By each test inlet pressure drop from initial value to the value kept on the valve outlet by the use of pressure regulator and outlet container. Measurement of the pressure and temperature in the inlet container allowed to estimate the mass of the gas present inside this container in each time instant and – as well – mass flow rate of the gas passing the investigated valve by various inlet and outlet pressures.

4. Results and conclusions

The comparison between mass flow rates of a gas passing two investigated valves led to conclusion that the multiplication of the actuator stroke by use of APA® gave no significant advantage from the point of view of maximum achievable mass flow rates of the gas. It exceeded 30 g/s by 1.2 MPa inlet pressure and 290 K inlet temperature. Replacing the poppet with Hörbiger plates ensured to achieve the same flow characteristics by two times shorter actuator strokes performed by cylindrical actuator.

Acknowledgments

Financial support of Structural Funds in the Operational Programme – Innovative Economy (IE OP) financed from the European Regional Development Fund – Project “Modern material technologies in aerospace industry”, No. POIG.01.01.02-00-015/08-00 and Polish National Science Centre Project ‘AIA’ (DEC-2012/05/B/ST8/02971) are gratefully acknowledged.

References

1. R. Wiszowaty, J. Biczysk (2013). Piezoelectric Valve for Controlled Pneumatic Shock Absorber, *IPPT Reports on Fundamental Technological Research*, **47**, 4, 43–47.
2. G. Mikulowski, R. Wiszowaty, J. Holnicki-Szulc (2013). Characterization of a piezoelectric valve for an adaptive pneumatic shock absorber, *Smart Materials & Structures*, **22**, 12, 1250011-1-12.
3. CeramTec. Advanced Ceramics in Piezo Applications, Multifunctional Ceramics Division [Online]. Available: http://www.ceramtec.de/files/mf_broschure-piezoapplications_en_de.pdf.

Session

Experimental Mechanics

organized in memory of

Professor Wojciech Szczepiński

Professor Wojciech Szczepiński (1924–2010)



Wojciech Szczepiński was born in Warsaw, Poland on January 1st, 1924, in a family of civil servants. After early loss of both his parents in 1937, care of him took over the family of his aunt. The World War II starting in September 1939 substantially complicated his education process. Due to abolition of secondary and higher education under Nazi occupation of Poland, he attended underground courses. After the end of the war he studied at the Engineering School of Wawelberg and Rotwand and in 1954 graduated from the Faculty of Mechanics and Technology of the Warsaw University of Technology. Between 1954 and 1957 he was the Head of the Department of Aviation Technology in the Institute of Aviation. Independently, he started his scientific career as early as in 1949 under supervision of Professor Zbigniew Brzoska at the Engineering School of Wawelberg and Rotwand and continued it later at the Faculty of Aviation of the Warsaw University of Technology. In 1960 Wojciech Szczepiński obtained his PhD degree presenting thesis on theoretical analysis of plastic deformation of metals which was recognized with the M.T. Huber award of Division IV of the Polish Academy of Sciences.

Wojciech Szczepiński spent one year 1961/62 as a post-doctoral research fellow at the Massachusetts Institute of Technology, where he carried out experimental work in the field of metal plasticity. Upon return to Warsaw, he continued his scientific activity at the Institute of Fundamental Technological Research (abbreviated as IPPT) of the Polish Academy of Sciences. He earned his D.Sc. (habilitation) degree based on the thesis entitled “Strain hardening at generalized plane stress in plastic medium” and became associated professor at IPPT in 1964. In the year 1977 Wojciech Szczepiński was conferred the title of Full Professor in Technical Sciences by the State Council of Poland. He held positions of importance at IPPT such as Chairman of the Scientific Council of the Institute in the years 1984–1986 and head of the Department of Continuous Media in 1986–1993.

Wojciech Szczepiński was elected a Corresponding Member of the Polish Academy of Sciences (PAN) in 1976 and a Full Member of PAN in 1989. His activities in the Academy were significant and multilateral; he was a Member of the Presidium of the Polish Academy of Sciences in the years 1993–1998, Chairman of Division IV of Technical Sciences of PAN in 1993–1995, Chairman of the Committee of Mechanics of PAN in 1984–1986. As a delegate of the Academy, he was active in international organizations in the field of mechanics. Between 1980 and 1997 he was a Member of Scientific Council of the International Centre for Mechanical Sciences (CISM) in Udine, Italy, a Member of Administrative Council of CISM in 1980–1988, a Member of General Assembly of International Union of Theoretical and Applied Mechanics (IUTAM) in 1980–1991. In the years 1992–1994 he was Chairman of Section of Technical Sciences of the Central Commission for Scientific Degrees and Titles in Poland.

Besides his organizational skills, Prof. Wojciech Szczepiński was first of all a remarkable scientist and teacher. His main fields of interest were: experimental and theoretical mechanics of materials, mechanics of plastic flow of metals and soils, strength design of machine parts by limit analysis, error analysis in engineering. He published over 120 papers in scientific journals; his most widely recognized papers are those on experimental studies of yield surfaces of metals subjected to a complex loading history. He frequently pointed out that in successful research on mechanics, both in the theoretical and experimental work, a good fresh idea plays a predominant role. His lectures were well-organized and clear, included a number of instructive examples illustrating major concepts and basic steps.

Professor Wojciech Szczepiński had supervised 14 completed PhD Theses. 8 of his co-workers gained degrees of Doctors of Sciences, and 5 became professors. Professor also inspired many other researchers, and the value of scientific discussions with him could not be underestimated. He was a researcher who excellently and effectively directed research topics of discussion participants or seminar panelists. There is a numerous group of co-workers who do not change the presented statistics, but who truly belong to the group of his students; thanks to Professor, Polish mechanics maintains and strengthens its position in the scientific world. The names of his doctoral students in the alphabetical order are: J. Białkiewicz, Z. Bogusz, E. Dreszerowa, L. Dietrich, R. Marjanović, J. Miastkowski, H. Petryk, J. Supel, J. Szlagowski, D.D. Tien, K. Turski, W. Trąmpczyński, M. Woźniakowa, J. Zawada.

As the author of 15 books, seven of which written individually, Wojciech Szczepiński demonstrated his exceptional ability to present apparently difficult theories, concepts and results from a variety of fields in a remarkably simple and transparent way. For example, in the monograph “Introduction to the Mechanics of Plastic Forming of Metals”, PWN and Sijthoff & Noordhoff, 1979, an English translation of the first edition in Polish in 1967, translated also to Chinese, he presented in a clear way a rigorous and at that time modern approach to the analysis of stress and velocity distributions in metals undergoing plastic deformation processing. In another book “Limit States and Kinematics of Soils” (in Polish), PWN, 1974 he elaborated the extension of the methods developed for metals to soils. His book “Plastic Design of Machine Parts” (in Polish), PWN, 1968 was later significantly extended in cooperation with his co-workers to four monographs, one published in English: “Plastic Design of Complex Shape Structures”, PWN and Ellis Horwood, 1990. In the last year he co-authored a book “Error Analysis with Applications in Engineering”, Springer, 2010 lying in his another field of interest. A next book, being in preparation, could not have been finished.

Professor Szczepiński was the winner of prestigious awards. In 1960, the M.T. Huber Prize, Division IV of the Polish Academy of Sciences. For his achievements in scientific work, he was awarded the Officer’s Cross of the Polonia Restituta Order. Wojciech Szczepiński earned honorary doctorates from Military University of Technology in Warsaw in 1989 and from Kielce University of Technology in 2002.

We will remember Professor Wojciech Szczepiński as a noble man, great scientific authority, inspirer, respected teacher and an outstanding scientist in the field of experimental and theoretical mechanics of solids, a specialist in problems of mechanics of plastic flow of metals and soils, strength design of machine parts by limit analysis and error analysis in engineering.

SENSING OF CEMENT MORTAR WITH EMBEDDED POLYVINYL ALCOHOL–CARBON NANOTUBE FIBER

N.D. Alexopoulos^{1,2}, S.K. Kourkoulis², P. Poulin³

¹Department of Financial Engineering, University of the Aegean, Chios, Greece

²Laboratory of Testing and Materials, National Technical University of Athens, Athens, Greece

³Université de Bordeaux, Centre de Recherche Paul Pascal – CNRS, Bordeaux, France

This research investigates the possibility of using polyvinyl alcohol fiber reinforced with carbon nanotubes (PVA-CNT) as a strain sensor in cement mortars used in the restoration of Cultural Heritage Monuments. Different types of PVA-CNT fibers were embedded in the matrix at a short distance from the bottom of the beam. The electrical resistance change of the embedded fiber was monitored during the mechanical testing of the four-point bending test. It was found that the PVA-CNT fiber's electrical resistance changed during the applied mechanical loading, indicating that its possible exploitation as a strain sensor is feasible.

1. Introduction

The ad-hoc accurate and thorough knowledge of the mechanical behaviour of building materials used in the restoration of Cultural Heritage Monuments is fundamental for the protection of their structural integrity. However, most of the traditional techniques used in the laboratory and in the field, such as strain-gauges, dial-gauges, extensometers, and LVDTs, provide data drawn from the materials' external surface. Therefore, gathering information about the internal events, for example local failures and micro-fracture, which precede those detected on the materials' surface, is challenging. This problem could be dealt by replacing (or parallel using) the traditional techniques by new innovative ones.

In this study, the use of different types of advanced fibers made from polyvinyl alcohol (PVA) reinforced with carbon nanotubes (CNTs) for sensing the mechanical performance of the cement mortar used for the restoration of Acropolis' Parthenon was investigated. These new innovative PVA-CNT fibers have the size of a human hair ($d = 40$ to $60 \mu\text{m}$) and exhibit excellent piezoresistive characteristics and ductility that exceeds 100% elongation [1]. Manufacturing of the specific fibers is patented by CNRS in Bordeaux. The structure of a PVA-CNT fiber as well as a SEM image of the cross section of the fiber is presented in Fig. 1. Previous research on epoxy resin composites reinforced with glass

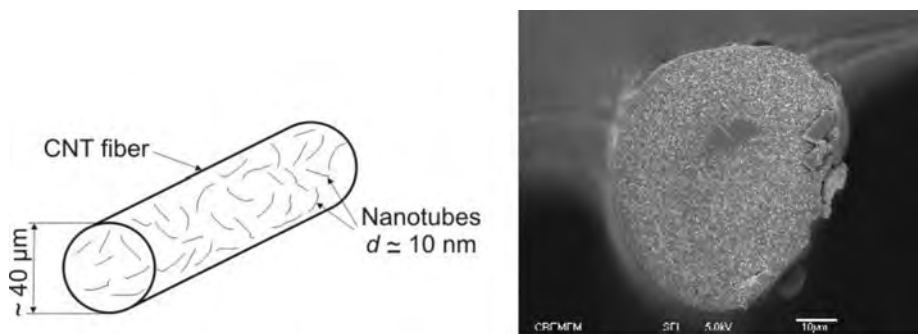


Fig. 1. Schematic representation of the structure of a typical PVA-CNT fiber (left) and SEM image of the cross section of the fiber (right); the white spots are the CNTs [2].

fibers and the aforementioned PVA microfiber has shown that it can be successfully used to assess the composites' deformation in tensile and bending tests [2, 3].

2. Experimental procedure

The samples were prepared using white cement and sand. Three different types of PVA-CNT fibers (reference, coated and coated and annealed) were used in different specimens. Before casting the PVA-CNT fibers were placed into the mold, at a distance of 4 mm from the bottom of the sample, as shown in Fig. 2a. A typical specimen with embedded fiber can be seen in Fig. 2b. The samples were tested under monotonic four-point bending with the loading span being 1/2 of the support span (Fig. 2c). For comparison and calibration reasons a suitable strain gage was used to measure the strain at the bottom of the beam. The resistance of the fiber was continuously monitored and recorded during testing.

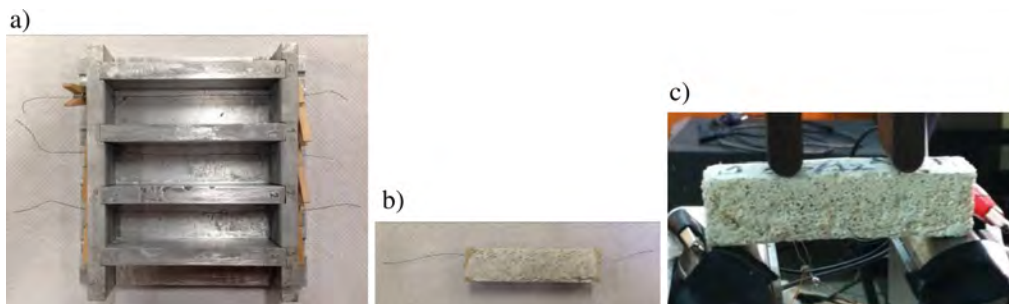


Fig. 2. a) Placement of the PVA-CNT fibers in the mold before casting, b) specimen after demolding and c) experimental test set up.

3. Results and conclusions

It was found that the PVA-CNT fibers can be used to monitor the mechanical response of the mortar. All fiber types exhibited a similar behavior; at the beginning of loading the electrical resistance of the fibers increased linearly to the applied stress. At approximately 30% of the fracture stress, a sudden change was observed, possibly attributed to microcracking. Following, the electrical resistance was analogous to the strain measured by the strain gage. Preliminary test results showed that the coated type of fibers gave better electrical resistance measurements.

Acknowledgments

The authors acknowledge the financial support of the European Union (European Social Fund – ESF) and Greek national funds through the Operational Program “Education and Lifelong Learning” of the National Strategic Reference Framework (NSRF) – Research Funding Program: “Thales – National Technical University of Athens – Development and assessment of innovative experimental techniques for the study of the mechanical behaviour of natural building stones: Applications to the conservation and restoration of monuments of Cultural Heritage” (MIS 380147).

References

1. B. Vigolo, A. Penicaud, C. Coulon, C. Sauder, R. Pailler, C. Journet, P. Bernier, P. Poulin (2000). Macroscopic fibers and ribbons of oriented carbon nanotubes, *Science*, **290**, 1331–34.
2. N.D. Alexopoulos, C. Bartholome, P. Poulin, Z. Marioli-Riga (2010). Structural health monitoring of glass fiber reinforced composites using embedded carbon nanotube (CNT) fibers, *Comp. Sci. Technol.*, **70**, 260–271.
3. N.D. Alexopoulos, C. Jaillet, C. Zakri, P. Poulin, S.K. Kourkoulis (2013). Improved strain sensing performance of glass fiber polymer composites with embedded pre-stretched polyvinyl alcohol-carbon nanotube fibers, *Carbon*, **59**, 65–75.

STRESS EVALUATION IN STEEL ELEMENTS WITH NOVEL BARKHAUSEN EFFECT METER

B. Augustyniak, M. Chmielewski, L. Piotrowski, P. Maciakowski

Department of Technical Physics and Applied Mathematics, Gdansk University of Technology,
Gdansk, Poland

1. Introduction

High tensile residual stress in steel elements of (e.g. pipe and tubes in power plant boilers and turbines) increases considerably risk of damage due micro crack creation and development. Quick and low cost technique of residual stress assessment is thus desired. In the case of ferromagnetic elements one can use well known nondestructive technique based on so called classical Barkhausen effect (HBE). This Barkhausen effect is related to abrupt jumps of magnetic domain wall (DW) when tested element is magnetized with varying magnetic field. DW is unpinned from microstructure defects (precipitates, dislocation tangles). Magnetic domain structure and thus DW activity are sensitive to local as well as to long range stress. It is known that the HBE intensity is higher when vector of magnetization provided by HBE probe is parallel to the direction of tensile stress, while the HBN intensity is lower on opposite case. Evaluation of stress level by means of HBE measurement is possible knowing the so called calibration function. In fact it is dependence of HBE intensity on surface strain level. Strain is measured with gages. This calibration function should be made for biaxial stress condition using cross shape reference sample. Residual stress evaluation at a given place with HBE technique can be deduced when HBE intensity is measured at different angles. Such evaluation is based on information about angular dependence of HBE intensity. In standard devices the probe is positioned by hand at a given directions. Such measurement is relatively time consuming procedure. This is why we have invented and produced a novel HBE meter with original probe. This probe magnetizes material at different angles automatically. We like present general description of this novel meter and provide some indicative examples of its application for residual stress evaluation in welded plates.

2. Meter description

Magnetic field inside the investigated material is generated with the help of a probe containing two perpendicular electromagnets (see Fig. 1). The HBE signal is detected in the detecting coil with a ferrite core, placed in the centre between the electromagnets poles. The change of field direction is obtained by changing the ratio of magnetic flux intensity in the cores of these electromagnets. Both the magnetisation and measurement processes are controlled with the help of multifunction data acquisition device under control of the LabVIEW based software. It allows to obtain any chosen ratio of the magnetisation flux density in magnetising cores. The apparatus may work in one of two regimes – performing either a single measurement or full rotation of the magnetic field. In the latter case two sets of magnetizing current amplitudes are generated. The number of amplitudes depends on the number of magnetizing

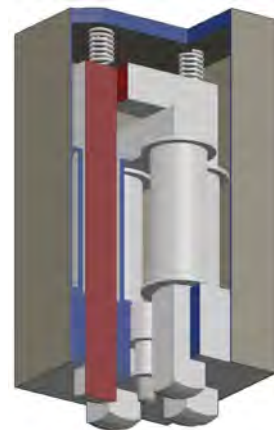


Fig. 1. Schematic view of the probe.

field orientations required. During the measurement, for every chosen orientation the measurement of HBE signal is performed, and its envelopes are numerically determined. On the basis of the obtained envelopes two parameters are calculated – a peak-to-peak (Ub_{PP}) value and an integral of the envelope (after background noise intensity deduction) over the magnetisation period ($Ub Int$). Both the parameters are recorded as a function of the magnetizing field direction.

3. Examples of application

Figure 2 shows polar plots of HBE intensities ($Ub Int$) obtained for the given strain levels (e_x and e_y) within elastic limits; steel S235. The strain values ε are in mikro-deformation units ($1 \mu def = 1 \cdot 10^{-6}$). The x direction corresponds to angle $\alpha = 0$. One can find that the tested steel grade S235 is quite isotropic against direction of magnetisation (plot 1) and also against applied strain. Those plots are used for construction of calibration function at or x or y direction, respectively. These function are transformed to the function type $\varepsilon_i = F(Ub Int)_i$. Such functions are applied for transformation of the as measured in the field condition HBE intensities into the strain level. This strain level can be deduced knowing calibration functions for both two directions of magnetisation.

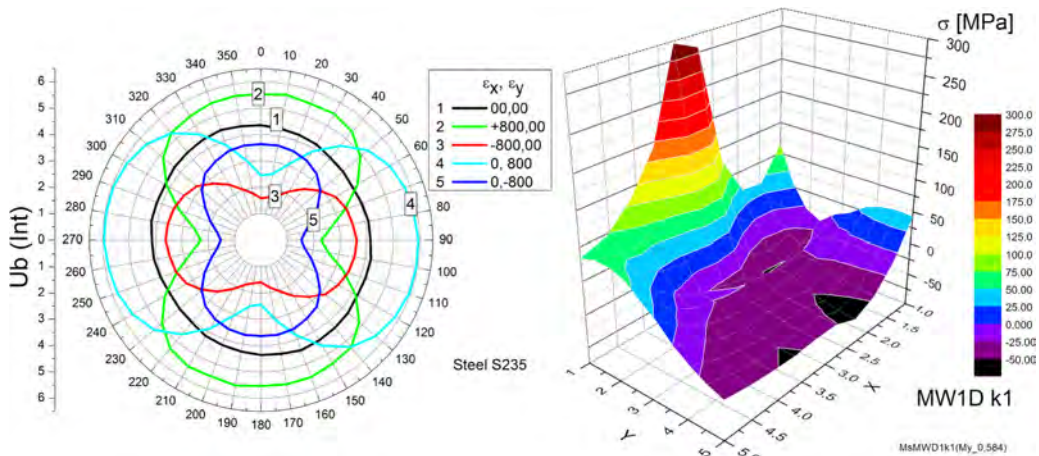


Fig. 2. Polar plots of HBE intensity (integrals) obtained for the given strain levels (ε_x and ε_y); steel S235.

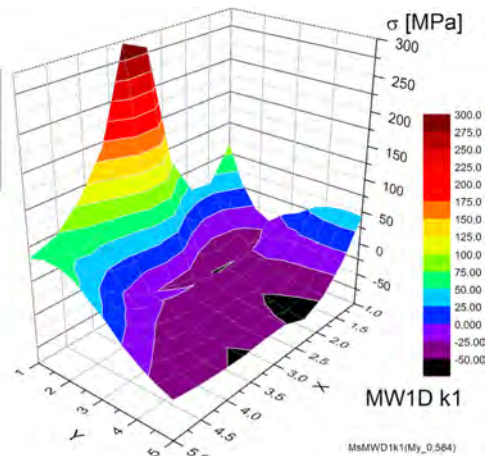


Fig. 3. Distribution of residual stress (σ_x) over the welded plate of steel M460.

An example of such analysis is 3D plot in Fig. 3. Axis x is parallel to the seam direction, and y is perpendicular, respectively. There are evident areas with as expected relatively high level of residual stress, just near the weld seam (stress of order of 300 MPa).

4. Conclusions

It is worth stressing that such measurements are easy to perform and very fast. The full process takes about 30 seconds. In addition to the obtained angular dependence the fitting procedure, is performed. From those parameters the maximum and minimum values as well as the main axis rotation are calculated. This novel meter allows thus very quick detection of material anisotropy as well as evaluation of residual stress components. However, separation of these two factors on the HBE intensity needs complementary information about residual stress. Such information can be obtained from the hole drilling method (Mathar method). Those types of experiments are in progress.

Acknowledgments

This work has been performed under the Project No PBS1/A9/14/2012, supported by The National Centre for Research and Development (Poland)

NATURAL TIME ANALYSIS OF ACOUSTIC EMISSIONS WHEN CEMENT MORTAR SPECIMENS ARE SUBJECTED TO THREE POINT BENDING LOADING

G. Hloupis¹, I. Stavrakas¹, I. Dakanali², A. Kyriazopoulos¹, D. Triantis¹

¹Technological Educational Institution of Athens, Department of Electronics
Laboratory of Electrical Characterization of Materials and Electronic Devices, 12210, Athens, Greece

²National Technical University of Athens, Department of Mechanics, Laboratory of Testing
and Materials, Theocaris Building, Zografou Campus, 15773, Athens, Greece

1. Introduction

Acoustic Emissions (AE) in brittle materials are subjected to complex correlations between space, time, and magnitude. This is a representative example of complex time series with features similar to that of other equilibrium or non-equilibrium critical systems. Projection of a time-series in Natural Time Domain (NTD) where the time is not continuous reveals novel dynamical features hidden behind time series in complex systems which cannot be captured the analysis is carried out within the frame of conventional time. Several studies from Biology, Earth Sciences, Environmental Sciences, Physics and Cardiology reporting that Natural Time plays a key role in predicting impending catastrophic events in general [1, 2].

In the current study, representative AE parameters were analyzed in NTD in order to follow the dynamical evolution of the system and identify its entrance to critical stage (i.e. fracture).

2. Experimental details and methods

Prismatic sample with dimensions 5x5x19cm exposed to three point bending (3PBD) test. The specimen was made by mortar of white cement and quartz sand. The load was applied in the middle of the length of the sample and the distance between the restraints was 13cm. The load pattern that was followed included multiple steps with increasing load and maintaining it constant for a while. In each step the final load was larger than the previous one. The AE sensors were installed on the right and left face of the prism.

The transformation of a time-series of AE hits from the conventional time domain to the natural time domain is performed by ignoring the time-stamp of each hit and retaining only their normalized order of occurrence (index of occurrence by number of events). This way, the k^{th} event corresponds to the natural time $\chi_k = k/N$, (N : total number of successive events). On the contrary the “energy”, Q_k , of each hit is retained. The quantity Q_k represents different physical quantities for different time series [3]; for earthquake time series it has been assigned to seismic energy released while at the current study corresponds to the energy burst described by RA parameter (RA = rise time of AE hit (s) / amplitude (db)). A system is considered to approach criticality when the parameter

$$\kappa_1 = \sum_{k=1}^N p_k \chi_k^2 - \left(\sum_{k=1}^N p_k \chi_k \right)^2$$

converges to a value $\kappa_1 = 0.07$ while at the same time the entropy in natural time, S , as well as the entropy in natural time under time reversal, S^* , are both less than $S_u = 0.0966$ which stands for the entropy value in natural time domain of uniform distribution (indicating randomness) [1].

3. Results

The spatial analysis of the AE events showed that during the initial loading values parasitic AEs, attributed to the friction of the steel rods and the specimen, were recorded. While the load was further increased the AE activity, as expected, was mainly located at the low-middle side of the specimen where maximum tensional load is recorded.

NTD analysis results indicate that during the subsequent loading cycles there are well defined time slots where the criticality conditions were met and thus the forthcoming fracture can be identified in advance. Representative results from the last loading step (before fracture) as presented in Fig. 2 clearly dictated that the criticality conditions were met a along before the fracture. More specific it is possible to identify the time slot where the increasing stress (σ) exceeds 40% (σ^*) of the ultimate compressional strength (σ_f) as observed in previous studies using marble specimens [4].

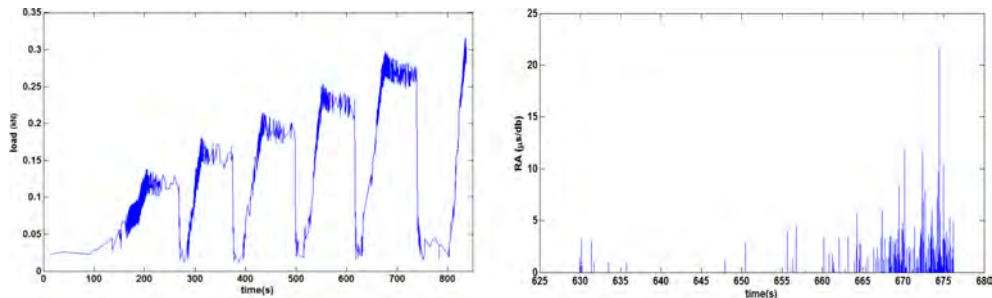


Fig. 1. The load profile of the experiment (left) and the evolution of RA parameter during load increase of 5th step (right).

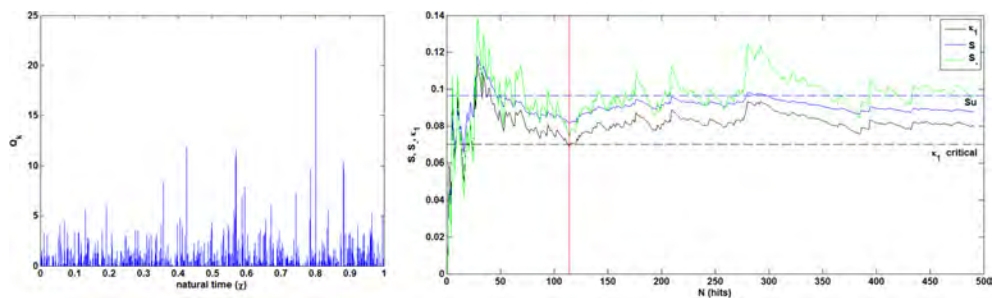


Fig. 2. The projection of RA parameter during load increase of 5th step in Natural Time Domain (left) and the results of NTD analysis for the same time excerpt. Vertical red line indicates the moment where criticality conditions fulfilled (right).

Acknowledgments

This research has been co-financed by the European Social Fund (ESF) and Greek national funds through the THALES-MIS380147 Program.

References

1. P.A. Varotsos, N.V. Sarlis, E.S. Skordas (2011). *Natural Time Analysis: The new view of time. Precursory Seismic Electric Signals, Earthquakes and other Complex Time-Series*, Springer-Verlag, Berlin, Heidelberg.
2. P. Varotsos, N.V. Sarlis, E.S. Skordas, S. Uyeda, M. Kamogawa (2011). Natural time analysis of critical phenomena, *PNAS*, **108**, 28, 11361–11364, Jul., doi: 10.1073/pnas.1108138108.
3. P.A. Varotsos, N.V. Sarlis, H.K. Tanaka, E.S. Skordas (2005). Similarity of fluctuations in correlated systems: The case of seismicity, *Phys. Rev. E*, **72**, 4, 041103/1–8, Oct., doi: 10.1103/PhysRevE.72.041103.
4. G. Hloupis, I. Stavrakas, F. Valianatos, D. Triantis (2013). Compressive Strength Estimation of Marble Specimens using Acoustic Emission Hits in Time and Natural Time Domains: Preliminary Results, *Geophysical Research Abstracts*, **15**, EGU201311623.

METHODOLOGICAL REMARKS ON CONDUCTING HIGH-STRAIN RATE TESTING WITH THE USE OF SHPB TECHNIQUE

J. Janiszewski

Military University of Technology, Warsaw, Poland

1. General overview

A split Hopkinson pressure bar (SHPB), also known as a Kolsky bar, is the most common technique for determination of the mechanical properties of materials deforming at high strain rates ($10^2 - 10^4 \text{ s}^{-1}$) [1, 2]. There are various setups and techniques, currently in use for the SHPB method, allowing studies of dynamic behavior of materials under different states of stress (e.g. compression, tension, torsion etc.). Although the general principles of the SHPB technique are not relatively complicated, a high strain rate tests with the use of this method may create significant errors in characterization of mechanical response for a given material. The main reason for the emergence of errors during conducting the SHPB experiments is an inadequate adjustment of the testing conditions (e.g. striker impact velocity, sample geometry) to the specific specimen response, as a result of a failure in satisfying methodological requirements of the SHPB technique.

The present paper summarizes the author's current experience in performing the compression split Hopkinson pressure bar tests and it focuses on the experimental methods that facilitate the material sample to deform under desirable valid testing conditions. In the work, there were presented the methodological considerations and results examples extracted from dynamic tests conducted for several various materials, such as: high strength steel, copper, aluminum alloy and rubber.

2. Experimental setup

At Military University of Technology in Warsaw, the experiments at high rate of strain have been performed for many years. For these purposes, the Taylor impact test and the expanding ring test have been used among others [3, 4]. SHPB technique has been especially exploited for characterization of mechanical properties of materials. A classical compression split Hopkinson pressure bar was applied in the present work. The apparatus presented in Fig. 1 consists mainly of a striker launching system (air pressure gun),

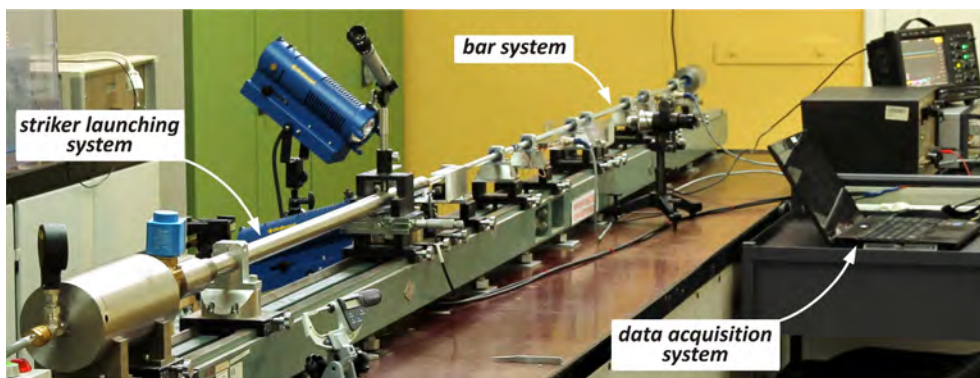


Fig. 1. Split Hopkinson Pressure Bar applied for investigations.

a striker, an incident bar, a transmission bar (bar system) and a high-frequency data acquisition system.

The incident bar and the transmission bar were each 1218 mm long, while the striker lengths were 200 or 300 mm. Both the bars and the striker had a common diameter of 12.05 mm and were made of commercial maraging steel grade 350 and 7075-T6 aluminum alloy or PMMA (plexiglass) in the case of testing low strength materials. Each bar was supported by 4 linear bearing stands, which were mounted on an optical bench allowing precise alignment of the bars system.

3. Results examples

The main considerations presented in the work were focused on the use of a pulse shaping technique to facilitate an achievement of stress equilibrium and constant strain rate deformation in the specimen during SHPB experiments [2]. The proper modification of the incident pulse profile was obtained through using pulse shapers, that is, the different diameters and thickness discs made of miscellaneous materials placed on the front surface of the incident bar. The pulse shapers were usually manufactured from copper sheets with various thicknesses by the use of a sheet metal punching technique. As an example, the history of stress on the contact specimen surfaces during the SHPB testing without and with applying a copper pulse shaper is presented in Fig. 2.

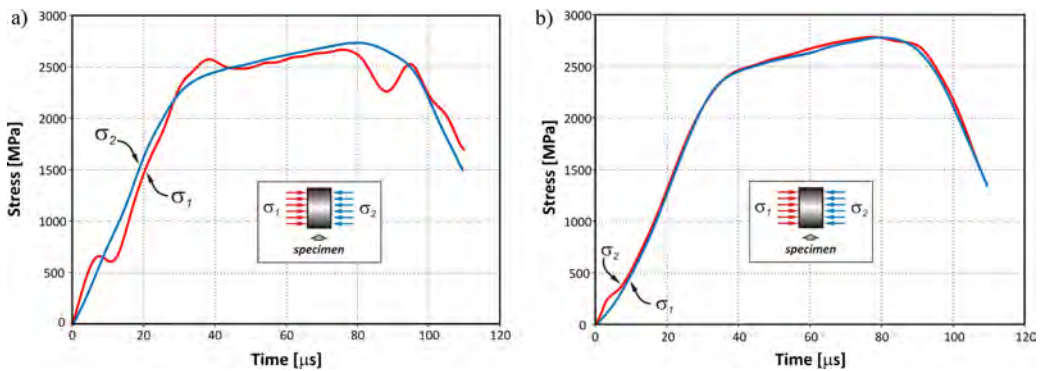


Fig. 2. Comparison of stresses at front and rear ends of the high strength steel specimens (4 mm in diameter; 2 mm in thickness) for the SHPB experiments conducted without (a) and with (b) the use of pulse shaper (impact velocity of striker bar ~ 19 m/s).

As demonstrated in Fig. 2, through repeated attempts, it was found that the use of the 5.56 mm diameter copper pulse shaper with the 0.32 mm thickness guarantees the satisfactory stress equilibrium for high strength steel specimen deformed with an average strain rate of $1.7 \times 10^3 \text{ s}^{-1}$. The above example validates the essential role of pulse shaping technique to meet methodological requirements of the SHPB test.

References

1. M.A. Meyers (1994). *Dynamic behaviour of materials*. John Wiley and Sons, INC, New York-Chichester-Brisbane-Toronto-Singapore.
2. W. Chen, B. Song (2011). *Split Hopkinson (Kolsky) bar, Design, testing and applications*, Springer.
3. W. Moćko, J. Janiszewski, M. Grażka (2013). Application of an extended Rusinek-Klepaczko constitutive model to predict the mechanical behavior of 6082-T6 aluminum under Taylor impact test conditions, *The Journal of Strain Analysis for Engineering Design*, **48**, 364–375.
4. J. Janiszewski (2012). Ductility of selected metals under electromagnetic ring test loading conditions, *International Journal of Solids and Structures*, **49**, 1001–1008.

AN EXPERIMENTAL STUDY OF THE MECHANICAL RESPONSE OF A TYPICAL EPISTYLES' CONNECTION UNDER PURE SHEAR

S.K. Kourkoulis¹, E.D. Pasiou¹, I. Stavrakas², G. Hloupis², D. Triantis², K. Moutzouris¹

¹National Technical University of Athens, Department of Mechanics, Athens, Greece

²Technological Educational Institution of Athens, Department of Electronics, Athens, Greece

1. Introduction

The Parthenon Temple on the Acropolis of Athens is a dry stone construction. Its epistyles were joined together with the aid of “T”-shaped steel connectors which were placed in grooves of appropriate geometrical shape filled with molten lead. Today, one of the major problems confronted during the conservation project in progress is the restoration of the damaged connections [1]. Pure shear is one of the main loading modes the epistyles' connections are subjected to. A pure laboratory shear test is a difficult task. In this direction a sophisticated experimental set up is here proposed, permitting successful implementation of almost pure shear as it was checked with the aid of both the Digital Image Correlation (DIC) technique and two clip gauges. Special attention was paid to pump data from the interior of the specimens since failure mechanisms are activated within the specimens' bulk before final failure. For this purpose the Pressure Stimulated Currents (PSC) – [2] and the Acoustic Emission (AE) – techniques were used in juxtaposition to traditional strain gauges.

2. Experimental procedure

The specimens used simulate a typical restored connection of the Parthenon's epistyles under a 2 : 3 scale. They consist of two blocks of Dionysos marble (Fig. 1a) which is used due to its mechanical compatibility with the authentic stone [3]. A 7 cm depth groove is sculptured, a titanium connector (Fig. 1b) is placed in the groove and then it is filled with a cementitious material. Before placing the connector three strain gauges were attached on its middle part, covered with silicone for protection from mortar's moisture (Fig. 1b). A pair of electrodes (for the application of the PSC technique) and eight acoustic sensors were glued on the specimen. In addition, a dots' pattern was sprayed on its front surface while two clip gauges were fixed at its back surface to measure any possible “opening” of the epistyles. In order to realize a pure shear test, a series of rigid metallic custom-made components were constructed: One marble block is kept fixed by means of three plates and six threaded bars. The load is applied on the other block with the aid of a metallic structure and two rods passing through the specimen (Fig. 1c). Attention was paid for the

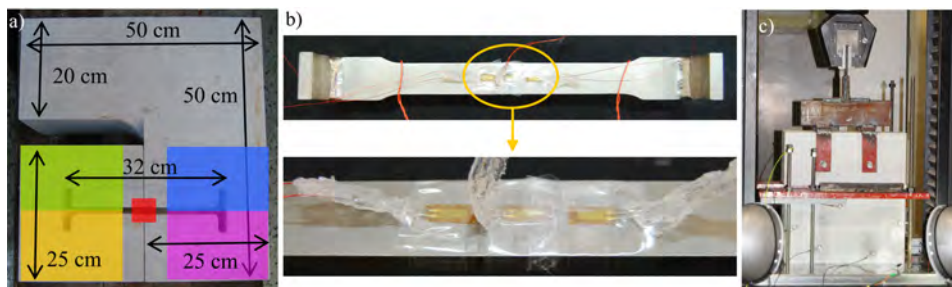


Fig. 1. a) The geometry of a typical specimen and the five auxiliary volumes for the AE technique. b) The three strain gauges glued on the connector. c) The experimental set up.

load to be applied exactly above the connector's position and along the epistyles' interface. The tests were realized under displacement control at a rate equal to 0.2 mm/min, using an Instron loading frame of capacity 250 kN.

3. Results

The connection collapses at a load equal to about 27.5 kN when the epistyle on which the load is applied is fractured (Fig. 2a). Careful examination of the load-time curve (Fig. 2b) reveals two slope changes around 17 kN and 23 kN. In order to explore their chargeable event, the specimen was divided in five volumes (Fig. 1a) and the cumulative number of the acoustic events detected in each one was plotted vs. time (Fig. 2b). After the level of 17 kN the rate of the acoustic events in the right epistyle starts increasing faster than the respective one in the left epistyle while after 23 kN it becomes even faster. In Fig. 2c the displacement component along the connector's axis is shown validating the realization of a pure shear test.

Measurable electrical current (PSC) emissions appear when the applied load exceeds 12 kN. For higher load values the PSC continues varying until the failure of the system. An intense spike-like PSC emission was recorded at approximately 22 kN, denoting severe abrupt damages, as it is also indicated by the AEs recorded. The characteristic pre-failure PSC peak [2] is also observed a few seconds before the failure of the system. The variation of the PSC emission exhibits two polarities indicating that the damage propagation direction changes during the experimental procedure. Such an indication may be used to estimate the stress concentration regions in the bulk of the epistyles.

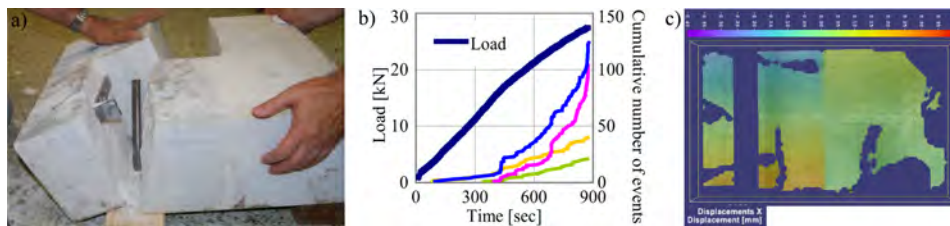


Fig. 2. a) The fracture plane. b) The acoustic events- and the load-time curves. c) The distribution of the horizontal component of the displacement field.

4. Conclusions

The mechanical response of interconnected epistyles under pure shear was studied by means of traditional and innovative techniques. It seems that failure of the marble-metal-cement complex starts from the fragmentation of the cement layer. Analysis of the experimental results indicates strong correlation between the PSCs and the AEs almost throughout the whole loading process.

Acknowledgments

This research has been co-financed by the European Social Fund (ESF) and Greek national funds through the THALES-MIS380147 Program.

References

1. C. Zambas (1994). *Study for the restoration of the Parthenon* (in Greek), Vol. 3b, Ministry of Culture, Committee for the Conservation of the Acropolis Monuments, Athens, Greece.
2. I. Stavrakas, C. Anastasiadis, D. Triantis, F. Vallianatos (2003). Piezo stimulated currents in marble samples: Precursory and concurrent-with-failure signals, *Natural Hazards and Earth System Sciences*, **3**, 243–247.
3. I. Vardoulakis, S.K. Kourkoulis (1997). *Mechanical properties of Dionysos marble*, Final report of the Environment Project EV5V-CT93-0300: Monuments Under Seismic Action, National Technical University of Athens, Greece.

EFFECT OF FIBRE CONTENT ON STATIC AND DYNAMIC PROPERTIES OF FIBRE REINFORCED CONCRETE

L. Kruszka¹, W. Moćko^{2,3}, E. Cadoni⁴, L. Fenu⁵

¹Military University of Technology, Warsaw, Poland

²Institute of Fundamental Technological Research, Warsaw, Poland

³Motor Transport Institute, Warsaw, Poland

⁴Scuola Universitaria Professionale della Svizzera Italiana, Lugano, Switzerland

⁵University of Cagliari, Cagliari, Italy

1. Introduction

The static and dynamic behaviour of glass and basalt fibre reinforced concretes (FRC) especially as high performance building materials is still important taking into account applications those materials to protective structures. Fibre reinforced concrete structures are one of solutions, which require suitable quantities of fibres in concrete, taking also into consideration type of fibres [1]. Certain quantity of fibres can be beneficial for enhancing the properties of plain concrete. But it is not necessary that all properties will be improved, the addition of fibres may increase certain properties and at the same time may decrease other ones. Therefore the fibres in appropriate quantity should be selected.

In this work, the effect of 3% and 5% fibres' content on properties of FRC is studied. To evaluate the efficiency of glass and basalt fibres in improving the properties of the concrete the performance of concrete matrix, i.e. plain concrete (PC) is used as a reference. Compressive strength, modulus of elasticity, and mod of fracture were determined for all FRC and PC specimens. Static and dynamic properties of the FRC and PC were investigated experimentally using: universal testing machine Instron 8802 equipped (Fig. 1) with Aramis measure system, and split Hopkinson pressure bar (Fig. 2) equipped in Phantom v1210 high speed camera, respectively [2, 3]. Quasi-static tests were carried out at strain rate equal to 0.005/s whereas dynamic tests were performed at strain rate equal to 800/s.

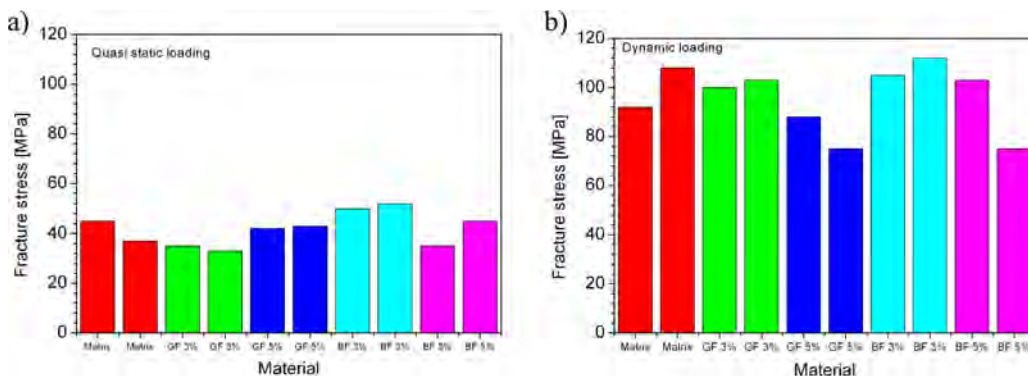


Fig. 1. Fracture stress of tested materials at: a) quasi-static and b) dynamic loading.

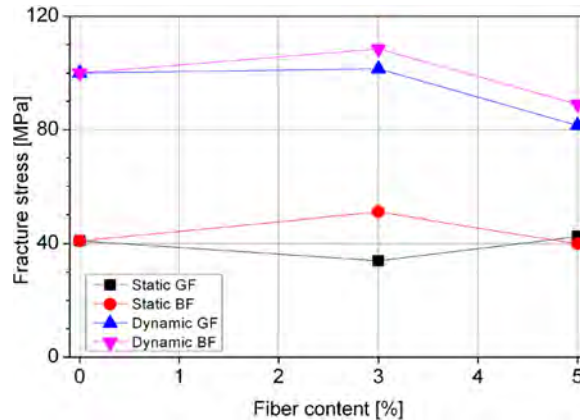


Fig. 2. Influence of glass (GF) and basalt fibers (BF) on the fracture strain at quasi-static and dynamic loading conditions.

2. Influence of the fiber content on the static and dynamic fracture stress

The fracture stress obtained during compression tests of matrix and fiber reinforced material as well is presented in Fig. 1. It may be observed that increase of the applied deformation rate induces clearly observed rise of the fracture stress in all cases. Analysis of the optimal content of fiber reinforcement in the concrete are shown in Fig. 2. Introducing of the 3% or 5% content of the glass fibers into concrete does not influence significantly fracture stress in the dynamic deformation regime. Under dynamic loading conditions 3% of the glass fibers reinforcement does not affect fracture stress, however further increase of the fibers share in the concrete up to 5% results in clearly observed drop of fracture stress, from 100 MPa to 80 MPa, in comparison to plain concrete. Application of 3% content of the basalt fiber induces increase of the fracture stress in both static and dynamic loading conditions. The fracture stress of the FRC concrete is 20–30 MPa higher than PC. Higher amount of the basalt fiber, i.e. 5% reduces fracture stress. For the static deformation rates stress of the 5% FRC drops to this same value as for the PC, whereas at the dynamic range the softening effect is even stronger, since the fracture stress drops to 90 MPa in comparison to 100 MPa for the PC.

3. Conclusions

Content of the glass fibers in the concrete does not influence the fracture stress at static loading conditions in a clearly observed way. Moreover at dynamic range 5% content of the fiber results in a significant drop of fracture stress. Analysis of the basalt fibers influence on the fracture stress shows that optimal content of this reinforcement is equal to 3% for both static and dynamic loading conditions. Further increase of the fiber share gives the opposite effect, i.e. drop of the fracture stress.

References

1. P. Baruah, S. Talukdar (2007). A comparative study of compressive, flexural, tensile and shear strength of concrete with fibres of different origins, *Indian Concrete Journal*, **81**, 17–24.
2. W. Mocko, Z.L. Kowalewski (2011). Dynamic Compression Tests – Current Achievements and Future Development, *Engineering Transactions*, **59**, 235–248.
3. L. Kruszka, W.K. Nowacki (1996). New applications of the Hopkinson pressure bar technique to determining dynamic behavior of materials, *Journal of Theoretical and Applied Mechanics*, **34**, 259–280.

PIEZOELECTRIC BEHAVIOR OF AERONAUTICAL GFRP WITH EMBEDDED STRAIN SENSOR UNDER BENDING LOADS

P. Lymperta¹, S.K. Kourkoulis², P. Poulin³, N.D. Alexopoulos¹

¹Department of Financial Engineering and Management, University of the Aegean, Chios, Greece

²School of Applied Mathematical and Physical Sciences, Section of Mechanics
Laboratory of Testing and Materials, National Technical University of Athens, Greece

³Université de Bordeaux, Centre de Recherche Paul Pascal – CNRS
Avenue Schweitzer, 33600 Pessac, France

1. Introduction

Innovative composite materials have been manufactured during the last five years in order to withstand the mechanical loads but besides to be themselves a sensor for cases of internal/external damages occurred. A significant technological innovation has been performed in the case of glass fiber reinforced composites, where carbon fibers were embedded in the matrix of the composite to be used as strain sensors. Carbon fibers have an intrinsic electrical conductivity that by monitoring their electrical resistance change can make feasible the monitoring of the material's structural integrity. However, due to significant problems, mainly due to difference in moduli of elasticity between host matrix and sensor, the carbon fibers could only prognose the time before fracture of the composite. Such a fiber from polyvinyl alcohol with carbon nanotubes (thereafter will be called PVA-CNT fiber) that could be used as an embedded sensor was manufactured by researchers of CRPP-CNRS [1, 2] and successfully tested in tensile tests [3].

The main objective of this work is to demonstrate the governing mechanism that this embedded fiber works under flexural loading. Therefore, it is essential to show the electrical resistance measurements of the fiber how can be correlated with typical flexural mechanical loadings along with the onset of material damage/failure of the specimen. To this cause, several three-point and four-point bending tests had been performed, simultaneously measuring bending flexure, applied bending force along with electrical resistance change of the embedded fiber during the mechanical tests.

2. Experimental procedure

The composite material used to embed the carbon nanotube fiber was a typical GFRP composite with the matrix being a typical epoxy resin currently used in aeronautical applications. The fibers used in the present study were produced by CNRS-CRPP at Bordeaux, France, by using the coagulation spinning process explicitly described in [1]. This process was in-house developed in 2000 and has improved since then [2]. Four different pre-stretched ratios were used, namely: (a) untreated fiber, pre-stretching at (b) 50%, (c) 100% and finally (d) 200%. The composites were manufactured by Vacuum Assisted Resin Infusion method and more details can be found in [3]. The dimensions and structure of testing coupons were rectangular and in accordance with ASTM D5947. The experimental setup and procedure was carried out in accordance to the ASTM D790 and D6272 standards for three and four point bending tests, respectively.

An Instron 10 kN testing machine of the Laboratory of Strength of Materials of the National Technical University of Athens was used. The diameter of the untreated fiber was of the order of 40 μm , while gauge length ranged between 35 and 50 mm. Bending tests

were performed under constant displacement rate of 0.1 mm/sec. An Agilent multimeter was also electrically attached to the fiber to record its electrical resistance change caused by the applied mechanical loading. Data for time, displacement, force and electrical resistance were continuously monitored, at a sampling frequency of 1 Hz. Additional strain gauges were surface attached in order to determine the material's deflection. Evaluations of these measurements included calculations and plots of the material's deflection, plots of strain versus stress and changes in intrinsic electrical resistance of the embedded fiber for all performed mechanical tests. Figure 1a shows the experimental setup for the four-point bending test configuration, with the arrangement of strain gauges, wired between specimen and machine.

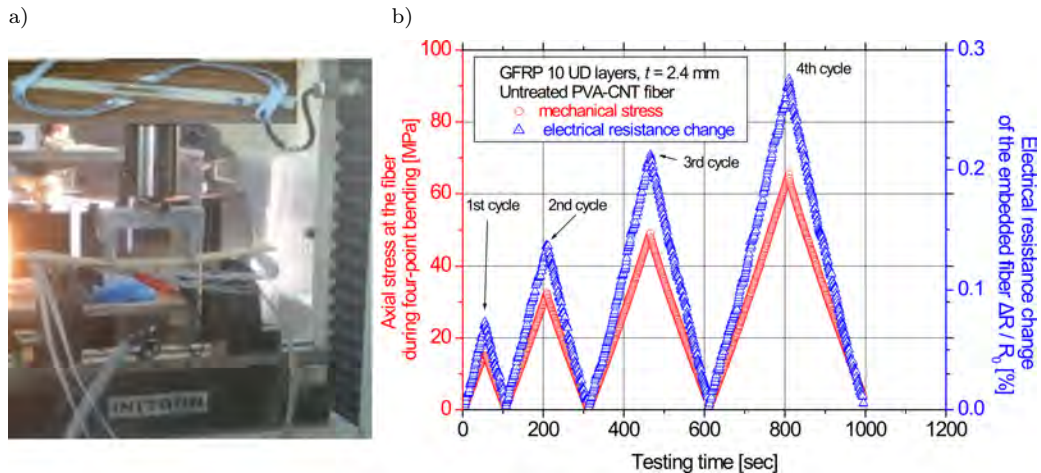


Fig. 1. a) The experimental setup with attached strain gages in four point bending test and b) available results showing the electrical resistance change, applied axial stress and vs testing time in 4pb configuration (untreated fiber).

3. Results

Figure 1b shows the combined electrical resistance change $\Delta R/R_0$ and mechanical stress results of the untreated fiber versus time during four bending loading and unloading branches. It was found that electrical resistance change of the fibers, in response to mechanical loading, is strongly dependent upon their pre-stretching degree. In tensile loading, the higher the pre-stretching ratio, the higher $\Delta R/R_0$ values were recorded, for the same axial strain value that was also noticed in [3]. Based on the observed experimental results and recordings, it was found that the pre-stretched fiber is a determining factor for the fiber's rate of change of electrical resistance, during the aforementioned described loadings – unloadings and under bending loadings.

References

1. B. Vigolo, A. Penicaud, C. Coulon, C. Sauder, R. Pailler, C. Journet, P. Bernier, P. Poulin (2000). Macroscopic fibers and ribbons of oriented carbon nanotubes, *Science*, **290**, 1331–1334.
2. P. Poulin, B. Vigolo, P. Launois (2002). Films and fibers of oriented single wall nanotubes, *Carbon*, **40**, 1741–1749.
3. N.D. Alexopoulos, C. Bartholome, P. Poulin, Z. Marioli-Riga (2010). Structural health monitoring of glass fiber reinforced composites using embedded carbon nanotube (CNT) fibers, *Composites Science and Technology*, **70**, 260–271.

MICROSTRUCTURAL ASSESSMENT AND MAGNETIC STRUCTUROSCOPY OF MIDDLE-CARBON STEEL AFTER SIMULATED CREEP

K. Makowska¹, Z.L. Kowalewski^{1,2}

¹Motor Transport Institute, Warsaw, Poland

²Institute of Fundamental Technological Research, Warsaw, Poland

1. General

The paper describes an application of magnetic methods for evaluation of the exploitation period, microstructural degradation and mechanical property variations of the middle carbon steel after simulated loadings at high temperature. The research dealing with an assessment of mechanical properties using magnetic non-destructive techniques is called as a magnetic structuroscopy [1–3]. In this paper, magnetic techniques based on measurements of the magnetic Barkhausen noise and magnetoacoustic emission were applied. These methods are potentially useful for damage identification of ferromagnetic materials.

Magnetic Barkhausen noise (MBN) is the result of the irreversible movement of magnetic domain walls during a magnetisation cycle [4]. Domain walls are pinned by microstructural barriers and released abruptly in the changing magnetic field [5]. The barriers that break domain wall movement are the grain boundaries, dislocations, precipitates [4] and voids [5], for example. A movement of the 90° domain walls generates acoustic waves that are known as the magnetoacoustic emission (MAE) [6]. This is a consequence of local volume changes in the materials having non-zero magnetostriction. The acoustic waves can be detected by the piezoelectric transducers.

2. Material and experimental procedure

Two series of specimens manufactured using the 40HNMA steel commonly applied in the power industry were tested. The specimens of the first series were cut out from a flat delivered in the as-received state, and subsequently, they were quenched and tempered (cooling in oil) at temperature of $T = 850^{\circ}\text{C}$ and $T = 500^{\circ}\text{C}$, respectively. The specimens of the second series were cut out from a piece of pipe after its prior exploitation. We decided to produce specimens from the exploited pipeline since we expected creating voids in them during laboratory creep tests in relatively short time.

Both series of specimens were subjected to accelerated creep ($\sigma = 250\text{ MPa}$, $T = 500^{\circ}\text{C}$). Additionally, the specimens cut out from the flat were subjected to plastic deformation at room temperature. Each prior deformation process was interrupted for a range of the selected time periods in order to achieve specimens with increasing level of strain. In the next step, non-destructive measurements were carried out. The yield point and ultimate tensile stress were determined on the basis of static tensile test. An evolution of material microstructure was extensively studied. Finally, the relationships between pre-strain level and parameters determined by means non-destructive methods were analysed.

3. Selected results

Figure 1 shows variations of the integral of half-period voltage signal of the magnetic Barkhausen emission $Int(U_b)$ and yield point $R_{0,2}$ of the 40HNMA steel cut out from the flat as a function of the creep pre-strain. As it is clearly seen, a trend of changes for both parameters is opposed. Moreover, both parameters are very sensitive into prior deformation either at the first or second stages of the accelerated creep. The relationships between $R_{0,2}$ and $Int(U_b)$ are presented in Fig. 2. In the case of plastic deformation linear relation between both parameters was found. It was also observed that the values of $Int(U_b)$ after plastic deformation are higher than those of $Int(U_b)$ after accelerated creep.

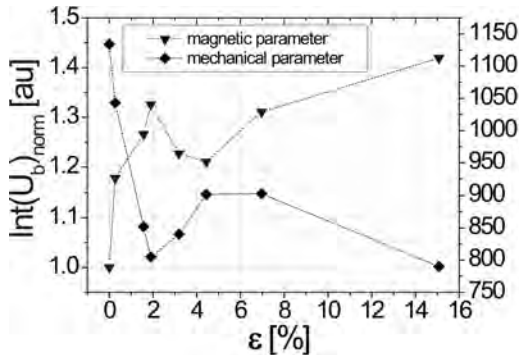


Fig. 1. Integral of half-period voltage signal of the magnetic Barkhausen emission $Int(U_b)$ and yield point $R_{0,2}$ versus pre-strain for the 40HNMA steel after laboratory creep.

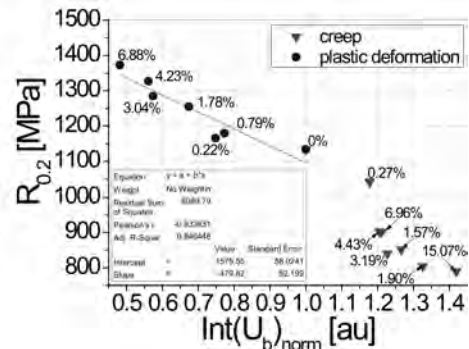


Fig. 2. Variation of yield point of the 40HNMA steel after accelerated creep/plastic deformation versus integral over half-period voltage signal of the magnetic Barkhausen emission: $Int(U_b)$.

4. Conclusions

The magnetic parameters, like the integral of voltage signal of the magnetic Barkhausen emission $Int(U_b)$ for example, are very sensitive into prior deformation at first and second stages of the accelerated creep. Parameters determined on the basis of non-destructive tests may be helpful in estimation of the basic mechanical properties of the prestress materials.

References

- G.V. Bida, A.P. Nichipuruk (2007). Multiparameter methods in magnetic structuroscopy and nondestructive testing of mechanical properties of steels, *Russian Journal of Nondestructive Testing*, **43**, 8, 493–509.
- B. Skrbek, J. Dočekal, I. Tomáš (2008). Quantitative NDT structuroscopy of cast iron castings for vehicles (cars and locomotives), *NDT for Safety*, 07-09, Prague, Czech Republic, 249–258.
- K. Makowska, Z.L. Kowalewski, B. Augustyniak, L. Piotrowski (2014). Determination of mechanical properties of P91 steel by means of magnetic Barkhausen emission, *Journal of Theoretical and Applied Mechanics (JTAM)*, **52**, 1, 181–188.
- M. Blaow, J.T. Evans, B.A. Shaw (2007). The effect of microstructure and applied stress on magnetic Barkhausen emission in induction hardened steel, *Journal of Materials Science*, **42**, 4364–4371.
- D. O'Sullivan, M. Cotterell, S. Cassidy, D.A. Tanner, I. Mészáros (2004). Magneto-acoustic emission for the characterisation of ferritic stainless steel microstructural state, *Journal of Magnetism and Magnetic Materials*, **271**, 381–389.
- D.J. Buttle, G.A.D. Briggs, J.P. Jakubovics, E.A. Little, C.S. Scruby (1986). Magnetoacoustic and Barkhausen emission in ferromagnetic materials, *Phil. Trans. R. Soc. Land.*, **A320**, 363378.

DESIGN WITH SADSF METHOD AND ANALYSES OF ELASTIC PROPERTIES OF TORSION-LOADED STRUCTURES BASED ON DOUBLE-TEE SECTIONS

I. Markiewicz

Kielce University of Technology, Kielce, Poland

1. Introduction

The paper presents results of design and elastic analysis of two tension-loaded thin-walled structures based on double-tee sections. The structures were designed with the use of application version of the method of statically admissible discontinuous stress fields (SADSF, [1, 2, 4]).

The present state of development of the SADSF method software [1, 4] makes it possible to design even very complex thin-walled structures (made of plane elements), applied, e.g., in aviation and automotive systems and in building engineering. This is a particular class of structures, in which small changes in boundary conditions (or constructional details) may cause large and non-local changes in stress fields [1]. Such problems are difficult to deal with even when using contemporary, most advanced methods of the so-called topology optimization based on iterative improvements. On the other hand, these problems often appear in everyday practice of an engineer.

In the SADSF method, one doesn't make use of iterations, moreover, the method may be applied already at the moment when only boundary conditions are known [1]. Virtually any engineer is able to use it, as the method's software is neither complicated nor costly, and the provided solutions are free of cardinal errors. Then, the SADSF method is worth being implemented to wider practical application.

In the SADSF method, one assumes the condition of equalized effort in the limit state, so the method is an approximate one. Therefore, this work contains also the results of elastic FEM analyses of the presented solutions. In this way, one verifies practical usefulness of the solutions and proves that the structures designed with the SADSF method have radically better properties than those designed intuitively.

2. Obtained results

The way of formulation of the considered design problem – typical for the SADSF method [1] – is illustrated in Fig. 1a. The only data (Fig. 1a) were: limit load on some parts of boundary S_p , which may be reduced to the system of forces \mathbf{P} , geometry of this part of the boundary (dimensions L , h , e , and δ), and the yield point of material assumed for the structure (σ_Y).

One should construct a statically admissible, discontinuous stress field (preferably a limit one), which would satisfy the given boundary conditions and define the structure of the designed construction, i.e. the number, spatial location and the system of mutual connections between component elements [1]. The field should also determine shapes and dimensions of the elements.

To solve the formulated problem, one uses the presently most advanced software package of the SADSF method application version, called the SADSFaM [1, 4]. Applying this software, one constructs structures by selecting ready-made solutions from a library and connecting them like building blocks. Equilibrium conditions and the assumed boundary conditions must be satisfied, as well.

The presented formulation leads to many solutions, however, the number of solutions is limited by the amount of fields available in the library. Such a multitude of solutions gives

the chance to satisfy some additional conditions, e.g. concerning simplicity of realization, strength, etc.

Two original solutions to the problem from Fig. 1a are presented in Figs. 1c and 1d. They have proportions typical for cross-bars of a vehicle frame bearer. Although all of their surfaces are accessible from the outside, the structures have high rigidity to torsion.

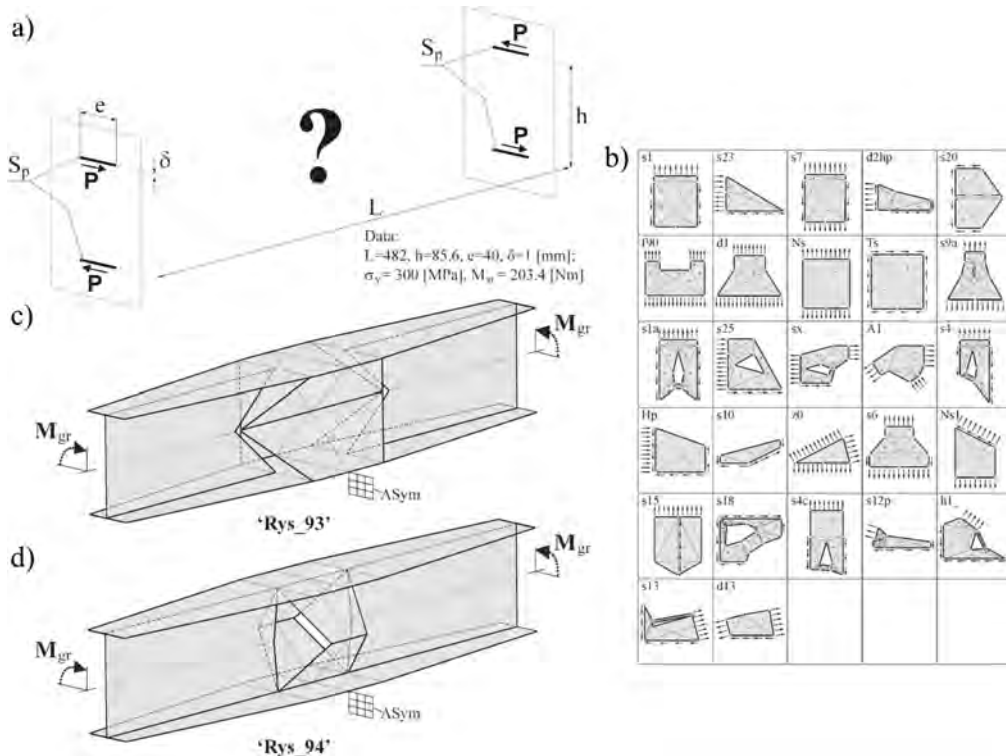


Fig. 1. Formulation and solutions to the problem of complex field construction: a) object illustration of design problem formulation [1, 2]; b) library of ready-made solutions from SADSFAm software package [1, 4]; c, d) solutions: contours of complex fields determining shape and dimensions of the sought-after structures.

Based on elastic FEM analyses, one finds that in the designed structures there are, among other things, maintained small deformations and domination of membrane states, well-equalized equivalent stress fields along free borders, relatively low concentrations of stress and similar levels of maximal equivalent stresses in component elements.

Additionally, it was shown that application of the SADSF method makes it possible to reduce the overall level of equivalent stress in this class of structures – compared to the systems designed intuitively – even several dozen times.

Similar properties have been found in a great number of all the thin-walled structures analyzed so far [3], therefore one can consider such properties as the expected ones.

References

1. W. Bodaszewski (2013). *Static analyses and shaping complex thin-walled structures* [in Polish], Wydawnictwo BEL Studio, Warszawa.
2. W. Bodaszewski, W. Szczepiński (2005/2006). *Shaping Structure Elements by the Method of Discontinuous Stress Fields* [in Polish], PWN/BEL Studio, Warszawa.
3. I. Markiewicz (2013). *Investigating the behaviour of structures designed with the SADSF method* [in Polish], MONOGRAFIE, STUDIA, ROZPRAWY M47, Wydawnictwo Politechniki Świętokrzyskiej, Kielce.
4. Web page: www.sadsf.net.

A NEW METHOD FOR MEASURING YOUNG'S MODULUS OF THIN MULTI-LAYERED MATERIALS USING POSTBUCKLING BEHAVIOR

A. Ohtsuki

Department of Mechanical Engineering, Faculty of Science and Technology, Meijo University
1-501 Shiogamaguchi, Tempaku-ku, Nagoya, 468-8502 Japan

1. Introduction

In recent years, flexible multi-layered materials with very high performance are widely used. Therefore, Young's modulus of these materials is very important to predict large deformation. This paper describes a new testing method (*Compression Column Method*) based on a nonlinear large deformation theory. Exact analytical solutions are obtained in terms of elliptic integrals. By using this method, Young's modulus of each layer in a thin flexible multi-layered material can be easily obtained by just measuring the horizontal displacement or the vertical displacement. The proposed new method is applicable to Young's modulus measurement in a thin layer formed by PVD, CVD, Electrodeposition, Coating, Paint, Cladding, Lamination, etc.

Besides the *Compression Column Method* studied here, the *Cantilever Method* [1], the *Circular Ring Method* [2, 3], the *Compression Column Method* [4] for a single-layered material have already been developed and reported, based on the nonlinear large deformation theory.

2. Theory

A typical illustration of a load-deflection shape for a multi-layered column, compressed between the fixed ends, is given in Fig. 1.

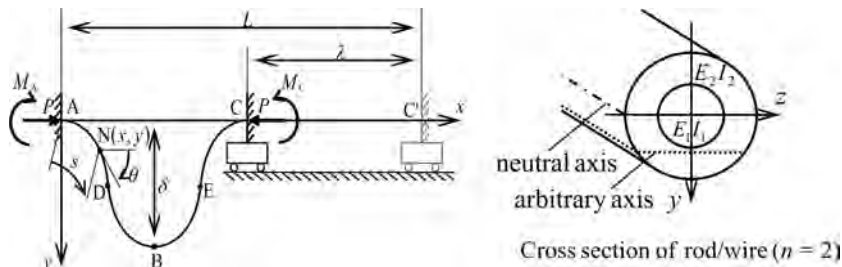


Fig. 1. Illustration of a typical load-deflection shape for a multi-layered buckled column.

Introducing the following non-dimensional variables,

$$(1) \quad \begin{aligned} \xi &= x/L, \quad \eta = y/L, \quad \zeta = s/L, \quad \rho = R/L. \\ \gamma &= PL^2 / \sum_{i=1}^n (E_i I_i), \quad \alpha = M_A L / \sum_{i=1}^n (E_i I_i). \end{aligned}$$

The basic equation is derived in the form of:

$$(2) \quad d^2\theta/d\zeta^2 + \gamma \cdot \sin\theta = 0.$$

Finally, the maximum non-dimensional arc length ζ_{AC} , the maximum non-dimensional vertical and horizontal displacements η_{AB} , ξ_{AC} are obtained as follows:

$$(3) \quad \zeta_{AC} = 1 = (4/\sqrt{\gamma}) \cdot F(k, \pi/2),$$

$$(4) \quad \eta_{AB} = \delta/L = 4k/\sqrt{\gamma},$$

$$(5) \quad \xi_{AC} = 1 - \lambda/L = (4/\sqrt{\gamma}) \cdot \{2E(k, \pi/2) - F(k, \pi/2)\},$$

where $F(k, \pi/2)$, $E(k, \pi/2)$: Legendre-Jacobi's complete elliptic integrals of the first and second kinds.

The following formula based on Eq. (1) is useful in calculating each Young's modulus E_i .

$$(6) \quad \sum_{i=1}^n (E_i I_i) = PL^2/\gamma.$$

The second moment of area I_i of each cross section for multi-layered rods/wires (diameter d_i) with respect to the neutral axis is shown as

$$(7) \quad I_i = \pi(d_i^4 - d_{i-1}^4)/64 \quad (d_0 = 0).$$

One quantity γ (: the non-dimensional load) is required to calculate Young's modulus E_i from Eq. (7). The value of γ is obtained from a chart (: Nonograph) of γ - λ relation (λ : the horizontal displacement) [Method 1] and γ - δ relation (δ : the vertical displacement) [Method 2].

3. Experimental investigation

Several experiments were carried out using a two-layered material [length: $L_1 = L_2 = L = 300.0$ mm, SWPA (1st layer): a piano wire, diameter: $d_1 = 0.7$ mm, + Cu (2nd layer): an electrodeposited Copper layer, thickness: $(d_2 - d_1)/2 = 0.02$ mm (i.e., d_2 : 0.74 mm)]. Young's moduli of Cu obtained by applying Method 1 and Method 2 [Note: experimental results of SWPA were omitted here.] are shown in Fig. 2. The measured values of Method 1 and Method 2 remain nearly constant for several axial compressive loads and the standard deviation is (S.D) very small although every method has a little scattered values. As a whole, the mean Young's moduli (shown as Av.: Average) determined by the two methods are in good agreement with each other.

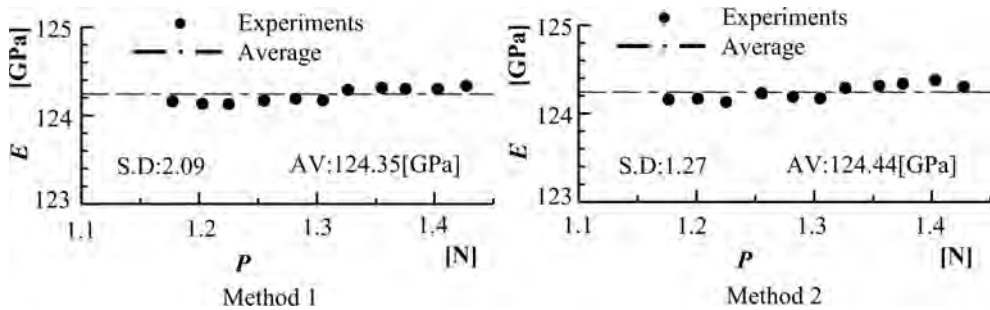


Fig. 2. Comparison of Young's moduli of an electrodeposited layer (Cu: E_2) between the two measuring methods for the axial load P (Note: E_1 of SWPA is known previously).

References

1. A. Ohtsuki (2005). A New Method of Measuring Young's Modulus for Flexible Thin Materials Using a Cantilever, *Proc. of the 4th Int. Conf. Adv. in Exp. Mech.*, **3-4**, 53-58.
2. A. Ohtsuki, H. Takada (2002). A New Measuring Method of Young's Modulus for a Thin Plate / Thin Rod Using the Compressive Circular Ring, *Tran. JSSR*, **47**, 27-31.
3. A. Ohtsuki (2005). A New Measuring Method of Young's Modulus for Flexible Materials, *Proc. of 2005 SEM Annual Conf.*, Sec. 72, 113(1)-113(8) [CD-ROM].
4. A. Ohtsuki (2004). A New Young's Modulus Measuring Method for Flexible Materials Using Post-buckling Behaviours, *4th Int. Conf. on Thin-Walled Structures*, 233-240.

ENERGY STORAGE RATE COMPONENTS

W. Oliferuk¹, M. Maj²

¹Białystok University of Technology, Białystok, Poland

²Institute of Fundamental Technological Research, Polish Academy of Sciences, Warsaw, Poland

Decomposition of energy storage rate into terms related to different deformation mechanisms has been presented. The energy storage rate is the ratio of the stored energy increment to the appropriate increment of plastic work. Experimental results show that the energy storage rate is dependent on plastic strain. This dependence is influenced by different microscopic deformation mechanisms. Then, the energy storage rate can be presented as a sum of particular components. Two of them are identified.

1. Introduction

When metals deform plastically energy conversion occurs; a part of the mechanical work w_p done during the single cycle of plastic straining is converted into a heat q_d . The rest of it remains in the strained material and it is known as the stored energy e_s , $e_s = w_p - q_d$.

The measure of energy conversion at each instant of the deformation process is the rate of energy storage de_s/dw_p . It has been shown experimentally, that at the initial stage of plastic deformation of annealed polycrystalline materials, the dependence of the de_s/dw_p on the work w_p expended on plastic deformation has a maximum [1, 2]. Such result can be explained by different influence of particular micro-scale deformation mechanisms on the energy storage rate at different deformation stages. Thus, de_s/dw_p is macroscopic quantity that depends on number of internal parameters H_1, H_2, \dots, H_n . Each of them is related to individual deformation mechanism. In order to distinguish the influence of the given internal parameter, the theoretical analysis of energy storage rate, on the basis of phenomenological thermodynamics of plastic deformation has been performed. The results of the analysis have been used to decompose the total energy storage rate, obtained for the initial stage of uniaxial tension of austenitic steel, into two components. On the basis of the Szczepiński's work [3] and our previous results [4] such decomposition has been done.

2. Decomposition of the energy storage rate

The energy storage rate has been obtained by differentiation of the stored energy e_s as a function of the plastic work w_p . The experimental method of the stored energy determination, as in the previous works by Oliferuk *et al.* [2, 4], was employed.

The stored energy can be divided into at least two parts: the energy of stress field connected with uniform deformation (statistically stored dislocations) and non-uniform one. The second part, connected with non uniform deformation at grain level, is a sum of a lattice stretch energy, energy of geometrically necessary dislocations and the energy of long-range internal stresses due to heterogeneous distributions of dislocations. As in our previous work [4] this part of the stored energy, indicated as e_{s1} has been estimated from experimentally obtained load-displacement curve.

The e_{s1} as a function of plastic work has been determined and the $Z_1 = de_{s1}/dw_p$ was calculated. The remaining term $Z_2 = de_{s2}/dw_p$ can be determined as a difference

between experimentally measured total energy storage rate de_s/dw_p and the component de_{s1}/dw_p calculated on the basis of the stress-strain curve.

The experiments were performed on the 304L austenitic stainless steel with mean grain size $7\ \mu\text{m}$. Specimens were strained using the MTS testing machine at the constant strain rate $\dot{\epsilon} = 4.3 \cdot 10^{-3}\ \text{s}^{-1}$. During tensile test the temperature distribution on the surface of the specimen was measured by IR camera. Simultaneously, the stress and strain were determined. On the basis of the thermo-mechanical characteristics, the stored energy as a function of plastic work was calculated (Fig. 1). In the same figure the part e_{s1} , obtained from the stress-strain curve, is shown. Differentiating the total stored energy e_s and the stored energy e_{s1} as a function of plastic work, the total energy storage rate $Z = de_s/dw_p$ and the $Z_1 = de_{s1}/dw_p$ are determined. A result of such operation is shown in Fig. 2. According to theoretical analysis the rate Z_2 of energy accumulated in statistically stored dislocations was calculated as the difference between Z and Z_1 .

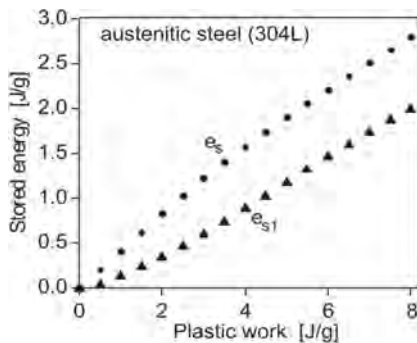


Fig. 1. The total stored energy e_s and the energy e_{s1} connected with non-uniform deformation as a function of plastic work at the initial stage of tensile deformation.

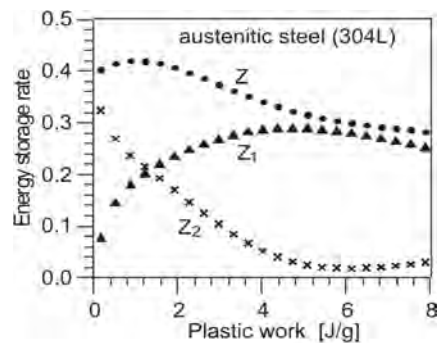


Fig. 2. The total energy storage rate Z as a sum of two components Z_1 and Z_2 .

References

1. A. Chrysochoos, O. Maisonneue, G. Martin, H. Caumon (1989). Plastic and dissipated work and stored energy, *Nucl. Eng. Design*, **114**, 3, 323–333.
2. W. Oliferuk, W. Świątnicki, M. W. Grabski (1995). Effect of grain size on the rate of energy storage during the tensile deformation of austenitic steel, *Mater. Sci. Eng.*, **A197**, 49–58.
3. W. Szczepiński (2001). The stored energy in metals and the concept of residual microstresses in plasticity, *Arch. Mech.*, **53**, 615–629.
4. W. Oliferuk, M. Maj, (2009). Stress-strain curve and stored energy during uniaxial deformation of polycrystals, *Eur. J. Mech. A/Sol.*, **28**, 266–272.

ESTIMATION OF THE EFFECTIVE PROPERTIES OF COMPOSITES WITH INCLUSIONS OF DIVERSE SHAPES AND PROPERTIES

P. Sadowski, S. Stupkiewicz

Institute of Fundamental Technological Research, Warsaw, Poland

1. Introduction

Multi-phase composites with inclusions which cannot be characterized by one representative shape and geometry, e.g., when different carbon allotropes (desired or not) can be found in the matrix (polymer or metal), are becoming more popular. Estimation, even rough, of the properties of such composites, is inevitably desired in the process of their design and production. Three classical methods, based on work of Eshelby [1] are used in this work, however the assumption concerning isotropy and similar shape of inclusions, which is commonly adopted in practice, is skipped in our analyses.

2. Classical estimation of the effective properties

Estimation of the effective elastic properties of the composites is summarized in e.g. [2]. Using the average strain theorem and the Hill's concept of the strain/stress concentration tensor [3], the effective stiffness tensor can be expressed as

$$(1) \quad C = C^m + \sum_{n=1}^N v_n (C_n^i - C^m) A_n^i,$$

where C_n^i and C^m are the stiffness tensors of the n -th type inclusions and the matrix respectively, v_n is the volume fraction of the n -th type inclusions, N – the number of types of inclusions and A_n^i is the strain concentration tensor.

Perfect bonding between inclusions and the matrix is assumed. Each family of inclusions can be characterized by a chosen shape which in turn can be approximated by an ellipsoid in order to use the concept of a single inclusion embedded in an infinite matrix. The effective elastic properties of the composite can be estimated once the strain concentration tensor for each type of inclusions is known. There are many micromechanical approaches to find A_n^i and results for three of them, namely Mori-Tanaka method¹⁾ (MT), the self-consistent scheme²⁾ (SC) and the effective-medium-field approximation³⁾ (EMF) [2] are presented. Although these classical equations are well known, they were mainly applied for single-phase composites. Equation (1) is solved without any simplifications in the considered problem, however its application is not trivial. Thanks to its general form, all isotropic as well as anisotropic elastic parameters can be evaluated from the obtained effective stiffness tensor. In the MT scheme the effective stiffness is given explicitly by Eq. (1). This is not the case in the other two approximations where Eq. (1) must be solved iteratively, e.g., by recurrent scheme. Furthermore, the well known simplified formulae for the Eshelby's tensor must be replaced by their general form, see [4],

¹⁾ $A_n^{\text{MT}} = A_n^{\text{dil}} \left[v_m I + \sum_{n=1}^N v_n A_n^{\text{dil}} \right]^{-1}$, $A_n^{\text{dil}} = [I + S_n (C^m)^{-1} (C_n^i - C^m)]^{-1}$, I – the unit tensor, S_n – the Eshelby's tensor.

²⁾ $A_n^{\text{SC}} = [I + S_n C^{-1} (C_n^i - C)]^{-1}$.

³⁾ $A_n^{\text{EMF}} = A_n^{\text{SC}} \left[v_m I + \sum_{n=1}^N v_n A_n^{\text{SC}} \right]^{-1}$.

to have the micromechanical approach consistent. As a consequence, additional numerical integration is needed. Another difficulty connected with the general form of Eq. (1), which is due to diverse shapes of inclusions, is the lack of convergence of the SC scheme due to a high contrast in the material properties of composite constituents. Relevant details will be discussed in the paper.

3. Numerical example

The effective elastic properties of the composite with three types of carbon inclusions embedded in the copper matrix have been estimated. These types of inclusions are following: #1 modelled as sphere has the properties of fullerene, #2 modelled as oblate spheroid with the properties of graphite and #3 modelled as disc with the properties of graphene. All constituents of the composite are assumed to have isotropic properties. Due to the Eshelby's tensor specified in the local coordinate system of the inclusion, transversely isotropic effective properties are obtained. Assumption of the isotropic effective properties [5] or averaging over orientations (for random distribution of inclusions) leads to the isotropic effective stiffness tensor, and an example of this kind of results is presented below.

The effective Young modulus of the composite with respect to Young modulus of the matrix is shown in Fig. 1 for (a) only one type of inclusions (volume fraction of other types is equal to 0) and (b) the mixture of all considered types of inclusions, with $v_1 = v_2 = v_3$. The influence of the considered approximation methods is also presented.

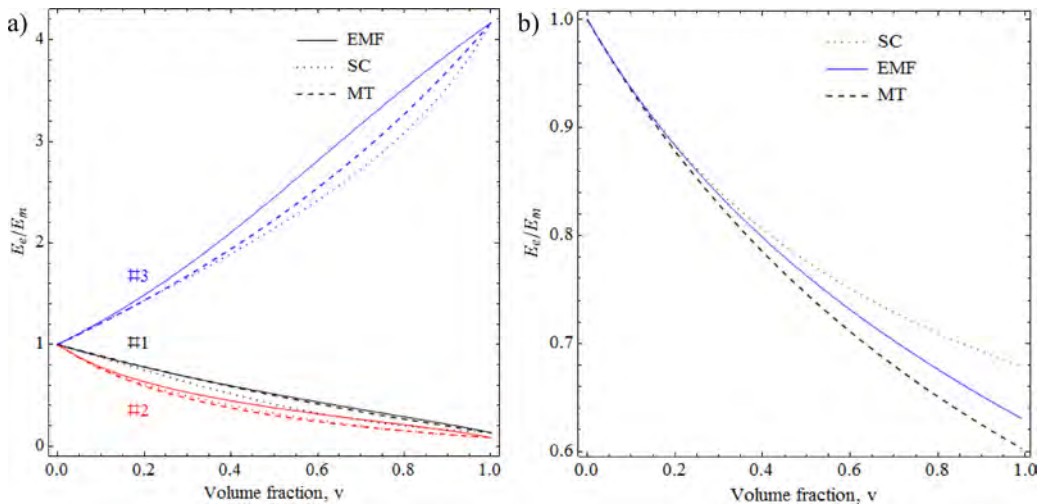


Fig. 1. Relative effective Young modulus E_e/E_m for three micromechanical approximations (MT – dashed line, SC – dotted line, EMF – solid line) for: a) only one type of inclusions ($v = v_n$) and b) three types of inclusions ($v = v_1 + v_2 + v_3$ and $v_1 = v_2 = v_3$).

References

1. J.D. Eshelby (1957). The determination of the elastic field of an ellipsoidal inclusion and related problems, *Proc. Roy. Soc. A*, **241**, 376–396.
2. J.Y. Li (1999). On micromechanics approximation for the effective thermoelastic moduli of multi-phase composite materials, *Mechanics of Materials*, **31**, 149–159.
3. R. Hill (1963). Elastic properties of reinforced solids: Some theoretical principles, *J. Mech. Phys. Solids*, **11**, 357–372.
4. A.C. Gavazzi, D.C. Lagoudas (1990). On the numerical evaluation of Eshelby's tensor and its application to elastoplastic fibrous composites, *Computational Mechanics*, **7**, 13–19.
5. S. Torquato (2002). *Random Heterogeneous Materials: microstructure and macroscopic properties*, Springer-Verlag, New York.

FRACTURE TOUGHNESS OF AERONAUTICAL ALUMINUM ALLOYS 6156 AND 2024 FOR DIFFERENT ARTIFICIAL AGING CONDITIONS

G. Stefanou¹, S.K. Kourkoulis², Z. Velonaki¹, E. Lymperaki¹, N.D. Alexopoulos¹

¹University of the Aegean, Department of Financial and Management Engineering, Chios Island, Greece

²National Technological University of Athens, Department of Applied Mathematical and Physical
Sciences Division of Engineering
Laboratory of Strength and Materials, Zografou, Athens, Greece

Aluminum alloys from the 6xxx series, e.g. 6056 were considered in fuselage sections where strength and damage-tolerance properties are required. However, future metallic airframes may contain laser beam welded structures to achieve lightweight integral airframes. Innovative 6156 fuselage sheets are particularly recommended for such a use as there exists an impression of having higher damage tolerance capabilities than its predecessor [1]. So far the literature review on the aluminum alloy 6156 remains very limited; the effect of aging treatments on microstructure and hardness are reported in the literature [2–4] as well as the effects of Ag addition on the long thermal stability of the alloy [5].

In this work an experimental study was conducted on the fracture toughness of aluminum alloys 6156-T4 and 2024-T3 as well as on its different artificial aging conditions. Tensile and fracture toughness specimens were manufactured according to the international specifications. Performed tensile tests showed that the innovative alloy presents higher mechanical strength and ductility values that exceed 25% elongation to fracture. Fracture toughness tests were also carried out which showed that the critical stress intensity factor K_{IC} is reduced by artificial aging at under-aging and peak-aging conditions. Reference tensile specimens were artificially aged for three different aging temperatures and various times. Yield stress, ductility and critical stress intensity factor values are reported and discussed in conjunction with the artificial aging condition.

1. Experimental procedure

The material used was 6156-T4 (Si 0.7-1.3%-Mg 0.6-1.2%-Cu 0.7-1.1%-Mn 0.4-0.7%-Fe < 0.2%-Cr < 0.25%-Zn 0.1-0.7%-Al remainder). Tensile and fracture toughness specimens were cut from flat sheets of geometrical dimensions 35×50 cm (L direction) and nominal thickness of 3.6 mm and according to standards ASTM E8 and E561, respectively. The same applied for the 2024-T3 alloy with nominal thickness of 3.2 mm. Three different aging temperatures, namely 150, 170 and 190°C were used for artificial aging, while aging times were chosen to be in the range between 1 and 166 hours and depending on the artificial aging temperature. Then tensile tests were performed (at least three tests per different aging time) and their tensile mechanical properties were evaluated. At the end fracture toughness tests were conducted and evaluated the critical stress intensity factor.

2. Fracture toughness tests

Representative resistance curves of force – crack mouth displacement of the edge crack can be seen in Figure 1a for different artificial aging times of AA6156 at 190°C. As seen in the diagram, by increasing artificial aging time, the maximum force increases while the displacement to achieve maximum force decreases. This was the case for all aging times and temperatures that belong to the under-aging condition. For example, after 1 hour aging the maximum force is 7.40 kN while the crack mouth displacement is 1.83 mm. After 4 hours of artificial aging, where the material is in the condition of peak aging, the maximum force is now 7.63 kN while the crack mouth displacement was essentially reduced to 1.65 mm.

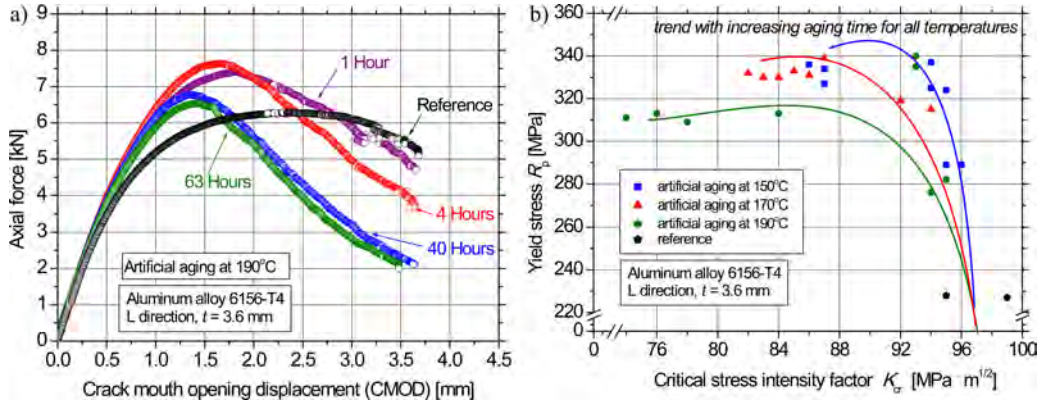


Fig. 1. a) Typical resistance curves of 6156-T4 for 190°C aging temperature and b) plot of critical stress intensity factor over yield stress for the investigated artificial aging conditions.

The resistance curves were evaluated according to the ASTM E561 standard and according to the compliance method. Figure 1b shows the available yield stress results for the investigated artificial aging conditions over the critical stress intensity factor test results for the same artificial aging conditions. Marked with arrows are the trends for $R_p - K_{cr}$ correlation for different aging temperatures with increasing aging time. As can be seen in the figure, the critical stress intensity factor decrease is essential when aged at higher temperatures due to over-aging conditions. It seems that all temperatures reach a “plateau” of yield stress (peak-aging condition), but the critical stress intensity factor appears to continuously decreasing with increasing aging time.

References

1. P. Lequeu, P. Lassince, T. Warner (2001). Engineering for the future: weight saving and cost reduction initiatives, *Aircraft Eng. Aerospace Technol.*, **73**, 147–159.
2. L. Lin, Z. Zheng, J. Li (2012). Effect of aging treatments on the mechanical properties and corrosion behavior of 6156 aluminum alloy, *Rare Metal. Mater. Eng.*, **41**, 1004–1012.
3. H.F. Zhang, Z.Q. Zheng, S. Zhong, X.F. Luo, J. Zhong (2012). Effects of two-step aging treatment on microstructure and properties of 6156 aluminum alloy, *Chin. J. of Nonferrous Met.*, **22**, 1025–1035.
4. K. Jin, Y.L. Deng, L. Zhou, L. Wan, X.M. Zhang (2011). Investigation on artificial aging and creep aging of 6156 aluminum alloy, *J. of Aeron. Mater.*, **31**, 18–29.
5. H. Zhang, Z. Zheng, Y. Lin, X. Luo, J. Zhong (2012). Effects of Ag addition on the microstructure and thermal stability of 6156 alloy, *J. Mater. Sci.*, **47**, 4101–4109.

ANALYSIS OF TENSILE FORCE VARIATION DUE TO APPLICATION OF CYCLIC TORSION FOR A RANGE OF FREQUENCY LEVELS

T. Szymczak¹, Z.L. Kowalewski²

¹Motor Transport Institute, Warsaw, Poland

²Institute of Fundamental Technological Research, Warsaw, Poland

1. Introduction

Experimental results of many research groups report a great influence of loading type on material behaviour. It is often expressed by material hardening due to deformation along non-proportional loadings in comparison to the typical response observed under proportional paths. This phenomenon depends on parameters of strain signals, i.e. shape, amplitude and frequency. An influence of loading type on material softening or hardening was also examined in experiments focused on investigations of KOBO method. It uses torsion-reverse-torsion cycles simultaneously with axial forces. Application of cyclic torsion enables a reduction of major forces in drawing, extrusion, forging or rolling. Previous investigations shown that a magnitude of axial force reduction in technological processes is connected with amplitude and frequency of torsion cycles. An effect of torsion cycle amplitude on tensile curves has been widely investigated by a number of researchers [1, 5, 6]. They have experimentally proved that technological force reduction decreased with increasing of torsion cycle amplitude. An influence of frequency of cyclic torsion on force variations in technological processes has not been efficiently determined up to now. Kong and Hodgson tested an extrusion of pure lead assisted by cyclic torsion at frequency within a range from 6.7 to 20 Hz [1]. They obtained lowering of the extrusion force when frequency decreasing. Similar tests on copper, however for drawing process, confirmed such observation. An opposite effect was discovered by Pawlicki and Grosman who performed compression tests in assistance of torsion cycles under a range of selected levels of frequency [2]. Their results expressed 50% force reduction with an increase of frequency from 0 to 1.8 Hz. Niewielski at al. also observed 20% reduction of compression force due to torsion cycles application to deform copper, however only for single level of frequency equal to 1.6 Hz [3]. In the case of the 7075 aluminium alloy tested by Korbelt et al. almost the same level of the compression force reduction was achieved for torsion cycles at frequency equal to 8 Hz [4]. Since the contradictory results related to the effect of frequency of cyclic torsion on tensile characteristics have been obtained, further investigations are necessary. Therefore, the paper is addressed to study this issue more accurately in laboratory tests.

2. Details of experimental procedure

Experimental procedure contained two stages:

- a) tensile tests assisted by torsion cycles for frequency levels equal of 0.005, 0.05 and 0.5 Hz;
- b) tensile tests assisted by torsion cycles under step increasing frequency from 0.25 to 1 Hz.

To determine material behaviour thin-walled tubular specimens and servo-hydraulic testing machine were used. All tests were conducted at room temperature. Axial and shear strain signals were used to enforce monotonic tension and shear cyclic deformation, Fig. 1. The axial strain monotonically increased while the shear strain was activated by torsion at constant amplitude equal to $\pm 0.4\%$ and frequency within a range from 0.005 to 0.5 Hz.

The 10H2M steel was selected to tests. It is commonly applied by engineers designing of some constructions used in power plant industry.

3. Analysis of tension assisted by cyclic torsion of various levels of frequency

The results of tests carried out on the 10H2M steel are presented in Fig. 2a, where the tensile characteristic (0) is compared to tensile curves obtained in assistance of cyclic torsion at a range of different frequency levels. They express gradual reduction of the axial stress with an increase of shear strain frequency. For the highest frequency applied it was reduced by 410 MPa. Another effect discovered during torsion cycles superimposed on tension is presented in Fig. 2b. It is manifested by more rapid decrease of the axial stress for higher magnitudes of frequency of torsion cycles applied.

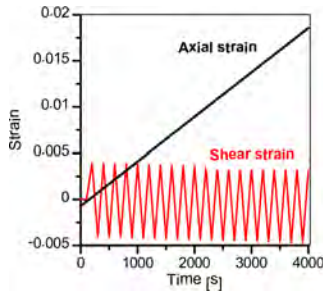


Fig. 1. Loading programme.

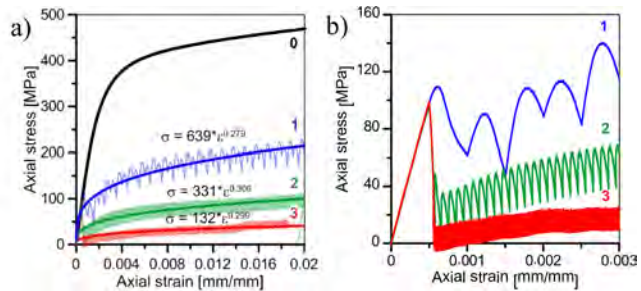


Fig. 2. Variations of stress-strain curves determined during typical tensile test (0) and in assistance of torsion cycles at frequency: (1) – 0.005 Hz, (2) – 0.05 Hz, (3) – 0.5 Hz.

For the higher frequency cycles applied in blocks of step-increasing frequency from 0.25 to 1 Hz for small amplitude of $\pm 0.1\%$ the 20% axial stress reduction was noticed. This effect was not so strong as that observed for higher value of strain amplitude and significantly lower frequency, Fig. 2a.

Calculations of total strain energy were performed to extend the knowledge of steel behaviour under simultaneously activated tension and cyclic torsion. In comparison to the total strain energy calculated on the basis of tensile curve (8.36 MJ/m^3) its level was significantly lower (92%) in the case of monotonic tension assisted by cyclic torsion realized under frequency equal to 0.5 Hz.

4. Summary

Torsion cycles frequency may reduce significantly the axial stress during monotonic tension. A level of axial stress reduction is dependent not only on the frequency, but also on the cyclic strain amplitude. An influence of both these parameters on the tensile stress drop is complex, hence in order to obtain optimal reduction of it for particular material a range of reasonable selected tests should be executed.

References

1. L.X. Kong, P.D. Hodgson (2001). Material properties under drawing and extrusion with cyclic torsion, *Mater. Sci. Eng.*, **A308**, 209–215.
2. J. Pawlicki, F. Grosman (2004). Analysis of power-energy effects for processes with forced deformation path, *Arch. Civil Mech. Eng.*, **4**, 3, 46–55.
3. G. Niewielski, D. Kuc, K. Rodak, F. Grosman, J. Pawlicki (2006). Influence of strain on the copper structure under controlled deformation path conditions, *J. Achiev. Mater. Manuf. Eng.*, **17**, 1–2.
4. A. Korbel, W. Bochniak, P. Ostachowski, L. Blaz (2011). Visco-plastic flow of metal in dynamic conditions, *Metall. Mater. Trans. A*, **42a**, 2881–2897.
5. T. Szymczak, Z.L. Kowalewski (2012). Variations of mechanical parameters and strain energy dissipated during tension-torsion loading, *Arch. Metall. Mater.*, **57**, 1, 193–197.
6. Z.L. Kowalewski, T. Szymczak, J. Maciejewski (2014). Material effects during monotonic-cyclic loading, *Int. J. Solid and Structures*, **51**, 3–4, 740–753.

MECHANICAL BEHAVIOUR OF ALUMINUM ALLOY 2198 UNDER DIFFERENT CORROSION EXPOSURE TIMES

Z. Velonaki¹, S.K. Kourkoulis², W. Dietzel³, N.D. Alexopoulos¹

¹University of the Aegean, Department of Financial and Management Engineering
Chios Island, Greece

²National Technological University of Athens, Department of Applied Mathematical
and Physical Sciences

Division of Engineering, Laboratory of Strength and Materials, Zografou, Athens, Greece

³Helmholtz-Zentrum Geesthacht, Institute of Materials Research, Materials Mechanics
Geesthacht, Germany

1. Introduction

Third generation Al-Li aluminum alloys such as the AA2198 is supposed to replace the conventional aluminum alloys (e.g. 2024) in aerostructures designed with the damage tolerance philosophy. The quasi-static mechanical properties of AA2198-T351 are scarcely reported in the open literature. For example, Chen *et al.* [1] performed tests on two different heat treated AA2198 (namely T351 and T851) and investigated their plastic and fracture behaviour. Seglich *et al.* [2, 3] investigated experimentally and analytically the anisotropic deformation of AA2198-T8 occurred during mechanical loading with and without the presence of artificial notches.

Lower density of AA2198 seems to be one of its advantages when compared to the conventional AA2024 that is currently used in aerostructures. In order the Al-Li alloy to replace the conventional one in aircraft structures, it has to be proven that its mechanical behaviour, damage tolerance capabilities and corrosion resistance are at least equal or superior to its predecessor.

In the present work the authors will try to report and compare AA2198 and AA2024 mechanical behaviour. To this end, a comparison of their tensile mechanical behaviour at T351 condition is essential. In addition, fracture toughness (R-curves) and fatigue crack propagation of laser beam-welded AA2198 butt-joints in T3 and T8 temper will be investigated.

2. Experimental procedure

Tensile test specimens were machined from sheets according to ASTM E8M with nominal cross-section 12.5 mm × 1.6 mm at the gauge length. Prior to corrosive solution exposure, all surfaces of the specimens were cleaned with alcohol according to ASTM G1 specification. Tensile specimens were afterwards exposed to the laboratory exfoliation corrosion environment (hereafter called EXCO solution) according to ASTM G34 specification.

A servo-hydraulic Instron 100 kN testing machine of the Laboratory of Strength and Materials of the National Technical University of Athens was used for the mechanical tests. Tensile tests were carried out according to ASTM E8 specification. An external extensometer was attached to the specimen surface and at the reduced cross-section gauge length. A data logger was used to store the data of axial force, displacement and axial strain from the attached extensometer in a digital file. To get representative average values of tensile properties, at least five tensile tests have been carried out for each test series.

3. Results

Typical tensile curves of pre-corroded AA2198-T351 specimens can be seen in Fig. 1a. The overall degradation mechanism due to corrosion exposure in exfoliation corrosion solution seems to be: (a) small degradation of ductility for small exposure times without an essential decrease in strength, (b) higher degradation of ductility for medium exposure times that is accompanied by a small decrease in strength and (c) even higher decrease in both, ductility and strength at the highest exposure times (24 hours for this case). For the latter case, a part of the ductility degradation was due to the heavily surface corroded areas that acted as surface notches that downgraded the specimen's tensile mechanical properties.

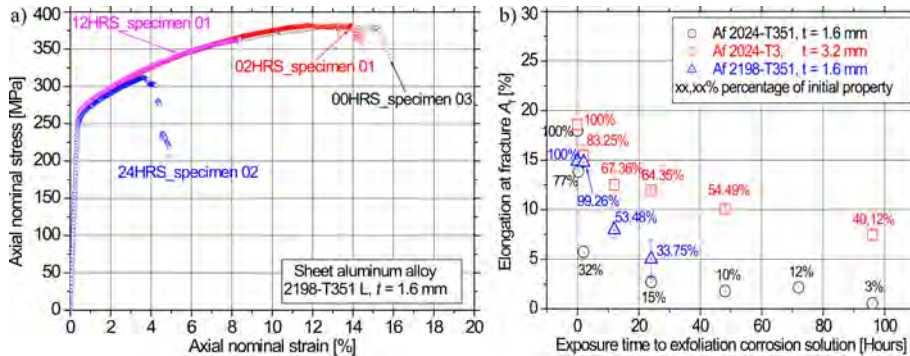


Fig. 1. a) Typical tensile flow curves of pre-corroded AA2198 specimens for various corrosion exposure times to exfoliation corrosion solution and b) evaluated tensile elongation at fracture A_f of pre corroded specimens for various corrosion exposure times.

Figure 1b shows the results of tensile elongation at fracture A_f . After only 2 hours EXCO exposure, AA2198 seems to maintain most of its ductility (99% of initial). On the contrary, AA2024 of same thickness lost almost 2/3 of its initial property; even in higher thickness AA2024 lost almost 20% of ductility after only 2 hours exposure. Of course this effect was well explained in the literature and was attributed to hydrogen embrittlement. Hydrogen is generated during the first corrosion stage that is being diffused inside the specimen's microstructure; this produces local surface embrittlement that influences the macro-property of ductility. For higher exposure times, the greatest A_f decrease was noticed for 12 hours exposure (was reduced to one half of its initial value); this EXCO exposure time should be carefully assessed to seek if this decrease is attributed to the synergistic effect of corrosion notches and hydrogen embrittlement. Finally, the last exposure time of 24 hours strongly influenced ductility (almost one third of initial ductility remained) but this is strongly affected by the formed surface corrosion notches. Again, AA2198 supersedes AA2024 in corrosion behavior as almost 15% ductility remains after 24 hours exposure, while more than 33% is the AA2198 remaining ductility.

Acknowledgments

The authors gratefully acknowledge the financial support of the European Union (Clean Sky EU-JTI Platform) under the thematic call: JTI-CS-2013-1-ECO-065 "Extrapolation and technical and economic study of a Laser Beam Welding technology" (Grant Agreement No: 620091).

References

1. J. Chen, Y. Madi, TF. Morgeneyer, J. Besson (2011). Plastic flow and ductile rupture of a 2198 Al-Cu-Li aluminum alloy, *Com. Mater. Sci.*, **50**, 1365–1371.
2. D. Steglich, H. Wafai, J. Besson (2010). Interaction between anisotropic plastic deformation and damage evolution in Al 2198 sheet metal, *Eng. Fract. Mech.*, **77**, 3501–3518.
3. D. Steglich, H. Wafai, J. Besson (2010). Anisotropic deformation and damage in aluminium 2198 T8 sheets, *Int. J. Damage. Mech.*, **19**, 131–152.

APPLICATION OF THE INHERENT STRAIN METHOD IN MODELING OF LASER THERMAL FORMING

J. Widłaszewski

Institute of Fundamental Technological Research, Polish Academy of Sciences, Warsaw, Poland

1. Thermal forming processes and their modeling methods

Processes of controlled producing plastic deformation of metal and non-metal objects by local heating are considered in the paper. Flame heating has been applied in shaping and shape correction of metal sheet and plates in manufacturing and repairs since a long time [1, 2]. Metal forming by a moving heat source has been recognized as an effective and economical method for forming flat metal plates into three-dimensional shapes for plating of ships, trains, airplanes, and for rapid prototyping of complex curved objects [3]. Application of the laser beam as a heat source in thermal forming processes results in reduction of the heat-affected zone and material degradation [4].

The non-contact method of controlled producing small deformations and displacements has found considerable interest and applications in the electronic industry for precise positioning, adjustment and alignment of micromechanical, optical and electronic parts and subassemblies in mass production [5, 6]. The technology of micro-adjustment with a laser beam and dedicated on-board structures (laser-driven actuators) overcomes difficulties related to the limited access for mechanical tools and to inaccuracies inherent to the production of individual elements and joining them together during the product assembly [7].

Modeling of thermal forming processes is necessary for better understanding the techniques once applied only manually by highly experienced and specialized workers, for the automation and improvement in today's applications, and for development of new manufacturing and repair methods. Even with the current performance of computer systems and commercially available software packages, the full 3D Finite Element Analysis (FEA) of industry-relevant thermo-elastic-plastic problems often requires too much time and cost. Therefore, simplified modeling methods are needed, that would enable effective process analysis, planning and optimisation. One of the approaches originates from analytical modeling of welding distortions [8] and can be generally termed the inherent strain method.

2. The inherent strain method

The method basically consists in estimation of thermoplastic deformation of a structure using the solution of the elastic problem with imposed plastic strain, which is produced in the heated zone (the inherent strain). The considered plastic strain results from thermal expansion under internal or external constraints (thermal upsetting).

Plastic strain can be estimated from thermal strain under condition that thermal stress has reached the material yield stress value. The size of the plastic zone is determined by the maximal extent of the isotherm of the so called critical temperature of the material. In some formulations the value of this temperature is defined as the temperature at which the material yield stress value becomes negligibly small.

The inherent strain approach is used both in analytical solutions and in numerical calculations. The method has a number of variants and implementations, e.g. in estimation of thermally-induced residual stresses. The operation of imposing plastic strain

to the structure model can be performed with the use of shrinkage forces and moments which produce equivalent straining. Another technique applied in numerical calculation of thermally-induced permanent deformation is the Artificial Temperature Field Analysis (AFTA), i.e. simulation of linearised plastic strains by the equivalent thermal contraction, combining artificial thermal expansion coefficient and temperature. In this case the linearised plastic strain is calculated from experimental or numerical results, and is collected in a data base of process parameters and corresponding plastic strains.

A short review of applications of the inherent strain approach for estimation of welding distortions [8], flame forming by line heating [9] and laser bending [10, 11] is presented in the article. Almost entirely analytical solution for laser adjustment using the two-bridge actuator is described [12]. Analytical modeling of such complex thermo-elastic-plastic processes seems to be impractical, if not impossible at all. However, closed form solutions that explicitly show the role of each significant process parameter are of great value for practicing engineers, who are involved in the application and development of new technologies. The analytical approach is able to extend our understanding of the basic physical mechanisms involved in the processes of interest [13]. The formulae derived due to the application of the inherent strain approach explicitly show the role of actuator design parameters, processing parameters (laser power and heating duration) and material data in thermo-elastic-plastic response of the structure to the laser pulse.

References

1. R.F. Arnoldy (1947). *Method of controlling distortion, straightening distorted objects and/or altering the shape of metal objects*, The Linde Air Products Company, US Patent No 2 428 825; issue date 1947-10-14.
2. R.E. Holt (1965). Flame Straightening Basics, *Welding Engineer*, Sept., 49–53.
3. G. Yu, R.J. Anderson, T. Maekawa, N.M. Patrikalakis (2001). Efficient Simulation of Shell Forming by Line Heating, *International Journal of Mechanical Sciences*, **43**, 10, 2349–2370.
4. K. Scully (1987). Laser line heating, *Journal of Ship Production*, **3**, 4, 237–246.
5. E. Steiger (1984). Führungsloses Justieren der Mittelkontaktfedern des Kleinrelais D2 in einem PulsLasersystem, *Siemens Components*, **22**, 3, 135–137.
6. W. Hoving (1997). Accurate Manipulation using Laser Technology, *Proceedings of SPIE*, **3097**, 284–295.
7. M. Schmidt, M. Dirscherl, M. Rank, M. Zimmermann (2007). Laser micro adjustment – from new basic process knowledge to the application, *Journal of Laser Applications*, **19**, 2, 124–132.
8. M. Watanabe, K. Satoh (1961). Effect of Welding Conditions on the Shrinkage Distortion in Welded Structures, *The Welding Journal, Welding Research Supplement*, **40**, 8, 377–384.
9. C.D. Jang, S.I. Seo, D.E. Ko (1997). A Study on the Prediction of Deformations of Plates Due to Line Heating Using a Simplified Thermal Elastoplastic Analysis, *Journal of Ship Production*, **13**, 1, 22–27.
10. Z. Mucha, J. Hoffman, W. Kalita, S. Mucha (1997). Laser Forming of Thick Free Plates, *Proceedings of the 30th International CIRP Seminar on Manufacturing Systems – LANE'97 (Laser Assisted Net shape Engineering 2)*, M. Geiger, F. Vollertsen (eds.), Meisenbach-Verlag, Bamberg, 383–392.
11. Z. Mucha, M. Cabaj, R. Gradoń, M. Pawłowski, J. Widłaszewski (2001). Laser forming of plates by use of beam with circular and rectangular cross-section, *Proceedings of the LANE 2001 (Laser Assisted Net Shape Engineering 3, International Conference)*, M. Geiger, A. Otto (eds.), Meisenbach-Verlag Bamberg, 527–536.
12. J. Widłaszewski (2009). *Modeling and experimental investigations of thermo-elastic-plastic deformations of the two-bridge actuator*, PhD Thesis, The Institute of Fundamental Technological Research of the Polish Academy of Sciences.
13. J. Dowden (ed.) (2009). *The Theory of Laser Materials Processing. Heat and Mass Transfer in Modern Technology*. Springer.

SESSION

**Fracture, Damage
and
Fatigue of Materials**

PARAMETRIC STUDY ON COLLAPSE INVESTIGATION IN STEEL VIERENDEEL BEAMS

Y. Akinci¹, O. C. Celik²

¹Ministry of Culture and Tourism, General Directorate for Cultural Heritage and Museums,
Ulus, Ankara, Turkey

²Istanbul Technical University, Faculty of Architecture, Taskisla, Taksim, Istanbul, Turkey

1. Motivation

This study describes a parametric investigation into the collapse analysis and design of steel Vierendeel beams using nonlinear pushover analysis. Limited studies are available in the inelastic or plastic limit analysis of Vierendeel beams [1–4]. Vierendeel beams are one of the viable solutions in spanning large areas of structures and have architectural advantages (e.g. they provide the designer with more open spaces) when compared to other trussed systems. Limit behavior and thus formation of plastic hinges in these beams are highly affected by several factors including bay configurations, joint flexibility of members, type of loading, and support conditions.

To address some of these issues and possibly reach some design recommendations for a group of beams, systems having four (even) and five (odd) bays of Vierendeel beams which are spaced at 10-meter intervals and spanning $L = 12$ m and $L = 15$ m are numerically investigated. Incremental collapse mechanisms are obtained. In this respect, an intense parametric study has been conducted using SAP2000. System height (b)/bay opening (a) ratio, different member sections having various strength (plastic moment capacity) and stiffness, the number of the bays in the system (odd or even number), and diagonal elements at the first and last bays (placed for retrofitting purposes for example) are taken as system parameters.

2. Numerical results

Each system composed of rectangular shaped bays is designed following the design criteria given in ASD89 and LRFD99 of American Institute of Steel considered. General views from the selected beams are given in Fig. 1. Construction (AISC). In total, 42 different systems covering many parameters mentioned above are analyzed following the standard pushover procedure. Rigid connections are assumed in nodal points. All mem-

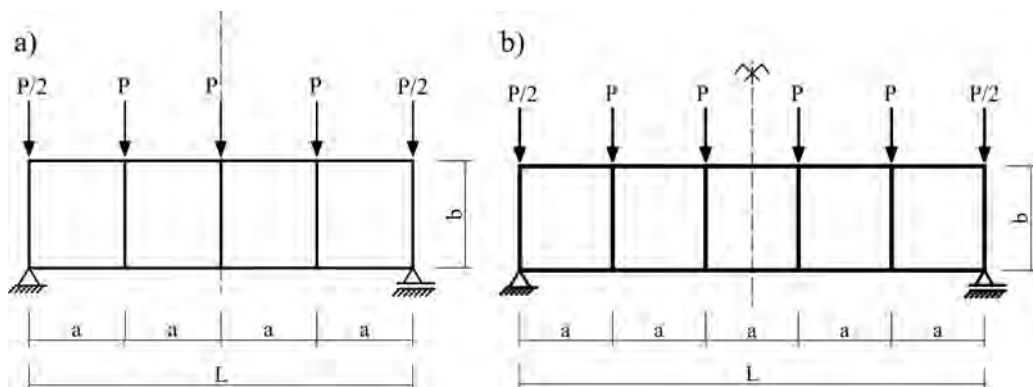


Fig. 1. Selected Vierendeel beams: a) with even bays, b) with odd bays.

bers were designed with HEA rolled steel sections with a yield stress of 235 MPa (i.e. a steel grade of S235JR was used). Total vertical load versus critical vertical displacement pushover curves are then obtained and presented for each system

As shear forces and secondary bending effects (also known as the Vierendeel action) from primary shear would dominate the behavior, first and last bays are given further attention. To improve the behavior and increase both strength and stiffness, retrofit of these bays using larger sectioned members (named as the stiffened bays) or placing a single diagonal brace are proposed. Their effect on the pushover curve, both overall ultimate capacity and stiffness are also investigated and compared with regular beam's numerical results. Pushover curves for a typical system designed with AISC-ASD and LRFD and having various aspect ratios for the bays are depicted in Fig. 2.

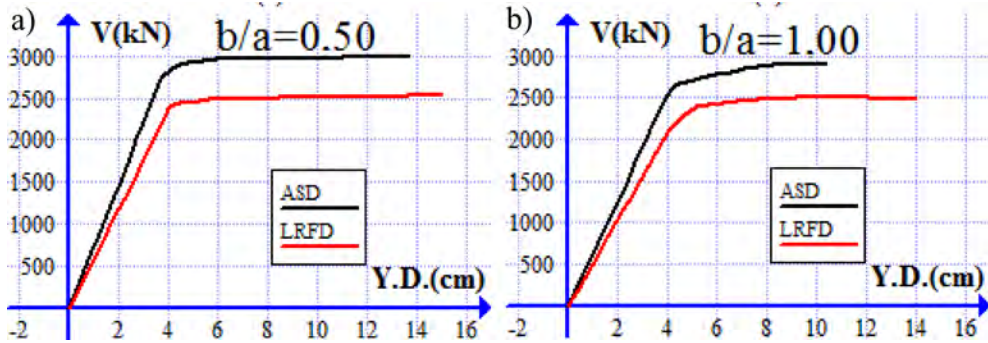


Fig. 2. Pushover curves for a beam with four bays ($L = 12$ m): a) $b/a = 0.50$, b) $b/a = 1.00$.

3. Conclusions

The following conclusions can be drawn from this numerical investigation:

- Determination of collapse mechanisms and the corresponding collapse load of Vierendeel beams may be complex as combined mechanisms usually govern the ultimate behavior.
- Static pushover analysis results are compatible with the results obtained from plastic limit analysis results using appropriate assumptions for plastic hinges.
- Systems designed with AISC-ASD provided higher capacity (15~20% more) under vertical loading when compared to the design with AISC-LRFD. However, larger ductility values were obtained in AISC-LRFD designs. Maximum ductilities of approximately $\mu = 4.00$ and $\mu = 8.00\sim 10.00$ are obtained for regular and retrofitted Vierendeel beams, respectively.
- Impact of vertical members on the behavior and ultimate capacity is noteworthy.
- When b/a ratio is about 1.00, the system becomes more convenient for strength, stiffness, and ductility.
- Maximum displacement at the mid-span and the relative vertical displacements at the first and last bays should be checked during collapse investigation. The latter may govern the mode of collapse and therefore structural design.

References

1. P.G. Hodge (1959). *Plastic Analysis of Structures*, McGraw Hill Book Company, New York.
2. O.C. Celik, K. Ozgen (1994). Ultimate strength of steel I-Beams at unreinforced web openings, *Proceedings of the 30th Polish Solid Mechanics Conference*, Zakopane, September 5-9, 72-73.
3. A. Del Savio *et al.* (2005). Structural modelling of Vierendeel beams with semi-rigid joints, *Proceedings of the XXVI Iberian Latin-American Congress on Computational Methods in Engineering – CILAMCE*, Brazil.
4. Y. Akinci (2010). *Collapse Investigation in Steel Vierendeel Beams and Parameters Affecting Collapse*, MS Thesis, Istanbul Technical University, Institute of Science and Technology, Istanbul.

DEFECTS AND NON-DESTRUCTIVE DETECTION METHODS FOR ADHESIVE BONDS IN COMPOSITE STRUCTURES – PRELIMINARY STUDY

P. Fiborek

Institute of Fluid-Flow Machinery, Gdańsk, Poland

1. Introduction

Composite structures can effectively replace steel or aluminum as a construction material for many years. The growing demand for lightweight and durable structures in aircraft and aerospace industry affected the intensive development of composites and nowadays they are used in almost every field of technology, from building materials to the medical implants. However, the lack of valuable non-destructive methods for the quality assessment of adhesive bonded structures strongly limits the further use of composites, especially in parts with high safety requirements. Currently being carried out by numerous scientific studies to develop effective methods of quality control.

2. Defects of adhesive bonds in composites

Strength of adhesive bonds is the weakest link in many engineering structure as well in the composite materials. Defects which arise as a result of mistakes during the manufacturing process or under storage and in-service operation have a significant effect on reducing the joint strength.

Defects in adhesive joints can be divided into two basic groups: defects in the adhesive layer and defects in the interface between adherend solids and adhesive.

Porosity and voids are mainly occurring defects in the adhesive layer as a result of insufficient application of adhesive by entrapping air or volatile substances such as water vapour. The pores and voids decrease the strength of the bonds and provide a place where moisture can be accumulated. Another disadvantage of adhesive layer are cracks that occurring by inadequate curing conditions or under the influence of external forces in case of brittle joints [1].

Delamination, debonding and weak bonds (also called “kissing bonds”) are the most common defects occurring in the interface between adhesive and adherend materials. Delamination is a defect of the composite structure, which leads to separation of the layers or reinforcements. Debonding occurs when an adhesive stops sticking to an adherend solids. Whereas, kissing bonds is defined as a perfect contact two surfaces where there is no shear stress between them [2].

In addition to the above cases, the quality of the composites structures can be decreased by contamination of the substrate. For example, the silicon which is remains of mould release agent or Skydrol hydraulic fluid used in hydraulic systems of aircraft navigation can occur on surface and reacts with water to form phosphoric acid that can etch material [3].

3. Detection methods of defects in adhesive bonds of composites

(a) *Vibration-based damage identification.* Physical properties such as mass, damping and stiffness alter by damages in structure will cause detectable changes in modal properties.

(b) *Methods based on laser vibrometer.* Analysis of propagation of elastic waves is an effective method for detection in composite materials such defects as cracks, delamination or weak bonds. Waves interact with material discontinuities like holes, rivets, damage, thickness change within the structural element thus detection defects are feasible [4]. One of the limitations is the thickness of material.

(c) *Ultrasonic Excitation and Infrared Imaging.* Likewise in previous method for the assessment of the material is used ultrasonic wave. When that wave is passing through the crack in the sample it causes rise of the defect surfaces temperature. This pulse of heat, generated by the friction process within the crack, is a source of heat propagation in the material, and is visible in the IR camera [5].

(d) *X-Ray Microtomographic.* 3D observation of internal microstructural features in materials is able by X-ray microtomography (XMT). A number of studies used XMT and image processing technique to reveal various types of damages in CFRP [6]. However, the obvious disadvantage of this method is the harmful effect of X-ray on the human body thus one must take special precautions during inspection. Moreover adsorption composites material i very low and defects oriented in a plane perpendicular to the X-ray beam are difficult to detect.

(e) *Assessment of kissing bonds based on digital image correlation.* Digital image correlation (DIC) is a non-contacting, optical method that involves capturing of digital images of the surface of an object and performs image analysis to obtain full-field deformation and/or motion measurements. Research has shown that digital image correlation technique could detect the kissing bonds even at 50% of the failure load [7]. Sensibility of this method is depending on magnitude of applied load.

4. Modeling of adhesive bonds in composites and application to detection of defects

There is still lack of useful models of adhesive bonds in composites taking into account their strength and damages. The strength of adhesive bonds is estimated usually with the aid of “interface elements”. Damages of adhesive bonds are modelled by various discontinuities in materials e.g. “gaps”. The models of adhesive bonds could help to determine positions, shapes and dimensions of a single defect or a group of defects in adhesive bonds of composite structures. This is the subject of our investigations.

References

1. R.A. Smith (1994). Composite Defects and Their Detection. <http://www.desware.net/Sample-Chapters/D07/E6-36-04-03.pdf>.
2. D. Jiao, J.L. Rose (1991). An ultrasonic interface layer model for bond evaluation, *Journal of Adhesive Science and Technology*, **5**, 631–646.
3. B. Ehrhart, B.Valeske, R. Ecault, M. Boustie, L.Berthe, C. Bockenheimer (2011). Extended NDT for the quality assessment of adhesive bonded CFRP structures, *International Workshop: Smart Materials, Structures & NDT in Aerospace*, Canada 2–4 November.
4. P. Malinowski, R. Ecault, M. Boustie, F. Touchard, L. Berth, W. Ostachowicz (2013). Damage detection method for composites based on laser vibrometer. *5th International Symposium on NDT in Aerospace*, 13-15th November, Singapore.
5. Xiaoyan Han, L.D. Favro, Zhong Ouyang, R.L. Thomas (2001). Thermosonics: detecting cracks and adhesion defects using ultrasonic excitation and infrared imaging, *Journal of Adhesion*, **76**, 151–162.
6. R. Huang, Z. Liu, Peifeng Li, T. Liu (2013). X-ray Microtomographic characterisation of damages in carbon fibre reinforced composites subjected to bending, *5th International Symposium on NDT in Aerospace*, 13-15th November, Singapore.
7. R.L. Vijaya Kumar, M.R. Bhat, C.R.L. Murthy (2013). Evaluation of kissing bond in composite adhesive lap joints using digital image correlation: Preliminary studies, *International Journal of Adhesion & Adhesives*, **42**, 60–68.

AN ANTICRACK IN A TRANSVERSELY ISOTROPIC SPACE UNDER A REMOTE UNIFORM HEAT FLOW

A. Kaczyński

Warsaw University of Technology, Warsaw, Poland

1. Introduction

This paper addresses a three-dimensional problem of determining the thermal stress distribution in a transversely isotropic space containing an insulated rigid sheet-like inclusion (an anticrack) situated in the plane of isotropy. It is assumed that the solid is under a vertically uniform heat flow at infinity and the stresses are absent far from the inclusion. The main idea of the author is to generalize the results obtained for the corresponding isotropic problem [1] to transversely isotropic materials characterized by five elastic constants c_{11} , c_{12} , c_{13} , c_{33} , c_{44} , two thermal moduli β_1 , β_3 and two conductivity coefficients k_1 , k_3 (Fig. 1).

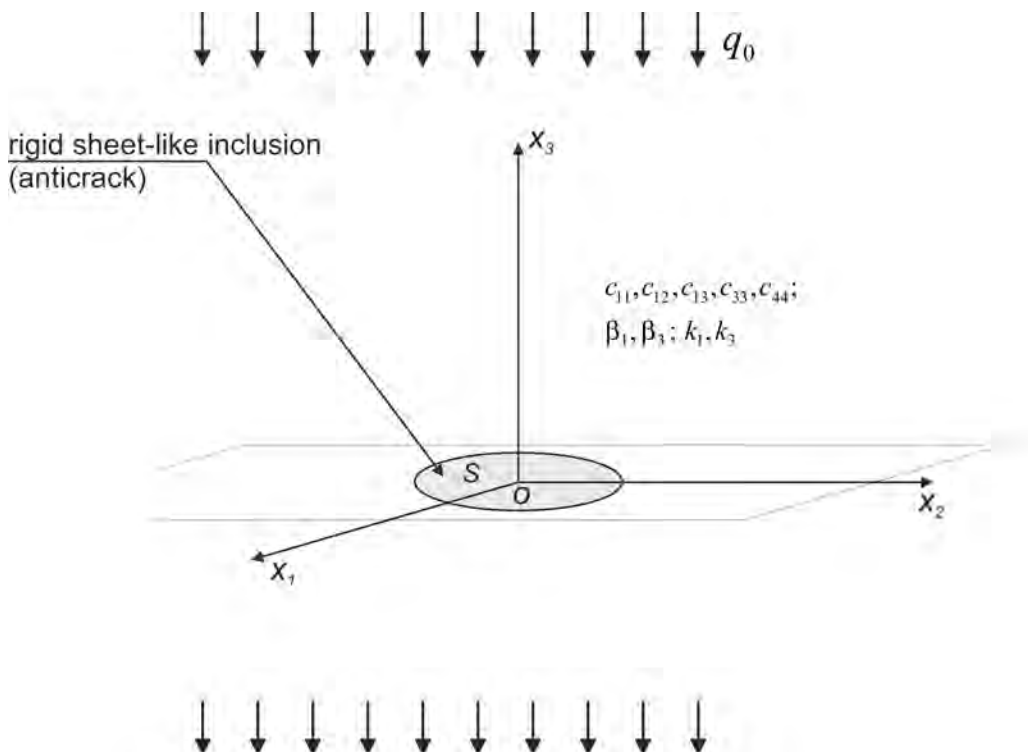


Fig. 1. A uniform heat flow in a transversely isotropic space weakened by an anticrack.

2. Method and results

A general solution scheme is presented for the resulting boundary-value problems. Effective results are obtained by constructing suitable potential functions and reducing

the thermal problem to its antisymmetric isothermal mechanical counterpart [2]. The governing boundary integral equation for a planar anticrack S of arbitrary shape is derived in terms of the normal stress jump $\sigma_{33}^+ - \sigma_{33}^-$ across the plane of the inclusion. It has the following form:

$$(1) \quad \tilde{H} \iint_S \frac{\sigma_{33}^+(\xi_1, \xi_2) d\xi_1 d\xi_2}{\sqrt{(x_1 - \xi_1)^2 + (x_2 - \xi_2)^2}} = -f_0(x_1, x_2), \quad (x_1, x_2) \in S,$$

where f_0 is given from the solution of the thermal anticrack problem, and the constant \tilde{H} is defined as follows:

$$(2) \quad \tilde{H} = \frac{\sqrt{c_{11} c_{33}} + c_{44}}{2\pi \sqrt{c_{44} c_{33}} \sqrt{(\sqrt{c_{11} c_{33}} - c_{13})(\sqrt{c_{11} c_{33}} + c_{13} + 2c_{44})}}.$$

It is interesting to note that the structure of (1) is the same as the one for punch problems in elasticity.

As an illustration, a complete solution in elementary functions is obtained and analysed for a circular inclusion. The expressions for the relevant field quantities (e.g., the displacements, stresses, temperatures, heat fluxes in the inclusion plane) in the solution in the corresponding isotropic problem differ only quantitatively. This solution is also compared with that corresponding to a penny-shaped crack problem.

References

1. A. Kaczyński, W. Kozłowski (2009). Thermal stresses in an elastic space with a perfectly rigid flat inclusion under perpendicular heat flow, *Int. J. Solids Struct.*, **46**, 1772–1777.
2. A. Kaczyński (2014). On 3D anticrack problems in a transversely isotropic solid, *Eur. J. Mech. A – Solid*, **43**, 142–151.

DAMAGE DETECTION IN PLATE STRUCTURES USING WAVELET TRANSFORMATION

A. Knitter-Piątkowska, M. Guminiak

Institute of Structural Engineering, Poznan University of Technology, Poznań, Poland

1. Introduction

Damage detection in engineering structures is significant for monitoring of a structural behaviour. There are different non-destructive techniques which enables an identification of defective part of a structure. This problem is extensively investigated by scientists and some approaches based on e.g. optimization of loads [6], information of natural frequencies [2], heat transfer [10], inverse analysis [3], soft computing methods such as evolutionary algorithms [1] or artificial neural networks [9] are applied. Damage can be effectively detected using relatively new method of signal analysis called wavelet transformation (WT) [8] also in its discrete form (DWT) [5]. Combining this method with, earlier mentioned, ANN [7] or inverse analysis [4] one can precisely identify damage details. The paper presents the issue of damage detection in thin plates excited by external static loads. The influence of the kind of structural response signal on obtained results is considered, too. Numerical examples are presented.

2. Problem formulation

The aim if this work is to detect the localization of defect provided that damage exists in the considered plate structure. Numerical investigation is conducted basing on signal analysis of structural static response. The plate bending is described and solved by the Boundary Element Method. The boundary integral equations are derived in singular and non-singular approach. Rectangular and skew plates supported on the edges and skew bridge plates resting on internal column supports are considered. The analysis of a structural response is conducted with the use of signal processing tool namely wavelet transformation in its discrete form. Damage in plates is modeled as a slot near the plate boundary.

3. Numerical example

A rectangular plate structure, simply-supported on boundary is considered. Damage is introduced by the additional edges forming a hole in relation to the basic plate domain. A static concentrated load is applied at selected points along direction parallel to the one plate dimension. As a structural response deflections and curvatures are taken into

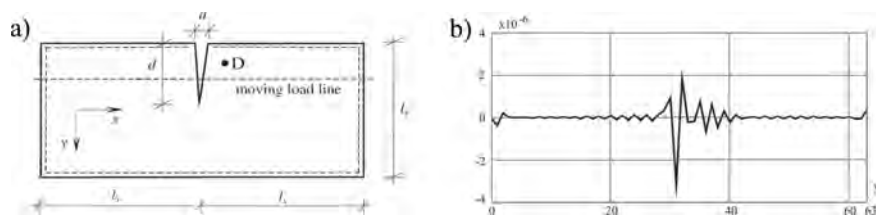


Fig. 1. Considered plate structure (a) and DWT of deflection (b) signal measured in D point, N – number of measurements.

account. The data are gathered in one measurement point, located near and slightly distal position in relation to the loss of plate basic domain, in equal time intervals. Decomposition of the obtained signal is carried out using DWT, Daubechies 4 wavelet. Proposed approach sufficiently precisely indicates the damage position which show Figs. 1b and 2. The plate properties are: $E = 205 \text{ GPa}$, $\nu = 0.3$, $l_x = l_y$, $a = 0.005 \cdot l_x$, $d = 0.5 \cdot l_y$.

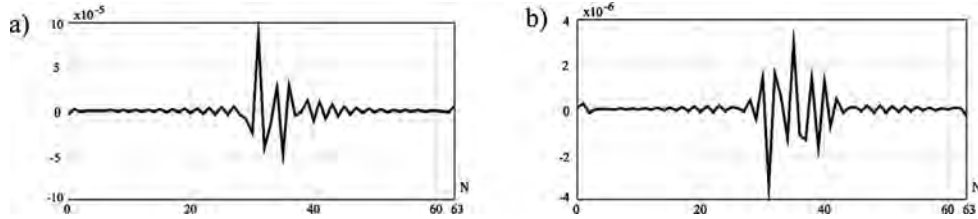


Fig. 2. DWT of curvature κ_x (a) and κ_y (b) signal measured in D point, N – number of measurements.

4. Concluding remarks

The implementation of discrete dyadic wavelet transformation to identification of signal discontinuity is presented in the paper. The analysis was carried out without any signal noise reduction. Considered examples proved that DWT of structural response signal expressed in deflections or curvatures established at selected domain point, quite correctly identifies the presence and position of damage. The influence of the location of measurement point with respect to the loss of a plate domain and reduction of number of measurements is studied too.

References

1. T. Burczyński, W. Kuś, A. Długosz, P. Orantek (2004). Optimization and defect identification using distributed evolutionary algorithms, *Engineering Applications of Artificial Intelligence*, 17, pp. 337–344.
2. K. Dems, Z. Mróz (2001). Identification of damage in beam and plate structures using parameter dependent frequency changes, *Engineering Computation*, 18, 1/2, 96–120.
3. T. Garbowski, G. Maier, G. Novati (2011). Diagnosis of concrete dams by flat-jack tests and inverse analysis based on proper orthogonal decomposition, *Journal of Mechanics of Materials and Structures*, 6, 1-4, 181–202.
4. A. Knitter-Piątkowska, T. Garbowski, A. Garstecki (2012). Damage detection through wavelet transform and inverse analysis, *Proc. 8th European Solid Mechanics Conference, ESMC 2012*, 9–13 July, Graz, Austria.
5. A. Knitter-Piątkowska, Z. Pozorski, A. Garstecki (2006). Application of discrete wavelet transformation in damage detection. Part I: Static and dynamic experiments, *Computer Assisted Mechanics and Engineering Sciences*, 13, 21–38.
6. Z. Mróz, A. Garstecki (2005). Optimal loading conditions in design and identification of structures. Part I: Discrete formulation, *Int. J. Struct. and Multidisciplinary Optim.*, 29, 11–18.
7. M. Rucka, K. Wilde (2010). Neuro-wavelet damage detection technique in beam, plate and shell structures with experimental validation, *Journal of Theoretical and Applied Mechanics*, 48, 3, 579–604.
8. Q. Wang, X. Deng (1999). Damage detection with spatial wavelets, *Journal of Solids and Structures*, 36, 3443–3468.
9. Z. Waszczyszyn, L. Ziemiański (2001). Neural networks in mechanics of structures and materials – new results and prospects of application, *Computers and Structures*, 79, 22-25, 2261–2276.
10. K. Ziopaja, Z. Pozorski, A. Garstecki (2011). Damage detection using thermal experiments and wavelet transformation, *Inverse Problems in Science and Engineering*, 19, 1, 127–153.

DEFORMATION AND FRACTURE OF THE PRELIMINARY DAMAGED MATERIAL UNDER THE IMPACT OF ELECTRIC CURRENT

C. V. Kukudzhanov, A. V. Kolomiets

Institute for Problems in Mechanics of the RAS, Moscow, Russia

1. Introduction

Thermoelectroplasticity is a comparatively young field in the theory of plasticity. The first experimental studies of this phenomena appeared only in the last few decades of the 20th century. They showed that the electric current action on metal samples made of hard-to-deform metals and alloys simplifies the subsequent mechanical working, improves the plastic properties of the material, and has advantages over the traditional methods of thermal processing such as annealing etc [1, 2]. A well-known technological method that has long been in use is to heat the sample with electric current of small density $J \approx 10^2$ A/m² and long duration $\tau \approx 10^3$ s. The study of the electromagnetic field action on the mechanical properties of conducting materials shows that the action of a current of density $J \approx 10^9$ A/m² and duration $\tau \approx 10^{-4}$ s significantly increases the plastic strains at fracture (up to 4–5 times). The phenomenon was called the “electroplasticity effect”. So far, there is no unified opinion about the nature and physical mechanism of this process, and discussion about the fundamental hypotheses are still continued [1–5].

2. Statement of the problem and basic equations of the model

Considered a coupled model of action of electromagnetic field on a sample made of a preliminary damaged material [4]. The problem is solved by the finite element method in two stages.

At the first stage, we study the thermal electrodynamic problem in order to obtain the temperature distribution in the sample. The problems on representative elements (volumes) of material with defects of different shapes (cracks, pores) and sample with an ordered (periodic) structure of these defects were solved To determine the temperature field distribution in the representative elements and samples with periodic distribution of defects solved a coupled thermoelectric problem of loading of the sample by applied electric flux.

To calculate the electric current (or electrical potential) and temperature in a conducting material, we use, at the first stage, the law of conservation of electric charge, Ohm’s law, the basic equation of the energy balance and the Fourier law. So using this equations in variational form, we obtain the basic equations of the finite-element model. In our simulation, we take account of the Joule–Lenz law describing the electric energy density scattered by the current flowing through the conductor. Here, the boundary conditions are set so that electric current (or potential) is applied at one of the sample ends, while the other end is kept at zero potential. As the time of the current impact is small $\tau \approx 10^{-4}$ s, so the sample is assumed to be thermally insulated.

At the second stage, we solve a coupled unsteady quasistatic thermomechanical problem of tensile deformation of the heated elastoplastic samples with finite displacements applied to its ends taking account of the initial temperature field distribution in the material obtained at the first stage: $\theta|_{t=0} = \theta_0(\mathbf{x})$. The main goal at the second stage is to

obtain the $R(U)$ diagram of the material, where R is the reaction force and U is the displacement applied. At this stage, we solve a quasistatic problem in which the magnitude of the applied displacement U is taken to be the parameter of the successive loading.

The total strain tensor of the material sample is equal to sum of the tensors of elastic, plastic, and temperature strains. In the elasticity field Hooke's law is assumed. The heat expansion in differential form can be written as $d\varepsilon^{th} = \alpha(\theta)d\theta$, where α is the coefficient of thermal expansion, θ is the temperature. In the plastic field the associated law of plastic flow is assumed, taking into account the formation of micropores according Garson model (GNT-model). The material considered is described by a plastically incompressible matrix and a continuum porosity, the presence of which leads to a dependence of the loading surface not only on the stress intensity but also on the first invariant of the stress tensor and the material porosity. The plasticity condition for the material was proposed [6] from the solution of the problem of a spherically symmetrical deformed spherical pore in an ideally plastic material.

3. Results of the numerical experiments

The main effect of the electromagnetic field is the change of the defect structure as a result of temperature concentration at the cut-shaped cracks of the original ordered structure which transforms into a structure consisting of cylinder pores [4]. Under the action of electric current, the plane cut-shaped defects are healed, and a cylindrical pore is formed at the crack tips because of the temperature concentration and melting (the melting condition $\theta = \theta_{\text{melt}}$ is satisfied at the boundary of this pore). While the significant normal displacements compressed crack in its middle part. The same result is obtained for a sample with an ordered structure of representative elements. Under same electric current action on the sample with cylindrical pores does not lead to complete the clamping of the pores ("healing") because of insufficient compressive stresses (displacements). Thus, from a sample with an ordered structure of plane cut-shaped defects, we obtain a material with an ordered structure of cylindrical defects. This phenomenon leads to an increase tensile strength and temperature softening of the material (the yield strength decreases, and the yield plateau increases).

The zones of nucleation, growth and coalescence of micropores around cylindrical defects in tension (after the current impact) are investigated: growth porosity leads to fracture of the material between the cylindrical defect and formation of a new defect in the form of cut (crack).

As a result of numerical experiments it was stated that the cyclical processes of thermoelectric treatment and stretching of a sample made of a preliminary damaged material (with an ordered structure of cut-shaped defect), improve its plastic properties. Thus, one can get a superplastic material.

References

1. N.N. Beklemishev, N.M. Gorbunov, N.I. Koryagin, V.N. Kukudzhano, V.A. Porokhov *et al.* (1989). *Plasticity and Strength of Metallic Constructions with Pulse Action of Highly-Energy Electromagnetic Field*, Preprint No. 372 IPM AN SSSR, Moscow.
2. V.I. Sinityn, O.A. Troitskii (1985). *Electroplastic Deformation of Metals*, Nauka, Moscow.
3. V.D. Klyushnikov, I.V. Ovchinnikov (1988). Plane Problem of Effect of an Instantaneous Point Heat Source, *Mech. Solids*, **23**, 4, 113–117.
4. V.N. Kukudzhano, A.V. Kolomiets-Romanenko (2011). A Model of Thermoelectroplasticity of Variations in the Mechanical Properties of Metals Based on Defect Structure Reorganization under the Action of Pulse Electric Current, *Mechanics of Solids (MTT)*, **46**, 6, 814–827.
5. V.M. Finkel, Yu.I. Golovin, A.A. Sletkov (1977). Disintegration of a Crack Tip with a Strong Electromagnetic Field, *Sov. Phys. Dokl.*, **22**, 683–685.
6. A.L. Gurson (1977). Continuum Theory of Ductile Rupture by Void Nucleation and Growth: Part I. Yield Criteria and Flow Rules for Porous Ductile Materials, *J. Engng. Mater. Technol.*, Vol. **99**, 2–15.

EFFECTIVE LINEAR ELASTIC PROPERTIES OF A SOLID WITH PERIODIC DISTRIBUTION OF PENNY SHAPED CRACKS

G. Mejak

University of Ljubljana, Faculty of Mathematics and Physics, Ljubljana, Slovenia

1. Introduction

One of the fundamental problems of micromechanics is to properly account for interactions between various defects such as are heterogeneities, voids or cracks. A common approach is to replace them with an appropriate distribution of the eigenstrains within the defects such that a comparison homogeneous material with this distribution of the eigenstrains has the same stress field as the original one. A critical point of the approach, known as the equivalent eigenstrain method, is to find the required distribution of the eigenstrains. The problem is that the underlying equivalent eigenstrain equation has a closed form solution only for an isolated elliptical inclusion. Using it gives a dilute model where the interactions are precluded. Although many ingenious methods were invented to somehow incorporate the interactions the basic issue of the interactions is not satisfactorily resolved.

2. A model problem

In a recent paper [1] a variational character of the equivalent eigenstrain method was established. This allows to consider the equivalent eigenstrain equation as the Euler-Lagrange equation and solve it approximately with the Ritz method. In this paper the above approach is used to compute the effective linear elastic properties of a solid with periodic distribution of penny shaped cracks. With reference to Fig. 1 a unit cell is a rectangular cuboid of dimensions $d \times d \times h$ with a centrally placed penny shaped crack with a radius $a \leq d/2$. Obviously, the solid has a tetragonal symmetry. The Euler-Lagrange equation of the functional

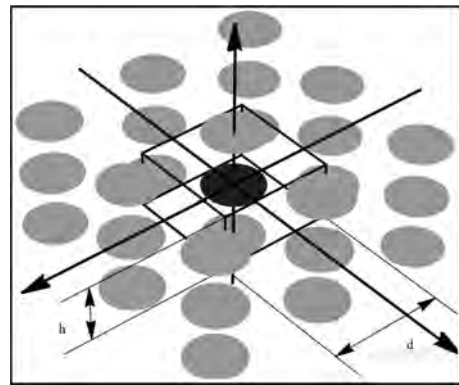


Fig. 1. Periodic array of penny shaped cracks.

$$(1) \quad I(\underline{\underline{\varepsilon}}^*) = \int_{\Omega_I} \underline{\underline{\varepsilon}}^* : \underline{\underline{C}} : (\underline{\underline{\varepsilon}}^* - S\underline{\underline{\varepsilon}}^* - 2\underline{\underline{e}}_b) dV$$

is

$$(2) \quad \underline{\underline{0}} = \frac{\partial I}{\partial \underline{\underline{\varepsilon}}^*} [\delta \underline{\underline{\varepsilon}}^*] = 2 \int_{\Omega_I} \delta \underline{\underline{\varepsilon}}^* : \underline{\underline{C}} : (\underline{\underline{\varepsilon}}^* - S\underline{\underline{\varepsilon}}^* - \underline{\underline{e}}_b) dV,$$

where $\underline{\underline{C}}$ is the elasticity tensor, S – the Eshelby operator, $\underline{\underline{e}}_b$ – the applied macro strain and Ω_I – the union of cracks, see [1]. Due to the periodicity all cracks have the same eigenstrain. If the functional I is restricted to the space of piecewise homogeneous eigenstrains, (2) is simplified to

$$(3) \quad (\underline{\underline{I}} - \langle \underline{\underline{S}} \rangle) : \underline{\underline{\varepsilon}}^* = \underline{\underline{e}}_b.$$

Here $\underline{\underline{S}}$ is the Eshelby tensor and $\langle \bullet \rangle$ is the volume average over the penny shaped crack of the unit cell. The Eshelby tensor is composed of the interior $\underline{\underline{S}}^I$ and exterior $\underline{\underline{S}}^E$ part. It is $\underline{\underline{S}}^E$ that takes the interactions into account. The Eshelby tensor of the penny shaped crack is computed as the limit $\varepsilon \rightarrow 0$ of the Eshelby tensor of the spheroidal inclusion with the semi axes a , a and εa . Then up to the first order $\underline{\underline{S}}^I = \underline{\underline{S}}_0^I + \varepsilon \underline{\underline{S}}_1^I$ and $\underline{\underline{S}}^E = \varepsilon \underline{\underline{S}}_1^E$. As $\lim_{\varepsilon \rightarrow 0} \underline{\underline{e}}^* = \infty$ Eq. (3) is replaced with

$$(4) \quad \left(\underline{\underline{I}} - \left\langle \underline{\underline{S}}_0^I + \varepsilon \underline{\underline{S}}_1^I \right\rangle + \left\langle \varepsilon \underline{\underline{S}}_1^E \right\rangle \right) : \frac{1}{\varepsilon} \underline{\underline{e}}^*(\varepsilon) = \underline{\underline{e}}_b.$$

For the periodic structure of Fig. 1 and the isotropic material the equation is for $\nu \in (0, 1/2)$ uniquely solvable for $\underline{\underline{e}}^*(\varepsilon)$. The effective properties are then given by

$$(5) \quad \underline{\underline{C}}^* = \underline{\underline{C}} : \left(\underline{\underline{I}} + \frac{4\pi}{3} f \underline{\underline{S}}_0^I : \underline{\underline{e}}_0^* \right)^{-1},$$

where $f = a^3/(hd^2)$ is the crack density parameter and $\underline{\underline{e}}_0^* = \lim_{\varepsilon \rightarrow 0} \underline{\underline{e}}^*(\varepsilon)$.

3. Numerical example

Results are given in Fig. 2. To obtain them the infinite structure of Fig. 1 was approximated with 125 unit cells. As can be seen our model gives more stiff results as the dilute model. This is due to the shielding which is, as expected, more pronounced in the case of Young modulus. For $h \geq d$ the dilute model is remarkably accurate. Using the above methodology effective properties of other structures can be readily computed with the full account of the interactions.

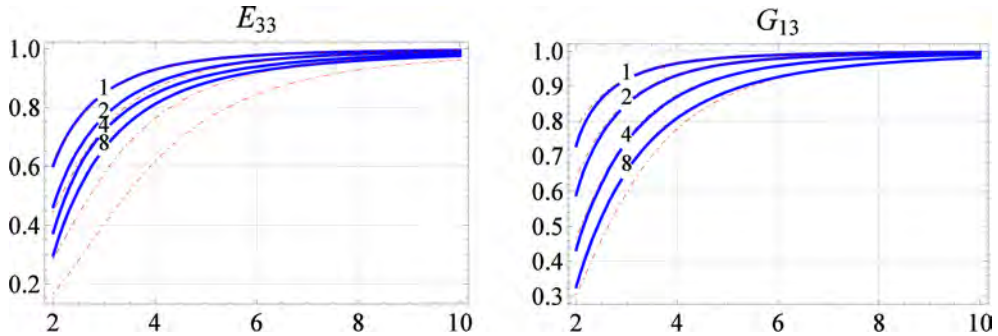


Fig. 2. Normalized effective Young (left) and shear (right) moduli (solid lines) with respect to $\delta = d/a$ for the material with the Poisson ratio $\nu = 1/4$ and the periodic structure with penny shaped crack from Fig. 1. The inset numbers 1, 2, 4 and 8 are equal to a/h . The dotted lines give the results of the dilute model.

References

1. G. Mejak (2014). Variational formulation of the equivalent eigenstrain method with an application to a problem with radial eigenstrains, *Int. J. Solids Struct.*, in press.

INFLUENCE OF THE FATIGUE LOADINGS ON THE RESIDUAL STRESS-STRAIN CHARACTERISTIC OF THE ENGINEERING MATERIALS

W. Moćko

Institute of Fundamental Technological Research, Warsaw, Poland

Motor Transport Institute, Warsaw, Poland

1. Introduction

Mechanical properties of the material are usually determined on the basis of test carried out using material in the as-received state. Obtained results may be applied for the purposes of design of structures. However, during normal exploitation process those structures may be subjected to fatigue loadings. Cyclic loading may substantially influence the observed macroscopically mechanical properties of the material [1, 2]. As a consequence mechanical behavior of the structure may be different from designed one, especially under extreme loading conditions.

This work presents the analysis of the influence of the fatigue loadings on the residual tensile curves of selected engineering materials, i.e. AISI 1045 [3, 4] steel and TiAl6V4 titanium alloy.

2. Experimental method

The first analysed material was titanium alloy. The hour-glass specimens, applied during the tests, were machined from an extruded rod made of TiAl6V4 titanium alloy, and subsequently polished in order to get roughness equal to 0.3. Therefore it was possible to induce localization of the fatigue damages and subsequently to determine true stress and strain values exactly in the place of fatigue damage accumulation. The diameter of the specimen grip and the necking was equal to 8 mm and 4 mm, respectively, and radius of the hour-glass was equal to 20 mm. The transversal extensometer has been applied for the purposes of strain measurement.

The latter tested engineering material was AISI 1045 steel. The specimens were machined from a drawn rod. Cylindrical specimens were fabricated with tangentially blended fillets between the gauge section and the ends. The gauge length and diameter were 12 mm and 4 mm, respectively. The surface was polished after machining.

The same specimen geometry was used for all of the analyses presented in this paper, including the tensile and fatigue tests. Three specimens were used for each tensile test under given loading conditions. The average value of the three replicate measurements was analysed. Fatigue test, pre-fatigue and tensile tests were carried out applying Instron servo-hydraulic testing machine. The experimental procedure has been divided into three steps:

- first, stress-controlled fatigue tests were carried out and followed by the analysis of ratcheting, plastic deformations and rupture surfaces;
- next, the initial material damage due to fatigue loadings was introduced into steel to reach the desired CFD values, i.e., 0.0, 0.25, 0.50, and 0.75; and
- finally, tensile tests of the pre-fatigued specimens were conducted to analyse the residual stress-strain characteristics of the steel.

3. Results

The tensile curves for both as-received and pre-fatigued materials are shown in Fig. 1a for the AISI 1045 steel and Fig. 1b for the TiAl6V4 titanium alloy. The stress-strain characteristic of both materials evolve as a consequence of initial fatigue loadings in different manner. In the case of steel, after pre-fatigue at stress controlled mode at magnitude equal to 557 MPa, material hardening is observed as the CFD increases to 0.25 and 0.50. A further increase to a CFD of 0.75 produces the opposite effect, a decrease in the flow stress. Thus, two different phenomena must be considered during fatigue loading. The first factor is related to cyclic hardening effects observed during the first few cycles and the second effect is softening due to the development of the fatigue damage [3].

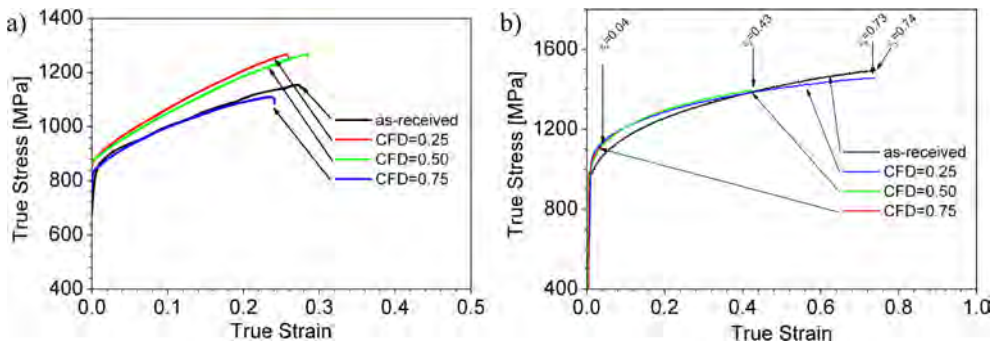


Fig. 1. Stress-strain curves of: a) AISI 1045 steel and b) TiAl6V4 titanium alloy.

Drop of the elongation due to pre-fatigue fatigue may be illustrated on the example of tensile tests of the titanium alloy initial loadings at amplitude equal to 557 MPa. Figure 2A and 2B shows fracture surface after tensile tests of the as-received material and after fatigue fracture, respectively. Initially the at CFD = 0.25 the fracture surface has ductile character (Fig. 2C), moreover the fracture strain equal to 0.74 is not strongly affected (Fig. 1b). The increase of the pre-fatigue cycles number to CFD = 0.50 induces drop of the elongation to 0.43 and ovalization of the fracture surface (Fig. 2D) which may be evidence of fatigue damage growth [3]. Further increase of CFD to 0.75 results in clearly observed decrease of the fracture strain to 0.04 followed by change of fracture mode to brittle (Fig. 2E).

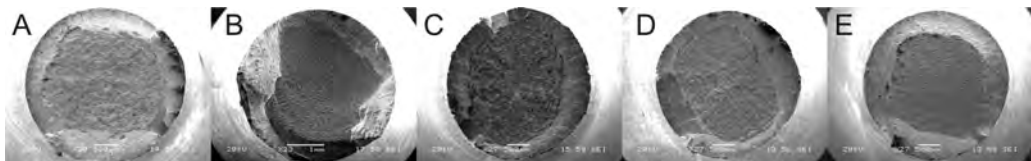


Fig. 2. Optical micrographs of the fracture surface.

References

1. C. Froustey, J.L. Lataillade (2009). Influence of the microstructure of aluminium alloys on their residual impact properties after a fatigue loading program, *Mat. Sci. Eng. A*, **A500**, 155–163.
2. U. Sánchez-Santana, C. Rubio-González, G. Mesmacque, A. Amrouche, X. Decoopman (2008). Effect of fatigue damage induced by cyclic plasticity on the dynamic tensile behavior of materials, *Int. J. Fatigue*, **30**, 1708–1719.
3. W. Močko (2014). The influence of stress-controlled tensile fatigue loading on the stress-strain characteristics of AISI 1045 steel, *Mater. Design*, **58**, 145–153.
4. W. Močko (2013). Effects of cumulative fatigue damage under tensional cyclic loading on the constitutive relation of AISI 1045 steel, *Proceedings of the 4th International Conference on Nonlinear Dynamics ND-KhPI2013 June 19-22, 2013, Sevastopol, Ukraine*, 412–418.

ABNORMAL FRACTURE IN TITANIUM ALLOY TA6V

T. Paris, A. Migliarini

Commissariat à l'Énergie Atomique, Centre de Valduc, 21120 Is sur Tille, France

1. Introduction

In the literature, many studies focus on abnormal phenomenon of fracture in titanium alloys. This kind of phenomenon is usually in the scope of 'sustained load cracking' or 'fatigue crack propagation threshold'. The first one is a delayed cracking after subcritical loading on notched specimen [1] whereas the second one is known as "Marci effect" [2] which is the disappearance of fatigue threshold at very high K_{\max} level. The clear connection between the two phenomenon is still an open debate but seems to be influenced by interstitials (O, C, N) and Hydrogen shielding [3]. These two points are also related to dynamic strain ageing (DSA) caused by interstitials hardening and room temperature creep enhanced by Hydrogen shielding.

Sustained load cracking and fatigue crack propagation threshold are addressed in this paper on a titanium alloy TA6V.

2. Experimental study

2.1. Fatigue Crack propagation threshold. Fatigue crack propagation tests were conducted on Compact Tension specimen of 12.5 mm thick. Three constant K_{\max} loading regimen were applied showing the fatigue crack propagation threshold disappearance for high value close to K_{Ic} (between 45% and 95% in Fig. 1). Other tests should be addressed to precise the exact value of the starting phenomenon.

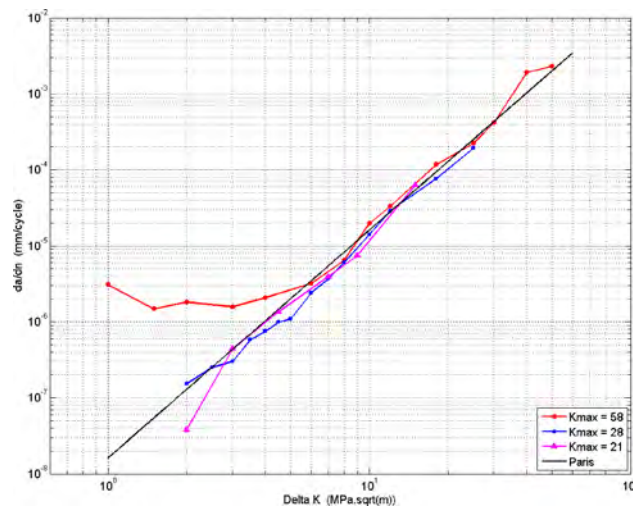


Fig. 1. Fatigue crack propagation threshold disappearance for high K_{\max} value (Crack growth rate versus stress intensity factor range in log-log scale).

2.2. Sustained load cracking. A different methodology was used in these tests involving KAHN specimen of 3 mm thick [4] rather than Compact Tension. Loading was sustained for half an hour steps starting from about 65% of maximum loading force to 80%. The phenomenon is clearly visible in Fig. 2.

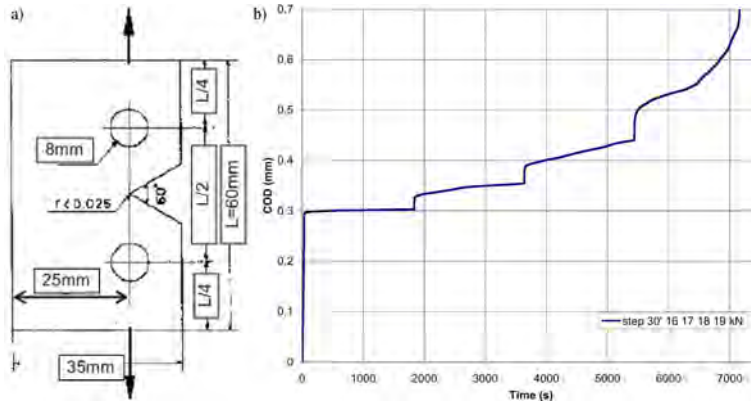


Fig. 2. Sustained Load Cracking test (clip gauge displacement versus time) (b) on KAHN specimen (a).

3. Numerical Study

A specific evolution of drag stress in the viscosity function [5] is trying to represent interstitials hardening. In this way, specific time dependency is introduced aiming to represent delayed cracking with sustained load. Actually, only monotonic crack growth test is conducted showing viscous stress relaxation in front of the crack tip (Fig. 3).

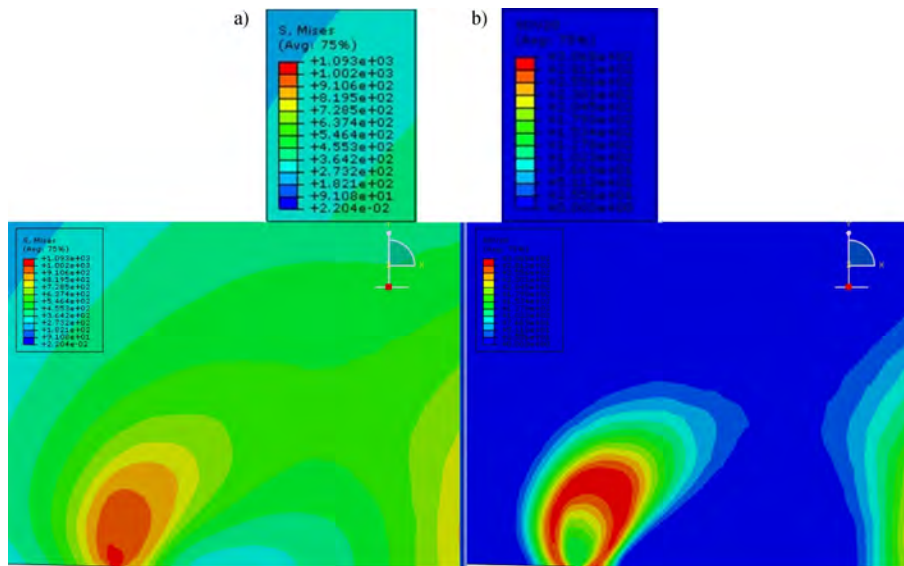


Fig. 3. Finite Element Simulation of KAHN specimen under monotonic loading: von-Mises stress (a) and viscous stress (b) at the crack tip (in MPa).

References

1. A. Vassel (1980). Etude du phénomène de rupture différée dans l'air de l'alliage TA6V, *Journal of the Less-Common Metals*, **69**, 293–299.
2. G. Marci (1994). Non-propagation conditions (ΔK_{th}) and fatigue crack propagation threshold (ΔK_T), *Fatigue Fract Engng Mater Struct*, **17**, 891–907.
3. F. Mignot, V. Doquet, C. Sarrazin-Baudoux (2004). Contributions of internal hydrogen and room-temperature creep to the abnormal fatigue cracking of Ti6246 at high K_{max} , *Materials Science and Engineering A*, **380**, 308–319.
4. ASTM B871-01 (2013). Standard Test Method for Tear Testing of Aluminum Alloy Products.
5. T. Paris (2008). Modélisation du comportement mécanique des liaisons soudées hétérogènes Ta/TA6V: Comportement et critère de rupture, *PhD Thesis University of Troyes*.

METAL MATRIX COMPOSITES UNDER FATIGUE CONDITIONS

A. Rutecka, P. Grzywna

Institute of Fundamental Technological Research, Warsaw, Poland

1. Introduction

Metal matrix composites (MMCs) are more and more commonly used in automotive and aerospace industries. The advantages of MMCs over conventional monolithic materials are, among others, improved strength and stiffness and simultaneously weight savings [1, 2]. Moreover, MMCs are often subjected to cyclic loadings. Thus, good fatigue resistance of the materials is required. Therefore, evolution of hysteresis loops under fatigue conditions was investigated as a first step to fatigue damage analysis of the materials [3].

2. Materials and experimental procedure

Metal matrix composites of two different matrixes, reinforced with SiC particles, were investigated. The first one, Al7,9Mg based MMC, was reinforced with 0; 2,5; 5; 7,5 and 10% of SiC. It was produced using the KoBo method. In the first stage of the process powders were blended and pressed. Finally they were extruded in the form of long rods. The second one, AA2124 based MMC, was reinforced with 17 and 25% of SiC. It was manufactured using powder metallurgy. Powders after high-energy mixing were compacted to fully dense billets and subsequently forged and subjected to T6 heat treatment.

Fatigue tests were performed on the MTS 858 servo-hydraulic testing machine. Sine shape tension-compression cycles were applied with frequency equal to 10 or 20 Hz. Tests were stress controlled with stress ratio $R = -1$. Stress amplitudes σ_a were equal to 220 and 240 MPa for AlMg/SiC, and 300 and 330 MPa for AA2124/SiC.

3. Fatigue tests results

During fatigue tests hysteresis loops were observed. AlMg/SiC exhibited three types of material behavior, depending on SiC content and stress amplitude values.

The first one was visible, among others, in the case of AlMg+2,5%SiC subjected to stress amplitude equal to ± 240 MPa. Hysteresis loops enlarged during first cycles and cyclic softening was identified (Fig. 1a). Subsequently cyclic hardening occurred (Fig. 2b).

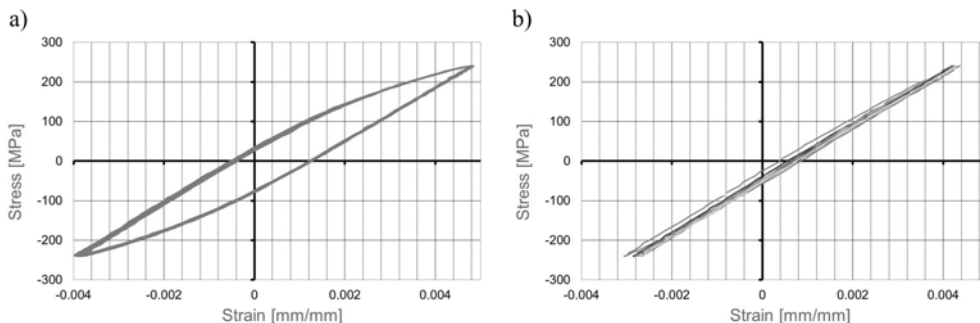


Fig. 1. Hysteresis loops for AlMg+2,5%SiC ($\sigma_a = \pm 240$ MPa): a) below one hundred cycles; b) over one hundred cycles.

The second type was represented by AlMg+7,5%SiC ($\sigma_a = \pm 240$ MPa). Hysteresis loops at the beginning of tests behaved elastically. Subsequently their width enlarged slightly. Above 100 cycles inelastic strain amplitude remained constant, while mean inelastic strain changed insignificantly.

The third type of material behavior was observed for AlMg+10%SiC ($\sigma_a = \pm 220$ MPa) and characterized by ratcheting towards negative values of the strain axis. Inelastic strain amplitude remained constant while mean inelastic strain decreased during subsequent cycles until stabilization.

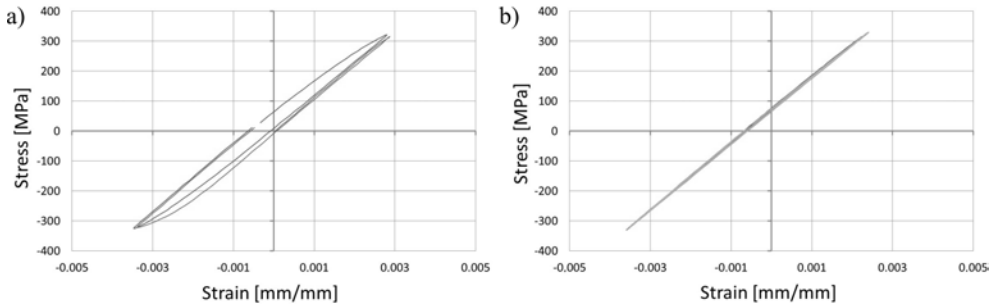


Fig. 2. Hysteresis loops for AA2124+25%SiC ($\sigma_a = \pm 330$ MPa): a) at the beginning of fatigue test; b) over 500 cycles.

In the case of preliminary tests of AA2124/SiC, cyclic plasticity followed by ratcheting was observed under fatigue conditions. Hysteresis loop width enlarged during first cycle towards negative strains (Fig. 2a) Subsequently hysteresis loops widths became narrower during next cycles and ratcheting towards negative strain values was observed (Fig. 2b). Afterwards hysteresis loops stabilized until specimen fracture.

Acknowledgments

The results presented in this paper have been obtained within the project “Kom-CerMet” (project no. POIG.01.03.01-00-013/08 with the Polish Ministry of Science and Higher Education) in the framework of the Operational Programme Innovative Economy 2007-2013 and within the project “KosDeKom” (project no. 1576/B/T02/2011/40) with the National Science Center, Poland

References

1. T.W. Clyne, P.J. Withers (2003). *An introduction to Metal Matrix Composites*. Cambridge University Press.
2. N. Chawla, Y.L. Shen (2001). Mechanical Behaviour of Particle Reinforced Metal Matrix Composites, *Advanced Engineering Materials*, **3**, 6, 357–370.
3. A. Rutecka, Z.L. Kowalewski, K. Pietrzak, L. Dietrich, K. Makowska, J. Woźniak, M. Kostecki, W. Bochniak, A. Olszyna (2011). Damage development of Al/SiC metal matrix composite under fatigue, creep and monotonic loading conditions, *Procedia Engineering*, **10**, 1420–1425.

EVOLUTION OF DAMAGE FOR P91 STEEL UNDER CYCLIC LOAD

G. Socha¹, L. Dietrich²

¹Institute of Aviation, Warsaw, Poland

²Institute of Fundamental Technological Research, Warsaw, Poland

1. Introduction

Damage evolution law for materials subject to monotonic load was used in its simplest form by many researchers, e.g. [1]. This simplest form can be written as follows:

$$(1) \quad dD = \frac{1}{\bar{\varepsilon}_f} d\bar{\varepsilon}_P,$$

which means that damage is liner function of accumulated plastic strain. Calculation of accumulated plastic strain in general case requires integration of the plastic strain intensity increment along the deformation path

$$(2) \quad \bar{\varepsilon}_P = \int d\bar{\varepsilon}_P.$$

For monotonic, proportional loading accumulated plastic strain equals strain intensity at the given instant. Final value of accumulated plastic strain (at the moment of material failure) is denoted as $\bar{\varepsilon}_f$. For general case of non-proportional, complex loading this calculation, however much more difficult, can be performed easily by most commercial FEM codes.

Uniaxial, cyclic load that is used in most of low and high cycle fatigue testing, e.g. [2] can be considered special case of proportional loading. Reported tests were stress controlled, fully reversible ($R = -1$) load cycles were applied with the frequency 20 Hz. Typical strain response for such program of loading is shown in Fig. 1 [3].

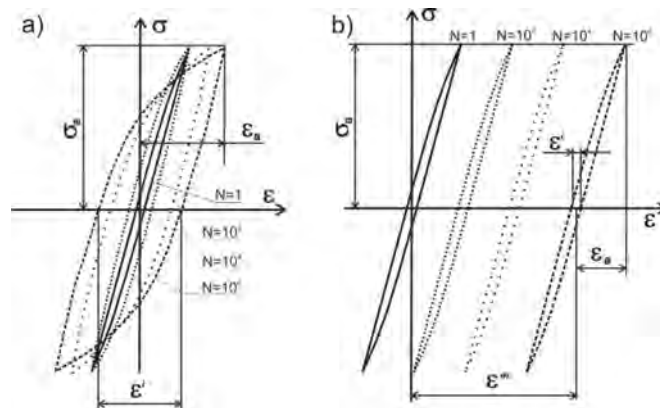


Fig. 1. Strain response for stress controlled, fully reversible load.

For each cycle of the load accumulated plastic strain intensity is composed of double inelastic response ε^i shown in Fig. 1a and ratcheting strain ε^m – see Fig. 1b. For N elapsed

cycles of load we can write that accumulated plastic strain intensity is:

$$(3) \quad \bar{\varepsilon}_P = \sum_{n=1}^N [2|\varepsilon_n^i| + |\varepsilon_n^m - \varepsilon_{n-1}^m|].$$

2. Experimental results

Most of experiments in the framework of presented experimental program was performed in high-cycle regime. Due to this fact, local observation of the damage had to be introduced in the manner described in [2]. Transversal strains were measured instead longitudinal, typically employed in the case of low-cycle fatigue. Since in the case of high-cycle fatigue it is inconvenient to record and analyze each load cycle, formula (3) was slightly modified to calculate damage indicator parameter using data recorded for selected cycles:

$$(4) \quad \varphi_N = \sum_{n=1}^N [|\varepsilon_n^i - \varepsilon_{n-1}^i| + |\varepsilon_n^m - \varepsilon_{n-1}^m|],$$

where n stands for sequential number of the recorded load cycle. Finally, value of damage parameter D was calculated using simple formula:

$$(5) \quad D = \frac{\varphi - \varphi_0}{\varphi_f - \varphi_0}.$$

Results of fatigue tests, obtained as the result of experimental program [3] are show in Fig. 2.

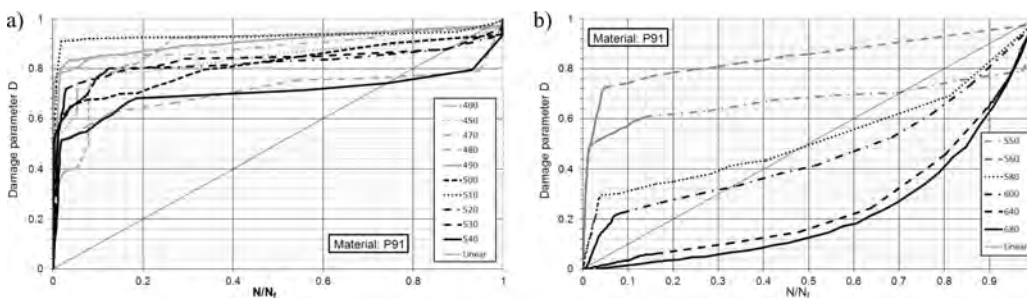


Fig. 2. Damage evolution for P91 steel: a) for low stress amplitudes (400–540 MPa), b) for high stress amplitudes (550–680 MPa).

Evolution of the damage parameter is shown in these plots as the function of the life fraction N/N_f for low (Fig. 2a) and high (Fig. 2b) stress amplitudes. Such kind of plot, usually referred as Damage Curve unambiguously describes damage evolution. Additionally, in Fig. 2a and b continuous line illustrates most popular damage evolution low – linear damage accumulation. In such a case damage is assumed to be linear function of the life fraction. As it can be easily noticed, evolution of damage for the material in question doesn't follow linear damage accumulation rule and more sophisticated, nonlinear model has to be applied in numerical simulations.

References

1. G.R. Johnson, W.H. Cook (1985). Fracture characteristics of three metals subjected to various strains, strain rates, temperatures and pressures, *Engng. Fract. Mech.*, **21**, 1, 31–48.
2. G. Socha (2003). Experimental investigations of fatigue cracks nucleation, growth and coalescence in structural steel, *Int. J. Fatigue*, **25**, 2, 139–147.
3. G. Socha, L. Dietrich (2014). A fatigue damage indicator parameter for P91 chromium-molybdenum alloy steel and fatigue pre-damaged P54T carbon steel, *Fatigue Fract. Engng. Mater. Struct.*, **37**, 195–205.

Session

Geomechanics

THE BRAZILIAN-DISC- AND THE RING-TESTS AS MEANS TO DETERMINE THE TENSILE STRENGTH OF BRITTLE MATERIALS: SOME NEW INSIGHTS

S. K. Kourkoulis

National Technical University of Athens, Department of Mechanics
5 Heroes of Polytechnion Avenue, Theocaris Bld., Zografou Campus, 157 73 Athens, Greece

The role of the boundary conditions prevailing at the disc-jaw interface, in case the Brazilian-disc test is implemented using the ISRM device, is studied analytically and experimentally. Attention is paid to the friction stresses and to the distribution of pressure along the contact arc. Weak points of the test are highlighted and possible solutions by using rings instead of compact discs are discussed.

1. Introduction

The Brazilian-disc test is nowadays considered as an irreplaceable tool for the determination of the tensile strength of brittle geomaterials. Hondros' analytic solution for the tensile stress at the disc's center is widely used, in spite of some rather unrealistic assumptions adopted (uniform pressure along two symmetric arcs of the disc's periphery of predefined length). In addition in some cases fracture starts far from the disc's center rendering the test's outcome erroneous. These weaknesses were highlighted already from mid-sixties and the ring-test was proposed as an alternative. In this study these factors are quantified taking advantage of some recently introduced closed form solutions [1, 2].

2. Theoretical considerations

The contact length 2ℓ and the distribution $P(\tau)$ of radial pressure for a disc of radius R and width w compressed (Fig. 1) between jaws of radius $1.5R$ (i.e. the ISRM device) read as [1]:

$$(1) \quad \ell = \sqrt{\frac{6RK P_o}{\pi}}, \quad P(\tau) = \frac{1}{3RK} \sqrt{\ell^2 - \tau^2}$$

with $K = [(\kappa_1 + 1)/4\mu_1 + (\kappa_2 + 1)/4\mu_2]$, $P_o = P_{\text{dev}}/w$ while κ_j and μ_j , $j = 1, 2$, are Muskhelishvili's [3] constants and the shear moduli for the disc's and jaw's materials, respectively. In case of non-smooth contact, friction stresses are generated along the contact length described by a two-branch function $T(\tau)$ as [2]:

$$(2) \quad T(\tau) = \begin{cases} f U(\tau) P(\tau), & \text{disc stuck to the jaw,} \\ n P(\tau), & \text{disc under impending slip conditions with respect to the jaw.} \end{cases}$$

The first branch of Eq. (2) is valid along the part of the contact arc where stick conditions prevail. Friction is here assumed proportional to $P(\tau)$ and to the relative motion tendency as it is quantified by the displacement mismatch $U(\tau)$ of any pair of points of the disc and the jaw facing each other [2]:

$$(3) \quad U(\tau) = |u_1^-(\tau)| - |u_2^+(\tau)| = \frac{1}{24RK} \left(\frac{\kappa_1 - 1}{\mu_1} - \frac{\kappa_2 - 1}{\mu_2} \right) \left(\tau \sqrt{\ell^2 - \tau^2} + \ell^2 \text{Arc sin} \frac{\tau}{\ell} \right).$$

The distributions of pressure $P(\tau)$ and friction $T(\tau)$, normalized over $P(\tau = 0)$, along the half-contact arc (normalized over ℓ) are shown in Fig. 2. Line (1) corresponds to stick conditions all-along the contact arc. Line (2) corresponds to partially stick conditions and con-

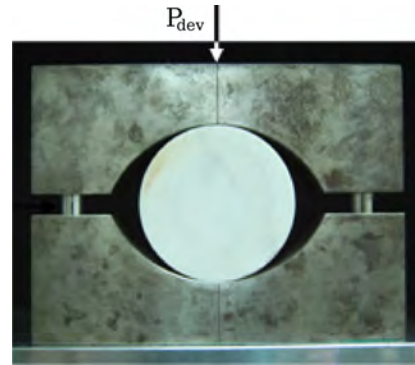


Fig. 1. The Brazilian-disc test realized according to the ISRM suggestions.

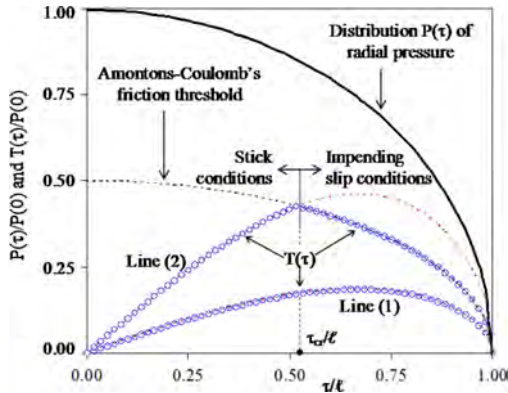


Fig. 2. Pressure and friction stresses along the contact semi-arc.

by a parabolic distribution of radial pressure was achieved recently [2]. It was concluded that even in the presence of friction the stress field at the critical points (intersection of loading axis of symmetry with the inner circle) ensures fracture away from the ring-jaw interface, at least for moderate friction coefficients.

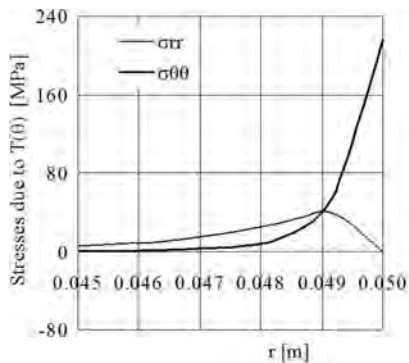


Fig. 3. Variation of stresses due to friction along the loading symmetry axis.

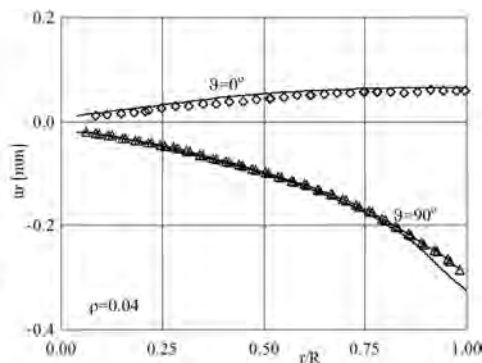


Fig. 4. Radial displacements in a ring with inner radius equal to 4% of the outer.

sists of two parts: For $0 \leq \tau \leq \tau_{cr}$ it represents stick conditions while for $\tau_{cr} \leq \tau \leq \ell$ it represents impending slip. The stress field imposed by the above friction forces is obtained using the complex potential technique [3]. Characteristic results are shown in Fig. 3. It is seen that the tangential stress $\sigma_{\theta\theta}$ as one approaches the disc-jaw interface reaches very high tensile values and local cracking is expected well before the stresses due to radial pressure cause cracking at the disc's center.

To avoid local cracking around the disc-jaw interface the substitution of the disc by ring-shaped specimens was proposed by Hobbs [4]. The analytic determination of the stress field in a ring loaded

The validity of the theoretical analysis for the ring under parabolic pressure was checked against experimental results for the displacement field obtained using the DIC technique. The results are satisfactory as long as linearity is ensured.

3. Conclusions

The friction stresses developed at the disc-jaw interface in case of non smooth contact are responsible for a strongly localized stress field in the disc which under certain conditions amplifies the field due to radial pressure, leading to premature local cracking far from the disc's center. In these cases the ring test offers a valuable alternative ensuring fracture at the ring's critical points.

References

1. S.K. Kourkoulis, Ch.F. Markides, P.E. Chatzistergos (2012). The standardized Brazilian disc test as a contact problem, *Int. J. Rock Mech. & Min. Sci.*, **57**, 132–141.
2. S.K. Kourkoulis, Ch.F. Markides, E.D. Pasiou (2014). A combined analytic and experimental study of the displacements field in a circular ring, *Meccanica*, DOI 10.1007/s11012-013-9846-0.
3. N.I. Muskhelishvili (1963). *Some basic problems of the mathematical theory of elasticity*, Groningen: Noordhoff, The Netherlands.
4. D.W. Hobbs (1964). The tensile strength of rocks. *Int. J. Rock. Mech. & Min. Sci.*, **1**, 385–396.

MICRO-MACRO DEPENDENCY FOR ELASTIC CONSTANTS IN A NUMERICAL MODEL OF GRANULAR MATERIAL

I. Marczewska¹, J. Rojek¹, R. Kačianauskas²

¹Institute of Fundamental Technological Research, Warsaw, Poland

²Vilnius Gediminas Technical University, Vilnius, Lithuania

1. Introduction

The discrete element method (DEM) is a suitable tool to model granular materials. In the DEM, a material is represented by an assembly of particles interacting among one another with contact forces. Interparticle interaction models can be based on different types of contact laws incorporating different physical effects such as elasticity, viscosity and friction. The contact model in the DEM can be treated as a micromechanical material model. Determination of micromechanical parameters is a key issue in the use of the DEM. Appropriate micromechanical allow us to obtain desired macroscopic behaviour. There is still a lack of full understanding of many micromechanical mechanisms which are inherent in the DEM and influence macroscopic behaviour of DEM models [1]. This paper is devoted to investigation of micro-macro dependency for elastic constants in a DEM model of granular material.

2. Numerical and analytical methodology for determination of micro-macro relationships

Macroscopic behaviour of a granular material has been investigated numerically performing simulation of the triaxial compression test which is a standard laboratory test procedure widely used to measure mechanical properties of soils and other granular materials. The discrete element simulations have been carried out using the DEM program Dompok [2]. A cylindrical specimen of 5,500 particles with confining membrane walls has been generated. Similar to the experimental procedure, after application of the confining pressure, the axial strain has been increased monotonically while keeping constant the pressure on the lateral walls. The elastic moduli, the Young's modulus and Poisson's ratio, have been determined in a standard way from the initial slopes of the stress–axial strain and volumetric–axial strain curves.

Numerically determined macroscopic properties have been compared with theoretical analytical predictions according the Voigt and best fit hypotheses described in [3]. The analytical formula are presented in Table 1, where the elastic macroscopic moduli, E and ν are expressed in terms of the micromechanical parameters: k_n and k_t – the contact stiffness in the normal and tangential direction, r – the average radius of the particles, N – the total number of inter-particle contacts in the volume V .

Table 1. Analytical estimation of the elastic moduli of the particle assembly.

Parameter	Voigt hypothesis	Best fit hypothesis
Young's modulus	$E = \frac{4Nr^2}{3V} \cdot \frac{2k_n + 3k_t}{4k_n + k_t}$	$E = \frac{20Nr^2}{3V} \cdot \frac{k_t}{2k_n + 3k_t}$
Poisson's ratio	$\nu = \frac{k_n - k_t}{4k_n + k_t}$	$\nu = \frac{k_n - k_t}{2k_n + 3k_t}$

3. Discussion of the results

Numerical simulations have been performed for the confining pressure 100 kPa, the contact stiffness in the normal direction k_n from the interval 9 kN/m–1.3 MN/m and the k_t/k_n ratio from the interval (0.1–1.0). The results are presented in Figs. 1 and 2 in the form of the curves showing the relationships between the dimensionless parameters: $Er/2k_n$, ν and k_t/k_n for different values of k_n . The dependence of the Poisson's ratio on the k_t/k_n ratio for different values of k_n is plotted in Fig. 2. Numerical results in Figs. 1 and 2 are compared with the analytical estimations according to the Voigt and best fit hypotheses. Quite a good agreement can be observed especially for lower values of k_n and k_t/k_n . The dependence of the Young's modulus E on the microscopic stiffness k_n is shown in Fig. 3 in comparison with the results obtained by other authors.

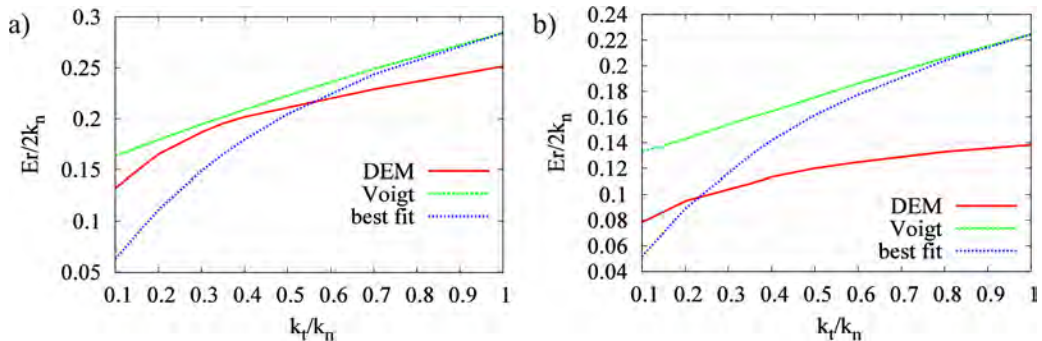


Fig. 1. Dimensionless micro-macro relationship for the Young's modulus for different values of k_n : a) 9 kN/m, b) 34 kN/m.

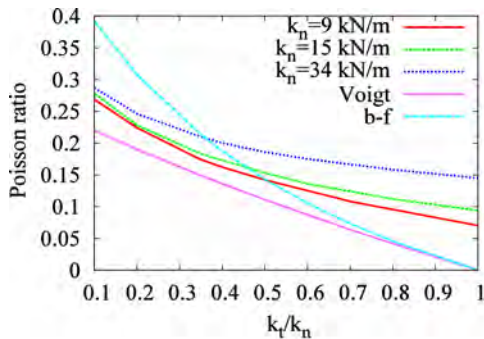


Fig. 2. Micro-macro relationships for the Poisson's ratio. relationships from different works.

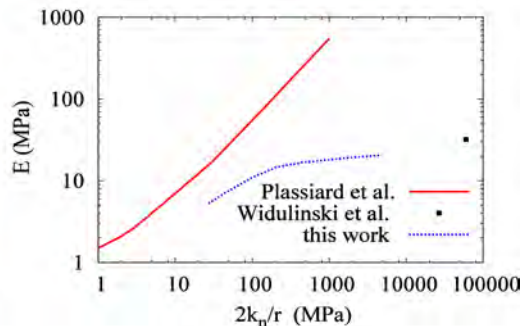


Fig. 3. Comparison of the numerical results from different works.

References

1. J. Rojek, C. Labra, O. Su, E. Oñate (2012). Comparative study of different discrete element models and evaluation of equivalent micromechanical parameters, *International Journal of Solids and Structures*, **49**, 1497–1517.
2. CIMNE (2010), *Dempack, explicit nonlinear dynamic analysis by the finite and discrete element method*, web:www.cimne.upc.edu/dempack.
3. C.L. Liao, T.P. Chang, D.H. Young (1997). Stress-strain relationship for granular materials based on the hypothesis of best fit, *Int. J. Solid. Structures*, **34**, 4087–4100.
4. J. Plassiard, N. Belheine, F. Donze (2009). A spherical discrete element model: calibration procedure and incremental response, *Granular Matter*, **11**, 293–306.

ON THE DESCRIPTION OF INHERENT/INDUCED ANISOTROPY IN POROUS MEDIA

S. Pietruszczak, M. Oboudi

McMaster University, Hamilton, Ontario, Canada

1. General

Many naturally occurring geomaterials are anisotropic at the macroscale, which is strongly related to their microstructure. Sedimentary rocks (like shales), for example, display an inherent anisotropy, which results from the presence of bedding planes. In granular materials, the anisotropy may originate from the shape of the grains. It is well known, for example, that the strength properties of sand with elongated angular-shaped aggregates are strongly affected by the direction of loading in relation to the direction of deposition. But even if the skeleton itself may be considered as isotropic, e.g., sand with nearly spherical particles, there is usually a bias in the distribution of void space, due to initial compaction, which also triggers the anisotropy that may evolve during the deformation process. Whether inherent, induced or a combination of both, the anisotropy in microstructure may have a significant effect on both the strength and deformation characteristics of the material and should be accounted for in the context of analysis and design of geotechnical structures.

2. The scope of research

In materials with *inherent* anisotropy, the principal material directions are often defined a priori and remain constant during the deformation process. In this case, one of the classical approaches to formulate the failure criteria is to invoke linear as well as quadratic terms in stress components referred to the coordinate system associated with the axes of symmetry of the material. An example of such an approach is an extension of the well-known Hill's criterion, as proposed in refs. [1, 2]. An alternative approach is the one which makes use of the general representation theorems and employs mixed invariants of stress and microstructure tensors [3]. The main issue with implementation of these approaches is the fact that they require a large number of material functions/parameters to be identified. Furthermore, the correlation of these parameters with the material microstructure is rather ambiguous. Given these difficulties, a simplified approach has been introduced in refs. [4] which employs a scalar anisotropy parameter defined in terms of mixed invariants of stress and microstructure tensors. This parameter is a homogeneous function of stress of degree zero, so that it depends only on the relative orientation of the principal stress triad with respect to the eigenvectors of the microstructure tensor.

In certain geomaterials, in particular in granular materials, the inherent anisotropy is weak and can easily be altered in the course of deformation process. The research on correlating the changes in material microstructure with the applied mechanical load has been quite limited. This stems primarily from difficulties associated with experimental setups providing more general loading paths e.g. rotation of principal stress axes. In addition, a continuous monitoring of the changes in structural arrangement, e.g. via computed tomography (CT) measurements, is required which is quite complex in itself. An alternative approach, which is the main focus in this work, involves examining the evolution of fabric based on numerical simulations of the mechanical response of a particulate assembly. Such a study is conducted here using the Discrete Element Method (DEM).

It should be noted that the description of anisotropy typically entails specification of the spatial distribution of strength parameters with respect to the coordinate system associated with material axes (cf. ref. [4]). For geomaterials with a strong inherent anisotropy (e.g., sedimentary rocks), the distribution of strength parameters can be assessed directly from appropriate experimental tests and no explicit measure of fabric is required. This is in contrast to the class of materials which initially have no preferred orientation but experience an induced anisotropy. Here, the principal material directions change and the formulation of an appropriate evolution law requires an explicit fabric descriptor and its correlation with stress/strain rates. It should be emphasized that a specific fabric measure is, in general, needed only to monitor the evolution of the principal material axes, and it's not necessarily employed in the formulation of the constitutive relation.

In this work, the notion of *inherent* anisotropy in porous media is addressed first. Both experimental and numerical studies are presented, which involve a granular material with nearly spherical grains (Ottawa sand). The samples are prepared so that there is a distinct bias in spatial the distribution of void space which triggers the strength/deformation anisotropy at the macroscale. The basic experimental trends are simulated numerically and the methodology is explained for the description of the mechanical response of this class of materials.

Later, the modeling of *induced* anisotropy is addressed. First, the notion of the description of microstructure of granular media is examined and some descriptors, which are based on stereological measurements, are reviewed [5]. Later, a series of DEM simulations are carried out examining the correlation between the external load and the evolution of microstructure. It is demonstrated that in a typical granular medium, like sand at different degrees of initial compaction, the evolution law may be formulated by imposing coaxiality between the microstructure and the total strain tensors. A comprehensive parametric is carried out to examine the influence of various material parameters on the general conclusion emerging from this work. The proposed evolution law is suitable for describing the effects of *induced* anisotropy in granular materials that are isotropic in terms of the grain architecture.

References

1. S.W. Tsai, E. Wu (1971). A general theory of strength of anisotropic materials. *Journ. Comp. Mat.*, **5**, 58–80.
2. W. Pariseau (1972). Plasticity theory for anisotropic rocks and soils. *Proceedings 10th Symposium on Rock Mechanics, AIME*.
3. P. Boehler, J. Sawczuk (1970). Equilibre limite des sols anisotropes, *Journ. de Mecanique*.
4. S. Pietruszczak, Z. Mroz (2001). On failure criteria for anisotropic cohesive frictional materials. *Intern. Journ. Numer. Anal. Meth. Geomech.*, **25**, 509–524.
5. D. Inglis, S. Pietruszczak (2003). Characterization of anisotropy in porous media by means of linear intercept measurements, *Intern. Journ. Solids and Structures*, **40**, 1243–1264.

SOFT COMPUTING IN MECHANICAL CHARACTERIZATION OF PAVEMENT STRUCTURES

A. Pożarycki¹, T. Garbowski²

¹Institute of Civil Engineering, Poznan University of Technology, Poznań, Poland

²Institute of Structural Engineering, Poznan University of Technology, Poznań, Poland

1. Background and motivation

In case when the pavement fatigue life, one of the most important element for pavement degradation monitoring, is still determined based on classic fatigue criteria [6], the priority is an accurate diagnosis of pavement parameters. Creating an analytical model of pavement structure based on commonly applicable standards in engineering practice, one needs to indicate the actual thickness of pavement structure in sections spaced at e.g. 500 m. Estimated pavement thickness affects directly the pavement fatigue life [2], hence precise identification of such parameters is critical for the proper prediction of pavement behavior over time, which is also essential for modelling purposes. The importance of thickness identification can be clearly evidenced by the contour plots of the root mean square (RMS) error when inverse analysis is employed in order to find the layer's moduli in a three layer pavement model. Depending on the adopted variables in 2D space, the moduli identification error occurs with a form of characteristic broad shape of contour line, denoting the minimum value of RMS (Fig. 1), which strongly depends on the input layer thickness.

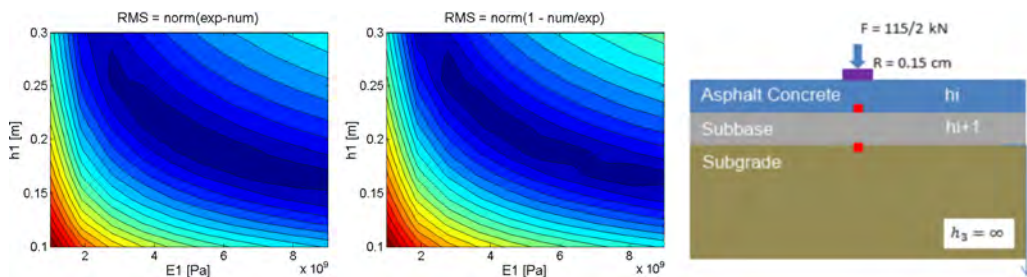


Fig. 1. Contours plots of cost function with analyzed 3-layered pavement model.

As far, the most reliable source of information about the pavement structure and thickness of its layers are invasive methods (see e.g. [4]). However, pavement structures belonging to certain road category, traffic class and type can be also correctly classified by using the artificial neural networks (ANNs). Successful implementation of classification-based ANN algorithm has been introduced in the paper [3]. In [5] a total of 6000 sets of deflection basin data have been used in order to estimate, predict and simulate the real pavement geometry and layer material properties.

2. Computer-aided identification of pavement parameters

Making use of computer generated set of pavement deflections, the neural network can be trained to perform (a) a prediction, (b) an estimation, (c) a simulation or (d) a classification. Here the mechanistic model based on layered elastic theory assumptions (LET)

is employed for data generation. The synthetic deflections are calculated using a general form of the integral of vertical displacements in linear elastic media:

$$(1) \quad w = \frac{1 + \nu}{E} [2 - 2\nu] \nabla^2 \Phi - \frac{\partial^2 \Phi}{\partial z^2}$$

where w – vertical displacement, ν – Poisson coefficient, ∇ – Laplacian, Φ – stress function, E – modulus of elasticity.

In contrast to classical gradient-based optimization algorithms no seed values are required when using the ANN, which is one of the main advantages when comparing to standard inverse analysis as it is used in this research area. Anyway, training data (layer moduli, layer thicknesses and Poisson coefficients together with discrete deflection) are crucial in soft computing methods. So far as recognized in design of computer experiments it is important to be able to obtain information from the entire design space (see e.g. [1]). Therefore, design points (vector of pavement parameters) are carefully distributed over the entire region of admissible parameters values. Among the chosen techniques of experiment designs the points based on regular scheme is the most convenience for further formulation of input and output in ANN structure. The sample distribution in 2D space (thickness h_1 and h_2) and thickness identification results are illustrated in Fig. 2.

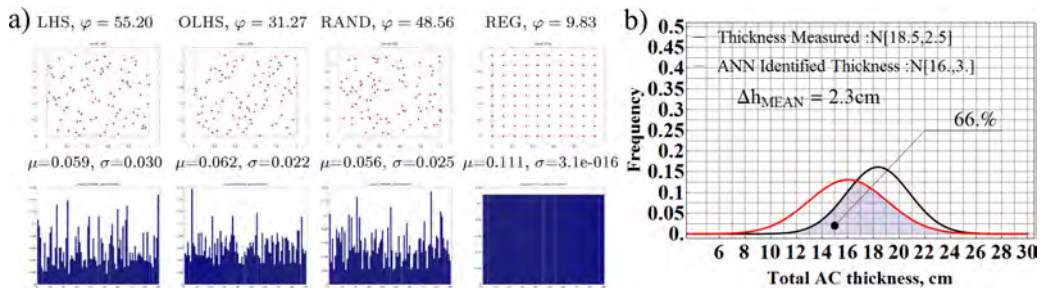


Fig. 2. Input and output ANN data, a) design spaces for various sampling techniques, b) best thickness identification results (h_1) based on data from computer simulations.

3. Conclusions

Limited solely to identification of the pavement layer thickness based on the ANN trained with computer generated data (8000 input data were used here) and mechanistic LET models, the 66% convergence with laboratory results can be observed. The ability to create the training sets of ANN for identification of layers thickness of asphalt pavement is a very attractive alternative, especially when results reveals the missing information about a thickness in between the distant drilling locations in pavement.

References

1. V. Buljak, T. Garbowski (2014). Efficient methods for optimal space filling in model reduction techniques, In: *Recent Advances in Computational Mechanics*, CRC Press, 285–292.
2. A.C. Collop (2007). The effect of asphalt layer thickness variations on pavement evaluation using the FWD, *Int. Journal of Pavement Eng.*, 247–263.
3. S. Kim, K. Gopalakrishnan, H. Ceylan (2009). Neural Networks Application in Pavement Infrastructure Materials, In: *Intelligent and Soft Computing in Infrastructure Systems Engineering*, Springer-Verlag Berlin Heidelberg, 47–66.
4. M. Mooney, G. Miller, S. Teh, W. Bong (2000). Importance of Invasive Measures in Assessment of Existing Pavements, *J. Perform. Constr. Facil.*, 14, 4, 149–154.
5. S. Sharma, D. Animesh (2008). Backcalculation of pavement layer moduli from falling weight deflectometer data using an artificial neural network, *Can. J. Civ. Eng.*, 3, 57–66.
6. J. Yu, B. Tsai, X. Zhang, C. Monismith (2012). Development of asphalt pavement fatigue cracking prediction model based on loading mode transfer function, *Road Materials and Pavement Design*, 13, 3, 501–517.

MODELLING OF SEA ICE FLOW BY THE SMOOTHED PARTICLE HYDRODYNAMICS METHOD

R. Staroszczyk

Institute of Hydro-Engineering, Polish Academy of Sciences, Gdańsk, Poland

1. Introduction

Sea ice dynamics is concerned with the complex motion of a large ice pack, composed of a multitude of interacting floes of vastly different sizes, driven by ocean currents, wind drag stresses and, on geophysical scale, the Coriolis forces. The floating ice cover is subject to surface accumulation due to the atmospheric precipitation, and undergoes surface/basal freezing or melting. The individual floes move about continuously, break, merge and rotate because of inter-floe collisions. As a result, large variations in the local ice thickness and ice concentration can occur. Moreover, large displacements and deformations of the ice pack domain and its boundaries take place under a prolonged action of wind and water currents.

The equations describing the dynamic behavior of sea ice are derived by treating the problem as a two-dimensional on the ‘horizontal’ surface (the free surface of the ocean), and by integrating the mass, momentum and energy balances of the ice and lead water through the ice pack thickness. The fundamental variables involved in the description are the mean ice thickness, the ice concentration (the area fraction of ice) and two components of the velocity field. Sea ice is usually treated as an elastic-viscous-plastic material (though the elastic effects are frequently neglected, Hibler [1]), and its rheology is described by a constitutive law that relates the depth integrated stresses to the two-dimensional deformation-rate. Since the strength of ice in tension is considerably smaller than in compression, the behavior of ice dramatically depends on whether the flow is locally converging or diverging. As a consequence, the structure of equations changes across interfaces separating converging and diverging flow regions, which can give rise to instabilities (Schulkes et al. [2]) when solving the sea ice flow equations by a numerical method.

2. Smoothed particle hydrodynamics method

The Smoothed Particle Hydrodynamics (SPH) method was invented as early as in 1977 by Lucy [3] and Gingold and Monaghan [4], but for nearly two decades its use was solely restricted to the field of astrophysics. Only in the mid 1990s some attractive features of the SPH method brought attention of the solid mechanics community, and ever since the interest in the method has been steadily growing and it has found applications in many branches of physics, applied mechanics and engineering, see Monaghan [5, 6].

The SPH method is a fully Lagrangian and mesh-free approach, in which a physical system under consideration is represented by a collection of arbitrarily distributed discrete particles, each of which carries individual information on all local properties relevant to the problem concerned, such as mass, density, momentum, temperature, etc. Owing to its conceptual simplicity, the fact that no connectivity between the particles is needed, and a relative ease of programming, the method has a natural capability of dealing with problems in which large deformations occur and surfaces of material discontinuity develop and subsequently propagate through the medium. Therefore, it seems that the SPH approach

is particularly well suited to solving the above-described sea ice dynamics problems, in which the application of conventional mesh-based discrete methods (such as the finite difference or finite element techniques) fails or entails significant numerical difficulties.

3. Sea ice flow simulations

The SPH method has been implemented to simulate the evolution of a large sea ice pack (of horizontal dimensions measured in hundreds of kilometers) subject to the action of wind. For simplicity, all thermodynamic effects have been ignored. Two different rheological models for ice have been applied: the viscous-plastic model of Hibler [1], and the non-linearly viscous model of Gray and Morland [7], the latter based on the theory of two-phase (ice and lead water) interacting continua theory. By the analogy with previously investigated problems solved by the finite element method by Schulkes et al. [2] and Morland and Staroszczyk [8], an idealized, initially rectangular, geometry of the ice pack has been adopted, with two or three adjacent sides of the rectangle at solid boundaries (representing a sea coast), and the remaining two or one side(s) at open sea boundary. The pack, initially of a uniform thickness, is driven by either a wind of constant speed and direction, or a vortex geostrophic wind field, acting over a few days, with the wind vortex centre located at the open sea off the rectangular ice field. It seems that such boundary value problems contains all the essential features which occur in realistic sea ice flows, and thus can serve as test cases for assessing the stability and performance of a numerical scheme. The results of the proposed discrete particle model have been compared with those obtained earlier by employing the finite element method, in order to see the advantages/disadvantages of the SPH approach compared to the mesh-based techniques.

The results of simulations illustrate the effects of the two rheological theories on the behavior of the ice pack, including the variation of the ice thickness and the ice area fraction in space and time. Also, the effects of different boundary conditions assumed at the coast-ice interface are explored. Of particular interest are the changes in the position of the open sea boundary, as the tracking of the sea ice pack extent under given weather conditions is of practical importance to the navigation and the oil industry in the Arctic.

References

1. W.D. Hibler (1979). A dynamic thermodynamic sea ice model, *J. Phys. Ocean*, **9**, 815–845.
2. R.M.S.M. Schulkes, L.W. Morland, R. Staroszczyk (1998). A finite element treatment of sea ice dynamics for different ice rheologies, *Int. J. Num. Anal. Meth. Geomech.*, **22**, 3, 153–174.
3. L.B. Lucy (1977). A numerical approach to the testing of the fission hypothesis, *Astron. J.*, **82**, 12, 1013–1024.
4. R.A. Gingold, J.J. Monaghan (1977). Smoothed particle hydrodynamics: theory and application to non-spherical stars, *Mon. Not. R. Astron. Soc.*, **181**, 375–389.
5. J.J. Monaghan (1992). Smoothed particle hydrodynamics, *Annu. Rev. Astron. Astrophys.*, **30**, 543–574.
6. J.J. Monaghan (2012). Smoothed particle hydrodynamics and its diverse applications, *Annu. Rev. Fluid Mech.*, **44**, 323–346.
7. J.M.N.T. Gray, L.W. Morland (1994). A two-dimensional model for the dynamics of sea ice, *Phil. Trans. R. Soc. Lond. A*, **347**, 219–290.
8. L.W. Morland, R. Staroszczyk (1998). A material coordinate treatment of the sea-ice dynamics equations, *Proc. R. Soc. Lond. A*, **454**, 2819–2857.

ANALYSIS OF SOIL–FLUID–STRUCTURE INTERACTION PROBLEMS BY MATERIAL POINT METHOD

Z. Więckowski

Łódź University of Technology, Łódź, Poland

1. Problem description

The material point method (MPM) has been successfully used in the large strains problems of solid mechanics, particularly in problems of granular flow [2]. The method deals without difficulties with free surface problems. The origin of the method is a particle-in-cell method introduced by Harlow [1] in fluid dynamics. Two types of space discretisation are utilized in MPM: Lagrangian material points which represent sub-domains of an analysed body and an Eulerian computational element grid which is used for field interpolation. State variables are traced at the material points the motion of which is followed by means of nodal values and interpolation functions defined on the computational grid. MPM can be regarded as a point-based (mesh-free) method as the material points are defined independently of the grid or an arbitrary Lagrangian–Eulerian formulation of the finite element method. As the computational grid can be defined in an arbitrary way—it can remain constant or be redefined during computations—the difficulty existing in purely Lagrangian approaches related to element distortions does not appear in MPM. The non-slip contact of two bodies is solved in MPM automatically which makes the method attractive when solid–fluid or soil–structure interaction problems are investigated. MPM allows for avoiding difficulties related to treatment of highly non-linear convective terms which exist in the case of Eulerian formulations. An explicit time integration algorithm is utilized to solve the discrete dynamic system of ordinary differential equations.

Using a single-phase model of the solid (or soil, in particular), the fluid–solid interaction problems like sinking and buoyancy as well as installing geo-containers, large geo-textile bags filled with soil, are analysed in the paper. The latter problem is very interesting from the engineering view point as dropping geo-containers from a barge with a movable bottom is one of useful methods of repairing dikes damaged by water.

A two-phase material model has been also applied in the paper to describe the mechanical behavior of a soil–fluid mixture. Two independent fields of velocity for the soil and fluid has been chosen as main variables. This two-phase model allows to analyse such complex phenomena as soil state transitions like liquefaction, sedimentation or erosion [3]. The Ergun law (the linear Darcy law enhanced with a quadratic term) is employed to describe the interaction between the two phases, soil and fluid.

2. Example

The plane problem of a geo-container dropped into a water basin is considered. The dimensions of the cross-section of the basin are 18 m × 8 m. The initial position of the geo-container is shown in the left-top corner of Figure 1. The circumference of the geo-textile material is slightly larger than the circumference of the volume occupied by the soil in order to increase the flexibility in changing shape of the geo-container. The soil is considered as a cohesion-less elastic–viscoplastic body with the Drucker–Prager yield condition and non-associative flow rule [2]. The following material parameters have been used in the calculations: Young's modulus $E = 1 \cdot 10^6$ Pa, Poisson's ratio $\nu = 0.3$,

mass density $\rho = 1400 \text{ kg/m}^3$, angle of internal friction $\varphi = 15^\circ$, viscosity parameter $\gamma = 100 \text{ s}^{-1}$, and exponent in the viscoplastic flow rule $N = 1$. The mechanical behaviour of the geo-membrane has been described by the linearly elastic material model. The material parameters for the geo-textile membrane used in the computations are as follows: elastic stiffness $6 \cdot 10^5 \text{ N/m}$, mass of the unit area 0.5 kg/m^2 . In the case of the liquid (water), the following values for the material parameters have been chosen: mass density $\rho = 1000 \text{ kg/m}^3$, bulk modulus $K = 2.1284 \cdot 10^9 \text{ Pa}$, viscosity $\mu = 0.8905 \cdot 10^{-3} \text{ Pa}\cdot\text{s}$.

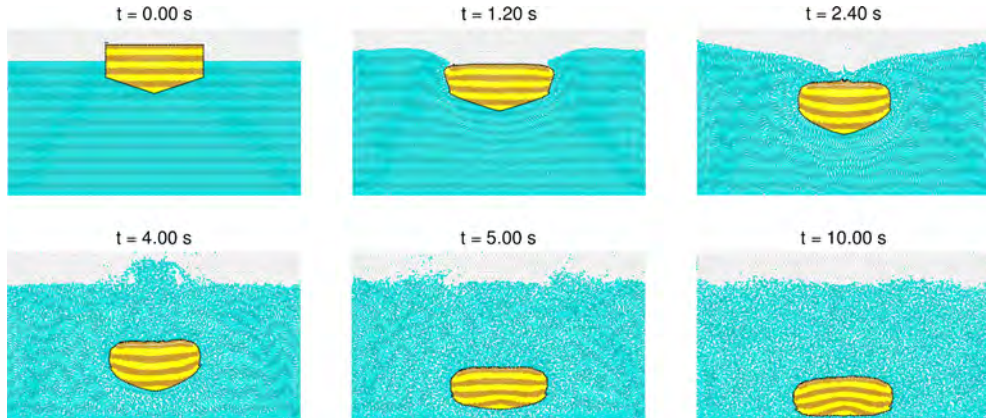


Fig. 1. Several phases of sinking geo-container process.

Some phases of the process of dumping the geo-container are shown in Figure 1. Large strains are observed not only in the fluid but for the soil as well. The bottom part of the geo-container with a corner at the initial state changes its shape to a rounded one when falling and becomes flat after touching the ground of the basin. The present example shows that the material point method can handle such complex problems like the interaction between fluid, soil and some structural elements like a membrane.

Despite the use of the explicit time integration procedure for the dynamic equations of the method, the computation time was only about 26 minutes for one second of the analysis time; a PC computer equipped with Intel Core2 Quad Q6600 processor (2.40 GHz) was utilized. In the calculations, a computational mesh with 4120 nodes and 8012 triangular elements with linear interpolation functions has been employed. Totally, 26670 material points have been introduced, 2816 for the soil, 23720 for the fluid and 134 for the membrane.

Acknowledgments

The financial support from the European Community's Seventh Framework Programme (Marie Skłodowska-Curie Intra European Fellowship) through grant PIEF-GA-2010-274335 is gratefully acknowledged (project title: Enhancement of the Material Point Method for Fluid–Structure Interaction and Erosion, GEO FLUID).

References

1. F.H. Harlow (1964). The particle-in-cell computing method for fluid dynamics, in: B. Adler, S. Fernbach and M. Rotenberg (eds.), *Methods for Computational Physics*, Vol. III, Academic Press, 319–343.
2. Z. Więckowski (2004). The material point method in large strain engineering problems, *Comput. Methods in Appl. Mech. Eng.*, **193**, 4417–4438.
3. Z. Więckowski (2013). *Enhancement of the Material Point Method for Fluid–Structure Interaction and Erosion*, Report, FP7 GEO FLUID project, Deltares, Delft, The Netherlands.

EXACT ANALYTICAL SOLUTIONS TO PROBLEMS ON EQUILIBRIUM STATE OF ELASTIC ANISOTROPIC HEAVY SPHERES AND CYLINDERS AND THEIR APPLICATIONS TO GEOMECHANICAL PROBLEMS

A. V. Zaitsev, A. V. Kutergin, Yu. V. Sokolkin, A. A. Fukalov

Perm National Research Polytechnic University, Perm, Russian Federation

1. Introduction

The need to solve problems for anisotropic heavy spheres and cylinders is due to a wide range of applications in various industries, construction, and geology. For instance, the problems of geomechanics of storing and mining (i.e. monolithic mine working supports) and road construction (i.e. tunnel lining) must be solved taking into account central and axial symmetry, uniform and/or nonuniform distribution of external and/or internal pressure. Obtaining of new analytical solutions is important and urgent for development of engineering methods of amended strength analysis, for testing computational algorithms of solving complex problems in which individual elements of designs and constructions are similar in geometry and boundary conditions and for working out methods for the experimental research of heavy bodies with simple geometry.

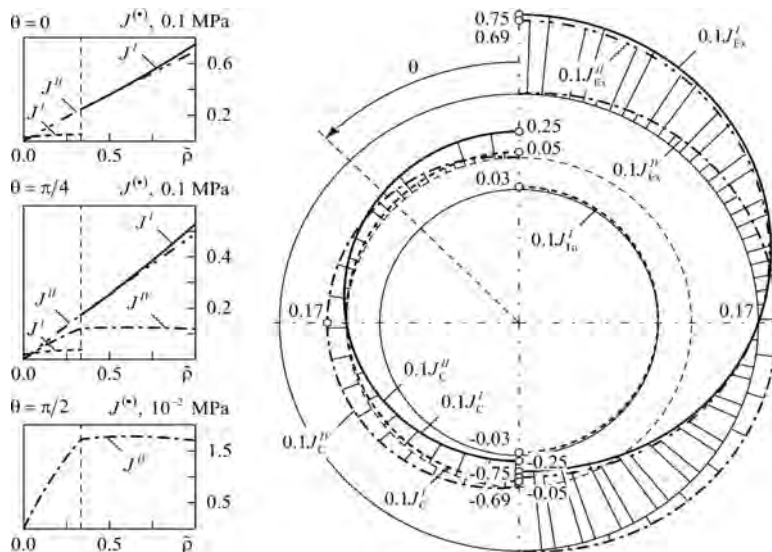


Fig. 1. Distribution of the independent invariant of stress tensor (MPa) on the fixed external ($J_{Ex}^{(\bullet)}$), free from pressures internal ($J_{In}^{(\bullet)}$) and contact ($J_C^{(\bullet)}$) surfaces, with radiuses $\rho_{In} = 2.5$ m, $\rho_C = 3.1$ m

$$\text{and } \rho_{Ex} = 4.3 \text{ m; } J^I = \sigma_{\phi\phi} = \sigma_{\theta\theta}, J^{II} = \sigma_{\rho\rho}, J^{IV} = \sqrt{\sigma_{\phi\rho}^2 + \sigma_{\theta\rho}^2}.$$

2. Method for solving

New exact analytical solutions to problems on equilibrium state of hollow and combined thick-walled heavy transversally-isotropic spheres [1, 2] and orthotropic cylinders [3], which are fixed on the interior or exterior surfaces and are subject to the action of uniform and/or nonuniform external or internal lateral pressure, are obtained. When integrated heterogeneous system of Lamé differential equations in cylindrical and spherical

orthogonal coordinates, the variable separation method led us to reduce the dimension of the problem, and the usage of generalized power series enabled us to write a general solution. The obtained solutions can set a pattern for exact solutions in particular cases of the relations for displacements, stresses and strains at the points inside hollow and combined heavy isotropic spheres and cylinders with the similar boundary conditions [4].

3. Applications to geomechanical problems

The reinforced concrete monolithic roof supports of spherical mining and the surrounding array of sedimentary rocks are considered as a single mechanical system [2]. The influence of construction geometries and material properties on the distribution of the independent invariants of stress tensor for spherically transversally-isotropic bodies in cross-sections (Fig. 1) is analyzed in the directions of meridian θ and dimensionless radial $\bar{\rho}$ coordinates. The estimation of an initial strength is carried out on the basis of a multicriteria approach taking into account various fracture mechanisms and areas where the fracture may be initiated and defined.

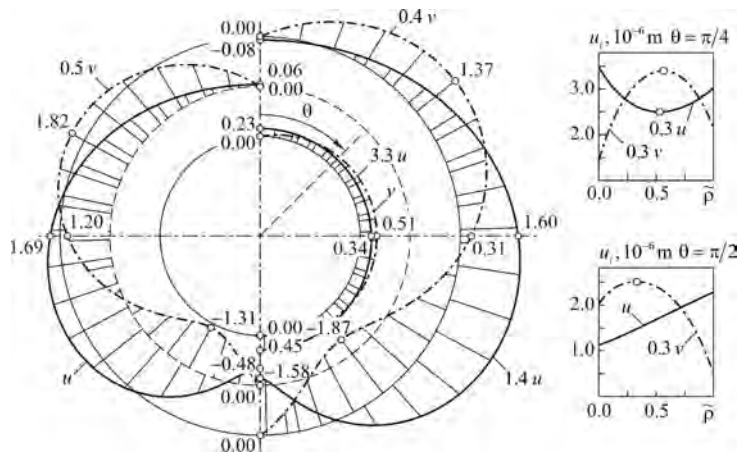


Fig. 2. Distribution of radial (u , 10^{-6} m) and hoop (v , 10^{-6} m) displacement in reinforced concrete cylinder on external, internal and median surfaces, with radiuses $\rho_{In} = 3.0$ m, $\rho_{Ex} = 5.5$ m.

The problem on equilibrium state of heavy reinforced concrete cylinder located on foundation soil is considered. Contact surface area was assumed to be known and unchanged. The reaction of soil is given in the form of a quadratic function which meets the condition that its integral sum equals weight of the constructions. The assumption allows us to write the boundary conditions for the determination of the integration constants of partial solution. On the basis of this the distribution of displacements (Fig. 2) and stresses in transversal cross-sections of horizontal monolithic reinforced concrete cylinders are shown, the lower half of which are dug into the soil.

References

1. Zaitsev A.V., Fukalov A.A. (2010). Elastic equilibrium state of thick-walled heavy transversally-isotropic spheres fixed on the interior surface, *Samara State Techn. Univ. Mech. Bulletin*, **5**, 21, 85–95 (in Russian).
2. Zaitsev A.V., Sokolkin Yu.V., Fukalov A.A. (2013). Initial damage mechanisms of reinforced concrete monolithic supports for spherical mine workings located in sedimentary rock mass, *PNRPU Mechanics Bulletin*, **4**, 59–71 (in Russian).
3. Fukalov A.A., Kutergin R.V. (2011). Exact analytical solutions to problems of the equilibrium state of elastic anisotropic heavy central and axial-symmetric bodies and their applications, *Vestnik of Lobchevsky State Univ. of N. Novgorod*, **4**, 3, 1831–1833 (in Russian).
4. Kuznetsov G.B. (1979). *Elastic, viscoelastic and long-term strength of cylindrical and spherical bodies*, Nauka, Moscow (in Russian).

Session

**Mechanics of Composites,
Porous Media**

ATOMISTIC MODELS OF POLYCRYSTALLINE AND POROUS STRUCTURES

T. Burczyński¹, A. Mrozek²

¹Institute of Fundamental Technological Research, Polish Academy of Sciences
Pawinskiego 5B, 02-106, Warsaw, Poland

²AGH University of Science and Technology, al. Mickiewicza, 30-059 Kraków, Poland

1. Introduction

The main purpose of this contribution is to present and discuss the features of the Molecular Dynamics (MD) methods [6] of building polycrystals with randomly orientated grains of given size and porous structures of adjustable density. Such atomic models can serve as initial solutions for the further MD simulations e.g. investigation of the behaviour of the nanodefects or determination of the mechanical characteristics where models built of ideal, regular lattices, which reveal anisotropic properties are not suitable. Although computationally expensive, MD-based methods have one main advantage compared to the artificial-geometrical ones: they produce stable, equilibrated structures, in almost all cases ready to the further use [3].

2. Methods of creation of molecular models

The following approaches are presented in this presentation: controlled cooling, compression of the nanoparticles and controlled range of interatomic interactions [3, 5]. All described approaches are illustrated with the appropriate numerical examples. Due to limited space of this abstract, only a few results of the simulations are shown. Two nanocrystalline structures, obtained using the third of mentioned methods are presented in Fig. 1.

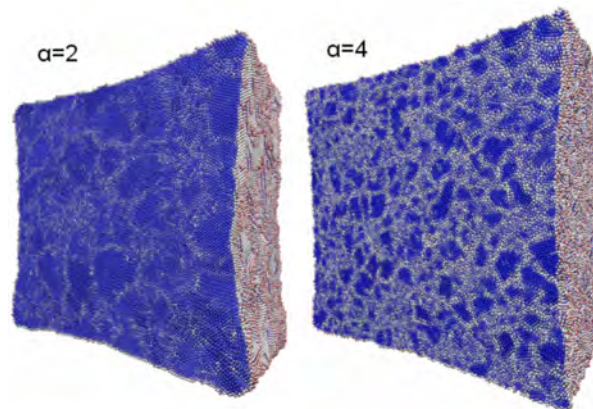


Fig. 1. Polycrystalline structures.

Both structures were obtained in the same conditions, during cooling a 32 nm ideal FCC cube (c.a. 2 mln of atoms) from 3000 K to 300 K in constant time of 2 ns. Only the scaling parameter α [4] which defined the curvature (thus interaction range) of the Morse potential was changed from 2 \AA^{-1} to 4 \AA^{-1} . The influence of this parameter on the average size of the grains is clearly visible.

Creation of the atomistic models with different, adjustable porosity is presented in Fig. 2. All the assumptions remain unchanged, but initial solution was prepared by random deleting certain number of atoms from regular FCC lattice. The EAM potential [2], dedicated to modelling metallic materials, was applied in this case.

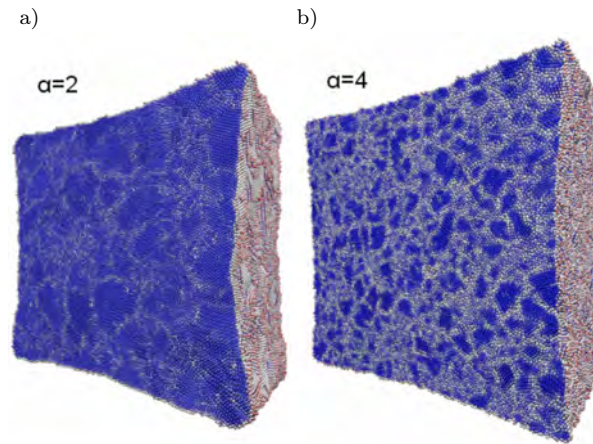


Fig. 2. Structures with: a) 15% and b) 30% porosity (respect to the ideal FCC lattice).

3. Estimation of the mechanical parameters

The methods of the estimation of the effective macroscopic mechanical properties, based on the nano-level tensile and shearing tests and so-called Non-Equilibrium Molecular Dynamics [7] will be performed, and computed for the various types of obtained atomistic structures. Obtained results, such as strain-stress relations, Young's and Kirchoff's moduli will be presented and compared with the results available in scientific literature and discussed during presentation.

In addition to potential applications of such atomistic models mentioned in the first paragraph, created structures can be also used in the methods of numerical homogenization or multiscale modelling e.g. in the author's developed versions of the multiscale modeling algorithms [1].

References

1. T. Burczyński, A. Mrozek, R. Górski, W. Kuś (2010). The molecular statics coupled with the subregion boundary element method in multiscale analysis, *Int. J. Multi. Comp. Eng.*, **8**, 319–330.
2. M.S. Daw, S.M. Foiles, M.I. Baskes (1993). The embedded-atom method: a review of theory and applications, *Mat. Sci. Rep.*, **9**, 7-8, 251–310.
3. A.M. Krivtsov (2003). Molecular dynamics simulation of impact fracture in polycrystalline materials, *Meccanica*, **38**, 61–70.
4. P.M. Morse (1929). Diatomic molecules according to the wave mechanics. II. Vibrational levels, *Phys. Rev.*, **34**, 57–64.
5. A. Mrozek, T. Burczyński (2012). Computational models of nanocrystalline materials, *Applied Sciences and Engineering (ECCOMAS 2012)* J. Eberhardsteiner *et al.* (eds.).
6. D. Rapaport (2005). *The Art of Molecular Dynamics Simulation*, Cambridge University Press.
7. M.E. Tuckerman, Ch.J. Mundy, S. Balasubramanian, M.L. Klein (1997). Modified nonequilibrium molecular dynamics for fluid flows with energy conservation, *J. Chem. Phys.*, **106**, 13, 5615–5621.

NEW HYBRID WEIGHT HOMOGENIZATION RULE FOR FIBER-REINFORCED ORTHOTROPIC COMPOSITE

S. Hernik

Cracow University of Technology, Cracow, Poland

1. Introduction

This paper deals with the unidirectionally long fiber reinforced composites of various representative unit cell symmetries, e.g. tetragonal or hexagonal. There are a lot of papers dealing with the modelling of effective mechanical properties of composite materials and its experimental verification, however only few of them describe the connection between the topology of fibers and group symmetry of constitutive models of composite materials (eg. Sun and Vaidya [1], Gan, Orozco and Herakovich [2], Liu, Feng and Zang [3] and others). In above papers two types of repeating unit cells: tetragonal array (six independent material constants in Hooke's law (1)) and hexagonal array (five independent material constants in Hooke's law (1)) are usually analysed.

$$(1) \quad \bar{\varepsilon} = \mathbf{S}^* \bar{\sigma}.$$

The following relation between Young's modulus, Poisson's ratio and Kirchhoff's modulus allows to precisely distinct between tetragonal and hexagonal symmetries of composites:

$$(2) \quad \bar{G}_{12} = \frac{\bar{E}_{11}}{2(1 + \bar{\nu}_{12})}.$$

In literature, there are at least two homogenization rules. The first one, proposed by Voigt [4], is based on isostrain assumption for estimation of the effective elements of constitutive matrix, contrary to the other proposal by Reuss [5], which is based on isostress assumption. Obviously both approximations suffer from some inconsistencies. For instance, Reuss approximation leads to incorrect results for magnitude of Young's modulus in fiber direction, whereas Voigt's approximation gives overestimate in case of shear modulus in transverse plane. This of course is a consequence of the fact that the Voigt and Reuss approximations represent upper and lower bounds for the stiffness or compliance matrix coefficients of a given composite (Hill 1952, after Aboudi *et al.* [6]).

2. New mixture rule

In this paper authors propose new simple rule (supermixture) as a hybrid weight interpolation method [7], between Voigt and Reuss isotropic estimates for given orthotropic composite, as follows:

$$(3) \quad \bar{\mathbf{S}}_{ij}(V_f) = \alpha_k \bar{\mathbf{S}}_{ij}^V(V_f) + (1 - \alpha_k) \bar{\mathbf{S}}_{ij}^R(V_f), \quad k = 1, \dots, 9$$

where α_k stands the weight coefficient vector. Elements of this vector are calculated from the consistency condition and compared to the compliance matrix coefficient, obtained from (3) and the experimental results for the given volume fraction V_f . In the present paper authors assume that results of SCMS method [2] play role of experimental data.

Table 1. Elastic constants.

	Aluminium	Boron
E [GPa]	55.16	413.7
ν [-]	0.3	0.2

3. Results

In numerical experiment the composite microstructures consist isotropic boron fibers embedded in an aluminum matrix. The elastic constants are presented in Table 1.

The comparison between new mixture rule proposed by authors and the Gan *et al.* results [2] of effective Young modulus for Boron/Al composite are presented in Fig. 1.

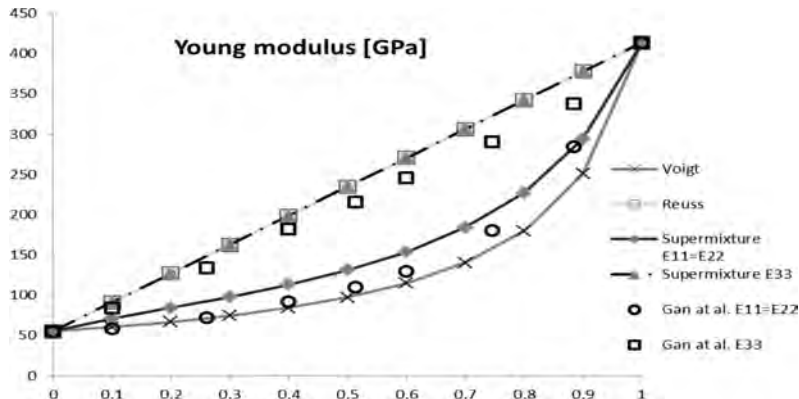


Fig. 1. Comparison of Young modulus between new homogenization rule and Gan *et al.* [2].

Acknowledgments

The financial support under Grant No. UMO-2011/03/B/ST8/05132 from the National Science Centre is gratefully acknowledgment.

References

1. C.T. Sun, R.S. Vaidya (1996). Prediction of composite properties from a representative volume element, *Composites Science Technol.*, **56**, 171–179.
2. H. Gan, C.E. Orozco, C.T. Herkovich (2000). A strain-compatible method for micromechanical analysis of multi-phase composites, *Int. J. Solids Struct.*, **37**, 5097–5122.
3. B. Liu, X. Feng, S.-M. Zhang (2009). The effective Young's modulus of composites beyond the Voigt estimation due to the Poisson effect, *Comp. Sci. Technol.*, **69**, 2198–2204.
4. W. Voigt (1889). Über die Beziehung Zwischen Den Beiden Elastizitätskonstanten Isotroper Körper, *Wied. Ann.*, **38**, 573–87.
5. A. Reuss (1929). Berchnung der Fiessgrenze von Mischkristallen auf Grund der Plastizitätsbedingung für Einkristalle, *Z. Angew. Math. Mech.*, **09**, 49–58.
6. J. Aboudi, S.M. Arnold, B.A. Bednarczyk (2013). *Micromechanics of composite materials*, Elsevier, 151–152.
7. A.W. Ganczarski, J.J. Skrzypek (2013): *Mechanika nowoczesnych materiałów*, Wydawnictwo PK, Cracow, 164 (in Polish).

INELASTIC BUCKLING OF THIN-WALLED FML COLUMNS BY ELASTIC ASYMPTOTIC SOLUTIONS

K. Kowal-Michalska, Z. Kołakowski

Department of Strength of Materials, Lodz University of Technology, Poland

1. Introduction

Fiber Metal Laminates (FMLs) are hybrid materials, built from thin layers of metal alloy and fiber reinforced epoxy resin. These materials are manufactured by bonding composite plies to metal ones. FMLs, with respect to metal layers, can be divided into FMLs based on aluminum alloys (among them ARALL reinforced with aramid fibers, GLARE – glass fibers, CARALL – carbon fibers) and others including titanium or magnesium based plies [1]. Nowadays materials such as GLARE (glass fiber/aluminum) due to their very good fatigue and strength characteristics combined with the low density find increasing use in aircraft industry.

When the plate structures made of GLARE subject to in-plane loading in the elasto-plastic range of stresses the buckling occurs in such a way that aluminum layers become plastic but the glass layers remain elastic. Therefore the inelastic behavior of such structures differs significantly from the behavior of pure aluminum ones.

2. Subject of consideration

Thin-walled columns of open cross-sections (channel or top-hat section) subject to uniform compression are investigated. The columns are built of rectangular flat plates. The material of the structures is GLARE 3 with an even number of glass reinforced layers, the outer layers are always aluminum. The plies are arranged in such a way that overall laminate is always symmetric. The dimensions of structures are chosen in such a way that the stability loss occurs in the elasto-plastic range for aluminum layers. The aluminum inelastic behavior is described by Ramberg-Osgood formula [2].

3. Method of solution

The problem of inelastic buckling is examined using the method elaborated for the analysis of the elastic stability of multi-layered thin-walled columns. The layers can be isotropic or orthotropic. The relationships between stress and strain for a component elasto-plastic layer are derived on the basis of the J2-deformation theory and/or J2-flow theory (incremental theory) of plasticity. Accordingly to the classical laminate plate theory the same relations can be written for an orthotropic/composite elastic layer. Comparing the appropriate coefficients in both relations the instantaneous “conventional” parameters of orthotropy can be found out.

The elastic problem is solved by the asymptotic Koiter’s method, formulated by Byskov and Hutchinson – the detailed method of solution can be found e.g. in works [2, 3]. The most important advantage of this method is that enables one to describe a complete range of behavior of thin-walled structures from global (flexural, flexural-torsional, lateral, distortional and mixed) to local stability. In the solution obtained, the co-operation between component walls of the structure, shear-lag phenomenon and the effect of cross-sectional distortions are included. The solution of the first order approximation enable to determine the critical loads of global and local values and the buckling modes.

This method is applied to calculate the critical load values for thin-walled FML columns in the inelastic range. The procedure is based on the fact that the relations between stresses and strains in the elastic and elasto-plastic range for aluminum layers have the identical form:

Elastic range for an orthotropic material

$$(1) \quad \sigma_x = K_{11}\varepsilon_x + K_{12}\varepsilon_y, \quad \sigma_y = K_{12}\varepsilon_x + K_{22}\varepsilon_y, \quad \tau_{xy} = K_{33}\gamma_{xy}.$$

Inelastic range for an isotropic material

$$(2) \quad \sigma_x = A_{11}\varepsilon_x + A_{12}\varepsilon_y, \quad \sigma_y = A_{12}\varepsilon_x + A_{22}\varepsilon_y, \quad \tau_{xy} = A_{33}\gamma_{xy}.$$

The coefficients A_{11} – A_3 (2) determined on the basis of the deformation theory of plasticity are as follows:

$$(3) \quad \begin{aligned} A_{11} &= E \frac{3E/E_s + E/E_t}{A_0}, & A_{12} &= E \frac{2E/E_t - 2(1-2\nu)}{A_0}, & A_{22} &= E \frac{4E/E_t}{A_0}, \\ A_{33} &= E \frac{1}{3E/E_s - (1-2\nu)}, & A_0 &= 3 \frac{E}{E_s} \frac{E}{E_t} - 2(1-2\nu) \frac{E}{E_t} - (1-2\nu)^2. \end{aligned}$$

In the equations (3) the following notation is introduced: E – Young’s modulus, ν – Poisson’s ratio, E_t – tangent modulus, E_s – secant modulus for the considered material characteristics in the inelastic range.

On the other hand, the elastic coefficients for orthotropic material K_{11} – K_{33} are defined as:

$$(4) \quad \begin{aligned} K_{11} &= \frac{E_x^*}{(1 - \nu_{xy}^* \nu_{yx}^*)}, & K_{12} &= \nu_{yx}^* K_{11} = \nu_{xy}^* K_{22}, \\ K_{22} &= \frac{E_y^*}{(1 - \nu_{xy}^* \nu_{yx}^*)}, & K_{33} &= G_{xy}^*, \end{aligned}$$

and $\eta^* = E_x^*/E_y^* = \nu_{xy}^*/\nu_{yx}^*$.

Equating $K_{11} = A_{11}$, etc., the instantaneous fictitious parameters of “elastic orthotropy” E_x^* , E_y^* , G_{xy}^* , ν_{yx}^* can be found out as functions of the parameters describing the inelastic behavior of an aluminum layer. Therefore, the method used to estimate the buckling behavior of elastic multi-layered columns can be applied to determine (for the assumed half-wave number m) the buckling load value and buckling modes for considered thin-walled FML columns subjected to pure compression in the inelastic range.

The problem is solved in a numerical way.

The results of numerical calculations will be presented in diagrams as the dependence between the dimensionless buckling stress versus number of axial half waves for different number of layers and varying arrangement of glass fiber layers. The shapes of buckling modes in the elasto-plastic range will be also depicted.

Acknowledgment

This contribution is a part of the project funded by the National Science Centre, Poland allocated on the basis of the decision No. 2012/07/B/ST8/0409.

References

1. T. Sinmazcelik *et al.* (2011). A review: Fibre metal laminates, background, bonding types and applied test methods, *Materials and Design*, **32**, 3671–3685.
2. Z. Kołakowski, K. Kowal-Michalska (eds.) (1999). *Selected problems of instabilities in composite structures*, Technical University of Lodz, Series of Monographs, Lodz.
3. Z. Kołakowski, M. Królak (2006). Modal coupled instabilities of thin-walled composite plate and shell structures, *Composite Structures*, **76**, 303–313.

A PRELIMINARY STUDY ON THE DEVELOPMENT OF GRAPHENE/CEMENT BASED NANOCOMPOSITES

Z. S. Metaxa¹, E. P. Favvas², C. Mercader³, F. Poulin⁴, N. D. Alexopoulos¹

¹Department of Financial Engineering, University of the Aegean, Chios, Greece

²Division of Physical Chemistry, NCSR “Demokritos”, Ag. Paraskevi, Attica, Greece

³Technological Center for Advanced Materials and Composites in Aquitaine (CNO), France

⁴Centre de Recherche Paul Pascal, CNRS, Université de Bordeaux, France

The present research work is focused on the implementation and utilization of novel nano-graphene platelets for the development of multifunctional nanocomposite cement based materials. More specific, the main goal was the development of innovative nanocomposites so that themselves can be used as sensors to monitor the structural health of structures. To take advantage of the excellent mechanical and electrical properties of the graphene nanoplatelets, initially, a method to effectively disperse them in the cementitious matrix was developed. Specifically, the dispersion of the nanoplatelets using a 3rd generation superpasticizer, typically used in cementitious materials, at different concentrations was studied. Following, the optimum sonication energy was defined. Finally, the effect of graphene nanoplatelets concentration on the electrical properties of the nanocomposites was studied.

1. Introduction

In Civil Engineering applications, the increasing structural needs, nowadays dictate that new high-technology composite materials should have additional functions, e.g. to be used simultaneously as sensors. Currently available technologies to monitor the cementitious materials are mainly based on sensors that are attached with appropriate adhesive at their surface. Experimental data obtained from such sensors remains rather limited and gives more or less information on the outer surface and not from the inside of the composite. Instead of using sensors in the outer surface of the composites, the use of embedded sensors could provide the engineers direct and more accurate information regarding the deformation and generally the structural health of the cementitious materials. Despite the above benefits, an embedded sensor could possibly act as a defect or will downgrade the material's mechanical properties.

The nanomaterials offer today the opportunity of developing embedded sensors that exhibit a high sensitivity without sacrificing the material's properties. Graphene, especially, is the newest and most advantageous nanoscale material for reinforcement. Due to its extremely high stiffness (Young's modulus of 0.5 to 1 TPa) and ultimate strength (130 GPa), single-layer graphene has been established as the strongest material ever measured [1]. Moreover, it has a very high electrical conductivity [2, 3].

In this study, various graphene/cement based nanocomposites were developed. Initially, in order to fully take advantage of the excellent mechanical and electrical properties of NGPs, an effective method to disperse the graphene nanoplatelets for use in cementitious composites, utilizing a 3rd generation superpasticizer and high power sonication, was developed. To optimize the method, the effects of both the concentration of the chemical admixture and the sonication energy on the dispersion of the nanoplatelets were studied. Finally, following the aforementioned dispersion method, the electrical characteristics of nanocomposites reinforced with different graphene nanoplatelets concentrations, with the objective to define the percolation threshold, i.e. the volume fraction of fillers at which the resistivity decreases sharply by several orders of magnitude, were studied.

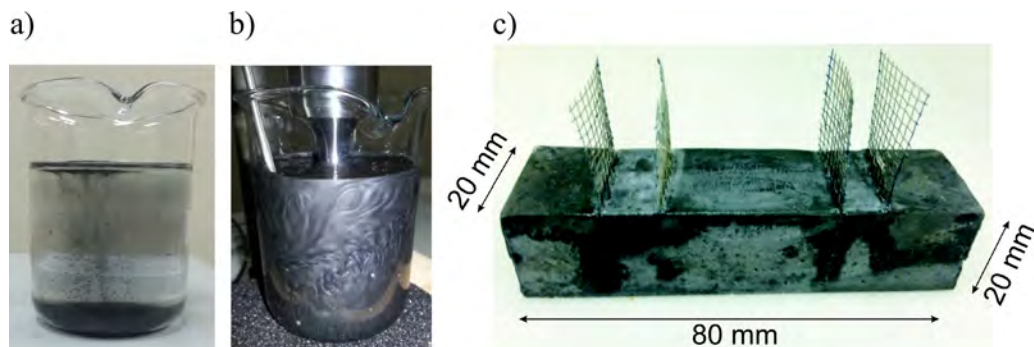


Fig. 1. Typical suspension (water, chemical admixture and graphene): a) before and b) during the sonication process.

2. Experimental procedure

The samples were prepared using cement CEM II 32.5 and two different types of graphene nanoplatelets having the same thickness (< 100 nm) and different width (8 and 100 μm). Before casting the graphene nanoplatelets were dispersed in the mixing water using a polycarboxylate-ether-based water reducing admixture and applying ultrasonic energy using a cup-horn ultrasonic processor. A typical suspension before and during sonication can be seen in Fig. 1a and b, respectively. The resulting suspensions were mixed with the cement following the ASTM 305.

The morphology of the graphene/cement based nanocomposites' fracture surfaces was investigated using both ultra-high-resolution scanning and transmission electron microscopes (SEM & TEM) while their crystalline characteristics were investigated by XRD measurements. The electrical resistivity of the nanocomposites was measured using the four-probe method. During specimen preparation four electrical contacts were embedded along the length of the specimen (Fig. 1c). During testing, the outer contacts were used for measuring the current and the inner contacts for measuring the voltage.

3. Results and conclusions

Initially, the effect of the chemical admixture concentration on the dispersion of the 8 μm graphene nanoplatelets at a constant concentration of 0.1 wt% of cement was studied. The nanoplatelets dispersion has been shown to be effected by the admixture concentration. To further optimize the dispersion method the effect of ultrasonic energy was also determined. The electrical properties results have shown that graphene nanoplatelets can be used to reduce the electrical resistivity of the cementitious matrix.

Acknowledgments

The authors would like to acknowledge the financial support of the John S. Latsis Public Benefit Foundation under the "Scientific Projects 2014", project entitled "Self sensing graphene/cement based nanocomposites for structural integrity monitoring".

References

1. C. Lee, X. Wei, J. Kysar, J. Hone (2008). Measurement of the elastic properties and intrinsic strength of monolayer graphene, *Science*, **321**, 385–388.
2. X. Du, I. Skachko, A. Barker, E.Y. Andrei (2008). Approaching ballistic transport in suspended graphene, *Nat Nanotechnol*, **3**, 491–495.
3. M. Pumera (2010). Graphene-based nanomaterials and their electrochemistry, *Chem. Soc. Rev.*, **39**, 4146–4157.

FINITE ELEMENT MODELLING OF THE MECHANICAL BEHAVIOR OF POLYMERS REINFORCED BY RANDOMLY DISTRIBUTED CARBON NANOTUBES

P. Papanikos

Department of Product and Systems Design Engineering, University of the Aegean, Greece

1. Introduction

Due to extraordinary mechanical properties and fiber-like structure, carbon nanotubes (CNTs) offer unique potential for reinforcing polymers either as replacements of conventional fibers or as fillers to enhance the existed advanced composites. It has been demonstrated that with only 1% (by weight) of carbon nanotubes added in a matrix material, the stiffness of a resulting composite film can increase between 36% and 42% and the tensile strength by 25% [1]. Yokozeki *et al.* [2] observed a clear retardation in matrix cracking onset and accumulation in composite laminates filled with carbon nanotubes.

Recent studies have shown that effectiveness of CNT-reinforcement in polymers depends on many parameters such as nanotube volume fraction, strength of nanotube/polymer interface and nanotube orientation. To ascertain the effects of these parameters, an extensive investigation is currently being conducted mainly by experimental means. Due to the difficulties in preparing and testing CNT-based materials, modeling serves as an attractive alternative. However, due to the enormous differences in scales involved in the correlation of macroscopic properties with the physical mechanisms of the nanotubes, different modeling levels need to be integrated. This can be achieved only by multi-scale approaches combining atomistic with continuum methods.

2. Representative volume element

An integrated multi-scale approach for modeling the tensile behavior of CNT-reinforced composites is proposed. The first step involves the evaluation of the mechanical properties of a single CNT using a FE model and by considering the bonds as connecting load-carrying elements, and atoms as joints of the connecting elements. In this way, the hexagonal lattice may be simulated as a frame structure [3].

The second step refers to the parametric modeling of various types of CNTs and evaluation of the mechanical properties of a continuum solid element, referred to as “equivalent beam” [4]. The concept of the “equivalent beam” is based on the condition of identical mechanical behavior between the CNT and the beam, which corresponds to identical tensile, bending and torsional behaviors (Fig. 1). As for elastic beams, these behaviors are designated by the corresponding rigidities and in order to fully define the equivalent beam, it suffices to evaluate its equivalent properties (geometrical characteristics and elastic properties) from the nanotube’s rigidities.

Using the properties of the equivalent beam, a FE-based representative volume element (RVE) of the reinforced polymer is developed. This element represents a unidirectional nanotube/polymer composite whose orthotropic properties are evaluated by considering different types of loading, i.e. axial tension and compression in the three axes and in-plane and out-of-plane shear. The dimensions of the RVE are evaluated as a function of the nanotube volume fraction, the nanotube length and the dispersion of the nanotubes in the polymer matrix. A typical RVE model is shown in Fig. 1. In this step, the results of the RVE model were compared with literature results and very good agreement was

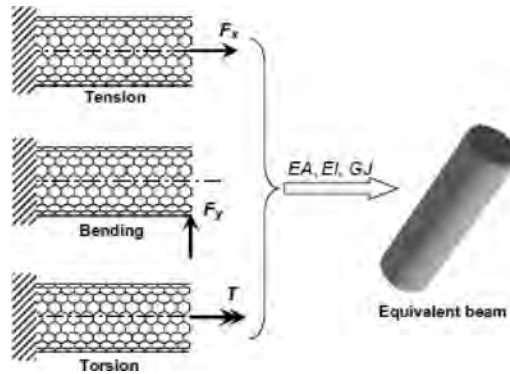


Fig. 1. The equivalent beam concept.

observed. However, it was found that the non-linear behavior of both the nanotube and the matrix have to be considered in order to evaluate more accurately the RVE behavior.

3. Mechanical behavior of reinforced polymer

Having derived the material properties of the RVE, a FE model of a CNT-composite specimen is developed (Fig. 2). Assigned to the elements of the FE model are the homogenized properties of the RVE. Then, the stiffness of the CNT-composite is evaluated as a function of nanotube orientation, which is either random or described by a given distribution. In the FE model, the nanotube orientation is considered by appropriately rotating the element coordinate system. The overall approach is validated by comparing the predicted values of stiffness with experimental values obtained from the literature. The proposed methodology can be easily applied to examine the mechanical behavior of fiber-reinforced laminates with nanotube-reinforced matrix.

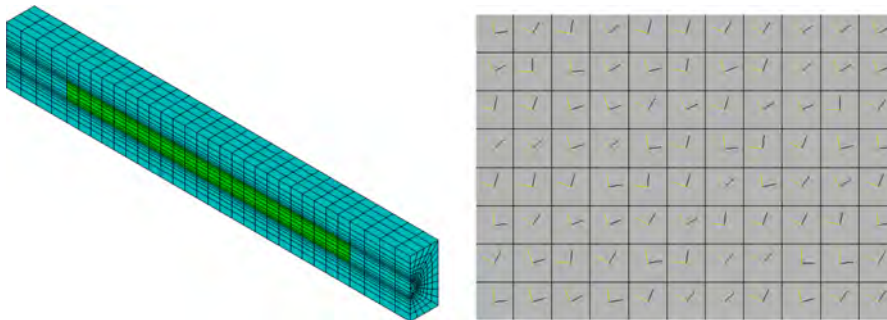


Fig. 2. Models of RVE (left) and reinforced composite (right).

References

1. D. Qian, E. Dickey, R. Andrews, T. Rantell (2000). Load transfer and deformation mechanisms in carbon nanotube-polystyrene composites, *Applied Physics Letters*, **76**, 20, 2868–2870.
2. T. Yokozeki, Y. Iwahori, S. Ishiwata (2007). Matrix cracking behaviors in carbon fiber/epoxy laminates filled with cup-stacked carbon nanotubes (CSCNTs), *Composites Part A*, **38**, 917–924.
3. K.I. Tserpes, P. Papanikos (2005). Finite element modelling of single-walled carbon nanotubes, *Composites Part B*, **36**, 468–477.
4. P. Papanikos, D.D. Nikolopoulos, K.I. Tserpes (2008). Equivalent beams for carbon nanotubes, *Computational Materials Science*, **43**, 345–352.

THE ANALYSIS OF PORE DISTRIBUTION AND PORE CONNECTIVITY IN CONCRETE SAMPLES USING X-RAY MICROTOMOGRAPHY

Z. Ranachowski¹, D. Józwiak-Niedźwiedzka¹, P. Ranachowski¹, A. Pawełek²,
S. Kudela Jr.³, T. Dvorak³

¹Institute of Fundamental Technological Research, Warsaw, Poland

²Institute of Metallurgy and Materials Science, Cracow, Poland

³Institute of Materials and Machine Mechanics, Bratislava, Slovak Republic

1. Introduction

The durability of concrete in outdoor structures is closely related to its resistance against the aggressive gaseous actions coming from the environment and including influence of oxygen, nitrogen, carbon dioxide. The pore system and its interconnectivity in the concrete matrix directly influence the possibility of penetration of various aggressive gaseous media into concrete structure. The X-ray microtomography (micro-CT) is a modern, non-invasive technique enabling for determination of existing pores in the microstructure of concrete matrix. In the paper the results of investigation of two different concretes by the application of micro-CT method to micro-cores are presented. The quantitative information on the parameters of the analysed microstructure can improve the methods of material characterization available up to now.

2. Application of X-ray microtomography in concrete microstructure analysis

The micro-CT technique and the material testing systems employed with this technique are produced by a few companies only. They are capable to perform tests on the small specimens of a few millimetres size or on larger elements. They include the micro-focal source of X-ray radiation, the movable table to place a specimen, and the flat panel with a radiation detector. The microstructure of concrete is visualized on the tomograms of the investigated specimen using grey scale convention related directly to the amount of local radiation absorption of the material. The grey scale is ordered from white related to maximum of absorption to black related to the minimum, respectively. Unhydrated cement particles and aggregate grains analysed in the micro-CT are objects of the greatest absorption. The hydration products as calcium silica hydrates that cover major part of the concrete matrix develop slightly lower absorption ability, then plates of calcium hydroxide and at the end of the scale are the regions of high porosity. The image resolution of tomograms is usually in the order of a few micrometers. The application of the micro-CT technique allows to reconstruct a real 3-dimensional image of investigated concrete micro cores and to determine the volumetric part of the material occupied by bulk matrix, aggregates, voids, pores, cracks, etc.

Slate and Olsefski [1] visualized the crack growth in compressed concrete specimens in early sixties of twentieth century. On their radiograms with resolution of 100 μm only large cracks, aggregate grains and matrix were visible. Landis *et. al.* [2] carried on compression tests of small mortar cylinders. During the experiments in compressed specimens the process of material decohesion was captured and rapid onset of the system of microcracks after exceeding the critical stress in tested mortar. On the basis of a qualitative analysis of the test results it was concluded that the area most affected by cracks appeared in the mortar of low density. Provis *et. al.* [3] tested concretes with addition of siliceous fly ash and ground granulated blast furnace slag in different proportions. The scanning

was performed on small agglomerates of particles of approx. $1 \times 1 \times 1$ mm. The aim of investigation was to trace the volume evolution of pores and to determine the time changes of connectivity within the pore system. To characterise the connectivity of pores a diffusive tortuosity T was determined. The latter parameter is constructed on the basis of the measurements of the paths created by the traces of migrating abstract particles, called ‘walkers’ using the special algorithm. The authors have reported that the pore volume decreased in linear proportion to the hardening time of specimens made with all investigated concretes. The decrease of pore volume was accompanied by the increase of their tortuosity.

3. The details of a ‘random walk’ procedure

Random walk algorithm was intended to simulate the diffusion of gases and liquids in the interconnected network of pores. At the starting point of the action a certain number of walkers was distributed randomly across the space reconstructed by means of the micro-CT scanning procedure. The walkers migrated on discrete voxels obeying the information on voxels brightness (i.e. material density). The walkers executed jumps in randomly chosen direction but the jumps could be performed if the neighbouring voxel belonged to a pore and otherwise the jumps are discarded. After refreshing the position of all walkers one epoch of its action was completed by the algorithm. The number of epochs was measured by the dimensionless integer time τ . The output of the random walk procedure is the walkers mean-square displacement $\langle r(\tau)^2 \rangle$ as a function of time (x_i, y_i, z_i are the coordinates of a current walker position and n is a number of executed epochs):

$$(1) \quad \langle r(\tau)^2 \rangle = \frac{1}{n} \sum_{i=1}^n (x_i(\tau) - x_i(0))^2 + (y_i(\tau) - y_i(0))^2 + (z_i(\tau) - z_i(0))^2.$$

The mean-square displacement is important because the diffusion coefficient D of the porous medium is related to the time-derivative of $\langle r(\tau)^2 \rangle$ and the key transport property called *tortuosity* T can be expressed as:

$$(2) \quad T = \frac{A}{d\langle r(\tau)^2 \rangle / d\tau} \quad \text{as } \tau \rightarrow \infty,$$

where A is a constant depended of image lattice parameters and when a tortuosity of the samples of the same dimensions are compared A can be assumed as 1.

4. Experimental Results

Two concrete specimens were tested using a micro-CT method and their analysed volume was appr. 410 mm^3 . The total porosity of the first one was 7.1% and of the other – 4.9%, thus their porosity ratio equalled 1.41. The total number of pores found in the reconstructed micro-CT image of the first sample was 84684 and it was 1.36 times greater than that in the other one. The mean-square displacements ratio of determined for these samples was 1.38 what means that the diffusion parameter remained in good agreement with porosity of the samples reported in [3], however it was not possible to calculate the certain values of their tortuosity.

References

1. F. Slate, S. Olsefski (1963). X-ray study of internal structure and microcracking of concrete, *J. of American Concrete Institute*, **60**, 575–588.
2. E. Landis, E. Nagy et. al. (1996). Observations of Internal Crack Growth in Mortar using X-ray Microtomography, *Proc. of the Fourth Mat. Eng. Conf., Washington, D.C., ASCE*, 82–96.
3. J.L. Provis, R.J. Myers, C.E. White (2012), X-ray microtomography shows pore structure and tortuosity in alkali-activated binders, *Cement & Concrete Research*, **42**, 855–864.

BOUNDARY VALUE PROBLEMS IN THE THEORY OF THERMOELASTICITY OF DOUBLE-POROSITY MATERIALS

M. Svanadze

Institute for Fundamental and Interdisciplinary Mathematics Research
Ilia State University, Tbilisi, Georgia

1. Introduction

The materials with double porosity play an important role in many branches of engineering, e.g., the petroleum industry, chemical engineering, geomechanics, and, in recent years, biomechanics. The theory of elasticity of double porosity media, as originally developed for the mechanics of naturally fractured reservoirs, has found applications in blood perfusion (for details, see [1]).

The quasi-static theory of elasticity for materials with double porosity is presented in [2]. In the recent years, a great attention has been paid to the theories of poroelasticity taking into account the thermal effects. The basic equations of the one and two-temperatures thermo-hydro-mechanical coupling theories for elastic materials with double porosity are presented by several authors [3, 4, 5]. In this connection, the linear theory of elastodynamics for anisotropic nonhomogeneous materials with double porosity is studied by Straughan [6], where uniqueness and stability for solutions of the initial-boundary value problem (BVP) are proved. The fundamental solutions in the theory of elasticity for materials with double porosity are constructed in [7, 8].

In the present paper, we shall consider the linear theory of thermoelasticity of double-porosity materials [4]. The properties of plane harmonic waves are established, the fundamental solutions of equations of steady vibrations are constructed, the basic external BVPs are formulated and the uniqueness theorem is proved, the basic properties of the surface (single-layer and double-layer) and volume potentials are established, the singular integral operators are studied, and finally, the existence theorems for the external BVPs are proved by means of the boundary integral equation method (potential method) and the theory of singular integral equations.

The investigation of BVPs of mathematical physics by the classical potential method has a hundred year history. This method is developed in the classical linear theories of elasticity and thermoelasticity in [9]. For an extensive review of works on the potential method, see [10].

2. Basic Equations

Let $\mathbf{x} = (x_1, x_2, x_3)$ be a point of the Euclidean three-dimensional space \mathbb{R}^3 , $\mathbf{u}(\mathbf{x})$ is the displacement vector in solid, $\mathbf{u} = (u_1, u_2, u_3)$; $p_1(\mathbf{x})$ and $p_2(\mathbf{x})$ are the pore and fissure fluid pressures, respectively, θ is the temperature measured from some constant absolute temperature T_0 , $T_0 > 0$. The system of homogeneous equations of steady vibrations in the linear theory of thermoelasticity of double-porosity materials has the following form [4]:

$$\begin{aligned}
 \mu\Delta\mathbf{u} + (\lambda + \mu)\nabla\operatorname{div}\mathbf{u} - \beta_1\nabla p_1 - \beta_2\nabla p_2 - \gamma_0\nabla\theta + \rho\omega^2\mathbf{u} &= \mathbf{0}, \\
 (k_1\Delta + a_1)p_1 + a_3p_2 + i\omega\beta_1\operatorname{div}\mathbf{u} + i\omega\gamma_1\theta &= 0, \\
 (k_2\Delta + a_2)p_2 + a_3p_1 + i\omega\beta_2\operatorname{div}\mathbf{u} + i\omega\gamma_2\theta &= 0, \\
 (k\Delta + i\omega aT_0)\theta + i\omega\gamma_0T_0\operatorname{div}\mathbf{u} + i\omega\gamma_1T_0p_1 + i\omega\gamma_2T_0p_2 &= 0,
 \end{aligned}
 \tag{1}$$

where Δ is the Laplacian operator, $a_1 = i\omega\alpha_1 - \gamma$, $a_2 = i\omega\alpha_2 - \gamma$, $a_3 = i\omega\alpha_3 + \gamma$; λ , μ , k , k_j , α_j , β_j , γ_j ($j = 1, 2$), a , γ , γ_0 and α_3 are the constitutive coefficients, ω is the oscillation frequency, $\omega > 0$, ρ is the reference mass density, $\rho > 0$.

Let S be a closed smooth surface surrounding the finite domain Ω^+ in \mathbb{R}^3 , $\bar{\Omega}^+ = \Omega^+ \cup S$, $\Omega^- = \mathbb{R}^3 \setminus \bar{\Omega}^+$, $\mathbf{n}(\mathbf{z})$ is the external unit normal vector to S at $\mathbf{z} \in S$. The basic external BVPs of steady vibrations in the linear theory of thermoelasticity of double-porosity materials are formulated as follows: find a regular (classical) solution $\mathbf{U} = (\mathbf{u}, p_1, p_2, \theta)$ to system (1) in Ω^- satisfying the boundary condition $\lim_{\Omega^- \ni \mathbf{x} \rightarrow \mathbf{z} \in S} \mathbf{U}(\mathbf{x}) \equiv \{\mathbf{U}(\mathbf{z})\}^- = \mathbf{f}(\mathbf{z})$ in the problem $(I)_{\mathbf{f}}^-$, and $\lim_{\Omega^- \ni \mathbf{x} \rightarrow \mathbf{z} \in S} \mathbf{R}(\mathbf{D}_{\mathbf{x}}, \mathbf{n}(\mathbf{z}))\mathbf{U}(\mathbf{x}) \equiv \{\mathbf{R}(\mathbf{D}_{\mathbf{z}}, \mathbf{n}(\mathbf{z}))\mathbf{U}(\mathbf{z})\}^- = \mathbf{f}(\mathbf{z})$ in the problem $(II)_{\mathbf{f}}^-$, where \mathbf{f} is the known six-component vector function and \mathbf{R} is the stress operator in the considered theory.

3. Basic results

Theorem 1. Through a solid with double porosity four longitudinal and two transverse plane harmonic waves propagate; the longitudinal plane waves are attenuated and the transverse plane waves have the constant amplitude.

Theorem 2. The external BVPs $(I)_{\mathbf{f}}^-$ and $(II)_{\mathbf{f}}^-$ have one regular solution.

Theorem 3. If $S \in C^{2,\nu}$, $\mathbf{f} \in C^{1,\tau}(S)$, $0 < \tau < \nu \leq 1$, then a regular solution of the external BVP $(I)_{\mathbf{f}}^-$ exists, is unique and is represented by sum $\mathbf{U}(\mathbf{x}) = \mathbf{Z}^{(2)}(\mathbf{x}, \mathbf{g}) - i\mathbf{Z}^{(1)}(\mathbf{x}, \mathbf{g})$ for $\mathbf{x} \in \Omega^-$, where $\mathbf{Z}^{(1)}(\mathbf{x}, \mathbf{g})$ and $\mathbf{Z}^{(2)}(\mathbf{x}, \mathbf{g})$ are the single-layer and double-layer potentials, respectively, and \mathbf{g} is a solution of the singular integral equation $\frac{1}{2}\mathbf{g}(\mathbf{z}) + \mathbf{Z}^{(2)}(\mathbf{z}, \mathbf{g}) - i\mathbf{Z}^{(1)}(\mathbf{z}, \mathbf{g}) = \mathbf{f}(\mathbf{z})$ for $\mathbf{z} \in S$ which is always solvable for an arbitrary vector \mathbf{f} .

Theorem 4. If $S \in C^{2,\nu}$, $\mathbf{f} \in C^{0,\tau}(S)$, $0 < \tau < \nu \leq 1$, then a regular solution of the external BVP $(II)_{\mathbf{f}}^-$ exists, is unique and is represented by sum $\mathbf{U}(\mathbf{x}) = \mathbf{Z}^{(1)}(\mathbf{x}, \mathbf{g}) + \mathbf{V}(\mathbf{x})$ for $\mathbf{x} \in \Omega^-$, where \mathbf{g} is a solution of the singular integral equation $-\frac{1}{2}\mathbf{g}(\mathbf{z}) + \mathbf{R}\mathbf{Z}^{(1)}(\mathbf{z}, \mathbf{g}) = \mathbf{f}_1(\mathbf{z})$ for $\mathbf{z} \in S$ which is always solvable for an arbitrary vector \mathbf{f}_1 , \mathbf{V} is a solution of the BVP $(I)_{\mathbf{f}_2}^-$, \mathbf{f}_1 and \mathbf{f}_2 are the known six-component vector functions.

References

1. S.C. Cowin (1999). Bone poroelasticity, *J. Biomechanics*, **32**, 217–238.
2. R.K. Wilson, E.C. Aifantis (1982). On the theory of consolidation with double porosity – I, *Int. J. Engng. Sci.* **20**, 1009–1035.
3. N. Khalili, A.P.S. Selvadurai (2003). A fully coupled constitutive model for thermo-hydro-mechanical analysis in elastic media with double porosity, *Geophys. Res. Letters*, **30**, 2268.
4. R. Gelet, B. Loret, N. Khalili (2012). Borehole stability analysis in a thermoporoelastic dual-porosity medium, *Int. J. Rock Mech. Mining. Sci.*, **50**, 65–76.
5. M. Bai, J.C. Roegiers (1994). Fluid flow and heat flow in deformable fractured porous media, *Int. J. Engng. Sci.*, **32**, 1615–1633.
6. B. Straughan (2013). Stability and uniqueness in double porosity elasticity, *Int. J. Engng. Sci.*, **65**, 1–8.
7. M. Svanadze (2013). Fundamental solution in the linear theory of consolidation for elastic solids with double porosity, *J. Math. Sci.*, **195**, 258–268.
8. M. Svanadze, S. De Cicco (2013). Fundamental solutions in the full coupled linear theory of elasticity for solid with double porosity, *Arch. Mech.*, **65**, 367–390.
9. V.D. Kupradze, T.G. Gegelia, M.O. Bashaishvili, T.V. Burchuladze (1979). *Three-Dimensional Problems of the Mathematical Theory of Elasticity and Thermoelasticity*, North-Holland, Amsterdam, New York, Oxford.
10. T. Gegelia, L. Jentsch (1994). Potential methods in continuum mechanics, *Georgian Math. J.*, **1**, 599–640.

FINDING SECOND-ORDER NONSYMMETRIC THERMOELASTIC PROPERTIES OF GRAPHENE MONOLAYER USING LATTICE STATICS APPROACH

I. Yu. Zubko, V. I. Kochurov, R. S. Gorodilov

Perm National Research Polytechnic University, Perm, Russia

1. Introduction

Graphene has recently been one of the most intensively researched crystal materials. It is partly due to the production of composite materials reinforced with carbon nanotubes and other carbon nanoparticles which are actually different structures based on graphene; and due to challenges in predicting physical and mechanical properties of such composites.

The known graphene experimental studies are performed using the atomic force microscopy methods. The obtained results are identified according to exact solutions for elastic rods or membranes. Such methods of the elastic moduli estimation are quite rough. Another method of experimental determination of some graphene mechanical characteristics provides tests with graphite samples which are sets of graphene layers. Usually the Young's modulus and the Poisson's ratio are studied in experiments. One of the serious disadvantages of the experimental methods is that they are not suitable for more or less complicated carbon nanostructures. Another shortcoming of *in-situ* experiments is impossibility to directly measure the second-order elastic moduli. But the discrete computational lattice approach is supposed to give enough adequate estimation of any elastic properties for any carbon nanoparticles in the case of the appropriately chosen interatomic potential and the values of their parameters.

So the aim of this paper is to ground the choice of interatomic potential, identification of its parameters using experimental data for the Young's modulus, Poisson's ratio and bending rigidity and finding the second-order elastic moduli of graphene monolayer. Also the questions of heating simulation in the lattice statics approach and changing of elastic moduli under the heating are of the great interest in this study.

2. Basic assumptions and methods of elastic properties computation

In order to eliminate the influence on the elastic moduli values caused by the mutual superposition of the sample and lattice symmetry classes, the computational experiments are performed with graphene sample of the hexagonal shape possessing the triad axis symmetry.

The crystal structure in any configuration is considered to be homogeneous along the sample and fully characterized with a parameter value of the interatomic distance. We impose that the initial configuration of graphene monolayer is characterised only by the value of parameter a , which is considered to be a variable and calculated as a minimiser for the full potential energy. The homogeneous crystal deformation is obtained according to the Cauchy-Born rule as a result of changes of lengths and angles between the straight lines connecting the atoms, they are described with the second-rank tensor corresponding to an affiner (or a deformation gradient tensor) \mathbf{F} used in continuum mechanics (although it is not a gradient of any continuous displacement field).

The density of elastic energy is adopted in the following form for small deformations

$$(1) \quad u = \frac{1}{2}(\mathbf{F} - \mathbf{I} - \mathbf{w}_{\#}) : \mathbf{C} : (\mathbf{F} - \mathbf{I} - \mathbf{w}_{\#}) + \frac{1}{2}(\nabla \omega_{\#})^T : \mathbf{D} : (\nabla \omega_{\#})^T,$$

where \mathbf{I} is the unit second rank tensor, $\mathbf{w}_{\#}$ is tensor of small lattice rotation, $\omega_{\#}$ is the axial vector for the tensor $\mathbf{w}_{\#}$, \mathbf{C} and \mathbf{D} are nonsymmetric fourth rank tensor of elastic moduli and the second-order elastic properties correspondently. Tensor $\nabla \omega_{\#}$ imposes

the in-plane lattice curvature (Fig. 1a, b) and bending deformation as well (Fig. 1c). Such form is obtained from general formulation for the elastic energy density of Cosserat continuum, introduced in [3] for the case of large deformation. In order to compute the elastic moduli of graphene using the lattice statics approach, the potential energy in the actual configuration is found, divided by the area of the deformed graphene layer and equated with the elastic energy density (1). All elastic moduli are found as second derivatives of the potential energy density by components of deformation measures.

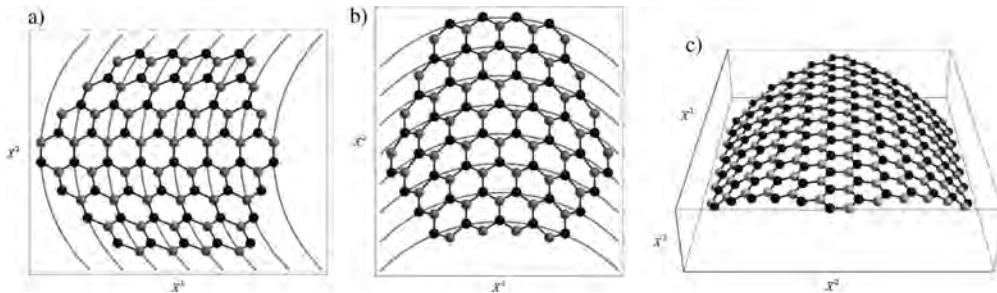


Fig. 1. In-plane curved and bended configurations of graphene monolayer.

The set of interatomic potentials including Tersoff, Brenner [1–2, 4] and other formulations was considered. The new empiric potential reflecting the geometry of sp^2 -gibritised covalent bonding and partially based on the Mie family potentials was suggested. After identification of parameters this potential allows obtaining very precise estimations simultaneously for the atom spacing, Young’s modulus, Poisson’s ratio and bending rigidity of graphene lattice.

For the aim of the crystal temperature control the computational-statistical approach to studying thermo-mechanical properties for finite sized crystals is presented. We suggest imitating heat oscillations of the atoms by applying random perturbations with the fixed amplitude A on the system of atoms under the uniform distribution of directions for the atoms shifts in space.

3. Results

It is shown that the homogeneous deformation of graphene monolayer transfers it into the non-equilibrium state. It is necessary to take into account inner displacements of one “triangular” sublattice with respect to another sublattice in order to provide the sample minimum potential energy in a deformed state, while each sublattice is deformed homogeneously. It was found that the inner displacements vector is linearly connected to the distortion tensor or linear tensor of small deformations by the third-rank tensor introduced in this work.

All graphene parameters are found to be depended on the specimen size and temperature. The bending rigidity is isotropic. The elastic moduli tensor \mathbf{C} is symmetric and isotropic at low temperature. Tensor \mathbf{D} of the second-order elastic properties is non-symmetric at any temperature. It is also shown that tensor \mathbf{C} for graphene becomes nonsymmetric under heating.

References

1. D.W. Brenner (1990). Empirical potential for hydrocarbons for use in simulating the chemical vapor deposition of diamond films, *Phys. Rev. B*, **15**, 9458–9471.
2. D.W. Brenner, O.A. Shenderova, J.A. Harrison, S.J. Stuart, B. Ni, S.B. Sinnott (2002). A second-generation reactive empirical bond order (REBO) potential energy expression for hydrocarbons, *J. Phys.: Condens. Matter.*, **14**, 783–802.
3. W. Pietraszkiewicz, V.A. Eremeyev (2009). On natural strain measures of the nonlinear micropolar continuum, *International Journal of Solids and Structures*, **46**, 774–787.
4. J. Tersoff (1988). New empirical approach for the structure and energy of covalent system, *Phys. Rev. B*, **37**, 6991–7000.

Session

**Micromechanics, Interfaces
and
Multi-Scale Modelling**

MODELLING OF MICROSTRUCTURE EVOLUTION IN HCP POLYCRYSTALS ON NON-PROPORTIONAL STRAIN PATHS

K. Frydrych, K. Kowalczyk-Gajewska, S. Stupkiewicz

Institute of Fundamental Technological Research, Warsaw, Poland

1. Introduction

Microstructure evolution in hcp polycrystals subjected to severe plastic deformation, in particular in the KOBO extrusion [1] and the equal channel angular pressing (ECAP) processes [2], are examined in this work, using the crystal plasticity framework. The ECAP process consists in pressing a billet through the bent equal channel (without changing billet dimensions). Often there are many passes with rotations about the billet longitudinal axis. Standard sequences of such rotations are named routes A, Ba, Bc or C. Texture evolution in ECAP differs depending on the route and the number of passes [2]. The KOBO process consists in extruding material at room temperature with assistance of cyclic rotation of a die. Deformation paths in KOBO process are strongly position-dependent, which affects microstructure of obtained material. Both processes lead to considerable grain refinement, so they could be considered as tools enabling tailoring of material microstructure. In order to use these tools effectively, valid modeling approach is necessary.

2. Modelling framework

Modelling approach combines the large strain crystal plasticity model accounting for twinning [3] and the tangent variant of the self-consistent (SC) scale transition scheme [4]. Since elastic stretches are much smaller than plastic strains, elastic part of deformation gradient is neglected. Averaging responses of individual grains in the representative volume element (RVE) provides the response of polycrystalline aggregate. Calculations have been made using the VPSC code [4] with own procedures for the probabilistic twin volume consistent (PTVC) reorientation scheme and the hardening model accounting for slip-twin interactions [3] implemented into the program.

Simulations have been performed for two materials of high specific strength i.e.: titanium and magnesium alloys. Material parameters for titanium (Table 1) have been estimated by comparing pole figures, stress-strain curves and slip activity graphs with those shown in [5]. Four slip systems have been taken into account: prismatic $\{0110\}\langle 2110 \rangle$, basal $\{0001\}\langle 2110 \rangle$, pyramidal $\langle c+a \rangle\{1011\}\langle 1210 \rangle$. Tensile twinning mode $\{1012\}\langle 1011 \rangle$ has been also considered. Slip and twin systems and material parameters in AZ31B magnesium alloy have been taken from [3].

Table 1. Active slip and twinning modes for Ti and their parameters (notation as in [3]).

Slip/Twin mode	τ_{c0}	τ_r^{sat}	β	h_0^{ss}/h_0^{ts}	$f_{\text{sat}}^{st}/f_{\text{sat}}^{tt}$	h_0^{st}/h_0^{tt}	μ	$q_{rq}^{*\text{PI}}$	$q_{rq}^{*\text{bas}}$	$q_{rq}^{*\text{PVT}}$	q_{rq}^{*tt}	$\gamma = c/a$
prismatic	30	70	1	50	1.0	10^{-5}	2.00	1	1	1	10	–
basal	40	42	1	86	1.0	10^{-5}	1.50	1	1	1	10	–
pyramidal $\langle c+a \rangle$	159	–	–	0	2.0	10^{-5}	2.00	1	1	1	2	–
tensile twinning	40	–	–	240	1.0	10^{-5}	0.75	1	1	1	10	0.514

3. Results

Selected results of texture simulation for initially untextured hcp materials are presented in Figs. 1–2. Microstructural changes have been investigated along the deformation trajectories according to the procedure described in [6]. The results will be compared with available experimental data.

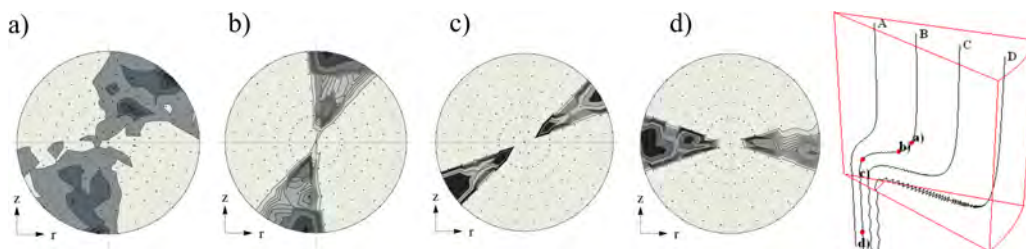


Fig. 1. (0001) pole figures of pure Ti in the KOBO process (process parameters $\phi_0 = \pm 6^\circ$, $do : d = 35 : 8$ [mm], $f = 5$ [Hz], $V_0 = 0.5$ [mm/s]) for trajectory B ($r_0 = 8$ mm) for accumulated plastic strain: a) 0.26, b) 1.11, c) 3.26, d) 3.74.

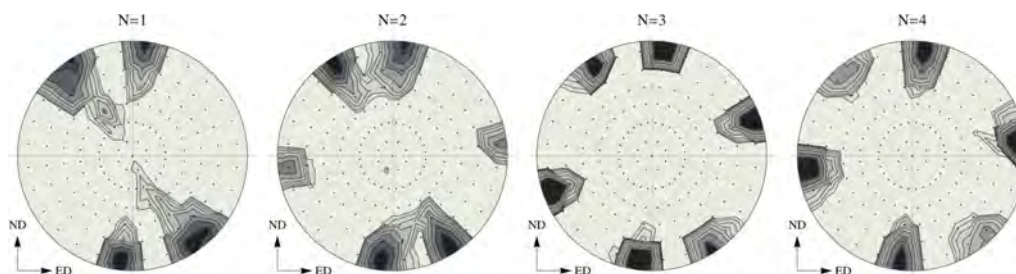


Fig. 2. (0001) pole figures of AZ31B Mg alloy after 1–4 ECAP passes (Route C).

Acknowledgments

The research were partially supported by the project of the National Science Center (NCN) granted by the decision No. DEC-2013/09/B/ST8/03320.

References

1. A. Korbel, W. Bochniak (1995). The structure based design of metal forming operations, *J. Mat. Proc. Technol.*, **53**, 229–237.
2. I.J. Beyerlein, L.S. Toth (2009). Texture evolution in equal-channel angular extrusion, *Progress Mater. Sci.*, **54**, 427–510.
3. K. Kowalczyk-Gajewska (2011). *Micromechanical Modelling of Metals and Alloys of High Specific Strength*, IFTR Reports, Warsaw.
4. R.A. Lebensohn, C.N. Tome (1993), A self consistent anisotropic approach for the simulation of plastic deformation and texture development of polycrystals: application to zirconium alloys, *Acta metall. Mater.*, **41**, 2611–2624.
5. A.A. Salem, S.R. Kalidindi, S.L. Semiatin (2005). Strain hardening due to deformation twinning in α -titanium: Constitutive relations and crystal-plasticity modeling, *Acta Mater.*, **53**, 3495–3502.
6. K. Kowalczyk-Gajewska, S. Stupkiewicz, K. Frydrych, H. Petryk (2014). Modelling of texture evolution and grain refinement on complex SPD paths, *IOP Conf. Ser.: Mater. Sci. Eng.*, (submitted) NanoSPD6 Conference.

EVOLVING MICROSTRUCTURES FOR SCALABLE ACTUATION IN PROGRAMMABLE MATTER

P. Hołobut¹, M. Kursa¹, A. Macios², J. Lengiewicz¹

¹Institute of Fundamental Technological Research, Warsaw, Poland

²Faculty of Mathematics and Information Science, Warsaw University of Technology, Poland

1. Introduction

Programmable Matter (PM) is a class of future meta-materials of programmable and controllable properties and behavior, e.g., able to autonomously transform into an arbitrary shape [1]. Currently, the most advanced approach towards PM comes from the field of self-reconfigurable robots. The main concept is a cooperation of millions of microrobots (modules), collectively imitating deformation of a macroscopically continuous material. The modules' connection topology can change, which distinguishes PM from simpler active structures like the actuated truss [2].

Much research has been done on the geometric problem of planning reconfiguration of a group of cooperating modules, to transform their initial arrangement into a desired one. On the other hand, the problem of using PM for performing mechanical tasks, like lifting external objects, has rarely been discussed [3, 4]. The present work partially addresses this issue.

2. Concept of evolving microstructures

The present analysis is based on a spherical module design, the so-called *catom* [3, 4]. It is superior to many other designs in that it has no moving parts and can be miniaturized more easily. It uses electrostatic forces for attachment and actuation – the charging of electrodes inside adjacent modules causes their attraction/repulsion and rotation (Fig. 1a). This type of actuation, however advantageous, has limited strength. Therefore structures, built only from electrostatically connected catoms, are not expected to perform useful mechanical work, since they are roughly only as strong as the sum of electrostatic connections in their cross-sections.

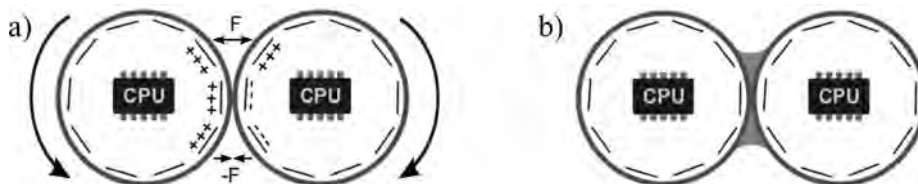


Fig. 1. Electrostatic (a) and fixed/strong (b) connections between modules.

In the present work a special arrangement of modules is therefore proposed, the *evolving microstructures*, which can potentially produce forces that scale with the volume of a structure. The modules are divided into groups connected by *fixed* connections and groups of *active* modules, propelled electrostatically (Fig. 2). The fixed connections do not need to reconfigure while the structure is moving, and can be assumed significantly stronger inasmuch as some other physical mechanism than electrostatic can be used for attachment. The first (fixed) group form supporting frames for the structure (gray and blue modules in Fig. 2), which transform PM into a macroscopic mechanism and integrate local stresses into an overall force. The second group of modules (red and yellow) provide

the basic micro-actuation mechanism. In the exemplary structure shown in Fig. 2, the red (yellow) modules roll over the wall of gray (blue) modules without sliding, and push adjacent gray and blue walls in opposite directions.

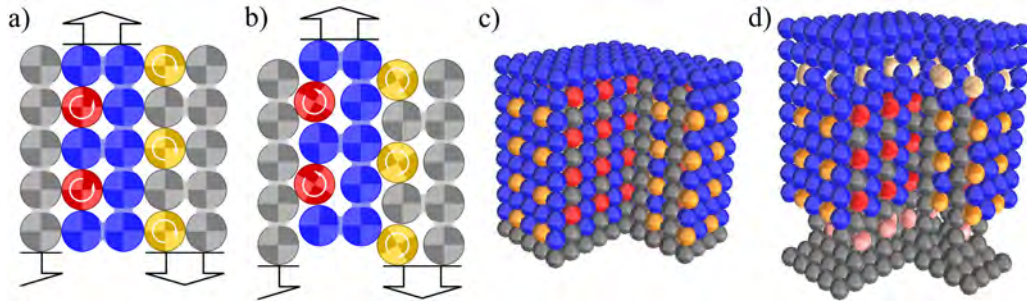


Fig. 2. Exemplary evolving microstructure at an initial stage and in motion: schematics, (a) and (b), and snapshots from a DEM simulation of a square linear actuator, (c) and (d).

3. Results

The behavior of evolving microstructures has been simulated using the Yade DEM system [5], modified to allow controllable attachment and detachment of modules. Fixed connections are modeled as strong cohesive interactions, which prevents unwanted detachment or sliding. The employed 6-degree-of-freedom contact law enforces elastic moments at contact points, preventing modules from rolling over one another. Electrostatic connections are modeled using similar cohesive interactions, but without elastic moments at contacts, which allow free rolling between modules. Additionally, torques are imposed on active modules to simulate electrostatic actuation.

In parallel with the DEM model, a simple micromechanical analytical model has also been developed. Analyses conducted with both models, for several types of actuators, show good agreement of results. Exemplary quasi-static force-elongation responses for square linear actuators, built from modules of radius $r = 65 \mu\text{m}$, each exerting an electrostatic torque of 16 pNm, are shown in Fig. 3. The expected result that the overall force scales with volume is shown in Fig. 3b.

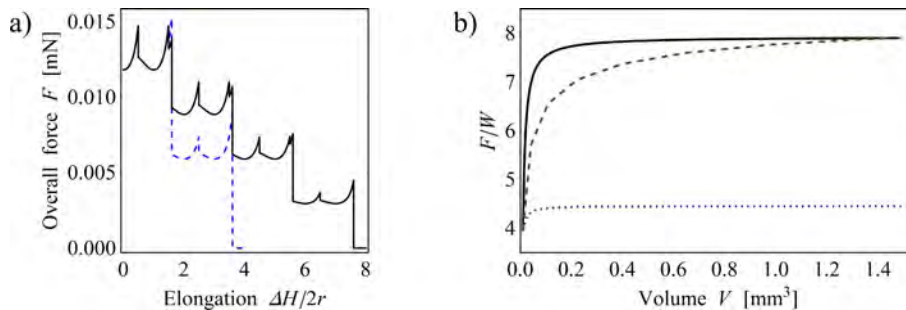


Fig. 3. Force vs elongation (a) and force/weight vs volume (b) plots for actuators as in Fig. 2 of different relative dimensions.

References

1. S.C. Goldstein, J.D. Campbell, T.C. Mowry (2005). Programmable Matter, *IEEE Computer*, **38**, 99–101.
2. C.J. Thore, A. Klarbring (2012). Modeling and optimal design of Neuro-Mechanical Shape Memory Devices, *Struct. Multidisc. Optim.*, **45**, 257–274.
3. J. Campbell, P. Pillai (2008). Collective actuation, *Int. J. Rob. Res.*, **27**, 299–314.
4. D.J. Christensen, J. Campbell, K. Stoy (2010). Anatomy-based organization of morphology and control in self-reconfigurable modular robots, *Neural Comput. Appl.*, **19**, 6, 787–805.
5. Yade – Open Source Discrete Element System, <http://yade-dem.org>.

RECENT DEVELOPMENTS IN ATOMISTIC AND ATOMISTIC-CONTINUUM MODELLING FOR MATERIALS DEVELOPMENT

S. Schmauder

Institute for Materials Testing, Materials Science and Strength of Materials
University of Stuttgart, Stuttgart, Germany

1. Summary

In recent years, innovations in materials development require more and more information from all length scales, as material properties are based on atomistic and on microstructural features as well as on properties on macroscopic scales. Therefore, multiscale material modelling (MMM) has become an ever increasing market and the nucleation point for improved and new materials. In this contribution, several examples of material innovations are presented which are based on numerical approaches taking relevant scale dependent properties into account.

This multiscale approach requires different numerical methods ranging from atomistic to continuum methods in order to simulate molecular and non-molecular processes for metallic and non-metallic materials as well as for composites made of strongly different components.

2. Methods

In this presentation, the methods required for successfully developing innovative improved materials are presented first. These methods comprise ab initio, Monte Carlo (MC) and Molecular Dynamics (MD) methods on the atomistic length scales and Phase Field Modelling (PFM) on the mesoscale as well as Finite Element Methods (FEM) on micro and macro length scales.

The combination of different length scales is shown to be dependent on transfer parameters which provide the relevant information from length scale to length scale.

3. Material systems

The material systems discussed here range from classical steels [1] via Dual Phase (DP) steels to metal matrix composites (MMCs) and metal/ceramic interface dominated materials. However, this approach is not limited to classical materials but also polymer matrix composites, fiber matrix composites or hybride layered materials.

4. Procedures

In the present paper, it will be shown that not only several length and time scales are required but also several methods have to be involved for performing successful hierarchical analyses with quantitative results in the field of modern materials research.

In addition, studies will be presented which provide the basis for the development of new material alloys when taking ab-initio, Monte Carlo or Molecular Dynamics modelling approaches into account. As an example solid solution hardening is considered for Fe-base materials where property predictions are in close agreement to experimental findings

5. Results

Results comprise the mechanical or thermal behavior of these materials [2] which is shown to be in very good agreement with experiments. Experimental findings on small, medium and macroscopic length scales are compared to the numerical results.

Amongst those are typically strengthening levels of solid solution strengthened materials with different dissolved atoms e.g. in Fe [3] or Al light metals. Other strengthening mechanisms such as particle [4] or fiber reinforced materials are also successfully modeled and compared with experiments and similarly particles which can be cut by dislocations are simulated successfully.

A typical macroscopic strengthening result of solid solution hardened Fe-based materials is shown in Fig. 1.

Furthermore, present day approaches are even dedicated to fatigue modelling on all length scales which may even have the potential to predict fatigue life based on coupled atomistic-microscale-macroscale analyses for individual structural materials with well-defined microstructures [5].

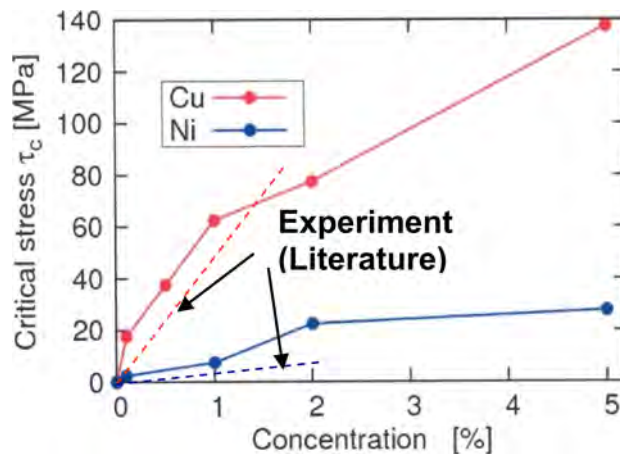


Fig. 1. Comparison of experimentally and numerically derived strengthening levels of solid solution hardened Fe-based materials.

References

1. S. Schmauder, D. Uhlmann, G. Zies (2001). Experimental and numerical investigations of two material states of the material 15 NiCuMoNb (WB 36), *Computational Materials Science*, **25**, 174–192.
2. S. Schmauder (2009). Simulation als Instrument der Werkstoffentwicklung, *Metall*, **63**, 295–297.
3. S. Schmauder, C. Kohler (2011). Atomistic simulations of solid solution strengthening of α -Fe, *Computational Materials Science*, **50**, 1238–1243.
4. S. Schmauder, U. Weber, A. Reuschel, M. Willert (2011). Simulation of the Mechanical Behaviour of Metal Matrix Composites, *Materials Science Forum*, **678**, 49–60.
5. Z. Bozic, S. Schmauder, M. Mlikota, M. Hummel (2014). Multiscale fatigue crack growth modelling for welded stiffened panels, *Fatigue & Fracture of Engineering Materials & Structures* (accepted).

VARIATIONAL SETTINGS IN MECHANICS OF WEAR

A. Zmitrowicz

Institute of Fluid-Flow Machinery, Gdańsk, Poland

1. Introduction

In the published literature, the principle of stationary total potential energy, the virtual work principle and their generalizations are often used in variational formulations of contact problems, i.e. in deformation descriptions of contacting solids. Several techniques are applied to fulfil the kinematic contact constraints and to calculate contact forces: variational inequalities, the Lagrange multiplier method, the penalty method, mathematical programming methods and others [1, 2].

An effective way to solve wear problems could be given by variational formulations and an approximation with the aid of finite element method. In this contribution we proceed using the variational formalism. Our aim is to obtain the complete set of governing relations describing mechanics of wear. Several generalizations of classical variational principles are presented in the case of wear problems. An advantage of this approach is that more accurate models of friction and wear can be easily implemented.

2. Key factors in wear analysis

Wear is identified with a gradual removal of material from rubbing surfaces of solids. Irreversible changes in bodies contours and an increase of a clearance gap between contacting solids are the main results of wear. An amount of the removed material can be estimated with the aid of a wear profile. A definition of a clearance gap between two contacting bodies includes deformations of the bodies and the gap evolution as a result of the wear process [3, 4].

The mechanism of wear involves formation of loose wear particles detached from the rubbing surfaces. The wear particles are trapped and accumulated between the sliding surfaces for some period of time. They form almost continuous intermediate layer which separates the rubbing surfaces. The wear particles transmit loads and displacements at the contact interface. The presence of wear particles between sliding surfaces affects friction and wear processes significantly [5].

Different constitutive models describe quasi-solid, quasi-fluid and granular-like behaviour of wear debris. In the discrete formulation each particle is considered as the isolated solid body (granular material) and motion equations are applied to each particle. In the continuum formulation the wear debris are treated as a single two-dimensional layer. In this contribution, the layer is considered as a continuum with own morphology, kinematics and constitutive models (micropolar thermoelastic layer). Small deformations and small micro-rotations are considered in the layer. Two governing equations define displacements and micro-rotations.

3. Wear effects and variational formulations of deformations and heat conduction

The objective of mechanics of wear is to determine profiles of external boundaries of wearing out solids, and to include an effect of wear debris on deformations of the rubbing bodies. Strong forms of governing equations for the contacting solids are constructed

from general balance laws: mass, momentum, moment of momentum, energy and entropy. Additional terms in the governing equations define a mass of wear debris supplied to the intermediate layer during the course of the wear process.

For numerical solutions of the contact problems with the aid of the finite element method one needs weak forms of the governing equations. A variational description of deformations of the contacting bodies is presented with the aid of the principle of stationary total potential energy. The total potential energy is defined in a deformed configuration of two contacting solids and the thin intermediate layer of wear particles. Furthermore, variational settings of the heat conduction (in the contacting bodies) and the mass continuity problem (in the layer) are discussed. The heat is generated by the friction process.

To solve the contact problems the incremental formulation and iteration procedures must be taken. We search such fields of displacements, temperatures and the mass intensity which guarantee the stationarity of the variational functionals at the given step of incremental approach and the iteration process. The stationarity condition of the total potential energy for any finite element leads to equations of displacements in the bodies and in the layer, and to equations of micro-rotations in the layer. The variational formulations and constrained methods (the Lagrange multiplier method, the penalty method and their generalizations) provide a powerful tool to solve the contact and wear problems.

4. Conclusions

In the contribution strong and weak formulations are given in the case of contact problems for wearing out solids. Classical variational formulations are extended by including an increase of the gap due to the wear process, and by taking into account the intermediate layer of wear particles. In this way the wear effects are introduced into the variational formulations of deformations and heat conduction. Proposed formulations can be useful in numerical analysis of machine parts subject to the wear process. There is a great need to improving the wear-resistance machinery components.

References

1. J.J. Telega (1988). Nierówności wariacyjne w zagadnieniach kontaktowych mechaniki, [w:] *Mechanika kontaktu powierzchni*, Z. Mróz (ed.), Ossolineum, Wrocław, 51-165.
2. R. Weyler, J. Oliver, T. Sain, J.C. Cante (2012). On the contact domain method: A comparison of penalty and Lagrange multiplier implementations, *Comput. Methods Appl. Mech. Engrg.*, **205-208**, 68–82.
3. I. Pączelt, Z. Mróz (2012). Solution of wear problems for monotonic and periodic sliding with p -version of finite element methods, *Comput. Methods Appl. Mech. Engrg.*, **249-252**, 75–103.
4. J. Langiewicz, S. Stupkiewicz (2012). Continuum framework for finite element modelling of finite wear, *Comput. Methods Appl. Mech. Engrg.*, **205-208**, 178–188.
5. A. Zmitrowicz (2001). Variational descriptions of wearing out solids and wear particles in contact mechanics, *Journal of Theoretical and Applied Mechanics*, **39**, 3, 791–808.

Session

Plates and Shells

SOME ASPECTS OF BUCKLING IN GEOMETRICALLY AND MATERIALLY NONLINEAR CYLINDRICAL SHELLS

S. Burzyński, J. Chróścielewski, W. Witkowski

Gdańsk University of Technology, Gdańsk, Poland

1. Introduction

We discuss some aspects of the elastic buckling and elastoplastic analysis of cylindrical shell. The constitutive relations for the shell stress resultants and stress couples are formulated by through-the-thickness integration of the Cosserat plane stress, [1]. A J_2 -type theory is taken into account in the plastic analysis. The formulated incremental equations are solved using the closest point projection scheme.

2. Constitutive relation

Components of the kinematic relations $\varepsilon_\beta = \mathbf{u}_{,\beta} + (\mathbf{1} - \mathbf{Q})\mathbf{t}_\beta^0$, $\kappa_\beta = \text{axl}(\mathbf{Q}_{,\beta} \mathbf{Q}^T)$, [2], are collected in the vector

$$(1) \quad \boldsymbol{\varepsilon} = \{\varepsilon_{11} \ \varepsilon_{22} \ \varepsilon_{12} \ \varepsilon_{21} \mid \varepsilon_1 \ \varepsilon_2 \mid \kappa_{11} \ \kappa_{22} \ \kappa_{12} \ \kappa_{21} \mid \kappa_1 \ \kappa_2\}^T = \{\boldsymbol{\varepsilon}_m \mid \boldsymbol{\varepsilon}_s \mid \boldsymbol{\varepsilon}_b \mid \boldsymbol{\varepsilon}_d\}^T,$$

where labels m, s, b, d denote, respectively: the membrane, shear, bending and drilling parts. To Eq. (1) we adjoin the vector of shell stress resultants and stress couples

$$(2) \quad \mathbf{s} = \{N^{11} \ N^{22} \ N^{12} \ N^{21} \mid Q^1 \ Q^2 \mid M^{11} \ M^{22} \ M^{12} \ M^{21} \mid M^1 \ M^2\}^T = \{\mathbf{s}_m \mid \mathbf{s}_s \mid \mathbf{s}_b \mid \mathbf{s}_d\}^T.$$

The constitutive relation $\mathbf{s} = \mathbf{C} \boldsymbol{\varepsilon}$ relates (2) to (1). The elastic or elastoplastic operator \mathbf{C} is developed from integrals (see [5])

$$(3) \quad \mathbf{s}_m = \int_{-h^-}^{+h^+} \boldsymbol{\sigma}_m \mu \, d\zeta, \quad \mathbf{s}_b = \int_{-h^-}^{+h^+} \boldsymbol{\sigma}_m \zeta \mu \, d\zeta, \quad \mathbf{s}_d = \int_{-h^-}^{+h^+} l \cdot \boldsymbol{\sigma}_d \mu \, d\zeta,$$

where $\boldsymbol{\sigma} = \{\boldsymbol{\sigma}_m \mid \boldsymbol{\sigma}_d\}^T = \{\sigma_{11} \ \sigma_{22} \ \sigma_{12} \ \sigma_{21} \mid m_1/l \ m_2/l\}^T$ are stress and couple-stress components of the plane stress state in the Cosserat continuum (see [2]). These are conjugated with shell strain and bending components $\mathbf{e} = \{\mathbf{e}_m \mid \mathbf{e}_d\}^T = \{e_{11} \ e_{22} \ e_{12} \ e_{21} \mid \kappa_1/l \ \kappa_2/l\}^T$ obtained from (1) under the Reissner-Mindlin kinematical assumption. It is necessary to introduce additional material parameters: l – characteristic length and G_c – shear modulus (for constitutive relations see [3]). Elastoplastic formulation is of J_2 -type, with generalization [3] of the second invariant of deviatoric stresses

$$(4) \quad J_2 = \frac{1}{3}\sigma_{11}^2 + \frac{1}{3}\sigma_{22}^2 - \frac{1}{3}\sigma_{11}\sigma_{22} + \frac{1}{4}\sigma_{12}^2 + \frac{1}{2}\sigma_{12}\sigma_{21} + \frac{1}{4}\sigma_{21}^2 + \frac{1}{2}((m_1/l)^2 + (m_2/l)^2).$$

3. Numerical example

In the numerical example we consider the cylindrical shell with imposed shear deformation (Fig. 1a) [4]. Due to symmetry, we use 12x12 16-node CAM elements (see [2]) for one half of the shell. At graphs, on vertical axis, we present sum of reactions in z -direction on upper edge. Elastoplastic analysis (Fig. 1b) shows excellent agreement with reference elastoplastic solution [4], shell deforms with visible action of the tension field. We next

extend the research to non-linear stability analysis in elastic regime (Fig. 1c). Here shell deformation is practically smooth until the bifurcation point is reached, where secondary paths lead to two possible shapes of sheared shell, with the point (B) having inward or outward translation (Fig. 1d, paths 1, 2, 3 refer to points marked in Fig. 1c).

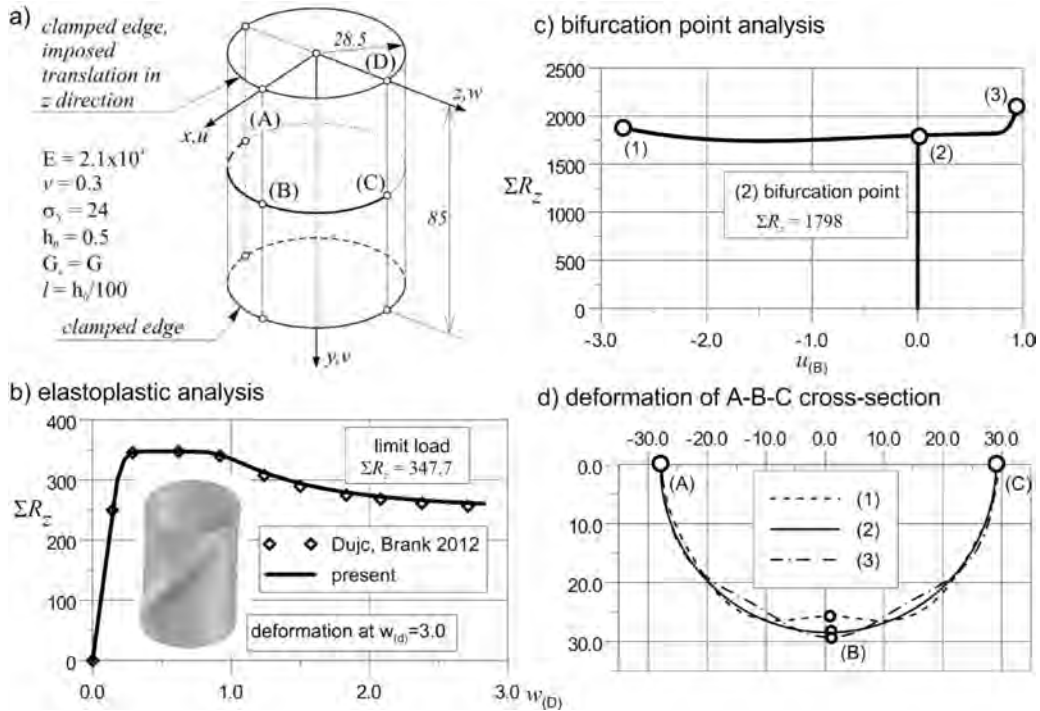


Fig. 1. Cylinder under shear load a) geometry b), c), d) results.

Acknowledgment

Stanisław Burzyński is supported by National Science Centre of Poland grant DEC-2012/05/D/ST8/02298.

References

1. S. Burzyński, J. Chrościelewski, W. Witkowski (2014). Elastoplastic material law in 6-parameter non-linear shell theory, In: W. Pietraszkiewicz, J. Górski (eds.), *Shell Structures: Theory and Applications*, Vol 3, CRC Press, London, 377–380.
2. J. Chrościelewski, J. Makowski, W. Pietraszkiewicz (2004). *Statics and Dynamics of Multifold Shells: Nonlinear Theory and Finite Element Method* (in Polish), Wydawnictwo IPPT PAN, Warsaw.
3. R. De Borst (1991). Simulation of strain localization: a reappraisal of the Cosserat continuum, *Engineering Computations*, **8**, 317–332.
4. J. Dujc, B. Brank (2012). Stress resultant plasticity for shells revisited, *Computer Methods in Applied Mechanics and Engineering*, **247-248**, 146–165.
5. T. Lewiński, J.J. Telega (2000). *Plates, Laminates and Shells, Asymptotic Analysis and Homogenization*, World Scientific.

ON A VARIATIONAL PROBLEM FOR A CUSPED ELASTIC PRISMATIC SHELLS
IN CASE OF THE THIRD MODEL OF VEKUA'S HIERARCHICAL MODEL

N. Chinchaladze

I. Javakhishvili Tbilisi State University

I. Vekua Institute of Applied Mathematics & Faculty of Exact and Natural Sciences, Tbilisi, Georgia

The elastic body is called a prismatic shell if it is bounded above and below by, respectively, the surfaces (so called face surfaces)

$$x_3 = \overset{(+)}{h}(x_1, x_2) \quad \text{and} \quad x_3 = \overset{(-)}{h}(x_1, x_2),$$

laterally by a cylindrical surface Γ of generatrix parallel to the x_3 -axis and its vertical dimension is sufficiently small compared with other dimensions of the body.

In other words, the 3D elastic prismatic shell occupies a bounded region $\bar{\Omega}$ with boundary $\partial\Omega$, which is defined as:

$$\Omega := \left\{ (x_1, x_2, x_3) \in \mathbb{R}^3 : (x_1, x_2) \in \omega, \quad \overset{(-)}{h}(x_1, x_2) < x_3 < \overset{(+)}{h}(x_1, x_2) \right\},$$

where $\bar{\omega} := \omega \cup \partial\omega$ is the so-called projection of the prismatic shell $\bar{\Omega} := \Omega \cup \partial\Omega$.

We assume that

$$\overset{(\pm)}{h}(x_1, x_2) \in C^2(\omega) \cap C(\bar{\omega}),$$

and

$$2h(x_1, x_2) := \overset{(+)}{h}(x_1, x_2) - \overset{(-)}{h}(x_1, x_2) \begin{cases} > 0 & \text{for } (x_1, x_2) \in \omega, \\ \geq 0 & \text{for } (x_1, x_2) \in \partial\omega \end{cases}$$

is the thickness of the prismatic shell $\bar{\Omega}$ at the points $(x_1, x_2) \in \bar{\omega}$. $\max\{2h\}$ is essentially less than the characteristic dimensions of ω . If the thickness of the prismatic shell vanishes ($2h = 0$) on some subset of $\partial\omega$, it is called cusped one.

In what follows X_{ij} and e_{ij} are the stress and strain tensors, respectively, u_i are the displacements, Φ_i are the volume force components, ρ is the density, λ and μ are the Lamé constants, δ_{ij} is the Kronecker delta. Moreover, repeated indices imply summation (Greek letters run from 1 to 2, and Latin letters run from 1 to 3, unless otherwise stated), bar under one of the repeated indices means that we do not sum.

By u_{ir} , X_{ijr} , e_{ijr} , Φ_{jr} we denote the r -th order moments of the corresponding quantities u_i , X_{ij} , e_{ij} , Φ_j as defined below:

$$(u_{ir}, X_{ijr}, e_{ijr}, \Phi_{jr})(x_1, x_2, t) := \int_{\overset{(-)}{h}(x_1, x_2)}^{\overset{(+)}{h}(x_1, x_2)} (u_i, X_{ij}, e_{ij}, \Phi_j)(x_1, x_2, x_3, t) P_r(ax_3 - b) dx_3, \quad i, j = \overline{1, 3}.$$

where

$$a(x_1, x_2) := \frac{1}{h(x_1, x_2)}, \quad b(x_1, x_2) := \frac{\tilde{h}(x_1, x_2)}{h(x_1, x_2)},$$

and

$$P_r(\tau) = \frac{1}{2^r r!} \frac{d^r(\tau^2 - 1)^r}{d\tau^r}, \quad r = 0, 1, \dots$$

are the r -th order Legendre Polynomials.

I. Vekua's hierarchical models for elastic prismatic shells are the mathematical models [1, 2, 3]. Their constructing is based on the multiplication of the basic equations of linear elasticity: **Motion Equations**, **Generalized Hooke's law (isotropic case)**, **Kinematic Relations** by Legendre polynomials $P_r(ax_3 - b)$ and then integration with respect to x_3 within the limits $\overset{(-)}{h}(x_1, x_2)$ and $\overset{(+)}{h}(x_1, x_2)$. So, we get the infinite system with respect to the so called r -th order moments X_{ijr}, e_{ijr}, u_{ir} . Then, in usual way, we construct infinite system with respect to the r -th order moments u_{ir} [1]. After this, if we suppose that the moments whose subscripts, indicating moments' order, are greater than N equal zero and consider for each $j = 1, 2, 3$ only the first $N+1$ equations ($r = \overline{0, N}$) in the obtained infinite system of equations with respect to the r -th order moments u_{ir} , we obtain the N -th order approximation (hierarchical model) governing system consisting of $3N+3$ equations with respect to $3N+3$ unknown functions $\overset{N}{u}_{ir}$ (roughly speaking $\overset{N}{u}_{ir}$ is an "approximate value" of u_{ir} , since $\overset{N}{u}_{ir}$ are solutions of the derived finite system), $i = \overline{1, 3}, r = \overline{0, N}$. Each of these approximations for $r = 0; 1; \dots$ can be considered as an independent mathematical model of plates. For example, $r = 0$ approximation coincides with plane stress, generalized plane stress and plane deformation; $r = 1$ approximation coincides with Kirchoff-Love plate model see [3].

The following model (third model of Vekua's hierarchical model) is considered [4]:

On the face surfaces a normal to the projection of the prismatic shell component of a stress vector and parallel to the projection of the prismatic shell components of a displacement vector are given.

The well-posedness of the boundary value problems (BVPs) under the reasonable boundary conditions at the cusped edge and given displacements at the non-cusped edge is studied. The classical and weak setting of the BVPs in the case is considered. Appropriate weighted functional spaces are introduced. Uniqueness and existence results for the variational problem are proved. The structure of the constructed weighted space is described and its connection with weighted Sobolev spaces is established.

Acknowledgment

The present work was supported by the Shota Rustaveli National Science Foundation within the framework of the projects D-13/18 and 30/28.

References

1. I.N. Vekua (1955). On one method of calculating of prismatic shells, *Trudy Tbilis. Mat. Inst.*, **21**, 191–259 (in Russian).
2. I.N. Vekua (1985). *Shell Theory: General Methods of Construction*. Pitman Advanced Publishing Program, Boston-London-Melbourne.
3. G. Jaiani (2011). *Cusped Shell-like Structures*. Springer Briefs in Applied Science and Technology, Springer-Heidelberg-Dordrecht-London-New York.
4. G. Jaiani (2013). Hierarchical models for prismatic shells with mixed conditions on face surfaces, *Bulletin of TICMI*, **17**, 2, 24–48.

QUADRILATERAL FLAT SHELL FINITE ELEMENT FOR SIMULATION OF REINFORCED CONCRETE STRUCTURAL ELEMENTS

S. Fialko

Tadeusz Kościuszko Cracow University of Technology, Kraków, Poland

1. Problem formulation

The objective of paper is the presentation of approach for analysis of behavior of thin-walled reinforced concrete structural elements – plates, shells, bearing walls and pylons, subjected by action of static load as well as cyclic and dynamic ones.

The concrete is considered as homogeneous isotropic material. The deformation theory of plasticity with unsymmetrical $\sigma - \varepsilon$ diagram (Fig. 2) for compression and tension [1], formulated in terms of residual strains, is used. The steel rods are considered as a layers, which work only in tension/compression in the direction coinciding with orientation of rods. For example, the rectangular bending plate contains two reinforced layers for upper rods in directions OX, OY and two reinforced layers for bottom rods. Axis OZ is directed along normal to middle surface. The deformation theory of plasticity and symmetrical $\sigma - \varepsilon$ diagram is applied.

The Mindlin-Reissner shell theory is applied for reduction of source 3D problems to 2D. The kinematic condition of equality of longitudinal displacements of rods and concrete ensures the compatibility of deformations of concrete and reinforcement.

2. Finite element formulation

The principle of virtual work is applied to obtain the element stiffness matrix and right-hand side vector.

$$(1) \quad \iint_{\Omega} \int_{-h/2}^{h/2} (\delta \vec{\varepsilon}^T \cdot \vec{\sigma} + \delta \vec{\gamma}^T \cdot \vec{\tau}) dz d\Omega + \sum_s \iint_{\Omega} \frac{A_s}{h_s} \sigma_s \delta \varepsilon_s(z_s) d\Omega - \delta A_{\text{ext}} = 0,$$

where $\vec{\sigma}^T = (\sigma_x \ \sigma_y \ \tau_{xy})$, $\vec{\tau}^T = (\tau_{xz} \ \tau_{yz})$, $\sigma_z = 0$, $\vec{\varepsilon}^T = (\varepsilon_x \ \varepsilon_y \ \gamma_{xy})$, $\vec{\gamma}^T = (\gamma_{xz} \ \gamma_{yz})$, $\vec{\sigma}$, $\vec{\varepsilon}$ – membrane components of stress and strains tensors in concrete layer with coordinate $z \in [-h/2, h/2]$, $\vec{\tau}$, $\vec{\gamma}$ – the transvers shear stresses and strains, h – thickness of shell, A_s , h_s , σ_s , ε_s , z_s – cross-section area of rod, step between the rods, stress and strain in rods and coordinate of reinforcement layer s , δA_{ext} – virtual work of external loads. The sum in (1) covers all reinforcement layers. The Lagrange poly-linear shape functions and mixed interpolation of tensorial shear components [2] for avoiding of shear lock effect is applied during discretization. Such approach allows us to take into account the effects, caused by discrete location of reinforcements over thickness, and simulates the structural anisotropy, involved by different properties of concrete and reinforcement layers. We suppose that the step between rods is essentially less than dimension of finite elements. It allows us to replace the finite sums, which describe the virtual works of separate rods, by integral in transverse direction, and to obtain the integral over reinforcement layer.

The incremental Newton-Raphson method is applied to solve the set of nonlinear algebraic equations. The multi-threaded parallelization is applied on the stage of aggregation of tangent stiffness matrix, factorization stage and evaluation of residual vector.

3. Numerical results

The simply supported quadratic plate 2×2 m, $h = 12.2$ cm, $z_{s,x} = 5.4$ cm, $z_{s,y} = 5.05$ cm, $A_{s,x} = A_{s,y} = 0.407$ cm², $h_{s,x} = h_{s,y} = 10$ cm, $\sigma_c = 26.5$ MPa, $\sigma_t = 1.3$ MPa, $\sigma_y = 408$ MPa, $E_c = 30\,000$ MPa, $E_s = 201\,000$ MPa. Here subscripts x, y denote the directions OX, OY, σ_c, σ_t – ultimate stresses of compression and tension in concrete, σ_y – yield stress in steel, E_c – deformation modulus in concrete, E_s – Young’s modulus in steel. The plate is subjected by action of 16 concentrated forces (the quarter part is presented in Fig. 2), uniformly distributed over the domain of plate. The load – vertical displacement in point A diagram is presented in Fig. 1. The “load” is taken as $16P/a^2$, where P is a concentrated force and a is the width of plate. The experimental data is taken for specimen 825 from [3]. Curve 1 corresponds to bilinear $\sigma - \varepsilon$ diagram for steel and curve 2 – for exponential approximation of bilinear diagram

$$(2) \quad \sigma_s = (E\lambda^{-1} + E_1\varepsilon_s)(1 - e^{-\lambda\varepsilon_s}), \quad \lambda = E^2/[\sigma_y(E - E_1)].$$

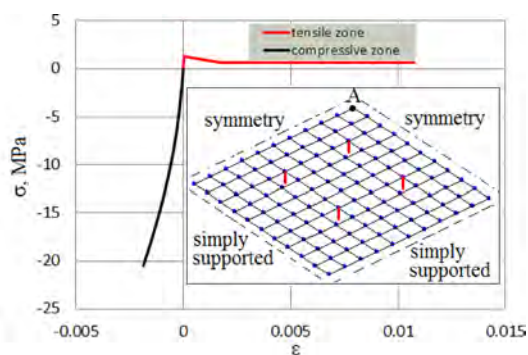
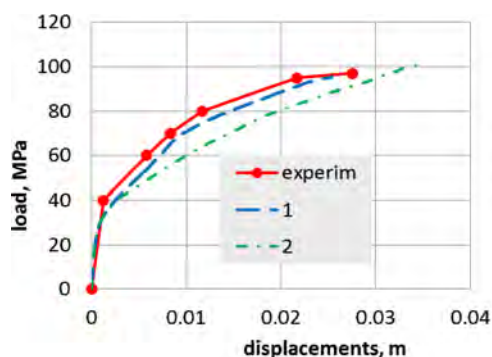


Fig. 1. Load-displacement diagram.

Fig. 2. Reduced stresses via reduced strains for concrete.

The reduced stresses – reduced strains diagram for the most compressed and most stretched fibers of concrete, which are located at the top and bottom surfaces in the middle of plate (point A), is presented in Fig 2. The descending branch simulates the degradation of concrete due to the appearance of cracks in the tensile zone. The process of intensive cracking corresponds to part of equilibrium states diagram with fast changing of slope at a load of about 30 MPa (Fig. 1). The horizontal branch in Fig. 2 presents the destructed concrete, which is almost switched off from work, and steel rods receive the main part of tensile forces.

The compressive part of diagram has the strong nonlinear character.

The proposed approach demonstrates a satisfactory prediction of load-carrying capacity of thin-walled shell structures (Fig. 1), is relatively simple and does not require a snapping of the finite element mesh to location of rods. These peculiarities make it applicable to analysis of real-life problems.

Acknowledgments

This work was supported by Narodowe Centrum Nauki on the basis of decision DEC-2011/01/B/ST6/00674.

References

1. K.J. Bathe, J. Walczak, A. Welch, N. Mistry (1989). Nonlinear analysis of concrete structures, *Computers & Structures*, **32**, 563–590.
2. K.J. Bathe (1996). *Finite element procedures*, Prentice Hall, Inc., 420–430.
3. N.I. Karpenko (1976). *The theory of deformation of reinforced concrete with cracks* (in Russian), Stroyisdat, Moscow, 135–138.

NATURAL SHAPES APPLIED TO SHELL STRUCTURES

M. Gohnert

School of Civil and Environmental Engineering, University of the Witwatersrand, South Africa

1. Introduction

The engineering and architectural profession seems to be largely unaware of the important role of natural structures. Natural structures are shapes created by nature and have geometrical properties that are resistant to local environmental conditions, such as earthquakes, temperature and metrological events. Few engineers and architects have recognized the significance of natural structures and have incorporated these shapes in the design of shell structures. Most of the structures are political or religious buildings with the primary focus, or motivation, was to span large areas without columns. Furthermore, most of the shells are hemispheres. Catenary shapes, however, are specialized shells in which the shape is dictated by local environmental conditions, and therefore a natural shape (i.e., a shape that is closely aligned with nature). Catenaries are characterized as pure compressive structures – an ideal shape if built of unreinforced masonry or other materials that have poor tension resistance.

Natural structures have, perhaps, evolved over millions of years into optimum shapes that are resistant to local environmental conditions. There are numerous examples of where buildings have been decimated due to excessive climatic conditions or earthquakes. In many instances, the natural environment remains intake but the manmade structures have failed. Would it not be prudent to learn from these structures and emulate them in our designs [1]?

Nature possesses and persistently reproduces several universal features – all natural structures have curved surfaces and solid forms are not solid, but composed of cellular or tubular shell like substructures. The curvature of the shapes is directly related to the flow of stress, dictated by the imposition of environmental conditions. The curvature of bone constitutes resistance to the action of walking, running, jumping, pulling or lifting. Leaves, which are miniature solar panels engaged in the act of photosynthesis, are designed to resist wind flutter, rain, snow and the invasion of insects. Each shape takes on a suitable form, to optimize the resistance to environmental forces and to ensure the species ultimate survival.

2. General principles of carrying load efficiently

An important concept in understanding the strength of curved structures is to understand how loads are efficiently carried by structures. Table 1 is a list of stress ratios for a variety of simple load and beam support conditions. The stress ratio represents the increase in beam stress compared to an axially loaded member. As indicated in the first row of Table 1, the stress in a simply supported beam subjected to a point load is 24 times higher than the stress in an axially loaded member. Similarly, the stress increase in other beam load/support configurations range from 12 to 18 times the stress in a column.

Table 1 demonstrates that greater efficiency is achieved by directing the flow of force along the axis of the member. The axis, however, does not necessarily have to be straight. A stress will flow along an axis of a curved member or along the curvature of a shell if the shape is catenary. The catenary is a natural form, where stresses will flow in pure

Table 1. Stress ratios of various loading and support configurations.

Load condition	L/h	Stress ratio (r) Beam stress/column stress
Simply supported, central point load	16	24
Simply supported, UDL	16	12
Fixed supports, UDL	24	12
Fixed supports, central point load	24	18

compression or tension. Unlimited variations of the catenary are also possible by varying the loads and corresponding shape

3. Lessons from the past

The discovery and importance of natural structures seems to have occurred around the 17th century from the work of Robert Hooke [2], the same who developed the theory of elasticity (i.e., Hooke's law). Hooke, a celebrated scientist, discovered the significance of a hanging chain and its relationship to structural forms. Hooke recognised that a hanging chain is in complete tension, without bending and shears. If the chain is locked and inverted, the stress in the chain is reversed and in pure compression. The importance of this discovery is that loads may be carried in pure compression, eliminating shears and bending. In building structures, the catenary is a natural structure and the most appropriate shape to resist excessive climatic loads and earthquakes.

References

1. Bejan A., Lorente S. (2006). Constructional theory of generation of configuration in nature and engineering, *J. App. Phys.*, 100 (041301).
2. O'Dwyer D. (1999). Funicular analysis of masonry vaults, *Comp. & Struct.*, **73**, 187–197.

VEKUA'S HIERARCHICAL MODELS OF THE SECOND TYPE FOR ELASTIC SHELLS

B. Gulua

Department of Mathematics & I. Vekua Institute of Applied Mathematics
of Iv. Javakhishvili Tbilisi State University, Tbilisi, Georgia
Sokhumi State University, Tbilisi, Georgia

I. Vekua constructed several versions of the refined linear theory of thin and shallow shells, containing the regular processes by means of the method of reduction of 3-D problems of elasticity to 2-D ones, when on upper and lower face surfaces stress-vectors are assumed to be known [1–2].

In the present paper, by means of Vekua's method, the system of differential equations for thin and shallow shells is obtained, when on upper and lower face surfaces displacements are assumed to be known.

The equilibrium equation of the continuous medium and stress-strain relations (Hooke's law) can be written in the form

$$(1) \quad \frac{1}{\sqrt{g}} \partial_i (\sqrt{g} \bar{\sigma}^i) + \bar{\Phi} = 0,$$

$$(2) \quad \bar{\sigma}^i = \lambda (\bar{R}^j \partial_j \bar{u}) \bar{R}^i + \mu (\bar{R}^i \partial_j \bar{u}) \bar{R}^j + \mu (\bar{R}^i \bar{R}^j) \partial_j \bar{u} \quad (i, j = 1, 2, 3),$$

where $\partial_i = \frac{\partial}{\partial x^i}$, x^i are curvilinear coordinates, g is the discriminant of the metric tensor of the space, $\bar{\Phi}$ is the volume force, $\bar{\sigma}^i$ are contravariant stress vectors, λ and μ are Lamé's constants, \bar{R}^i and \bar{R}_i are covariant and contravariant base vectors of the space and \bar{u} is the displacement vector.

To construct the theory of shells, we use the more convenient coordinate system which is normally connected with the midsurface S of the shell [1–2].

For thin or shallow shells we can write [1–2]

$$\bar{R}_\alpha \cong \bar{r}_\alpha, \quad \bar{R}^\alpha \cong \bar{r}^\alpha, \quad \bar{R}^3 = \bar{R}_3 = \bar{n}, \quad g \cong a,$$

where \bar{r}_α and \bar{r}^α are covariant and contravariant base vectors of the midsurface, \bar{n} is the unit vector of the normal of the midsurface, a is the discriminant of the metric tensor of the midsurface.

Multiplying both sides of equations (1) and (2) by Legendre polynomials $P_m\left(\frac{x^3}{h}\right)$ and then integrating with respect to x^3 from $-h$ to h we obtain the equivalent infinite system of 2-D equations

$$\begin{aligned} & \frac{1}{\sqrt{a}} \frac{\partial \sqrt{a}}{\partial x^\alpha} \bar{\sigma}^\alpha + \frac{2m+1}{h} \left(\bar{\sigma}^3 + \bar{\sigma}^3 + \dots \right) + \bar{\Phi} = 0, \\ & \bar{\sigma}^\alpha = \lambda \left[\bar{r}^\beta \partial_\beta \bar{u} - \frac{2m+1}{h} \left(\bar{u}^3 + \bar{u}^3 + \dots \right) \right] \bar{r}^\alpha \\ & + \mu \left[\left(\bar{r}^\alpha \partial_\beta \bar{u} \right) \bar{r}^\beta + \partial^\alpha \bar{u} - \frac{2m+1}{h} \left(\bar{u}^\alpha + \bar{u}^\alpha + \dots \right) \right] \bar{n} + \bar{F}^\alpha, \end{aligned}$$

$$\begin{aligned} \vec{\sigma}^3 &= \lambda \left(\vec{r}^\beta \partial_\beta \vec{u}^{(m)} \right) \vec{n} - (\lambda + \mu) \frac{2m+1}{h} \left(u^3^{(m-1)} + u^3^{(m-3)} + \dots \right) \vec{n} \\ &+ \mu \left[\left(\vec{n} \partial_\beta \vec{u}^{(m)} \right) \vec{r}^\beta - \frac{2m+1}{h} \left(\vec{u}^{(m-1)} + \vec{u}^{(m-3)} + \dots \right) \right] + \vec{F}^3, \end{aligned}$$

where

$$\left(\vec{\sigma}^i, \vec{u}, \vec{\Phi} \right) = \frac{2m+1}{2h} \int_{-h}^h \left(\vec{\sigma}^i, \vec{u}, \vec{\Phi} \right) P_m \left(\frac{x_3}{h} \right) dx_3 \quad (m = 0, 1, 2, \dots),$$

$$\vec{F}^\alpha = \lambda \frac{2m+1}{2h} \left(u^3^{(+)} - (-1)^m u^3^{(-)} \right) \vec{r}^\alpha + \mu \frac{2m+1}{2h} \left(u^\alpha^{(+)} - (-1)^m u^\alpha^{(-)} \right) \vec{n},$$

$$\vec{F}^3 = (\lambda + \mu) \frac{2m+1}{2h} \left(u^3^{(+)} - (-1)^m u^3^{(-)} \right) \vec{n} + \mu \frac{2m+1}{2h} \left(\vec{u}^{(+)} - (-1)^m \vec{u}^{(-)} \right),$$

$$\vec{u}^{(\pm)} = \vec{u}(x^1, x^2, \pm h).$$

x^1, x^2 are the Gaussian parameters of the midsurfaces, $x^3 = x_3$ is the thickness coordinate and h is the semi-thickness. So, we get the equivalent to (1), (2) infinite system.

Then we consider $N = 1$ order approximation for plates. In other words, in the previous equations it is assumed that

$$\vec{u}^{(m)} = 0, \quad \vec{\sigma}^i = 0, \quad \text{if } m > 1.$$

Concrete problem has been solved.

Acknowledgment

The designated project has been fulfilled by financial support of the Shota Rustaveli National Science Foundation (Grant No 52/48).

References

1. I.N. Vekua (1965). *Theory on Thin and Shallow Shells with Variable Thickness*, Tbilisi, Metsniereba (in Russian).
2. I.N. Vekua (1985). *Shell Theory: General Methods of construction*, Pitman Advanced Publishing Program, Boston – London – Melbourne.

ON PARALLELIZATION OF THE LOOP OVER ELEMENTS FOR COMPOSITE SHELL COMPUTATIONS

P. Jarzębski, K. Wiśniewski

Institute of Fundamental Technological Research, Warsaw, Poland

1. Introduction

The multi-scale models used in computation of composite shells require a significant computational power and, therefore, a finite-element code should take advantage of such techniques as: 1) parallel solvers, e.g. PARDISO, MUMPS, PaStiX, 2) parallelization of the loop over elements using e.g. OpenMP, and 3) domain decomposition and spreading tasks over a cluster of computers, using e.g. MPI. A significant programming effort is needed to convert a large and complicated existing FE code into a parallel one, especially when implementing the most effective hybrid approach.

In this paper, we focus on parallelization of the loop over elements using OpenMP standard [2], which we apply to the finite element program FEAP [1]. We shall discuss basic features of our implementation as well as demonstrate correctness and speed up ratio of the code. Several numerical examples of shell benchmarks will be presented.

2. Parallelization of the loop over elements

Personal computers have processors with several (2–32) cores, which makes them shared memory architectures, for which communication is implicit. An appropriate parallelization technique for such architectures is a threading parallelism, which may be based on the OpenMP standard [2], specifying parallelization in terms of compiler directives, library routines and environment variables. OpenMP defines the 'fork-join' parallelism, because it launches multiple parallel threads (fork) in parallel regions of the code and joins them into a single thread (the master one) for serial processing in non-parallel regions [3].

To parallelize FEAP, we apply the "*parallel do*" directive to the loop over elements, for which OpenMP creates a set of threads and distributes the iterations of the loop across them for parallel execution. The pivotal question is the choice as to whether a variable is shared or private. If too many variables are made private then OpenMP has to make additional and unnecessary work of initialization and copying extra variables for each thread. On the other hand, for shared variables more critical sections are needed to synchronize data. The additional difficulty is that FEAP uses many common blocks, and passes varying data through them. Finally, we have to properly treat critical sections, as they have a tremendous impact on the speed up ratio. These issues will be discussed in more detail during the presentation.

3. Pinched hemisphere shell example

Our OMP parallelization of FEAP was tested on the pinched hemispherical shell with 18° hole loaded by two pairs of equal but opposite external forces, applied in the plane $z = 0$, along the X and Y axes, so the shell undergoes strong bending, see [4] p. 445. The geometry of the shell and the load are shown in Figure 1a. The shell was computed for two thicknesses, $h = 0.4$ and $h = 0.04$ using three different elements. The numerical

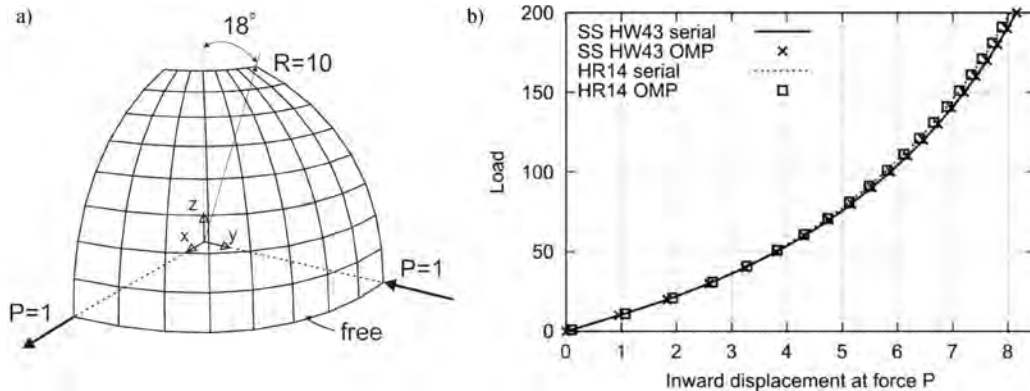


Fig. 1. Pinched hemispherical shell. $E = 6.825 \times 10^7$, $\nu = 0.3$: a) initial geometry and load, b) displacement ($-u_y \times 100$) for serial and parallel version for thin shell.

tests were performed on 1 node of the cluster GRAFEN [6]. One node has two 6-core processors Xeon X5650 2.66 GHz and 24 GB RAM.

The thick shell ($h = 0.4$) was computed using our 3D displacement-type 8-node solid element using 10 elements through the shell thickness. The mesh consisted of $316 \times 316 \times 10$ elements (about 3.3 millions unknowns). The results for computation of a tangent matrix and a residual vector for a linear problem are given in Table 1, and we see a good speed up ratio with the number of threads.

Table 1. Time of computation and speed up ratio for thick shell.

Version	Serial	OMP, number of threads						
		1	2	4	6	8	10	12
Time [secs]	52.48	53.61	27.08	13.63	9.45	7.11	5.68	4.79
Speed up ratio	0.98	1	1.98	3.93	5.67	7.54	9.44	11.19

The thin shell ($h = 0.04$) was computed using two non-linear elements: our solid shell element HW43 as well as the shell element with 2 rotational dofs of FEAP [5] (which we denote HR14), to demonstrate that the user as well as the FEAP elements are operational in the parallel version. The Newton method was used. The results of nonlinear analyses are given in Fig. 1b, and we see that both versions, the serial and the parallel one, give exactly the same results. This indicates that our implementation of the OpenMP standard in FEAP is correct indeed.

References

1. Taylor R.L. (2013). FEAP 8.3, <http://www.ce.berkeley.edu/projects/feap>.
2. OpenMP Architecture Review Board, OpenMP Application Program Interface (2013). <http://www.openmp.org/mp-documents/OpenMP4.0.0.pdf>.
3. Pantale O. (2005), Parallelization of an object-oriented FEM dynamics code: influence of the strategies on the Speedup, *Advances in Engineering Software*, 361–373.
4. Wisniewski K. (2010). *Finite Rotation Shells*, Springer.
5. Simo J.C., Tarnow N. (1992). On a stress resultant geometrically exact shell model. Part VI 5/6 dof treatments, *Int. J. Numerical Methods in Engineering*, **34**, 117–164.
6. GRAFEN, <http://info.grafen.ippt.pan.pl/>

MODELLING PROPAGATION OF LAMB WAVES IN CFRP PLATES FOR DAMAGE DETECTION

G. Knor, J. Holnicki-Szulc

Institute of Fundamental Technological Research, Warsaw, Poland

1. Introduction

The scope of this paper is the presentation of application of modeling acoustic waves propagation in carbon fiber reinforced plastic elements for damage detection. This task is a part of the non-destructive testing methods which are very important in many industry branches. Many of construction elements are made of composite materials (e.g. plane's wings, components of cars coachwork). Due to importance of these elements they must be tested by means of NDT techniques during manufacturing and exploitation. The main reason to do that is to ensure the reliability of the whole constructions made of CFRP materials. One of the ways to detect flaws in laminate structure are techniques based on so called Lamb wave propagation. The mathematical background for this phenomenon was published by Horace Lamb in 1917 and since 1980s Lamb waves have been successfully used in SHM and NDT [1]. Theoretical models and experimental methods are still being developed mainly because of their advantages.

2. Mathematical formulation

The wave propagation in stress-free isotropic and anisotropic bulk media can be adequately described using theory based on linear stress-strain relationships: the stress equation of motion [2]: $\sigma_{ij,j} + \rho f_i = \rho \ddot{u}_i$. Hooke's law: $\sigma_{ij} = C_{ijkl} \varepsilon_{kl}$ and linear strain-displacement relationship: $\varepsilon_{ij} = \frac{1}{2}(u_{i,j} + u_{j,i})$ where σ is the Cauchy stress tensor, ε is the Cauchy strain tensor, ρ is the material density, \mathbf{u} is the displacement, \mathbf{f} is a vector of the external force, \mathbf{C} is fourth-order stiffness tensor. Combining the above three equations one can obtain the system of differential equations of motion. This set of equations with associated boundary conditions can be solved analytically only for limited number of cases. One of the examples with existing analytical solution is the propagation of Lamb waves in thin isotropic plate (for example made of aluminum). In this case elastic oscillations are described by the Rayleigh-Lamb equations:

$$\frac{\tan(pd)}{\tan(qd)} = - \left[\frac{4k^2 pq}{(k^2 - q^2)^2} \right]^{\pm 1}$$

where: $p^2 = \frac{\omega^2}{c_L^2} - k^2$ and $q^2 = \frac{\omega^2}{c_T^2} - k^2$, k is wave number, ω is angular frequency, c_L is longitudinal phase velocity, c_T is shear phase velocity and d is half thickness of plate. In most cases the geometry, boundary conditions and potential defects complicate the situation and the only possible solution is to use a numerical model. A number of different numerical computational techniques have been developed and can be used for this type of analysis, for example finite difference method, finite element method, spectral element method, etc. In this work FEM is used because of its versatility and wide availability of both commercial and free software. The advantages of FEM include the ability to study Lamb wave propagation almost in any kind of the structure including geometry, inhomogeneities, defects, etc.

3. Results

The FEM model was first tested on thin isotropic plate. Obtained dispersion curves agree very well with analytical solution (Fig. 1). Next the method of determining elasticity constants was investigated to develop material properties by means of homogenization of representative volume element – RVE (Fig. 3). Based on obtained material properties a full-scale model for various scenarios was solved to find a potential defects in plates. It can be done for example by means of short time Fourier transform (Fig. 2) or wavelet transform. Finally the calculation for object with nontrivial geometry were performed to show that proposed method is robust and can be applied for real object made of CFRP materials (Fig. 4).

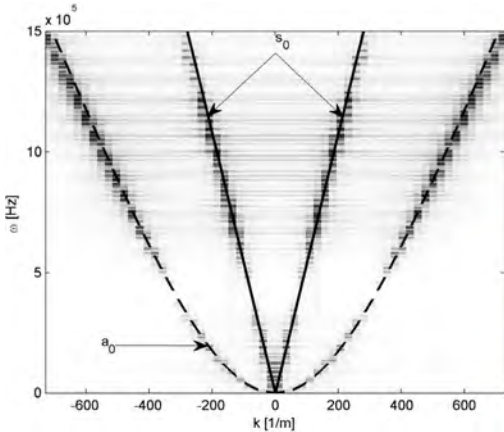


Fig. 1. Dispersion curves for isotropic plate.

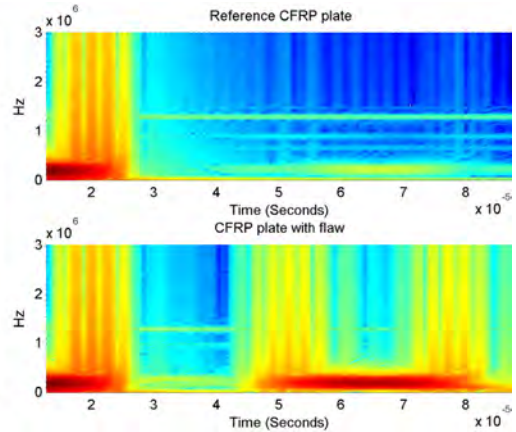


Fig. 2. Spectrograms of CFRP plates.

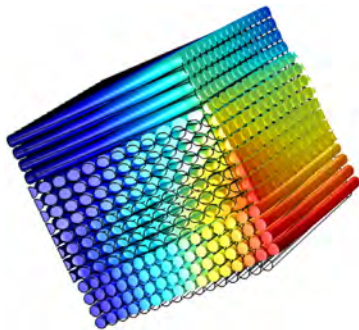


Fig. 3. Total displacement in RVE.

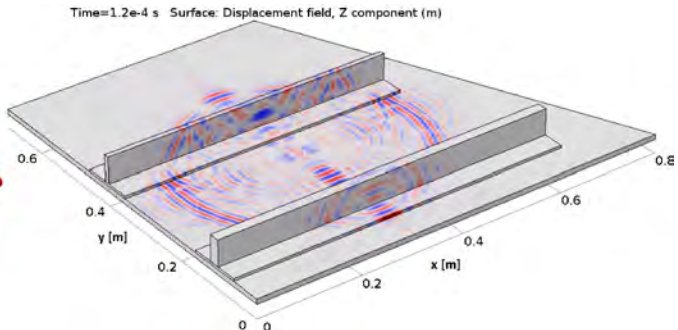


Fig. 4. Wave propagation in CFRP plate.

Acknowledgment

Financial support of Structural Funds in the Operational Programme - Innovative Economy (IE OP) financed from the European Regional Development Fund - Project "Modern material technologies in aerospace industry", No. POIG.01.01.02-00-015/08-00 and Polish National Science Centre Project 'AIA' (DEC-2012/05/B/ST8/02971) are gratefully acknowledged.

References

1. Y. Lu, L. Ye, D. Wang, Z. Zhong and I. Herszberg (2009). *Damage detection in a large composite panel of five stiffeners using lamb wave signals*, Materials Forum, 33.
2. J.L. Rose (1999). *Ultrasonic Waves in Solid Media*, Cambridge University Press.

WRINKLING OF INFLATED ELASTIC CURVED TUBE UNDER PURE BENDING

A.M. Kolesnikov

Southern Federal University, Rostov on Don, Russia

1. Introduction

The approach to solve the nonlinear pure bending problem of pressurized curved tubes is given in [1]. In [2] the approach for solving the strong bending problem of pressurized straight and curved tubes is presented. These approaches are based on the decomposition the deformation into two parts: in-plane deformation of cross-sections, plus rigid rotation of each of these cross-sections by a constant relative angle.

Based on this decomposition pure bending of a pressurized thin-walled cylinder made of nonlinear elastic material is studied in [3–5]. In [5] the bending of straight tube is studied using ordinary nonlinear theory of elastic membrane. It obtains that there is the ultimate bending moment. After that the tube collapses due to its ovalization. We note that the compressive stresses occur in the tube before the ultimate moment.

The thin-walled structures are unstable under compressive stresses. The wrinkling of membranes may be studied by tension-field theory. For isotropic elastic membrane under large strains the tension-field theory is developed in [7,8] using a relaxed strain energy. Using this approach the bending of a cylindrical membrane is investigated in the papers [3, 4].

In [6] the in-plane bending of curved tube is studied using ordinary nonlinear membrane theory. There are two ultimate bending moments for curved tube. They are corresponded by direct and inverse bending of a curved tube.

In this work we study the in-plane bending of straight and curved tubes using a tension-field theory.

2. Results

We denote r_1 and r_2 radii of an elliptical cross section of tube, β an initial curvature of curved tube, B a curvature of deformed tube, p^* a dimensionless internal pressure, M^* a dimensionless bending moment.

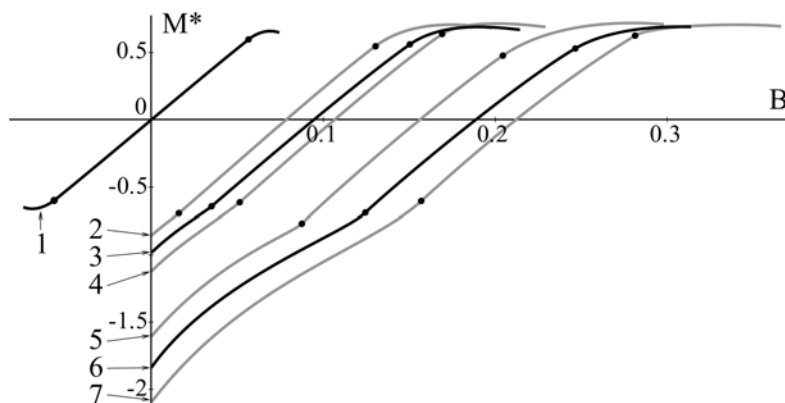


Fig. 1. The dependence of bending moment on curvature" for $p^* = 0.3$.

Figures 1, 2 show dependences between the bending moment and the curvature of deformed tube for the pressure $p^* = 0.3$ and 0.65 respectively. Table 1 presents parameters of tubes.

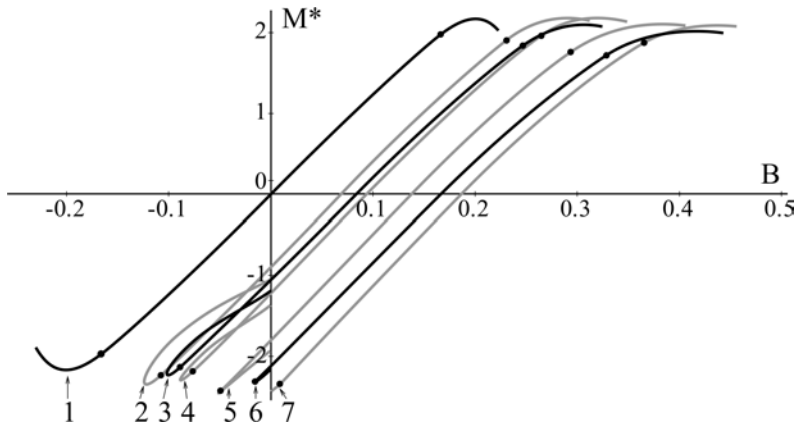


Fig. 2. The dependence of bending moment on curvature" for $p^* = 0.65$.

Table 1. The parameters of tubes.

No.	1	2	3	4	5	6	7
r_1	1	1.2	1	0.8	1.2	1	0.8
r_2	1	0.8	1	1.2	0.8	1	1.2
β	–	0.1			0.2		
	straight			curved tube			

Acknowledgments

This research was supported by the Russian Foundation for Basic Research (Grant 12-01-00038).

References

1. A. Libai, J.S. Simmonds (1998). *The Nonlinear Theory of Elastic Shells*, 2nd ed., Cambridge Univ. Press., Cambridge.
2. L.M. Zubov (2001). Semi-inverse solution in non-linear theory of elastic shells, *Archives of Mechanics*, **53**, 599–610.
3. E. Haseganu, D. Steigmann (1994). Theoretical flexure response of a pressurized cylindrical membrane, *International Journal of Solids and Structures*, **31**, 27–50.
4. D. Haughton, B. McKay (1996). Wrinkling of inflated elastic cylindrical membranes under flexure, *International journal of engineering science*, **34**, 1531–1550.
5. A.M. Kolesnikov, L.M. Zubov (2009). Large bending deformations of a cylindrical membrane with internal pressure, *ZAMM*, **89**, 288–305.
6. A.M. Kolesnikov (2011). Large bending deformations of pressurized curved tubes, *Archives of Mechanics*, **63**, 507–516.
7. A.C. Pipkin (1986). The relaxed energy density for isotropic elastic membranes, *IMA Journal of Applied Mathematics*, **36**, 85–99.
8. D.J. Steigmann (1990). The relaxed energy density for isotropic elastic membranes, *Proc. R. Soc. Lond. A*, **429**, 141–173.

IRREGULAR BASE SURFACE IN THE RESULTANT THERMOMECHANICS OF SHELLS

V. Konopińska¹, W. Pietraszkiewicz²

¹Gdańsk University of Technology, Gdańsk, Poland

²Institute of Fluid-Flow Machinery, Polish Academy of Sciences, Gdańsk, Poland

Pietraszkiewicz [1] formulated the resultant balance laws of mass, linear and angular momenta, and energy as well as entropy inequality of 2D shell thermomechanics by direct through-the-thickness integration of corresponding 3D laws of rational thermomechanics proposed by Truesdell and Noll [2]. In [1] the undeformed (reference) and deformed (current) placements of the shell base surface were assumed to be regular geometric surfaces with piecewise smooth boundaries. Also all the surface fields appearing in the resultant 2D laws were assumed to be smooth everywhere. In [3] we have additionally assumed that the 2D surface fields appearing in the resultant shell thermomechanics of [1] may not be differentiable at a moving, non-material, singular surface curve. This has allowed us to formulate in [3] the corresponding jump conditions across the singular moving surface curve.

But real shell structures are often irregular ones such that already their undeformed base surface may contain folds, branches, intersections and additional design elements such as stepwise thickness changes, parts made of different materials, stiffeners, technological junctions etc. A thin-walled turbine blade with inside cooling channels is an example of a shell with thermal singular curves. All such 1D discontinuities are associated with the material singular curves which remain to be material during an arbitrary thermodynamic process in the shell.

In this lecture we discuss thermomechanical jump conditions in shells whose undeformed base surface may be irregular one as for example in Fig. 1.

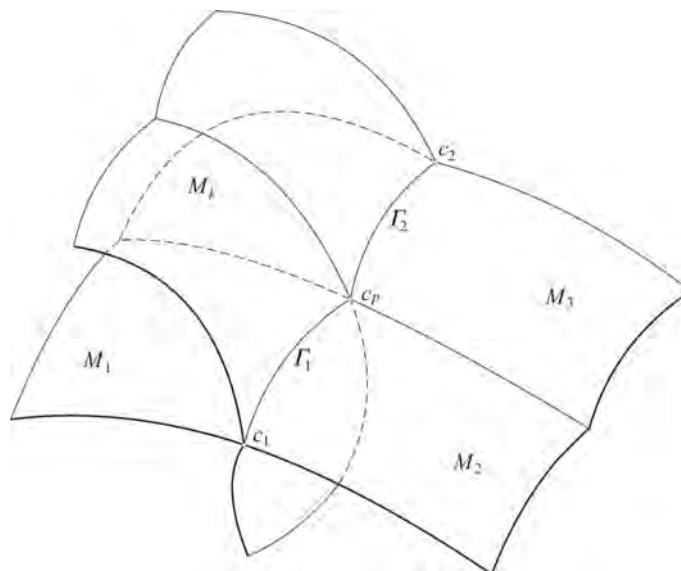


Fig. 1. Example of the piecewise smooth surface M .

Thermomechanical processes in such types of shell structures are governed by the resultant 2D laws in the regular parts of the shell structure formulated in [1]. But across any stationary surface curve of irregularity of the base surface additional 1D jump conditions are required to be satisfied. The explicit forms of the jump conditions depend on the type of irregularity and follow directly from the extended surface divergence theorems formulated on the piecewise smooth base surface. Details of these theorems are given in [4].

For example, let the shell base surface consist of two smooth parts joined together along the surface curve Γ , i.e. the base surface has a fold along Γ . Then for the piecewise smooth 2nd-order tensor field $\mathbf{S}(\mathbf{x}) \in E \otimes T_x M$ we obtain the patchwork surface divergence theorem

$$\int_{\partial \Pi} \mathbf{S} \boldsymbol{\nu} ds = \iint_{\Pi} \text{Div } \mathbf{S} da - \int_{\Pi \cap \Gamma} \llbracket \mathbf{S} \boldsymbol{\nu} \rrbracket ds,$$

$$\llbracket \mathbf{S} \boldsymbol{\nu} \rrbracket = \mathbf{S}_1 \boldsymbol{\nu}_\Gamma - \mathbf{S}_2 \boldsymbol{\nu}_\Gamma \cos \alpha = -(\mathbf{S}_2 \cos \alpha - \mathbf{S}_1) \boldsymbol{\nu}_\Gamma$$

on any $\Pi \subset M$ having a part of Γ in its interior, with an angle $180^\circ - \alpha(x_\Gamma)$ in the plane orthogonal to Γ between exterior normal vectors of two surface parts along Γ , see [4].

Applying appropriate patchwork divergence theorems to 2D scalar, vector and/or tensor fields applied on irregular base surface with various types of irregularities, the corresponding jump conditions across various material singular curves are formulated for the resultant shell thermomechanics.

Acknowledgments

The research reported in this paper was supported by the National Centre of Science of Poland with the grant DEC – 2012/05/D/ST8/02298.

References

1. W. Pietraszkiewicz (2011). Refined resultant thermomechanics of shells, *Int. J. Engng Sci.*, **49**, 1112–1124.
2. C. Truesdell, R. Toupin (1960). The Classical Field Theories. In: S. Flügge (Ed.), *Handbuch der Physik*, Band III/1. Springer-Verlag, Berlin.
3. V. Konopińska, W. Pietraszkiewicz (2014). On jump conditions at non-material singular curves in the resultant shell thermomechanics. In: W. Pietraszkiewicz, J. Górski (Eds.), *Shell Structures: Theory and Applications*, Vol. 3, pp. 117–120, CRC Press/Balkema, Taylor & Francis Group, London.
4. W. Pietraszkiewicz, V. Konopińska (2014). Singular curves in the resultant thermomechanics of shells, *Int. J. Engng Sci.* (accepted).

ELLIPTICALLY PERFORATED CIRCULAR DISCS UNDER PARABOLIC PRESSURE

Ch. F. Markides, S. K. Kourkoulis

National Technical University of Athens, Department of Mechanics
5 Heroes of Polytechnion Avenue, Theocaris Bld., Zografou Campus, 157 73 Athens, Greece

A centrally elliptically perforated disc under parabolic radial pressure along two symmetric arcs of its periphery is studied. The loaded arc is either arbitrarily prescribed or, in case of small cracks, it is obtained from the respective contact problem. Adopting Muskhelishvili's [1] complex potentials method a solution is obtained for both the stress- and displacement-fields in infinite series form.

1. Theoretical assumptions

A disc (O, R_O) of thickness t , with a central elliptic crack (a, b), lies in the complex plane $z = x + iy = re^{i\varphi}$, with the origin of the Cartesian reference as its centre (Fig. 1). The radial pressure σ_r acting on its periphery L_O is given as:

$$(1) \quad \sigma_r = -P(\varphi) = -P_c \left[1 - \frac{\sin^2(\varphi_o - \varphi)}{\sin^2 \omega_o} \right] \quad (P_c = P(\varphi)_{\max}).$$

Assuming the potentials φ_o, ψ_o obtained for a ring of outer radius R_O and inner one $R_I = b$ [2] predominate on L_O of the elliptically perforated disc, its solution will be:

$$(2) \quad \varphi = \varphi_o + \varphi_*, \quad \psi = \psi_o + \psi_* \quad (\varphi_*, \psi_* \text{ due to } L).$$

Mapping the ring in the plane $\zeta = \rho e^{i\theta}$ with the unit hole through the transformation $z = \omega(\zeta) = R(\zeta + m/\zeta)$ where $R = (\alpha + b)/2$ and $m = (\alpha - b)/(\alpha + b)$, and demanding L to be stress-free yields:

$$(3) \quad \varphi_*(s) + \frac{s^2 + m}{s(1 - ms^2)} \overline{\varphi'_*(s)} + \overline{\psi_*(s)} = - \left[\varphi_0(s) + \frac{s^2 + m}{s(1 - ms^2)} \overline{\varphi'_0(s)} + \overline{\psi_0(s)} \right] \quad (s = e^{i\theta}).$$

Solving (3) and using (2) it is finally obtained that:

$$(4) \quad \varphi(\zeta) = \frac{P_c R}{\pi} \left\{ (b_0 + mR^2 B_2) \zeta + R^2 B_2 \zeta^3 / 3 - \left[mb_0 + \overline{B'_0} + R^2 \left[(1 + 2m^2) \overline{B_2} + m \overline{B'_2} \right] \right] / \zeta \right. \\ - R^2 (m \overline{B_2} + \overline{B'_2} / 3) / \zeta^3 + \sum_{n=1}^{\infty} \left[R^{4n} \left(\frac{B_{4n}}{4n+1} G_{4n+1}^{\infty}(\zeta) - \overline{B_{4n}} G_{4n}^0(\zeta) - \frac{\overline{B'_{4n}}}{4n+1} G_{4n+1}^0(\zeta) \right) \right. \\ \left. \left. + R^{2(2n+1)} \left(\frac{B_{2(2n+1)}}{4n+3} G_{4n+3}^{\infty}(\zeta) - \overline{B_{2(2n+1)}} G_{2(2n+1)}^0(\zeta) - \frac{\overline{B'_{2(2n+1)}}}{4n+3} G_{4n+3}^0(\zeta) \right) \right] \right\},$$

$$\begin{aligned}
(5) \quad \psi(\zeta) = & \frac{P_c R}{\pi} \frac{\zeta^2}{\zeta^2 - m} \left\{ -R^2 \left(8m\overline{B}_2/3 + \overline{B}'_2 \right) / \zeta^5 - \left[R^2 \left[4(1 + 3m^2)\overline{B}_2/3 + 2m\overline{B}'_2 \right] + \overline{B}'_0 \right] / \zeta^3 \right. \\
& - \left[2(1 + m^2)(b_0 + 2mR^2\Re B_2) + m\Re(B'_0 + mR^2 B'_2) \right] / \zeta + (B'_0 + 2mR^2 B'_2/3)\zeta + R^2 B'_2 \zeta^3 \\
& + (1 + m\zeta^2) \sum_{n=1}^{\infty} \left[R^{4n} \left(\frac{\overline{B}_{4n}}{B_{4n}} \frac{dG_{4n}^0(\zeta)}{d\zeta} - \frac{B_{4n}}{4n+1} \frac{dG_{4n+1}^{\infty}(\zeta)}{d\zeta} + \frac{\overline{B}'_{4n}}{4n+1} \frac{dG_{4n+1}^0(\zeta)}{d\zeta} \right) \right. \\
& + R^{2(2n+1)} \left(\frac{\overline{B}_{2(2n+1)}}{B_{2(2n+1)}} \frac{dG_{2(2n+1)}^0(\zeta)}{d\zeta} - \frac{B_{2(2n+1)}}{4n+3} \frac{dG_{4n+3}^{\infty}(\zeta)}{d\zeta} + \frac{\overline{B}'_{2(2n+1)}}{4n+3} \frac{dG_{4n+3}^0(\zeta)}{d\zeta} \right) \left. \right] \\
& - (1 - m/\zeta^2) \sum_{n=1}^{\infty} \left[R^{4n} \left(\frac{\overline{B}_{4n}}{4n+1} G_{4n+1}^0(\zeta) - B_{4n} G_{4n}^{\infty}(\zeta) - \frac{B'_{4n}}{4n+1} G_{4n+1}^{\infty}(\zeta) \right) \right. \\
& + R^{2(2n+1)} \left(\frac{\overline{B}_{2(2n+1)}}{4n+3} G_{4n+3}^0(\zeta) - B_{2(2n+1)} G_{2(2n+1)}^{\infty}(\zeta) - \frac{B'_{2(2n+1)}}{4n+3} G_{4n+3}^{\infty}(\zeta) \right) \left. \right] \left. \right\},
\end{aligned}$$

with b_0 , B_j and B'_j constants follow from [2] and $G_j^{\infty}(\zeta)$, $G_j^0(\zeta)$ the principal parts at ∞ and 0 of functions involved. Inserting (4) and (5) in the familiar Muskhelishvili's [1] formulae:

$$\begin{aligned}
(6) \quad \sigma_r - i\sigma_{r\varphi} = & 2\Re\varphi'(\zeta) - \frac{\zeta^2}{\rho^2\omega'(\zeta)} \left[\overline{\omega(\zeta)}\varphi''(\zeta) + \omega'(\zeta)\psi'(\zeta) \right], \quad \sigma_r + \sigma_{r\varphi} = 4\Re\varphi'(\zeta), \\
2\mu(u + iv) = & \kappa\varphi(\zeta) - \frac{\omega(\zeta)}{\overline{\omega'(\zeta)}}\varphi'(\zeta) - \overline{\psi(\zeta)},
\end{aligned}$$

the stresses and displacements are obtained at any z through $\zeta = (z + \sqrt{z^2 - 4mR^2})/(2R)$. Setting $m = 0$ or $m = 1$ one obtains the solution of the ring or the disc with the straight cut 2α , respectively. In Fig. 2 its deformed shape and stress state along x -axis are shown of a disc with $R_O = 0.05$ m, $\alpha = R_O/2$, $b = R_O/10$, $t = 0.01$ m, made of PMMA ($E = 3.19$ GPa, $\nu = 0.36$), squeezed between the ISRM's curved ($R_J = 1.5R_O$) steel jaws ($E_J = 210$ GPa, $\nu_J = 0.3$) under an overall load $P_{\text{frame}} = 40$ kN at $\varphi_0 = 30^\circ$. 4 additional terms of the infinite series were used to draw the deformed L , while 40 ones to plot stresses. According to the basic assumption, the ring's solution $\{\varphi_0, \psi_0\}$ was employed to draw the outer deformed boundary of the disc. The rotation and rolling of the elliptic hole's lips and the increased stress values obtained at α are clearly seen.

Acknowledgments

This research has been co-financed by the European Social Fund (ESF) and Greek national funds through the THALES-MIS380147 Program.

References

1. N.I. Muskhelishvili (1963). *Some Basic Problems of the Mathematical Theory of Elasticity*, 4th ed. P. Noordhoff Groningen, Netherlands.
2. S.K. Kourkoulis, Ch.F. Markides, E.D. Pasiou (2014). A combined analytic and experimental study of the displacements field in a circular ring, *Meccanica*, DOI 10.1007/s11012-013-9846-0.

NUMPRESS – INTEGRATED COMPUTER SYSTEM FOR ANALYSIS AND
OPTIMIZATION OF INDUSTRIAL SHEET METAL FORMING PROCESSES:
NUMERICAL INVESTIGATION OF SQUARE CUP DRAWING

P. Kowalczyk, J. Rojek, R. Stocki, T. Bednarek, P. Tazowski, R. Lasota,
D. Lumelsky, K. Wawrzyk

Institute of Fundamental Technological Research, Warsaw, Poland

1. Introduction

This paper presents basic features of the NUMPRESS system and some examples of use. The system has been developed at IPPT PAN as a result of a project financially supported by European Regional Development Fund and is dedicated to small and middle enterprises (SME) dealing with sheet metal forming. The program consists of (i) an analytical finite element method module (ii) an optimization module, (iii) a reliability analysis module, and (iv) a graphical user interface enabling communication between modules. The analytical module consists of two independent programs up to the user's choice: NUMPRESS-Flow, a faster and less accurate program for implicit quasi-static analysis of rigid-viscoplastic shells (based on the flow approach) and NUMPRESS-Explicit, a program for explicit dynamical analysis of elastic-plastic shells. Both programs are interfaced to a well-known commercial graphical pre-and postprocessor GiD.

2. Program description

The NUMPRESS-Explicit is based on the explicit FE solution of the equations of motion. The theoretical formulation is based on that of Oñate *et al.* [1]. Sheet is discretized by the basic shell triangular (BST) elements [2]. The BST element features linear approximation of displacements within each triangle. Kinematics of the element is based on the Kirchhoff shell theory. The material properties are considered assuming the Hill'48 model. The implementation of the material model includes anisotropy of the sheet described by Lankford coefficients.

The program NUMPRESS-Flow is another FEA system in which a simplified rigid-viscoplastic material model is used for sheet. Elastic part of the deformation is neglected which limits its applicability. The flow approach formulation for large deformation shells [3, 4] is adopted. The constitutive model is based on the classical J_2 theory with the given nonlinear yield function $\sigma_y(\bar{\varepsilon})$ and with the viscoplastic effects included, based on Perzyna formulation. As a result, a formulation is obtained in which a visible analogy to nonlinear elasticity equations exists (with all displacement and strain fields and arrays replaced with velocities and strain rates, respectively), which makes it easy to implement it in a FE code. This simple formulation has not yet gained wide interest by developers of academic and commercial FE codes dedicated for sheet metal forming problems.

The module NUMPRESS-Explore has been developed to facilitate the design process by providing tools to find the optimal forming parameters and to allow for a variety of probabilistic analyzes like scatter analysis or reliability analysis. NUMPRESS-Explore automates and manages the process of calling the external computational modules (Explicit and Flow), which, depending on the problem, are executed in serial or parallel mode. NUMPRESS-Explore's GUI controls problem definition, submission of computations and post-processing of the results.

3. Numerical investigation of square cup drawing

To illustrate some of the software capabilities, analysis of stamping process of an aluminum square cup is performed. Numerical results of stamping calculations is presented in Figs. 1 and 2. Comparison of the thickness strain distribution calculated by both analytical modules and experimental results is presented in Fig. 1. Results received by the module NUMPRESS-Explicit using planar and transversal anisotropy formulations are close to each other. Good agreement is seen between numerical and experimental results. For the square cup model on stamping depth 20 mm, we expect that we obtain failure because during experiments failure in specimen occur for the same depth. It is seen on the forming limit diagram presented in Fig. 2a. Strains marked by red color are close to forming limit curve, so we can take that such strains are in almost in failure zone. Such strains occurs in corners of the square cup (Fig. 2b).

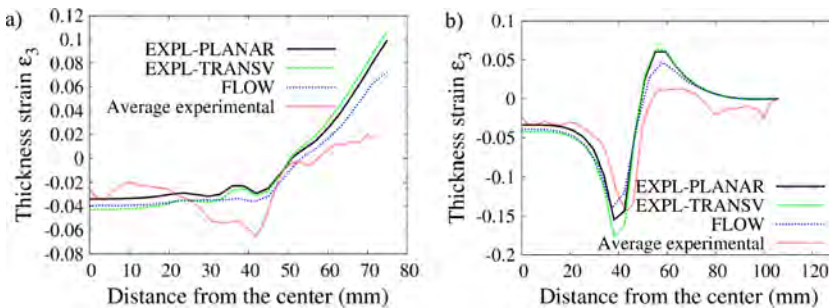


Fig. 1. Numerical results of thickness strain distribution in square cup specimen, stamping depth 15 mm, along the cross section: a) centerline, b) centerline rotated 45°.

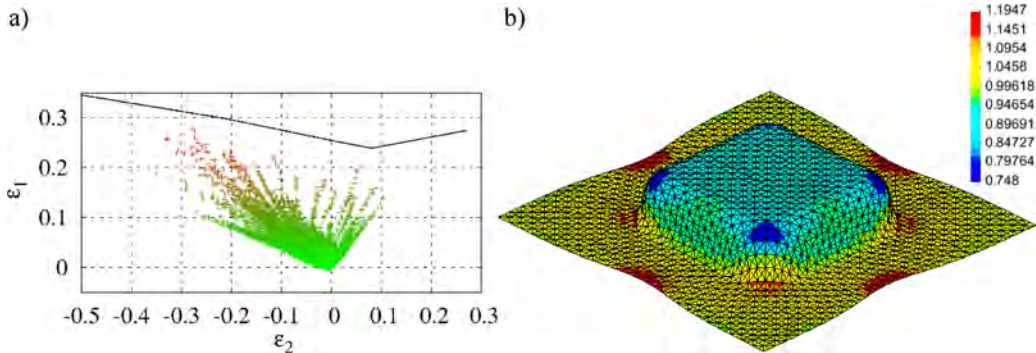


Fig. 2. Numerical results of strain distribution (a) in square cup specimen compared with experimental forming limit curve and thickness ratio (b), stamping depth 20 mm.

Acknowledgments

Financial support from European Regional Development Fund within the framework of the Innovative Economy Programme (project no. POIG.01.03.01-14209/09, acronym NUMPRESS) is gratefully acknowledged.

References

1. Oñate E., Rojek J., Garcia Garino C. (1995). NUMISTAMP: a research project for assesment of finite element models for stamping processes, *Journal of Material Processing Technology*, 50, 17–38.
2. Oñate E., Cervera M. (1993). Derivation of thin plate bending elements with one degree of freedom per node: a simple three node triangle, *Engineering Computations*, 10, 6, 543–561.
3. Oñate E., Zienkiewicz O.C. (1983). A viscous shell formulation for the analysis of thin sheet metal forming, *International Journal of Mechanical Sciences*, 25, 305–335.
4. Agelet de Saracibar C. (1990). *Finite Element Analysis of Sheet Metal Forming Processes*, PhD thesis (in Spanish), Universitat Politecnica de Catalunya, Barcelona.

**TWO-DIMENSIONAL MODEL OF FIFTH ORDER FOR THE COMBINED BENDING,
STRETCHING AND SHEARING OF SHELLS DERIVED FROM
THREE-DIMENSIONAL ELASTICITY: GENERAL APPROACH
AND APPLICATION TO CYLINDRICAL SHELLS**

E. Pruchnicki

Ecole Polytechnique Universitaire de Lille, Cité Scientifique
Avenue Paul Langevin F 59655 Villeneuve d'Ascq Cedex, France

The problem of deriving approximate lower-dimensional models from three-dimensional elasticity to describe the behavior of beams, plates and shells is one of the major open problems of Mechanics (Ball [1]). For homogeneous shells, the problem is addressed through the use of gamma convergence method (Friesecke, James and Müller [2]) or the method of asymptotic expansion applied to the weak forms of the three dimensional problem (Ciarlet [3]). Further works for heterogeneous nonlinear shells can be found in Pruchnicki [4]. These methods have given results for pure membrane behavior and for inextensional bending and thus separate the scale associated with membrane and bending behavior. In general, as remarked in Friesecke [5], the bending is not inextensional and it would be interesting to have a two-dimensional coupled membrane-bending model which is valid whatever is the order of magnitude of the loads. Ciarlet and Roquefort [6] proposed in the spirit of the work of Koiter [7] a two-dimensional model independent of the order of magnitude of the loads which generalizes the two-dimensional membrane modeling (Ciarlet and Lods [8]) and the two-dimensional pure bending modeling obtained by asymptotic analysis (Ciarlet *et al.* [9]). Nevertheless this coupled model was not directly deduced from three-dimensional elasticity. By using a thickness-wise expansion of the displacement field, Steigmann [10] deduced from three-dimensional elasticity, a two-dimensional modeling for thin elastic homogeneous shell depending on the thickness and combining both membrane and bending effects.

However it can be noted that for homogeneous shells, h^3 truncation of the internal energy contains a term of order h^3 which is not sign definite (Steigmann [10]) and then equilibria generated by the model may not minimize the associated approximation to the potential energy. If we add transverse shear internal energy (Pruchnicki [11]), the Legendre-Hadamard condition will be satisfied then this term appears as a regularization term of the internal energy even if it is of order higher than h^3 . Here we propose to extend this model to order h^5 . The outline of this paper reads as follows. For shells, we derive a two-dimensional model for combined stretching, bending and shearing in the presence of boundary conditions. According to the results of Fichera [12], the displacement field can be approximated in each layer by a Taylor-Young expansion up to fifth-order in thickness. The potential energy is truncated at fifth-order and for consistency with the exact theory, exact equilibrium equation is considered as a constraint. In the case of cylindrical shell, we obtain an analytical approximate expression of the potential energy of the laminated shell in terms of the displacement field at the interface and its derivatives which satisfies the Legendre-Hadamard stability condition. We present the mathematical formulation at Zakopane.

References

1. J.M. Ball (2002). Some open problems in elasticity, in: *Geometry, Mechanics and Dynamics*, 3–59, Springer, New-York.
2. G. Friesecke, R.D. James, S. Müller (2002). Derivation of nonlinear bending theory for shells from three-dimensional nonlinear elasticity theory by Gamma-convergence, *C.R. Acad. Sci. Paris, Ser I*, **336**, 697–702.
3. P.G. Ciarlet (1998). *Introduction to Linear Shell Theory*, Elsevier.
4. E. Pruchnicki (2006). Nonlinearly elastic membrane model for heterogeneous shells: a formal asymptotic approach, *J. Elasticity*, **84**, 245–280.
5. G. Friesecke, R.D. James, S. Müller (2006). A hierarchy of plate models derived from nonlinear elasticity by gamma-convergence, *Arch. Ration. Mech. Anal.*, **180**, 183–236.
6. P.G. Ciarlet, A. Roquefort (2001). Justification of a two-dimensional nonlinear shell model of Koiter's type, *Chin. Ann. of Math.*, **22B**, 129–144.
7. W.T. Koiter (1966). On the nonlinear theory of thin elastic shells, *Proc. Kon. Ned. Akad. Wetensch.*, **B69**, 1–54.
8. P.G. Ciarlet, V. Lods (1996). Asymptotic Analysis of Linearly Elastic Shells. I. Justification of Membrane Shell Equations, *Arch. Rational Mech. Anal.*, **136**, 119–161.
9. P.G. Ciarlet, V. Lods, B. Miara (1996). Asymptotic analysis of linearly elastic shells. II. Justification of Flexural Shell Equations, *Arch. Rational Mech. Anal.*, **136**, 163–190.
10. D.J. Steigmann (2012). Extension of Koiter's linear shell theory to materials exhibiting arbitrary symmetry, *Int. J. Engng. Sci.*, **46**, 654–676.
11. E. Pruchnicki (2013). Two-dimensional model for the combined, stretching and shearing of shells: A general approach and application to laminated cylindrical shells derived from three-dimensional elasticity, *Mathematics and Mechanics of Solids*, DOI: 1081286512470676.
12. G. Fichera (1972). Existence theorems in elasticity, in: C. Truesdell (ed.), *Handbuch der Physik*, vol VIa/2, Springer, Berlin, 347–389.

DISTORTION-IMMUNE 9-NODE QUADRILATERAL THICK PLATE FINITE ELEMENTS THAT SATISFY CONSTANT-BENDING PATCH TEST

D. Ribarić, G. Jelenić

University of Rijeka, Faculty of Civil Engineering, Rijeka, Croatia

1. Linked interpolation concept

We employ the linked interpolation concept to develop two higher-order 9-node quadrilateral plate finite elements with curved sides that pass the constant bending patch test for arbitrary node positions. The linked interpolation for the plate displacements is expanded to get polynomial completeness necessary to satisfy the patch test. The resulting plate element (proposed element $Q9 - L2$) involves all twenty-five monomials of the bi-quartic parametric polynomial for the displacement interpolation and full bi-quadratic interpolation with nine monomials for rotations in both directions necessitating as many as sixteen additional degrees of freedom more than the pure Lagrangean 9-node element ($Q9$). However, taking advantage of the linked interpolation concept, the number of associated parameters is reduced by as many as twelve degrees of freedom, leaving the distortion-immune element with thirty-one degrees of freedom (of which four are internal).

If the internal element node is further taken to be in the central position (relative to the side nodes), three of the remaining four internal bubbles cease to be necessary to pass the patch test (proposed element $Q9 - L1$). It needs to be emphasized that the position of the central node may be defined automatically by the procedure making this element particularly efficient.

All elements presented here retain invariance to the coordinate rotation and show no singularity when the element shape is distorted from a quadrilateral to a triangle and they are free of zero energy modes (other than those relating to the three rigid body motions) regardless of the plate thickness.

2. Shear strain reduction

The proposed interpolation concept follows from the idea of reducing the derived shear strain expressions to the linear form, for the all six element sides of the 9-node plate element (Fig. 1). For example, along the chosen element side ($a - b - c = 1 - 2 - 3$) after coordinate transformation, shear is expressed:

$$(1) \quad \gamma_{s,\xi} = \left\{ \frac{w_3 - w_1}{2} + \frac{w_{b3}}{4} + \xi \left(w_1 - 2w_2 + w_3 + \frac{w_{b9}}{2} + \frac{\theta_{y3} - \theta_{y1}}{2} \frac{\Delta x_{13}}{2} - \frac{\theta_{x3} - \theta_{x1}}{2} \frac{\Delta y_{13}}{2} \right) + \xi^2 \left[-\frac{3w_{b3}}{4} + (\theta_{y1} - 2\theta_{y2} + \theta_{y3}) \frac{\Delta x_{13}}{4} - (\theta_{x1} - 2\theta_{x2} + \theta_{x3}) \frac{\Delta y_{13}}{4} + \frac{\theta_{y3} - \theta_{y1}}{2} (\Delta x_{23} - \Delta x_{12}) - \frac{\theta_{x3} - \theta_{x1}}{2} (\Delta y_{23} - \Delta y_{12}) \right] + \xi^3 \left[-w_{b9} + (\theta_{y1} - 2\theta_{y2} + \theta_{y3}) \frac{(\Delta x_{23} - \Delta x_{12})}{2} - (\theta_{x1} - 2\theta_{x2} + \theta_{x3}) \frac{(\Delta y_{23} - \Delta y_{12})}{2} \right] \right\} \frac{1}{\partial s / \partial \xi}.$$

In order to eliminate the higher order terms associated with ξ^2 and ξ^3 , which prevent the shear strain to take the linear form, we can set the free parameters w_{b3} and w_{b9} to be dependent from the nodal rotations and the coordinate differences (Fig. 1).

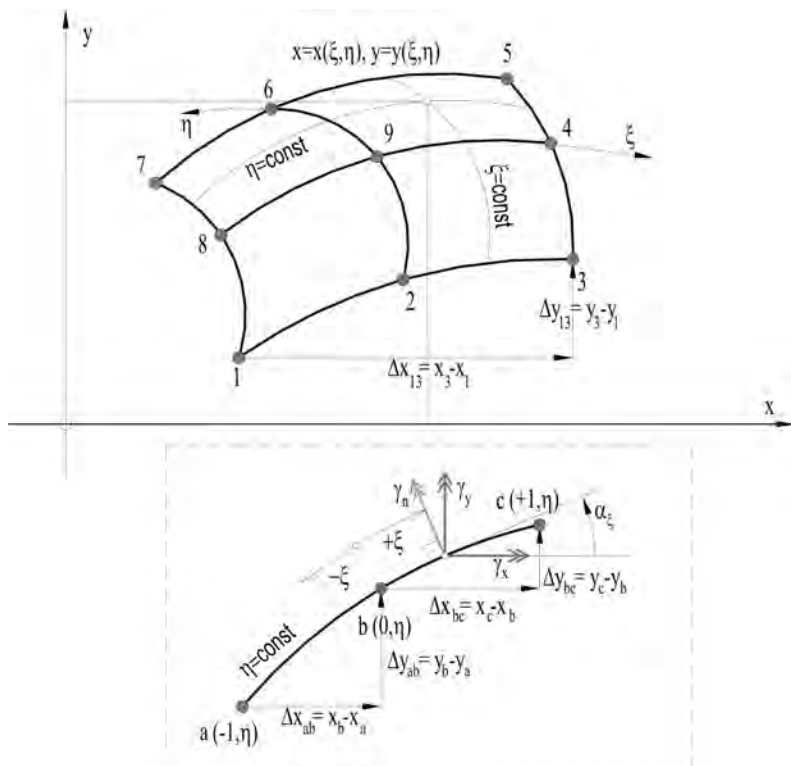


Fig. 1. Distorted 9-node quadrilateral plate element – relations between the global and the natural coordinates.

3. Conclusions

In contrast to some other techniques [1–4], the elements developed in this way retain a symmetric stiffness matrix at a marginal computational expense at the element level. The new elements generated using this concept, are tested on several examples with curved sides or some other kind of geometric distortion, showing superiority to the other elements from literature with the same number of degrees of freedom.

The concept of freely chosen node positions over the element is suitable for extending the interpolations used on $Q9 - L2$ element to develop an efficient shell element, where the present interpolation for the transverse displacement can be used to interpolate the shell surface perpendicular displacement, with the rotation interpolations describing the shell section rotations, and combined with in-plane membrane displacements.

References

1. N.S. Lee, K.J. Bathe (1993). Effects of element distortions on the performance of isoparametric elements, *Int. J. Num. Meth. Eng.*, **36**, 3553–3576.
2. S. Rajendran (2010). A technique to develop mesh-distortion immune finite elements, *Comput. Methods Appl. Mech. Engrg.*, **199**, 1044–1063.
3. G. Castellazzi (2011). On the performances of parametric finite elements when geometry distortions occur, *Finite Elements in Analysis and Design*, **47**, 1306–1314.
4. S. Cen, X.-R. Fu, M.-J. Zhou (2011). 8- and 12-node plane hybrid stress-function elements immune to severely distorted mesh containing elements with concave shapes, *Comput. Methods Appl. Mech. Engrg.*, **200**, 2321–2336.
5. D. Ribarić, G. Jelenić (2012). Higher-order linked interpolation in quadrilateral thick plate finite elements, *Finite Elements in Analysis and Design*, **51**, 67–80.

TOLERANCE MODELS OF STABILITY PROBLEMS FOR MICRO-PERIODIC CYLINDRICAL SHELLS

B. Tomczyk

Department of Structural Mechanics, Technical University of Lodz, Lodz, Poland

1. Formulation of the problem

Thin linearly elastic Kirchhoff-Love-type circular cylindrical shells with a periodically heterogeneous structure in circumferential direction are analysed. Shells of this kind are termed *uniperiodic*. Periodic inhomogeneity means here periodically variable shell thickness and/or periodically variable inertial and elastic properties of the shell material. The period of inhomogeneity is assumed to be very large compared with the maximum shell thickness and very small compared to the midsurface curvature radius as well as the smallest characteristic length dimension of the shell midsurface. As an example we can mention shells with periodically and densely spaced stiffeners in circumferential direction.

The properties of such shells are described by highly oscillating and non-continuous periodic functions, so the exact equations of the shell theory are too complicated to apply to investigations of engineering problems. That is why a lot of different approximate modelling methods for shells of this kind have been proposed. Periodic cylindrical shells (plates) are usually described using *homogenized models* derived by means of *asymptotic methods*, cf. [2]. Unfortunately, in the models of this kind *the effect of a cell size* (called *the length-scale effect*) on the overall shell behaviour is neglected in the first approximation which is usually employed. The periodically densely stiffened shells are also modelled as homogeneous orthotropic structures, cf. [1]. The orthotropic model equations with coefficients independent of the cell size cannot be used to the analysis of phenomena related to the existence of microstructure length-scale effect (e.g. the dispersion of waves).

In order to analyse the length-scale effect in selected dynamic or/and stability problems, the new averaged non-asymptotic models of thin cylindrical shells with a periodic microheterogeneity either along two directions tangent to the shell midsurface (*biperiodic structure*) or along one direction (*uniperiodic structure*) have been proposed and discussed by Tomczyk in a series of publications and summarized as well as extended in [4]. These, so-called, *tolerance models* have been obtained by applying *the non-asymptotic tolerance averaging technique* presented and discussed by Woźniak in many monographs, e.g. [5]. This technique is based on the concept of *tolerance relations* between points and real numbers related to the accuracy of the performed measurements and calculations. These tolerance relations are determined by *the tolerance parameters*. The second basic concept of this method is *a function slowly-varying within a cell*. It is a function which, together with its derivatives occurring in the problem under consideration, can be treated in the framework of tolerance as constant within every cell. Contrary to starting equations of theories of microheterogeneous structures (partial differential equations with functional, highly oscillating, non-continuous coefficients), *governing equations of the tolerance models have coefficients which are constant or slowly-varying and depend on the period length of inhomogeneity*. Hence, these equations make it possible to analyze the length-scale effect.

Applications of the tolerance averaging technique to the investigations of selected dynamical and/or stability problems for various periodic structures are shown in many works. The extended list of papers and books on this topic can be found in [4, 5].

A certain extended version of the known tolerance modelling technique has been proposed by Tomczyk and Woźniak in [3]. This version is based on a new notion of *two kinds of slowly-varying functions*, contrary to “classical” tolerance modelling procedure based on a concept of only one kind of these functions. In work [3], for the first time it was shown that application of two kinds of slowly-varying functions leads to a number of different tolerance models describing this same modelling problem. It means that the formulated engineering problem does not have the unique solution. In work [3], the considerations were carried out in the framework of the linear elastodynamics of thin cylindrical uniperiodic shells being in *the membrane state*.

In contribution presented here, using the new notion of two kinds of slowly-varying functions introduced in [3], *we will formulate two new tolerance non-asymptotic models for the analysis of selected dynamic and stability problems for the uniperiodic shells under consideration*. The considerations will be carried out in the framework of the well-known linear Kirchhoff-Love second-order theory of thin elastic shells being in *the bending state*. Contrary to starting exact shell equations with highly oscillating non-continuous periodic coefficients, *the proposed general and standard tolerance models have constant coefficients depending also on a cell size*. Hence, *the tolerance models make it possible to analyze the effect of a length scale on the global shell dynamics and stability*. *The general model equations* derived by means of the concept of *weakly slowly-varying function* contain a bigger number of terms depending on the microstructure size than *the standard model equations* obtained by means of the concept of *slowly-varying function*, so they allow us to investigate the length-scale effect in more detail. Moreover, a certain homogenized (asymptotic) model, being independent of a microstructure size, will be also derived applying the extended tolerance averaging technique presented in [3].

2. Applications and concluding remarks

The tolerance and asymptotic models, proposed here, will be applied to analyse the length scale effect in stability of an open simply supported circular cylindrical shell reinforced by thin stiffeners periodically and densely distributed in circumferential direction. In order to evaluate this effect the critical forces derived from the tolerance non-asymptotic models will be compared with the results obtained from the asymptotic model. Moreover, critical forces derived from the general tolerance model will be compared with those obtained from the standard tolerance one.

We are to show, under what conditions the effect of a microstructure length on the values of critical forces in microperiodic shells under consideration plays an important role and hence only the non-asymptotic models have to be used to analyse the stability problem under consideration. We are also show under what conditions this effect can be neglected and hence the asymptotic model being independent of a cell size is sufficient to determination and analysis of the critical forces in microheterogeneous cylindrical shells.

In the framework of the non-asymptotic tolerance models proposed here, *the fundamental lower and new additional higher critical forces* can be derived. These new higher critical forces depending on a cell size cannot be determined using the asymptotic model.

References

1. S.A. Ambartsumyan (1974). *Theory of anisotropic shells*, Nauka, Moscow, (in Russian).
2. T. Lewiński, J.J Telega (2000). *Plates, laminates and shells. Asymptotic analysis and homogenization*, Word Scientific Publishing Company, Singapore.
3. B. Tomczyk, C. Woźniak (2012). Tolerance models in elastodynamics of certain reinforced thin-walled structures, in: *Statics, dynamics and stability of structural elements and systems*, Z. Kołakowski, K. Kowal-Michalska (eds.), Technical University of Lodz Press, Lodz, 123–153.
4. B. Tomczyk (2013). *Length-scale effect in dynamics and stability of thin periodic cylindrical shells*, Scientific Bulletin of the Lodz University of Technology, No. **1166**, series: Scientific Dissertations, Technical University of Lodz Press, Lodz.
5. C. Wozniak *et al.* (eds.) (2008). *Thermomechanics of microheterogeneous solids and structures. Tolerance averaging approach*, Technical University of Lodz Press, Lodz.

A COMPARATIVE STUDY OF NEW DUAL-MIXED h - AND p -VERSION CYLINDRICAL SHELL FINITE ELEMENTS FOR ELASTOSTATIC PROBLEMS

B. Tóth

Institute of Applied Mechanics, University of Miskolc, Miskolc-Egyetemváros, Hungary

1. Introduction

The widely-used standard, displacement-based finite element techniques have some significant disadvantages. The conventional structural finite elements built in the commercial finite element softwares can give low convergence rates and inaccurate solutions particularly for the stress field, which is often more important in the engineering practice than the knowledge of the displacement field. The primal-mixed and displacement-based methods can provide especially inaccurate numerical results and slow convergences mainly when bending-dominated plate and shell problems are investigated for small thicknesses. This phenomenon is known as numerical locking effects including the shear- and membrane locking [1–2]. One of the possible ways to avoid these numerical difficulties in shell finite element modeling is to use dual-mixed variational formulations within the context of the linear elasticity. These complementary energy-based principles are suitable for the direct approximations of the stress field. Therefore they can provide better convergence rates and higher accuracy for the stresses than the strain energy-based primal-mixed formulations and conventional displacement-based models.

2. Objectives and the basic assumptions

The main goal is to present the similarities and differences between the new, dimensionally reduced cylindrical shell models based on the three-field dual-mixed Hellinger-Reissner-type and the two-field dual-mixed Fraeijs de Veubeke variational principles using *a priori* non-symmetric stresses [3–5].

During the dimensional reduction procedure all the variables are expanded into power series with respect to the thickness coordinate. Assuming thin cylindrical shells the translational equilibrium equations in terms of the expanded stresses are obtained. The only hypothesis for *a priori* satisfaction of the second- and higher-order equilibrium equations is employed. According to this assumption the stress coordinates are approximated by linear and parabolic functions across the thickness. Therefore the symmetry of the stress tensor should be satisfied in a weak sense. The applied variational principles allow me to use this requirement [3–5].

The approximation of the stresses prescribes the approximation of the other variables such as the first-order stress functions, the displacements and the infinitesimal rotations [3–5]. Another important property of the shell models developed is that the classical kinematical hypotheses regarding the deformation of the normal to the shell mid-surface are not used, i.e., the inverse unmodified three-dimensional constitutive equations are applied.

3. Summary about FEM and the numerical results

Dual-mixed h - and p -version finite element models are demonstrated for bending-shearing (including tension-compression) cylindrical shell problems. The computational

performances of the constructed shell elements are compared through two representative, boundary-value problems proving the efficiency and reliability of these hp elements [3–5]. The convergence rates in the energy norm as well as in the maximum norm of stresses and displacements are presented not only for h - but also for p -approximations.

It will be presented that no sensitivity of the convergence rates to the thickness change is experienced for both h - and p -extensions, i.e., the shell finite elements developed is shear locking-free. The further results and conclusions will be presented on the conference.

References

1. K.-U. Bletzinger, M. Bischoff, E. Ramm (2000). A unified approach for shear-locking-free triangular and rectangular shell finite elements, *Comput. Struct.*, **75**, 321–334.
2. K. Gerdes, A.M. Matache, C. Schwab (1998). Analysis of membrane locking in hp FEM for a cylindrical shell, *ZAMM, J. Appl. Math. Mech.*, **78**, 663–686.
3. L.G. Kocsán (2011). Derivation of a dual-mixed hp -finite element model for axisymmetrically loaded cylindrical shells, *Arch. Appl. Mech.*, **81**, 1953–1971.
4. B. Tóth (2012). Dual-mixed hp finite element model for elastic cylindrical shells, *ZAMM, J. Appl. Math. Mech.*, **92**, 236–252.
5. B. Tóth, L.G. Kocsán (2013). Comparison of dual-mixed h - and p -version finite element models for axisymmetric problems of cylindrical shells, *Finite Elements in Analysis and Design*, **65**, 50–62.

ON THE INFLUENCE OF SHELL-KINEMATICS ON THE FAILURE BEHAVIOUR OF COMPOSITE SHELL STRUCTURES

W. Wagner, J. Läufer

Institute of Structural Analysis, Karlsruhe Institute of Technology, Karlsruhe, Germany

1. Introduction

Nowadays composite material is often used in combination with thin structures. Classical applications are different types of shell panels introduced as parts of cars, aircrafts, racing yachts and other structures, where the question of low weight together with high stiffness and strength values is of high interest. Here the material behaviour will be described more and more in detail. Thus questions of geometrical and material nonlinearities were discussed. One aspect describing the complete failure of the structure is the intra- and interlaminar damage behaviour of the used composite materials. This may depend strongly on the chosen structural approach and will be discussed in this paper.

2. Structural approach

The classical approach is the application of a geometrical nonlinear shell model together with a layerwise description of the material behaviour, e.g. [1, 2]. Within the kinematical description one straight director is introduced. To describe the behaviour in thickness direction more in detail multi-director theories have been presented, e.g. [3] among others. Typically a straight director is introduced for each layer. A further refinement is possible using numerical and physical layers. The advantage of such a formulation is the completely 2D-description of the structure. Thinking in degrees of freedom of the overall FE-problem a 3D-FE-model leads to the same number of unknowns. Thus simple 3D-hexahedral elements could also be used but having the deficiency of locking. This could be overcome very efficiently using so called solid shell concepts, e.g. [4, 5], here in the sense that at least one solid shell element for each layer in thickness direction exists. Thus a multi-director kinematical approach is employed with respect to the overall thickness of the structure. Based on the efficiency of these solid shell concepts, a model with only one solid element in thickness direction together with the layerwise approach, is another option being very close to the classical shell concept. Differences may occur especially in defining boundary conditions.

As a third approach one can operate with multi-scale methods, see e.g. for the application to shell structures [6]. Here the structural behaviour is described on the shell level, whereas the material behaviour is described on a representative volume element at each integration point of the structural elements. Special focus has to be set on the choice of boundary conditions, see e.g. [6]. A graphical interpretation of these different options is depicted in Fig. 1.

3. Material approach

In addition to these different discretization models we will describe material nonlinear effects. Here we will restrict us on the intralaminar damage behaviour based on the models of Hashin and Cuntze, e.g. in [7]. These damage models consist of failure criteria and degradation models. The degradation simulates the post-failure behaviour resulting in strong influences on the problem.. Interlaminar failure is not addressed in this paper.



Fig. 1. Different discretization models for thin laminated structures.

4. Examples

Within examples we will discuss the described different discretization models and with that the different kinematical assumptions used on structural level with respect to the damage behavior of thin shell structures.

References

1. W. Wagner, F. Gruttmann (2005). A robust nonlinear mixed hybrid quadrilateral shell element, *Int. J. Num. Meth. Eng.*, **64**, 635–666.
2. F. Gruttmann, W. Wagner (2006). Structural analysis of composite laminates using a mixed hybrid shell element, *Comp. Mech.*, **37**, 479–497.
3. F. Gruttmann, W. Wagner (1996). Delamination Analysis of thin Composite Structures using a Multi-Director Formulation, in: B.H.V. Topping (ed.), *Advances in Analysis and Design*, Civil-Comp. Press, Edinburgh, 51–59.
4. S. Klinkel, W. Wagner, W. (1997). A Geometrical Nonlinear Brick Element based on the EAS-Method, *Int. J. Num. Meth. Eng.*, **40**, 4529–4545.
5. S. Klinkel, F. Gruttmann, W. Wagner (2006). A Robust Non-Linear Solid Shell Element Based on a Mixed Variational Formulation, *Comp. Meth. Appl. Mech. Eng.*, **195**, 179–201.
6. F. Gruttmann, W. Wagner (2013). A coupled two-scale shell model with applications to layered structures, *Int. J. Num. Meth. Eng.*, **94**, 1233–1254.
7. J. Läufer, S. Lauterbach, W. Wagner (2014). Analysis and finite element modeling of composite structures using the damage models of Hashin and Cuntze, submitted to *Computational Mechanics*.

MODELLING OF THIN SKELETONAL ANNULAR PLATES WITH DENSE SYSTEM OF RIBS

A. Wirowski, M. Rabenda, B. Michalak

Department of Structural Mechanic, Technical University of Lodz, Poland

The subject of this contribution is a certain thin skeletal annular plate. The aim of analysis is to derive and apply a macroscopic model for annular plate with the non-uniformly oscillating microstructure. The main feature of the proposed mathematical model is that the microstructure length parameter l is similar compared to thickness h of the plate ($l \cong h$). The formulation of approximate mathematical model of these plates is based on a tolerance averaging approximation [3]. The general results of the contribution will be illustrated by the analysis of a specific problem.

1. Introduction

The considered skeletal plate is made of two families of thin beams with axes intersecting under the right angle. The regions situated between the beams are filled with a homogeneous matrix material (Fig. 1). It is assumed that midplane of the plate represents a certain plane microheterogeneous structure which is periodic along angular ξ^2 -coordinate but has slowly varying apparent properties in the radial direction. The generalized period $l = \sqrt{l_1 l_2}$ of inhomogeneity is assumed to be sufficiently small when compared to the measure of the domain of coordinates ξ^α . At the same time it is assumed that the microstructure length parameter l is similar compared to thickness h of the plate. Thus we deal with a composite plate having what can be called space-varying periodic microstructure. From a formal point of view, the structure under consideration can be described in the framework of the well-known theories for thin elastic plates. However, due to the inhomogeneous microstructure of the plate, this direct description of the structure leads to plate equations with discontinuous and highly oscillating coefficients. The aim of the contribution is to formulate and apply the macroscopic mathematical model describing the composite plate under consideration. The formulation of the macroscopic mathematical model for the analysis of dynamic behaviour of these plates will be based on the tolerance averaging technique. The applications of this technique for the modelling of various dynamic problems of elastic microheterogeneous composites are given in a series of papers [1, 2].

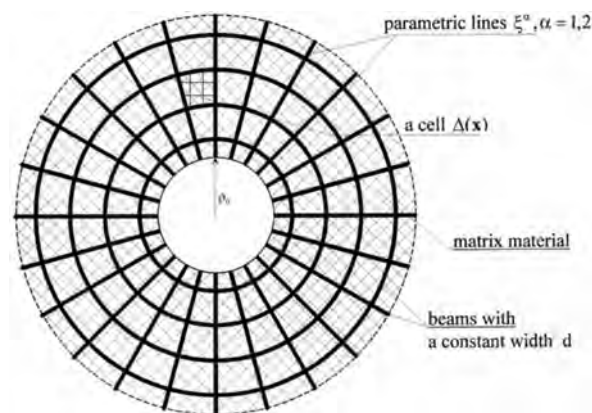


Fig. 1. Fragment of skeletal plate.

2. Direct description

The starting point of this contribution is the direct description of the structure in the framework of the well known theory of thin plates. The displacement field of the arbitrary point of the plate we write in form

$$(1) \quad w_3(x, z) = w_3(x), \quad w_\alpha(x, z) = w_\alpha^0(x) - \partial_\alpha w_3(x) z.$$

Denoting by $\mathbf{p}(\mathbf{x}, t)$ the external forces, by ρ the mass density, setting $\partial_k = \partial/\partial x^k$ we also introduce gradient operators $\nabla \equiv (\partial_1, \partial_2)$, in the framework of the linear approximated theory for thin plates, we obtain the following system of equations: strain-displacement relations (2) and strain energy averaged over the plate thickness (3):

$$(2) \quad \varepsilon_{\alpha\beta}(x, z) = \varepsilon_{\alpha\beta}^0(x) + \kappa_{\alpha\beta}(x) z, \quad \varepsilon_{\alpha\beta}^0 = \partial_{(\beta} w_\alpha^0), \quad \kappa_{\alpha\beta} = -\nabla_{\alpha\beta} w_3;$$

$$(3) \quad E(x) = \frac{1}{2} B^{\alpha\beta\gamma\delta} \nabla_{\alpha\beta} w_3 \nabla_{\gamma\delta} w_3 + \frac{1}{2} D^{\alpha\beta\gamma\delta} \partial_{(\beta} w_\alpha^0 \partial_{(\delta} w_\gamma^0).$$

3. Averaged description

Let us introduce the orthogonal curvilinear coordinate system $O\xi^1\xi^2\xi^3$. Setting $\mathbf{x} \equiv (\xi^1, \xi^2)$ and $z = \xi^3$ it is assumed that the undeformed plate occupies the region $\Omega \equiv \{(\mathbf{x}, z) : -h/2 \leq z \leq h/2, \mathbf{x} \in \Pi\}$, where $\Pi = [0, \varphi] \times [R_1, R_2]$ is the plate midplane and h is the plate thickness. Denote Π_Δ as a subset of Π for points with coordinates determined by conditions $(\xi^1, \xi^2) \in (\Delta\varphi/2, \varphi - \Delta\varphi/2) \times (R_1 + l_1/2, R_2 - l_1/2)$. An arbitrary cell with a center situated on the radial coordinate at point $(\xi^1)_j = l_1/2 + (j - 1)l_1$, $j = 1, \dots, n$ will be determined by $\Delta(\xi^\alpha) \equiv (-\Delta\varphi/2, -\Delta\varphi/2) \times ((\xi^1)_j - l_1/2, (\xi^1)_j + l_1/2)$. The modeling technique will be based on the tolerance averaging approximation and on the restriction of the displacement field under consideration given by

$$(4) \quad \begin{aligned} w_3(x, z, t) &= V_3(x, t), \\ w_\alpha(x, z, t) &= V_\alpha(x, t) + \varphi^A(x) V_\alpha^A(x, t) + (-\partial_\alpha V_3(x, t) + \varphi^A(x) u_\alpha^A(x, t)) z, \end{aligned}$$

The governing equations derived from stationary action principle of the averaged lagrangian $\langle \Lambda \rangle = \langle K \rangle - \langle E \rangle + \langle F \rangle$ have the form

$$(5) \quad \begin{aligned} \nabla_{\alpha\beta} \left((\tilde{B}^{\alpha\beta\gamma\delta} - \tilde{B}^{\mu B\alpha\beta} K^{\mu B\tau A} \tilde{B}^{\tau A\gamma\delta}) \nabla_{\gamma\delta} V_3 \right)_3 + \langle \tilde{\rho} \rangle \ddot{V}_3 &= \langle f^3 \rangle, \\ \nabla_\delta (\tilde{D}^{\alpha\beta\gamma\delta} \nabla_\beta V_\alpha + \tilde{D}^{\alpha A\gamma\delta} V_\alpha^A) - \langle \tilde{\rho} \rangle \ddot{V}_\gamma - \langle \tilde{\rho} \varphi^A \rangle \ddot{V}_\gamma^A &= -\langle f^\gamma \rangle, \\ \tilde{D}^{\alpha A\gamma\delta} \nabla_\delta V_\gamma + \tilde{D}^{\alpha A\gamma B} V_\gamma^B + \langle \tilde{\rho} \rangle \varphi^A \varphi^B \ddot{V}_\alpha^B + \langle \tilde{\rho} \varphi^A \rangle \ddot{V}_\alpha &= \langle f^\alpha \varphi^A \rangle. \end{aligned}$$

The above equations have the smooth and functional coefficients in contrast to equations in direct description with the discontinuous and highly oscillating coefficients.

References

1. Kaźmierczak M., Jędrysiak J. (2013). A new combined asymptotic-tolerance model of vibrations of thin transversally graded plates, *Engineering Structures*, **46**, 322–331.
2. Michalak B., Wirowski A. (2012). Dynamic modeling of thin plate made of certain functionally graded materials, *Meccanica*, **47**, 1487–1498.
3. Woźniak Cz., Michalak B., Jędrysiak J. (eds.) (2008). *Thermomechanics of Heterogeneous Solids and Structures*, Wydawnictwo Politechniki Łódzkiej, Łódź.

COMPARISON OF BUCKLING RESISTANCE OF COLUMNS MODELLED BY BEAM AND SHELL ELEMENTS USING NON-LINEAR ANALYSIS

Ł. Żmuda-Trzebiatowski

Gdansk University of Technology, Gdansk, Poland

1. Introduction

Buckling analysis for engineering structures, like columns, is usually carried out by means of linear buckling analysis (LBA) of a perfect structure and non-linear static analysis of an imperfect structure, forming load-displacement equilibrium paths. The aim of this paper is to investigate the stability process in axially compressed columns using linear buckling analysis, non-linear static and dynamic finite element analysis, incorporating both geometric and material non-linearity. The non-linear results are compared with the linear buckling analysis results. In the paper columns are modelled by beam-column elements with six degrees of freedom in node and shell elements in order to determine the relevant models to obtain fairly accurate results.

In order to capture the unstable post-buckling behaviour in static analysis the arc-length Riks method is used. This method is a fundamental one for a stable process analysis under a global load control, but it does not work well for all types of structures. The solution may be impossible due to convergence loss caused by localized instability, general local buckling or material instability. The solution depends on the shape and amplitude of initial imperfections of a structure. Dynamic analysis, according to [1–5], is applied, tracing time history of structure response due to an increasing load. Convergence is achieved due to inertia and damping forces. A long time interval of load action results in a quasi-static solution. Comparison of static and dynamic solutions is presented in the paper.

A non-linear dynamic explicit and static finite element analysis are presented in the paper. Geometric and material non-linearity were introduced for perfect and imperfect columns, using bar and shell elements in their modelling. Various initial imperfections of columns were taken into account. A linear buckling analysis of perfect columns resulted in the lowest buckling load and the corresponding buckling modes, taken next as initial geometric imperfections. The attention is focused on the comparison of two models (1D and 3D) of the column.

2. Numerical models

Two I-section columns with different boundary conditions were numerically analysed. Both were fixed at the bottom, two variants at the top end – the first column was free at its top, the second has fork support at the top where horizontal displacement and in-plane rotation of cross-section are restrained. In both cases the column length $L = 8$ m. They are made of HEB 320 profile. Both columns were subjected to axial constant pressure at the top edge. The steel of the columns is elastic-perfectly plastic (without hardening) of the following parameters: elastic modulus $E = 210$ GPa, Poisson's ratio $\nu = 0.3$, yield stress $f_y = 355$ MPa and mass density $\rho = 7850$ kg/m³. A constant edge load applied at the column top was used for linear buckling analysis.

The computations were carried out by means of FEM packages: Abaqus/Explicit for dynamic analysis and Abaqus/Standard for static analysis. First of all assessment was made how the mesh and the finite element type acts on the linear buckling analysis results. Next, finite element mesh for each variant of analysis was defined.

In static analysis the automatic Riks method was used to determine the buckling load factor in terms of vertical displacement of the column top edge. In non-linear explicit dynamic analysis time of load duration was assumed in the range $t_a = 2, 3, 4, 5, 10, 20$ and 30 seconds in order to obtain quasi-static results. Standard damping parameter (linear bulk viscous parameter 0.06, quadratic bulk viscous parameter 1.2) and an automatic time increment were applied. In FEM analysis both perfect and imperfect columns models were considered. Geometrical imperfections of columns were defined by means of a linear buckling analysis. Various shapes of initial column imperfections and various imperfection amplitudes were taken into account.

3. Results

Two cases of non-linearity: only geometric and geometric-material, were considered in the paper. In both cases it was not possible to obtain limit load for the perfect columns in the static analysis due to the lack of imperfection. In turn, the same columns buckled in a dynamic analysis. The maximum dynamic load factor λ was sensitive to the load duration – decreasing with the time increment. The load-displacement relation of the entire buckling process was found only by means of the dynamic analysis. In static cases the equilibrium path was not stated due to the loss of convergence.

In the cases of imperfect columns for low load action time maximum dynamic and static load factors λ are similar. Decrement of the load action time t_a makes the columns buckling strength increase even by 50% for the perfect structure and 25% for structural imperfections of amplitude $w = 100$ mm.

Differences of the maximum load factor λ due to static and dynamic solutions, related to the static results are: 3.5% for load action time $t_a = 5$ s and about 40% for $t_a = 30$ s. The maximum dynamic load factor λ obtained for a different time of load action reduces while increasing an imperfection amplitude w . Thus the differences between maximum load factors due to imperfections related to different buckling modes are relatively low (about 5%). A higher decrement of the column strength is caused by an increasing loading time (21.5%). The material non-linearity significantly decreases the load-bearing capacity of the column (even by 50%). Comparison of results of LBA and GNA yields that the first critical force is nearly equal to the highest non-linear analysis result. Most of them exhibit the decrement of the column load-carrying capacity (even twice). Load capacity and critical forces for beam models are higher than for shell models. In some cases the results are similar.

References

1. C. Bottasso, O. Bauchau, J.-Y. Choi (2002). An energy decaying scheme for nonlinear dynamics of shells, *Computer Methods in Applied Mechanics and Engineering*, **191**, 3099–3121.
2. K.K. Choong, E. Ramm (1998). Simulation of buckling process of shells by using the finite element method, *Thin-Walled Structures*, **31**, 39–72.
3. J. Chróścielewski, I. Lubowiecka, W. Witkowski (2006). Dynamics based on six-field theory of shells in the context of energy-conserving scheme, *Shell Structures: Theory and Applications*, **1**, 303–307.
4. T. Kobayashi, Y. Mihara, F. Fujii (2012). Path-tracing analysis for post-buckling process of elastic cylindrical shells under axial compression, *Thin-Walled Structures*, **61**, 18–187.
5. T. Kubiak (2007). Criteria of dynamic buckling estimation of thin-walled structures, *Thin-Walled Structures*, **45**, 888–892.

Session

**Smart Materials
and
Structures**

PARTITIONED THERMO-MECHANICAL COUPLING OF SMA CONSTITUTIVE MODEL

V. Dunić¹, E.A. Pieczyska², N. Busarac¹, R. Slavković¹, V. Slavković¹

¹Faculty of Engineering, University of Kragujevac, Kragujevac, Serbia

²Institute of Fundamental Technological Research, Warsaw, Poland

1. General

For many kinds of materials (e.g. metals, shape memory alloys, etc.), thermal changes coupled with the deformation process can have significant effect on the mechanical response and also on the accuracy of numerical analysis. In order to take them into account, monolithic coupling algorithms have been used, however a partitioned approach can also be applied. An advantage of the partitioned thermo-mechanical coupling is the possibility to re-use already developed software to simulate various kinds of multiphysics scenarios, i.e. various coupled fields: structure, heat transfer, fluids, magnetic, etc. To realize the partitioned approach, communication protocols for exchange of information between the used codes are needed [1]. To this end, Component Template Library (CTL) [2], developed at the Institute of Scientific Computing, TU Braunschweig, Germany, is used as a middleware between the FEM programs for the structural analysis (PAKS) and the heat transfer analysis (PAKT).

2. Methods

The CTL is a library which provides an exchange of information between the program codes through communication protocols. The PAKT and PAKS programs, developed at the Faculty of Engineering, University of Kragujevac, are transformed into the components with the communication interface. The SMA constitutive model based on the Lagoudas theory [3] is modified and adopted to depend only on scalar values of effective stress, strain and martensitic volume fraction and is implemented into the PAKS program. The martensitic phase transformation is related to a dissipation of internal energy and a change of the material temperature what violates the thermodynamic equilibrium in the structure. The PAKS program has been extended to compute the energy released during the phase transformation which behaves as an internal heat source in the heat transfer component PAKT. The partitioned coupling approach, based on assumptions of Block-Gauss-Seidel numerical procedure [1, 4] is employed to re-establish the balance.

3. Partitioned coupling algorithm

In order to use the partitioned approach, a thermo-mechanical problem has to be defined as a nonlinear system of equations $f(\approx, T) = 0$ and $g(\approx, T) = 0$ where f , g are thermal and structural subproblems and \approx and T are displacement and temperatures, respectively [4]. The first equation is solved by PAKT, while the second one is solved by PAKS. To calculate the influence of a run of the phase transformation on the temperature field, the dissipative energy [3, 5] is calculated in each integration point as follows:

$$W_i = (\psi_i - \rho \Delta s_0 T_i) \Delta \xi_i,$$

where i is the current number of integration point, ψ is the thermodynamic force, $\rho \Delta s_0$ is the stress influence coefficient, T is the temperature in integration point and $\Delta \xi$ is the increment of martensitic volume fraction in the time step. The dissipative energy of the whole construction and the global convergence criterion can be defined as:

$$W^k = \sum_{i=1}^P W_i^k, \quad \frac{W^k - W^{k-1}}{W^{k-1}} < tol_w,$$

where P is the number of integration points, k is the iteration counter and tol_w is the minimal desired tolerance.

4. Numerical results

This coupling algorithm has been verified using the experimental results of TiNi SMA subjected to tension with various strain rates carried out at the IPPT PAN [5]. The stress (black line) and temperature changes (red line) obtained at the strain rate 10^{-3} s^{-1} are presented by solid line, whereas the numerical results of the stress and the temperature changes by dotted lines, respectively (Fig. 1). A good agreement between the experimental and numerical data has been obtained.

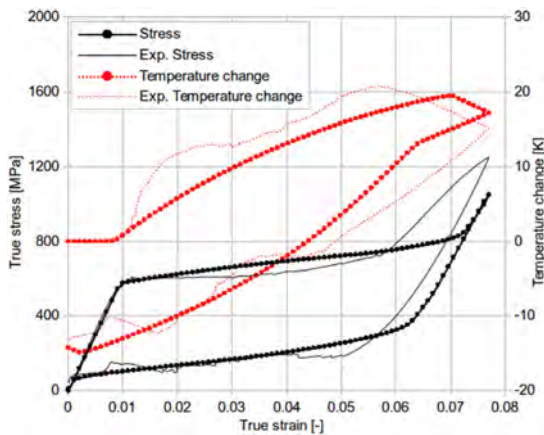


Fig. 1. Comparison of numerical and experimental results for TiNi SMA at strain rate 10^{-3} s^{-1} .

5. Conclusions

The partitioned coupling algorithm, based on the CTL, PAKS and PAKT programs, proved to be a good approach for the accurate numerical analysis of the stress-induced martensitic transformation developing in TiNi SMA subjected to tension. A similar approach can be used for advanced thermo-mechanical analysis in the case of other thermo-sensitive materials.

Acknowledgment

The research has been supported by KMM-VIN Research Fellowship; 1.08-13.09.2013, Polish National Center of Science, Grant No. 2011/01/M/ST8/07754 and Serbian Ministry of Education, Science and Technological Development Grant No. TR32036 and III41007.

References

1. H.G. Matthies, R. Niekamp, J. Steindorf (2006). *Comput. Method. Appl. M.*, **195**, 17-18, 2028–2049.
2. R. Niekamp (2005). *CTL Manual for Linux/Unix for the Usage with C++*, Institut für Wissenschaftliches Rechnen – TU Braunschweig, Germany.
3. D.C. Lagoudas (2010). *Shape Memory Alloys: Modeling and Engineering Applications*, Springer.
4. A. Yeckel, L. Lun, J.J. Derby (2009). *J. Comput. Phys.*, **228**, 23, 8566–8588.
5. V. Dunić, E.A. Pieczyska, H. Tobushi, M. Staszczak, R. Slavković (2014). *Smart. Mater. Struct.*, **23**, 055026 (11pp).

ANALYSIS OF EFFECT OF LOADING FREQUENCY ON STRESS-STRAIN-TEMPERATURE RELATIONSHIP OF SHAPE MEMORY ALLOYS

T. Ikeda

Nagoya University, Nagoya, Japan

1. Introduction

Shape memory alloys (SMAs), having unique properties such as shape memory effect and superelasticity, are applied in wide range of field such as aerospace, medical, and livingware. However, deformation behaviour based on phase transformation is complicated depending on temperature, hysteresis, and loading frequency. Accordingly, to understand the mechanism of such a complicated behaviour and design products including SMAs optimally, fundamental experimental data and mathematical models are necessary and many experimental and mathematical researches are performed [1–10]. It has been found from the researches that temperature variation is one of the most important factors to understand the complicated behaviour.

In this paper a constitutive model “one-dimensional phase transformation model” proposed by the author and his coworkers [7–10] is simplified by introducing some assumptions so that the temperature variation can be obtained analytically. Using the obtained formula, factors causing temperature variation depending on the loading frequency are analyzed.

2. Governing equations

The temperature variation can be calculated using the following formula,

$$(1) \quad \Theta = \Theta_1 e^{-Ht} + \Theta_2 \sin(2\pi ft - \phi) + \Theta_3,$$

which is derived from the energy balance equation of “the one-dimensional phase transformation model” [7–10] under the assumptions that the thermal expansion is negligible, martensite volume fraction varies as $0.5\{1 - \cos(2\pi ft)\}$, and $\Psi dz/2$. In Eq. (1), $\Theta_1 = \Theta_2 \sin \phi - \Theta_3$, $\Theta_2 = S\pi f / \sqrt{(2\pi f)^2 + H^2}$, $\Theta_3 = F\pi f / (2H)$, and $\phi = \tan^{-1}(2\pi f/H)$, where $\Theta = T - T_s$, $H = hA/(VC)$, $S = \Delta s T_s / C$, $F = \Psi / C$, T is temperature, T_s is the environmental temperature, h is the coefficient of conduction, A/V is the area/volume, C is the specific capacity, Δs is the entropy difference between martensite phase and austenite phase, Ψ is the required transformation energy, and f is the loading frequency.

3. Numerical example and discussion

It is seen from Eq. (1) that the temperature vibrates sinusoidally. The first term becomes 0 as $t \rightarrow \infty$ since H is positive. The mean temperature increases when Θ_1 is negative and decreases when Θ_1 is positive. Θ_2 is the amplitude of the vibrating temperature, and it becomes larger as f becomes larger and becomes $S/2$ as $f \rightarrow \infty$. Θ_3 is the mean temperature at $t \rightarrow \infty$. Here the mean temperature at $t = 0$ is given by $\Theta_1 + \Theta_3$.

H , S , and F , which are calculated from assumed material and environmental constants, are given as listed in Table 1, and the values of Θ_1 , Θ_2 , ϕ , and Θ_3 are calculated as listed in Table 2 for some loading frequencies.

It is seen from Table 2 that the amplitude of temperature is 15 K and the mean temperature decreases from 14.6 K at $t = 0$ to 1.6 K at $t \rightarrow \infty$ for 0.1 Hz, and that the

Table 1. Constants H , S , and F .

H [s^{-1}]	S [K]	F [K]
0.1	30	1

Table 2. Θ_1 , Θ_2 , φ , and Θ_3 for several loading frequencies.

f [Hz]	Θ_1 [K]	Θ_2 [K]	φ [deg]	Θ_3 [K]
0.001	0.043	0.94	3.6	0.016
0.01	4.1	8.0	32	0.16
0.1	13	15	81	1.6
1	-0.71	15	89	16

amplitude of temperature is 15 K and the mean temperature increases from 15.3 K at $t = 0$ to 16 K at $t \rightarrow \infty$ for 1 Hz. Figure 1 shows the temperature variation at a frequency of (a) 0.1 Hz and (b) 1 Hz, obtained from Eq. (1). From this figure the trend mentioned above is confirmed. Comparing this analytical result with the experiment, it was confirmed that this analysis using simplified equation captures the trend of the experimental data qualitatively.

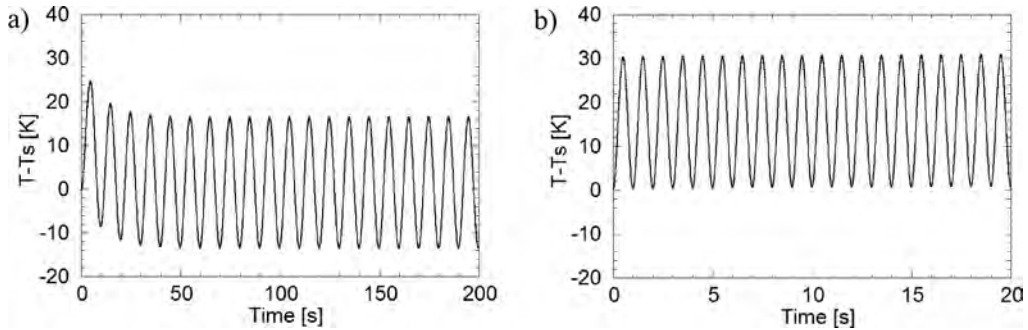


Fig. 1. Calculated temperature variation: a) 0.1 Hz, b) 1 Hz.

4. Conclusions

A constitutive model “one-dimensional phase transformation model” proposed by the author and his coworkers [8–11] was simplified by introducing some assumptions and the formula giving temperature variation was obtained. From the formula, the factors affecting the temperature variation depending on loading frequency was analyzed. The obtained temperature variation agreed with the measured data qualitatively.

References

- Otsuka K., Wayman C.M. (eds.) (1998). *Shape Memory Materials*, Cambridge Univ. Press.
- Shaw J.A., Kyriakides S. (1995). *J. Mech. Phys. Solids*, **43**, 8, 1243–1281.
- Liu Y., Xie Z., van Humbeeck J., Delaey L. (1998). *Acta Mater.*, **46**, 12, 4325–4338.
- Falk F. (1983). *Arch. Mech.*, **35**, 1, 63–84.
- Tanaka K. (1986). *Res Mech.*, **18**, 3, 251–263.
- Boyd J.G., Lagoudas D.C. (1996). *Int. J. Plasticity*, **12**, 6, 805–842.
- Ikeda T., Nae F.A., Naito H., Matsuzaki Y. (2004). *Smart Mater. Struct.*, **13**, 916–925.
- Ikeda T. (2005). Proc. SPIE, 5757, 344–352.
- Ikeda T. (2006). Proc. SPIE, 6166, 61660Z (8p).
- Ikeda T. (2008). *J. Intel. Mater. Syst. Struct.*, **19**, 533–540.

TWO-PHASE MODEL OF SHAPE MEMORY POLYMERS AT FINITE STRAINS: FORMULATION AND EXPERIMENTAL VERIFICATION

K. Kowalczyk-Gajewska¹, E.A. Pieczyska¹, M. Maj¹, M. Staszczak¹, M. Majewski²,
M. Cristea³, H. Tobushi⁴

¹Institute of Fundamental Technological Research, Warsaw, Poland

²Faculty of Civil Engineering, Warsaw University of Technology, Poland

³“Petru Poni” Institute of Macromolecular Chemistry, Iasi, Romania

⁴Aichi Institute of Technology, Toyota, Japan

1. Introduction

Shape memory polymers (SMP) can play different functions, such as sensing, actuating and crack-healing. They have good physical properties and favorable economical indicators. The shape memory effect is temperature driven. The elastic modulus and the yield stress are high at temperatures below the glass transition temperature T_g and low above T_g . If SMP is deformed at temperatures above T_g and cooled down to temperatures below T_g , the deformed shape is fixed and SMP can carry large load. If the shape-fixed SMP element is heated up to temperatures above T_g under no load, the original shape is recovered [1]. Physical explanation for such behavior is as follows. Thermoplastic polyurethanes are block copolymers composed of hard and soft segments distributed randomly within volume element. With the increased volume fraction of domains dominated by hard segments, these domains are better cross-linked and interconnected. Two types of domains are usually well separated although such separation is never complete. Hard domains are responsible for the inelastic properties of polyurethanes. Deformation of the material above the glass transition temperature, when soft domains dominate, is mainly entropic being caused by changes in the alignment of polymer chains. Numerous works can be found that concern the characterization and applications of various types of SMP. Much less work is dedicated to modelling of these materials. Departing from the proposal [2] a constitutive model of SMP, formulated at large strain format, is developed. SMP is described as a two-phase material composed of a soft rubbery phase and a hard glassy phase.

2. Model formulation

Within the model at a given temperature SMP is assumed to be composed of two phases: a soft rubbery phase and a hard glassy phase. The volume fraction of each phase is postulated as a logistic function of temperature using the relation proposed in [2]. Furthermore, during cooling yet another phase is assumed to be formed: a frozen rubbery phase. This phase behaves similarly to a native glassy phase. The constitutive relations are formulated separately for each phase and the resulting behavior of the material depends on the actual material composition. The relations are written in the large strain framework. For the rubbery phase the hyperelastic Arruda-Boyce model is used, which accurately describes the behavior of isotropic homogeneous elastomers. The glassy phase is assumed to be hyperelastic-viscoplastic with the Zener-type behavior. Effective behavior of the shape memory polyurethane is the resultant response of individual phases. When we do not have to do with cooling, a simple Voigt-type averaging scheme is used, i.e. each phase is assumed to share the same deformation gradient being equal to the macroscopic one. The overall Cauchy stress tensor in the material is a volume average of stresses in the

individual phases. The first assumption is modified when a frozen rubbery phase is formed during cooling. More advanced averaging schemes can be used in the future [3]. Further details of model formulation can be found in [2, 4].

3. Comparison with experimental results

Identification of model parameters has been performed using the experimental tensile loading-unloading tests with different strain rates conducted in IPPT at thermal chamber at temperatures $T_g - 20^\circ\text{C}$ and $T_g + 20^\circ\text{C}$, with the help of the similar tests performed at the intermediate temperatures. Glass transition temperature $T_g = 25^\circ\text{C}$ is identified for the considered SMP. The parameters have been optimized with a focus on valid predictions for low strain rates and a room temperature. In Fig. 1 selected comparisons of experimental results with the model predictions are shown.

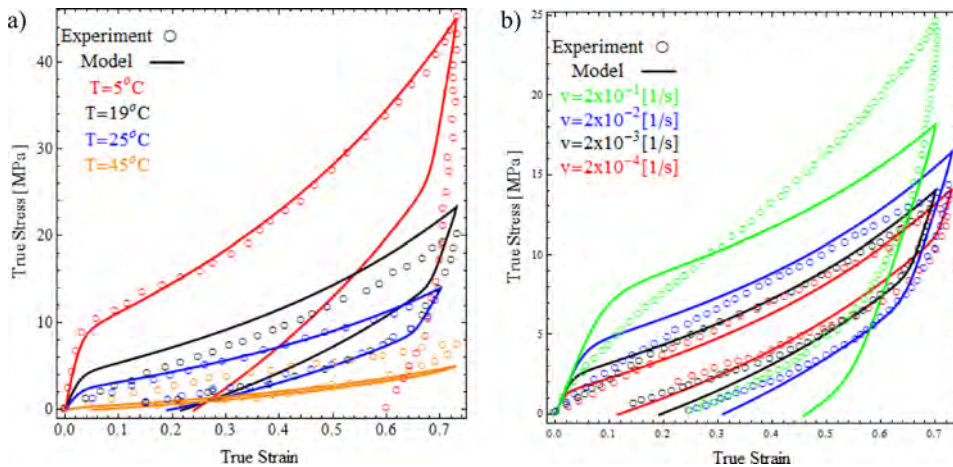


Fig. 1. Comparison of experimental results and modelling predictions for SMP tension: a) with strain rate $2 \times 10^{-3} \text{ s}^{-1}$ at different temperatures, b) with different strain rates at temperature 25°C .

It is seen that the model satisfactorily predicts the dependence of material response on temperature (Fig. 1a), although some discrepancies are visible as concerns the unloading part of the curve for the lowest temperature and the width of hysteresis loop for the highest strain rate. The second discrepancy is due to the model assumption that the rubbery phase is purely hyperelastic. As seen in Fig. 1b, influence of the strain rate at constant temperature 25°C is also well accounted for by the model for the strain rate up to 2×10^{-2} . The stress level is underestimated for the highest strain rate.

Acknowledgments

The research has been carried out with the support of the Polish National Center of Science under Grant No. 2011/01/M/ST8/07754.

References

1. J. Hu, Y. Zhu, H. Huang, J. Lu (2012). Recent advances in shape-memory polymers: Structure, mechanism, functionality, modeling and applications, *Progress in Polymer Science*, **37**.
2. H.J. Qi, T.D. Nguyen, F. Castro, Ch.M. Yakacki, R. Shandas (2008). Finite deformation thermomechanical behavior of thermally induced shape memory polymers, *J. Mech. Phys. Solids*, **56**, 1730–1751.
3. K. Kowalczyk-Gajewska, H. Petryk (2011). Sequential linearization method for viscous/elastic heterogeneous materials, *Eur. J. Mech. A/Solids*, **30**, 650–664.
4. E.A. Pieczyńska, M. Maj, K. Kowalczyk-Gajewska, M. Staszczak, L. Urbański, H. Tobushi, S. Hayashi, M. Cristea (2014). Mechanical and Infrared Thermography Analysis of Shape Memory Polyurethane, *Journal of Materials Engineering and Performance* (accepted).

TRANSFORMATION AND DEFORMATION PROPERTIES OF FUNCTIONALLY GRADED SHAPE MEMORY ALLOY FABRICATED BY SPS AND ROLLING PROCESSES

R. Matsui¹, R. Takenouchi²

¹Aichi Institute of Technology, Toyota, Japan

²Tokai Rika Co. Ltd., Oguchi, Japan

1. Introduction

The martensitic and reverse transformation temperatures of TiNi shape memory alloy (SMA) are directly related to its bending rigidity [1]. In this study, we developed a new fabrication process that combines powder metallurgy and plastic working to obtain a functionally graded TiNi SMA stripe that varies in bending rigidity from high to low along the stripe axis. First, a multilayered TiNi green compact in which the Ti–Ni compositions varied layer by layer was sintered using a spark plasma sintering (SPS) process; the compact was then hot and cold rolled into stripes. In this study, we investigated the functionally graded properties of the transformation temperatures and the local deformation properties of the resulting rolled thin stripes.

2. Fabrication processes

In this study, we developed a process to fabricate functionally graded TiNi SMA stripes. The multilayered TiNi green compact was sintered at 1023 K for 1.8 ks using the SPS process. Solution treatment was subsequently performed at 1273 K for 43.2 ks to encourage interdiffusion between Ti and Ni, and we obtained a solution-treated compact, which was 20 mm in diameter and 29 mm in height. The stripes were cut to a width of 5 mm and a thickness of 1 mm using a wire electric discharge machine and were subsequently hot and cold rolled. The hot rolling process was performed twice at different rolling reductions at 1073 K. The reduction in area was $5\% \pm 2\%$ for the hot rolling (HR; 5% HR) process and $10\% \pm 2\%$ for the cold rolling (CR; 10% CR) process.

3. Experimental procedure

We investigated the transformation and deformation properties before and after the hot and cold rolling processes under the described conditions. In addition, we performed a shape memory heat treatment at 773 K for 3.6 ks before all experiments.

Differential scanning calorimetry (DSC) was performed at heating and cooling rates of 5 K/min at seven representative positions along the longitudinal direction of the rolled stripes to determine the transformation properties. In the tensile tests, local strain of the SMA stripes was detected by strain gauges attached to two points of the specimen corresponding to a Ni content of 50.2 and 50.6%.

4. Experimental results and discussion

DSC curves of the cooling process for the 5% HR and 10% CR stripes are shown in Fig. 1. The transformation peaks gradually shifted to lower temperatures with increasing

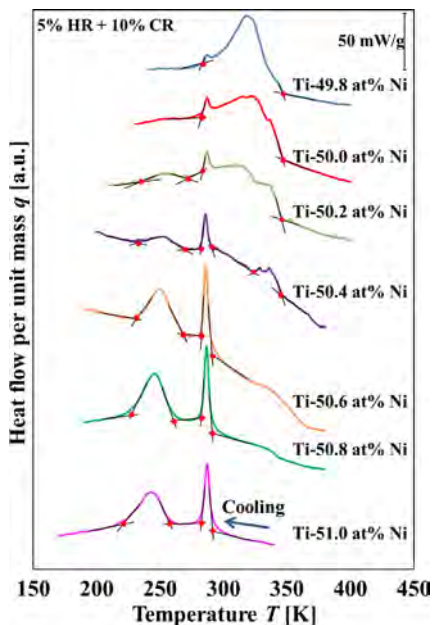


Fig. 1. DSC curves of the TiNi SMA stripes subjected to the rolling process.

Ni content. The trends of these results are similar to that of a cast TiNi SMA. We have already confirmed that the transformation temperatures of the TiNi SMA stripes before the hot and cold rolling processes are functionally graded. Hence, these results indicate that the functionally graded properties of the transformation behaviors are still retained after the HR and CR processes.

Figure 2 shows the stress-local strain curves at two points of the hot- and cold-rolled TiNi SMA stripes. At the positions on the hot- and cold-rolled stripes that correspond to a Ni content of 50.6%, the maximum local strain was smaller and the position of the stress plateau due to the martensitic transformation was higher than that at the positions corresponding to a Ni content of 50.2%. These differences in the stress plateaus and maximum local strains appear to be based on the martensitic transformation temperatures and correspond to the results shown in Fig. 1. As previously explained, the deformation behavior of the hot- and cold-rolled TiNi SMA stripes was also functionally graded.

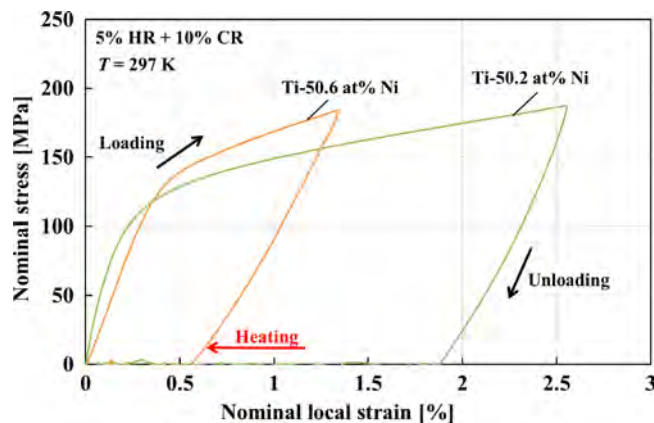


Fig. 2. Stress-local strain curves of the TiNi SMA stripes before and after being subjected to the rolling processes.

5. Conclusions

In this study, using stripes that already exhibit functionally graded properties, we observed that the transformation temperatures of hot- and cold-rolled TiNi SMA stripes are also functionally graded. As a result, the deformation behaviors of the rolled stripes differ depending on the Ni content at a given position.

References

1. H. Tobushi, R. Matsui, K. Takeda, E.A. Pieczyska (2013). *Mechanical Properties of Shape Memory Materials*, Nova Science Publishers, New York, 1–7.

FERROMAGNETIC SINGLE CRYSTAL SHAPE MEMORY ALLOY SUBJECTED TO SUBSEQUENT COMPRESSION CYCLES

E. A. Pieczyska

Institute of Fundamental Technological Research, Warsaw, Poland

1. Introduction

The paper presents effects of thermomechanical coupling related to pseudoelastic deformation of NiFeGaCo single crystal of ferromagnetic shape memory alloy (FSMA) subjected to subsequent loading-unloading compression cycles. The stress-strain parameters were obtained by mechanical and laser extensometers, whereas infrared measurement system (IR) enabled measurement of the sample temperature during the SMA deformation process. The obtained thermograms exposure localized character of the stress-induced martensitic transformation (SIMT), initiating in form of inclined bands of higher temperature and developing throughout the sample. High repeatability of both mechanical and temperature changes obtained in the subsequent loading cycles indicates good thermomechanical properties of the FSMA crystal and confirms high accuracy of the measurement.

2. Results and discussion

Ferromagnetic shape memory alloys discovered by Ullakko (1996) exhibit magnetic field- or stress-induced reversible strains of up to 10% and can operate with 50–100 Hz frequency [1]. Similarly to classical SMA, these alloys are characterized by a high-symmetry cubic structure in the high-temperature phase and a low-symmetry tetragonal structure in the low-temperature phase. The goal of the research was to investigate the NiFeGaCo single crystal behavior in subsequent compression loading cycles and check whether the SIMT occurs macroscopically homogeneously or not. And if the transformation is localized, how it nucleates and develops. As a result, it was found that during the first cycle of the loading a band inclined by 45° and characterized by higher temperature by approximately 0.4 K appeared manifesting localized character of the transformation (Fig. 1a). At higher strain a second family of bands appears, emerging at the angle close to 90° according to the loading direction (Fig. 1b), followed by many transformation bands developing towards the upper grip of the testing machine (Fig. 1c). After reaching the grip area, a strong band in the upper part of the sample emerged developing again at the

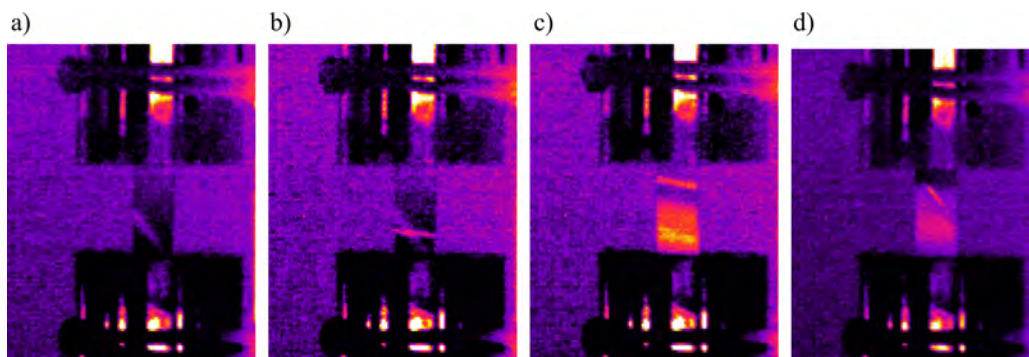


Fig. 1. Subsequent stages of FSMA single crystal loading shown in infrared: a) 1st transformation band, b) 1st and 2nd bands, c) many developing bands, d) a band developing from upper grip.

angle close to 45° (Fig. 1d). Similar localization effects were recorded in the subsequent loading-unloading cycles. The bands behavior seems to reflect a compromise between the alloy structure and the sample boundary conditions.

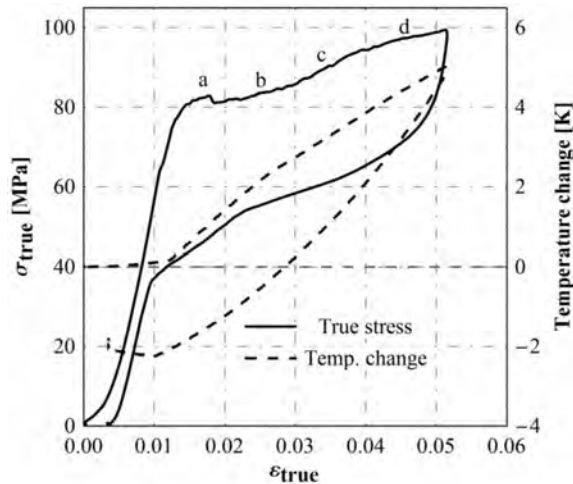


Fig. 2. Stress and temperature change vs. strain curve for 1st cycle of FSMA single crystal loading; a, b, c, d denote subsequent transformation stages shown in thermograms presented in Fig. 1.

Nucleation and development of the bands are especially valuable in the case of single SMA crystal, since the localization phenomena are not influenced by the grains and by the grain boundaries interactions. Due to that the observed effects are almost directly related to the SIMT mechanisms, according to its thermodynamics and the SMA microstructure. The reverse transformation is also not uniform; however the recorded localization effects are not so significant, like observed during the forward transformation. Shape memory alloys are very sensitive to the temperature. Therefore, the awareness of the stress and temperature changes accompanied the martensitic transformation is important for their thermodynamics study. In order to estimate the global heat effects, related to the transformation, average values of the sample temperature were calculated and compared to the stress vs. strain in the presented diagrams (Fig. 2) [3]. The values of the maximal temperature changes related to the exothermic martensitic forward transformation and measured in non-contact manner by high-performance IR camera are about 4.6 K. After the unloading, the sample temperature drops below its initial state by approximately 2.2 K (Fig. 2). These thermomechanical coupling effects, observed in SMA and confirmed in FSMA, are important for developing other directions of the alloys applications as cooling elements and will be a subject of our future research.

Acknowledgment

The financial support of the Polish National Center of Science under Grant No. 2011/01/M/ST8/07754 is acknowledged. Author is grateful to E. Cesari for valuable advices and supplying the ferromagnetic SMA specimens, to M. Maj for elaborating the temperature changes and to L. Urbański and R. Maciak for obtaining and processing experimental mechanical data.

References

1. K. Ullakko (1996). Magnetically controlled shape memory alloys: A new class of actuator materials, *J. Mat. Eng. Perf.*, **5**, 405–409.
2. H. Tobushi, R. Matsui, K. Takeda, E. Pieczyńska (2013). *Mechanical Properties of Shape Memory Materials. Materials Science and Technologies, Mechanical Engineering Theory and Applications*, NOVA Publishers, New York.
3. E.A. Pieczyńska (2014). Mechanical behavior and infrared imaging of ferromagnetic NiFeGaCo SMA single crystal subjected to subsequent compression cycles, *Meccanica*, DOI 10.1007/s11012-013-9868-7.

ORDERING AND SEGREGATION PROCESSES IN BINARY INTERMETALLIC NANOFILMS WITH TRIPLE DEFECTS: ATOMISTIC SIMULATIONS

P. Sowa¹, A. Biborski², R. Kozubski¹, E. V. Levchenko³, A. V. Evteev³,
I. V. Belova³, G. E. Murch³

¹M. Smoluchowski Institute of Physics, Jagiellonian University in Krakow, Poland

²AGH University of Science and Technology Academic Centre for Materials and Nanotechnology
al. Mickiewicza 30, 30-059 Krakow, Poland

³Centre for Mass and Thermal Transport in Engineering Materials, School of Engineering
The University of Newcastle, Callaghan, Australia

Despite having been extensively studied for several decades, the B2-ordering intermetallic compound NiAl is still of great research and technological interest. The compound crystallises in the B2 superstructure which remains stable up to the melting point $T_M = 1911$ K.

Except for the wide application of the compound in the technology of structural materials, its low density and high oxidation resistance make it an ideal candidate for the base substrate for the production of protective coatings [1, 2]. Due to the high melting point and high thermal conductivity of NiAl films most turbine blades made of super-alloys are virtually covered with coatings of this material. Detailed knowledge of structural-defect density, as well as of ordering and surface segregation phenomena in NiAl films has considerable importance for understanding its oxidation resistance, fracture crack propagation, and other properties. Accordingly, many contemporary studies are focused on such problems.

The present study consists of atomistic Monte Carlo simulations of equilibrium vacancy and antisite defect concentration and configuration, as well as the kinetics of chemical ordering and surface segregation in thin films of a model binary system AB mimicking NiAl and showing the tendency for triple defect formation – i.e. manifesting a strong preference for the A-antisite and A-vacancy formation. The basic concept was to consistently treat the equilibrium atomic configuration, ordering kinetics and self-diffusion by using two atomistic Monte Carlo techniques: Semigrand-Canonical Monte Carlo (SGCMC) and Kinetic Monte Carlo (KMC) simulations.

An Ising model of a binary A-B system with vacancies V and with nearest-neighbour (nn) pair-interaction energies V_{ij} ($i, j = A, B, V$) was considered. The nn pair-interaction energies yielded the tendency for triple-defect formation in the bulk AB system, whose signature is the existence of a finite temperature range, where the concentrations of antisites and vacancies are proportional [3].

For the sake of the planned KMC simulations, the model was completed by the saddle-point energies E^+ assigned to atomic jumps to nn vacancies and effectively dependent on the local configuration of the atom-vacancy pairs exchanging their positions [4].

The AB films limited by (001)-oriented free surfaces were generated by imposing 2D periodic boundary conditions in the [100] and [010] directions upon cubicoidal supercells built of bcc unit cells. The three different shapes of the supercells allowed the simulation of AB films defined by their thickness $d = 54, 24$ and 6 atomic planes (27, 12 and 3 bcc unit-cells), respectively. The particular supercell sizes were chosen with reference to the test which indicated stability of the SGCMC result for the number of lattice sites $N > 10\,000$. In the present study $N \approx 30\,000$ was almost equal in all supercells.

The results obtained within the presented work may be summarised as follows:

- The effect of the decreasing B2 superstructure stability with decreasing film thickness was demonstrated.
- The value of the thermodynamic activation energy for vacancy formation resulting from the SGCMC simulations and corresponding to the “inner” parts of the films – i.e. to the film body free from the surface effects, appeared equal to the value estimated for the bulk AB system, however, the vacancy concentration in the “inner” parts of the films decreased with decreasing film thickness.
- While strong vacancy surface segregation was observed in all the simulated films, the equilibrium B-termination of both film surfaces did not follow from the B-atom surface segregation, but was a consequence of the A-atom diffusion into the films mediated by vacancy surface segregation.
- The two-stage character of the “order-order” kinetics in the simulated films and the very low rate of their final evolution towards the equilibrium configuration suggests the structural metastability of the deposited NiAl layers.

Acknowledgments

Support is acknowledged from the COST Action MP0903 NANOALLOY, Foundation for Applied Thermodynamics and from the programme “Society, Environment and Technology” realised at the Jagiellonian University in Krakow, Poland.

References

1. Y. Tamarin (2002). *Protective Coatings for Turbine Blades*, ASM International, Materials Park, OH.
2. M. Hetmanczyk, L. Swadzba, B. Mendala (2007). *Journal of Achievements in Materials and Manufacturing Engineering*, **24**, 372.
3. A. Biborski, L. Zosiak, R. Kozubski, R. Sot, V. Pierron-Bohnes (2010). *Intermetallics*, **18**, 2343.
4. P. Sowa, R. Kozubski, A. Biborski, E. Levchenko, A. Evteev, I.V. Belova, G. Murch, V. Pierron-Bohnes (2013). *Philos. Mag.*, **93**, 1987.

ESTIMATION OF SHAPE FIXITY AND SHAPE RECOVERY – CRUCIAL PARAMETERS FOR SHAPE MEMORY POLYMER APPLICATIONS

M. Staszczak¹, E. A. Pieczyska¹, M. Maj¹, K. Kowalczyk-Gajewska¹, M. Cristea²,
H. Tobushi³, S. Hayashi⁴

¹Institute of Fundamental Technological Research, Warsaw, Poland

²Institute of Macromolecular Chemistry, “Petru Poni” Iasi, Romania

³Aichi Institute of Technology, Toyota, Japan

⁴SMP Technologies Inc., Tokyo, Japan

1. Introduction

Shape memory polymers (SMP) are new unique and attractive materials which demonstrate shape memory properties. It means that the materials, as a result of an external stimulus such as temperature, can recover their original (permanent) shape from deformed (temporary) shape. The mechanical characteristics of SMP, e.g. the elastic modulus and the yield stress, change significantly below and above their glass transition temperature T_g . It can be explained by differences of molecular motion of the polymer chains below and above T_g [1, 2]. Two phenomena due to this can be observed in the SMP. The first one is a shape fixity which means that it is possible to fix a temporary shape by cooling the deformed SMP below T_g . The second phenomenon, called a shape recovery, denotes the property that the original shape, changed due to deformation, is recovered during subsequent heating above the SMP T_g temperature. Preliminary estimation of these two parameters, crucial to assess SMP potential applications, is the subject of this paper [1].

2. Experimental procedure, results and discussion

The research was carried out on a new shape memory polyurethane PU-SMP, produced by SMP Technologies Inc., Tokyo, Japan. In order to learn more about the new material, a dynamic mechanical analysis (DMA) was performed. The characteristics of the SMP shown in Table 1 suggest that the material fulfills some preliminary demands to function as shape memory polymer. Namely, a high glass elastic modulus E'_g (1500 MPa) that renders good shape fixity of the polymer, proper value of the rubber modulus E'_r (15 MPa) that ensures both large deformations in the rubbery state and high elastic recovery at high temperatures, as well as a high ratio of E'_g/E'_r (100) were obtained. The SMP glass transition temperature T_g defined by a midpoint of glass transition temperature region is equal to approximately 25°C.

Table 1. DMA results: values of elastic modulus E'_g , rubber modulus E'_r , T_g and E'_g/E'_r ratio.

Sample	E'_g	T_g (determined as midpoint of glass transition temperature region)	E'_r	E'_g/E'_r
PU-SMP	1500 MPa	25°C	15 MPa	100

The thermomechanical properties, such as the shape fixity and the shape recovery, crucial for the SMP applications, were estimated.

Initial thermomechanical tests were performed for the SMP samples subjected to tension on MTS 858 testing machine in thermal chamber at various temperatures. The loading and unloading rates were $2 \times 10^{-3} \text{ s}^{-1}$ and $2 \times 10^{-4} \text{ s}^{-1}$, respectively. The SMP sample temperature was controlled by three thermocouples located at the sample area as well as in upper/lower grips of testing machine.

At first, max. strain (20%) was applied at high temperature $T_h = 45^\circ\text{C}$ ($T_g + 20^\circ\text{C}$). Next, while maintaining the strain, the sample was cooled down to $T_l = 5^\circ\text{C}$ ($T_g - 20^\circ\text{C}$) and then unloaded. During the subsequent heating from T_l to T_h under no-load conditions the SMP sample almost recovered its original shape; however a residual strain ε_{ir} was recorded. Schematic of the PU-SMP investigation is presented in Fig. 1.

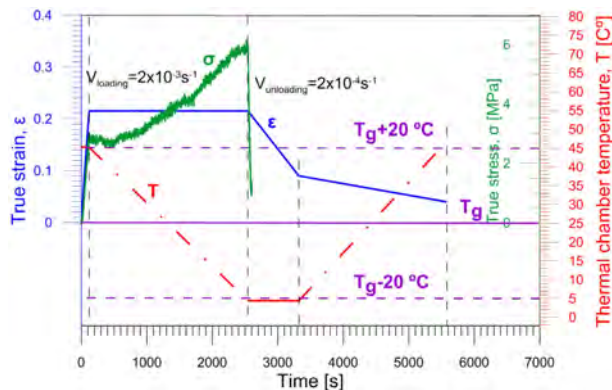


Fig. 1. Schematic of thermomechanical test; strain ε , stress σ and chamber temperature T vs. time.

The shape recovery R_r and shape fixity R_f parameters were calculated by following equations respectively:

$$(1) \quad R_r = \frac{\varepsilon_{\max} - \varepsilon_{ir}}{\varepsilon_{\max}} \cdot 100\%, \quad R_f = \frac{\varepsilon_{un}}{\varepsilon_{\max}} \cdot 100\%,$$

where ε_{\max} is maximum strain, ε_{un} denotes the strain obtained after unloading at T_l and ε_{ir} is irrecoverable strain, i.e. strain obtained after heating up to T_h under no-load conditions [1].

An example of estimated shape fixity and shape recovery parameters is presented in Table 2.

Table 2. Example of shape fixity and shape recovery parameters estimated for PU-SMP.

Sample No.	Shape fixity parameter, %	Shape recovery parameter, %
1	97.1	72.1
2	96.9	79.6
3	95.8	83

3. Conclusions

Results of dynamic mechanical analysis confirm the PU-SMP good shape memory properties.

Initial estimation of the PU-SMP application parameters, e.g. shape fixity and shape recovery, carried out at 20% max strain and at temperature range $T_g - 20^\circ\text{C}$, $T_g + 20^\circ$, gave reasonable values.

Acknowledgments

The research has been carried out with the support of the Polish National Center of Science under Grant No. 2011/01/M/ST8/07754.

References

1. H. Tobushi, R. Matsui, K. Takeda, E. Pieczyska (2013). *Mechanical Properties of Shape Memory Materials*, Materials Science and Technologies, NOVA Publishers, New York.
2. M. Staszczak, E.A. Pieczyska, M. Maj, L. Urbański, H. Tobushi, S. Hayashi (2013). Właściwości mechaniczne oraz zmiany temperatury polimeru z pamięcią kształtu w procesie rozciągania, *POMIARY AUTOMATYKA KONTROLA*, **59**, 9, 1002–1005.

DEFORMATION AND FATIGUE PROPERTIES OF NITROGEN ION IMPLANTED TiNi SHAPE MEMORY ALLOY

K. Takeda¹, R. Matsui¹, H. Tobushi¹, N. Levintant-Zayonts², S. Kucharski²

¹Aichi Institute of Technology, Toyota, Japan

²Institute of Fundamental Technological Research, Warsaw, Poland

1. Introduction

Shape memory alloy (SMA) is expected to be applied as intelligent materials since it shows the unique characteristics of the shape memory effect (SME) and superelasticity (SE). Most SMA elements with using these characteristics perform cyclic motions. In these cases, fatigue of SMA is one of the important properties in view of evaluating functional characteristics as SMA elements. Fatigue properties of SME and SE are complex since they depend on stress, strain, temperature and time which are related to the martensitic transformation (MT). If SMA is implanted by high energy ions, the thermo-mechanical properties may change, resulting in long fatigue life. In the present paper, the nitrogen ion implantation was applied to modify TiNi SMA tape surface and the influence of implantation treatment on the tensile deformation and bending fatigue properties is investigated.

2. Transformation temperature

The TiNi SMA tape of a width of 2.5 mm and a thickness of 1.0 mm was ion-implanted on both surfaces from two opposite directions by nitrogen ion beam with acceleration energy of 50 keV. The total doses of implanted ion are 8×10^{16} , 3×10^{17} and 2.5×10^{18} J/cm². The DSC thermograms for non-implanted and ion-implanted with 2.5×10^{18} J/cm² tapes are shown in Fig. 1. If the nitrogen ion was implanted, the transformation temperatures R_s , R_f , A_s and A_f increase a little.

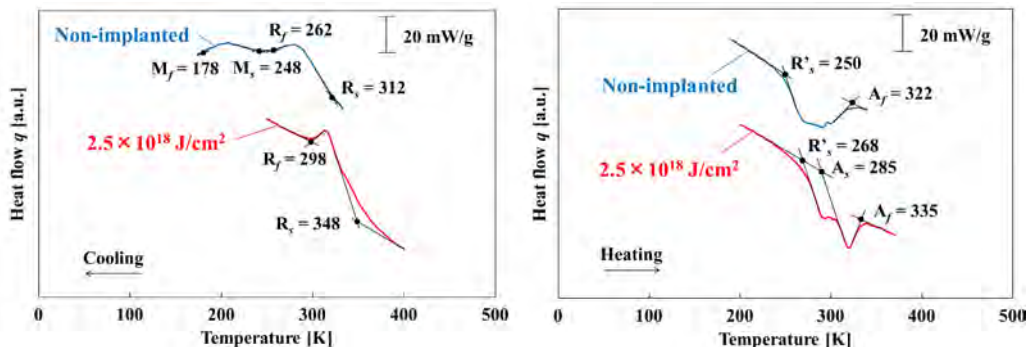


Fig. 1. DSC thermograms for two kinds of tapes with non-implanted and 2.5×10^{18} J/cm².

3. Tensile deformation property

The stress-strain curves of non-implanted and ion-implanted with 2.5×10^{18} J/cm² tapes obtained by the tension test at room temperature are shown in Fig. 2. The stress-

strain curve with non-implanted tape draws a hysteresis curve during loading and unloading, showing the SE. The curve with 2.5×10^{18} J/cm² shows the partial SE. As observed in Fig. 1, if the nitrogen ion is implanted, the transformation temperatures increase a little. Both upper and lower yield stresses therefore decrease and the partial SE appears in place of the SE.

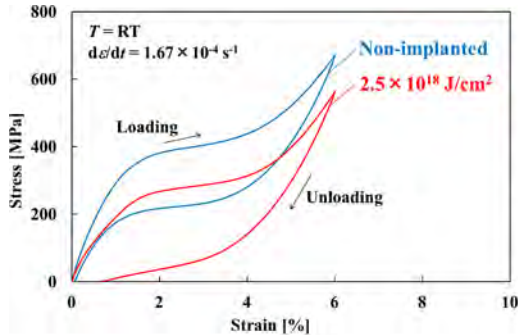


Fig. 2. Stress-strain curves of two kinds of tapes obtained by the tension test at room temperature.

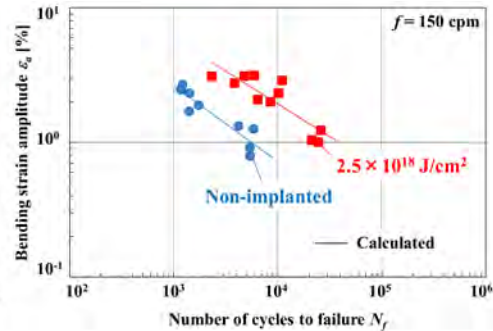


Fig. 3. Relationships between maximum bending strain and the number of cycles to failure obtained by the alternating-plane bending fatigue test.

4. Bending fatigue property

The relationships between the maximum bending strain and the number of cycles to failure for two kinds of tapes obtained by the alternating-plane bending fatigue test at room temperature are shown in Fig. 3. The larger the maximum bending strain, the shorter the fatigue life is. If the nitrogen ion is implanted, the bending fatigue life becomes longer.

5. Fatigue fracture surface

Figure 4 shows SEM photographs of a fracture surface of two kinds of tapes obtained by the alternating-plane bending fatigue test. In Fig. 4, F_c denotes the initiation point of the fatigue crack. In the case of the non-implanted tape, the crack nucleates at a certain point F_c in the central position of the surface and propagates towards the center in an ellipsoidal pattern. In the case of the ion-implanted with 2.5×10^{18} J/cm² tape, the crack nucleates at a corner of the tape and propagates towards the center and along the surface of the tape with the higher speed of progression.

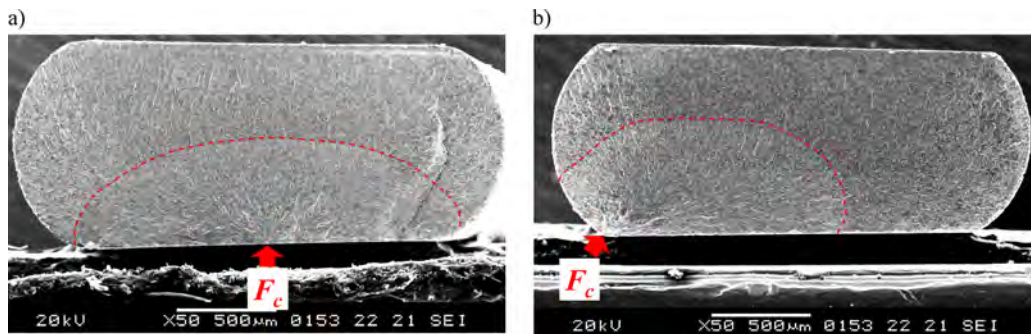


Fig. 4. SEM photographs of a fracture surface of two kinds of tapes obtained by the alternating-plane bending fatigue test: a) non-implanted, b) implanted with 2.5×10^{18} J/cm².

STRESS RELAXATION AND STRESS RECOVERY OF TiNi SHAPE MEMORY ALLOY IN STRESS-CONTROLLED SUBLOOP LOADING

K. Takeda¹, R. Matsui¹, H. Tobushi¹, E.A. Pieczyska²

¹Aichi Institute of Technology, Toyota, Japan

²Institute of Fundamental Technological Research, Warsaw, Poland

1. Introduction

Since the shape memory alloy (SMA) has the superior functions as intelligent materials, the application of the SMA has drawn the worldwide attention. In the case of the subloop in which strain, temperature and stress vary in the range prior to the martensitic transformation (MT) completion, the starting and finishing conditions of the MT prescribed in the full loop are not satisfied. If the condition of the MT to progress is satisfied, stress relaxation and stress recovery occur under constant strain and the load to hold the position varies.

In the present study, the transformation-induced relaxation and stress recovery in the stress-controlled superelastic subloop loading under a constant strain are discussed by the tension test for the TiNi SMA.

2. Stress-strain relationship in the stress-controlled subloop loading

The stress-strain curve and variations in stress σ and strain ε with time t obtained by the test under a stress rate $d\sigma/dt = 5 \text{ MPa/s}$ till a point H_1 at a strain $\varepsilon_1 = 6\%$ followed by holding the strain ε_1 constant and thereafter unloaded under a stress rate $d\sigma/dt = -5 \text{ MPa/s}$ till a point H_3 at a strain $\varepsilon_3 = 2\%$ followed by holding the strain ε_3 constant are shown in Figs. 1 and 2, respectively.

As can be seen in Fig. 1, in the strain holding process at $\varepsilon_1 = 6\%$, stress decreases from σ_1 to σ_2 , resulting in stress relaxation $\Delta\sigma = \sigma_2 - \sigma_1$. In the strain holding process at $\varepsilon_3 = 2\%$, stress increases from σ_3 to σ_4 , resulting in stress recovery $\Delta\sigma = \sigma_4 - \sigma_3$.

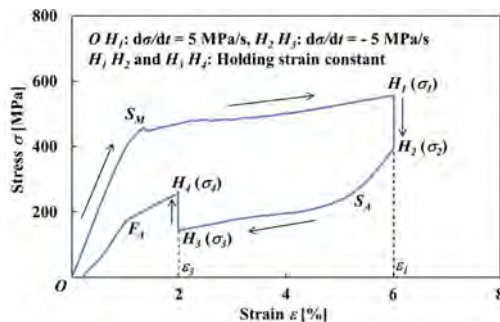


Fig. 1. Stress-strain curve.

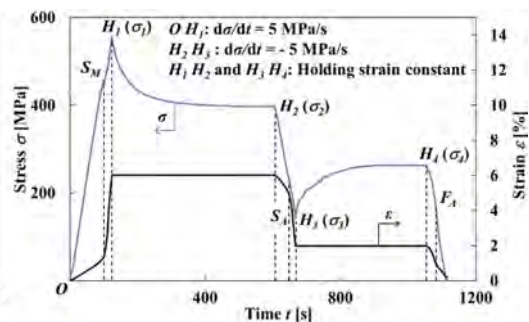


Fig. 2. Variation in stress and strain with time.

As can be seen in Fig. 2, after the strain holding start point H_1 , stress decreases rapidly in the early stage and thereafter decreases gradually. The stress σ_2 at a point H_2 after relaxation is 397 MPa. Similarly, in the unloading process, after the strain holding start point H_3 , stress increases rapidly in the early stage and thereafter increases gradually. The stress σ_4 at a point H_4 after recovery is 263 MPa.

3. Behavior of transformation band

Figure 3 shows the photographs of specimen surface at various strains taken by a microscope during the test. In the loading process under a constant stress rate of 5 MPa/s, strain rate increases from a strain of 2% to 3%, and the transformation bands appear on the whole specimen surface. After a strain of 3%, the interfaces of the appeared transformation bands propagate and strain increases. In the strain holding stage from the point H_1 at a strain of 6% to the point H_2 , the MT progresses and the region of the martensite-phase expands a little. In the unloading process after stress relaxation (point H_2), the reverse transformation progresses from the initiation location at the interfaces of the transformation bands and strain decreases. In the strain holding stage from the point H_3 at a strain of 2% to the point H_4 , the reverse transformation progresses and the region of the parent-phase expands a little.

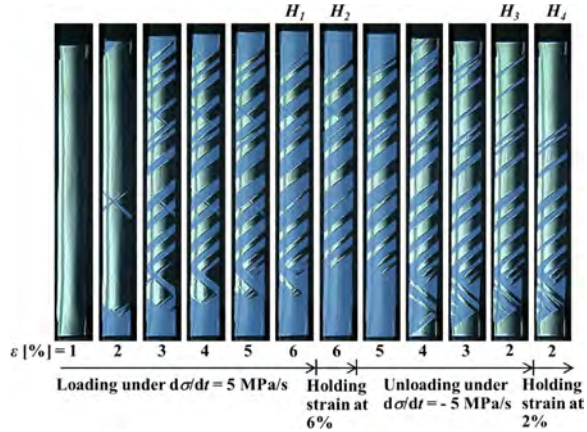


Fig. 3. Photographs of specimen surface at various strains ε .

4. Temperature change due to transformation

Figure 4 shows the temperature distributions on specimen surface at various strains during loading and at various stresses during holding strain constant obtained by the thermography. Figure 5 shows the relationship of stress σ and temperature change ΔT between the average temperature on the specimen surface and the atmosphere temperature with time t during loading and holding strain constant.

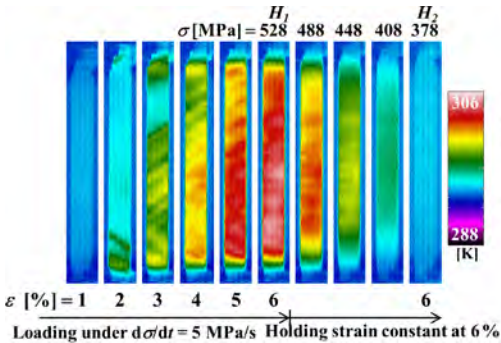


Fig. 4. Thermograms of temperature distribution on specimen surface at various strains ε .

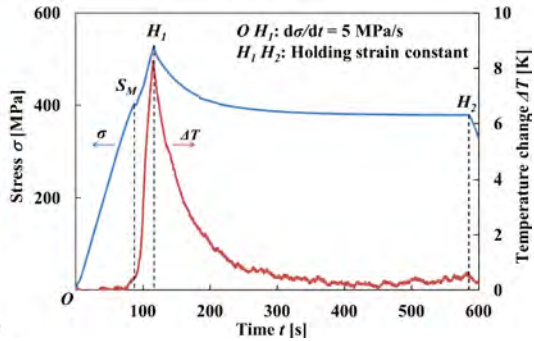


Fig. 5. Variation in stress σ and average temperature change ΔT on specimen surface.

As can be seen in Figs. 4 and 5, in the loading process from the MT start point S_M to the point H_1 , strain rate becomes high as shown in Fig. 2 and there exists less time for the heat generated due to the exothermic MT to transfer to the atmosphere air, resulting in an increase in temperature of the specimen. In the strain holding stage from the point H_1 to the point H_2 , temperature decreases by the air and the condition for the transformation to progress is satisfied, resulting in the progress of the MT. As a result, stress relaxation appears during holding strain constant.

As can be seen in Fig. 5, temperature varies markedly in the early stage during holding strain constant and thereafter saturates a certain value. Corresponding to this temperature change, stress relaxation appears markedly in the early stage during holding strain constant.

References

1. Tobushi H., Matsui R., Takeda K., Pieczyska E.A. (2013). *Mechanical Properties of Shape Memory Materials*, Nova Science Publishers, Inc., 400 Oser Avenue, Suite 1600, Hauppauge, N.Y. 11788-3619, USA, 1–271.
2. Pieczyska E.A., Staszczak M., Dunić V., Slavković R., Tobushi H., Takeda K. (2014). Development of stress-induced martensitic transformation in TiNi Shape Memory Alloy, *Journal of Materials Engineering and Performance* (in print).

JUMP PHENOMENON OF THERMOMECHANICAL RESPONSES IN NONLINEAR TORSIONAL VIBRATION OF NiTi TUBE

M. Xia^{1,2}, Q. Sun¹

¹Hong Kong University of Science and Technology, Hong Kong SAR, China

²Wuhan University, Wuhan, China

1. Introduction

Due to the outstanding superelasticity and damping capacity originating from the first order martensitic phase transition, *Shape Memory Alloy* (SMA) has attracted growing academic and industrial interests. When phase transition occurs, SMA exhibits nonlinear hysteretic constitutive relation and consequent softening stiffness, which will induce classical jump phenomenon in a vibration system. Li and Feng [1] first measured the frequency response functions of SMA bars under traction-compression and a slight resonance frequency shift was observed in experiments. Olivier [2] studied the dynamic behavior of NiTi wire in torsion and observed the jump of rotational angle in the frequency domain. However, the thermal aspect of NiTi SMA was not considered in their work.

In this abstract, we perform experimental investigations on the jump phenomenon of both mechanical response and thermal response in the frequency domain, the amplitude domain and the time domain respectively in a nonlinear torsional vibration system with NiTi tube as the spring.

2. Experimental setup

The torsional vibration tests were conducted on BOSE ElectroForce Test Instruments with a polycrystalline superelastic NiTi tube. A rotary stepping motor provided sinusoidal angular excitations at the lower clamp. The upper clamp was attached with a rotating pendulum, whose angle of rotation was instantly measured by a rotary motion sensor. An infrared camera simultaneously measured the surface temperature field of the NiTi tube and calculated the mean temperature.

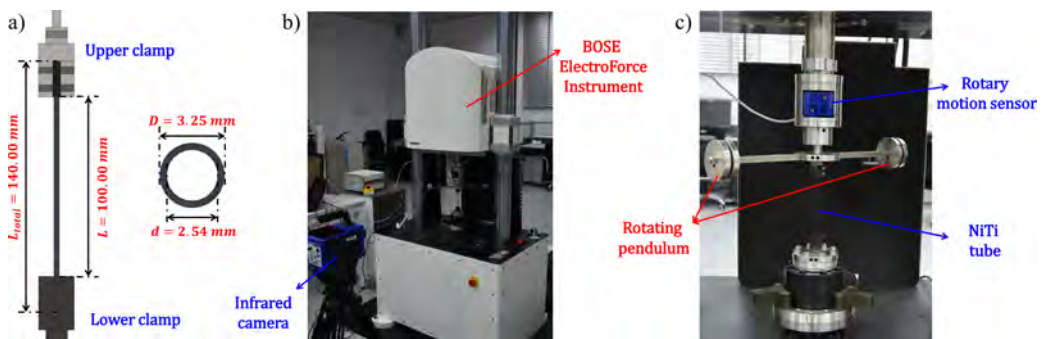


Fig. 1. a) Dimension of NiTi tube, b) testing platform overview and c) clamping configurations.

3. Results and discussion

At a given excitation amplitude, the experiments were performed on ascending and descending frequency orders respectively (see Fig. 2a). At each frequency, the steady stage rotational angle and temperature oscillation amplitude were taken as the mechanical and thermal responses of the vibration system. It is seen that both the mechanical and thermal

responses in the frequency domain are strongly path-dependent. There is significant jump-up (on ascending frequency order at 0.810 Hz) and jump-down (on descending frequency order at 0.790 Hz) on the frequency response curves.

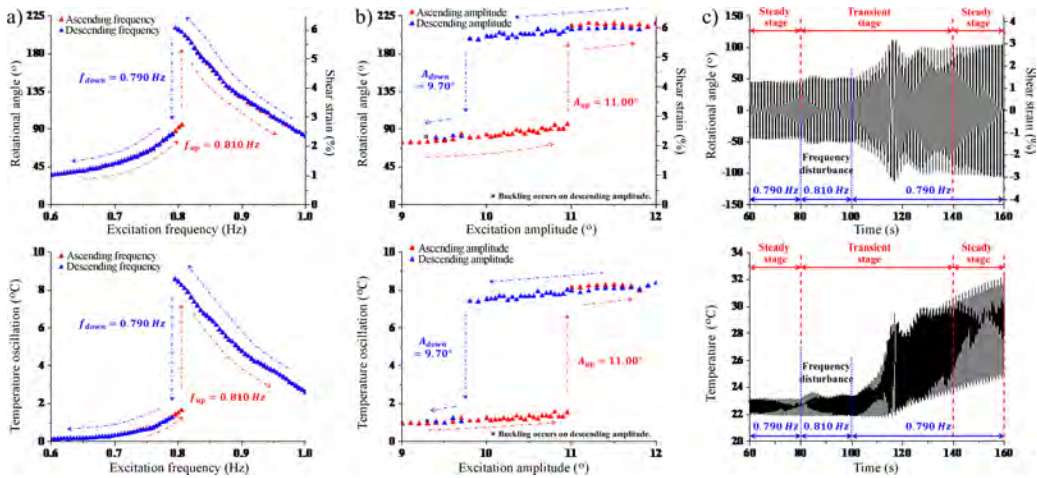


Fig. 2. Mechanical and thermal responses of the torsional vibration system with NiTi tube: a) in the frequency domain at excitation amplitude of 10° , b) in the amplitude domain at excitation frequency of 0.820 Hz and c) in the time domain at excitation amplitude of 10° and frequency of 0.790 Hz.

Similar to the jump in the frequency domain, the vibration tests were performed on ascending and descending amplitude orders (see Fig. 2b) to observe the jump in the amplitude domain at a given excitation frequency. It is shown that the thermomechanical responses in the amplitude domain are also path-dependent. The jump-up phenomenon occurs at 11.00° on ascending amplitude path and jump-down happens at 9.70° on descending amplitude path in the excitation amplitude domain.

To observe the jump phenomenon in the time domain, a metastable testing condition ($0.790 \text{ Hz}/10^\circ$ excitation) was chosen so that the external disturbance could trigger the dynamic bifurcation. When the steady stage was reached under the metastable testing condition, a slight disturbance (excitation frequency increased by 0.020 Hz) was introduced to the system lasting 20s and then removed (see Fig. 2c). Thus, the jump phenomenon was brought about in experiments. From the thermomechanical responses, it is seen that the external disturbance will induce a new transient stage and help the vibration system overcome the energy barrier to reach another steady stage with larger rotational angle. It is directly evidenced that the jump of mechanical response and jump of thermal response happen simultaneously, originating from the thermomechanical coupling of NiTi SMA.

4. Conclusions

The typical jumps of thermomechanical responses in the frequency domain, the amplitude domain and the time domain of a nonlinear torsional vibration system with NiTi tube component are examined in this abstract. Thermal aspect of the softening-type nonlinear vibration system is addressed and simultaneous jumps of thermal and mechanical responses in multiple domains are captured in experiments. The effect of softening-type nonlinear hysteretic constitutive relation of NiTi SMA on a mechanical vibration system is investigated by the characteristic jump phenomenon.

References

1. D.Z. Li, Z.C. Feng (1997). Dynamic properties of pseudoelastic shape memory alloys, *Smart Structures and Materials 1997: Smart Structures and Integrated Systems*, 715–725.
2. O. Doaré et al. (2001). Experimental analysis of the quasi-static and dynamic torsional behaviour of shape memory alloys, *Int. J. Solids. Struct.*, **49**, 32–42.

Session

**Structural Mechanics,
Optimization
and
Reliability Analysis**

**PROBABILISTIC APPROACH TO THE LOAD-CARRYING CAPACITY
 ESTIMATION OF THIN-WALLED STRUCTURAL MEMBERS**

M. Kotełko, P. Lis

Łódź University of Technology, Department of Strength of Materials, Łódź, Poland

1. Introduction

Sensitivity and uncertainty analysis methods are of two types: deterministic and stochastic. While deterministic analysis (parametric study) is a relatively known method in structure design, the stochastic one is a relatively new method, still under intensive investigation and exploration. The research into an application of probabilistic approach to the structural sensitivity analysis goes back to 70th of the XXth Century. Pioneers in Poland were Mróz, Murzewski, Szymczak [1] and Szefer. Publications of Szymczak, Budkowska and Iwicki [1] were the first, concerning results of the probabilistic sensitivity analysis of thin-walled structures. Fundamental, in the area of stochastic sensitivity analysis of thin-walled columns under compression and girders subjected to bending are works carried out by Z. and J. Kala, Melcher and Skaloud from Czech Republic [2].

TWS members display a significant post-elastic capacity. It means, that the actual load-carrying capacity of any TWS member (particularly column or beam) is situated between a lower- and upper-bound value of the load-carrying capacity [3]. The probabilistic sensitivity analysis of both load-carrying capacity estimations and of a difference between them is an important issue, still under intensive research.

2. Sensitivity analysis of load-carrying capacity of box-section girders

In the paper selected results of the load-carrying capacity stochastic variance based sensitivity analysis of thin-walled box-section girder subjected to pure bending are presented. The lower- and upper-bound load-capacity estimation (OD and OG, respectively) is performed. The methodology of the sensitivity analysis was based on the Monte-Carlo method. The sensitivity analysis was performed to determine the sensitivity of OD and OG with respect to the variance of several random input quantities, i.e. dimensions of the girder and material parameters. The input random quantities are indicated in Table 1.

Table 1.

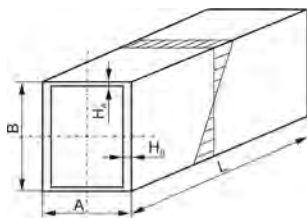


Fig. 1. Box-section girder.

Random variable	Unit	Mean value	Standard deviation	Type of distribution
width A	M	0.1	0.0005	Norm. (Gauss)
height B	M	0.1	0.5, 0.6, 0.7 [mm]	Norm. (Gauss)
length L	M	0.1	0.0005, 0.0006, 0.0007	Norm. (Gauss)
wall thickness H ($H_A = H_B$)	M	0.001	1, 2, 7, 8, 9, 10, 15 [%]	Norm. (Gauss)
Young modulus E	GPa	210	12.6	Norm. (Gauss)
Poisson ratio ν	–	0.27	0.03	Norm. (Gauss)
yield stress R_e	MPa	284.5	21.5, 22.5, 23.5	Norm. (Gauss)

The analysis consisted in the polynomial decomposition, carried out using the multi-dimensional linear regression. The calculations were performed using the program Minitab [4]. Knowing the distribution of input variables, using the Monte-Carlo method, adequate

data files were generated. After generating the data files the values of out-put variables were determined, using the code “NOSNOSC” [3]. Then, after generating in-out files equations of regression, performing the decomposition to polynomial through linear regression were derived [3]. Exemplary results of the sensitivity analysis of OG in terms of the variance of girder’s height B (Fig. 2a) and material yield stress Re (Fig. 2b) represented by pie charts are shown below.

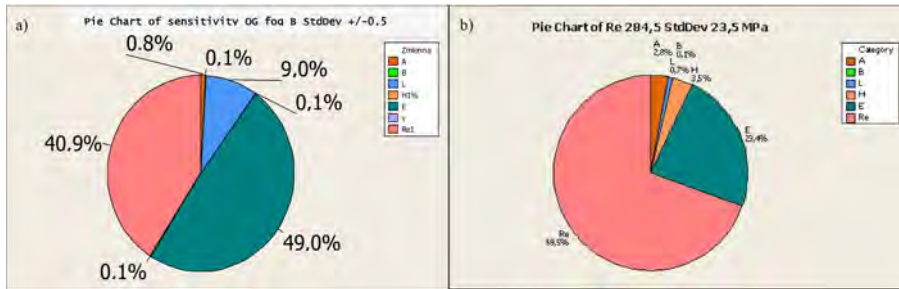


Fig. 2. Exemplary pie charts for OG: a) sensitivity analysis of height B variance (± 0.5 standard deviation), b) sensitivity analysis of yield stress variance (standard deviation 23.5 MPa).

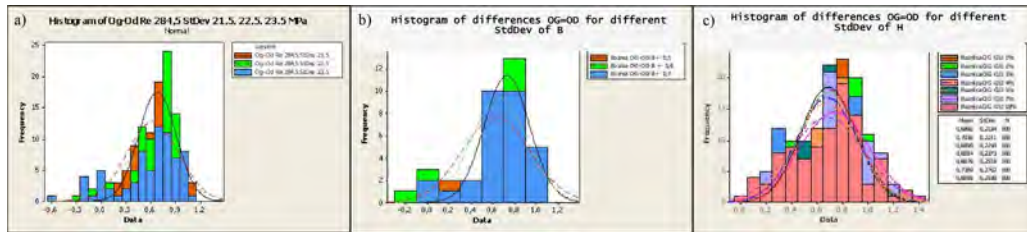


Fig. 3. Visualization of OG and OD differences by histograms: a) for yield stress variance, b) for height variance, c) for wall thickness variance.

3. Final remarks

The results of research obtained by the authors previously [4] and that presented herein indicate, that statistically significant is the variance of the yield stress only, while the significance of geometrical parameters is much lower. The regression analysis confirms that a statistically significant empirical multi-dimensional model exists for the lower-bound estimation (OD) in terms of considered input random quantities. However, its efficiency is weak. Accuracy of the model based on the least squares method was connected with 25% error. On the contrary, the efficiency of analogous empirical model for the upper-bound estimation – (OG) is high (above 98%). It concerns both the yield stress and geometrical dimensions. The increase of the yield stress and geometrical dimensions (except wall thickness) standard deviation induces an increase of the differences of OG and OD (see the “shift” of the histograms in Fig. 3a and 3b)). The distribution of OG-OD differences is not normal for about 95% confidence level. For the wall thickness variance at the same confidence level this distribution is normal (Fig. 3c)

References

1. Szymczak C. *et al.* (2003). *Sensitivity analysis of beams and frames made of thin-walled members*, Gdansk University of Technology, Gdańsk.
2. Kala Z. (2007). Stability problems of steel structures in the presence of stochastic and fuzzy uncertainty, *Int. Journal of Thin-Walled Structures*, **45**, 10–11.
3. MINITAB PRODUCTION GROUP (2000). *Minitab User’s Guide 2: Data Analysis and Quality Tools*, Release 13, *Minitab Inc.*
4. Lis P., Kotelko M. (2013). Sensitivity analysis of steel box-section girder, *Mechanics and Mechanical Engineering*, **25**, 4, 165–176, Technical University of Lodz.

SENSITIVITY ANALYSIS IN HOMOGENIZATION PROCESS OF CORRUGATED PAPERBOARDS

A. Marek, T. Garbowski

Institute of Structural Engineering, Poznan University of Technology, Poznan, Poland

1. Introduction and motivation

The corrugated paperboard is a product that has extremely big number of applications in various fields, e.g. transportation boxes, protection covers, supplementary material in furniture structures, to list just a few. Due to its complicated geometry (sine-like corrugated core) it is demanding task to perform numerical simulations of large structures consisting of such material. This is because the appropriate meshing of fluting dramatically increase the number of degrees of freedom of Finite Element (FE) model. In order to cope with this problem many researchers took attempts to homogenize corrugated board by replacing structural model with homogeneous shells of equivalent properties.

Due to a microscopic structure of paperboard material its mechanical properties are different along different directions. Three main directions are induced by manufacturing process of paperboard, as cellulose fibers align mainly in rolling direction. This direction of typically greatest stiffness is referred to as MD (machine direction), in-plane transverse direction is known as CD (cross direction) and out of plane direction is called ZD. Experiments show that stiffness in MD differs from CD typically by a factor of 2–3, while from ZD by a factor of 2 orders [9].

In order to simulate failure of corrugated board structures it is vital to include post-elastic response of material. In order to capture such response a number of constitutive models of paperboard were proposed which includes e.g. Hill model [4], Hoffman model [5] (an extension of Hill model that distinct tension and compression and is pressure-dependent) or Xia et al. [9] model with anisotropic hardening. These models differ in complexity of plastic surface description and in number of parameters to be characterized in a laboratory work (see e.g. [6]), ranging from 6 in Hill, through 9 in Hoffman to 10 in Xia *et al.*

Having selected a proper material model for cardboard one needs to choose a method of homogenization of corrugated boards. There are various homogenization techniques that can be applied to cardboards among which one can name Classical Laminate Theory (CLT) [1, 8], Hill-Mandel (HM) approach [2], Asymptotic Expansion Method (AEM) [3]. Those methods base on both geometry of RVE (representative volume element – unit cell of corrugated board) and stiffnesses of constituents. The CLT assumes that equivalent plate stiffness is computed through integration of stiffness parameters of all constituents. The HM approach uses energy equivalence of RVE and equivalent homogeneous shell. It was shown [3, 7] that those method provide very similar elastic parameters which give accurate response of homogenous shell in comparison to response of structural model. Unfortunately those approaches fail in providing equivalent inelastic parameters such as initial yield stresses, hardening controls etc. In literature there are not many attempts of establishing effective inelastic parameters in systematic way.

Therefore here authors would like to show a preliminary work in selecting a proper numerical model that will be capable of reproducing an experimental data both in elastic and inelastic region. The experiment which will activate the biggest possible number of model's parameters can be later used for a calibration of average inelastic parameters

in homogenized model. In this communication authors present a study on sensitivity of Edge Crush Test (ECT) and Bending Stiffness Test (BST) of cardboard with respect to parameters embedded in selected orthotropic elasto-plastic constitutive models. This helps in careful separation of cardboard's constituents properties which are important in homogenization procedure from those which can be safely neglected.

2. Methods and conclusions

Sensitivity analysis is great tool which can either establish importance of parameters that are taken into account during design process or identify crucial parameters in certain models. This information can be then used in construction of effective model that can capture necessary mechanics. Simplest measure of sensitivity is change of appropriate scalar output of model with respect to perturbation of one of inputs in model. Such scalar can be for example deflection or displacement in ECT and BST tests. Sensitivity can be then calculated as partial derivative of outcome with respect to input:

$$(1) \quad s_i = \frac{\partial u}{\partial x_i} \approx \left(\frac{u_i}{u_{\text{ref}}} - 1 \right) \frac{1}{\Delta_i}$$

where: s_i is sensitivity of i -th parameter, u_{ref} is reference displacement, u_i is displacement when i -th parameter is changed, Δ_i is change factor of i -th parameter.

Such approach is called local sensitivity and is limited to given set of initial parameters. In order to obtain more thorough results global sensitivity analysis is also performed, that is analysis is performed on finite number of initial parameters sets randomly distributed in space of interest (i.e. in the space of admissible values of paperboard material parameters).

Sensitivity brings here two very important informations for those who would like to perform a clever homogenization of corrugated paperboards structures: (i) it points out the parameters of cardboard's constituents which are not active in a particular test and, therefore one should be careful in taking them into account during homogenization (ii) it orders an importance of the parameters. Those two informations are meaningful only if experimental setups triggers in the specimen the same strain or stress states which can be observed in service life of a real structures. Here two main strain-stress states are considered in two tests: (a) axial compression test (ECT) and (b) bending test (BST) in various material directions. Having a full list of sensitivities of measured quantities in the tests with respect to model parameters one can perform a conscious homogenization of corrugated paperboard structures both in elastic and inelastic range.

References

1. S. Allaoui, M.L. Benzeggagh, Z. Aboura, N. Talbi (2004). Elastic behaviour of corrugated cardboard: experiments and modeling, *Compos. Struct.*, **63**, 53–62.
2. M.E. Biancolini (2005). Evaluation of equivalent stiffness properties of corrugated board, *Compos. Struct.*, **69**, 322–328.
3. N. Buannic, P. Cartraud, T. Quesnel (2003). Homogenization of corrugated core sandwich panels, *Compos. Struct.*, **59**, 299–312.
4. R. Hill (1948). A theory of the yielding and plastic flow in anisotropic metals, *Proceedings of the Royal Society*, **193**, 281–297.
5. O. Hoffman (1967). The brittle strength of orthotropic materials, *J. Compos. Mater.*, **1**, 200–206.
6. T. Garbowski, G. Maier, G. Novati (2012). On calibration of orthotropic elastic-plastic constitutive models for paper foils by biaxial tests and inverse analyses, *Struct. Multidisc. Optimization*, **46**, 111–128.
7. A. Marek (2014). *Homogenization techniques and constitutive modeling of sandwich panels*, Bachelor Thesis, Poznan University of Technology.
8. N. Talbi, A. Batti, R. Ayad, Y.Q. Guo (2009). An analytical homogenization model for finite element modelling of corrugated cardboard, *Compos. Struct.*, **88**, 280–289.
9. Q.S. Xia, M.C. Boyce, D.M. Parks (2000). A constitutive model for the anisotropic elastic-plastic deformation of paper and paperboard, *Int. J. Solids Struct.*, **6**, 1–48.

ANALYSIS OF STEADY WEAR STATES FOR MONOTONIC AND PERIODIC SLIDING

I. Páczelt¹, Z. Mróz²

¹University of Miskolc, Miskolc, Hungary

²Institute of Fundamental Technological Research, Warsaw, Poland

1. Introduction

In many practical industrial applications it is very important to predict the form of wear shape and the related contact stress distribution. The wear process on the frictional interface of two bodies in a relative sliding motion induces shape evolution. In the earlier paper [1] it was shown that the contact shape evolution tends to a steady state. The steady state conditions were specified for both monotonic and periodic sliding motion. In the case when the contact zone is fixed on body B_1 and translates on body B_2 in monotonic sliding, then the rigid body velocity of B_1 specifies the wear rate form of B_1 and the related contact pressure, satisfying the minimum principle of the wear dissipation power. In this work a fundamental assumption has been introduced, namely, *in the steady state the wear rate vector is collinear with the rigid body wear velocity of body B_1* allowed by the boundary constraints. Similarly, for the periodic sliding motion the steady state satisfies the periodicity condition and the accumulated wear in one cycle is compatible with the rigid body motion of B_1 . The numerical simulation of the contact shape evolution is based on time integration of the modified Archard wear rule expressed in terms of relative slip velocity and contact pressure.

Several classes of wear problems are distinguished and discussed for specified loading and support conditions for two bodies in the relative sliding motion: *Class 1.* The rigid body wear displacements are constrained by the boundary supports and the steady state corresponds to vanishing contact pressure [1]. *Class 2.* The contact zone S_c does not evolve in time and is specified. The rigid body wear velocity is compatible with the specified boundary conditions. The steady state condition is reached when the contact pressure distribution corresponds to the wear rate proportional to the rigid body velocity [1]. *Class 3.* The contact surface S_c evolves in time due to wear process, for instance, in the case of a spherical indenter sliding on a substrate with varying size of the contact domain $a = a(t)$. The stress distribution and the shape of contact zone are then dependent on the size parameter $a(t)$. In this case the quasi-steady distribution of contact pressure and the surface shape can then be specified for the selected values of the size parameter [2]. *Class 4.* Similarly as for *Class 2* the contact surface S_c is specified but the wear process occurs for periodic sliding motion. The periodic solution for one cycle remains steady for consecutive cycles [1, 3]. *Class 5.* Similarly to *Class 3*, the contact zone S_c evolves during consecutive cycles of sliding or loading and the periodic quasi-steady state depends on the contact size parameter [2].

2. Wear rule and variational method applied to steady state conditions

The modified Archard wear rule [1] specifies the wear rate $\dot{w}_{i,n}$ of the i -th body in the normal contact direction. Following the previous work [1] it is assumed that

$$(1) \quad \dot{w}_{i,n} = \beta_i (\tau_n)^{b_i} \|\dot{\mathbf{u}}_\tau\|^{a_i} = \beta_i (\mu p_n)^{b_i} \|\dot{\mathbf{u}}_\tau\|^{a_i} = \beta_i (\mu p_n)^{b_i} v_r^{a_i} = \tilde{\beta}_i p_n^{b_i} v_r^{a_i}, \quad i = 1, 2$$

where μ is the friction coefficient, β_i , a_i , b_i are the wear parameters, $\tilde{\beta}_i = \beta_i \mu^{b_i}$, $v_r = \|\dot{\mathbf{u}}_{R,\tau}^{(s)}\|$ is the relative sliding velocity. The shear stress at the contact surface is denoted by τ_n and calculated in terms of the contact pressure p_n by using the Coulomb friction law $\tau_n = \mu p_n$. Assuming existence of J contact zones in Body 1, it can be proved that for the wear problem of *Class 2* the minimization of the following wear dissipation power

$$(2) \quad D_w^= \sum_{j=1}^J \sum_{i=1}^2 \left(\int_{S_c^{(j)}} (\mathbf{t}_i^c \cdot \dot{\mathbf{w}}_i) dS \right) = \sum_{j=1}^J \sum_{i=1}^2 C_i^{(j)}$$

with the equilibrium constraints of body B_1 : $\mathbf{f} = \mathbf{0}$, $\mathbf{m} = \mathbf{0}$, provides the contact pressure

$$(3) \quad p_n^{(j)\pm} = \left(\frac{1}{K^{(j)}} \left(\dot{\boldsymbol{\lambda}}_F \cdot \boldsymbol{\rho}_c^\pm + \left(\dot{\boldsymbol{\lambda}}_M \times \mathbf{r} \right) \cdot \boldsymbol{\rho}_c^\pm \right) \frac{1}{Q} \right)^{1/b} \quad x \in S_c^{(j)}$$

where $K^{(j)} = \sum_{i=1}^2 (\tilde{\beta}_i v_r^{a_i})^{(j)}$, $Q = 1 \pm \mu \tan \chi \cos \chi_1 + \mu_d \tan \chi \sin \chi_1$, $\dot{\boldsymbol{\lambda}}_F$ and $\dot{\boldsymbol{\lambda}}_M$ are the vectors induced by wear, briefly called *rigid body wear velocities*. The solution is valid if $p_n^{(j)\pm} \geq 0$ at each point $x \in S_c^{(j)}$. The contact traction can now be written as follows $\mathbf{t}^c = \mathbf{t}_1^c = -\mathbf{t}_2^c = -p_n^\pm \boldsymbol{\rho}_c^\pm$, where the vector $\boldsymbol{\rho}_c^\pm = \mathbf{n}_c \pm \mu \mathbf{e}_{\tau 1} + \mu_d \mathbf{e}_{\tau 2}$ specifies the orientation and magnitude of the traction on S_c referred to the contact pressure p_n^\pm . The friction coefficients μ and μ_d specify the shear stresses in sliding and transverse directions [1]. The non-linear equations can be solved by applying Newton-Raphson technique.

3. Periodic sliding motion

During a periodic reciprocal sliding, the steady wear state is expressed in terms of contact pressure in progressive and reverse sliding semi-cycles [1, 3], that is $p_n^+ + p_n^- = 2p_m = \text{const}$. Using this fact the optimization problem for calculation of the contact shape of body B_1 is stated and an analytical method is formulated for prediction of the number of cycles to reach the periodic steady wear state.

4. Numerical experiments

The lecture will present numerous examples for different classes of wear problems with neglect or account for the generated temperature field. The presented examples demonstrate that the thermal distortion affects essentially the optimal contact shape in the steady state and for periodic sliding motion it affects also the contact pressure distribution.

Acknowledgments

The present research was partially supported by the Hungarian Academy of Sciences, by grant OTKA K67825, by program TÁMOP-4.2.1.B-10/2/KONV-2010-0001.

References

1. I. Páczelt, Z. Mróz (2012). Solution of wear problems for monotonic and periodic sliding with p-version of the finite element method, *Comput. Methods Appl. Mech. Engng.*, **249-252**, 75–103.
2. I. Páczelt, S. Kucharski, Z. Mróz (2012). The experimental and numerical analysis of quasi-steady wear processes for a sliding spherical indenter, *Wear*, **274-275**, 127–148.
3. I. Páczelt, Z. Mróz (2014). Analysis of thermo-mechanical wear problems for reciprocal punch sliding, submitted to Civil-Comp Press, Reference: S2012/2013/00063.

SENSITIVITY ANALYSIS FOR THE INDIRECT EXTRUSION OF Mg ALLOY WITH Al COATING

T. Tokunaga^{1,2}, D. Szeliga², K. Matsuura³, M. Ohno³, M. Pietrzyk²

¹Research Fellow of Japan Society for the Promotion of Science, Hokkaido University, Sapporo, Japan

²AGH University of Science and Technology, Krakow, Poland

³Hokkaido University, Sapporo, Japan

1. Introduction

Mg alloys have attracted much attention in the aerospace, automotive and telecommunication equipment industries owing to their high strength-to-weight ratio and good recyclability. However, the use of the Mg alloys has been limited due to their extremely poor corrosion resistance. In order to solve this problem, the present authors have developed a new process for thick Al coating on Mg alloys using a hot extrusion technique and have found that the Al-coated Mg alloy extruded bar exhibits an excellent corrosion resistance comparable to that of pure Al [1]. We also found that the uniformity of Al coating thickness can be controlled by changing extrusion parameters such as die angle. However, the optimal extrusion condition for a uniform coating thickness to be achieved remains unclear, because effects of extrusion parameter on the uniformity of coating thickness are not elucidated. In the present study, the optimal extrusion conditions are investigated by means of numerical simulations using a finite element (FE) code. The validity of the model for the extrusion is investigated and the sensitivity analysis is conducted in order to clarify the influence of each parameter.

2. Methodology

An AZ80 Mg alloy and a commercial pure Al were used as the core and coating material, respectively. The flow stress model of the Mg alloy was developed from plastometric tests and the inverse analysis. The flow stress model of the pure Al was taken from the FPDBase [2]. The extrusion temperature was 583 K, the ram speed was 0.033 mm/sec and extrusion ratio was 92%. The details of the extrusion conditions can be found in [1]. The initial geometry for the simulation was identical with billet, plate, die and container geometries used in the experiments [1]. The model was implemented with the commercial FORGE 2011 software, and the FE code based on the Norton-Hoff viscoplastic flow rule was used in the simulations. After the simulations, the thickness of coating was measured in a length of 40 mm of the simulated extrusion product. The response, y , for the sensitivity analysis was set as the uniformity of Al coating thickness, which is defined as:

$$(1) \quad y = \frac{\sum_{i=1}^n (d_i - d_{\text{ave}})^2}{d_{\text{ave}}^2}$$

where d_i is the thickness of Al coating layer at the i -th position numerated from the tip of the extruded bar, n is the number of measurements and d_{ave} is the average thickness of the coating layer.

In the sensitivity analysis, full two-level factorial design (FD) was adopted in light of low computational costs of the method and high computational costs of the extrusion process [3]. Five parameters were used in this study: initial thickness of pure Al plate, d ,

(2–5 mm), extrusion temperature, T , (523–623 K), ram speed, v (0.033–1 mm/sec), flow stress ratio of the calculation to the original pure Al, K (0.9–1.2) and die angle, θ , (90–110°). These parameter levels were chosen based on our preliminary experiments. In FD, the average response from high-level runs was compared with the average response from the low-level runs to determine the parameter effect:

$$(2) \quad Effect_{FD} = \frac{\sum y^+}{m^+} - \frac{\sum y^-}{m^-}$$

where y is the model output, “+” and “–” are the upper and lower limits of the parameter range, respectively; m is the number of model simulations at each level.

3. Results

Figure 1a) illustrates the comparison between the experimental and simulation results which show the changes of Al coating thickness with respect to the distance from the tip of the extruded bar produced with different die angles. The simulation results fairly agree with the experimental results especially regarding the uniformity of the coating layer. Thus, the developed 2D FE model of hot extrusion is considered to be reliable from the point of the uniformity of Al coating thickness. The results of sensitivity analysis are presented in Fig. 1b). The higher absolute value of the $Effect_{FD}$ means the higher effect on the extrusion process. From the figure, it was found that the magnitudes of the initial thickness d and the die angle θ affect the uniformity the most. The extrusion temperature T , the extrusion velocity v and the flow stress ratio K are comparable and the effects are not so significant.

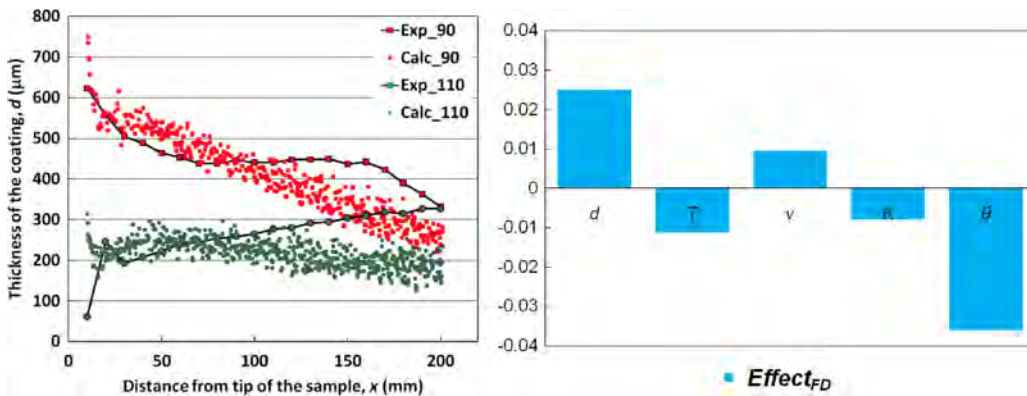


Fig. 1. a) Changes of Al coating thickness with respect to the distance from the tip of samples extruded with different die angles. The results were obtained by experimental and simulation processes, b) effects of the factorial design for the process parameters.

References

1. T. Tokunaga, K. Matsuura, M. Ohno (2012). Aluminum Coating on Magnesium-Based Alloy by Hot Extrusion and Its Characteristics, *Mater. Trans.*, **53**, 1034–1041.
2. FPDBASE 1.3 TRANSVALOR S.A., September 2005.
3. A. Saltelli, K. Chan, E.M. Scott (2000). *Sensitivity analysis*, Wiley, New York.

FLANGE VERTICAL BUCKLING OF HYBRID STEEL GIRDERS UNDER BENDING

T. Ueda¹, S. Shimizu¹, G. Fujita², N. Tanaka²

¹Department of Civil Engineering, Shinshu University, Nagano, Japan

²Miyaji Engineering Co. Ltd, Tokyo, Japan

1. General

This paper describes flange vertical buckling behaviour of a hybrid steel I-shaped girder under bending.

The authors have made a series of studies on hybrid steel girders experimentally and numerically, and the shear behaviour of the hybrid steel girder was presented in the Solmech 2008 conferece [1].

In the experimental test by authors on hybrid steel girders, unexpected flange vertical buckling under bending was observed in one of the test models as shown in the photo in the Fig. 1 [2]. Flange vertical buckling is believed to occur in an I-shaped steel girder having very weak web plate, and a hybrid steel girder just has the weak web plate. Thus, it is considered that flange vertical buckling may be one of the important failure patterns of the hybrid girders.

With this background, we tried to reproduce the test result on the vertical buckling with the numerical analyses, and to study the basic characteristics of bending behaviour of hybrid girders. The principal results are summarized in the authors' previous paper [3]. An existing formula for vertical buckling refers the width-thickness ratio of the web plate. However, in the paper [3], the authors pointed out that the web depth has small contribution on the occurrence of vertical buckling.

In the current paper, a new collapse model of the flange vertical buckling will be proposed.

2. Numerical models and loadings

The numerical models used in this study have nominally same shapes and dimensions to those of the author's experimental model, expect the flange thickness and the web depth. In this study, the flange thickness and the web depth are considered as parameters. Figure 2 shows the outlines of typical numerical model with the FEM mesh

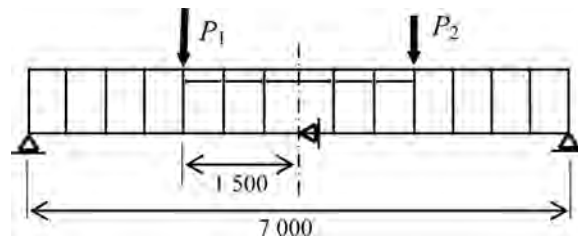


Fig. 2. Numerical model layout.

pattern. The model has an I-shaped section with the flange width of 200 mm and the web thickness of 45 mm. The flange thickness t_f and the web depth b_w are varied as $t_f = 10$ to 20 mm and $b_w = 600$ to 1200 mm. The grade SM570 high strength steel having yield stress $\sigma_y = 596$ MPa and SM400 normal steel with $\sigma_y = 360$ MPa are used for the flange and web plates respectively, although the LY235 low yield steel with $\sigma_y = 273$ MPa for the center part of the web. In the experimental test, 2 point loadings P_1 and P_2 are applied



Fig. 1. Observed flange vertical buckling [2].

on the test model as illustrated in Fig. 1. Investigating the test result carefully, it is found that the left-sided load P_1 is greater by about 1% than P_2 . Therefore, in the analyses, the load P_1 is kept to be greater by 1% than P_2 throughout the incremental procedure.

3. Numerical results and a bar model on the elastic foundation

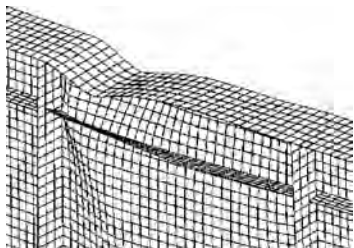


Fig. 3. Deformation pattern of vertical buckling.

In the Fig. 3, the deformation pattern of the numerical model with $b_w = 900$ mm and $t_f = 15$ mm is shown. The typical vertical buckling deformation pattern is observed in the figure. As mentioned in [3], this vertical buckling pattern is found for the numerical models with the flange thickness greater than 15mm or 16mm, and with the thinner flange thickness the flange torsional buckling or the coupled pattern of the vertical and the torsional buckling. In the results, the web depth has very small contribution for the occurrence of the vertical buckling.

Here, the authors will present a new model of the flange vertical buckling. The flange can be considered a compressed bar element supported by many springs as illustrated in the Fig. 4, just like the compressed bar on the elastic foundation proposed by Timoshenko. The reaction from the springs in the figure is corresponding with the web plate, and the spring constant is equivalent to the stiffness of the web plate.

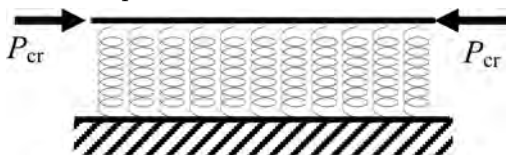


Fig. 4. A column on the elastic foundation.

Timoshenko presented a formula to estimate the buckling load P_{cr} in the figure, approximately $P_{cr} = \sqrt{\alpha EI}$ here the constant α [N/mm/mm] is corresponding with the spring constant per a unit length. By using the maximum load obtained through the analyses, the spring constant can be calculated. The obtained

values of the constant are summarized in the Table 1. It is found from this table that the values are mainly owing to the flange thickness.

Table 1. Coefficients α for Flange vertical buckling.

flange thickness	web depth				
	600 mm	750 mm	900 mm	1050 mm	1200 mm
15 mm			71.5	71.6	68.5
16 mm	64.3	68.8	67.7	68.0	65.2
17 mm	64.1	65.5	64.4	65.3	62.0
18 mm	62.9	61.9	61.4	61.0	58.9
19 mm	60.8	58.1	57.9	57.0	56.0
20 mm	58.1	64.3	55.8	54.3	53.4
					N/mm/mm

Hereafter, the mechanical (theoretical) values of the constant shall be discussed.

References

1. S. Shimizu, K. Hara (2008). Shear Behaviour of Hybrid Steel Girders, Selected Topics of Contemporary Solid Mechanics, *36th Solid Mechanics Conference, Gdansk, Poland*, 288–289.
2. S. Shimizu, J. Zhang, N. Tanaka, K. Akehashi, H. Nakai (2003). An Experimental Study on Ultimate Strength Behaviour of Hybrid Steel Plate Girders, *Steel Construction Engineering, JSSC (Japanese Society of Steel Construction)*, **10**, 51–60 (in Japanese).
3. T. Ueda, Y. Matoge, S. Shimizu, G. Fujita, N. Tanaka (2013). A Parametric Study on Flange Vertical Buckling of Hybrid Steel Girders, *Shell Structures: Theory and Applications*, Vol. 3, W. Pietraszkiewicz et al. (eds.), CRC Press, 445–448.

MATHEMATICAL MODEL FOR INELASTIC DEFORMATION OF FLEXIBLE GRAPHITE O-RING SEALS AND SEAL PACKS UNDER THEIR EXPLOITATION IN STOP VALVES

A.V. Zaitsev¹, I.Yu. Zubko¹, O.Yu. Isaev², D.M. Karavaev¹, V.S. Koksharov¹,
D.V. Smirnov², A.M. Khanov¹

¹Perm National Research Polytechnic University, Perm, Russian Federation

²Sealur Ltd., Perm, Russian Federation

1. Introduction

Flexible graphite (i.e. FG) is a unique composite material with temperature-independent high thermo-chemical durability, low coefficient of friction and high elastic properties. FG seals are easily breaking-in without erosive affection on the contact metal surfaces, fit for multifunctional usage in high-corrosive and high-reactive gas (i.e. oxygen, nitrogen, hydrogen, etc.) and fluid (i.e. solutions of acids, alkalis and salts, organic solvents, petroleum and petroleum derivatives, sweet and sea-water, etc.) media [1, 2]. FG o-ring seals and seal packs have high reliability, they do not require additional hermetization during long-term usage and work at temperatures up to 560°C with pressures up to 40.0 MPa. Currently FG o-ring seals are greatly used in aerospace, metallurgical, oil-and-gas and chemical plants, power industry facilities, housing and communal service companies. Traditional experimental schemes (i.e. full scale in-situ experiments with structures with prototypes) for the development and optimization of seals are unreasonable due to a high risk of accidents with serious environmental and economic damage. Therefore, mathematical modelling makes it possible to predict thermophysical and mechanical properties of FG, describe mechanical behaviour and optimum design of o-ring seals and seal packs corresponding to survivability and safety usage.

2. Thermomechanics model for initial operation mode

A thermomechanics model for initial operation mode description of large-scale production seals (intended for plunger seal in the stop valves) is developed with the account of a cylindrical nature of anisotropy type of FG, obtained experimental data and results of numerical predictions by modification of particle method for elastic, friction, strength and thermophysical characteristics of FG. It was supposed that o-ring seal is a thick-walled, limiting homogeneous transversally-isotropic cylinder fixed in a oil-seal housing by sealing bush (i.e. in all points of an external surface radial, hoop and axial displacements are dropped out). On one of the end surfaces hermetization pressure has been set from a sealing bush, and on the other end surfaces — work pressure. Axial displacements that modelled plunger reciprocation in burn-in regimes in the direction of a closing ring and in the opposite side have been set on the internal lateral surface. The quasistationary mode of o-ring seal behaviour assumed absence of FG entrainment which was modelled by the set of the friction law for contact surfaces in the form of proportionality between radial and shear stresses. With consideration of given conditions analytical solutions for boundary-value problems have been received and stresses, strains and displacements have been defined.

The influence of thermoforce loading conditions on the character of stress-strain distributions along cross-sections of o-ring seals and seal packs has been investigated by the use of numerical FEM solutions of 3D stationary boundary-value problems. Calculations have been made of estimation of real damage mechanisms (i.e. damage from tension or compression in radial, hoop and axial directions, and from transversal and antiplane shear)

affection on initial strength, of a comparison of different loading modes (i.e. reciprocating motion in sealing bush or opposite direction, and torsion of the rod), height and conditions on contact surfaces (i.e. ideal contact, friction or slip) between seals on the maximum values of radial, hoop, axial, and shear stresses. It was supposed that external and internal radii of o-ring seals were the following $a = 15.0$ mm and $b = 22.5$ mm; the high was $H = 8.0$ mm; external lateral temperature got the value $T_{\text{ext}} = 20^\circ\text{deg. C}$, axial displacements for the point on internal lateral surface were $u_z^{\text{int}} = 0.1$ mm, uniform hermetization and work pressures were $p_{zz}^{\text{lat}} = 60.0$ MPa and $p_{zz}^{\text{appl}} = 30.0$ MPa consequently; elastic and thermo-physical properties of FG were $E = 0.51$ GPa, $\tilde{E} = 0.41$ GPa, $G = 0.21$ GPa, $\tilde{G} = 0.16$ GPa, $\nu = 0.03$, $\tilde{\nu} = 0.05$; $\lambda = 122.0$ W/(m·K) and $\tilde{\lambda} = 90.0$ W/(m·K), $\tilde{\lambda} = 87.0$ W/(m·K) and $\tilde{\lambda} = 70.0$ W/(m·K) for temperatures 300°deg. C and 550°deg. C consequently; $\alpha = 1.21 \cdot 10^{-6}$ K $^{-1}$, $\tilde{\alpha} = 2.77 \cdot 10^{-6}$ K $^{-1}$.

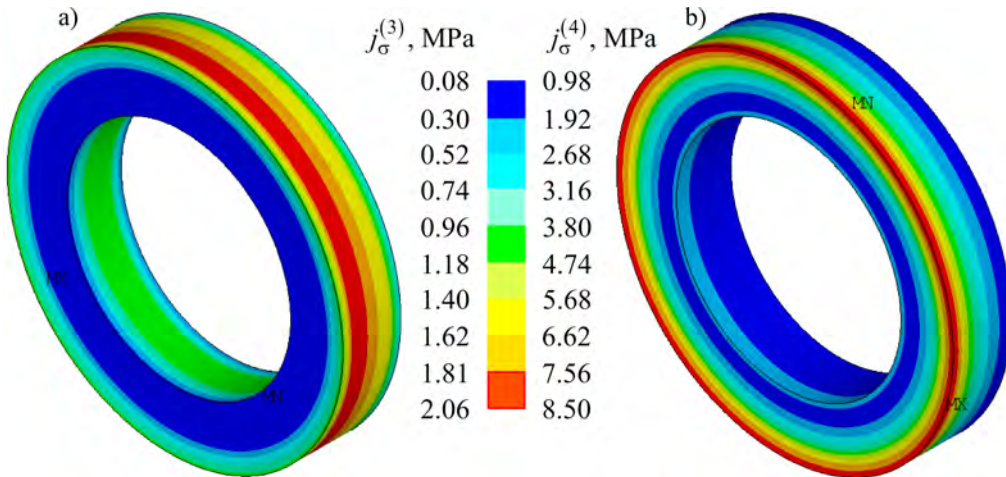


Fig. 1. Distribution of the third $j_\sigma^{(3)}$ (a) and the fourth $j_\sigma^{(4)}$ (b) invariants of stresses tensor for FG o-ring seal under reciprocating motion of the plunger in sealing bush direction. Internal temperature was $T_{\text{int}} = 550^\circ\text{deg. C}$.

The locations of damaged domains (i.e. red zones at Fig. 1) obtained from computational experiments correspond with the results of o-ring seals experience. That allows us to define an optimum hermetization pressure, justify recommendations to modify existing structures of o-ring seal packs and develop engineering techniques for refined strength analysis.

Acknowledgments

The authors acknowledge the support of the Ministry of Education and Science of the Russian Federation (project No 1911 within the context of the state assignment No 2014/152).

References

1. M.Yu. Belova, I.A. Malkova, T.M. Kuzinova, A.S. Kolishkin, O.Yu. Isaev (2006). The modified flexible graphite seals, *J. Russ. Sci. & Industr. Valve Manufact.*, **3**, 67–71 (in Russian).
2. M.Yu. Belova, O.Yu. Isaev, A.S. Rozovskiy, D.V. Smirnov (2006). The flexible graphite seals: safe application conditions in the environment of liquid and gaseous oxygen, *J. Russ. Sci. & Industr. Valve Manufact.*, **2**, 70–75 (in Russian).
3. A.P. Andreev, B.V. Burmistrov, A.K. Matushak, O.I. Fedorov, O.Yu. Isaev, M.Yu. Belova (2006). The first joint standard on the flexible graphite seals for valves, *J. Russ. Sci. & Industr. Valve Manufact.*, **6**, 50–55 (in Russian).

Poster Session

DYNAMIC MODEL AIRCRAFT ENGINE FROM THE SOLID TO MULTICOUPLING SYSTEM (ON EXPERIMENTAL STUDIES OF DYNAMIC COMPLIANCE ENGINE HOUSING)

V. Baklanov

Tupolev Design Bureau, Moscow, Russia

Rigid body model for the aircraft engine is widely used in aviation, for example in the calculation of aircraft flutter, design vibration isolating engine mounts on the classical theory of vibration isolation. But vibration sensors mounted on the engine mounts zones on the plane, fix not only different levels of vibration, but also significantly different spectrum of vibration.

Knowledge of real dynamic characteristics of the aircraft engine opens the way for assessing the interaction of natural frequencies and frequency engine disturbance impacts work flow engine.

A well-known impedance testing technique was used: for the determination of these characteristics the structures were excited by an electrodynamic shaker while the harmonic input force amplitude was constant and its frequency was varying automatically within the studied range 10...500 Hz [1].

The dynamic characteristics enabled us to make the dynamic model for an aviation gas-turbine engine more precise, especially in the rotor frequency range [2].

Modifications of frequency characteristics of engine's dynamic compliances are presented in Fig. 1.

The straight line in double-log scale (*x*-axis – frequency, *y*-axis – compliance) with slope factor 12 dB per an octave corresponds to the function $C(f) = 1/m(2\pi f)^2$, ($C(f)$ – dynamic compliance), which is a feature of a rigid body.

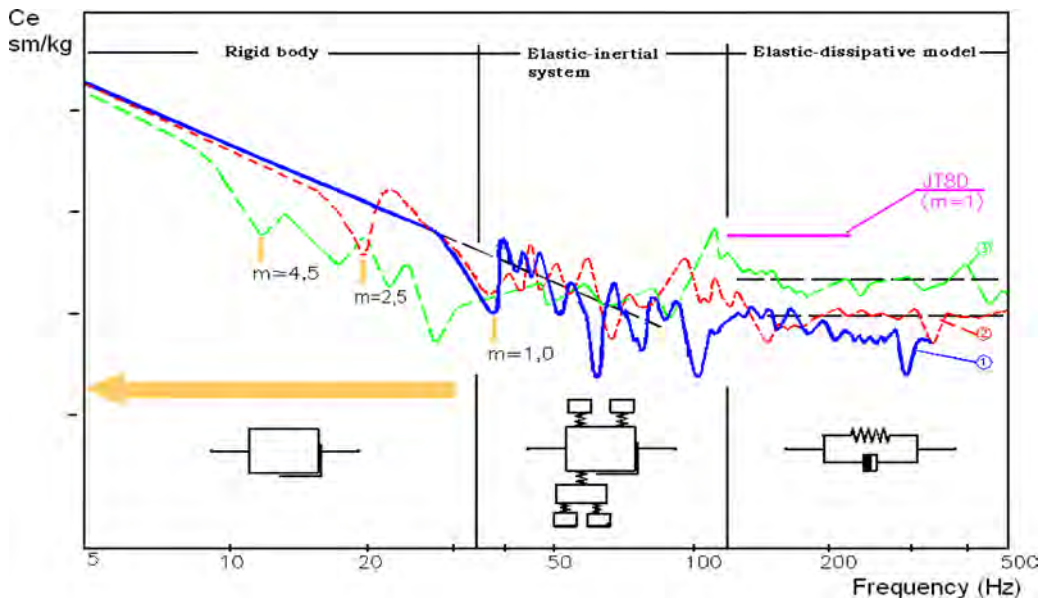


Fig. 1. Dynamic compliances of engine body at attachment points, 1 – $m = 1$; 2 – $m = 2.5$; 3 – $m = 4.5$.

The straight line parallel to x -axis is a feature of an elastic element, whereas the one with the slope of 6 dB per an octave belongs to an elastic-dissipative element.

Analysis of obtained data makes it possible to divide the frequency range of investigation into three sub-ranges characterized by certain dynamic behavior of the engine and consequently each of said ranges can be provided with its special mathematical model – simple and clear enough (Fig. 1).

Dynamic compliances of engine body at the attachment points has revealed that the body of engines with by-pass ratio (m) of 0.5...1.1 corresponds to the rigid body model for frequencies below 40 Hz, while for engines with by-pass ratio of 2.5...4.5 the upper boundary of the rigid body model behaviour is shifted to 20 Hz.

It has been found out that at frequencies between 20...40 Hz and 120 Hz the engine body behaves as an elastic-inertial system with a large number of resonances of various damping degrees.

Identification of these resonances (by comparison of results of various researches) allowed to connect them with own frequencies of a number of elements of the engine (rotors, a box of the drives, the separate units fixed on the case) [3].

Within the frequency range 120...500 Hz the engine body corresponds to the model of elastic – dissipative element. The case of engine JT8D also corresponds to this model at the indicated frequency range [4].

Thus, the study of dynamic characteristics of the engines showed that for aviation turbofan engine bypass ratio 2.5–5.0 rigid body model is valid up to 20 Hz.

The next 10–15 years we will have to deal with aircraft equipped with turbofan engines extra high by-pass ratio (8.5–12): GE9X, Leap-1B, Leap-1A, PD-14 and engine family type PW1000G.

Thus, a wide range of rotor speed engines (20–200 Hz) the dynamic behavior of the engine case corresponds to the model of elastic-inertial system or elastic-dissipative element with a significant difference from the idealized model of aircraft turbine engine as solid as largest unit of dynamic compliance and the nature of the dynamic behavior.

Dynamic engine model will significantly increase the accuracy of the analysis of structural failure of the aircraft engine in his typical complex loading conditions: high static load under dynamic loads in a wide range of frequencies.

References

1. V.K. Agafonov, V.S. Baklanov, V.M. Vul, V.I. Popkov, A.V. Popov (1990). The Investigation of Dynamic and Vibroacoustic Characteristics of Aircraft and an Engine by Calibration Test Methods, in: *VII Aero-acoustic Conference*, TsAGI, Moscow, 141–144.
2. V.S. Baklanov (2002). Dynamic model of Engine-Mount-Airframe System of Trunk-Aircraft Basing on Results of Impedance Data Tests at Attachment Points, *Ninth Int. Congress on Sound and Vibration*, Orlando, Florida, USA.
3. V.S. Baklanov (2002). Identification of Engine-Attachment-Airframe System Model Basing on Impedance Test Results, *Proceedings of International Conference on Structural Dynamics Modeling*, Madeira Island, Portugal.
4. S. Rubin, F.A. Biehl (1967). Mechanical Impedance Approach to Engine Vibration Transmission into an Aircraft Fuselage, *Aeronautic and Space Engineering and Manufacturing Meeting*, SAE Paper No 670873.

THE ROLE OF MICROSTRUCTURE IN DEFORMATION MECHANISMS IN EXTRUDED AZ31 MAGNESIUM ALLOY

P. Drzymała¹, J. Bonarski¹, Z. Ranachowski²

¹Institute of Metallurgy and Materials Science, PAN, Cracow, Poland

²Institute of Fundamental Technological Research, PAN, Warsaw, Poland

1. Introduction

Contemporary trends in vehicle and airplane designing place great emphasis on the reduction of the weight. This contributes to energy saving and to reduction of their negative environmental impact. One of the methods of weight reduction is use of magnesium alloys. Magnesium is the lightest structural element with desirable mechanical properties and its use is environment-friendly. However, due to hexagonal close-packed crystal structure, resulting in insufficient independent number of slip systems, magnesium alloys exhibit poor formability at ambient temperature.

2. The microstructure of Mg-AZ31 alloy

Conventional methods of hot extrusion of results in formation of inhomogeneous microstructure consisting of α -Mg matrixes and fine particles identified as Al-Mn phase with presence of inclusions and pores. The grain size and shape is remarkably diversified. Typically elongated coarse grains are surrounded by much smaller equiaxed recrystallized grains (Fig. 1 left). Such microstructure is not beneficial for plastic properties of magnesium alloys. The elongated coarse grains have base planes mostly parallel to the direction of extrusion so their rotation due to base slip at room temperature is very limited. These grains undergo contraction or tensile twinning depending on applied strain tensor. The result of this process is that many twinning boundaries are formed inside elongated grains and they are recognized as spots of crack initiation during cold deformation [1].

Hot extruded rods typically have strong fiber texture with base planes and $\langle 01-10 \rangle$ direction lying parallel to the extrusion direction. Such texture formation is ascribed to preference of base slip even at high temperatures due to large difference in critical resolved shear stress (CRSS) between the base slip and non-base slips [2]. Strong texture decreases the ability of Mg-AZ31 alloy extrusions to deform at room temperature, because again base slip is the main deformation mode. But the effect of deformation twinning in coarse grains enables some strain until twin saturation. It has been observed that almost whole initial grains can be consumed by following generations of twins [3].

We discuss the possibility of enhancing plasticity of magnesium alloys by proper modification of microstructure. The application of new method of hot extrusion prevents formation of coarse elongated grains having a detrimental effect on the Mg-AZ31 alloy plasticity. Grain refinement can also support activation of additional prismatic slip, which has relatively low CRSS, due to stress concentration at grain boundary [2].

In the paper the results of investigations of ductile Mg-AZ31 alloy are presented. The rod extrusions, favorably oriented for $\{10-12\}$ $\langle 10-11 \rangle$ twinning were tested in compression to various extent. Analysis of grain orientation, twinning saturation and crystallographic texture supports description of the microstructure changes. An acoustic emission (AE) technique was also used in this approach to detect the moment of twinning or slip activation during compression tests (Fig. 2). The comparison of AE diagrams with

orientation image maps shows correlation between microstructure changes and AE peak occurrence. The effect of texture and grain size on twinning and deformation mechanisms was considered.

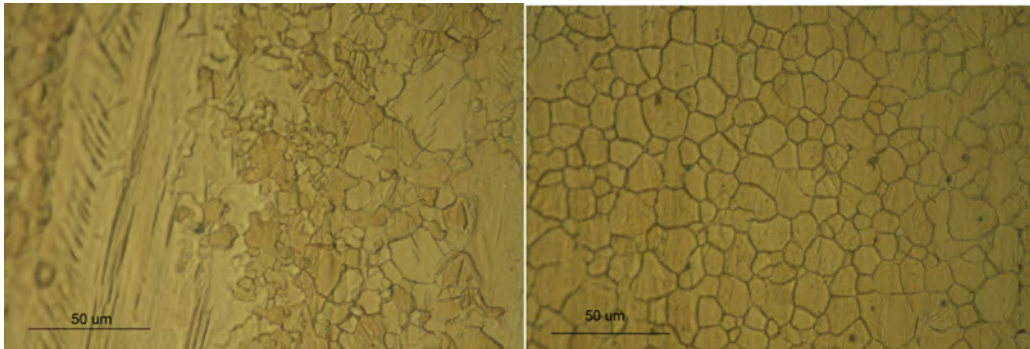


Fig. 1. Microstructures of conventionally hot extruded Mg-AZ31 alloy with elongated coarse grains (left) and refined hot extruded with equiaxed grains (right).

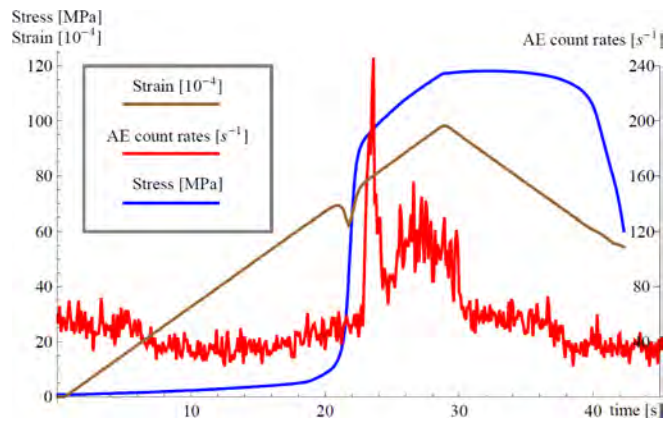


Fig. 2. Stress-strain curve, AE count rates and strain in interrupted compression test for Mg-AZ31 alloy at room temperature and strain rate of 0.00035 1/s.

References

1. L. Lu, T. Liu, Y. Chen, Z. Wang (2012). Deformation and fracture behavior of hot extruded Mg alloys AZ31, *Mater. Charact.*, **67**, 93–100.
2. Y. Chino, K. Kimura, M. Mabuchi (2008). Twinning behavior and deformation mechanisms of extruded AZ31 Mg alloy, *Mater. Sci. Eng.*, **A 486**, 481–488.
3. S. Mu, J.J. Jonas, G. Gottstein (2012). Variant selection of primary, secondary and tertiary twins in a deformed Mg alloy, *Acta Mater.*, **60**, 2043–2053.

WETTING-BONDING RELATIONSHIP IN LEAD-FREE SOLDER JOINTS FOR HIGH TEMPERATURE APPLICATIONS

A. Klasik¹, K. Pietrzak¹, N. Sobczak^{1,2}, K. Makowska¹, D. Rudnik¹

¹Motor Transport Institute, Warsaw, Poland

²Foundry Research Institute, Cracow, Poland

1. Introduction

In response to serious health and environmental safety problems related to the use of lead, the regulatory actions have been taken in many countries to eliminate this element from solder materials for electronic devices [1]. Up till now, various solder alloys have been proposed as potential Pb-free solders and in consequence the most efforts have been oriented on the alloy families of Sn–Ag, Sn–Ag–Cu and Sn–Cu. Unfortunately, these alloys are characterized by the higher melting temperature than Sn–Pb alloy used till now in conventional joints [2]. Moreover, higher soldering temperature may lead to the damage of electronic components. Therefore, Sn–Zn solders have been highly recommended as a substitute for eutectic Sn–Pb solder due to their low melting point, excellent mechanical properties and low cost [3]. The shear resistance is one of the mechanical properties that have to be taken into account in producing joints based on Sn–Zn solders. Consequently, many aspects of this behaviour are still under discussion and several examples of such analyses are quoted in [4–7]. This research is focused on the analysis of the effect of alloying addition of Cu, Ag, and Zn to Sn, on the solder wetting properties and their influence on the shear resistance of solder joints with Cu as candidates for Pb-free high temperature applications.

2. Experimental procedures

The model solder/substrate couples were produced with Pb-free alloys of Sn–Zn and Sn–Zn–X systems as follows: binary alloys: SnZn4.5, SnZn9, SnZn13.5, ternary alloys: SnZn4.5Cu1, SnZn9Cu1, SnZn13.5Cu1, SnZn4.5Ag1, SnZn9Ag1, SnZn13.5Ag1. Then the joints with Cu substrate were subjected to research on: their wettability, shear-strength and the microstructure characteristics, especially in the interfacial area. Wetting properties of binary Sn–Zn (Zn = 0–13 wt.%) and ternary Sn–Zn–X alloys (where X – alloying

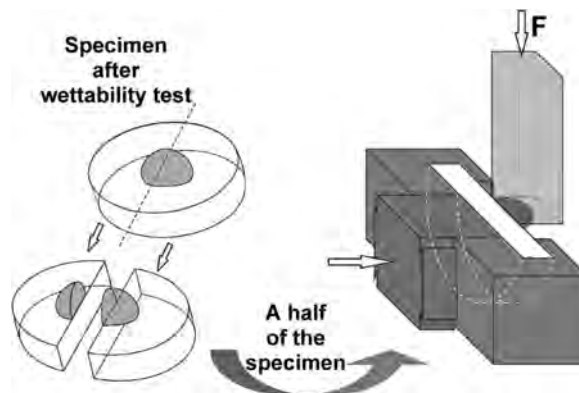


Fig. 1. Scheme showing push-off shear test of a solder/substrate couple.

additions of Cu or Ag) were characterized by measurements of contact angle (θ) values using a sessile drop method at a temperature of 230°C for 5 min contact time. After the wettability tests, a half of each solidified sessile drop specimen of Sn–Zn/Cu and Sn–Zn–X/Cu couples was subjected to shear strength measurement by improved push-off shear test (Fig. 1). The shear tests were performed by means of specific appliances adapted for INSTRON machine.

3. Results

The results of wettability assessment and shear tests are summarized in Table 1.

Table 1. Contact angle and shear strength values of different solder/Cu couples produced with binary and ternary Pb-free alloys.

Alloy/substrate	θ [deg]	τ_{\max} [MPa]	Alloy/substrate	θ [deg]	τ_{\max} [MPa]
SnZn4.5/Cu	52	45.5	SnZn9Ag1/Cu	80	51.4
SnZn4.5Cu1/Cu	56	43.0	SnZn13.5/Cu	60	33.9
SnZn4.5Ag1/Cu	62	41.1	SnZn13.5Cu1/Cu	70	43.9
SnZn9/Cu	68	32.4	SnZn13.5Ag1/Cu	88	55.8
SnZn9Cu1/Cu	75	45.7			

4. Concluding remarks

For binary Sn–Zn alloys, the lowest shear strength value of the solder/Cu couples was obtained with the alloys containing higher amount of zinc (9.0% and 13.5%) because of increase in relatively coarse needle-like Zn-rich precipitates observed near Cu_5Zn_8 interfacial layer.

For ternary Sn–Zn–Cu alloys containing the same amount of 1 wt.% Cu, the shear strength of the solder/Cu couples remains at the similar level, independently of Zn content in the solder. This fact is related to the addition of Cu to the solder resulting in the formation of Cu_5Zn_8 (mainly globular) precipitates close to Cu_5Zn_8 interfacial layer, instead of needle-like Zn-rich precipitates.

The most remarkable effect of shear strength improvement was observed with Sn–Zn–Ag ternary alloys containing 1 wt.% Ag. The shear strength of solder/Cu couples increases with the increase of Zn content because of the formation of AgZn_3 precipitates of small sizes and more beneficial spherical morphology.

Acknowledgments

The research was carried out in frame of the EU COST ACTION MP0602 with financial support from the Ministry of Science and Higher Education of Poland.

References

1. K.J. Puttlitz, K.A. Stalter (2004). *Handbook of Lead-Free Solder Technology for Microelectronic Assemblies*, New York Basel.
2. L. Zhang, S. Xue, G. Li et al. (2010). Development of Sn–Zn lead-free solders bearing alloying elements, *J. Mater. Sci: Mater. Electron.*, **21**, 1, 1–15.
3. M. McCormack, S. Jin, G.W. Kammlott (1995). The design of new, Pb free solder alloys with improved properties, *IEEE Int. Symp. Electron. Environ.*, 171–176.
4. J.W. Yoon, S.B. Seung-Boo Jung (2006). Reliability studies of Sn–9Zn/Cu solder joints with aging treatment, *J. Alloy Compd.*, **407**, 141–149.
5. A. Sharif, Y.C. Chan (2006). Effect of reaction time on mechanical strength of the interface formed between the Sn–Zn(–Bi) solder and the Au/Ni/Cu bond pad, *JEM*, **35**, 10, 1812–1817.
6. T. Takahashi, S. Komatsu, H. Nishikawa, T. Takemoto (2010). Improvement of High-Temperature Performance of Zn–Sn Solder Joint, *JEM*, **39**, 8, 1241–1247.
7. J.W. Yoon, S.B. Jung (2006). Interfacial reactions and shear strength on Cu and electrolytic Au/Ni metallization with Sn–Zn solder, *Journal of Materials Research*, **21**, 1590–1599.

PRISMATIC BEAMS MADE OF SHELLSTONE UNDER THREE-POINT BENDING: IMPLICATIONS DUE TO THE TRANSVERSE ISOTROPY

S.K. Kourkoulis¹, G.E. Exadaktylos²

¹National Technical University of Athens, Dept. of Mechanics, 157 73 Athens, Greece

²Technical University of Crete, Dept. of Mineral Resources Engng, 731 00 Chania, Greece

1. Introduction

The problem of a simply supported prismatic beam under a central force (Fig. 1) concerns engineering community already from the end of 19th century. For isotropic materials a solution was first obtained by Stokes [1] and it was improved by Boussinesq, Filon, Lamb and Seewald [1]. On the contrary a concise theory in case of even the simplest anisotropy is not available. In this context a theory is here developed, based on Reissner's [2] work, for a special class of transversely isotropic rocks.

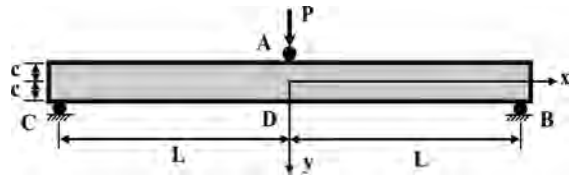


Fig. 1. The configuration of the problem.

Following Reissner [2] equilibrium is written as:

2. Theoretical considerations

A transversely isotropic slender beam is subjected to 3PB. Consider that plane stress conditions prevail and denote by σ_{xx} and σ_{yy} the normal stress components along x - and y -axes, by $\sigma_{xy} = \sigma_{yx}$ the shear stress components and by u, v the displacements.

$$(1) \quad \frac{\partial \sigma_{xx}}{\partial x} + \frac{\partial \sigma_{xy}}{\partial y} = 0, \quad \frac{\partial \sigma_{xy}}{\partial x} + \frac{\partial \sigma_{yy}}{\partial y} = 0.$$

It is further assumed that the moduli of elasticity and Poisson's ratios E_x, E_y, ν_x, ν_y , of the material are mutually related (due to the existence of a strain energy function) through the equation:

$$(2) \quad E_x \nu_y = E_y \nu_x,$$

From this point the study is restricted to transversely isotropic materials with elasticity modulus normally to the isotropy plane negligibly small, i.e. $E_y \rightarrow 0$. Then from Eq. (2) it is concluded that ν_y tends also to zero, and the non-vanishing independent constants, necessary for the mechanical description of the material are three, i.e. E_x, ν_x and G . Combination of Hooke's law with Eq. (1) yields:

$$(3) \quad E_x \frac{\partial u}{\partial x} = \sigma_{xx} - \nu_x \sigma_{yy}, \quad \sigma_{yy} = 0, \quad G \left(\frac{\partial u}{\partial y} + \frac{\partial v}{\partial x} \right) = \sigma_{xy}.$$

According to Reissner [2] the condition $\sigma_{yy} = 0$ follows from Hooke's law as a natural consequence, otherwise a finite normal stress along the y -axis would cause infinite normal strain in the y -direction.

In practice, however, no material exists with $E_y = 0$ and the theory developed here is to be considered as a limiting case for materials with $E_y/E_x \rightarrow 0$. In this simplified case,

Eqs. (1), (2) yield the following expressions for the non-vanishing stress components, σ_{xx} , σ_{xy} and the displacements u , v :

$$(4) \quad \begin{aligned} \sigma_{xy} &= f(y), & \sigma_{xx} &= -xf'(y) + g(y), \\ u &= \frac{1}{E_x} \left[-\frac{x^2}{2}f'(y) + xg(y) + h(y) \right], \\ v &= \frac{1}{E_x} \left[\frac{x^3}{6}f''(y) - \frac{x^2}{2}g'(y) + \frac{E_x}{G}xf(y) + k(y) \right] \end{aligned}$$

where f , g , h , k are arbitrary functions. Using the boundary conditions along lines $x = \text{const}$ one obtains the equations for the determination of the four functions f , g , h , k . Using then the conditions along the lines $y = \text{const}$ one obtains the equations for the determination of the constants in the solutions of the boundary differential equations. After lengthy algebra it is obtained for the stress components:

$$(5) \quad \sigma_{xx} = -\frac{2xCGe^{-\alpha c}\alpha \sinh(\alpha c)}{L(1 + e^{-2\alpha c})}, \quad \sigma_{xy} = -\frac{CG}{L} + \frac{2CGe^{-\alpha c} \cosh(\alpha y)}{L(1 + e^{-2\alpha c})}$$

with $C_1e^{\alpha c} + C_2e^{-\alpha c} = \frac{CG}{L}$, $C_1e^{-\alpha c} + C_2e^{\alpha c} = \frac{CG}{L}$ and $C_1 = C_2 = \frac{CGe^{-\alpha c}}{L(e^{-2\alpha c} + 1)}$. Constant C is determined by equating the externally applied load P with the force developed by the action of the stress σ_{xy} as:

$$(6) \quad C = \frac{PL\alpha}{2be^{-\alpha c}} [-Gc\alpha e^{\alpha c} + C'_1L(e^{2\alpha c} - 1)], \quad \text{with} \quad C'_1 = \frac{C_1}{C} = \frac{Ge^{-\alpha c}}{L(e^{-2\alpha c} + 1)}.$$

Applying this solution for a fictitious material with $E_x = 10$ GPa, $E_y/E_x = 10^{-3}$, $\nu_x = 0.30$ and $G = 5$ GPa, the ratio β_σ of the maximum stress, according to the present approach, over that of Bernoulli-Euler's solution is plotted in Fig. 2, vs. the L/c ratio. It is seen that the present solution tends to the classical one only for L/c ratios exceeding 5. It is also noticed that the longitudinal stress at the central section according to the transversely isotropic analysis systematically exceed that of the classical solution.

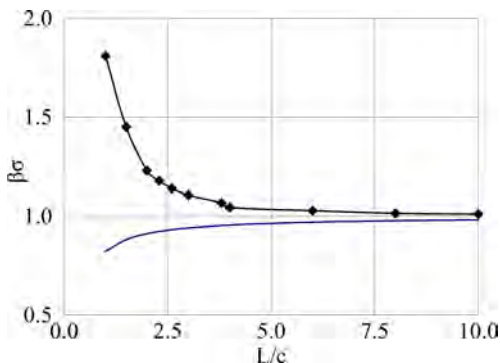


Fig. 2. Normalized maximum stress over the L/c ratio.



Fig. 3. Conchyliates shellstone.

3. Experimental study

Prismatic beams were prepared from the building stone (Fig. 3) used by ancient Greeks for the erection of the Zeus Temple at Olympia, a soft shellstone called conchyliates. The specimens were cut parallel to the material layers and their longitudinal axis was oriented parallel to them, while the y -axis (Fig. 1) was normal to them, resulting to $E_x/E_y \cong 50$. The strains were measured using electrical strain gauges. Three L/c ratios were tested. In Table 1 the axial stresses, σ_{xx} , are shown together with the respective predictions of

Table 1. Reduced axial stress, σ_{xx} , at the mid-point of the lowest fiber.

L/c	2	4	6
Theoretical analysis	1.23	1.05	1.03
Experimental results	1.67	1.23	1.17

the theoretical analyses. The values are normalized over the ones corresponding to the Bernoulli-Euler theory. For the transverse stress, σ_{yy} , the values obtained varied between 1/50 and 1/70 of the respective axial one, validating the assumption $\sigma_{yy} \rightarrow 0$ adopted in the theoretical analysis.

4. Conclusions

The predictions of the theory introduced are in good agreement with experimental evidence, although systematically lower. The discrepancies increase for low L/c ratios indicating the importance of the punch effect, which is not taken into account by the theoretical analysis. The assumption $E_y \rightarrow 0$ is not absolutely true for the stone tested, introducing additional discrepancies, although the transverse stress measured do tend to zero.

Acknowledgments

This research has been co-financed by the European Social Fund (ESF) and Greek national funds through the THALES-MIS380147 Program.

References

1. S.P. Timoshenko (1953). *History of Strength of Materials*, Mc Graw Hill Inc., New York.
2. E. Reissner (1949). A Contribution to the Theory of Elasticity of Non-Isotropic Materials (with Applications to Problems of Bending and Torsion, *Philosophical Magazine*, **30**, 418–429.

A VALIDATED NUMERICAL MODEL FOR THE RESPONSE OF TYPICAL PARTHENON EPISTYLES' CONNECTIONS UNDER PURE SHEAR

S.K. Kourkoulis, E.D. Pasiou

National Technical University of Athens, Department of Mechanics, Laboratory of Testing and Materials
Theocarlis Building, Zografou Campus, 15773, Athens, Greece

1. Introduction

The epistyles of the Parthenon Temple in Greece are interconnected by means of “T”-shaped metallic connectors which are placed in grooves of appropriate shape. Then the grooves are filled with a suitable material. Ancient Greeks used steel connectors and molten lead as filling material while today, during the restoration project, connectors made of titanium substitute the authentic destroyed ones and the groove is filled with mortar. Although no one could question the use of titanium concerning its great resistance to corrosion, there are some objections concerning its strength. More specific it seems that it is stronger than it should be in order to protect the marble volume in case of excessive pure shear. In this context, a numerical analysis is carried out aiming to the determination of the optimum combination of mechanical characteristics of the materials constituting the connection. The problem is confronted exclusively from the mechanical point of view.

2. The numerical analysis

The geometry of the numerical models constructed matches exactly the connection of two epistyles of the Parthenon Temple under a 2:3 scale. They consist of two identical marble blocks simulating the epistyles, one “T”-shaped connector and filling material (Fig. 1a). Four cases were studied: (i) The restored connection-TMM (Titanium-Mortar-Marble), (ii) The ancient connection-SLM (Steel-molten Lead-Marble), (iii) A hypothetical one-GLM (Gold connector ($\sigma_y = 75$ MPa) – Lead-Marble) and (iv) A hypothetical one-GLM-30 (Gold connector ($\sigma_y = 30$ MPa) – Lead-Marble). The three material interfaces characterizing the sequence of the materials (Fig. 1b) and the contact between the epistyles were modeled using contact elements. In all cases, the linear elastic model was adopted for marble while the other materials were simulated with multi-linear constitutive laws.

Pure shear was achieved by: (i) Keeping fixed the nodes of the upper surface of the left epistyle, (ii) Restricting the “opening” of the epistyles along the x -axis and (iii) Applying a vertical upwards displacement on the upper surface of the right epistyle (Fig. 1a). In order to adjust the element size for the meshed volumes a series of preliminary analyses were carried out checking the von Mises stress developed along a characteristic path. The meshes finally chosen are shown in Figs. 1a, c.

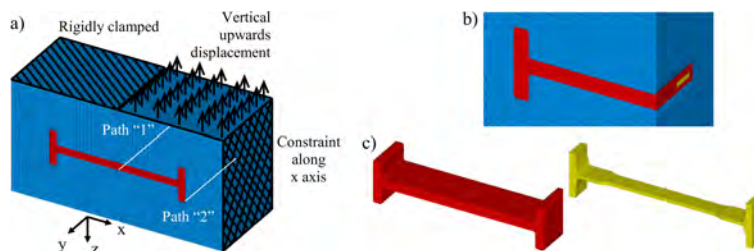


Fig. 1. a) A typical numerical model; b) The sequence of the three materials; c) The meshed volumes of the connector and the filling material.

The reference model, TMM, was validated based on the force-displacement curve obtained in the respective experimental study [1]. Although the geometry of the specimen's part on which the load is imposed is slightly different this does not affect the overall response of the system. This is clearly seen in Fig. 2a and it was to be expected since the specimen's most stressed areas are located around the groove (Fig. 2b) and are not influenced by the moving volume's detailed geometry.

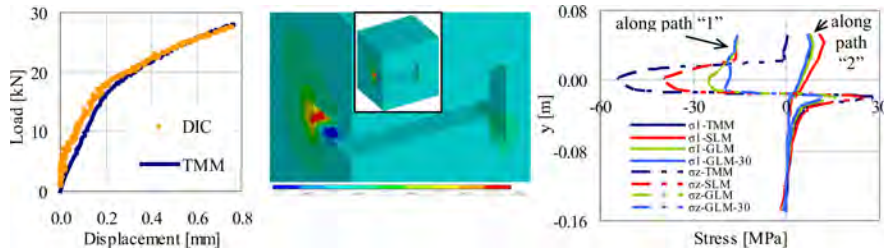


Fig. 2. a) Validation of the reference model; b) The distribution of the maximum principal stress in the right marble volume [Pa]; c) The variation of the stress components in marble along paths “1” and “2”.

3. Results

Keeping the displacement induced constant it was concluded that the titanium connector remains in its elastic region while the other three materials (steel and the two types of gold) yield. The filling material (ductile lead or brittle mortar) seems to strongly affect the stress distribution along path “1” (Fig. 1a) as it is seen in Fig. 2c, where the σ_z stress component (along the loading axis) is plotted. Lead distributes more uniformly the stresses developed in marble along the groove's depth (especially in case of gold with $\sigma_y = 30$ MPa) in contrast to mortar which leads to stresses localized only along the connector's height. On the other hand, concerning the stress field around the groove's flange (path “2” in Fig. 1a), the SLM connection seems to be the worst among the ones studied. The maximum principal stress developed in the epistyle of the SLM model is almost 60% higher compared to the one developed when gold with yield stress equal to 30 MPa is used (Fig. 2c).

4. Conclusions

According to a detailed inspection [2] of all in-situ epistyles (the ones that were never removed from their initial position) of the Parthenon Temple, fractures are located around the grooves' flanges. Therefore path “2” is proved to be the critical one. Taking into account the relatively low tensile strength of Dionysos marble (about 8 MPa) [3], it can be said that both titanium and gold are more “friendly” to marble in the critical region (path “2”). On the contrary the higher stress values developed along path “1” in case of titanium connector ($\sim 200\%$ higher than the respective stress in GLM-30) indicate superiority of gold, ignoring of course additional factors like cost per unit weight.

Acknowledgments

This research has been co-financed by the European Union (European Social Fund-ESF) and Greek national funds through the Operational Program “Education and Lifelong Learning” of the National Strategic Reference Framework (NSRF) – Research Funding Program: THALES: Reinforcement of the interdisciplinary and/or inter-institutional research and innovation.

References

1. S.K. Kourkoulis *et al.* (2014). An experimental study of the mechanical response of a typical epistyles' connection under pure shear, *SolMech 2014*, September 1-5, Zakopane, Poland.
2. M. Mentzini (2006). Structural Interventions on the Acropolis Monuments, *The Acropolis Restoration News*, **6**, 15–18.
3. I. Vardoulakis, S.K. Kourkoulis (1997). *Mechanical properties of Dionysos marble*, Final report of the Environment Project EV5V-CT93-0300: Monuments Under Seismic Action, NTUA, Greece.

FORMULATION OF THE SPECTRAL DIRECT METHOD FOR CYCLE COUNTING OF BIMODAL MULTIAXIAL STRESS

M.S. Kozień, D. Smolarski

Cracow University of Technology, Cracow, Poland

1. Introduction

The response of engineering structures on external excitations, are often the multi-modal type. It means, that in spectrum of the response can be identified a few important frequencies. Let us assume, as in [1, 2, 4, 7], that the considered stress responses have the bimodal character. Moreover let us assume that for identified stress responses have a multiaxial type.

The well known in literature methods which can be applied to analyze of the non-harmonic stress functions are connected with the two attempts:

- counting of the cycles based of the especially defined procedure, among them the most popular is the rain-flow one [3] (formulation in time domain),
- application of the power spectra density function [2, 4, 6, 7] (formulation in frequency domain).

In the analysis of dynamics of structures, the frequency analysis based on the FFT and STFT procedures applied directly to the functions defined in time domain are commonly used.

The authors propose leading the cycle counting procedure base on the information which can be get from the spectrum of the stress functions, each of stress components. The analysis is reduced to the case of bimodal spectrum with no taking into account the phase shift.

2. Theoretical background of the method

The proposed method, which basis are presented in [5], is based on the fundamental assumption about existency of the major cycle and the secondary ones. The secondary ones are described by non-zeroes and variable with time the mean values, as it is described for simpler cases in [3].

The basic ideas of the proposed method, which can be applied for multiaxial stress cases can be described by the following steps:

- For a given stress components functions, variable with respect to time, the amplitudes and phase spectrums are determined. Let us assume, that in spectrum the two frequencies f_1 and f_2 ($f_1 < f_2$) are identified. These components are moreover described by periods T_1 and T_2 , amplitudes A_1 and A_2 and phases ϕ_1 and ϕ_2 . In the discussed attempt, the phase shift are not taken into account. But the proposed algorithm allow to take them into account in easy way if it is necessary.
- Period of the major cycle T_1 is the basic period of the stress sequence.
- The main stress cycle, existing one in the sequence, has the amplitude of stress equal to $A_1 + A_2$ for each stress components, and if there is no other reasons (as e.g. the constant non-zeroes component in FFT spectrum, existences of static thermal stress) the mean values equal to zero. It is the base to obtain the equivalent amplitude of stress, e.g. by application of the Huber-Mises-Hencky (von Mises) formula [3] and

them to obtain the equivalent stress for completely reversed cycle, e.g. of the Morrow type [3].

- The secondary cycles have the variable in time amplitudes, depend on the value of A_2 and on influence of the major cycle form with frequency f_1 and variable mean value depends on the major cycle frequency f_1 too for each components of stress tensor. The obtained values are base to obtain the equivalent amplitude of stress, e.g. by application of the Huber-Mises-Hencky (von Mises) formula [3], equivalent mean value of stress, e.g. in the form of Sines stress [3] and them to obtain the equivalent stress for completely reversed cycle e.g of Morrow type [3]. The number of identified cycles can be not integer.
- The obtained data, describe the identified stress cycles for given sequence, are the attempt to further fatigue analysis with application of the chosen hypothesis of cycle cumulation, e.g. the Palmgren-Miner one [3].

3. Final remarks

The presented method is an alternate attempt to the cycle counting problem for the bimodal stress cycles. The application of the method will be presented during the Conference for the realistic structure. The formulation allow to its expand for the case of damped structural response e.g. just after series of pulse type excitation of the structure.

References

1. D. Benasciutti, R. Tovo (2007). On fatigue damage assessment in bimodal random process, *Int. J. Fatigue.*, **29**, 232–244.
2. C. Braccisi, F. Cianetti, G. Lori, D. Pioli (2005). Fatigue behaviour analysis of mechanical component subject to random bimodal stress proces: frequency domain approach, *Int. J. Fatigue.*, **27**, 335–345.
3. N.E. Dowling (1993). *Mechanical behaviour of materials. Engineering methods for deformations, fracture and fatigue*, Prentice-Hall International Editors Inc., Englewood Cliffs.
4. T.-T. Fu, D. Cebon (2000). Predicting fatigue lifes for bi-modal stress spectral density, *Int. J. Fatigue.*, **22**, 11–21.
5. M.S. Kozieln, D. Smolarski (2007). Analytical simulation of application of FFT based spectral method of fatigue cycle counting for multiaxial stress on example of pulse excited beam, *Engineering Mechanics*, **19**, 5, 1–7.
6. A. Nieslony, E. Macha (2007). *Spectral method in multiaxial random fatigue*, Springer, Berlin-Heidelberg.
7. S. Sakai, H. Okamura (1995). On the distribution of rainflow range for Gaussian random proces with bimodal PSD, *JSME International Journal, Serie A*, **38**, 440–445.

ASSESSMENT OF DAMAGE DEVELOPMENT DUE TO FATIGUE OF 2017 ALUMINUM ALLOY ON THE BASIS OF CONDUCTIVITY MEASUREMENTS

D. Kukla, P. Grzywna, Z. L. Kowalewski

Institute of Fundamental Technological Research, Warsaw, Poland

1. Introduction

The study concerns experimental capability of conductivity measurements application for damage development analysis of the 2017 aluminum alloy subjected to various fatigue loading conditions. It is well known that a process of degradation due to fatigue is developing locally around structural notches, where stress concentration may lead to crack initiation before the fracture of a specimen will occur. Such a structural degradation enforces a local changes of conductivity, which allow to indicate a damage initiation place and monitoring of the dominant crack growth.

2. Material and research methodology

The tests were performed on specimens of the 2017 aluminum alloy cut from sheets of thickness equal to 1, 2, and 3 mm. Figure 1 shows the geometry of specimen and places of conductivity measurements during fatigue tests.

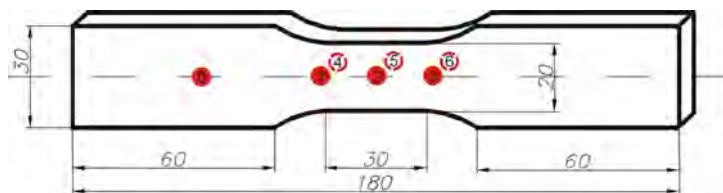


Fig. 1. Specimen geometry and conductivity measurement points.

The measurement points were located on both sides of specimen gauge length (points 1, 3, 4, 6) as well as on its gripping part as a reference point (0). Additionally, another two points were selected in the points (2, 5) where the highest stress concentration was expected.

The geometry and size of the specimen enable the conductivity measurements to be done using the manual Ferster device (Fig. 2a). During fatigue tests the specimens were

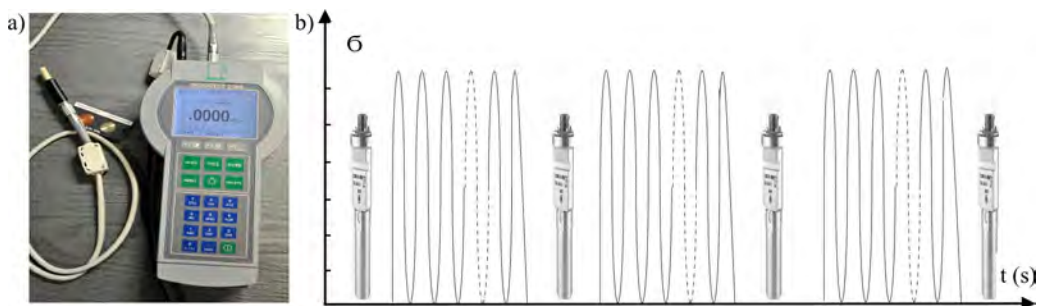


Fig. 2. Sigmatrust 2.069 equipment (a), and a scheme of the loading programme (b).

subjected to cyclic tensile stress using the MTS 810 servo-hydraulic testing machine. Each test was stopped after selected number of cycles, and subsequently the conductivity measurements were carried out on the unloaded specimen, Fig. 2b.

Deformation changes during subsequent cycles of the fatigue test were monitored using the MTS axial extensometer. Tests were carried out up to a dynamic increase of specimen deformation indicating an initiation of the dominant crack and its fast growth.

3. Results

The conductivity variations versus number of cycles are presented in Fig. 3 for all points selected on the specimens for measurements. For three specimens of different thickness one can see local reduction of the conductivity on both specimen sides.

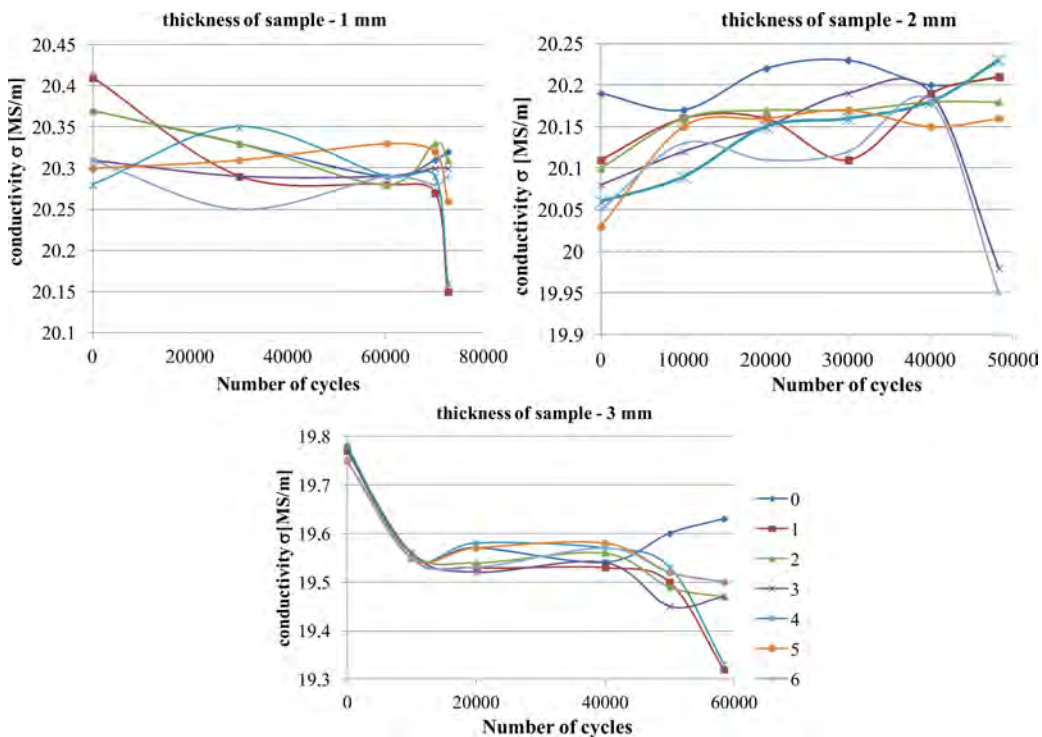


Fig. 3. Changes of conductivity of aluminum alloy for three specimens of different thickness.

A decrease of the conductivity in the final stage of fatigue test is clearly visible, Fig 3. It was located at that point, where the cumulative fatigue damage was most advanced. It has been found for all tested specimens that the measuring point corresponding the conductivity decrease in subsequent cycles represents the point where specimen fracture was obtained. This enables to conclude that the conductivity measurements may be promising technique for fatigue damage analysis, especially for an identification of areas where the dominant crack propagation takes place.

References

1. Kukla D., Grzywna P., Zagórski A. (2012). Development evaluation fatigue degradation of P91 steel on the basis of changes in the phase angle of the Eddy current signal, *Welding Technology Review*, 13, 8–11.
2. Kukla D., Szlagowska-Spychalska J., Grzywna P., Zagórski A. (2013). Identification of fatigue damage in 2017 aluminum alloy based on conductivity measurements, *Welding Technology Review*, 12, 88–91.

INNOVATIVE MICRO WELDING TECHNOLOGIES

P. Kulak¹, J. Piwnik², T. Węgrzyn³, D. Sieteski³, Ł. Wszolek⁴

¹LaserTec Sp. z o.o.

²Białystok University of Technology

³Silesian University of Technology

⁴Diagno-Test Sp. z o.o.

1. Introduction

In thin steel structure the best mechanical properties of weld correspond with acicular ferrite (AF) amount. Amount of acicular ferrite (AF) is treated as the most beneficial phase in steel WMD [1–5]. Laser and micro-jet technology give chance to obtain artificially high amount of AF in weld that corresponds with good impact toughness of weld [1–5]. In this paper there is presented comparison of laser welding with innovative welding method with micro-jet. Weld metal deposit (WMD) was prepared by welding with two methods: dioxide laser with a max output of 5 kW in the continues wave mode and micro-jet cooling after MIG welding.

Both CO₂ laser beam welding and welding with micro-jet injector are regarded as high energy density and low heat input process. In both methods there is observed narrow heat affected zone and high amount of acicular ferrite (AF) in weld. Laser welding involves such main parameters as: power, welding speed, defocusing distance, type of shielding gas. Parameters of micro-jet injector are varied by: cooling steam diameter, number of jets in injector micro-jet gas pressure and also type of shielding gas. Optimal parameters of both processes for thin structure welding was mainly compared in terms of oxygen in WMD and metallographic structure.

2. Experimental procedure

One type of low alloy S355J2G3 steel was used in both welding methods. The thickness always was 1 mm of upper sheet and 2 mm of lower sheet in all tested cases. Butt weld joints were made using firstly a carbon dioxide laser capable of producing max output of 5 kW in the continues wave mode. The main laser parameters are summarized in Table 1. Parameters of micro-jet injector are presented in Table 2. Argon was chosen for shielding gas in both cases.

Table 1. Laser welding parameters.

Power, kW	Speed, m/min	Heat input, kJ/mm	Defocusing, mm	Flow rate, l/min
3	1.2	0.4	2	15

Table 2. Parameters of welding process with micro-jet cooling.

Micro-jet cooling gas	Gas pressure	Diameter of jet	Number of jet
Ar	0.4 MPa	40 μm	1

Thus weld metal deposit was prepared by welding with two methods: MIG welding with micro-jet cooling and laser welding.

3. Results and discussion

There were tested and compared various welds of standard laser welding and MIG welding with innovative micro-jet cooling technology. A typical weld metal deposit had similar chemical composition in all tested cases. Both laser and micro-jet gas could have only influence on more or less intensively cooling conditions, but do not have strong influence on chemical WMD composition, except oxygen amount.

For laser welding there were observed much lower amount of oxygen (280 ppm) in WMD than in MIG welding with micro-jet cooling (380 ppm). Study shows that in standard MIG/MAG welding process (without micro-jet cooling) and in laser welding there were usually gettable higher amounts of another structure: MAC (self-tempered martensite, retained austenite, carbide) phases on the level of 4%. Acicular ferrite with percentage above 70% was gettable only in one case after MIG welding with argon micro-jet. The higher amount of MAC phases was especially gettable for more intensive laser welding and welding without micro-jet cooling. Various AF amount in tested cases corresponds with respectable various amount of oxygen in WMD. After that compared penetration and weld quality in tested cases. It was observed that quality is rather good in all cases, nevertheless penetration is perfect only during welding with micro-jet cooling. In the nearest future micro-jet cooling will be checked for laser welding process.

4. Summary and conclusions

In steel welding there is main type of test performed: metallographic structure. Acicular ferrite and MAC phases (self-tempered martensite, upper and lower bainite, retained austenite, carbides) were analyzed and counted for each weld metal deposit. This two methods (laser welding and MIG welding with micro-jet cooling) proved that micro-jet technology gives more beneficial properties of welds. The innovative micro-jet technology was firstly recognized with great success for thin sheet welding. On the basis of investigation it is possible to deduce that micro-jet technology could be important alternative for laser welding.

Final conclusions:

- a) micro-jet cooling could be treated as an important element of thin sheet welding process,
- b) micro-jet cooling after welding can prove amount of ferrite AF, the most beneficial phase in low alloy steel WMD,
- c) laser welding could give weld with comparable quality, but with lower amount of AF in weld metal deposit,
- d) laser welding corresponds with higher amount of not beneficial MAC phases in weld metal deposit in comparison with micro-jet process,
- e) laser welding process should be checked together with micro-jet process.

References

1. T. Węgrzyn (2011). Proposal of welding methods in terms of the amount of oxygen, *Archives of Materials Science and Engineering*, **47**, 1, 57–61.
2. T. Węgrzyn, J. Mirosławski, A. Silva, D. Pinto, M. Miros (2010). Oxide inclusions in steel welds of car body, *Materials Science Forum*, 6.
3. A.M. El-Batahgy (1997). Effect of laser welding parameters on fusion zone shape and solidification structure of austenitic stainless steels, *Materials letters*, **32**, 115–163.
4. J. Słania (2005). Influence of phase transformations in the temperature ranges of 1250–1000°C and 650–350°C on the ferrite content in austenitic welds made with T 23 12 LRM3 tubular electrode, *Archives of Metallurgy and Materials*, 3.
5. T. Węgrzyn, J. Piwnik, D. Hadryś, R. Wieszała (2011). Car body welding with micro-jet cooling, *Archives of Materials Science and Engineering*, **49**, 1.

A NEW VERSION OF HOPKINSON BAR TESTING STAND FOR DETERMINATION OF DYNAMIC TENSILE CHARACTERISTICS

T. Libura¹, W. Moćko^{1, 2}, Z.L. Kowalewski¹

¹Institute of Fundamental Technological Research, Warsaw, Poland

²Motor Transport Institute, Warsaw, Poland

1. Introduction

There is an increasing demand for determination of tensile characteristics of engineering materials under static and dynamic loading in order to assess an influence of the strain rate on their course. The paper presents a new testing stand for tensile characteristics determination under dynamic loading covering strain rate range up to 5000 1/s. This device was used to determine the stress-strain curves of the TRIP and DP steels. They have been determined for the materials in the as-received state as well as for the same materials after preloading due to fatigue.

2. Details of the testing stand

A construction of the testing stand was based on the technology proposed by G.H. Staab and A. Gilat [1]. The device (Fig. 1) consists of three independent mobile steel parts that are connected together in one rigid unit. There are 7 fences mounted on the device foundation. Thanks to them two 20 mm diameter rods (first stretching and second freely moving) made of 7075-T651 aluminum alloy may move freely, and assure simultaneously mutual alignment of them. A stretching specimen is fixed between the rod according to standard [2].

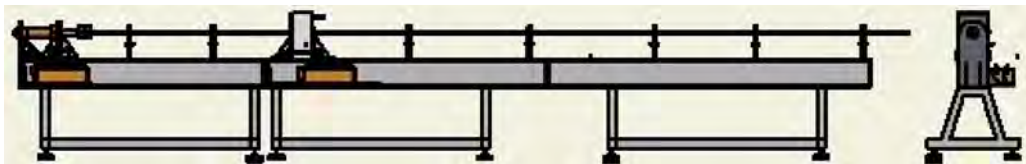


Fig. 1. A scheme of the testing stand for dynamic investigations of materials subjected to tensile loading.

The stretching rod has a length of 3.6 m, and its first tip is connected loosely to the piston of the hydraulic actuator, Fig. 2, which introduces a force giving tensile stress in the range of 20–30 kN. At a distance of 1.6 m from the hydraulic actuator there is a hydraulic lock (Fig. 3). It enables fixing of the stretching rod by clamping jaws before an introduction of the tensile force. A value of this force is measured by means of a special sensor synchronized with the hydraulic actuator. The freely moving rod with a length of 2.2 m, is embedded loosely in the teflon frames, and joined with the stretching rod through the fixed specimen. The whole unit is designed and constructed in such a way that enables to fit a special furnace of the temperature capacity up to 1000°. However, in such high temperature a special material for rods should be applied.



Fig. 2. A general view of the hydraulic actuator connection to the stretching rod.



Fig. 3. Hydraulic lock.

3. Results

Two kinds of steel, i.e. DP560 and TRIP690, were investigated in a wide range of strain rates ranged from 0.005 1/s to 2000 1/s. The results are presented in Fig. 4. The standard servo-hydraulic testing machine was used for tests under quasi-static loading conditions, while for the dynamic ones the Hopkinson bar testing stand was applied [3–5]. Both materials exhibited substantial sensitivity in to the level of strain rate. After analysis of the captured characteristics one can conclude that a stress responses in the plastic range increase with the strain rate increase. Also the elongation takes higher magnitudes.

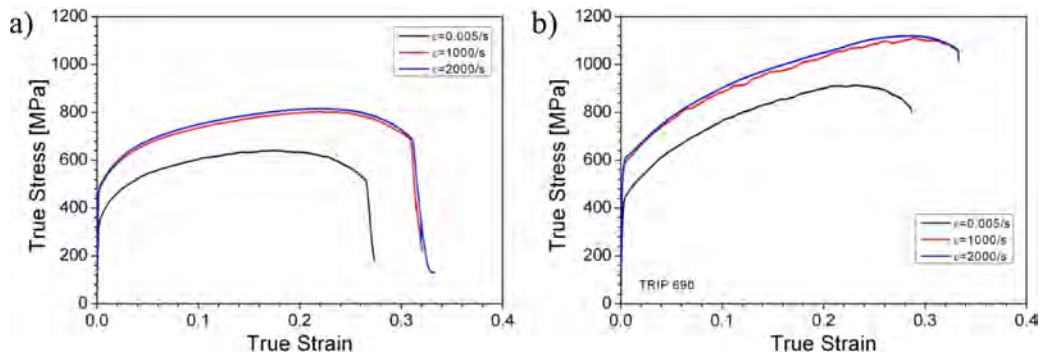


Fig. 4. Comparison of the tensile characteristics for a range of strain rates, the results for: a) DP 560 steel; b) TRIP 690 steel.

References

1. G.H. Staab, A. Gilat (1991). A Direct Tension SHB for high strain rate testing, *Exp. Mech.*, 232–235.
2. EN ISO 26203-1 (2010). *Metallic materials – Tensile testing at high Strain rates – Part 1: Elastic – Bar – Type Systems* (ISO 26203-1: 2010).
3. H. Kolsky (1949). An Investigation of the Mechanical Properties of Materials at Very High Rates of Loading, *Proc. Phys. Soc. London*, **62B**, 676.
4. U.S. Lindholm (1964). Some experiments with the Split Hopkinson Pressure Bar, *J. Mech. Phys. Solids*, **12**, 317–335.
5. W. Mocko, Z.L. Kowalewski (2011). Dynamic compression tests – current achievements and future development, *Eng. Trans.*, **59**, 235–248.

MECHANICAL LOW CYCLE FATIGUE (LCF) TEST AND ITS MODIFIED (MLCF) VERSION

M. Maj¹, A. Klasik², K. Pietrzak², D. Rudnik²

¹University of Science and Technology, Cracow, Poland

²Motor Transport Institute, Warsaw, Poland

1. Introduction

Cyclically varying stresses shorten the service life of structural components, since their destruction can occur under stresses much below the value of the static strength of a material [1]. There are many factors that directly may affect the number of cycles for failure. Up to now, the data for fatigue characteristics have been derived from the fatigue tests carried out in a high- or low-cycle regime (HCF and LCF, respectively) [2, 3]. The fatigue life of materials is very often evaluated on a basis of low-cycle fatigue test (LCF) [3–5]. Application of such conditions limits the number of cycles to failure of the specimen, and moreover the results of tests carried out on a single specimen correspond to single point of the curve reflecting the low-cycle fatigue strength. However, for both HCF and LCF testes, the measurements are more accurate, much more number of the specimens are necessary. Moreover, the LCF technique applicability is limited to materials that have good plastic properties, since usually the entire measuring range is substantially above the yield strength [3]. In this study, the fatigue life was examined using the own original modified low cycle test (referred here as MLCF), described in detail in [4].

2. Experimental procedures

The following test materials were used: 40H (41Cr4) steel and Al 6082 (AlSi1MgMn) alloy. The 40H (41Cr4) steel were quenched in oil at 850°C and tempered for 2 h at 450°C, while the Al 6082 alloy was heated according to T6 condition. Fatigue life analysis was performed using static tensile test (Instron 8874). A comparative study of the fatigue life of 40H (41Cr4) steel and Al 6082 alloy was carried out by both LCF method and its modified version (MLCF). In the stress-controlled MLCF method, specimens were subjected to tensile loading cycles. In the first step, a specimen was loaded with an extra load of $\sigma_{\min} = 10$ MPa in order to avoid its distortion. The research programme consisted of N_p “packages”, with stress amplitude increased in each successive “package”. Each “package” contained $N_c = 20$ tensile cycles of the same amplitude.

3. Results

A microstructure of the 40H steel (Fig. 1a) contained a highly tempered fine-grain martensite (formerly sorbite). A microstructure of the Al 6082 alloy consisted of a solid solution with fine precipitates of the α -Al (FeMn)Si phase.

The selected fatigue parameters obtained by LCF and MLCF methods are compared with the data given in literature in Table 1 for the 40H steel and Al 6082 alloy.

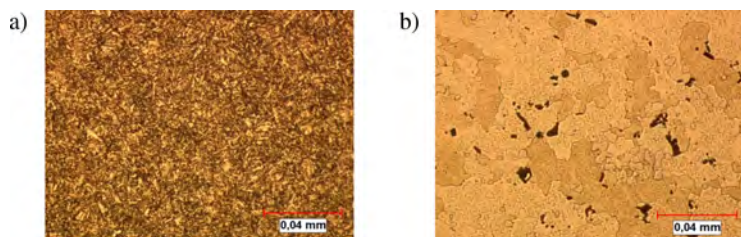


Fig. 1. The microstructure of: a) heat-treated 40H steel, b) Al 6082 alloy. Etched state magn. $500\times$.

Table 1. Selected fatigue parameters for 40H and Al 6082 alloy in comparison with the literature data.

Fatigue parameters	40H steel				Al 6082 alloy			
	Own results		Literature data		Own results		Literature data	
	LCF	MLCF	LCF [11]	MLCF [4]	LCF	MLCF	LCF [12]	MLCF [4]
b	-0.062	-0.062	-0.082	-0.07	-0.09241	-0.09306	-0.095	-0.08650
c	-0.866	-0.523	-0.791	-0.66	-0.8185	-0.79649	-0.690	-0.68818
K'	1 077	1 560	1 269	808	591	723	940	639
n'	0.043	0.129	0.137	0.017	0.13113	0.13006	0.110	0.02671

4. Concluding remarks

A good agreement was achieved between fatigue parameters coming from own research carried out using the common LCF test and its modified MLCF version and literature data. Application of the MLCF method can enable to obtain a set of several mechanical parameters, modulus of elasticity for different stress ranges eg. E_0 , E_{10} , E_{80} , E_{180} , the stress limits for selected offset strains ($R_{0.02}$, $R_{0.05}$, $R_{0.1}$, and $R_{0.2}$), ultimate tensile strength (UTS), fatigue strength at rotary bending (Z_{go}) and parameters of the low-cycle fatigue test (b , c , ε_{max}) on the basis of single measurement taken on a single specimen.

Acknowledgments

The research was carried out within the framework of the projects No N N507295440 financed by the Ministry of Science and Higher Education of Poland and No 6232/CBM/ITS financed by Motor Transport Institute.

References

1. Z.L Kowalewski (2011). 17th Seminary on Nondestructive Testing of Materials, Fatigue of materials – fundamentals, directions of investigations, damage assessments, Zakopane, Poland.
2. Z. Cheng-Cheng, Y. Wei-Xing (2011). An improved multiaxial high-cycle fatigue criterion based on critical plane approach, *Fatigue & Fracture of Engineering Materials & Structures*, **34**, 5, 337–344.
3. I. Brunner, D. Schwerdt, C. Berger, B. Pyttel (2012). Influence of defects on fatigue strength and failure mechanisms in the VHCF-region for quenched and tempered steel and modular cast iron, *International Journal of Fatigue*, **41**, 107–118.
4. M. Maj (2012). *Fatigue life of selected casting alloys*, Archives of Foundry Engineering, monography of Polish Academy of Sciences, Commission of Foundry Engineering.
5. A. Rutecka, Z.L. Kowalewski, K. Pietrzak, L. Dietrich, W. Rehm (2011). Creep and Low Cycle Fatigue Investigations of Light Aluminium Alloys for Engine Cylinder Heads, *Strain, International Journal of Experimental Mechanics*, **47**, s2, 374–381.
6. L. Blacha, A. Karolczuk, R. Bański, P. Stasiuk (2011). Eksperymental Study of Fatigue Life of Cruciform Welded Joints with Reference to Scale Effect, *Acta Mechanica et Automatica*, **5**, 3, 16–20.

NUMERICAL AND EXPERIMENTAL ANALYSIS OF A BRIDGE

J. Melcer

University of Žilina, Faculty of Civil Engineering, Žilina, Slovak Republic

1. Introduction

The problem of vehicle-bridge interaction can be followed in the literature from the year 1849. It was induced by the collapse of the Chester Rail Bridge in England in the year 1847, [1]. While the problem of dynamic of railway bridges was followed from the year 1847 the problems of dynamic of highway bridges start to be followed in the 20th century only. The 1st important report on this topic was published by the American Society of Civil Engineers [2]. Total review about results of solution to the year 1975 was published by Tseng Huang in [3]. Also in the Czech and Slovak Republic important works arose in this field. In the area of railway bridges they were published by Frýba [4] and in the area of highway bridges they were published by Melcer [5]. Numerical modeling of the vehicle motion along bridge structure requires paying attention minimally to these facts: creation of computing models of vehicles, creation of computing models of bridges, creation of computing programs for the solution of the equations of motion and displaying of obtained results. The Finite Element Method and Component Element Method are widely used. But classical computing models give very good results too.

2. Vehicle computing model

Vehicle computing model can be created on three qualitative different levels: 1D – quarter model, 2D – plane model and 3D – space model. For the purpose of this contribution the plane 2D model of a lorry was adopted, Fig. 1. It is discrete computing model with 8 degrees of freedom. The equations of motion are derived in the form of ordinary differential equations and they are solved numerically.

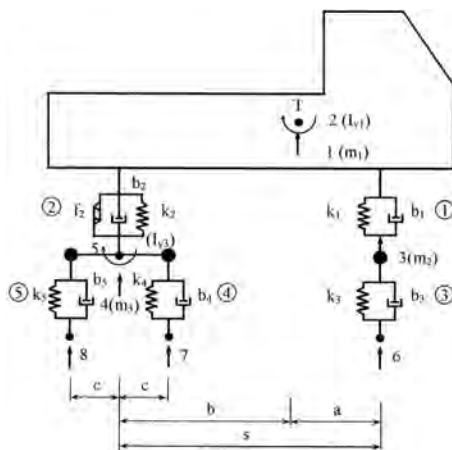


Fig. 1. Plane computing model of a lorry.

3. Bridge computing model

The computing model of the bridge was created as the simply supported Euler beam with uniformly distributed mass. The equation of motion is the 4th order partial differen-

tial equation. To avoid the solution of partial differential equation the assumption about the shape of dynamic deflection curve was adopted. It is assumed that the dynamic deflection curve is proportional to static deflection curve form vehicle in every time moment. On the basis of this assumption the partial differential equation is transformed on the ordinary differential equation for the coefficient of proportionality. This equation is solved numerically. The adopted assumption was experimentally tested on the beam model in laboratory conditions.

4. Road surface unevenness

Road surface unevenness represents the integral part of numerical modeling. It is the main source of kinematical excitation of vehicle. It was numerically simulated by the known power spectral density of unevenness for very good road profile, category B, ISO 8608.

5. Numerical modeling and experimental testing

Numerical modeling of vehicle motion along the bridge with various speeds was carried out in the environment of program system MATLAB. The Runge-Kutta step-by-step integration method was used for the solution of equations of motion. The experimental test on the so call Varin Bridge was carried out. It is single span bridge of the length 30 m. The dynamic deflection in the mid-span of the bridge was followed. The inductive sensors Bosch were applied. The signal from sensor was leaded by coaxial cable via analog digital interface into the computer and than it was operated by the program system Disys. The experimentally obtained results were compared with numerically obtained ones. As the example the mutual comparison of dynamic mid-span deflection obtained by numerical and experimental way at the speed of vehicle motion 14.23 km/h is plotted in the Fig. 2.

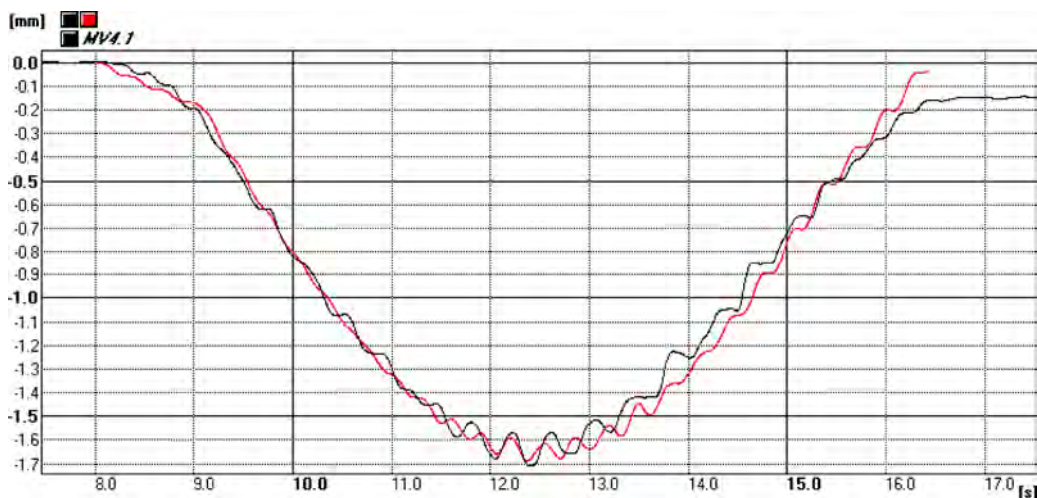


Fig. 2. Experimentally (back) and numerically (red) obtained results, speed 14.23 km/h.

References

1. R. Willis (1849). *Appendix, Report of the Commissioners Appointed to Inquire into the Application of Iron to Railway Structures*, Stationary Office, London.
2. *Impact on Highway Bridges* (1931). Final Report of the Special Committee on Highway. Bridges, *Transactions ASCE*, **95**, 1089–1117.
3. T. Huang (1976). Vibration of Bridges, *Shock and Vibration Digest*, **8**, 3, 61–76.
4. L. Frýba (1992). *Dynamics of railway bridges* (in Czech), ACADEMIA, Praha.
5. J. Melcer (1997). *Dynamic calculation of highway bridges* (in Slovak), EDIS, Žilinská Univerzita v Žiline.

FAILURE FREQUENCY OF STEAM PIPELINES – OPERATIONAL CONCLUSIONS

D. Mężyk

Institute of Power Engineering, Warsaw, Poland

1. Introduction

During long-term operation of power units, structural materials used in the power industry operate under variable stress field conditions and at variable temperatures. These materials are exposed to the impact of gaseous and liquid media as well as mechanical loads. These factors cause continuous changes in the microstructure of materials in their service life, which in result may deteriorate their mechanical properties. Cracking of welded joints and failures of shaped components of high temperature and pressure systems in power facilities result from increased stress values and concentrations.

2. Technical diagnosis

Special diagnostic care should be given to high pressure pipelines due to their unique character. High temperature – within a range of 540°C and pressure values up to 20 MPa causes that components of the system are not always able to transfer loads and pipelines may be damaged.

Interaction of the pipeline – turbine system is a major concern during operation of power equipment. The mechanism of such interaction of the aforementioned components has not been clearly defined. Considering the seriousness of this problem for the majority of domestic power plants and combined heat and power plants, diverse research is carried out in order to determine the interaction of mentioned components of power units.

Mechanical loads from the weight of a pipeline and fittings installed on this pipeline as well as from the limited movement of thermal expansion and from the quality of performance of a fixing system have an impact on the residual strength of pressure parts, except for stresses caused by internal pressure and by temperatures. Due to operational conditions and any related loads, the most important are the live steam pipelines, and mainly their shaped components (elbows, tees, four-way pieces, steam mixing valves, main gate valves).

Hot reheat pipelines operate at high temperatures but at much lower pressures. Safety valves are installed on hot reheat pipelines. This section of a pipeline operates in a periodic cycle, which causes sudden drops and rises in temperature resulting in low-cycle damage. Therefore, special care should be given to this section of the pipeline.

The test scope for cold reheat pipelines includes periodically operating pipelines, shaped components and drains. Other pipelines should be included in the material diagnostic program according to the applicable operation manual, and if any noticeable changes occur in the material or in the shape, the frequency of tests should be increased.

Land surveying under cold pipeline conditions and under conditions of full thermal load is essential for monitoring of spatial position of high pressure pipelines. Results of these measurements constitute a basis for determining the temperature stress distribution along the pipeline route, including in particular the shaped components.

Important features of the process station: “main steam pipelines”, are the fittings installed on the pipelines. The fittings are mainly located under the turbine but installed on the pipelines, and considered jointly with the pipelines.

The fittings include: quick-closing valves, main steam gate valves and by-pass gate valves of the main steam valves. Quick-closing valves are the essential components of the system because in emergency situations they cut off the steam flow to the turbine. Almost all the systems of the power unit protection, in the scope of heat, process and electricity control, may give a signal to immediately close the quick-closing valves and to cut off the steam flow to the turbine. These valves are hydraulically controlled and directly linked to the turbine control oil system. Since their full working order is essential for safe operation of the power unit, they should also be included in the diagnostic program.

Safe operation of the facility involves the service life parameter which may be included in the scope of generally defined residual strength.

Such long-term operation of pipeline components under creep conditions causes the material to deteriorate due to structural changes, which may result in reduction of the creep strength and in transfer of the transition temperature to the brittle condition to higher temperatures.

However, this does not have to cause such components to be replaced with the new ones. In most cases these components may operate significantly exceeding the design service life, which involves the presence of the residual service life.

3. Conclusion

During long-term operation of pipelines, despite all the diagnostic processes carried out in order to ensure failure-free operation of pipeline systems, emergency situations occur sometimes as a result of structural, operational and material causes. Testing aims at comprehensive evaluation of the material with the use of state-of-the-art test methods for early detection of any changes in the microstructure and strength properties of the material used in the production of tested critical components, and as a consequence for the evaluation of the degree of wear and for the forecast of the service life of power systems. Deterioration of strength properties of the material does not mean that the used components must be absolutely and explicitly replaced with new ones. In most cases these components may operate significantly exceeding the design service life, which involves the presence of the residual service life. The residual strength of critical points has the most significant impact on the safe and reliable operation of power facilities, which is inseparably linked with the correct diagnostic policy. Generally, the condition of individual components subject to the greatest operational loads, i.e. critical components, decides on the condition of pipelines. For high pressure pipelines these are the shaped components such as elbows, tees and four-way pieces. Areas of diameter and wall thickness changes, which can be observed at the meeting point of the pipeline and the tee, are also subject to great loads. These are the areas of stress concentrations that may cause cracking of welded joints. In the event of further long-term operation of the pipelines at present operational parameters, it should be considered to replace the most worn shaped components.

GEOMETRY OPTIMIZATION METHOD OF THE CORES OF THE ENERGY-ABSORBING PROTECTIVE PANELS

G. Mura

Department of Theoretical and Applied Mechanics
Silesian University of Technology, Gliwice, Poland

Key words: energy-absorbing protective panels, explosion.

1. Introduction

The aim of this work is to develop a model of an impact from shockwave which originates from a explosive material and affects the structure of a tracked vehicle, and then to work out a method to minimize the impact, by way of an optimum choice of the design features of energy-absorbing protective panels.

2. The essence of this work

The essence of this work consists in research based upon numerical simulations imitating shockwave impact from blasting block on both the energy-absorbing protective panels and the floor of special-purpose vehicles. The results of this research will form the input data to the subsequent research aimed at minimizing the explosion impact from e.g. mines on structure of the special-purpose vehicles through development of optimum design features of the energy absorbing panels.

This work presents a proposal of optimization method of the geometry of the cores of the energy-absorbing panels using the finite element method and genetic algorithm. The algorithm has been developed in the MATLAB software, but calculation of the impact of the explosion of explosive material on energy-absorbing panel, with the change of geometrical parameters on each iteration of the optimization, was performed in LS-Dyna.

Figures below shows numerical model of protective panels and example results of optimization of panels core geometry reached during this work.

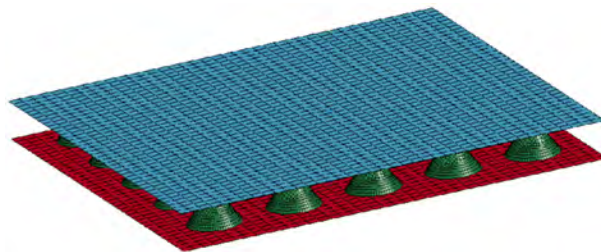


Fig. 1. Numerical model of protective panel prepared in LS-Dyna.

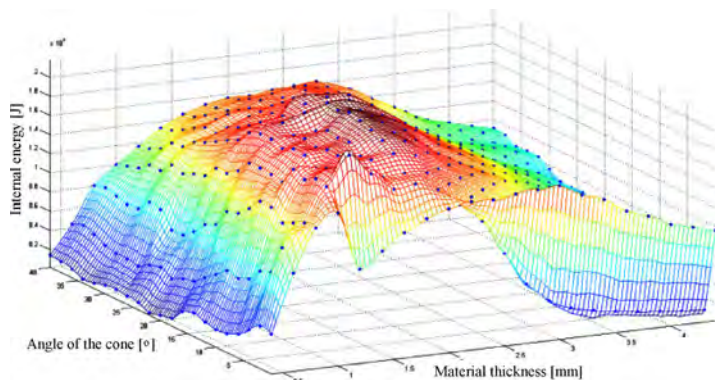


Fig. 2. Progress of the objective function of core of protective panels.

Acknowledgment

Work is realized under project no. 2011/01/N/ST8/04636.

References

1. Barnat W. (2010). *Wybrane problemy energochłonności nowych typów paneli ochronnych obciążonych falą wybuchu*, BEL Studio Sp. z o.o., Warszawa.
2. Rybak P. (2010). Protecting panels for special purpose vehicles, *Journal of Kones Powertrain and Transport*, **17**, 1, 357–364.
3. Barnat W. (2010). Dobór podstawowych parametrów warstwy dennej lekkiego pojazdu wojsk powietrzno desantowych, *Szybkobieżne Pojazdy Gąsienicowe*, **24**, 1, 79–89.
4. Babul W. (1980). *Odształcanie metali wybuchem*, WNT, Warszawa.
5. Panowicz R., Miedzińska D., Niezgoda T., Barnat W. (2011). Wstępne modelowanie oddziaływania fali ciśnienia na półsferyczny element kompozytowy o zmiennej grubości, *Mechanik*, **84**, 2, 142.
6. Larcher M. (2008). *Pressure-time functions for the description of air blast waves*, JRC Technical Notes, Ispra.
7. Baker W.E. (1973). *Explosions in the Air*, University of Texas Pr., Austin.

MECHANICAL PROPERTIES OF ALUMINUM COMPOSITES REINFORCED WITH Al_2O_3 PARTICLES AFTER MULTIPLE REMELTING

K. Pietrzak¹, A. Klasik¹, K. Makowska¹, J.J. Sobczak², D. Rudnik¹

¹Motor Transport Institute, Warsaw, Poland

²Foundry Research Institute, Cracow, Poland

1. Introduction

Nowadays in the case of many materials received for various practical applications the producing process is the one problem and utilization method of these materials is the second question has to be resolved. For many years the efforts are oriented on the production of composites included aluminium matrix composites. This fact results first of all from their attractive useful properties obtained for example due to the lower weight of composites compared to the steel or cast irons. In consequence there is research necessity of economically well-founded methods of their recycling. In general the necessity of the usage of several or at least two technological stages results from many theoretical-practical conditionings [1, 2]. This fact complicates the course of the recycling process as well as causes its cost increase. Instead earlier positive results of research were obtained by means of multiple repeated remelting of A359 matrix composites reinforced with SiC particles [3, 4]. In this research it was to decide to conduct the same multiple remelting method in the case of commercial A359 matrix composites but reinforced with Al_2O_3 particles.

2. Experimental procedures

Examined composites were subjected to 9-times repeated remelting of the original material as the simulation of the recycling process. In any time the gravity casts or squeeze-casts were got as ready tensile samples. In the case of squeeze-casting technique the liquid metal fills the mould cavity in laminar way, without the turbulence, and the effect of gas occlusion does not appear in the microstructure. In additional the high pressure under which the metal solidifies affects the better results compared to other casting methods. Composites received with both gravity casting and squeeze-casting methods were subjected to the tensile tests and microstructure examination.

3. Results

The strength properties were determined by means of tensile test versus the remelting number. The results after gravity casting and squeeze-casting are presented in Fig. 1a, b, respectively.

Microstructures of composites after the gravity casting and squeeze-casting are presented in Fig. 1a, b respectively. In the case of gravity casting the shrinkage porosity is observed (Fig. 2a) whereas after the squeeze-casting the porosity is not identified (Fig. 2b).

Determined mechanical properties confirm the efficiency of the proposed recycling method by means of directly multiple remelts of A359 matrix composite reinforced with Al_2O_3 particles. Simultaneously, in the case of squeeze-casting the mechanical properties are practically the same as in as received state (Fig. 1b). In opposite the successive decrease of mechanical properties is observed after the gravity remelts. For gravity castings the biggest differences are visible between the UTS values (Fig. 1a). This effect is connected with successive increase of shrinkage porosity versus remelts number.

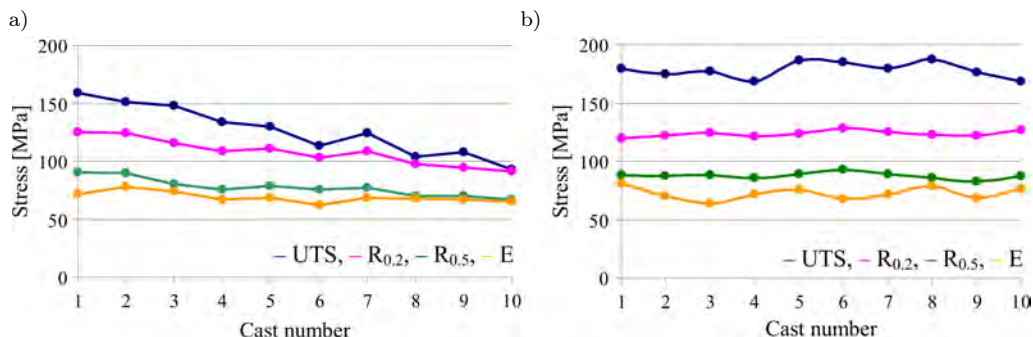


Fig. 1. Mechanical properties of A359 matrix composite reinforced with Al₂O₃ particles versus remelted number: a) gravity casting, b) squeeze-casting.

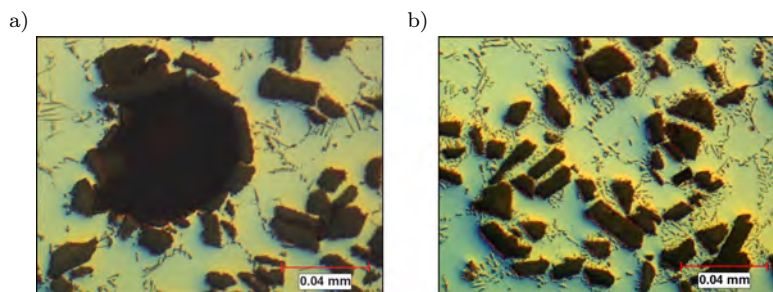


Fig. 2. Microstructure of A359 matrix composite reinforced with Al₂O₃ particles after the last remelt: a) gravity casting, b) squeeze-casting.

4. Concluding remarks

Based on the results it was ascertained that A359 matrix composite reinforced with Al₂O₃ particles could be subjected to the multiple remelting process. The better results were obtained for squeeze-casting because of lack of shrinkage porosity and in consequence the mechanical properties were on the same level as in as received state. Simultaneously it should be underlined that proposed method could be treated as economically well-founded alternative for other recycling methods. However, it is necessary to remember that this method requires the verification for any composite type separately.

Acknowledgments

The research was carried out in frame of the project no N N507 242740 with financial support from the Ministry of Science and Higher Education of Poland.

References

1. K.R. Ravi, R.m. Pillai, B.C. Pai, M. Chakraborty (2007). Separation of matrix alloy and reinforcement from aluminum metal matrix composites scrap by salt flux addition, *Bull. Mater. Sci.*, **30**, 4, 393–398.
2. M. Muzimoto, T. Oghai, A. Agawa (2009). Separation of PRMMC into matrix alloy and reinforcement by nozzle filtering method, *Journal of Material Processing Technology*, **209**, 9, 4264–4267.
3. A. Klasik, A. Wojciechowski, J. Sobczak, N. Sobczak (2008). Effect of multiple remelting on selected properties of dispersed reinforced aluminum matrix composite, *Journal of Kones*, **15**, 3, 233–238.
4. A. Klasik, J. Sobczak, K. Pietrzak, N. Sobczak, A. Wojciechowski (2012). *Influence of multiple remelting of particulate reinforced cast aluminum composites on their properties and structure*, Warsaw-Cracow, Poland.

SOFT ELASTOHYDRODYNAMIC LUBRICATION PROBLEMS IN THE FINITE DEFORMATION REGIME: EXPERIMENTAL TESTING AND MODELLING

P. Sadowski, S. Kucharski, J. Lengiewicz, S. Stupkiewicz

Institute of Fundamental Technological Research, Warsaw, Poland

1. Introduction

An increased interest in soft elastohydrodynamic lubrication (soft-EHL) problems is recently observed which is due to important applications in technology (elastomeric seals, tyres, etc.), but also because this lubrication regime occurs in many biotribological systems (e.g., synovial joints, human skin contact, etc.). In hydrodynamic lubrication, contact interaction occurs through a thin film of lubricant in which hydrodynamic pressure builds up when the lubricant is dynamically entrapped between the contacting surfaces. In the elastohydrodynamic lubrication regime, the hydrodynamic pressure is sufficiently high to significantly deform the contacting bodies, which introduces a strong coupling between the fluid flow and the elastic deflections of the contacting members. Finally, the characteristic feature of soft-EHL contacts is that the pressure is relatively low, but the elastohydrodynamic coupling is crucially important because one or both contacting bodies are soft.

When the contacting bodies are soft, relatively low contact pressures may lead to finite deformations of the contacting bodies. The corresponding effects have so far attracted little attention. In this work, the related effects are investigated experimentally and theoretically.

2. Experimental setup

A ball-on-disk setup, see Fig. 1, has been used to experimentally test friction in lubricated contact. The setup has been designed such that a rubber ball can be tested under the normal force that is high enough to result in finite deformations of the ball. The rotation speed, the normal force and the lubricant properties are controlled and the friction force is measured using a load cell.

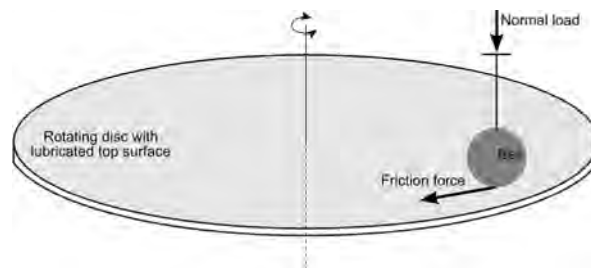


Fig. 1. Scheme of the ball-on-disk experimental setup.

3. Finite-element-based modelling approach

A general framework for the modelling of soft-EHL problems in the finite deformation regime has been developed by Stupkiewicz and Marcinişzyn [1, 2], and this framework is adopted in this work. The finite element model of an EHL problem involves the fluid

part, the solid part and the elastohydrodynamic coupling. The fluid part is conveniently modelled using the classical Reynolds equation. In the classical EHL theory, the solid part is usually modelled using the linear elasticity framework and an elastic half-space approximation. A distinct feature of the present approach is that the finite deformation effects are consistently treated.

The solid part is modelled using the finite element (FE) method so that an arbitrary (hyperelastic) material model and an arbitrary geometry can be analyzed. The Reynolds equation is formulated on the contact boundary of the solid and is discretized using the finite element method. The solid-fluid coupling (lubricant film thickness depends on the deformation) and the fluid-solid coupling (the hydrodynamic pressure and the shear stress are applied to the body as the surface traction) are fully accounted for. The Reynolds equation is formulated in an Eulerian frame which introduces an additional coupling due to the finite configuration changes.

The resulting nonlinear finite element equations are solved monolithically for all unknowns, i.e., displacements of the solid, lubricant pressures, and also other quantities, such as Lagrange multipliers, depending on the specific problem and specific formulation adopted. The nonlinear FE equations are consistently linearized so that the Newton method can be efficiently used. The model employs a recently developed mixed formulation of the mass-conserving cavitation model, see [3]. This formulation is particularly suitable for the specific mesh refinement technique used in the computational model. Mesh refinement is a crucial element of the finite element model because adequate description of the EHL coupling requires locally a very fine mesh. This is seen in Fig. 2a which shows the finite element mesh used to solve the problem of a hyperelastic ball sliding against a rigid surface in the hydrodynamic lubrication regime. Finite deformations of the ball are clearly seen in the Fig. 2b.

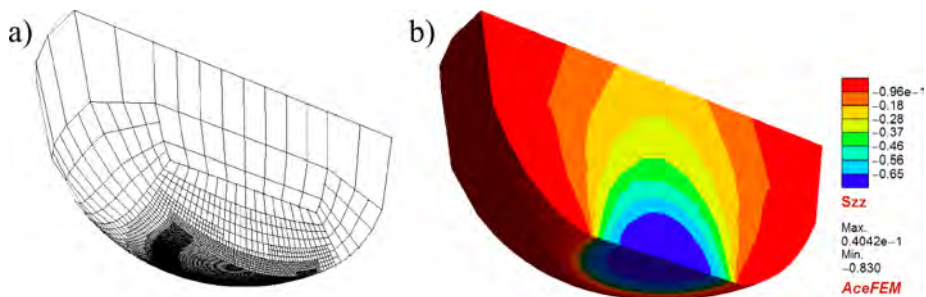


Fig. 2. Hyperelastic ball sliding against a rigid surface: a) undeformed mesh, b) distribution of σ_{zz} stresses (in MPa) in the deformed configuration [3].

References

1. S. Stupkiewicz, A. Marcinişzyn (2009). Elastohydrodynamic lubrication and finite configuration changes in reciprocating elastomeric seals, *Tribol. Int.*, **42**, 615–627.
2. S. Stupkiewicz (2009). Finite element treatment of soft elastohydrodynamic lubrication problems in the finite deformation regime, *Comp. Mech.*, **44**, 605–619.
3. J. Lengiewicz, M. Wichrowski, S. Stupkiewicz (2014). Mixed formulation and finite element treatment of the mass-conserving cavitation model, *Tribol. Int.*, **72**, 143–155.

AN EFFECT OF TECHNOLOGICAL NOTCHES ON STRESS AND STRAIN DISTRIBUTION DURING MONOTONIC TENSION

T. Szymczak¹, A. Brodecki¹, Z.L. Kowalewski^{1,2}

¹Motor Transport Institute, Warsaw, Poland

²Institute of Fundamental Technological Research, Warsaw, Poland

1. Introduction

It is widely known that the stress produced by various type of geometric discontinuities reduces material resistance. A level of such reduction depends on the loading type.

An influence of notches on material behaviour is usually determined either experimentally [1, 2, 6] or theoretically [3, 5]. The laboratory tests are very often focused on determination of details related to variations of stress-strain curve, fracture force, ultimate tensile strength and lifetime. An effect of hole diameter on the SMC-R50 composite behaviour under tension was investigated by Mallick [4]. He obtained strength decrease from 140 MPa to 60 MPa when the diameter increased three times. An opposite effect was achieved for the 2024 and 7075 aluminium alloys [6]. Bennett and Weinberg [1] tested the 248-T4 aluminium alloy under cyclic loading applying specimens with two various fillets. An effect of radius change from 1.6 mm to 0.6 mm was manifested by 50% lowering of the strength curve. Another experiments also confirmed a significant influence of notches on high cyclic fatigue life [2]. In order to extend knowledge concerning material behaviour due to geometrical discontinuities modern testing devices are necessary such as digital image correlation (DIC) systems for example.

The paper reports results from monotonic tension tests in which the DIC device was applied to measure a distribution of strain components.

2. Experimental procedure

The experimental procedure contained two stages: (a) determination of mechanical properties applying digital image correlation system; (b) examination of an influence of technological notch on the stress-strain curve variations.

The 40H steel widely applied by automotive and machinery branches of industry was selected for investigations. All tests were performed at room temperature, using servo-hydraulic testing machine and DIC measurement system (4M Aramis). The plane specimens of gauge length and thickness equal of 50 mm and 6 mm, respectively, were used. In order to validate axial strain measurements by the Aramis system the 2620 Instron extensometer was applied. Monotonic tension was conducted at constant displacement velocity equal to 0.5 mm/s.

3. Experimental results

The results validation process was performed on the basis of data comparison captured by extensometer and DIC system, Fig. 1. It enabled to distinguish only small differences in the last part of the tensile curve considered. Young's modulus values determined using testing methods were close i.e. 148 672 and 164 866 MPa for extensometer and DIC techniques, respectively.

An influence of technological notches on the steel properties under monotonic tension was investigated for two types of notch, i.e. 3×15 and 5×25 mm, Fig. 2. It was determined on the basis of the Mises strain evolution from the start (Fig. 2a) up to the end of test

(Fig. 2b) and as well as fracture and sub-zones localization (Fig. 2b). A field distribution of the Mises strain calculated on the basis of DIC system measurements was illustrated in Fig. 2a. The maximum values of the effective strain were detected in four zones of the groves edges. A strain increased with increasing tension force and achieved the critical value at zone where decohesion was observed, Fig. 2b. As it is indicated in Fig. 2b besides of the dominant fracture zone one can also notice a subzone, where deformation level is increased with respect to the other places of the specimen.

An effect of technological notch on the tensile characteristic can be evaluated on the basis of taking comparison of tensile characteristic (0) for specimen without artificial defects to stress-strain curves determined by the use of specimens with notches, Fig. 2c. As it is clearly seen both types of notch accelerated material yielding. In the case of notched specimen yield point was equal 350 MPa, what means that it was more than 200 MPa lower than for the standard specimen obtained. The differences between maximum stress from tests performed on the notched and unnotched specimens were almost negligible, less than 5%.

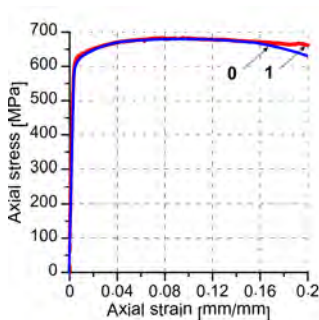


Fig. 1. Comparison of tensile characteristic determined by the use of extensometer (0) and 4M Aramis system (1).

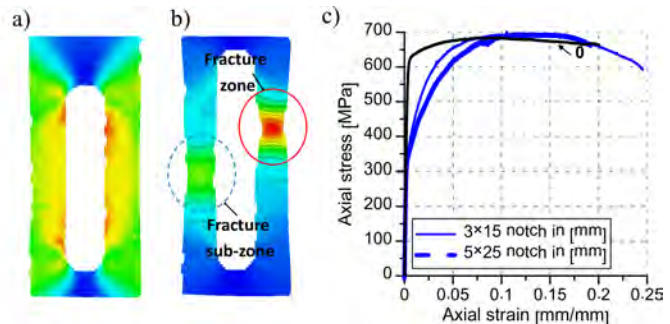


Fig. 2. The results of tensile tests: distribution of Mises's effective strain at the beginning (a) and the final stage of monotonic tension (b); comparison of stress-strain curves for specimens having two types of notch, i.e. 3×15 and 5×25 [mm] to the characteristic (0) captured for unnotched specimen (c).

4. Summary

The digital image correlation (DIC) system may be used to determine not only strain distribution but also to capture data necessary to calculate material mechanical properties e.g. Young's modulus, yield point or ultimate tensile strength. The DIC system allows to identify places of geometrical discontinuities. Although the results exhibited 67% decrease of the yield point due to the notch, the ultimate tensile strength remained almost the same for notched and unnotched specimens.

References

1. J.A. Bennett, J.G. Weinberg (1954). Fatigue notch sensitivity of some aluminium alloys, *Journal of Research of the National Bureau Standards*, **52**, 5, 235–245.
2. A. Fatemi, Z. Zeng, A. Plaseied (2004). Fatigue behavior and life predictions of notched specimens and of QT and forged microalloyed steels, *Int. J. Fatigue*, **24**, 663–672.
3. M. Fillipini (2000). Stress gradient calculations in notches, *Int. J. Fatigue*, **22**, 397–409.
4. P.K. Mallick (1988). Effect of hole stress concentration and its mitigation on the tensile strength of sheet moulding compound (SMC-R50) composites, *Composites*, **19**, 4, 283–287.
5. N. Noda, Y. Takase (2006). Stress concentration formula useful for all notch shape in a round (comparison between torsion, tension and bending), *Int. J. Fatigue*, **28**, 151–163.
6. R. E. Whaley (1962). Fatigue and static strength of notched and unnotched aluminium-alloy and steel, *Exp. Mech.*, **11**, 329–334.

EXPERIMENTAL ASSESSMENT OF BALL JOINTS OPERATION USING SERVO-HYDRAULIC TESTING SYSTEMS

T. Szymczak¹, A. Brodecki¹, A. Eminger¹, Z. L. Kowalewski²

¹Motor Transport Institute, Warsaw, Poland

²Institute of Fundamental Technological Research, Warsaw, Poland

1. Introduction

A progress in many branches of industry has spurred the elaboration and application of modern materials [2, 3]. This push is related to the current requirements concerning the lifetime extension of the responsible parts or elements of engineering constructions. For the automotive industry, ball joints are selected for modification by application of materials exhibiting better properties in comparison to the typical ones. Among these materials, the tungsten carbide (WC) is noteworthy [1]. Its melting temperature of around 2700°C, enables an operation at extreme environmental conditions. Moreover, the value of Young's modulus of this composite (around 690 GPa) is three times higher than that of typical steel. Although the ultimate tensile strength of the tungsten carbide is only equal to 530 MPa, its compressive strength is very impressive, i.e. it is almost thirteen times higher (around 6800 MPa). The producers' catalogue data [1] indicate that the WC composite is highly resistant to wear. Taking into account given advantages of the WC, one can conclude that it may be used as a thin layer to cover exploitation surfaces, and thus, protect base materials from temperature, reduce friction and non-typical loading effects.

The main aim of this paper was to check a possibility of using ball joints coated by the tungsten carbide under wear conditions.

2. Experimental procedure

All experiments were conducted using an anti-vibration platform with T slots and hydraulic servomotors. The typical ball joint (denoted as W11) and its modified version obtained by means of the tungsten carbide (WC) coating on the ball or/and cups surfaces were tested with or without application of the lubricant. The following configurations of the sliding pairs were considered, i.e.: W14 (WC-steel ball – polyamide cups with lubrication); W23 (WC-steel ball – polyamide cups) and W24 (WC-steel ball – WC-steel cups) – both without lubrication. These elements were mounted using a special gripping system, which enabled a load to be applied to the rocker arm. The loading conditions were defined based on realistic data. The amplitude reached 35 mm, and the frequency was equal to 2 Hz. Moreover, the following experimental stages were realized prior to the main test: (a) loading systems were designed and implemented; (b) software enabling identification of the effects due to the applied loading conditions was developed; (c) data acquisition system was implemented. A comparison of the experimental results obtained from the testing of modified and standard ball joints enabled an examination of the composite layer behaviour. It was evaluated on the basis of changes registered after every 500 cycles and elaborated in the form of diagrams of the force or temperature versus time, diameters, mass or roughness.

3. Results

Figure 1 illustrates some changes in the force as a function of time during the examination of the composite ball joint at the beginning (blue line) and final stage (green line) of the test. Important differences between both curves are especially visible for the compressive force. Comparison of the results achieved at the first and last cycle shows 25% reduction of the acting compressive force. Also, significant temperature variation can be observed over the entire test (Fig. 2). It increased linearly over a few initial cycles independently of the composite surface type and friction conditions. For the W14, W23 and W24 layers, an increase of temperature was equal to 60%. The smallest variations of temperature (less than 30%) were achieved for the typically lubricated surface, denoted as W11. Such a small increase of temperature reflects a stabilisation of the wear process. It was not observed for the other types of the WC composite layers.

An analysis of the weight variations of the composite coated ball exhibited its increase equal to 0.017 g, when the polyamide cups were applied. It was related to the wear product deposition. An opposite effect occurred when the WC coated steel cups were used. The weight reduction achieved a level of 0.19 g.

The results of the profilometric investigations (Fig. 3) showing irregular discontinuities in the WC layer enabled to take a conclusion that significant changes in the composite surface were observed when the WC-steel cups were used. Comparison to the roughness measured for the composite coated steel ball sliding on the polyamide cups in the received state and after cyclic loading history exhibited its reduction due to exploitation from 3.3 to 2.1 μm .

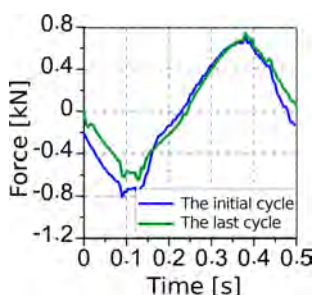


Fig. 1. Force versus time at the initial and final stage of test.

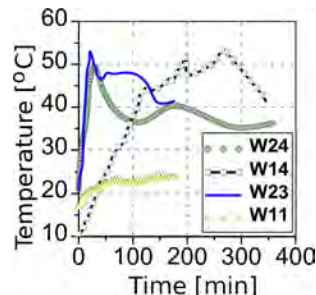


Fig. 2. Variations of temperature versus time for various sliding pairs.

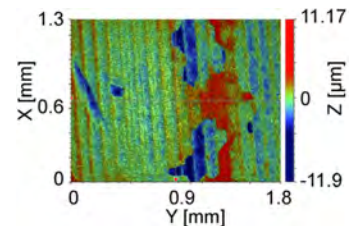


Fig. 3. A surface topography of the composite coated ball after test.

4. Conclusions

Profilometric investigations were used to examine a degree of homogeneity of the ball joint coated by the tungsten carbide layer. The composite coating on the sliding joints of the steel ball-steel cups type increased the wear coefficient. It was expressed by a reduction of the ball weight and appearance of the metallic powder. A magnitude of the ball mass reduction was dependent on the wear conditions, i.e. sliding of the joint elements with or without of the lubricant.

References

1. *The designer's Guide to Tungsten Carbide* (2009). General Carbide Corporation, 60 pages.
2. L.A. DOBRZAŃSKI, A. KLOC-PTASZNA, A. DYBOWSKA, G. MATULA, E. GORDO, J.M. TORRALBA (2007). Effect of WC concentration on structure and properties of the gradient tool materials, *Archives of Metallurgy and Materials*, **20**, 1–2.
3. T. MOSKALEWICZ, B. WENDLER, S. ZIMOWSKI, B. DUBIEL, A. CZYRSKA-FILIMONOWICZ (2010). Microstructure, micro-mechanical and tribological properties of the nc-WC/a-c nanocomposite coating magnetron sputtered on non-hardened and oxygen hardened Ti-6Al-4V alloy, *Surface & Coatings Technology*, **205**, 268–277.

DEGRADATION OF MATERIAL PROPERTIES DUE TO EVOLUTION OF RADIATION INDUCED DAMAGE

A. Ustrzycka, B. Skoczeń

Institute of Applied Mechanics, Cracow University of Technology, Poland

1. General

The problem undertaken in the present work concerns the kinetics of evolution of radiation induced damage under mechanical loads. Furthermore, coupling between the radiation induced nano-damage and the mechanically induced micro-damage is taken into account. During irradiation, energetic particles penetrating a solid displace the lattice atoms from their original positions. Exposure to a flux of particles leads inevitably to creation of clusters of defects in the material, provided that the energy of incident particles is large enough. Collisions of particles of enhanced energy with the lattice atoms ejects the atoms from their initial position and transfers the energy to the next collisions with the neighboring atoms. These atomic interactions lead to creation of the cascade of atoms moving inside lattice and to production of radiation induced defects in the lattice. Thus, as a result of the cascade process, the pairs of interstitial atoms and vacancies (the so-called Frenkel pairs) are created [3]. The evolution of radiation induced damage is combined with the evolution of classical mechanically induced damage within the common framework of Continuum Damage Mechanics (CDM). An additive formulation with respect to damage parameters or tensors has been used. A multiscale constitutive model comprising the evolution of radiation induced damage under mechanical loads has been formulated [1]. Two kinetic laws of damage evolution were taken into account: the Rice and Tracey model and the Gurson model. Both of them address the evolution of porosity in the form of spherical or ellipsoidal voids in a different way. The Rice & Tracey model predicts the evolution of radius of spherical void as a function of triaxiality ($3\sigma_m/2\sigma_{eq}$) and the equivalent plastic strain dp . The Rice & Tracey model [5] is expressed in the form of differential equation:

$$(1) \quad dr_c = r_c \alpha_r \exp\left(\frac{3\sigma_m}{2\sigma_{eq}}\right) dp.$$

Thus, in order to obtain the radius increment dr_c a differential equation has to be solved and the current radius can be updated. In order to compute the damage parameter, the volume or the surface density of voids has additionally to be known. On the other hand, the Gurson model [2] is based on the definition of the porosity parameter ξ :

$$(2) \quad \dot{\xi} = (1 - \xi)\dot{\varepsilon}_{kk}^p,$$

where $\dot{\varepsilon}_{kk}^p$ denotes trace of the plastic strain rate tensor. The porosity parameter can be directly recalculated to obtain the classical damage parameter in the sense of CDM. Here, a simple differential equation has also to be solved in order to obtain the porosity increment. Both Rice & Tracey and Gurson kinetics may conveniently be applied to describe the evolution of radiation induced damage in the form of clusters of voids embedded in the metallic matrix [4, 6]. As an application, estimation of lifetime of coaxial target embedded in a particle detector configuration, subjected to combination of irradiation and mechanical loads, has been carried out (Fig. 1).

The shell is subjected to pulsed irradiation by the flux of secondary particles generated by solid target located coaxially and hit periodically by high energy particles beam.

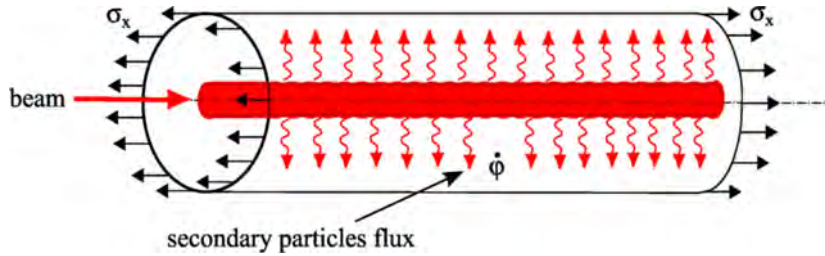


Fig. 1. Coaxial target – detector configuration (round bar and cylindrical shell).

In addition, the shell is subjected to cyclic mechanical loads which leads to build-up of cyclic stress state containing localization. Combined radiation and mechanical loads lead to evolution of both damage components as a function of the number of cycles (time). The lifetime prediction has been expressed in terms of number of beam cycles as a function of maximum dpa (displacement per atom) on cycle [7]. New closed form analytical solutions for the problem of periodic irradiation combined with cyclic axial load, and corresponding to Rice & Tracey and Gurson models were obtained.

References

1. C. Garion, B. Skoczen (2003). Combined model of strain-induced phase transformation and orthotropic damage in ductile materials at cryogenic temperatures, *Int. J. Damage Mech.*, **12**, 331–356.
2. A.L. Gurson (1977). Continuum theory of ductile rupture, by void nucleation and growth: part I—yield criteria and flow rules for porous ductile media, *ASME J. Eng. Mater. Technol.*, **99**, 2–15.
3. D. Li, H.X. Sun, M. Khaleel (2013). Predicting plastic flow and irradiation hardening of iron single crystal with mechanism-based continuum dislocation dynamics, *International Journal of Plasticity*, <http://dx.doi.org/10.1016/j.ijplas.2013.01.015>.
4. K. Nahshon, J.W. Hutchinson (2008). Modification of the Gurson model for shear failure, *Eur. J. Mech. A/Solids*, **27**, 1–17.
5. J.R. Rice, D.A.I. Tracey (1969). On the ductile enlargement of voids in triaxial stress fields, *J. Mech. Phys. Solids*, **17**, 201–217.
6. V. Tvergaard (2012). Effect of stress-state and spacing on voids in a shear-field, *International Journal of Solids and Structures*, **49**, 3047–3054.
7. E. Verbiest, H. Pattyn (1982). Study of radiation damage in aluminum, *Physical Review B*, **25**, 8, 5097–5121.

Authors Index

- Adamowicz A., 77
Adamski M., 73
Akinci Y., 151
Alexopoulos N.D., 37, 117, 129, 141, 145, 195
Altenbach H., 17
Antoš J., 83
Arias A., 109
Augustyniak B., 119
- Bajkowski A., 63
Baklanov V., 293
Bednarek T., 237
Belova I.V., 265
Biborski A., 265
Biczuk J., 111
Bobra P., 105
Bonarski J., 295
Brodecki A., 325, 327
Burczyński T., 189
Burzyński S., 217
Busarac N., 255
- Cadoni E., 127
Celik O.C., 151
Chinchaladze N., 219
Chmielewski M., 119
Chróścielewski J., 217
Chudzicka-Adamczak M., 65
Cristea M., 259, 267
Cohen T., 29
- Dakanali I., 121
Dębski D., 33
Dietrich L., 169
Dietzel W., 145
Dłużewski P., 35
Domagalski Ł., 101
Drzymała P., 295
Dunić V., 255
Dvorak T., 199
- Eberhardsteiner J., 19
Egner H., 67, 69, 71
Egner W., 67
Eminger A., 327
Eremeyev V.A., 17
Evtcev A.V., 265
Exadaktylos G.E., 299
- Favvas E.P., 195
Fenu L., 127
Fernández-Sáez J., 29, 91
Fialko S., 221
Fiborek P., 153
Frydrych K., 207
- Fujita G., 287
Fukalov A.A., 185
Füssl J., 19
- Ganczarski A., 73
Garbowski T., 179, 281
Gialos A., 37
Gohnert M., 223
Goodarzi A., 103
Gorodilov R.S., 203
Grosman F., 45, 47
Grzywna P., 167, 307
Gulua B., 225
Guminiak M., 157
Gupta N.K., 21
- Hashemian B., 103
Hayashi S., 267
Hernik S., 191
Hénap G., 39
Hloupis G., 121, 125
Hoffmann T.J., 65
Holnicki-Szulc J., 229
Hołobut P., 209
- Ikedo T., 257
Isaev O.Yu., 289
- Janiszewski J., 123
Jarzębski P., 227
Jelenić G., 241
Jędrysiak J., 101
Jóźwiak-Niedźwiedzka D., 199
- Kabele P., 89
Kaczyński A., 155
Kačianauskas R., 175
Kandler G., 19
Karavaev D.M., 289
Karyakin M., N., 75
Kashaev N., 37
Keršner Z., 51
Khanov A.M., 289
Klasik A., 297, 313, 321
Kłosowski P., 81
Knitter-Piątkowska A., 157
Knor G., 229
Kochanowski K., 77
Kochurov V.I., 203
Kokot S., 105
Koksharov V.S., 289
Kolesnikov A.M., 231
Kolomiets A.V., 159
Kołakowski Z., 193
Konopińska V., 233

- Kosiński W., 77
Kotelko M., 279
Kourkoulis S.K., 117, 125, 129, 141, 145, 173, 235, 299, 303
Kowalczyk P., 237
Kowalczyk-Gajewska K., 207, 259, 267
Kowalewski Z.L., 131, 143, 307, 311, 325, 327
Kowal-Michalska K., 193
Kozień M.S., 305
Kozubski R., 265
Kruszka L., 127
Kucharski S., 269, 323
Kudela S. Jr., 199
Kukla D., 307
Kukudzhanov C.V., 159
Kulak P., 309
Kulchytsky-Zhyhailo R., 63
Kulczynska M., 93
Kursa M., 209
Kutergin A.V., 185
Kyriazopoulos A., 121
- Landkammer P., 41
Lasota R., 237
Läufer J., 247
Lehký D., 51
Lengiewicz J., 43, 209, 323
Levchenko E.V., 265
Levintant-Zayonts N., 269
Libura T., 311
Lis P., 279
Lukacevic M., 19
Lumelsky D., 45, 47, 237
Lymperaki E., 141
Lymperta P., 129
- Maciakowski P., 119
Macios A., 209
Macur J., 51
Maj M., 137, 259, 267, 313
Majewski M., 259
Makowska K., 131, 297, 321
Marczewska I., 175
Markides Ch.F., 235
Markiewicz I., 133
Matsui R., 261, 269, 271
Matsuura K., 285
Maździarz M., 35
McArthur D.R., 79
Meguid S.A., 23
Mejak G., 161
Melcer J., 315
Mercader C., 195
Marek A., 281
Metaxa Z.S., 195
Mężyk D., 317
Michalak B., 249
Migliarini A., 165
- Mikułowski G., 111
Misztańska E., 55
Mleczek A., 81
Moćko W., 127, 163, 311
Moutzouris K., 125
Mrozek A., 189
Mróz Z., 283
Mura G., 319
Murch G.E., 265
- Nalepka K., 25
Nežerka V., 83
Nowak M., 47
Nowak Z., 47
- Oboudi M., 177
Ohno M., 285
Ohtsuki A., 135
Oliferuk W., 77, 137
Ortwein R., 85
Osovski S., 29
- Pamin J., 97
Papanikos P., 197
Paris T., 165
Pasiou E.D., 125, 303
Pawełek A., 199
Pączelt I., 283
Pesci R., 29
Pęcherski R.B., 25, 45, 47
Pieczyńska E.A., 255, 259, 263, 267, 271
Pietraszkiewicz W., 233
Pietruszczak S., 177
Pietrzak K., 297, 313, 321
Pietrzyk M., 285
Piotrowski L., 119
Pisarski D., 107
Piwnik J., 309
Poulin P., 117, 129
Poulin F., 195
Pozdnyakov I., 75
Pożarycki A., 179
Pruchnicki E., 239
- Rabenda M., 249
Ranachowski P., 199
Ranachowski Z., 199, 295
Ribarić D., 241
Riekehr S., 37
Rittel D., 29
Rodríguez-Martínez J.A., 29, 109
Rojek J., 45, 47, 175, 237
Romanowicz M., 49
Rudnik D., 297, 313, 321
Rusinek A., 29
Rutecka A., 167
Ryś M., 69, 71

- Sadowski P., 43, 139, 323
Schmauder S., 211
Sekula K., 111
Shimizu S., 287
Shodja H.M., 103
Shubchinskaya N., 75
Sieteski D., 309
Skoczeń B., 53, 85, 87, 329
Slavković R., 255
Slavković V., 255
Smirnov D.V., 289
Smolarski D., 305
Sobczak J.J., 321
Sobczak N., 297
Socha G., 169
Sokolkin Yu.V., 185
Somr M., 89
Sowa P., 265
Staroszczyk R., 181
Staszczak M., 259, 267
Stavrakas I., 121, 125
Stefanou G., 141
Steinmann P., 41
Stocki R., 237
Stupkiewicz S., 43, 139, 207, 323
Sudak L.J., 79
Sulich P., 67
Sumelka W., 91
Sun Q., 275
Svanadze M., 201
Szabó L., 39
Szeliga D., 285
Szymczak T., 143, 325, 327

Šimonová H., 51

Tabin J., 53
Takeda K., 269, 271
Takenouchi R., 261
Tanaka N., 287
Taufowski P., 35, 237
Tesárek P., 83

Tkocz M., 45, 47
Tobushi H., 259, 267, 269, 271
Tokunaga T., 285
Tomczyk B., 243
Tóth B., 245
Triantis D., 121, 125
Turska E., 27

Ueda T., 287
Uscilowska A., 93
Ustrzycka A., 329

Vadillo G., 29
Vaz-Romero A., 109
Velonaki Z., 141, 145
Veselý V., 51

Wagner W., 247
Wawrzyk K., 237
Wcisło B., 97
Węgrzyn T., 309
Widłaszewski J., 147
Wirowski A., 249
Witkowski W., 217
Więckowski Z., 55, 183
Wiszowaty R., 111
Wiśniewski K., 27, 227
Wszolek Ł., 309

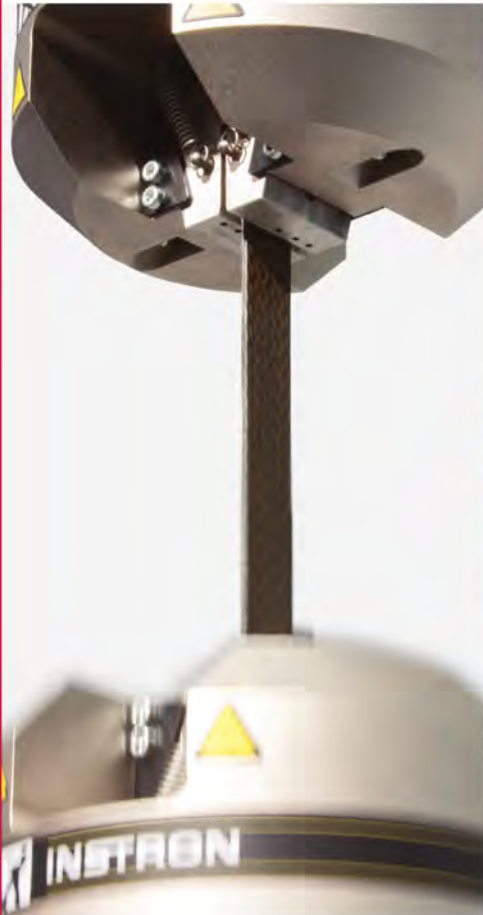
Xia M., 275

Zaera R., 29, 91
Zaitsev A.V., 185, 289
Zeimpekis V., 37
Zeman J., 83
Zembaty Z., 105
Zmitrowicz A., 213
Zubko I.Yu., 203, 289

Żach P., 33
Żmuda-Trzebiatowski Ł., 251

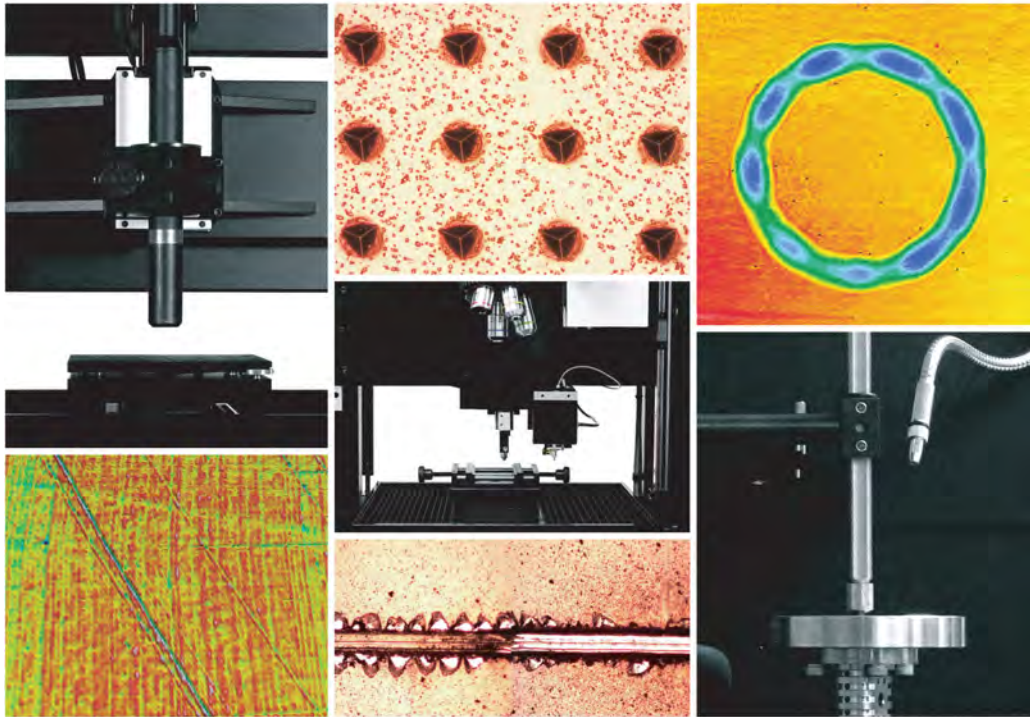
Instron®'s latest composites testing solutions enhance the scope, quality, and efficiency of your tests.

When Composite Performance is Critical... TRUST Instron



The difference is measurable®

Spectro-Lab, ul. Warszawska 100, 05-092 Lomianki, Poland | Tel: +48 675 25 67 | www.instron.pl



Nanovea began designing and manufacturing instruments after years of experience in providing solutions for profilometry, mechanical and tribology applications. Firmly aligned with its vision, Nanovea aims to simplify advanced measurement technology to stimulate materials engineering for the common good. Ease of use, advanced automation and the dedication to superior accuracy are the driving forces behind the design and manufacturing of its full range of Optical Profilometers, Mechanical Testers and Tribometers. Unlike other manufacturers, Nanovea also provides Laboratory & consulting services. Thus, clients are given access to years of experience in finding solutions to improve quality control and materials development. Nanovea offers many critically important tests including surface roughness, nanoindentation, scratch and wear testing among many others. Nanovea's instruments can be found internationally in distinguished educational and industrial organizations ranging from automotive to cosmetic, biotechnology to medical devices to microelectronics and space applications. Thousands of clients rely on Nanovea for accurate solutions, technically superior instruments, experienced assistance and comprehensive laboratory services.



EXPERTISE ACROSS THE SPECTRUM



A COMPLETE PORTFOLIO OF SOLUTIONS FOR YOUR EVOLVING NEEDS

Engineers and researchers worldwide rely on MTS for the testing expertise, technology and support required to pursue research and advanced development.

MTS offers solutions for a full spectrum of materials testing needs - from simple tension/compression to fracture mechanics to complex multi-axial fatigue.

Contact MTS today and explore how MTS solutions can help you adapt to evolving materials testing requirements.

www.mts.com
info@mts.com

MTS MATERIALS SOLUTIONS

be certain.